Transactions of the ASME®

Journal of Heat Transfer

Published Quarterly by The American Society of Mechanical Engineers

VOLUME 119 • NUMBER 4 • NOVEMBER 1997

Transactions of the ASME, Journal of Heat Transfer (ISSN 0022-1481) is published quarterly (Feb., May, Aug., Nov.) for $220.00 per year by The American Society of Mechanical Engineers, 345 East 47th Street, New York, NY 10017. Periodicals postage paid at New York, NY and additional mailing offices. POSTMASTER: Send address changes to Transactions of the ASME, Journal of Heat Transfer, c/o THE AMERICAN SOCIETY OF MECHANICAL ENGINEERS, 22 Law Drive, Box 2300, Fairfield, NJ 07007-2300.
CHANGES OF ADDRESS must be received at Society headquarters seven weeks before they are to be effective. Please send old label and new address. **PRICES:** To members, $40.00, annually: to nonmembers, $220.00. Add $40.00 for postage to countries outside the United States and Canada.

INDEXED by Applied Mechanics Reviews and Engineering Information, Inc. Canadian Goods & Services Tax Registration #126148048.

TECHNICAL PAPERS

(Contents continued on Outside Back Cover)

(Contents continued)

The Effect of Imprecisions in Thermal Sensor Location and Boundary Conditions on Optimal Sensor Location and Experimental Accuracy

A. F. Emery
emery@u.washington.edu

T. D. Fadale
Department of Mechanical Engineering,
University of Washington,
Seattle, WA 98195-2600

Optimal sensor locations and the information content obtained when estimating thermal parameters using the inverse method are significantly affected by uncertainties in sensor position and in the system parameters. This paper describes the effects of these uncertainties. It is shown that the effect of sensor location uncertainties can be reduced by placing temperature sensors in locations of minimum heat flux. In transient experiments, the uncertainties in the boundary conditions have the greatest effect at points of high heat flux and cause the optimal sensor locations to move from the boundary with the highest convective heat transfer coefficient to the boundary with the lowest in an abrupt manner.

Introduction

Almost all predictions and simulations of thermal systems require the specification of properties, boundary conditions, and other relevant parameters associated with the model of the system.[1] These are usually determined by specially designed experiments. For example, guarded hot box experiments are used to determine the thermal conductivity by measuring the temperature difference across a layer through which a known heat flux is conducted and applying Fourier's law directly. Other times, the measured quantities cannot be directly used and the theory of inverse problems must be employed. In this method a number of measured responses are compared with an analytical or numerical solution to estimate the desired properties. For example, if the temperature response of an infinite conductivity sample is measured, the surface heat transfer coefficient may be estimated through matching the results of the differential equation

$$\rho c V \frac{\partial T}{\partial t} = h(t)A(T_\infty - T) = Q(t) \tag{1}$$

with the temperatures measured over time by assuming values of $h(t)$. This is normally done by using a least squares approach in which the value of $h(t)$ is that which minimizes the sum of the squares of the difference between the measured temperatures, $T_m(t_k)$, and the predicted temperatures, $\Phi(t_k)$. As is well known, this is an ill conditioned problem and special mathematical techniques, such as regularization, must be employed (Alifanov 1994; Beck and Arnold 1977).

In previous papers (Emery and Fadale, 1996; Fadale, et al., 1995a), we have discussed how to optimize the design of an experiment to determine one or more parameters by choosing optimal sensor locations, sampling times, duration of the experiment, and the variables to be measured. By "optimizing" we mean minimizing the uncertainty in the sought-after quantity. This is most easily done by appealing to the work of Fisher (Helstrom, 1995; Linnik, 1961; Strang, 1986), who pointed out that the information content of a signal used to estimate properties or parameters, $\mathbf{u}$, could be expressed in terms of the Fisher Information matrix, $\mathbf{M}$

$$\mathbf{M} = E\left[\left(\frac{\partial \ln f(\Psi|\mathbf{u})}{\partial \mathbf{u}}\right)\left(\frac{\partial \ln f(\Psi|\mathbf{u})}{\partial \mathbf{u}}\right)^T\right] \tag{2}$$

where $f(\Psi|\mathbf{u})$ is the conditional probability distribution function, Ψ is the difference between the measured and predicted responses, and $\mathbf{u}$ is the vector of sought-after parameters. The theorem of Cramer-Rao states that the estimation error has a lower bound of $\mathbf{M}^{-1}$. The predicted response is a function of both the sought-after parameters and others which are assumed to be known. In its usual form, $\mathbf{M}$, does not admit the consideration of uncertainties in these "known" parameters. For example, the fluid temperature and the mass of the infinite conductivity sample are usually assumed to be known exactly.

Fadale et al. (1995b) have presented a theory which accounts for such uncertainties. In this extended theory, the components of $\mathbf{M}$ are given by

$$M_{lm} = \sum_{k=1}^{K}\left[\left(\frac{\partial \Phi_k}{\partial u_m}\right)^T V_k^{-1}\left(\frac{\partial \Phi_k}{\partial u_l}\right) + \frac{1}{2}\,\mathrm{tr}\left[V_k^{-1}\frac{\partial V_k}{\partial u_l}V_k^{-1}\frac{\partial V_k}{\partial u_m}\right]\right] \tag{3}$$

where Φ is the predicted response and the extended covariance matrix $\mathbf{V}_k$ is defined as

$$\mathbf{V}_k = E[\{\Phi_k - E(\Phi_k)\}\{\Phi_k - E(\Phi_k)\}^T] = \mathbf{S}_k + \mathbf{\Theta}_k\mathbf{G}\mathbf{\Theta}_k^T \tag{4}$$

where $\mathbf{S}_k$ is the usual covariance matrix of the measurement noise, $\mathbf{\Theta}$ is the matrix of sensitivity of the predicted temperature Φ to the "known" parameters, $\mathbf{b}$, which are presumed to have some uncertainty, and $\mathbf{G}$ is the covariance matrix of the uncertainties in $\mathbf{b}$.

[1] Although the concepts described in this paper are applicable to all systems, we treat only the estimation of thermal properties by measurements of temperature or heat flux.

Contributed by the Heat Transfer Division for publication in the JOURNAL OF HEAT TRANSFER. Manuscript received by the Heat Transfer Division September 3, 1996; revision received May 12, 1997; Keywords: Measurement Techniques; Modeling & Scaling; Transient & Unsteady Heat Transfer. Associate Technical Editor: T. L. Bergman.

The optimal protocol consists of choosing the sensor locations, x_i, y_i, z_i, the sampling times, t_k, and the duration of the experiment to minimize the uncertainty as characterized by $\mathbf{M}^{-1}$. This clearly depends upon the interaction between the measurement noise, $\mathbf{S}_k$, and the sensitivity of the system to these "known" parameters, $\Theta = \partial\Phi/\partial b$. When the "known" parameters have some uncertainty, this effect can be accounted for (at least to the first order) by including their covariance $\mathbf{G}$, as indicated in Eq. 4.

The different experiments that we have examined thus far (Emery and Fadale, 1996; Fadale, et al., 1995a, 1995b) have had only one "known" parameter with uncertainty, either the prescribed boundary temperature, heat flux, or convective heat transfer coefficient. In addition, we have assumed that it is possible to locate the sensor precisely (or equivalently, that the sensor measures the temperature at an exact location). In this paper, we wish to examine the effect of measuring the temperature using a sensor which is either positioned with some uncertainty or measures the temperature over a small but finite range of x. We also wish to examine what happens when two different, but interacting, boundary parameters are assumed to possess uncertainty.

New Results

Before discussing these new results, it is instructive to look at Eq. 3 for a simple case. Consider when there is only one sensor and one parameter to be estimated. In all of the thermal problems studied to date, when only one parameter is to be estimated the trace term has contributed negligibly to $\mathbf{M}$ (why this is so is currently not clear, but is related to the complex behavior of V_k). Neglecting the trace term and assuming that there is only one uncertain "known" parameter b, we may write

$$(\sigma^2(u)/u^2)^{-1} \le M = \sum_{k=1}^{K} \left(\frac{\left(\frac{\partial \Phi_k}{\partial u}\right)^2}{S_k + \left(\frac{\partial \Phi_k}{\partial b}\right)^2 G} \right). \quad (5)$$

The variance of u is inversely proportional to the sensitivity of the measurement to u, $\partial\Phi/\partial u$, and proportional to the sensitivity to b, $\partial\Phi/\partial b$. Thus, the variance of u will be minimized if the sensor is placed at the point of maximum sensitivity to the sought-after parameter u and the point of minimum sensitivity to the "known" parameter b. Unfortunately, these two points are rarely the same, and the optimal location is a competition between these two effects. Since both sensitivities vary with time and boundary conditions, the optimal sensor location for any given experiment changes with time and differs substantially for different experiments and with the relative importance of S_k and G.

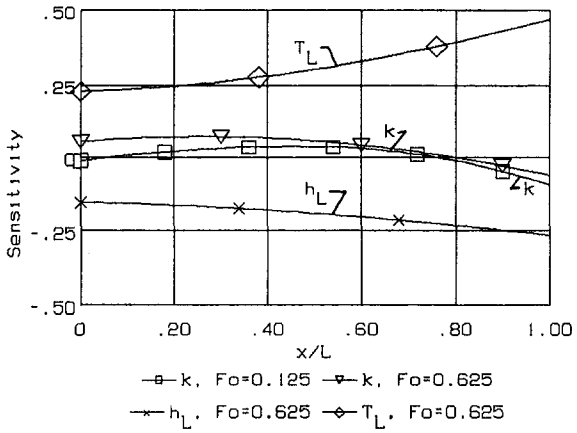

Fig. 1 Sensitivity of temperature to k, h_L and T_L for a slab with convective boundary conditions on both faces ($Bi_0 = 0.2$, $T_0 = 1000$, $Bi_L = 0.8$, $T_L = 1000$)

Consider a slab of thickness L, initial temperature of 0, convective heat transfer coefficients and fluid temperatures at $x = 0$, and L of $h_0 = 5$, $h_L = 20$, $T_0 = 1000$, $T_L = 1000$, $\rho c = 10^6$, and conductivity k of 1 (all in SI units), and let us examine the behavior at times long enough so that the temperature distribution is affected by heat conducted inward from both surfaces. We seek to determine the optimal position of a single sensor to estimate the conductivity, k, under conditions of uncertainty in the sensor location and the boundary conditions.

Figure 1 depicts the sensitivity of temperature to k and to the convective coefficient and the fluid temperature at $x = L$. The associated M for 1 percent noise and no uncertainty in h_L and T_L is shown in Fig. 2. Its peculiar shape is due to the time variation of $\partial T/\partial k$, Fig. 1. At any given time, a small increase in k increases the heat flux, lowering the surface temperature and the temperatures near the surface, thus $\partial T/\partial k < 0$. Farther from the surface, the increase in k leads to an increase in penetration depth and flux and an increase in temperature; thus, $\partial T/\partial k > 0$. Near $x = 0$, the temperature history at early times is similar to that at $x = L$. At later times, the much lower convection coefficient leads to a temperature distribution which is strongly affected by the heat conducted from the surface at $x = L$, leading to $\partial T/\partial k > 0$, but less than that near $x/L \approx 0.3$. Because M is formed from measurements taken over time, it is difficult to predict its behavior. For this experiment, the value of $\partial T/\partial k$ at $x = L$ is initially very high but decreases with time, while it increases with time near $x = 0$ and particularly at the intermediate point, $x/L \approx 0.3$ where the temperature is affected by heat flowing in from both surfaces. The value of M at $x = L$ is initially greater than at the other points. As time increases the value of M at $x = L$ decreases rapidly and that at $x/L \approx 0.3$ increases sufficiently to become the best region for locating

Nomenclature

$\mathbf{b}$ = vector of known parameters, b
c = specific heat capacity
$Cov[\ ]$ = covariance operator
$E[\ ]$ = expected value operator
f = probability Distribution Function
Fo = Fourier number ($=kt/\rho cL^2$)
$\mathbf{G}$ = known parameter covariance matrix
h = convective heat transfer coefficient
k = thermal conductivity
K = number of measurements
$\mathbf{M}$ = Fisher information matrix
q_x, Q = heat flux
$\mathbf{S}_k$ = error covariance matrix
t = time
tr = trace
T_0, T_L = fluid temperatures
T_o = initial temperatures
T_m = measured temperature
$\mathbf{u}$ = vector of parameters to be estimated, u
V = volume
x = position
X_s = sensor position
ρ = density
σ = standard deviation
Φ = predicted temperature
Ψ = error, $\Phi - T_m$
Θ = matrix of sensitivities, $\partial\Phi/\partial\mathbf{b}$

Superscripts and Subscripts

k = time
T = transpose

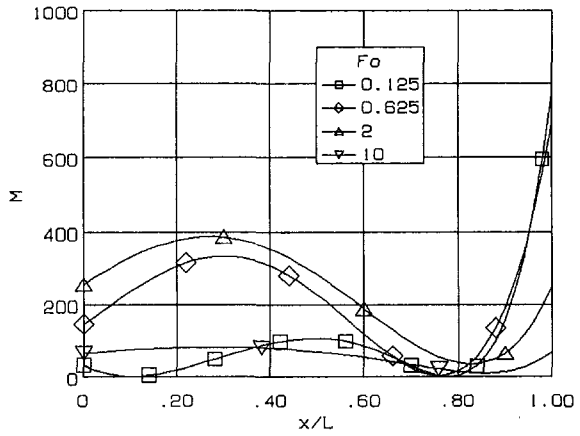

Fig. 2 Values of M as a function of sensor location and time for a slab with convective boundary conditions on both faces ($Bi_0 = 0.2$, $T_0 = 1000$, $Bi_L = 0.8$, $T_L = 1000$) and 1 percent noise in the measured temperature

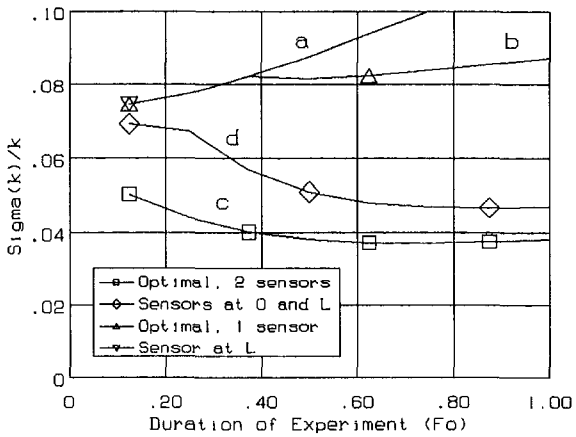

Fig. 4 Standard deviation of conductivity for one and two sensors placed at the optimal and fixed sensor locations for a slab with convective boundary conditions on both faces ($Bi_0 = 0.2$, $T_0 = 1000$, $Bi_L = 0.8$, $T_L = 1000$) with 1 percent noise in the measured temperature and $\sigma(h_L)/h_L = 10$ percent

the sensor. It is best in two senses: (a) measurements taken in this region provide the most information; and (b) the information is relatively constant over a wide spatial zone reducing the need to precisely locate the sensor. At very long times the temperature becomes constant, the sensitivity reduces, and the information approaches zero.

Effect of Imprecisions in h_L and T_L. The spatial distribution of the sensitivity of the temperature to both h_L and T_L is similar, Fig. 1. Both sensitivities are greatest at $x = L$, with the sensitivity to T_L being the larger. These spatial distributions are reasonably constant with respect to time. The effect of the imprecisions in h_L and T_L is to reduce M at all values of x, but more so at $x = L$, Fig. 3. It is interesting that uncertainties in h_L, T_L, or both do not lead to a different location of the maximum value of M.

As the temperature at $x = L$ approaches its steady-state value, the sensitivity to k quickly diminishes. Simultaneously, the value of M increases in the interior. The result is that the optimal sensor location moves inward with time. Figure 4 shows the history of $\sigma(k)/k$. When only one sensor is used and it is fixed at $x = L$, $\sigma(k)/k$ increases significantly with time (Fig. 4, curve a). If the sensor is always located at the optimal position, i.e., the point of maximum M, it is initially at $x = L$, but then later, at Fo $\approx$ 0.4, it begins to move towards $x = 0$. Positioning the sensor at the optimal location mitigates the strong increase in $\sigma(k)/k$ at later times (Fig. 4, curve b) but unfortunately it still remains large. From a practical point of view the sensor cannot move with time and the only way to conduct such an experiment is to install multiple sensors and use the reading of the appropriate sensor at each measurement time.

If two sensors are used and placed at the optimal positions, one of which turns out to be always at $x = L$, (Fig. 4, curve c) $\sigma(k)/k$ decreases continuously with time. Of course, it may be impractical to move the sensor or to make use of a large number of distributed sensors. Instead, we could place one at $x = L$ and the other at $x = 0$. Initially, the sensor at $x = 0$ contributes little to increasing the information (Fig. 4, curve d). As time goes on and the optimal location of the second sensor begins to approach 0, this second sensor adds considerable information and the curve for $\sigma(k)/k$ parallels that for curve c in Fig. 4, although always at a slightly higher uncertainty.

Effect of Imprecisions in X_s. The effect of imprecision in the sensor location, X_s, is illustrated in Fig. 5. For both a known and an uncertain h_L, the imprecision in X_s produces a very large reduction in M at all values of x except near a point in the interior. This effect can be understood by examining the nature of V. For an uncertainty in X_s, the relevant term, $\partial T/\partial b = \partial T/\partial X_s = -q_x/k$. Thus, V is equal to S where the heat flux is zero, and increases with increasing heat flux. Near the heated surface, since q_x is large, V is also large and the value of M is reduced, and thus the variance of k is substantially increased when com-

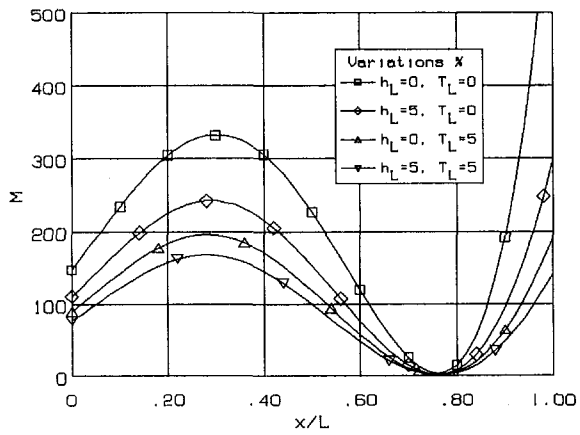

Fig. 3 Values of M at Fo = 0.625 for a slab with convective boundary conditions on both faces ($Bi_0 = 0.2$, $T_0 = 1000$, $Bi_L = 0.8$, $T_L = 1000$) with uncertainty in h_L and T_L, 1 percent noise in the measured temperature

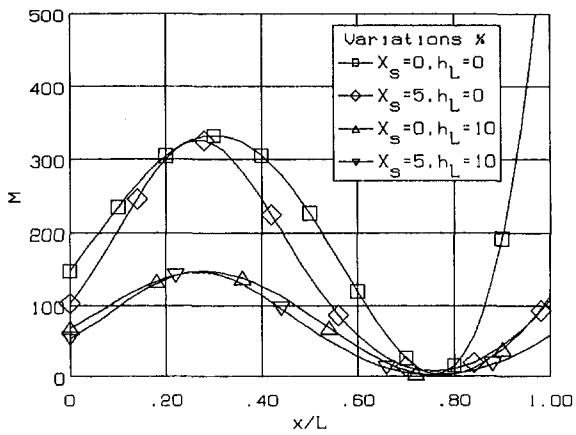

Fig. 5 Values of M at Fo = 0.625 for a slab with convective boundary conditions on both faces ($Bi_0 = 0.2$, $T_0 = 1000$, $Bi_L = 0.8$, $T_L = 1000$) with uncertainty in h_L and X_s and 1 percent noise in the measured temperature

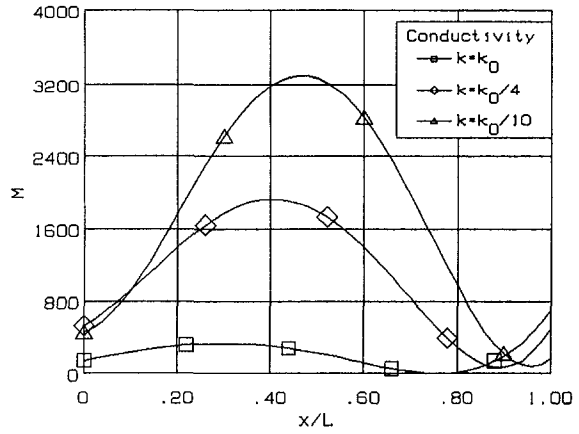

Fig. 6*a* **Effect of changing the conductivity on the values of M at Fo = 0.625 for a slab with convective boundary conditions on both faces (Bi_0 = 0.2, T_0 = 1000, Bi_L = 0.8, T_L = 1000) at a fixed value of Fo with 1 percent noise in the measured temperature**

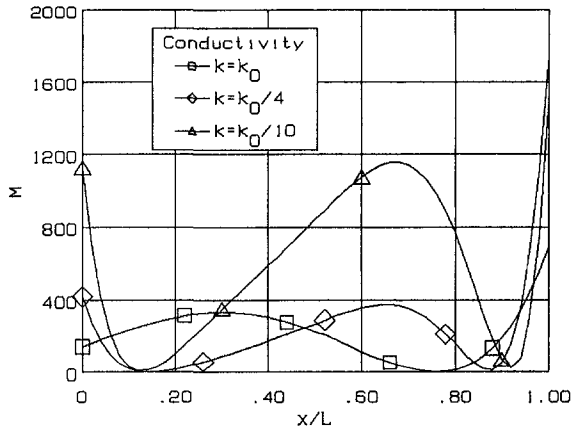

Fig. 6*b* **Effect of changing the conductivity on the values of M for a slab with convective boundary conditions on both faces (Bi_0 = 0.2, T_0 = 1000, Bi_L = 0.8, T_L = 1000) at a fixed value of t ($k_0 t/\rho c\, 2^2$ = 0.625) and 1 percent noise in the measured temperature**

pared to the case where there is no uncertainty in X_s. However, at the point at which the heat fluxes oppose and cancel each other, $V = S_k$, M is unaffected. The ideal sensor location is near this point and remains nearly constant with respect to time. When both X_s and h_L are uncertain, the uncertainty in h_L dominates, but there is still value in placing the sensor near the point of zero heat flux.

Effect of Conductivity k. The thermal conductivity defines the ratio of internal to surface resistance (Bi) and conduction to storage (Fo). Thus, changes in k lead to complex changes in the amount of information available from the experiment. The results presented thus far are for a relatively high conductivity leading to Biot numbers near 1 at both surfaces. It is of interest to explore how such a test will perform when used to measure the conductivity of insulators. Since the surface heat convective coefficients are controlled primarily by the test fixture, it is not likely that h_0 and h_L will change. For an insulator, then the changes in the Bi and Fo numbers will be due only to changes in k.

As the conductivity decreases, at the surface the temperature is essentially equal to the fluid temperature and constant with time. As a consequence, the values of M at $x = 0$ and L approach 0. The temperature in the interior becomes very sensitive to k and the interior values of M, Fig. 6(a). Because T_0 and T_L are equal, the point of maximum sensitivity moves towards the center. Since the experimental accuracy is defined by $\sigma(k)/k = 1/\sqrt{M}$, reducing the conductivity by a factor of 10 yields an increase in the accuracy of about 3, Fig. 6(a). From another point of view, if a desired level of accuracy has been defined, reducing the conductivity increases the range of x/L in which the sensor can be placed.

The conclusions drawn from Fig. 6(a) can be misleading from the experimenter's point of view since the curves are at a constant value of Fo. That is, when the conductivity is reduced by a factor of 10, the duration of the experiment increases by a factor of 10. Figure 6(b) illustrates the effect of conductivity at a fixed time measured in seconds. While the accuracy does increase for sensors placed in the interior of the slab, the optimal location of the sensor varies strongly with k. The greatest increase in accuracy occurs at the surfaces, and sensors placed there are to be preferred.

Effect of Different Boundary Conditions. The results described to this point have been strongly affected by the existence of opposing heat flows due to convection into the slab from both surfaces. It is of interest to examine the case of unidirectional heat flow which occurs when the fluid temperature at $x = 0$ is zero. Figure 7 illustrates the different aspects of this boundary condition. All of the results can be anticipated based upon the previous discussion. First, the temperature develops slowly at $x = 0$; thus, at early times M is greatest at $x = L$, passes through a near zero at $x/L \approx 0.7$, and remains quite low all the way to $x = 0$. Later, when the temperature at $x = 0$ begins to increase, the temperature at $x = L$ has stabilized and the highest values of M are found at $x = 0$, Fig. 7(a). Likewise, since the heat flux is always greatest near the heated surface at $x = L$, an uncertainty in X_s causes the greatest reduction in M for sensors located near $x = L$, Fig. 7(b). Finally, the effect of increasing the Biot number is to move the optimal sensor to $x = 0$ with a substantially increased value of M, Fig. 7(c). In contrast to the results shown on Fig. 6 where there was a strong effect of changing k regardless of the value of k, the incremental effect of reducing k shown in Fig. 7 diminishes as k decreases. For this case of unidirectional heat flow, the optimal sensor location once the temperature begins to rise at $x = 0$, Fo ≈ 0.1, is always at $x = 0$ regardless of the uncertainty in any of the "known" parameters.

It is of interest to examine the value of M for several different practical boundary conditions. Table 1 lists the values of M at the optimal sensor location.[2] The maximum values of M vary somewhat erratically as the sensor moves in time. It is clear that the best experiments for estimating the thermal conductivity are those in which one surface is maintained at a fixed temperature and the other surface temperature is controlled by some form of heat flux, either prescribed or convective. The last two cases, columns 5 and 6, show the strong effect of the convective coefficient. The optimal sensor location for estimating k is where the temperature is most sensitive to k. Initially, this is at the surface with the highest value of surface heat transfer coefficient, $x = L$. Later, when the temperature at $x = L$ approaches T_∞ and is insensitive to both h_L and k, the optimal location moves to the surface whose temperature is still changing, i.e., the surface with the lowest heat transfer coefficient, $x = 0$. Here the temperature is primarily controlled by h_0 and not k, and the information content is substantially reduced because of this low value of h_0, column 5. On the other hand, when h_0 is so large that the temperature at $x = 0$ is fixed, column 6, the temperature distribution is controlled by k, the optimal sensor location is always at $x = L$, and the information content is adequate ($\sigma(k)/k \approx 1.3$ percent). In all cases when the steady-state temperature distribution is a function of k, the best performance is at relatively long times.

[2] All results are presented in non-dimensional form with T normalized by $T_L - T_0$

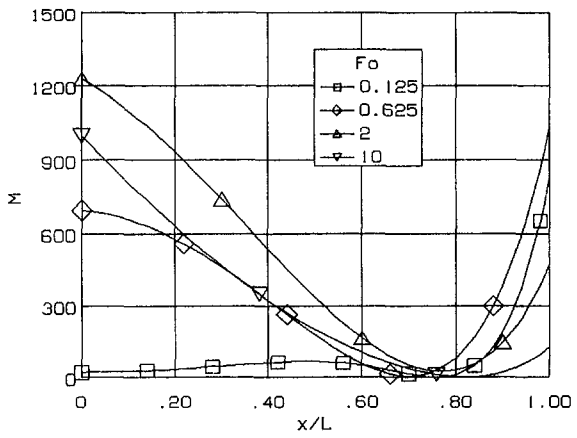

Fig. 7*a* **Values of M for a slab with convective boundary conditions on both faces ($Bi_0 = 0.2$, $T_0 = 0$, $Bi_L = 0.8$, $T_L = 1000$) as a function of sensor location and time with 1 percent noise in the measured temperature**

Fig. 7*b* **Effect of uncertainty in sensor location on the values of M at Fo = 0.625 for a slab with convective boundary conditions on both faces ($Bi_0 = 0.2$, $T_0 = 0$, $Bi_L = 0.8$, $T_L = 1000$) at a fixed value of Fo and 1 percent noise in the measured temperature**

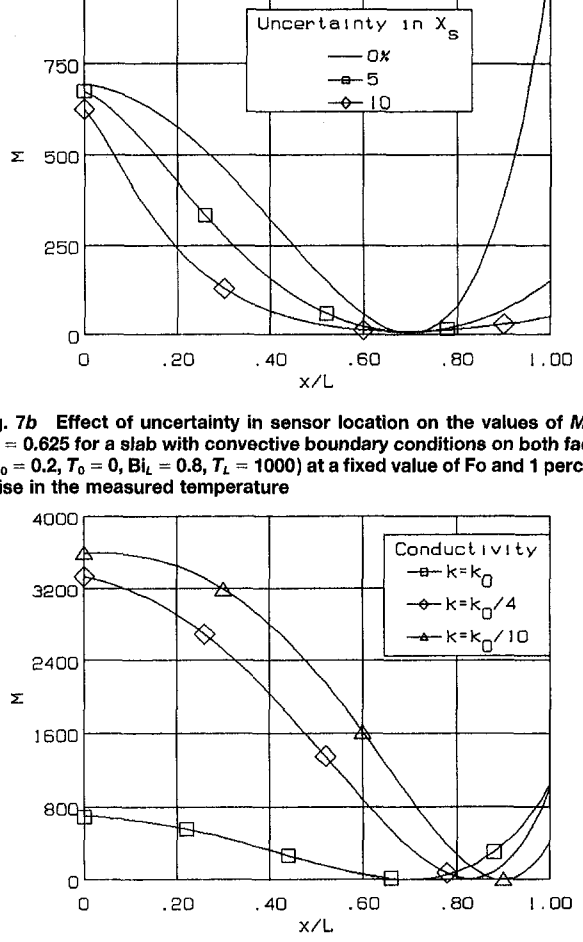

Fig. 7*c* **Effect of changing the conductivity on the values of M at Fo = 0.625 for a slab with convective boundary conditions on both faces ($Bi_0 = 0.2$, $T_0 = 0$, $Bi_L = 0.8$, $T_L = 1000$) at a fixed value of Fo and 1 percent noise in the measured temperature**

Conclusions

In transient experiments, the optimal temperatures sensor location is always in the region which experiences the greatest change in temperature. For convective boundary conditions, at early times this will be the surface with the largest convective heat transfer coefficient. Later, this region's temperature stabilizes and the optimal point moves. The new optimal point is either at another convective boundary or in the interior at a point where there is zero heat flux, depending upon the value of the Biot number. In cases with high Biot numbers, the optimal point is generally in the interior. In low Biot number cases, the optimal point is almost always at a convective boundary. Uncertainties in boundary conditions drive the optimal point to the interior. Uncertainties in sensor location, either in the form of an uncertain position or because the measured temperature represents an average over a finite region of space, force the optimal sensor location to points of minimum temperature gradient.

It might be thought that there cannot be uncertainty in sensor location at $x = 0$ or L since this simply calls for a surface temperature measurement. However, realistically, because of the sensor thickness, such surface sensors measure a temperature which is intermediate to the true surface temperature and the fluid temperature. This is particularly true of probes placed in the boundary layer. Thus, there is a natural uncertainty in sensor position. Because the temperature gradient is a maximum at the convective surface, the effect of this uncertainty is very degrading to the estimation of the conductivity by an inverse method and internal temperature sensors or heat flux sensors should be employed.

By using the simplification of the general form of $\mathbf{M}$ given in Eq. 5, the experimenter can successfully understand the time history of the optimal sensor location. While the sensitivities, $\partial\Phi/\partial\mathbf{u}$ and $\partial\Phi/\partial\mathbf{b}$, may be complex functions of time and space, even an approximate estimate of their behavior will often suffice. However, when several parameters are sought, the trace term of Eq. 3 is no longer negligible and ignoring it can lead to substantial errors in estimating $\mathbf{M}$ and the optimal sensor location.

Table 1 Maximum value of M for determining k, noise = 1 percent, no uncertainty in known parameters

Fo	Boundary Conditions				
x=0	T =0	T =0	$T_\infty = T_L$ Bi =0.8	T_∞=0 Bi=0.2	T =0
x=L	q_x=Q	T = T_L	$T_\infty = T_L$ Bi =0.8	$T_\infty = T_L$ Bi =0.8	$T_\infty = T_L$ Bi =0.8
0.01	112	169	90	89	89
0.05	519	178	314	316	316
0.10	1028	171	455	516	516
0.50	6172	172	374	998	1491
0.75	10989	171	395	873	2113
1.00	16129	171	381	903	2674
∞	10^5	0	0	905	6097
Optimal X_s	L	Varies	Varies	Varies	L

References

Alifanov, O. M., 1994, *Inverse Heat Transfer Problems,* Springer-Verlag New York, Inc., New York.

Beck, J. V., and Arnold, K. J., 1977, *Parameter Estimation in Engineering and Science,* John Wiley & Sons, Inc., New York.

Emery, A. F., and Fadale, T. D., 1996, "Design of Experiments using Uncertainty Information," ASME JOURNAL OF HEAT TRANSFER, Vol 118, No. 3, pp. 532–538.

Fadale, T. D., Nenarokomov, A. V., and Emery, A. F., 1995a, "Uncertainty in Parameter Estimation and the Inverse Problem," *International J. of Heat and Mass Transfer,* Vol 38, pp. 511–518.

Fadale, T. D., Nenarokomov, A. V., and Emery, A. F., 1995b, "Two Approaches to Optimal Sensor Locations," ASME JOURNAL OF HEAT TRANSFER, Vol 117, pp. 373–379.

Helstrom, C. W., 1995, *Elements of Signal Detection and Estimation,* Prentice-Hall, Inc. Englewood Cliffs, New Jersey.

Linnik, Y. V., 1961, *Method of Least Squares and Principles of the Theory of Observations,* Pergamon Press, Inc., Tarrytown, New York.

Strang, G., 1986, *Introduction to Applied Mathematics,* Wellesley-Cambridge Press.

X. Wang

R. J. Crawford
r.crawford@qub.ac.uk

Department of Mechanical and Manufacturing Engineering,
The Queen's University of Belfast,
Ashby Building,
Stranmillis Road,
Belfast, Northern Ireland BT9 5AH

ADE Type of Algorithms for Solving Diffusion Equations in Non-Cartesian Coordinates

This paper studies the use of ADE methods for solving diffusion equations in non-Cartesian coordinates. To retain unconditional stability and greater accuracy of computation when solving diffusion equations in non-Cartesian coordinates, a new explicit algorithm is developed by combining the advantages of those originally proposed by Saul'ev, Larkin, Barakat and Clark. Analysis of accuracy shows that the new algorithm can be as accurate as either that of Larkin or that of Barakat and Clark. Stability analysis is also carried out 'locally' based on the spectral stability, and this shows unconditional stability of the generalised algorithm. Numerical examples on transient heat conduction are used to support the conclusions from the analysis.

1 Introduction

The ADE (Alternating Direction Explicit) methods for the solution of diffusion equations based on rectangular or cubic regions in Cartesian coordinates were developed several decades ago (Barakat and Clark, 1966; Larkin, 1964; Saul'ev, 1957, 1958). Practical applications have shown that these algorithms possess great advantages over other numerical methods in regard to both the CPU time and memory if the problem to be solved is of the appropriate type (see Anderson et al., 1984).

The ADE type of algorithms were developed in such a way that the implicit computing scheme (Crank-Nicholson) was split into fractional explicit computations along positive and negative directions of coordinates. The purpose of this is to make the computation which was originally implicit become explicit and thus cancel the truncation errors during explicit computation in alternating directions. The first such algorithm was developed by Saul'ev (1957, 1958). In his method, computation along opposite directions was carried out at different time levels. This led to first order accuracy. To improve the accuracy, Larkin (1964) proposed another algorithm to do computation along opposite directions at the same time level. Subsequently, a slightly different approach was suggested by Barakat and Clark (1966). All of these algorithms were developed only for solving diffusion equations with standard expressions in rectangular or cubic areas. Unconditional stability exists for solving diffusion equations in these regular areas and since no simultaneous equations need to be generated and solved, a great amount of CPU time and storage can be saved with these explicit algorithms. It has been reported that for two-dimensional problems, the ADE method is at least ten times faster than the corresponding ADI method for large problems.

However, equations with standard forms in rectangular or cubic regions in Cartesian coordinates occur only in a relatively small number of practical problems. In order to make the ADE method capable of being used for a wider range of engineering problems, it is necessary to develop these algorithms further so that diffusion equations can be solved on irregular grids. In an attempt to achieve this, the authors realize that in developing numerical methods for solving diffusion problems the nature of the equations along with the boundaries change with the variation of the coordinate systems. In other words, the region has different shapes in different coordinate systems. This computing strategy has been widely used previously in techniques such as the Numerical Grid Generation method. As a first step in developing ADE types of algorithms for solving diffusion equations in arbitrary regions, diffusion equations in non-Cartesian coordinates, such as cylindrical and spherical (which are special cases of the general expressions of diffusion equations), are considered. This is also equivalent to solving complex expressions involving both lower order and mixed derivatives of diffusion equations in regular areas.

Firstly, ADE algorithms are developed for use with diffusion equations in two-dimensional cylindrical coordinates by considering the treatment of the first order derivatives. Their stability and accuracy are also studied. To retain unconditional stability of computation and maintain second order accuracy a new approach is developed. It is shown that all of the algorithms previously developed are actually special cases of this new method. This new algorithm is further developed for solving three-dimensional diffusion equations in cylindrical and spherical coordinate systems. It should be noted that the problems studied in this paper are differential equations with variable coefficients. A spectral stability analysis method in the sense of "local analysis" is employed. In carrying out this analysis, all of the problems are assumed to be properly posed. Finally, numerical experiments are carried out to show the stability of the proposed method. Since the new method is a generalization of the previous developed algorithms, exactly the same accuracy can be achieved when a corresponding approach is adopted. To make the expressions simpler and easier to understand, only constant mesh sizes are used in the analysis. Corresponding formulae for variable mesh sizes can be easily obtained from those provided in this paper. In addition to this, due to the unconditional stability of the new method, it is readily apparent that variable mesh sizes can be used in the solution of practical problems.

2 ADE Methods for the Solution of MultiDimensional Diffusion Equations in Non-Cartesian Coordinates

A two-dimensional linear diffusion equation in cylindrical/polar coordinates can be expressed as

$$\frac{\partial u}{\partial t} = \frac{a}{r}\frac{\partial u}{\partial r} + a\frac{\partial^2 u}{\partial r^2} + a\frac{\partial^2 u}{\partial z^2} \quad (1)$$

Contributed by the Heat Transfer Division for publication in the JOURNAL OF HEAT TRANSFER. Manuscript received by the Heat Transfer Division January 16, 1997; revision received August 4, 1997; Keywords: Computer Codes; Conduction; Transient and Unsteady Heat Transfer. Associate Technical Editor: R. W. Douglass.

or

$$\frac{\partial u}{\partial t} = \frac{a}{r}\frac{\partial u}{\partial r} + a\frac{\partial^2 u}{\partial r^2} + \frac{a}{r^2}\frac{\partial^2 u}{\partial \varphi^2} \tag{1a}$$

where $a > 0$. From the point of view of constructing numerical algorithms, there is no significant difference between (1) and (1a). Hence, only Eq. (1) is employed to evaluate the new algorithms.

In the algorithms developed below, the subscript j denotes the node number in the radial direction and k denotes the node number in the z direction. The superscript n denotes the nth time-step so that (j, k, n) can be used to denote a position in both space and time domains while computing. Central difference is employed for both first and second order derivatives for spatial variables.

As in the case for Cartesian coordinates, the ADE algorithms are based on the splitting of the Crank-Nicholson (C-N) method. For the two-dimensional equation given in (1), the following is the application of the C-N method

$$\frac{u_{jk}^{n+1} - u_{jk}^{n}}{\Delta t} = \frac{a}{4r_j\Delta r}\delta_r[u_{jk}^{n+1} + u_{jk}^{n}] + \frac{a}{2(\Delta r)^2}\delta_r^2[u_{jk}^{n+1} + u_{jk}^{n}] + \frac{a}{2(\Delta z)^2}\delta_z^2[u_{jk}^{n+1} + u_{jk}^{n}] \tag{2}$$

where δ and δ^2 are the central difference operators.

2.1 Handling of the First Order Derivative. It is apparent that the difference between the algorithms to be developed here and those studied by previous researchers is the handling of the first order derivative. To illustrate this problem, the following one-dimensional diffusion equation in polar coordinates is employed:

$$\frac{\partial u}{\partial t} = \frac{a}{r}\frac{\partial u}{\partial r} + a\frac{\partial^2 u}{\partial r^2}. \tag{3}$$

The following method, which is an analogue of that proposed by Barakat and Clark (1966), can be constructed to solve Eq. (3):

$$p_j^{n+1} = p_j^n + C_j[p_{j+1}^n - p_j^n + p_j^{n+1} - p_{j-1}^{n+1}] + A[p_{j+1}^n - p_j^n - p_j^{n+1} + p_{j-1}^{n+1}] \tag{4}$$

and

$$q_j^{n+1} = q_j^n + C_j[q_{j+1}^{n+1} - q_j^{n+1} + q_j^n - q_{j-1}^n] + A[q_{j+1}^{n+1} - q_j^{n+1} - q_j^n + q_{j-1}^n] \tag{5}$$

where $A = (a\Delta t)/(\Delta r)^2$, $C_j = (a\Delta t)/(2r_j\Delta r)$. The solution is given by

$$u_j^{n+1} = \frac{p_j^{n+1} + q_j^{n+1}}{2}. \tag{6}$$

Obviously, stability of the above method depends on the stability of both (4) and (5). Stability analysis is carried out by means of the spectral stability analysis method based on "local" stability. This method works in the following way: in an inner product space spanned by the standard Fourier bases, a periodical function can be expressed by the linear combination of the bases (Richtmyer and Morton, 1967). Denoting α and f as the angle variable and Fourier coefficient in the spectral stability analysis, analysis for (4) gives

$$[(1 + A - C_j) - (A - C_j)e^{-i\alpha}]f_j^{n+1} = [(1 - A - C_j) + (A + C_j)e^{i\alpha}]f_j^n \tag{7}$$

or

$$h_j = \frac{[1 - (A + C_j)(1 - \cos\alpha) + i(A + C_j)\sin\alpha]}{[1 + (A - C_j)(1 - \cos\alpha) + i(A - C_j)\sin\alpha]} = \frac{f_j^{n+1}}{f_j^n}. \tag{8}$$

We can obtain

$$|f_j^n|^2 - |f_j^{n+1}|^2 = 1 - 2C_j. \tag{9}$$

It can be seen that the condition for the stability of computation with (4) is $|C_j| \le \frac{1}{2}$ in the sense of "local stability". This example shows that unconditional stability is not always retained due to the appearance of the first order derivative (lower order term). Therefore, contrary to the normally accepted situation (Richtmyer and Morton, 1967), it can be seen that no general conclusion can be drawn about the influence of lower order terms on stability.

Alternatively, the method for solving Eq. (3) can be

$$p_j^{n+1} = p_j^n + C_j[p_{j+1}^n + p_j^n - p_j^{n+1} - p_{j-1}^{n+1}] + A[p_{j+1}^n - p_j^n - p_j^{n+1} + p_{j-1}^{n+1}] \tag{10}$$

and

$$q_j^{n+1} = q_j^n + C_j[q_{j+1}^{n+1} + q_j^{n+1} - q_j^n - q_{j-1}^n] + A[q_{j+1}^{n+1} - q_j^{n+1} - q_j^n + q_{j-1}^n] \tag{11}$$

where the only variation is the handling of the first order derivative and the final solution is also that given by (6). Stability analysis gives

$$[(1 + C_j + A) - (A - C_j)e^{-i\alpha}]f_j^{n+1} = [(1 + C_j - A) + (A + C_j)e^{i\alpha}]f_j^n \tag{12}$$

and

$$[(1 - C_j + A) - (A + C_j)e^{i\alpha}]g_j^{n+1} = [(1 - C_j - A) + (A - C_j)e^{-i\alpha}]g_j^n. \tag{13}$$

By analyzing the stability of (12) and (13) it can be concluded that the computation is unconditionally stable for recurrence in the time domain. However, if the recurrence in the radial direction is studied, another stability problem occurs. From (13), the following stability expression can be obtained:

$$(1 - C_j + A)\lambda_j = (A + C_j). \tag{14}$$

To make the computation stable, λ_j must satisfy $|\lambda_j| \le 1$ which leads once again to the condition $C_j \le \frac{1}{2}$. Therefore, in the following analysis the first order derivatives are to be treated in the same way as that in (4) and (5).

The stable region of the algorithm in (4) and (5) is quite small. To seek algorithms with greater stable regions, the following algorithm may be constructed

$$p_j^{n+1} = u_j^n + C_j[u_{j+1}^n - u_j^n + p_j^{n+1} - p_{j-1}^{n+1}] + A[u_{j+1}^n - u_j^n - p_j^{n+1} + p_{j-1}^{n+1}] \tag{15}$$

and

$$q_j^{n+1} = u_j^n + C_j[q_{j+1}^{n+1} - q_j^{n+1} + u_j^n - u_{j-1}^n] + A[q_{j+1}^{n+1} - q_j^{n+1} - u_j^n + u_{j-1}^n]. \tag{16}$$

The final solution is also that given in (6). This algorithm is an analog of that proposed by Larkin (1964). The accuracy of

this algorithm can be considered to be roughly second order since (15) and (16) are equivalent to

$$\frac{p_j^{n+1} + q_j^{n+1}}{2} = u_j^n + \frac{C_j}{2}[(u_{j+1}^n - u_{j-1}^n) + (q_{j+1}^{n+1} - p_{j-1}^{n+1})] + \frac{A}{2}[\delta^2 u_j^n + (q_{j+1}^{n+1} - q_j^{n+1} - p_j^{n+1} + p_{j-1}^{n+1})]. \quad (17)$$

If the angle variables in spectral stability analysis for (15) and (16) are considered to be identical which is denoted by α, the following non-negative condition for stability of computation can be obtained:

$$[1 + A(1 - \cos\alpha) + A^2 \sin^2\alpha - C_j^2(1 - \cos\alpha)^2] \times [A + A^2(1 - \cos\alpha) - C_j^2(1 + \cos\alpha)] - C_j^2(1 + \cos\alpha)[4A^2(1 - \cos\alpha)^2 - 1] \geq 0. \quad (18)$$

Denoting $C_j = \mu_j A$ and $\mu = \text{Max}\{\mu_j\}$, the stability condition in the sense of local analysis is

$$A_{\max} \leq \frac{1 + \sqrt{1 + 4\mu^2}}{4\mu^2}. \quad (19)$$

It can be seen that since the extreme of μ is $\frac{1}{2}$, Eq. (19) gives $A_{\max} = 1 + \sqrt{2}$. However, numerical tests have shown unconditional stability. Hence, due to the difficulty in analyzing the stable region of this method, it will not be studied further in this paper. Detailed discussion on general splitting of algorithms and associated stability analysis problems will appear in a separate paper (Wang & Crawford, in press).

2.2 ADE Algorithms for Solving Two-Dimensional Problems. On the basis of the above analysis for a one-dimensional problem, the construction of ADE algorithms for solving the two-dimensional equation in (1) is quite straightforward.

The first method for constant mesh sizes consists of

$$u_{jk}^{n+1} = u_{jk}^n + C_j[u_{j+1,k}^n - u_{jk}^n + u_{jk}^{n+1} - u_{j-1,k}^{n+1}] + A_1[u_{j+1,k}^n - u_{jk}^n - u_{jk}^{n+1} + u_{j-1,k}^{n+1}] + A_2[u_{j,k+1}^n - u_{jk}^n - u_{jk}^{n+1} + u_{j,k-1}^{n+1}] \quad (20)$$

and

$$u_{jk}^{n+2} = u_{jk}^{n+1} + C_j[u_{j+1,k}^{n+2} - u_{jk}^{n+2} + u_{jk}^{n+1} - u_{j-1,k}^{n+1}] + A_1[u_{j+1,k}^{n+2} - u_{jk}^{n+2} - u_{jk}^{n+1} + u_{j-1,k}^{n+1}] + A_2[u_{j,k+1}^{n+2} - u_{jk}^{n+2} - u_{jk}^{n+1} + u_{j,k-1}^{n+1}] \quad (21)$$

where A_1, A_2, and C_j are

$$A_1 = \frac{a\Delta t}{(\Delta r)^2}; \quad A_2 = \frac{a\Delta t}{(\Delta z)^2}; \quad C_j = \frac{a\Delta t}{2r_j\Delta r}. \quad (22)$$

This algorithm is a variation of that proposed by Saul'ev. It works in the following way: in the first step and the following odd steps, computation is carried out from the lower bottom corner to the right upper corner along the positive directions of R and z; in the second and the following even steps, computation is carried out along the inverse directions.

The second method for constant mesh sizes consists of

$$p_{jk}^{n+1} = p_{jk}^n + C_j[p_{j+1,k}^n - p_{jk}^n + p_{jk}^{n+1} - p_{j-1,k}^{n+1}] + A_1[p_{j+1,k}^n - p_{jk}^n - p_{jk}^{n+1} + p_{j-1,k}^{n+1}] + A_2[p_{j,k+1}^n - p_{jk}^n - p_{jk}^{n+1} + p_{j,k-1}^{n+1}] \quad (23)$$

and

$$q_{jk}^{n+1} = q_{jk}^n + C_j[q_{j+1,k}^{n+1} - q_{jk}^{n+1} + q_{jk}^n - q_{j-1,k}^n] + A_1[q_{j+1,k}^{n+1} - q_{jk}^{n+1} - q_{jk}^n + q_{j-1,k}^n] + A_2[q_{j,k+1}^{n+1} - q_{jk}^{n+1} - q_{jk}^n + q_{j,k-1}^n] \quad (24)$$

where A_1, A_2, and C_j are the same as those defined in Eq. (22) and the solution is given by

$$u_{jk}^{n+1} = \frac{p_{jk}^{n+1} + q_{jk}^{n+1}}{2}. \quad (25)$$

This algorithm is a variation of that suggested by Barakat and Clark. Computation with this algorithm is exactly the same as the first one, i.e., sweeping from different directions except that computation is in the same time level.

The accuracy of the second algorithm can be considered to be approximately second order (see Barakat & Clark, 1966). To analyse the accuracy of the first algorithm, the one-dimensional diffusion equation in (3) can be employed. The truncation error in Eqs. (20) and (21) at $t = (n + 1)\Delta t$ is apparent from the following expressions:

$$\mathcal{R}_1 = -\frac{\Delta t}{2}u_{tt} - \frac{a}{2_{r_j}}[-\Delta t_{u_{rt}}] - a\left(-\frac{\Delta t}{\Delta r}u_{rt} - \frac{\Delta t}{2}u_{rrt} + \frac{(\Delta t)^2}{2\Delta r}u_{rtt}\right) \quad (26)$$

and

$$\mathcal{R}_2 = \frac{\Delta t}{2}u_{tt} - \frac{a}{2_{r_j}}[\Delta t_{u_{rt}}] - a\left[\frac{\Delta t}{\Delta r}u_{rt} + \frac{\Delta t}{2}u_{rrt} + \frac{(\Delta t)^2}{2\Delta r}u_{rtt}\right]. \quad (27)$$

It can be seen that the principal error of the method is $[a\Delta t^2/\Delta r]u_{rtt}$. Hence, this method is considered to be accurate to the first order.

From the stability analysis carried out previously, the second method is only conditionally stable and numerical tests have confirmed this. To analyze the stability of the first algorithm, Eqs. (20) and (21) can be rewritten as

$$(1 - C_j + A_1 + A_2)u_{jk}^{n+1} + (C_j - A_1)u_{j-1,k}^{n+1} - A_2u_{j,k-1}^{n+1} = (1 - C_j - A_1 - A_2)u_{jk}^n + (C_j + A_1)u_{j+1,k}^n + A_2u_{j,k+1}^n \quad (28)$$

and

$$(1 + C_j + A_1 + A_2)u_{jk}^{n+2} - (C_j + A_1)u_{j+1,k}^{n+2} - A_2u_{j,k+1}^{n+2} = (1 + C_j - A_1 - A_2)u_{jk}^{n+1} + (A_1 - C_j)u_{j-1,k}^{n+1} + A_2u_{j,k-1}^{n+1}. \quad (29)$$

Based on the spectral stability analysis method (see section 2.1) and denoting the angle variables corresponding to R and z directions, respectively, by α, β and the Fourier coefficient by F, the following expressions for "local" stability can be obtained:

$$[(1 - C_j + A_1 + A_2) + (C_j - A_1)e^{-i\alpha} - A_2e^{-i\beta}]F_j^{n+1} = [(1 - C_j - A_1 - A_2) + (A_1 + C_j)e^{i\alpha} + A_2e^{i\beta}]F_j^n \quad (30)$$

and

$$[(1 + C_j + A_1 + A_2) - (C_j + A_1)e^{i\alpha} - A_2 e^{i\beta}]F_j^{n+2} = [(1 + C_j - A_1 - A_2) + (A_1 - C_j)e^{-i\alpha} + A_2 e^{-i\beta}]F_j^{n+1} \quad (31)$$

where α, β, and F are angle variables and the Fourier coefficient.

Cancelling F_j^{n+1} from Eqs. (30) and (31), the local amplification factor H_j can be obtained,

$$H_j = \frac{[1 - (A_1 + C_j) - A_2 + (A_1 + C_j)e^{i\alpha} + A_2 e^{i\beta}][1 - (A_1 - C_j) - A_2 + (A_1 - C_j)e^{-i\alpha} + A_2 e^{-i\beta}]}{[1 + (A_1 + C_j) + A_2 - (A_1 + C_j)e^{i\alpha} - A_1 e^{i\beta}][1 + (A_1 - C_j) + A_2 - (A_1 - C_j)e^{-i\alpha} - A_2 e^{-i\beta}]}. \quad (32)$$

When the modulus of H_j satisfies $|H_j| \leq 1$ for arbitrary α and β, computation with the method in (20) and (21) for solving Eq. (1) is stable. If the fact that $A_1 > C_j \geq 0$ is noted (since $r_j \geq \Delta r$), unconditional stability is readily apparent (see also Eq. (50)).

Although this algorithm is unconditionally stable, which facilitates computation and programming, its accuracy, being limited to the first order, is a drawback. However, an interesting thought is the possibility of combining the advantages of the first and second algorithms to develop a new approach. To achieve this, two computation schemes starting at different ends and proceeding in different directions based on (20) and (21) can be constructed. The following is the recommended computing strategy if the initial values of p and q are specified as

$$p_{jk}^0 = q_{jk}^0 = u_{jk}^0. \quad (33)$$

For $n = 0, 2, 4, \ldots$, the computation scheme, at time $t = (n + 1)\Delta t$, is

$$p_{jk}^{n+1} = p_{jk}^n + C_j[p_{j+1,k}^n - p_{jk}^n + p_{jk}^{n+1} - p_{j-1,k}^{n+1}] + A_1[p_{j+1,k}^n - p_{jk}^n - p_{jk}^{n+1} + p_{j-1,k}^{n+1}] + A_2[p_{j,k+1}^n - p_{jk}^n - p_{jk}^{n+1} + p_{j,k-1}^{n+1}] \quad (34)$$

and

$$q_{jk}^{n+1} = q_{jk}^n + C_j[q_{j+1,k}^{n+1} - q_{jk}^{n+1} + q_{jk}^n - q_{j-1,k}^n] + A_1[q_{j+1,k}^{n+1} - q_{jk}^{n+1} - q_{jk}^n + q_{j-1,k}^n] + A_2[q_{j,k+1}^{n+1} - q_{jk}^{n+1} - q_{jk}^n + q_{j,k-1}^n] \quad (35)$$

where A_1, A_2, and C_j are the same as those defined in Eq. (22). The solution for the output is $u^{n+1} = (p^{n+1} + q^{n+1})/2$. At time $t = (n + 2)\Delta t$, the computation scheme is

$$p_{jk}^{n+2} = p_{jk}^{n+1} + C_j[p_{j+1,k}^{n+2} - p_{jk}^{n+2} + p_{jk}^{n+1} - p_{j-1,k}^{n+1}] + A_1[p_{j+1,k}^{n+2} - p_{jk}^{n+2} - p_{jk}^{n+1} + p_{j-1,k}^{n+1}] + A_2[p_{j,k+1}^{n+2} - p_{jk}^{n+2} - p_{jk}^{n+1} + p_{j,k-1}^{n+1}] \quad (36)$$

and

$$q_{jk}^{n+2} = q_{jk}^{n+1} + C_j[q_{j+1,k}^{n+1} - q_{jk}^{n+1} + q_{jk}^{n+2} - q_{j-1,k}^{n+2}] + A_1[q_{j+1,k}^{n+1} - q_{jk}^{n+1} - q_{jk}^{n+2} + q_{j-1,k}^{n+2}] + A_2[q_{j,k+1}^{n+1} - q_{jk}^{n+1} - q_{jk}^{n+2} + q_{j,k-1}^{n+2}]. \quad (37)$$

The solution for output is $u^{n+2} = (p^{n+2} + q^{n+2})/2$. A variation of the above computing scheme can be obtained by specifying the u^{n+2} as the initial value for the next step computation.

It can be seen that all of the ADE algorithms developed previously are only special cases of the above computing strategy. For example, Eqs. (34) and (36) or (35) and (37) constitute the algorithm originally proposed by Saul'ev; Eqs. (34) and (35) are proposed by Barakat and Clark if the output is the average value of p and q as given above; the algorithm originally proposed by Larkin can be obtained if the solution for output is also used as the initial value for next step computation. Therefore, it is evident that the above computing strategy is accurate to the second order and retains unconditional stability.

2.3 Explicit Algorithms for Three-Dimensional Problems. The new ADE algorithm for solving the diffusion equation in both cylindrical and spherical coordinate systems is studied in this section. The diffusion equation in a cylindrical coordinate system is

$$\frac{\partial u}{\partial t} = \frac{a}{r}\frac{\partial u}{\partial r} + a\frac{\partial^2 u}{\partial r^2} + a\frac{\partial^2 u}{\partial z^2} + \frac{a}{r^2}\frac{\partial^2 u}{\partial \phi^2}. \quad (38)$$

The diffusion equation in spherical coordinates is

$$\frac{\partial u}{\partial t} = \frac{2a}{r}\frac{\partial u}{\partial r} + a\frac{\partial^2 u}{\partial r^2} + \frac{a}{r^2 tg\,\theta}\frac{\partial u}{\partial \theta} + \frac{a}{r^2}\frac{\partial^2 u}{\partial \theta^2} + \frac{a}{r^2 \sin^2\theta}\frac{\partial^2 u}{\partial \phi^2}. \quad (39)$$

On the basis of the study of two-dimensional problems, algorithms for solving three-dimensional problems can be readily constructed by extending those previously studied. For example, the extension of the algorithm in Eqs. (34)–(37) for solving three-dimensional diffusion equations in cylindrical coordinates for a constant mesh size consists of the following:

1 At $t = (n + 1)\Delta t$,

$$p_{jkl}^{n+1} = p_{jkl}^n + C_j[p_{j+1,kl}^n - p_{jkl}^n + p_{jkl}^{n+1} - p_{j-1,kl}^{n+1}] + A_1[p_{j+1,kl}^n - p_{jkl}^n - p_{jkl}^{n+1} + p_{j-1,kl}^{n+1}] + A_2[p_{j,k+1,l}^n - p_{jkl}^n - p_{jkl}^{n+1} + p_{j,k-1,l}^{n+1}] + A_{3j}[p_{jk,l+1}^n - p_{jkl}^n - p_{jkl}^{n+1} + p_{jk,l-1}^{n+1}] \quad (40)$$

and

$$q_{jkl}^{n+1} = q_{jkl}^n + C_j[q_{j+1,kl}^{n+1} - q_{jkl}^{n+1} + q_{jkl}^n - q_{j-1,kl}^n] + A_1[q_{j+1,kl}^{n+1} - q_{jkl}^{n+1} - q_{jkl}^n + q_{j-1,kl}^n] + A_2[q_{j,k+1,l}^{n+1} - q_{jkl}^{n+1} - q_{jkl}^n + q_{j,k-1,l}^n] + A_{3j}[q_{jk,l+1}^{n+1} - q_{jkl}^{n+1} - q_{jkl}^n + q_{jk,l-1}^n] \quad (41)$$

where

$$C_j = \frac{a\Delta t}{2r_j\Delta r}; \quad A_1 = \frac{a\Delta t}{(\Delta r)^2}; \quad A_2 = \frac{a\Delta t}{(\Delta z)^2}; \quad A_{3j} = \frac{a\Delta t}{r_j^2(\Delta\phi)^2}. \quad (42)$$

2 At $t = (n + 2)\Delta t$,

$$p_{jkl}^{n+2} = p_{jkl}^{n+1} + C_j[p_{j+1,kl}^{n+2} - p_{jkl}^{n+2} + p_{jkl}^{n+1} - p_{j-1,kl}^{n+1}] + A_1[p_{j+1,kl}^{n+2} - p_{jkl}^{n+2} - p_{jkl}^{n+1} + p_{j-1,kl}^{n+1}] + A_2[p_{j,k+1,l}^{n+2} - p_{jkl}^{n+2} - p_{jkl}^{n+1} + p_{j,k-1,l}^{n+1}] + A_{3j}[p_{jk,l+1}^{n+2} - p_{jkl}^{n+2} - p_{jkl}^{n+1} + p_{jk,l-1}^{n+1}] \quad (43)$$

and

$$q_{jkl}^{n+2} = q_{jkl}^{n+1} + C_j[q_{j+1,kl}^{n+1} - q_{jkl}^{n+1} + q_{jkl}^{n+2} - q_{j-1,kl}^{n+2}] + A_1[q_{j+1,kl}^{n+1} - q_{jkl}^{n+1} - q_{jkl}^{n+2} + q_{j-1,kl}^{n+2}] + A_2[q_{j,k+1,l}^{n+1} - q_{jkl}^{n+1} - q_{jkl}^{n+2} + q_{j,k-1,l}^{n+2}] + A_{3j}[q_{jk,l+1}^{n+1} - q_{jkl}^{n+1} - q_{jkl}^{n+2} + q_{jk,l-1}^{n+2}]. \quad (44)$$

To solve three-dimensional diffusion equations in spherical coordinates, the recommended algorithm for constant mesh size consists of the following:

1 At $t = (n + 1)\Delta t$,

$$p_{jkl}^{n+1} = p_{jkl}^{n} + C_{1j}[p_{j+1,kl}^{n} - p_{jkl}^{n} + p_{jkl}^{n+1} - p_{j-1,kl}^{n+1}] + A_1[p_{j+1,kl}^{n} - p_{jkl}^{n} - p_{jkl}^{n+1} + p_{j-1,kl}^{n+1}] + C_{2jk}[p_{j,k+1,l}^{n} - p_{jkl}^{n} + p_{jkl}^{n+1} - p_{j,k-1,l}^{n+1}] + A_{2j}[p_{j,k+1,l}^{n} - p_{jkl}^{n} - p_{jkl}^{n+1} + p_{j,k-1,l}^{n+1}] + A_{3jk}[p_{jk,l+1}^{n} - p_{jkl}^{n} - p_{jkl}^{n+1} + p_{jk,l-1}^{n+1}] \quad (45)$$

and

$$q_{jkl}^{n+1} = q_{jkl}^{n} + C_{1j}[q_{j+1,kl}^{n+1} - q_{jkl}^{n+1} + q_{jkl}^{n} - q_{j-1,kl}^{n}] + A_1[q_{j+1,kl}^{n+1} - q_{jkl}^{n+1} - q_{jkl}^{n} + q_{j-1,kl}^{n}] + C_{2jk}[q_{j,k+1,l}^{n+1} - q_{jkl}^{n+1} + q_{jkl}^{n} - q_{j,k-1,l}^{n}] + A_{2j}[q_{j,k+1,l}^{n+1} - q_{jkl}^{n+1} - q_{jkl}^{n} + q_{j,k-1,l}^{n}] + A_{3jk}[q_{jk,l+1}^{n+1} - q_{jkl}^{n+1} - q_{jkl}^{n} + q_{jk,l-1}^{n}] \quad (46)$$

where

$$C_{1j} = \frac{a\Delta t}{r_j \Delta r}; \quad A_1 = \frac{a\Delta t}{(\Delta r)^2}; \quad C_{2jk} = \frac{a\Delta t}{2r_j^2 \Delta\theta tg\theta_k};$$

$$A_{2j} = \frac{a\Delta t}{r_j^2(\Delta\theta)^2}; \quad A_{3jk} = \frac{a\Delta t}{r_j^2(\Delta\phi)^2 \sin^2\theta_k}. \quad (47)$$

2 At $t = (n + 2)\Delta t$,

$$q_{jkl}^{n+2} = q_{jkl}^{n+1} + C_{1j}[q_{j+1,kl}^{n+1} - q_{jkl}^{n+1} + q_{jkl}^{n+2} - q_{j-1,kl}^{n+2}] + A_1[q_{j+1,kl}^{n+1} - q_{jkl}^{n+1} - q_{jkl}^{n+2} + q_{j-1,kl}^{n+2}] + C_{2jk}[q_{j,k+1,l}^{n+1} - q_{jkl}^{n+1} + q_{jkl}^{n+2} - q_{j,k-1,l}^{n+2}] + A_{2j}[q_{j,k+1,l}^{n+1} - q_{jkl}^{n+1} - q_{jkl}^{n+2} + q_{j,k-1,l}^{n+2}] + A_{3jk}[q_{jk,l+1}^{n+1} - q_{jkl}^{n+1} - q_{jkl}^{n+2} + q_{jk,l-1}^{n+2}] \quad (48)$$

and

$$p_{jkl}^{n+2} = p_{jkl}^{n+1} + C_{1j}[p_{j+1,kl}^{n+2} - p_{jkl}^{n+2} + p_{jkl}^{n+1} - p_{j-1,kl}^{n+1}] + A_1[p_{j+1,kl}^{n+2} - p_{jkl}^{n+2} - p_{jkl}^{n+1} + p_{j-1,kl}^{n+1}] + C_{2jk}[p_{j,k+1,l}^{n+2} - p_{jkl}^{n+2} + p_{jkl}^{n+1} - p_{j,k-1,l}^{n+1}] + A_{2j}[p_{j,k+1,l}^{n+2} - p_{jkl}^{n+2} - p_{jkl}^{n+1} + p_{j,k-1,l}^{n+1}] + A_{3jk}[p_{jk,l+1}^{n+2} - p_{jkl}^{n+2} - p_{jkl}^{n+1} + p_{jk,l-1}^{n+1}]. \quad (49)$$

For both algorithms, the solution for the output at $t = (n + 1)\Delta t$ is $u^{n+1} = (p^{n+1} + q^{n+1})/2$. The solution for the output at $t = (n + 2)\Delta t$ is $u^{n+2} = (p^{n+2} + q^{n+2})/2$, which can also be used as the initial value for the next step computation.

Unconditional stability of the above algorithms can be seen from analysing the computation of either p or q. For example, stability analysis for p in the algorithm in Eqs. (45)–(49) results in the following "local" amplification factor:

$$H_{jk} = \frac{[1 - (A_1 + C_{1j}) - (A_{2j} + C_{2jk}) - A_{3jk}] + (A_1 + C_{1j})e^{i\alpha} + (A_{2j} + C_{2jk})e^{i\beta} + A_{3jk}e^{i\gamma}}{[1 + (A_1 + C_{1j}) + (A_{2j} + C_{2jk}) + A_{3jk}] - (A_1 + C_{1j})e^{i\alpha} - (A_{2j} + C_{2jk})e^{i\beta} - A_{3jk}e^{i\gamma}} \times \frac{[1 - (A_1 - C_{1j}) - (A_{2j} - C_{2jk}) - A_{3jk}] + (A_1 - C_{1j})e^{-i\alpha} + (A_{2j} - C_{2jk})e^{-i\beta} + A_{3jk}e^{-i\gamma}}{[1 + (A_1 - C_{1j}) + (A_{2j} - C_{2jk}) + A_{3jk}] - (A_1 - C_{1j})e^{-i\alpha} - (A_{2j} - C_{2jk})e^{-i\beta} - A_{3jk}e^{-i\gamma}}. \quad (50)$$

Table 1 One-dimensional computation

Δt	ONEDA	ONEDB	A
0.00001	STABLE	STABLE	1
0.00005	STABLE	STABLE	5
0.0001	STABLE	STABLE	10
0.001	STABLE (u_{max}=400.01, at N=9314, 2nd node)	STABLE	100
0.002	u_{max}=402.17 (at N=1000, 2nd node)	STABLE	200
0.005	UNSTABLE	STABLE	500
0.01	UNSTABLE	STABLE	1000
0.1	UNSTABLE	STABLE	10000
10^8	UNSTABLE	STABLE	10^{13}

The above equation can be denoted by $H_{jk} = H_{jk}^{(1)}H_{jk}^{(2)}$. Since $A_1 > C_{1j}$ and $A_{2j} > C_{2jk}$, $H_{jk}^{(1)}$ and $H_{jk}^{(2)}$ satisfy $|H_{jk}^{(1)}| < 1$ and $|H_{jk}^{(2)}| < 1$. This results in $|H_{jk1}| < 1$. The stability of computation for p in the algorithm in Eqs. (40)–(44) can be readily seen by simply letting $C_{2jk} = 0$ in (50).

3 Numerical Examples

Since the new method given from Eqs. (34) to (37) is a generalization of the algorithms previously developed, exactly the same accuracy can be achieved when a corresponding approach is adopted. Therefore, comparisons of accuracy of numerical solutions will not be shown. As has been pointed out, because the key is stability, numerical testing is focused on the stability of computation for various algorithms.

3.1 Stability of Explicit Algorithms for Solving One-Dimensional Equations. To verify the stability of the new ADE algorithms for solving diffusion equations in non-Cartesian coordinates, the following initial and boundary value problem of one-dimensional diffusion in the radial direction is considered:

$$\frac{\partial u}{\partial t} = \frac{a}{r}\frac{\partial u}{\partial r} + a\frac{\partial^2 u}{\partial r^2} \quad (51)$$

$$u(0, r) = u^0; \quad u(t, R_0) = u(t, R_1) = u_\Gamma; \quad r \in [R_0, R_1].$$

Two computer codes were programmed: (1) code ONEDA—based on the algorithm in Eqs. (4) and (5); and (2) code ONEDB—based on the algorithm in Eqs. (34)–(37).

Firstly, the codes were tested by comparing them with one based on the C-N algorithm, it was found that the numerical solutions were almost identical. To compare the stability of the different ADE algorithms, the following one-dimensional computational model was employed. A total of 1001 nodes along the radial direction were used in the computation. R_1 and R_0 were taken as 0.1001 and 0.0001 respectively so that $C_{max} = A/4$ due to the use of central difference. The parameter a in Eq. (51) is given as 0.001, that initial value at every internal node is $u^0 = 399$, and the value at every boundary node is $u_\Gamma = 400$. The use of this model is purely for the purpose of stability examination. Numerical tests

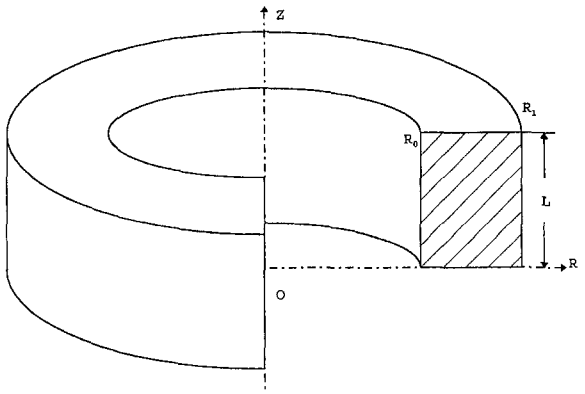

Fig. 1 The cross section used for computation

were carried out for various step lengths of Δt. The results observed at $N = 10{,}000$ are listed in Table 1. Single precision was used for the computation.

It can be seen from the results that the spectral stability analysis gives a very conservative stability prediction. It is also found that while ONEDA is conditionally stable, computation with ONEDB is unconditionally stable.

3.2 Stability of the Algorithms for Solving Two-Dimensional Equations. Two computer codes TWODA and TWODB were developed based on (1) the explicit method in Eqs. (23) and (24); and (2) the explicit algorithm in Eqs. (34)–(37).

To examine the stability of the explicit algorithms, transient heat conduction is computed for a cross section of a ring shown in Fig. 1.

In all of the computations carried out, $R_0 = 0.001$, $R_1 = 0.101$ and there are 101 nodes in the directions of both R and Z, respectively, so that $C_{\max} = A_1/4$. This is because the boundary condition is of the first kind, which means that the computation should start at the second node ($r_j = 2\Delta r_o$). The value of a in Eq. (1) is 0.1.

First of all, the validity of these codes was checked for $L = 10$. This makes the problem almost one-dimensional along the line of symmetry. Numerical solutions from all of the above codes were thus compared with those from the codes for one-dimensional problems. Then, numerical output from the above two codes are cross-checked for $L = 0.1$ and $\Delta t = 0.00001$. For the purpose of assessing stability, computation was carried out for $L = 10$, $L = 0.1$, and $L = 0.001$ to illustrate the influence of the variation of A_2. Numerical tests were carried out for the initial value $u^0 = 399$ and the boundary value $u_\Gamma = 400$ with various step lengths of Δt. The results observed at $N = 3000$ are listed in Tables 2, 3, and 4. Single precision is used in the computations.

Table 2 Two-dimensional computation, L = 10

Δt	TWODA	TWODB	A_1	A_2
0.0001	STABLE	STABLE	10	0.001
0.0002	u_{max}=400.14 (At N=100, j=2, k=100)	STABLE	20	0.002
0.0005	UNSTABLE	STABLE	50	0.005
0.1	UNSTABLE	STABLE	10^4	1
1	UNSTABLE	STABLE	10^5	10
100	UNSTABLE	STABLE	10^7	1000
10^8	UNSTABLE	STABLE	10^{13}	10^9

Table 3 Two-dimensional computation, L = 0.1

Δt	TWODA	TWODB	A_1	A_2
0.00001	STABLE	STABLE	1	1
0.00002	u_{max}=400.12 (At N=2, j=100, k=100)	STABLE	2	2
0.00005	u_{max}=400.3 (At N=2, j=100, k=100)	STABLE	5	5
0.0001	u_{max}=400.4 (At N=2, j=100, k=100)	STABLE	10	10
0.01	UNSTABLE	STABLE	1000	1000
1	UNSTABLE	STABLE	10^5	10^5
10	UNSTABLE	STABLE	10^6	10^6
10^9	UNSTABLE	STABLE	10^{13}	10^{13}

Table 4 Two-dimensional computation, L = 0.001

Δt	TWODA	TWODB	A_1	A_2
0.00001	STABLE	STABLE	1	10^4
0.00002	u_{max}=400.16 (At N=600, j=39, k=52)	STABLE	2	$2x10^4$
0.00005	u_{max}=400.2 (At N=1943, j=40, k=35)	STABLE	5	$5x10^4$
0.0001	u_{max}=400.2 (At N=1888, j=40, k=61)	STABLE	10	10^5
0.01	u_{max}=400.1 (At N=665, j=39, k=51)	STABLE	1000	10^7
1	u_{max}=400.3 (At N=1937, j=86, k=57)	STABLE	10^5	10^9
10	u_{max}=400.3 (At N=1999, j=12, k=53)	STABLE	10^6	10^{10}
10^8	u_{max}=400.144 (At N=1817, j=38, k=49)	STABLE	10^{13}	10^{17}

4 Conclusions

As a result of the analysis and numerical experiments in this paper, it is concluded that the new ADE algorithm described in this paper possesses roughly the same accuracy when compared with the ADI counterparts and the Finite Element method (based on linear interpolation). Since the algorithm proposed in this paper is explicit and no simultaneous equations need to be generated and solved, less CPU time and memory are required. Also, as a result of its unconditional stability, the use of larger Δt values is allowed, which may save CPU time and make programming easier. No restriction on Δt for the sake of stability indicates that the algorithm may be used for solving elliptic equations (steady-state problems) in the areas described in this paper.

Perhaps the most important contribution of this research is that it may have provided a way for solving diffusion equations in arbitrary areas when the general expressions of the equations are considered. This is because in practical situations, in addition to the first derivatives, mixed derivatives are required to be considered in constructing numerical algorithms (see Wang and Crawford, 1997). Such problems are readily solved using the proposed new approach.

References

Anderson, D. A. et al, 1984, *Computational Fluid Mechanics and Heat Transfer,* Hemisphere Publishing Corp., Bristol, PA.

Barakat, H. Z., and Clark, J. A., 1966, "On the Solution of the Diffusion Equations by Numerical Methods," ASME JOURNAL OF HEAT TRANSFER, pp. 421--427.

Larkin, B. K., 1964, "Some Stable Explicit Difference Approximations to the Diffusion Equation," *Mathematics of Computations,* pp. 196–202.

Richtmyer, R. D., and Morton, K. W., 1967, *Difference Methods for Initial-Value Problems,* Interscience Publishers, New York.

Saul'ev, K., 1957, "On a Method of Numerical Integration of the Equation of Diffusion," Doklady Akad. Nauk USSR, Vol. 115, pp. 1077–1079.

Saul'ev, K., 1958, "Methods of Increased Accuracy and Two-Dimensional Approximations to Solutions of Parabolic Equations," Doklady Akad. Nauk USSR, Vol. 118, pp. 1088–1090.

Wang, X. M., and Crawford, R. J., 1997, "Splitting-up Algorithms for Solving Diffusion Equations in Arbitrary Regions," in press.

A Global Time Treatment for Inverse Heat Conduction Problems

J. I. Frankel
Professor.
frankel@titan.engr.utk.edu

M. Keyhani
Professor.

Mechanical and Aerospace Engineering and Engineering Sciences Department,
University of Tennessee,
Knoxville, TN 37966-2210

A new global time treatment is proposed and demonstrated for inverse heat conduction problems. This exposition illustrates the methodology by carefully and meticulously investigating the classic Beck's problem. It is shown that accurate and stable numerical results occur without resorting to any stabilizing scheme beyond the implementation of a global basis representation for the temperature distribution. As a global time method the entire space-time domain is resolved in a simultaneous fashion. The approach is also extendable to multidimensional and multiprobe situations without difficulty. In direct problems the method has been successively applied to initial value problems, Volterra integral equations, and parabolic and hyperbolic partial and integro-partial differential equations.

1 Introduction

Inverse heat conduction involves the application of diffusion theory for estimating unknown boundary conditions, energy generation rates, or thermophysical properties through internal measured temperature histories at one or more locations. Typically, discrete data (Beck et al., 1985), as obtained from an embedded thermocouple, is used in the model. Applications involving atmospheric entry of space vehicles, heat treatment, and turbine blade design can utilize inverse analyses. In thermal design it is often desirable to be able to overspecify (or constrain) a location in order to assure a desired transient temperature distribution. In this case it is desired to know what boundary input would be required to generate this prescribed history. Areas involving heat treatment processes and inverse solidification design processes (Frankel and Keyhani, 1996) can benefit from such a methodology. The interested reader is referred to the exposition by Beck et al. (1985) for further applications and a detailed literature review.

Unlike direct problems, inverse problems possess several undesirable mathematical and numerical characteristics that must be addressed in order to obtain meaningful results. Direct problems possess clear mathematical theories for well-posedness, while inverse problems are typically ill-posed in the sense of Hadamard. That is, a small change in the input data can produce a large change in the output. Ill-posed problems of this sort seem to be paradoxical in that the condition number grows with the quality of the approximation. A large condition number may indicate that excessive roundoff errors may be looming which in turn can produce erratic or unstable results. Owing to this dilemma, numerical schemes involving Tikhonov regularization and future information (Beck et al., 1985) have been proposed for stabilizing the solution.

The present offering proposes a natural and unified treatment for resolving both inverse and direct problems. In this paper we demonstrate several fundamental features of the developing methodology without undue complication. This paper serves to introduce the concept and to lay down a foundation that allows multidimensional and multiprobe solutions to be developed.

This paper is organized as follows. The mathematical formulation for the transient, linear, one-dimensional heat conduction problem is presented in Section 2. Section 3 presents the formulation for the inverse heat conduction problem. Section 4 presents the new numerical solution method. Section 5 presents some preliminary results indicating that accurate and stable results occur. Section 6 discusses some applications where additional constraints can be imposed in the formulation. Finally, Section 7 presents some concluding remarks.

2 Forward Problem

In this section the mathematical formulation is developed for a well studied heat conduction problem. In order to demonstrate the merit of the proposed approach, a conventional test problem is investigated in some detail. Ozisik (1993) and Beck et al. (1985) consider the one-dimensional parallel plate geometry having unit dimensionless length. The surface at $x = 0$ is exposed to a transient dimensionless heat flux denoted by $q(t)$, while the back face is insulated at $x = 1$. These conventional dimensionless quantities (though renamed here) can be found in Ozisik (1993, p. 593). Using the dimensionless forms defined in Ozisik (1993), the heat conduction equation is

$$\frac{\partial^2 T}{\partial x^2}(x, t) = \frac{\partial T}{\partial t}(x, t), \quad x \in (0, 1), \quad t > 0, \qquad (1a)$$

subject to the boundary conditions

$$-\frac{\partial T}{\partial x}(0, t) = q(t), \qquad (1b)$$

$$\frac{\partial T}{\partial x}(1, t) = 0, \quad t > 0, \qquad (1c)$$

and the initial condition

$$T(x, 0) = 0, \quad x \in [0, 1]. \qquad (1d)$$

Here, continuous input data is given by the auxiliary condition displayed in Eq. (1b). The partial differential equation expressed in Eq. (1a) subject to the auxiliary conditions given in Eqs. (1b)–(1d) generate a well posed mathematical problem if $q(t)$ is known.

Using the finite integral transform technique (Ozisik, 1993), the solution of Eq. (1) for $T(x, t)$ in terms of $q(t)$ is

$$T(x, t) = \sum_{m=0}^{\infty} \frac{\cos(\lambda_m x)}{N(\lambda_m)} \int_{t'=0}^{t} q(t') e^{-\lambda_m^2 (t - t')} dt', \qquad x \in [0, 1], \quad t \geq 0, \qquad (2)$$

Contributed by the Heat Transfer Division for publication in the JOURNAL OF HEAT TRANSFER. Manuscript received by the Heat Transfer Division January 21, 1997; revision received August 11, 1997; Keywords: Conduction; Materials Processing and Manufacturing Process; Numerical Methods. Associate Technical Editor: R. W. Douglass.

where the discrete spectrum of eigenvalues is given as $\lambda_m = m\pi$, $m = 0, 1, \ldots$ and the normalizations integrals are $N(\lambda_0) = 1$, $N(\lambda_m) = \frac{1}{2}$, $m = 1, 2, \ldots$

Evaluating Eq. (2) at $x = 1$ produces

$$T(1, t) = \sum_{m=0}^{\infty} \frac{(-1)^m}{N(\lambda_m)} \int_{t'=0}^{t} q(t') e^{-\lambda_m^2 (t-t')} dt', \quad t \geq 0. \quad (3)$$

If $q(t)$ is known, then Eq. (2) is the formal solution. If $q(t)$ is unknown but $T(1, t)$ is given, then the problem is considered an inverse problem and it is viewed as being ill-posed. This ill-posedness is evident from viewing Eq. (3) which indicates that in order to determine $q(t)$, a Volterra integral equation of the first kind must be solved. This type of integral equation is considered mildly ill-posed (Wing, 1991).

3 An Inverse Heat Conduction Problem

Consider the classic inverse problem where overspecified data at a boundary is prescribed; namely,

$$T(1, t) = f(t) \quad (\text{or} = f_i;\ i = 1, 2, \ldots, M), \quad (4a)$$

and

$$\frac{\partial T}{\partial x}(1, t) = 0, \quad t > 0, \quad (4b)$$

where the heat equation given in Eq. (1a) and initial condition prescribed in Eq. (1d) are still valid. If discrete temperature data is specified at discrete values of time, t_i, $i = 1, 2, \ldots, M$, then we denote these values of temperature by f_i, $i = 1, 2, \ldots, M$.

For convenience in the analysis the temporal and spatial domains are mapped into a new computational domain through the linear transformations

$$\eta = 2x - 1, \quad \eta \in [-1, 1], \quad x \in [0, 1], \quad (5a)$$

and

$$\xi = \frac{t}{\lambda} - 1, \quad \xi \in [-1, 1], \quad t \in [0, t_{\max}], \quad (5b)$$

where $\lambda = t_{\max}/2$ and where $t_{\max}$ represents the maximum time of interest for the time evolution of the problem. These choices will become evident as the solution method is developed. Using these new independent variables, the mathematical formulation for the inverse heat conduction problem becomes

$$L[\theta(\eta, \xi)] = 0, \quad (\eta, \xi) \in [-1, 1], \quad (6a)$$

where the differential operator L is

$$L = \frac{\partial^2}{\partial \eta^2} - \frac{1}{4\lambda} \frac{\partial}{\partial \xi}. \quad (6b)$$

The prescribed one-sided boundary conditions become

$$\theta(1, \xi) = F(\xi) \quad (\text{or } F_i,\ i = 1, 2, \ldots, M), \quad (6c)$$

$$\frac{\partial \theta}{\partial \eta}(1, \xi) = 0, \quad \xi \in [-1, 1], \quad (6d)$$

with the initial condition

$$\theta(\eta, -1) = 0, \quad \eta \in [-1, 1], \quad (6e)$$

where $\theta(\eta, \xi) = T(1 + \eta/2, \lambda(1 + \xi))$, and $F(\xi) = f(\lambda(1 + \xi))$ or $F_i = \theta_i$, $i = 1, 2, \ldots, M$. For the time being it is assumed that $F(\xi)$ is a real and continuous function in the domain of $[-1, 1]$. (Note that $F(-1) = 0$ for continuity purposes.) From viewing the domain definition shown in Eq. (6a), it appears that (η, ξ) is defined in a square. Finally, the unknown surface heat flux can be expressed as

$$Q(\xi) = -2 \frac{\partial \theta}{\partial \eta}(-1, \xi), \quad \xi \in [-1, 1]. \quad (6f)$$

Beck's future information method (Beck et al., 1985) has generally been applied to such problems. Other approaches have also been considered (Beck et al., 1985) for solving this type of problem in the presence of discrete data. To indicate the versatility of the proposed approach, we present preliminary results for the following two situations: (i) continuous $F(\xi)$, and (ii) discrete $F_i = \theta_i$, $i = 1, 2, \ldots, M$.

Nomenclature

$a_m(\xi)$ = time varying expansion coefficients, Eq. (7a)
$a_m^{N+1}(\xi)$ = approximate time varying expansion coefficients, Eq. (8)
b_n^m = expansion coefficient, Eq. (10)
$c_m^N(\xi)$ = approximate time varying expansion coefficients, Eq. (9a)
c_n^m = expansion coefficient, Eq. (29)
$f(t)$ = time varying specified boundary temperature at $x = 1$, Eq. (4a)
f_i = discrete temperature at $x = 1$, Eq. (4a)
$F(\xi)$ = transformed time varying temperature boundary condition at $\eta = 1$, Eq. (6c)
F_i = transformed discrete temperature at $\eta = 1$, Eq. (6c)
l = length of slab
L = differential operator defined in Eq. (6b)
$N(\lambda_m)$ = normalization integrals
$Q(\xi)$ = transformed heat flux, Eq. (6f)
R_N = residual function defined in Eq. (13)
$R_N^i(\xi)$ = temporal residual defined in Eq. (22c)
$\hat{R}_N^1(\xi)$ = temporal residual function defined in Eq. (22a)
t = dimensionless time, $\alpha t_o/l^2$
t_o = dimensional time
$t_{\max}$ = maximum dimensionless time of interest
T = temperature
$T_m(\eta)$ = Chebyshev polynomial of the first kind
x = dimensionless space, x_o/l
x_o = dimensional space

Greek

α = thermal diffusivity
δ = dirac delta function
η = transformed spatial variable, Eq. (5a)
η_j = spatial collocation point, Eq. (14c)
θ = transformed temperature
θ_N = approximate transformed temperature, Eq. (9a)
Θ_{N+1} = approximate transformed temperature, Eq. (8)
λ = constant, $t_{\max}/2$
λ_m = eigenvalue
ξ = transformed time, Eq. (5b)
ξ_k = temporal collocation point, Eq. (14b)
σ = constant, Eq. (27)
$\Psi_m(\eta)$ = spatial trial function, Eq. (9b)
$\omega_m(\eta)$ = spatial trial function, Eq. (17b)
$\Omega_{m,n}(\eta, \xi)$ = space-time trial function, Eq. (19b)
$\hat{\Omega}_{m,n}(\eta, \xi)$ = space-time trial function with embedded constraint, Eq. (30b)

4 Solution Methodology

In this section a weighted-residual methodology is provided for developing an approximate solution for the unknown temperature $\theta(\eta, \xi)$ and, in particular, the resolution of the surface temperature $\theta(-1, \xi)$ and its corresponding surface heat flux, $Q(\xi)$. To begin, consideration is directed toward having continuous surface data, i.e., $F(\xi)$. Later we develop a corresponding method that directly utilizes discrete data. This second approach illustrates that presmoothing of the data is unnecessary. The proposed nontraditional time implementation follows from Frankel and Keyhani (1996), Frankel and Osborne (1996), and Frankel (1996b).

(i) Continuous Input, $F(\xi)$. To begin, let the unknown function $\theta(\eta, \xi)$ be represented by the series expansion

$$\theta(\eta, \xi) = \sum_{m=0}^{\infty} a_m(\xi) T_m(\eta), \quad (\eta, \xi) \in (-1, 1), \quad (7a)$$

where the spatial basis functions $\{T_m(\eta)\}_{m=0}^{\infty}$ are chosen as Chebyshev polynomials of the first kind (Rivlin, 1974) and are explicitly given by

$$T_m(\eta) = \cos [m \cos^{-1} \eta], \quad m = 0, 1, \ldots \quad (7b)$$

Chebyshev polynomials have several computational features and have been used with much success in solving problems that arise in fluid mechanics (Orszag, 1971), solid mechanics (Kaya and Erdogen, 1987), and radiative heat transfer (Frankel, 1995a, b). Though this study uses this basis set, other basis sets have yet to be explored and may possess attributes worth exploiting. Additionally, finite difference and finite element analogs will become evident as the method is presented. The unknown time varying expansion coefficients are denoted by the infinite set $\{a_m(\xi)\}_{m=0}^{\infty}$. In practice, this infinite series representation must be truncated after a finite number of terms, say $N + 1$, and thus Eq. $(7a)$ must be reconsidered as

$$\theta(\eta, \xi) \approx \Theta_{N+1}(\eta, \xi) = \sum_{m=0}^{N+1} a_m^{N+1}(\xi) T_m(\eta), \quad (\eta, \xi) \in (-1, 1), \quad (8)$$

where $a_m(\xi) \approx a_m^{N+1}(\xi), m = 0, 1, \ldots, N, N+1$ for sufficiently large N. It is possible to introduce the known auxiliary conditions expressed in Eqs. $(6c)-(6e)$ into the expansion. This removes a potential source of error from the numerical solution. Thus, with the basis set so chosen and given in Eq. $(7b)$, the trial functions can be devised in such a manner to incorporate the known boundary and initial conditions. Upon introducing the one-sided boundary conditions at $\eta = 1$, and after a straightforward set of analytic manipulations, the expansion for $\Theta_{N+1}(\eta, \xi)$ can be written as

$$\theta_N(\eta, \xi) = F(\xi) + \sum_{m=1}^{N} c_m^N(\xi) \Psi_m(\eta), \quad (9a)$$

where $\theta_N(\eta, \xi) = \Theta_{N+1}(\eta, \xi)$, and $c_m^N(\xi) = a_{m+1}^{N+1}(\xi)$, with

$$\Psi_m(\eta) = T_{m+1}(\eta) + (1 - \eta) \frac{dT_{m+1}}{d\eta}(1) - 1, \quad m = 1, 2, \ldots, N. \quad (9b)$$

Let

$$c_m^N(\xi) = \sum_{n=0}^{p_m} b_n^m T_n(\xi), \quad m = 1, 2, \ldots, N, \quad (10)$$

where the time varying expansion coefficients are expressed in terms of a finite sum of Chebyshev polynomials of the first kind and are given in Eq. $(7b)$ when $\eta \to \xi$ and $m \to n$. Substituting Eq. (10) into Eq. $(9a)$ for $c_m^N(\xi)$ produces

$$\theta_N(\eta, \xi) = F(\xi) + \sum_{m=1}^{N} \sum_{n=0}^{p_m} b_n^m T_n(\xi) \Psi_m(\eta). \quad (11)$$

Next, the initial condition is introduced into the series expansion shown in Eq. (11) to produce

$$\theta_N(\eta, \xi) = F(\xi) + \sum_{m=1}^{N} \sum_{n=1}^{p_m} b_n^m [T_n(\xi) + (-1)^{n+1}] \Psi_m(\eta), \quad (\eta, \xi) \in [-1, 1]. \quad (12)$$

With this expansion all known auxiliary conditions are exactly satisfied.

Clearly, from viewing Eq. (12), the expansion coefficients $b_n^m, n = 1, 2, \ldots, p_m, m = 1, 2, \ldots, N$ needs to be determined by some manner. The weighted-residual method of collocation is now incorporated to illustrate the principle of the proposed methodology. Following Finlayson (1972), we substitute the expansion for the temperature into the field equation displayed in Eq. $(6a)$ to arrive at the residual equation

$$R_N(\theta_N(\eta, \xi)) = L[\theta_N(\eta, \xi)], \quad (\eta, \xi) \in [-1, 1]. \quad (13)$$

The collocation method is defined through the orthogonality statement (Finlayson, 1972)

$$\langle R_N(\theta_N(\eta, \xi)), \delta(\eta - \eta_j, \xi - \xi_k) \rangle_1 = 0, \quad k = 1, 2, \ldots, p_j; \quad j = 1, 2, \ldots, N, \quad (14a)$$

where $\xi_k, k = 1, 2, \ldots, p_j$ and $\eta_j, j = 1, 2, \ldots, N$ are prescribed temporal and spatial collocation points, respectively. (For notational simplicity we omit the "j" dependency on ξ_k.) For the sake of demonstration purposes we define these points by the open rules (Delves and Mohamad, 1988)

$$\xi_k = \cos\left(\frac{(2k-1)\pi}{2p_j}\right), \quad k = 1, 2, \ldots, p_j, \quad (14b)$$

$$\eta_j = \cos\left(\frac{(2j-1)\pi}{2N}\right), \quad j = 1, 2, \ldots, N. \quad (14c)$$

Upon substituting Eq. (13) into Eq. $(14a)$ where Eq. (12) is explicitly used in place of $\theta_N(\eta, \xi)$, we arrive at

$$\sum_{m=1}^{N} \sum_{n=1}^{p_m} b_n^m L[(T_n(\xi_k) + (-1)^{n+1}) \Psi_m(\eta_j)] = -L[F(\xi_k)], \quad k = 1, 2, \ldots, p_j; \quad j = 1, 2, \ldots, N. \quad (15)$$

Equation (15) describes a system of linear algebraic equations for the unknown expansion coefficients $\{b_n^m\}, n = 1, 2, \ldots, p_m; m = 1, 2, \ldots, N$. Once these coefficients are determined we can reconstruct the solution for $\theta_N(\eta, \xi)$ through Eq. (12).

(ii) Discrete Input, $F_i, i = 1, 2, \ldots, M$. The direct use of the given probe data is highly appealing since no presmoothing is assumed. The data stream or streams can be directly imported into the numerical code and utilized as such in the actual computation. Also, the proposed approach possesses obvious generalization to multidimensional geometries and multiprobe inputs. In the context of the weighted-residual approach, we begin in a similar manner as outlined in the investigation of situation (i). Let

$$\theta(\eta, \xi) = \sum_{m=0}^{\infty} a_m(\xi) T_m(\eta), \quad (16a)$$

or upon truncating the series we write

$$\theta(\eta, \xi) \approx \theta_N(\eta, \xi) = \sum_{m=0}^{N} a_m^N(\xi) T_m(\eta). \qquad (16b)$$

Following our previous logic we can incorporate the known functionally explicit boundary condition displayed in Eq. (6*d*) to arrive at

$$\theta_N(\eta, \xi) = \sum_{m=1}^{N} b_m^N(\xi) \omega_m(\eta), \qquad (17a)$$

where

$$\omega_m(\eta) = \begin{cases} 1, & m = 1; \\ T_m(\eta) - \eta \dfrac{dT_m}{d\eta}(1), & m = 2, 3, \ldots, N, \end{cases} \qquad (17b)$$

with $b_1^N(\xi) = a_0^N(\xi)$ and $b_m^N(\xi) = a_m^N(\xi)$, $m = 2, 3, \ldots, N$. As before, we assume

$$b_m^N(\xi) = \sum_{n=0}^{p_m} b_n^m T_n(\xi), \qquad (18)$$

and upon substituting Eq. (18) into Eq. (17*a*) and making use of the known initial condition shown in Eq. (6*e*) we find

$$\theta_N(\eta, \xi) = \sum_{m=1}^{N} \sum_{n=1}^{p_m} b_n^m \Omega_{m,n}(\eta, \xi), \qquad (19a)$$

where the trial function becomes

$$\Omega_{m,n}(\eta, \xi) = [T_n(\xi) + (-1)^{n+1}] \omega_m(\eta)$$
$$n = 1, 2, \ldots, p_m; \quad m = 1, 2, \ldots, N. \qquad (19b)$$

Unlike our previous development the last known boundary condition, namely Eq. (6*c*) where it is understood that discrete data is provided, cannot be used at this juncture. It is clear from Eq. (19*a*) that the unknown expansion coefficients need resolution. Again, we call upon the weighted-residual method for assisting in acquiring these constants. Substituting the expansion shown in Eq. (19*a*) into Eq. (6*a*) produces the residual equation

$$R_N(\theta_N(\eta, \xi)) = L[\theta_N(\eta, \xi)] = \sum_{m=1}^{N} \sum_{n=1}^{p_m} b_n^m L[\Omega_{m,n}(\eta, \xi)],$$
$$(\eta, \xi) \in [-1, 1]. \qquad (20)$$

However, we now propose, when discrete data is prescribed at discrete times, to use spatial collocation while implementing a temporal, discrete least-squares approach. Though this presentation is in the context of a single spatial dimension, it is apparent that this approach is extendable to multidimensions. The traditional dilemma associated with these ill-posed problems typically manifests itself through the temporal variable. This

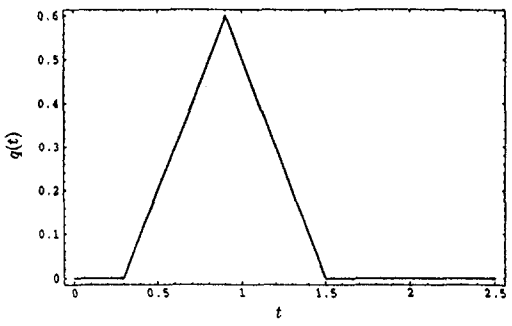

Fig. 1 Classic Beck's problem having triangular surface heat flux imposed at $x = 0$ for $t > 0$

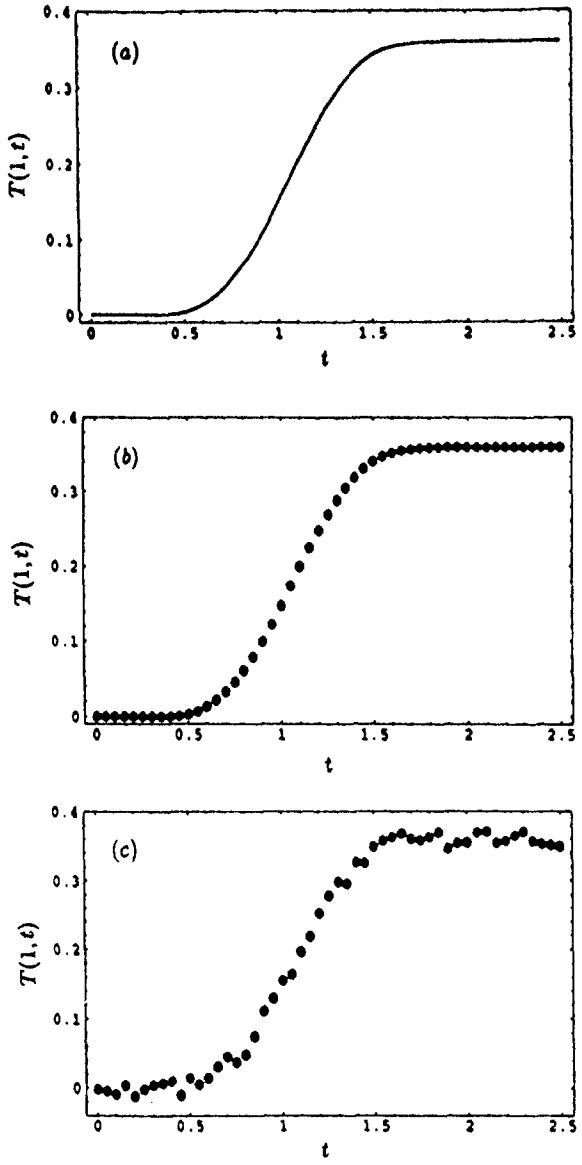

Fig. 2 Imposed overspecified surface temperature at $x = 1$ for (*a*) continuous input, (*b*) discrete noiseless data, and (*c*) discrete noisy data with $\sigma = 0.005$

fundamental treatment strongly suggests that the approach offered here may represent a fundamental clue on resolving a broad class of inverse problems. It should also be evident that conventional methods, such as the finite element method, can be used in these problems with the understanding that a nontraditional time treatment should be considered.

Two inner product statements are developed for probe and nonprobe locations. For the one-dimensional one-probe problem at hand we define the spatial collocation points by the closed rule (Delves and Mohamad, 1988).

$$\eta_j = \cos\left(\frac{(j-1)\pi}{N-1}\right), \quad j = 1, 2, \ldots, N \qquad (21)$$

The closed rule includes the end points. The rationale for presenting the closed rule is evident since we want the probe location to coincide with a point in the collocation set. With this set of collocation points the probe location at $\eta = 1$ corresponds to $\eta_1 = 1$, i.e., $j = 1$. At the probe location the data stream is discrete and known; therefore, the orthogonality statement for the discrete least-squares method is

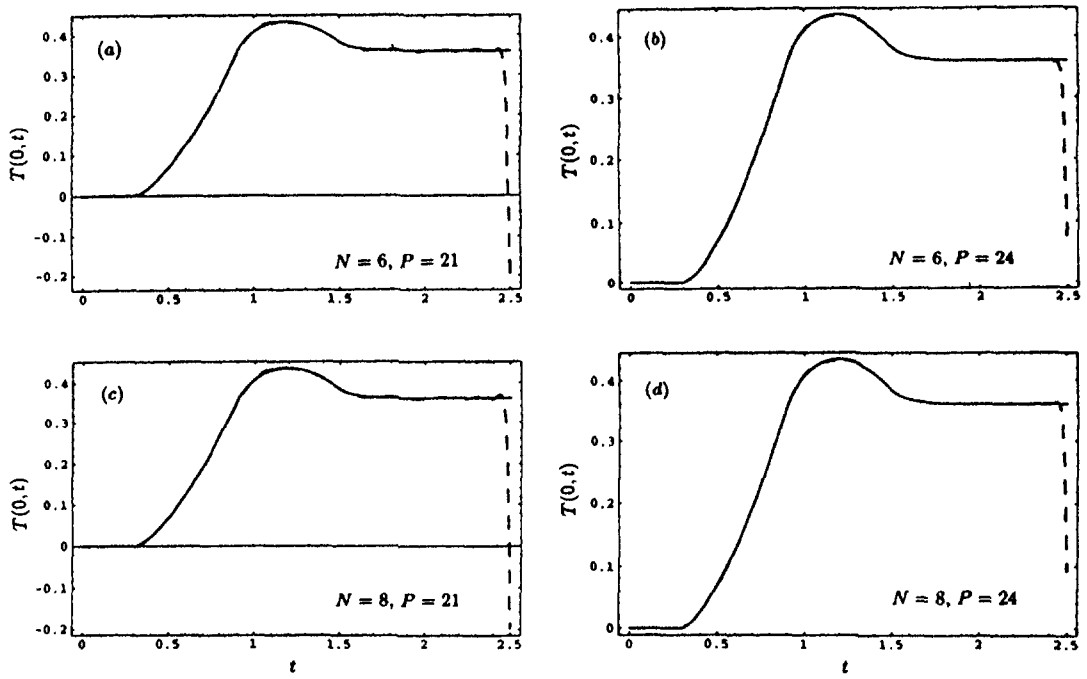

Fig. 3 Predicted surface temperature $T(0, t)$ for Case (i) using input data shown in Fig. 2*a* when: (*a*) $N = 6$, $P = 21$; (*b*) $N = 6$, $P = 24$; (*c*) $N = 8$, $P = 21$; and (*d*) $N = 8$, $P = 24$

$$\left\langle \hat{R}^1_N(\xi), \frac{\partial \hat{R}^1_N}{\partial b^1_k}(\xi) \right\rangle = 0, \quad j = 1, \tag{22a}$$

$$\left\langle R^j_N(\xi), \frac{\partial R^j_N}{\partial b^j_k}(\xi) \right\rangle = 0, \quad j = 2, 3, \ldots, N, \tag{22b}$$

while the orthogonality statement supporting spatial collocation and the discrete least-squares method at nonprobe ($j = 2, 3, \ldots, N$) locations is

where

$$R^j_N(\xi) = \langle R_N(\theta_N(\eta, \xi)), \delta(\eta - \eta_j) \rangle, \quad j = 1, 2, \ldots, N. \tag{22c}$$

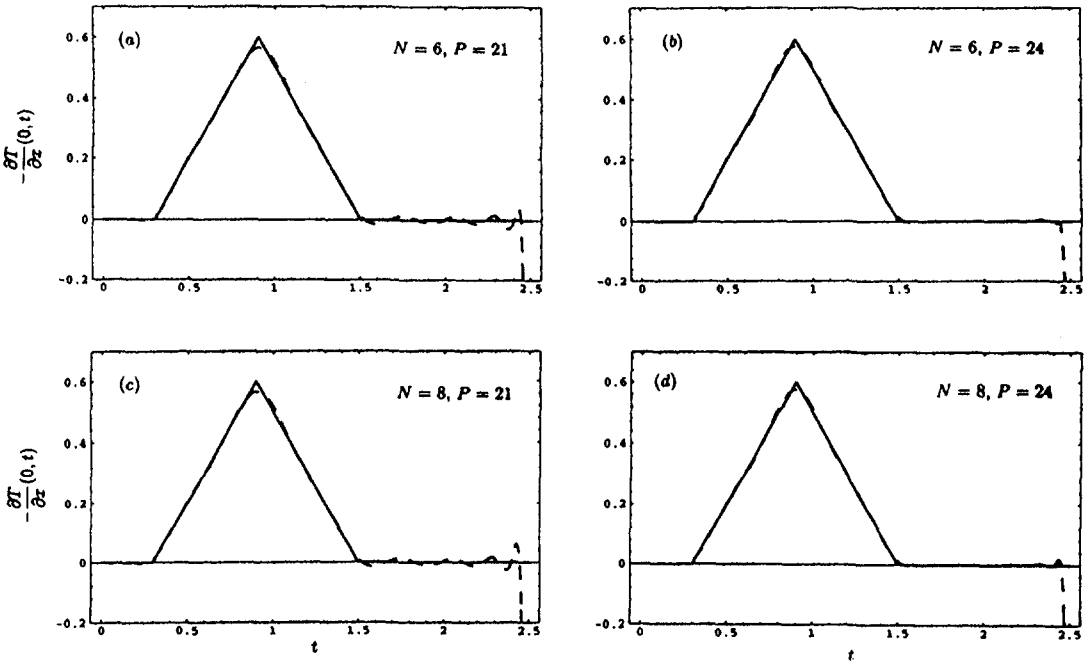

Fig. 4 Predicted surface heat flux $q(0, t) = -T_x(0, t)$ for Case (i) using input data shown in Fig. 2*a* when: (*a*) $N = 6$, $P = 21$; (*b*) $N = 6$, $P = 24$; (*c*) $N = 8$, $P = 21$; and (*d*) $N = 8$, $P = 24$

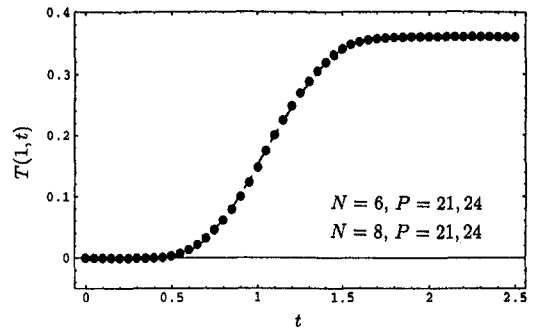

Fig. 5 Resulting surface temperature $T(1, t)$ for Case (ii) using the error-less discrete data shown in Fig. 2b

The residual function needed in Eqs. (22b) and (22c) is described by Eq. (20), while the residual function $\hat{R}_N^1(\xi)$ is determined from the data stream located at $\eta_1 = 1$ ($j = 1$).

The inner product shown in Eq. (22c) describes the action of collocation in the spatial variable. Upon substituting Eq. (20) into Eq. (22c) we explicitly find

$$R_N^j(\xi) = \sum_{m=1}^{N} \sum_{n=1}^{P_m} b_n^m L[\Omega_{m,n}(\eta_j, \xi)], \quad j = 1, 2, \ldots, N. \quad (23)$$

Clearly, at this point time is still represented by a continuous function at each distinct collocation point j. Equation (23) is valid at node $j = 1$, although we will disregard this equation at that node in lieu of using the data stream.

To develop explicit and usable relations for the inner product displayed in Eq. (22a) for the probe stream, we appeal to the classical definition of the discrete least-squares method, i.e.,

$$S_1 = \|\hat{R}_N^1\|_2^2 = \sum_{i=1}^{M} (\theta_N(\eta_1, \xi_i) - \theta_i)^2, \quad (24a)$$

or, upon substituting the expansion for $\theta_N(\eta, \xi)$ as shown in Eq. (19a) into Eq. (24a), we find that

$$S_1 = \sum_{i=1}^{M} \Big(\sum_{m=1}^{N} \sum_{n=1}^{P_m} b_n^m \Omega_{m,n}(\eta_1, \xi_i) - \theta_i \Big)^2. \quad (24b)$$

Minimizing this expression with respect to b_k^1 for $k = 1, 2, \ldots, p_1$ produces

$$\frac{\partial S_1}{\partial b_k^1} = 2 \sum_{i=1}^{M} \Big(\sum_{m=1}^{N} \sum_{n=1}^{P_m} b_n^m \Omega_{m,n}(\eta_1, \xi_i) - \theta_i \Big) \Omega_{1,k}(\eta_1, \xi_i) = 0,$$

$$k = 1, 2, \ldots, p_1, \quad (25a)$$

or, upon some simplification, we find that

$$\sum_{m=1}^{N} \sum_{n=1}^{P_m} b_n^m \Big(\sum_{i=1}^{M} \Omega_{m,n}(\eta_1, \xi_i) \Omega_{1,k}(\eta_1, \xi_i) \Big) = \sum_{i=1}^{M} \theta_i \Omega_{1,k}(\eta_1, \xi_i),$$

$$k = 1, 2, \ldots, p_1. \quad (25b)$$

Next, we present the methodology for the mathematical statement displayed in Eq. (22b). Let

$$S_j = \|R_N^j\|_2^2 = \sum_{i=1}^{M} \Big(\sum_{m=1}^{N} \sum_{n=1}^{P_m} b_n^m L[\Omega_{m,n}(\eta_j, \xi_i)] \Big)^2,$$

$$j = 2, 3, \ldots, N. \quad (26a)$$

Following Frankel (1996a), we minimize S_j with respect to each coefficient b_k^j for fixed j, $j = 2, 3, \ldots, N$ in the finite set. Doing so yields

$$\frac{\partial S_j}{\partial b_k^j} = 2 \sum_{i=1}^{M} \Big(\sum_{m=1}^{N} \sum_{n=1}^{P_m} b_n^m L[\Omega_{m,n}(\eta_j, \xi_i)] \Big) L[\Omega_{j,k}(\eta_j, \xi_i)] = 0,$$

$$k = 1, 2, \ldots, p_j; \quad j = 2, 3, \ldots, N, \quad (26b)$$

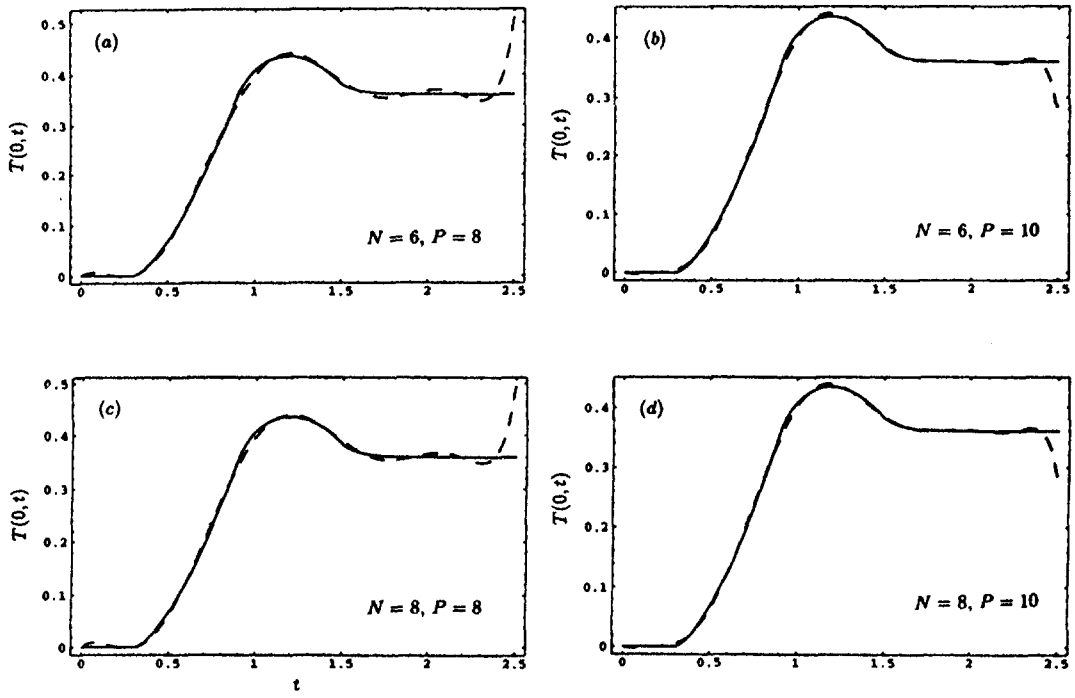

Fig. 6 Predicted surface temperature $T(0, t)$ for Case (ii) using the discrete input data shown in Fig. 2b when: (a) $N = 6$, $P = 8$; (b) $N = 6$, $P = 10$; (c) $N = 8$, $P = 8$; and (d) $N = 8$, $P = 10$

or

$$\sum_{m=1}^{N}\sum_{n=1}^{P_m} b_n^m\Big(\sum_{i=1}^{M} L[\Omega_{m,n}(\eta_j, \xi_i)]L[\Omega_{j,k}(\eta_j, \xi_i)]\Big) = 0,$$

$$k = 1, 2, \ldots, p_j; \quad j = 2, 3, \ldots, N. \quad (26c)$$

Notice that the expansion coefficients displayed in Eq. (25*b*) for $j = 1$ and Eq. (26*c*) for $j = 2, 3, \ldots, N$ are fully coupled through the two expressions. This linear system permits solution for the expansion coefficients.

5 Results

To test the proposed methodology we appeal to the benchmark case offered by Beck et al. (1985) involving a triangular surface heat flux at $x = 0$. This boundary condition permits an analytic solution for the temperature. Using this analytic result the surface temperature at $x = 1$ ($\eta = 1$) is obtained and used for setting up the inverse heat conduction problem. All figures and results are presented in the context of the original dimensionless variables x, t, T for convenience.

Using the analytic solution generated from the surface heat flux input shown in Fig. 1, we obtain $f(t)$, $t > 0$, ($F(\xi)$, and $\xi\epsilon[-1, 1]$). Figure 2 indicates the surface temperature history at $x = 1$ for the cases considered in this paper. Figure 2(*a*) illustrates the continuous input used for Case (i) to describe $f(t)(F(\xi))$. Figure 2(*b*) describes Case (ii), which involves discrete data at $x = 1$, where 50 equidistant samples are used when $\Delta t = t_{\max}/50$ with $t_{\max} = 2.5$. Figure 2(*c*) describes Case (iii) where random noise is introduced into the discrete set of 50 points through

$$T_i = T_{\text{exact}}(1, t_i) + \sigma\text{Random}(i), \quad (27)$$

where Random(i) is a random number between $[-1, 1]$, as generated through a random number generator. For this study σ was chosen as 0.005.

Following the mathematical development discussed in Section 4, Figs. 3 and 4 present the actual numerical outputs using the method of collocation when continuous input is provided at the overspecified boundary condition. In all the figures presented in this paper, the dashed line represents the numerical solution obtained using the methods of this paper. The solid line represents the analytic solution as obtained from Eq. (2) using the prescribed triangular heat flux shown in Fig. 1. Also, for convenience, $p_m = P$, $m = 1, 2, \ldots, N$, and thus no attempt has been made to optimize the methodology with regard to the selection of the temporal collocation set.

Figure 3 presents the predicted surface temperature $T(0, t)$ for $t\epsilon$ $(0, t_{\max} = 2.5)$ when a various number of terms are retained in the finite series representation shown in Eq. (12). From viewing this set of figures it is evident that the analytic solution can be graphically replicated by the proposed method with the exception of a small neighborhood near $t = t_{\max}$. Beck's future information method also suffers from not being able to resolve the solution to $t_{\max}$. From the physical viewpoint this is of no real significance since data can be collected beyond the value of $t_{\max}$, say to $t'_{\max}$, and then used to predict the results to value $t_{\max}$. The proposed methodology permits graphical convergence to be established independent of the effects of a free parameter. From viewing these plots it is evident that convergence is occuring as both N and P are increased. Additionally, no ill-conditioning effects are observed. If ill-conditioning effects would occur, then appearance of this condition would be observed as both N and P were increased.

Figure 4 presents the exact triangular surface heat flux input and predicted values using the method described in Section 4 when continuous data is specified at $x = 1$. It is interesting to note the accuracy of the method in resolving the triangular shape of the time varying surface heat flux. The Chebyshev basis adequately resolves the shape, and we can readily establish graphical convergence through the series of plots.

Figures 5–7 illustrate the predicted solution for Case (ii) using the method of temporal least-squares and the errorless data shown in Figure 2(*b*). It should be reiterated that this approach does not presmooth the data. A curve fit for the input data is obtained as part of the global solution for all space and time. Figure 5 displays the predicted solution for the surface temperature at $x = 1$. For convenience the data shown in Figure 2(*b*) is displayed in Figure 5. It is impossible to discern the difference among the predicted solutions for the displayed val-

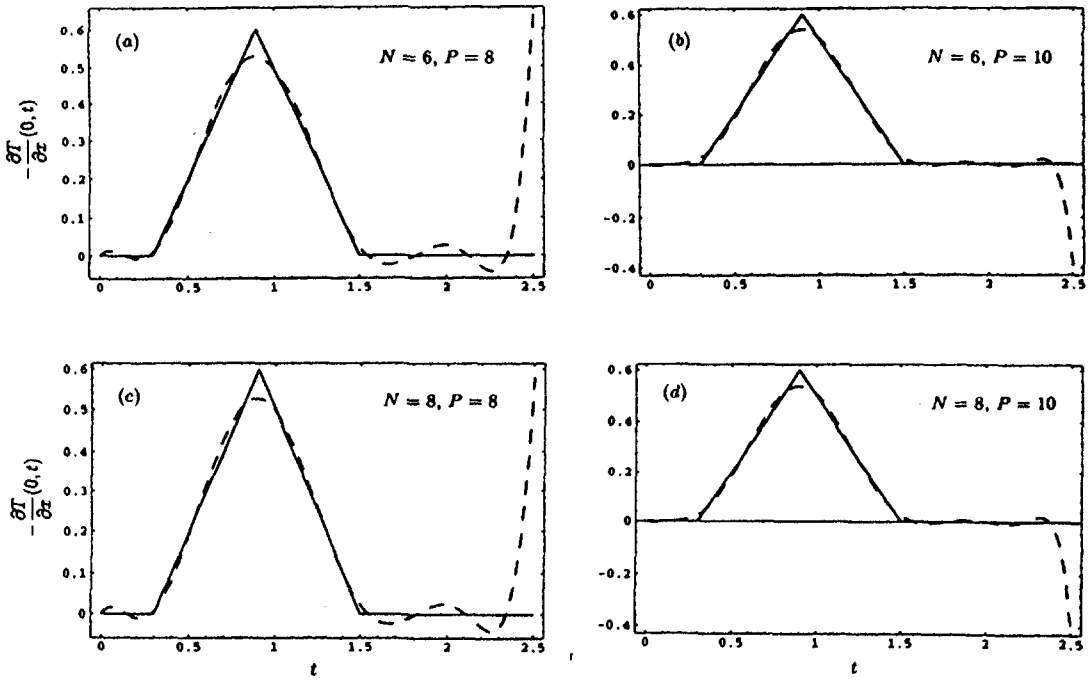

Fig. 7 Predicted surface heat flux $q(0, t) = -T_x(0, t)$ for Case (ii) using the discrete input data shown in Fig. 2*b* when: (*a*) $N = 6$, $P = 8$; (*b*) $N = 6$, $P = 10$; (*c*) $N = 8$, $P = 8$, and (*d*) $N = 8$, $P = 10$

Table 1 Maximum absolute error of the predicted surface heat flux using the indicated values of N and P for the errorless input case

N	P	$\epsilon_{N,P}$
6	8	0.0739
6	10	0.0621
8	8	0.0739
8	10	0.0621

ues of N and P. The curve fitted output for the input data is a result of the numerical determination of the expansion coefficients and thus eliminates the need to presmooth; in particular, to curve fit the data. Frankel and Keyhani (1996) have demonstrated that presmoothing data for inverse problems by curve fitting the input data set, can produce dramatically different output results depending on the degree of the polynomial fit. Frankel and Keyhani (1996) show that graphically comparable presmoothed inputs produce vastly different outputs owing to the ill-posed nature of the problem.

Figure 6 illustrates a set of plots indicating the effect of the number of terms retained in the finite series representation shown in Eq. (19*a*) on determining the surface temperature $T(0, t)$. The effect of the value for P on the behavior of the endpoint at $t = t_{max} = 2.5$ is shown in this set. Other than in the neighborhood about $t = t_{max}$, convergence is clearly being established as both N and P are increased. Figure 7 presents the surface heat flux predicted using the temporal least-squares method in conjunction with spatial collocation. Again, remarkable accuracy is displayed as well as the establishment of graphical convergence. To quantify the errors in the surface heat flux, let the standard error metric be defined as

$$\epsilon_{N,P} = \max_{i=1,\ldots,41} |q_{\text{exact}}(0, t_i) - q_i|,$$

where q_i represents the predicted surface heat flux at time t_i. Table 1 presents the maximum absolute error in the interval $t \in (0, 0.8t_{max} = 2)$ where $t_i = (i - 1)\Delta t$, $i = 1, 2, \ldots, 41$ and the values of N and P correspond to the values reported in Figs. 5–7. In this way a quantitative measure of the accuracy can be established for the exact data input case. Table 1 indicates that the maximum error is more strongly dependent on the value of P than N for this test case. Also, the maximum error in the defined time interval occurs at the peak of the triangular heat flux ($t = 0.9$), where the polynomial is attempting to reckon with the discontinuous derivative. Beck et al. (1985; pp. 182, 189, 193) also report that the maximum error coincides with the peak value of the surface heat flux. At all other times for $t < 2$ the error associated with the proposed technique does not exceed 0.025. In fact, the absolute error is typically less than 0.025, up to $t \approx 2.35$, which actually represents 94 percent of the chosen interval. By increasing the data set size, i.e., the number of samples M, the error will tend to decrease.

Figures 8–10 (Case (iii)) are intended to illustrate the effect of noise in establishing convergence of the solution. The noise level used in Figure 2(*c*) is higher than presented in Ozisik (1993). Figure 8 presents the surface temperature generated as part of the solution using the Case (iii) analysis. It is difficult to discern the four predicted solutions among each other as both N and P are varied. Figure 9 presents a set of solutions for the surface temperature at $x = 0$ using various polynomial orders for space and time. Again, it appears that convergence is established except in the small neighborhood about the temporal endpoint. Finally, Fig. 10 presents the predicted surface heat flux at $x = 0$ using various degrees of polynomials corresponding to Fig. 9. Again, it appears that convergence is established for the heat flux. It is expected that with this level of noise the predicted solution should be about the most noiseless solution.

6 Implications of the Application of the Proposed Methodology

The universal approach for solving transient phenomena, direct or inverse statements, involves a time-marching procedure, i.e., taking one step in time and solving for the spatial domain. In the present method, by inverting a matrix, a simultaneous solution for the entire domain is obtained. The fact that the solution for the entire time duration of interest is obtained through a matrix inversion gives an appearance that the time dependence is effectively formulated in an "elliptic" fashion. Therefore, it follows that specification of a constraint at $t = t_{max}$

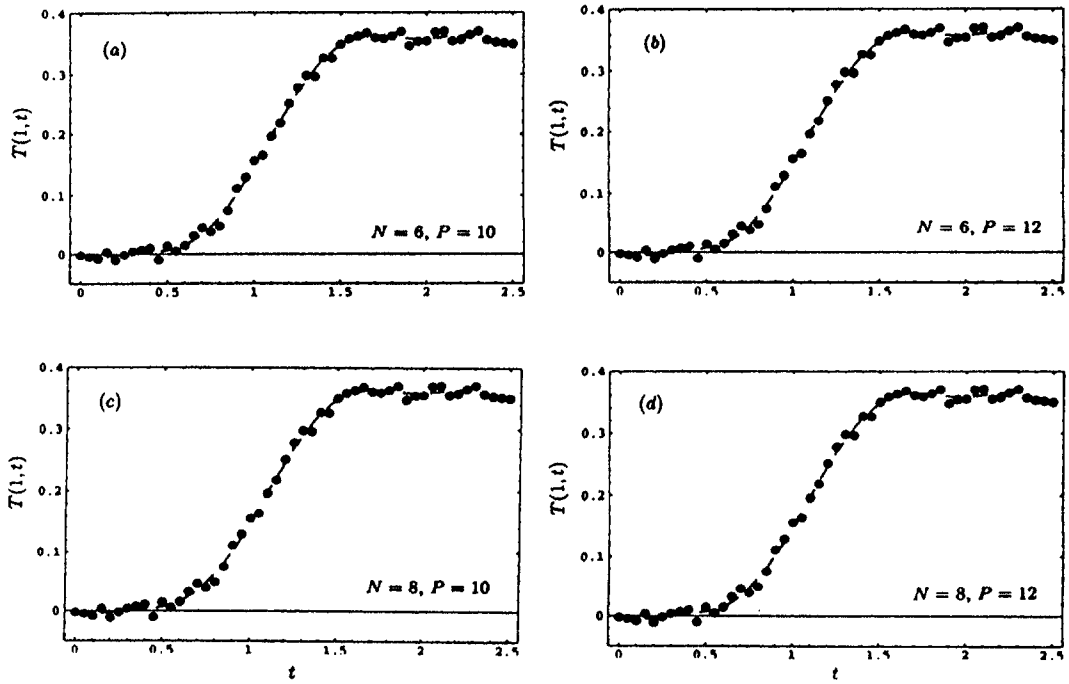

Fig. 8 Resulting surface temperature $T(1, t)$ for Case (iii) using the noisy discrete data shown in Fig. 2*c*

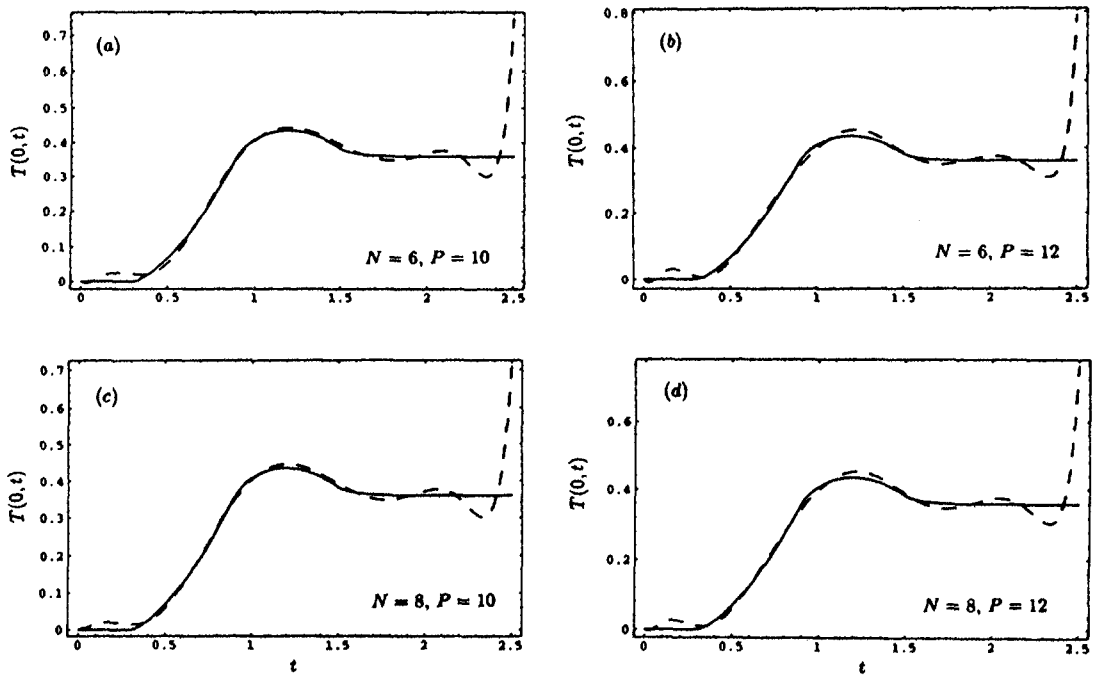

Fig. 9 Predicted surface temperature $T(0, t)$ for Case (iii) using the noisy discrete input data shown in Fig. 2c when: (a) $N = 6$, $P = 10$; (b) $N = 6$, $P = 12$; (c) $N = 8$, $P = 10$; and (d) $N = 8$, $P = 12$

(a "time boundary" condition) should improve the accuracy of the solution at $t = t_{\max}$.

Many problems subject to inverse analyses involve processes in which transition from one state of steady state to another occurs. For example, in a quenching process a heated specimen is quenched in a bath and allowed to cool to ambient temperature. Also, in experiments planned for the determination of properties, such as the thermal conductivity, one could collect temperature data until steady state is reached. It is clear that for an inverse analysis of such problems one could impose the constraint of

$$\frac{\partial T}{\partial t}(x, t_{\max}) = 0, \quad x \in [0, L], \tag{28a}$$

or in the present formulation

$$\frac{\partial \theta}{\partial \xi}(\eta, 1) = 0, \quad \eta \in [-1, 1]. \tag{28b}$$

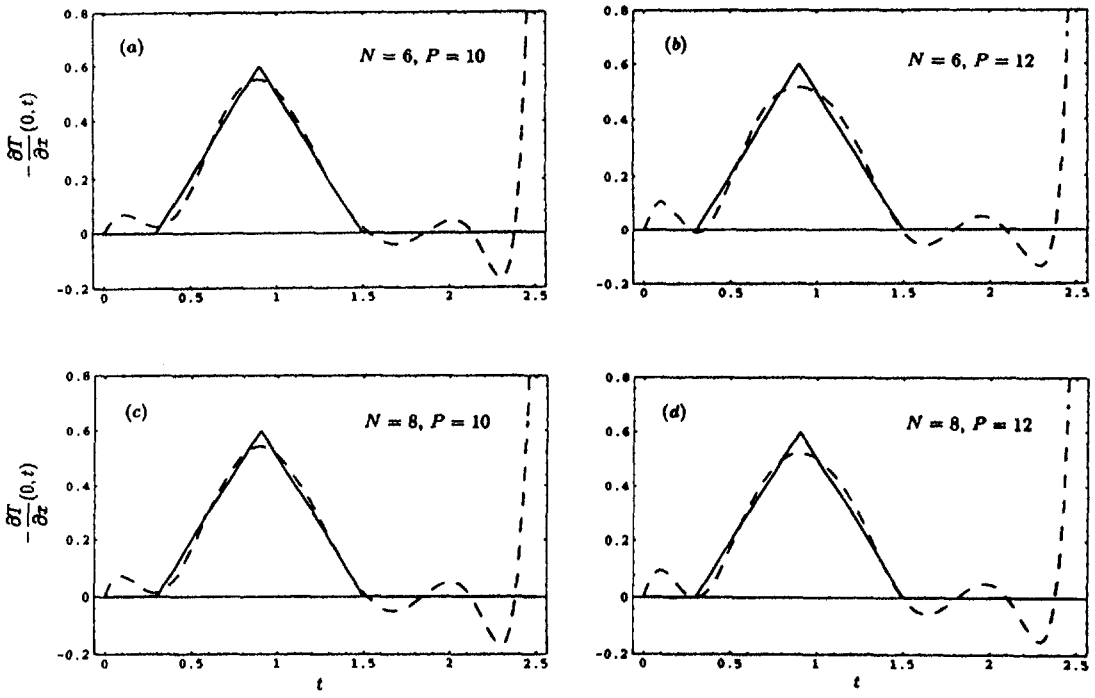

Fig. 10 Predicted surface heat flux $q(0, t) = -T_x(0, t)$ for Case (iii) using the noisy discrete input data shown in Fig. 2c when: (a) $N = 6$, $P = 10$; (b) $N = 6$, $P = 12$; (c) $N = 8$, $P = 10$, and (d) $N = 8$, $P = 12$

The temperature representation shown in Eq. (12) can be modified to include the constraint displayed in Eq. (28*b*). The resulting expansion for Case (i) becomes

$$\theta_N(\eta, \xi) = F(\xi) + \sum_{m=1}^{N} \sum_{n=1}^{r_m} c_n^m \left[T_{n+1}(\xi) + (-1)^n - (\xi + 1) \frac{dT_{n+1}}{d\xi}(1) \right] \Psi_m(\eta), \quad (\eta, \xi) \in [-1, 1], \quad (29)$$

when $dF/d\xi(1) = 0$ and where $c_n^m = b_{n+1}^m$ and $r_m = p_m - 1$. Meanwhile, the temperature representation shown in Eq. (19*a*) can be modified to include the constraint shown in Eq. (28*b*). The resulting expansion for Case (ii) becomes

$$\theta_N(\eta, \xi) = \sum_{m=1}^{N} \sum_{n=1}^{r_m} c_n^m \hat{\Omega}_{m,n}(\eta, \xi), \quad (30a)$$

where the trial function is

$$\hat{\Omega}_{m,n}(\eta, \xi) = \left[T_{n+1}(\xi) + (-1)^n - (1 + \xi) \frac{dT_{n+1}}{d\xi}(1) \right] \omega_m(\eta)$$

$$n = 1, 2, \ldots, r_m; \quad m = 1, 2, \ldots, N. \quad (30b)$$

The expansion coefficients $\{c_n^m\}$, $n = 1, 2, \ldots, r_m$, $m = 1, 2, \ldots, N$ are determined using the appropriate methodologies developed in section 4.

Using the constraint of steady state at $t = t_{\max}$, the solution for Cases (i) and (ii) are revisited and presented in Figs. 11 and 12, respectively. A comparison of Case (i) for the temperature and heat flux predictions shown in Fig. 11 with the corresponding unconstrained results presented in Figs. 3 and 4, clearly show that the solution at $t = t_{\max}$ is in excellent agreement with the exact solution. By contrasting the predictions shown in Fig. 12 with the corresponding results presented in Figs. 6 and 7, a similar observation can be made about the constraint results for Case (ii).

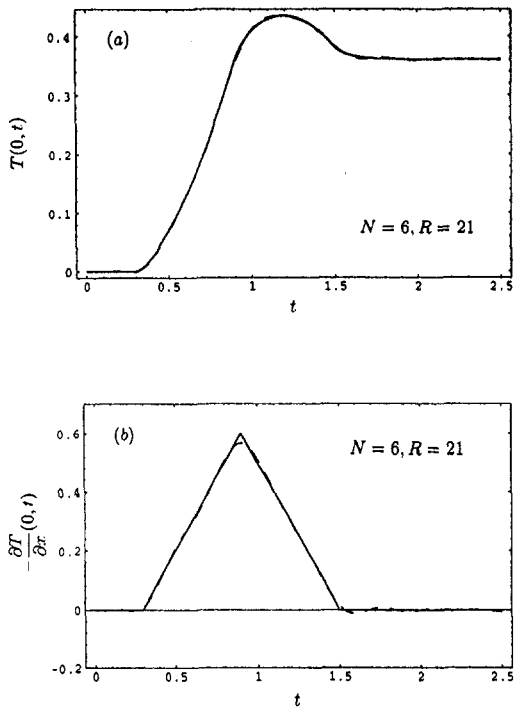

Fig. 11 Predicted (a) surface temperature $T(0, t)$ and (b) surface heat flux for Case (i) using input data shown in Fig. 2*a* and the imposed constraint shown in Eq. (28) when $N = 6$, $P = 21$

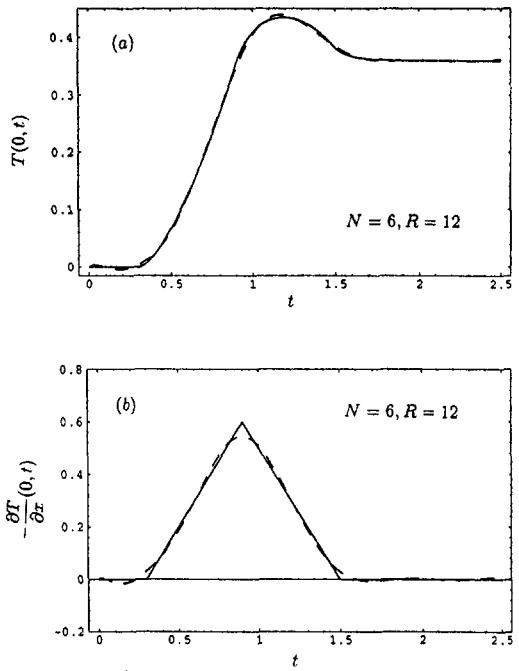

Fig. 12 Predicted (a) surface temperature $T(0, t)$ and (b) surface heat flux for Case (ii) using the discrete input data shown in Fig. 2*b* and the imposed constraint shown in Eq. (28) when $N = 6$, $P = 12$

7 Concluding Remarks

The simplified approach and appealing preliminary results offered in this paper indicate that the methodology should be investigated further. This observation is especially important since the methodology reported in Case (ii) has clear generalization to multiprobe and multidimensional situations without additional imagination. Extension to the multiprobe and multidimensional situation is on the agenda and will be reported in a later work. This approach allows for graphical convergence to be established, except possibly in the neighborhood of $t_{\max}$. This endpoint character is indicative of the ill-posed nature of the problem. The global time treatment "suppresses" or "pushes" the numerical instability toward the specified value of $t_{\max}$. This can be illustrated by varying the value of $t_{\max}$ and noting that the instability always appears in the neighborhood of $t_{\max}$. That is, by increasing the value for $t_{\max}$ and solving the $\eta - \xi$ domain, we effectively increase the domain of stability. This continual suppression can only take place through a global time treatment. Also, if additional physical constraints are available to the system, then the global time treatment can readily accommodate the inclusion of the constraints. The novel temporal time treatment offered here possesses several intriguing numerical features due to its global implicitness. This approach produces excellent results in direct problems and does not display any endpoint anamoly (Frankel and Osborne, 1996; Frankel, 1996b).

References

Beck, J. V., Blackwell, B., and St. Clair, C. R., 1985, *Inverse Heat Conduction*, John Wiley & Sons Inc., New York.

Delves, L. M., and Mohamad, J. L., 1988, *Computational Methods for Integral Equations*, Cambridge University Press, Cambridge, MA.

Finlayson, B. A., 1972, *The Method of Weighted Residuals and Variational Principles*, Academic Press, New York.

Frankel, J. I., 1995a, "A Galerkin Solution to a Regularized Cauchy Singular Integro-Differential Equation," *Quart. Appl. Math.*, Vol. 53, pp. 245–258.

Frankel, J. I., 1995b, "Cumulative Variable Formulation for Transient Conductive and Radiative Transport in Participating Media," *J. Thermophys. Heat Transfer*, Vol. 9, pp. 210–218.

Frankel, J. I., 1996a, "Direct Least-Square Solutions to Integral Equations Containing Discrete Data," *J. Thermophys. Heat Transfer*, Vol. 10, pp. 181–186.

Frankel, J. I., 1996b, "The Numerical Treatment of Time as a Fourth Computational Space in Hyperbolic Equations," *J. Thermophy. Heat Transfer,* in review.

Frankel, J. I., and Keyhani, K., 1996, "A New Approach for Solving Inverse Solidification Design," *Num. Heat Transfer, Part B,* Vol. 30, pp. 161–178.

Frankel, J. I., and Osborne, G. E., 1996, "A New Time Treatment for Solving Partial-Integro Differential Equations of Radiative Transport," *IMA J. Num. Anal.,* in review.

Kaya, A. C., and Erdogen, F., 1987, "On the Solution of Integral Equations with Strongly Singular Kernels," *Quart. Appl. Math.,* Vol. 45, pp. 105–122.

Orszag, S. A., 1971, "Accurate Solution of the Orr-Sommerfeld Stability Equation," *J. Fluid Mechanics,* Vol. 50, pp. 689–703.

Ozisik, M. N., 1993, *Heat Conduction,* John Wiley & Sons Inc., New York.

Rivlin, T. J., 1974, *The Chebyshev Polynomial,* John Wiley & Sons Inc., New York.

Wing, G. M., 1991, *A Primer on Integral Equations of the First Kind,* SIAM, Philadelphia, PA.

Thermal Contact Conductance of Spherical Rough Metals

M. A. Lambert
Assistant Professor.
Department of Mechanical Engineering,
San Jose State University,
One Washington Square,
San Jose, CA 95192-0087
lambertm@isc.sjsu.edu
Mem. ASME.

L. S. Fletcher
Thomas A. Dietz Professor.
Department of Mechanical Engineering,
Texas A&M University,
College Station, TX 77843-3123
Fellow ASME.

Junction thermal conductance is an important consideration in such applications as thermally induced stresses in supersonic and hypersonic flight vehicles, nuclear reactor cooling, electronics packaging, spacecraft thermal control, gas turbine and internal combustion engine cooling, and cryogenic liquid storage. A fundamental problem in analyzing and predicting junction thermal conductance is determining thermal contact conductance of nonflat rough metals. Workable models have been previously derived for the limiting idealized cases of flat, rough, and spherical smooth surfaces. However, until now no tractable models have been advanced for nonflat rough "engineering" surfaces which are much more commonly dealt with in practice. The present investigation details the synthesis of previously derived models for macroscopically nonuniform thermal contact conductance and contact of nonflat rough spheres into a thermomechanical model, which is presented in an analytical/graphical format. The present model agrees well with representative experimental conductance results from the literature for stainless steel 303 and 304 with widely varying nonflatness (2 to 200 μm) and roughness (0.1 to 10 μm).

2.0 Introduction

A successful model for thermal contact conductance must actually consist of a combination of three models: thermal, mechanical (contact), and metrological (surface geometry). The mechanical and metrological models, which are interdependent, provide estimations of contact spot size, density, and distribution for use in the thermal model. A model by which thermal contact conductance of spherical rough metals may be simply predicted from contact load, material properties, and surface profile measurements would be of great practical value. The model should also be sufficiently robust to predict the conductance for nominally flat (though typically arbitrarily nonflat) rough metals.

Solutions for thermal contact conductance for the two bounding cases of flat rough surfaces (e.g., Cooper et al. (1969); Mikic (1974); Yovanovich (1982)) and spherical, smooth surfaces (e.g., Clausing and Chao (1965)) have been developed. The models by Mikic and Rohsenow (1966), Thomas and Sayles (1974), and Yovanovich and Burde (1978) for the contact conductance of rough, spherical surfaces are difficult to use.

Nishino et al. (1993) combined the thermal model by Mikic (1970) with the mechanical/metrological models by Greenwood and Tripp (1967) and Tsukada and Anno (1979) to obtain a model for thermal contact conductance of spherical rough metals for which both roughness and nonflatness significantly affect conductance. Mikic (1970) derived a thermal model associated with two simple nonuniform contact pressure distributions (i.e., periodic in one direction or axisymmetric). Greenwood and Tripp (1967) and Tsukada and Anno (1979) developed mechanical/metrological models for contacting rough spheres that predict how roughness causes the pressure distribution to deviate from the solution for smooth spheres by Hertz (1896). However, in order to employ the model by Nishino et al. (1993), the pressure distribution must be laboriously measured with pressure sensitive films. Also, they did not reduce the integrals in the thermal model by Mikic (1970) to a more readily usable format.

Contributed by the Heat Transfer Division for publication in the JOURNAL OF HEAT TRANSFER. Manuscript received by the Heat Transfer Division February 8, 1996; revision received April 16, 1997; Keywords: Conduction; Direct-Contact Heat Transfer; Thermal Packaging. Associate Technical Editor: T. Tong.

3.0 Model Development

3.1 Assumptions of the Present Model.

1 Contacting surfaces are circular and macroscopically spherical (see section 3.2). Surfaces are microscopically rough with a Gaussian height distribution. It is unknown how significant deviations from a Gaussian distribution affect contact conductance.
2 The average flow pressure equals the contact microhardness, H_c, which is determined from H_V and σ/m (Hegazy, 1985). H_c corresponds to the mean pressure within the macroscopic contact region ($0 \leq r \leq a_L$).
3 Heat flux only occurs through solid contacts. That is, fluid gap conductance and radiative heat transfer are negligible.

3.2 Selection of Spherical Macroscopic Surface Profile. Though a model capable of dealing with completely arbitrary surface profiles would have universal applicability, it would probably be, at best, overly cumbersome if not intractable. One simplification that may be introduced without sacrificing wide applicability is the assumption that the macroscopic topography can be described by one or a few parameters, just as the microscopic topography is often adequately described by combined root-mean-square roughness, σ, and combined mean absolute profile slope, m. A sphere is the simplest macroscopic profile, because it is completely described by one parameter, its radius of curvature is ρ. The modeled geometry is illustrated in Fig. 1.

Clausing and Chao (1965), Mikic and Rohsenow (1966), Thomas and Sayles (1974), Yovanovich and Burde (1978), and Nishino et al. (1993) addressed spherical surfaces in their models for macroscopic thermal constriction resistance. This assumption is often justifiable because nominally flat engineering surfaces are often spherical, or at least are quite often crowned (convex) with a monotonic curvature in at least one direction.

3.3 Thermal Contact Resistance Model for Nonuniform Contact Pressure by Mikic (1970). Mikic (1970) derived expressions for the total (microscopic, $R_{c,S}$, plus macroscopic, $R_{c,L}$) thermal contact resistance due to a nonuniform, axisymmetric contact pressure distribution:

$$R_{c,S} = 0.345 \frac{\sigma}{km}\left[\int_0^\infty \frac{r}{b_L}\left(\frac{P}{H_c}\right)^{0.985} d\left(\frac{r}{b_L}\right)\right]^{-1} \quad (1)$$

$$R_{c,L} = 8\frac{b_L}{k}\sum_{n=1}^{\infty}\frac{\left[\int_0^\infty \frac{r}{b_L}\left(\frac{P}{P_{\text{avg}}}\right)^{0.985} J_0\left(\zeta_n \frac{r}{b_L}\right) d\left(\frac{r}{b_L}\right)\right]^2}{\zeta_n J_0^2(\zeta_n)}. \quad (2)$$

$R_{c,S}$ is the resistance to heat flux caused by imperfect contact at the microscopic level due to roughness; whereas $R_{c,L}$ is the resistance arising from macroscopic gaps between surfaces resulting from nonflatness. Radial distance, r, is measured from the center of the circular contact region, k is harmonic mean thermal conductivity, H_c is contact microhardness, and b_L is the radius of the contact surface. $P\,[=P(r)]$ and P_{avg} are the local and average contact pressure, respectively. Defining the pressure distribution remains the crux of the problem.

3.4 Pressure Distribution for Contact of Elastic Rough Spheres. The present thermal-mechanical model incorporates a contact model by Greenwood and Tripp (1967) for elastic deformation of rough spheres. However, at the microscopic level deformation is entirely or predominantly plastic, as borne out by the work of Sridhar and Yovanovich (1993) for all but possibly the smoothest surfaces ($\sigma \leq 0.2$ to 0.3 μm). For applications in which thermal contact conductance is relevant, contact loads are usually sufficient to cause only elastic deformation at the macroscopic level. Because macroscopic deformation is often much greater than microscopic deformation for spherical surfaces, the Greenwood and Tripp (1967) model was deemed appropriate.

According to Greenwood and Tripp (1967), the mean plane separation $u(r)$ and u_0 and deformation $w(r)$ and w_0 for deformable, rough, elastic spheres are related by:

$$u(r) = u_0 + r^2/2\rho + w(r) - w_0. \quad (3)$$

Greenwood and Tripp (1967) nondimensionalized variables by including σ and ρ.

$$u_0^* = u_0/\sigma \quad w_0^* = w_0/\sigma \quad r^* = r/\sqrt{2\rho\sigma}$$

$$u^*(r^*) = u(r)/\sigma \quad w^*(r^*) = w(r)/\sigma$$

$$u^*(r^*) = u_0^* + r^{*2} + w^*(r^*) - w_0^*$$

$$P^* = P/(E'\sqrt{\sigma/8\rho}) \quad L^* = 2L/(\sigma E'\sqrt{2\rho\sigma}) \quad (4)$$

L and L^* are dimensional load and dimensionless load, respectively. The pressure and displacement equations in dimensionless form are:

$$P^*(r^*) = \left(\frac{8}{3}\eta\sigma\sqrt{2\rho\beta}\right)\int_{u^*}^{\infty}(z^* - u^*)^{3/2}\frac{1}{\sqrt{2\pi}} \times \exp\left(-\frac{z^{*2}}{2}\right)dz^* \quad (5)$$

$$w^*(r^*) = \int_0^\infty r^* P^*(r^*\xi)\kappa d\xi \quad (r^* > 0) \quad (6)$$

$$w_0^* = \int_0^\infty P^*(\xi)d\xi \quad (r^* = 0) \quad (7)$$

where $z^* = z/\sigma$ is dimensionless height above mean plane of the rough surface, η is the number of microscopic asperities per unit area, β is the radius of curvature of the asperities, and κ is a function of the complete elliptic integral, $K(\xi)$.

To apply the model by Greenwood and Tripp (1967), a value for u_0^* is selected and initial values for $w^*(r^*)$ and w_0^* are

Nomenclature

a_L = radius of macrocontact region for rough spheres (L stands for large-scale), (m)
$a_{L,\text{Hz}}$ = radius of macrocontact region for smooth spheres from Hertz (1896), (m)
a_s = radius of microcontact (S stands for small-scale), (m)
b_L = radius of component (m)
b_s = radius of elemental heat flux channel supplying each microcontact (m)
E = modulus of elasticity (N/m^2)
E' = effective elastic modulus (N/m^2), $E' = [(1-\nu_1^2)/E_1 + (1-\nu_2^2)/E_2]^{-1}$
f_s, f_L = polynomial regression functions of b/a (Lambert, 1995)
g = polynomial regression function of b/a and L^* (Lambert, 1995)
h_c = thermal contact conductance (W/m^{2}K)
H_c = contact microhardness (N/m^2)
H_V = Vickers microhardness (N/m^2)
J_0, J_1 = Bessel functions of the first kind
k = harmonic mean thermal conductivity (W/mK), $k = 2k_1k_2/(k_1 + k_2)$
$K(\xi)$ = complete elliptic integral of modulus ξ
L = load (N)
m = combined mean absolute profile slope (m/m), $m = (m_1^2 + m_2^2)^{1/2}$
$P(r)$ = $[=P]$ local contact pressure at radius r from center of circular contact (N/m^2)
P_{app} = apparent contact pressure (N/m^2)
P_{avg} = average contact pressure (N/m^2)
P_0 = maximum contact pressure (at $r = 0$) for rough spheres (N/m^2)
$P_{0,\text{Hz}}$ = maximum contact pressure (at $r = 0$) for smooth spheres from Hertz (1986), (N/m^2)
r = radial displacement from center of axisymmetric contact (m)
R = thermal resistance (m^{2}K/W)
TIR = nonflatness (Total Included Reading), (m), TIR = TIR$_1$ + TIR$_2$
$u(r)$ = mean plane separation (m)
u_0 = mean plane separation at center of contact ($r = 0$) (m)
$w(r)$ = deformation due to load (m)
w_0 = deformation due to load at center of contact ($r = 0$) (m)
z = height above or below mean plane of surface (m)
β = radius of curvature of spherical asperity (m)
δ = crown drop of surface (m), $\delta = \delta_1 + \delta_2$
$\epsilon_L = b_L/a_L$
ζ_n = n^{th} root of Bessel function $J_1(\zeta_n)$
η = number of asperities (peaks) per unit area (1/m^2)
κ = function of complete elliptic integral K [$\kappa = K(\xi)$ for $\xi \leq 1$; $\kappa = K(1/\xi)$ for $\xi > 1$]
μ = micro = 10^{-6}, combined with meters or inches
ν = Poisson ratio
ξ = modulus of elliptic integral K
ρ = combined radius of curvature (m), $\rho = (1/\rho_1 + 1/\rho_2)^{-1}$
σ = combined root-mean-square (rms) roughness (m), $\sigma = (\sigma_1^2 + \sigma_2^2)^{1/2}$

Superscripts

$'$ = effective
$*$ = dimensionless, as defined in Eq. 4

Subscripts

L = large scale, macroscopic
n = index of summation
S = small scale, microscopic
0 = at center of contact ($r = 0$)
1 = specimen or surface 1
2 = specimen or surface 2

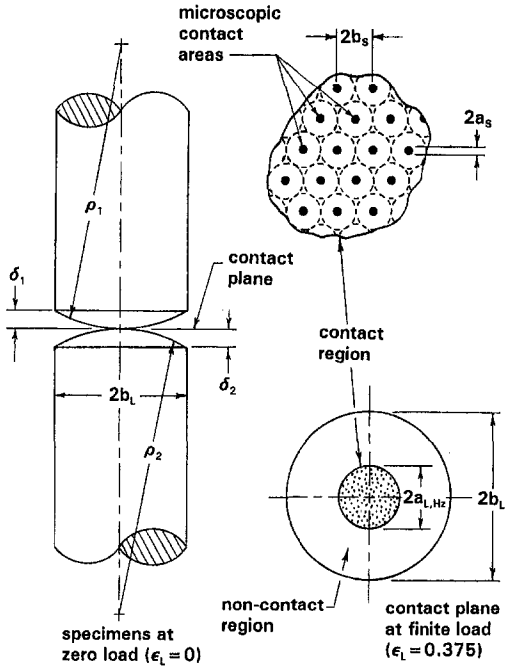

Fig. 1 Contacting spherical rough surfaces showing the macroscopic contact radius, $a_{L,Hz}$, predicted by Hertz (1896). Note that $a_{L,Hz} \leq a_L$. Also shown is an idealized array of microcontacts.

assumed. Equations 5, 6, and 7 are employed to alternately and iteratively to compute $w^*(r^*)$, w_0^*, and $P^*(r^*)$ until they converge. $P^*(r^*)$ is integrated and compared to L^*. If the two are significantly different, a new estimate of w_0^* is made, and the iterative displacement-pressure calculation procedure is repeated until the integrated load from $P^*(r^*)$ and L^* are essentially equal.

The value u_0^* may be varied over a wide range resulting in different solutions for $P^*(r^*)$, $w^*(r^*)$, and w_0^* for a single combination of load, surface profile, and elastic properties. Consequently, Greenwood and Tripp's (1967) model is under-constrained. A solution may be obtained even for the physically impossible case of a negative u_0^*, that is, a crossing of the mean planes of the two surfaces.

In the present study, realistic values of u_0^* were determined for each set of conditions (i.e., L, σ, ρ, and E'). The theoretical dimensional pressure, P_0, (the maximum contact pressure at the center ($r = 0$) of the circular contact region between rough spheres) was obtained from $P^*(r^*)$. P_0 was then normalized by dividing by the theoretical value of $P_{0,Hz}$, the maximum pressure at $r = 0$ for smooth spheres, according to Hertz (1896). Lambert (1995) determined correct values of u_0^* so that the computed $P_0/P_{0,Hz}$ equaled the experimental $P_0/P_{0,Hz}$ (plotted in Fig. 2) by Tsukada and Anno (1979) and Sasajima and Tsukada (1981). Their results are available for $L^* \geq 0.1$, that is, contacts for which the effect of sphericity is more pronounced. The trend in u_0^* was extrapolated for $L^* < 0.1$, then used to compute $P_0/P_{0,Hz}$ for $L^* < 0.1$.

Sasajima and Tsukada (1981) truncated the pressure distribution at an effective macroscopic contact radius, a_L, beyond which $P(r)$ becomes negligible. They defined $a_L/a_{L,Hz}$ to relate the actual macroscopic contact radius for rough spheres to the macroscopic contact radius for smooth spheres as predicted by Hertz (1896). Tsukada and Anno (1979) and Sasajima and Tsukada (1981) provided experimental values of $a_L/a_{L,Hz}$ for L^* greater than 4, as illustrated in Fig. 3. Values of $a_L/a_{L,Hz}$ for $L^* < 4$ were generated from the model by Lambert (1995).

The trends in Figs. 2 and 3 are explained as follows: $L^* = 2L/[\sigma E'(2\rho\sigma)^{1/2}]$ decreases as σ increases. Physically, this

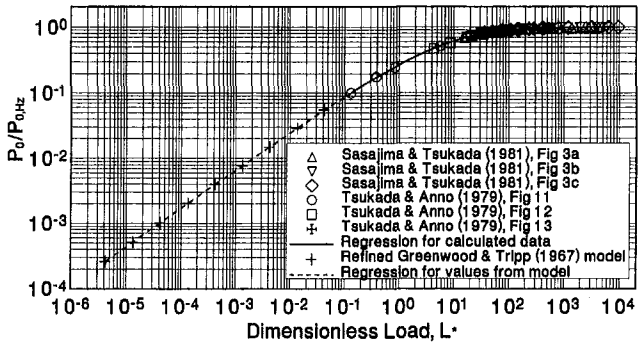

Fig. 2 Axial (maximum) pressure ratio, $P_0/P_{0,Hz}$, versus dimensionless load, L^*

means that load is spread over a greater portion of the surface by rising roughness. The pressure distribution becomes more uniform, reduced in intensity compared to the Hertz (1896) theory. Thus, $P_0/P_{0,Hz}$ decreases, while $a_L/a_{L,Hz}$ increases.

3.5 Model for Thermal Contact Conductance of Spherical Rough Metals. The present model was obtained by using the contact model by Greenwood and Tripp (1967), as refined herein, to define the pressure distribution, $P(r)$, in terms of L, H_c, E', σ, m, ρ, and b_L, then substituting $P(r)$ into Mikic's (1970) expressions (Eqs. 1 and 2) for $R_{c,S}$ and $R_{c,L}$. Lambert (1995) lists a FORTRAN 90 computer program implementing the present model.

Buckingham Pi dimensional analysis was applied to determine the effect of each physical parameter on $R_{c,S}^*$ and $R_{c,L}^*$, which resulted in the following correlations:

$$R_{c,S}^* = \frac{\left(\frac{R_{c,S}km}{\sigma}\right)\left(\frac{L}{H_c\rho\sigma}\right)^{0.95}\left(\frac{P_0}{P_{0,Hz}}\right)^{0.67}}{\left(\frac{b_L}{a_L}\right)^2 f_s\left(\frac{b_L}{a_L}\right)}$$

$$= 6.15(L^*)^{0.484} \tag{8}$$

$$R_{c,L}^* = \frac{\left(\frac{R_{c,L}kL}{\rho\sigma^2E'}\right)}{\left(\frac{P_0}{P_{0,Hz}}\right)^{0.20}\left(\frac{b_L}{a_L}\right)^2 f_L\left(\frac{b_L}{a_L}\right) g\left(\frac{b_L}{a_L}, L^*\right)}$$

$$= 1.44(L^*)^{0.954}. \tag{9}$$

Initially, component radius, b_L, was assumed to equal the macroscopic contact radius, a_L. Starting values of material prop-

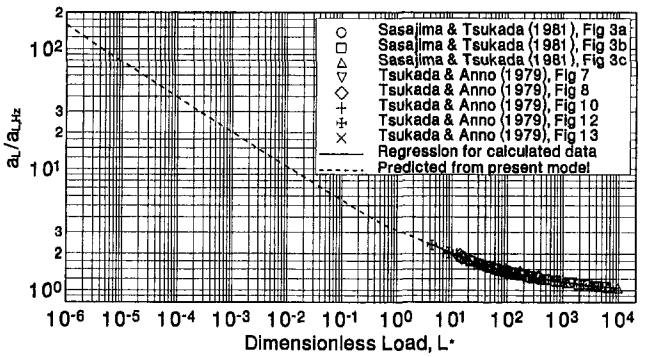

Fig. 3 Macrocontact radius ratio, $a_L/a_{L,Hz}$, versus dimensionless load, L^*

erties were selected as those for stainless steel 304 (H_c = 2800–4100 MPa, E = 207 GPa, ν = 0.30, and k = 14.9–16.2 W/mK). Next, wide ranges of load, L (10^{-4} to 10^6 N), and surface measurements, σ (0.1 to 10 μm), m (0.0316 to 0.316 m/m) ($m = (\sigma^{1/2} \times 10^6)/10$), and ρ (10^{-2} to 10^6 m), were used to compute a multitude of results for $R^*_{c,S}$ and $R^*_{c,L}$. Then, material properties were varied (H_c (490 to 4100 MPa), E (42.1 to 303 GPa), and k (6.7 to 391 W/mK)) to generate many additional results for $R^*_{c,S}$ and $R^*_{c,L}$. The ranges of material properties used encompass a host of structural alloys and metals, such as magnesium alloy AZ31B, aluminum alloys 2024-T4, 6061-T6, and 7075-T5, titanium alloy Ti-6A1-4V, copper, brass, nickel, beryllium, and stainless steel 304. Results were collapsed (superimposed) into single curves by the first two terms in the numerator of $R^*_{c,s}$ and the only term in the numerator of $R^*_{c,L}$, respectively.

The expressions for $R^*_{c,S}$ and $R^*_{c,L}$ were linearized into the power law regressions in terms of L^* on the right-hand sides of Eqs. 8 and 9 by inserting the term $P_0/P_{0,\mathrm{Hz}}$ raised to a different power in each equation. The dimensionless load, L^*, was varied from 4.2×10^{-5} (i.e., essentially optically flat for any realistically sized component) up to 1.3×10^4 (i.e., a smooth sphere for all practical purposes). The exponents of L^* have no readily apparent physical meaning. Finally, results were computed for the general case in which component radius, b_L, does not equal predicted macroscopic contact radius, a_L. The ratio b_L/a_L was varied from 10^{-4} (i.e., a nearly uniform pressure distribution, $P(r)$, since only the very center of the predicted $P(r)$ is actually brought to bear on the surface) up to 10^3 (i.e., a very small contact on very large surface, say a_L = 1 mm and b_L = 1.0 m). This considerably complicated the results, requiring inclusion of empirical correction factors, $1/f_s$, $1/f_L$, and $1/g$, in Eqs. 8 and 9 in addition to the expected term $(b_L/a_L)^2$. Polynomial functions for $P_0/P_{0,\mathrm{Hz}}$, $a_L/a_{L,\mathrm{Hz}}$, $1/f_s$, $1/f_L$, and $1/g$ are provided by Lambert (1995) and are plotted in Figs. 2–6, respectively. L^* is defined in Eq. 4, and b_L/a_L is determined from

$$\frac{b_L}{a_L} = \frac{b_L}{\left(\frac{a_L}{a_{L,\mathrm{Hz}}}\right)a_{L,\mathrm{Hz}}} = \frac{b_L}{\left(\frac{a_L}{a_{L,\mathrm{Hz}}}\right)\left(\frac{3L\rho}{4E'}\right)^{1/3}}. \qquad (10)$$

$R^*_{c,S}$ and $R^*_{c,L}$ yield the dimensionless contact conductance ($h^*_{c,S+L}$)

$$h^*_{c,S+L} = \frac{1}{R^*_{c,S} + R^*_{c,L}}. \qquad (11)$$

Both $R^*_{c,S}$ and $R^*_{c,L}$ increase with increasing L^*, which is directly proportional to load, L. This trend is opposite that exhibited by all other correlations of contact resistance versus load, which show that resistance decreases with increasing load. This departure of the present model from the common trend resulted from the way in which $R^*_{c,S}$ and $R^*_{c,L}$ were defined in terms of L^*, which is the most convenient and descriptive load parameter, since it includes load, elastic properties, roughness, and radius of curvature. Note that both $R^*_{c,S}$ and $R^*_{c,L}$ contain load, L, which is atypical of conductance correlations. However, because L is raised to different powers in $R^*_{c,S}$ and $R^*_{c,L}$, L could not be removed from these two parameters when combining them into a single dimensionless conductance, $h^*_{c,S+L}$, something not accomplished in any previous investigation. Predictions made via the present model are interpreted in the same manner as are other conductance models. That is, experimental data falling below $h^*_{c,S+L}$, as computed from the present model, are over-predicted by the model and vice versa.

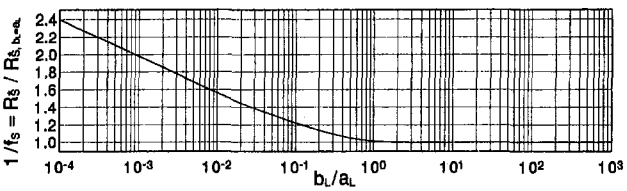

Fig. 4 Correction function $1/f_s$ versus radius ratio, a_L/b_L

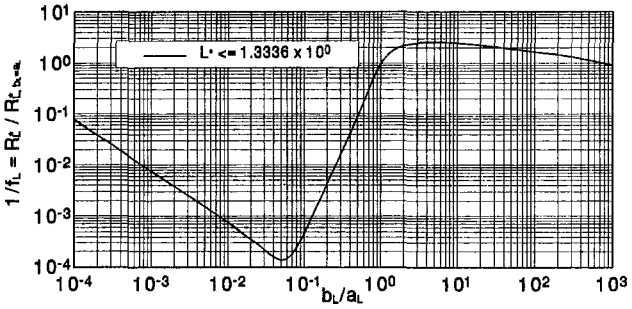

Fig. 5 Correction function $1/f_L$ versus radius ratio, a_L/b_L

4.0 Results and Discussion

The accuracy and robustness of the present model for contact conductance of spherical, rough metals are determined by comparing it to experimental results from the literature. Nearly all tractable empirical and theoretical correlations for predicting thermal contact conductance tacitly assume that surfaces are nearly optically flat. Such surfaces are herein defined as having nonflatness TIR (Total Included Reading) of less than 2 μm. TIR is the difference between the maximum and minimum height measurements of a surface.

Hegazy (1985) and Sridhar and Yovanovich (1993) demonstrated that the correlation by Yovanovich (1982) is the most accurate model for nearly optically flat surfaces. His model is included in the comparisons below to ascertain those cases for which flat surface models are no longer appropriate and the present model should be used. Also, the present model reduces to the theory by Yovanovich (1982) for optically flat surfaces.

4.1 Estimation of Unspecified Parameters. Mean absolute profile slope, m, was unspecified in most experimental investigations performed in the 1960s and 1970s. Lambert (1995) correlated σ and m for experiments in which both parameters were given, yielding an estimation for m of

$$m_{1\text{ or }2} = 0.076\,(\sigma_{1\text{ or }2} \times 10^6)^{0.52}. \qquad (12)$$

Uncertainty in this empirical correlation may, at the extremes, be plus or minus a factor of two. However, with sophisticated profilometers gaining increasingly widespread use, especially in such applications as electronic packaging and spacecraft thermal control, for which the expense of a profilometer is certainly justifiable, estimation of m should be unnecessary.

Also, the radii of curvature of the specimen surfaces are rarely provided in most experimental investigations. To circum-

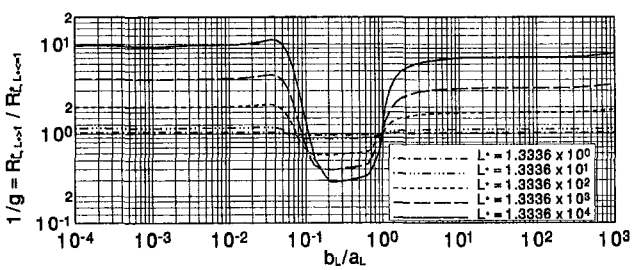

Fig. 6 Correction function $1/g$ versus a_L/b_L for a range of L^*

vent this difficulty, the combined radius of curvature, $\rho = (1/\rho_1 + 1/\rho_2)^{-1}$, is estimated from the combined nonflatness TIR. In the present study, the combined crown drop, $\delta = \delta_1 + \delta_2$, shown in Fig. 1 is assumed to equal TIR. The value of ρ is

$$\rho = b_L^2/2\delta. \tag{13}$$

The concept of radius-of-curvature loses relevance if the surfaces are decidedly nonspherical. In such instances the present model may substantially disagree (typically in an over-conservative fashion) with experimental data, but usually by no more than a factor of three.

For noncircular specimens, an effective component radius, b_L', is

$$b_L' = \sqrt{A_{\text{app}}/\pi}\ . \tag{14}$$

This expression is useful for commonly utilized square or rectangular surfaces (provided the length is not, say, more than twice the width for rectangular surfaces) or less frequently encountered triangular surfaces (approximately equilateral). This method of estimating b_L for noncircular contact surfaces is supported by the work of Yovanovich et al. (1977).

4.2 Comparison of the Present Model and the Model by Yovanovich (1982) to Experiments. The present model and the model by Yovanovich (1982) were compared to representative experimental conductance results for stainless steel 303 and 304 from the literature. These very similar materials were selected for comparisons because they are often used in applications for which contact conductance is a concern, as evidenced by the volume of available data (364 results for 33 contact pairs) compiled by Lambert (1995). Also, stainless steel is corrosion resistant, so that oxidation should not markedly affect experimental results. Comparisons are shown in Figs. 7(a) through 7(f) for surfaces ranging from nearly optically flat (TIR $\leq$ 2 μm) to highly spherical (TIR $\approx$ 200 μm) and very smooth ($\sigma \approx$ 0.15 μm) to very rough ($\sigma \approx$ 11 μm).

The present model and the model by Yovanovich (1982) are compared in Fig. 7(a) to experimental contact conductance results by Hegazy (1985) for three nearly optically flat (TIR $\leq$ 2.0 μm) stainless steel 304 contact pairs with small, medium, and large roughness (σ = 0.48, 2.71, and 10.95 μm, respectively). For these three cases, both models provide nearly identical predictions and agree very well with the data. The average root-mean-square (RMS) errors for the present model and the model by Yovanovich (1982) are 17.8 percent and 13.4 percent, respectively. The present correlation is slightly lower than the model by Yovanovich (1982) model because the present model predicts the presence of a minuscule macroscopic contact resistance, R_L, due to the very small nonflatness TIR. The present correlation differs slightly more from the model by Yovanovich (1982) for the smoothest contact pair (σ = 0.48 μm). This is because the computed R_L, though small for all three contact pairs, is slightly more significant in relation to the microscopic contact resistance, R_S, of the smoothest contact pair. Hegazy (1985) stated that each surface he tested exhibited a TIR of one to three light fringes (0.3 to 0.9 μm), as determined with an optical flat.

Both models are compared to experimental conductance measurements for three nearly optically flat (TIR $\leq$ 2 μm) contact pairs with very small roughness (σ = 0.14 to 0.16 μm) in Fig. 7(b). Note that the data, though somewhat scattered, fall evenly about the present model for which the average RMS error equals 49.6 percent. The model by Yovanovich (1982) is two to three times greater than the present model and has an average RMS error of 180 percent. The significantly different predictions by the two models arise because the present model accounts for the small R_L caused by the minuscule nonflatness, whereas the model by Yovanovich (1982) does not. R_L, though minimal, is considerably greater than the minute R_S resulting from the very small roughness.

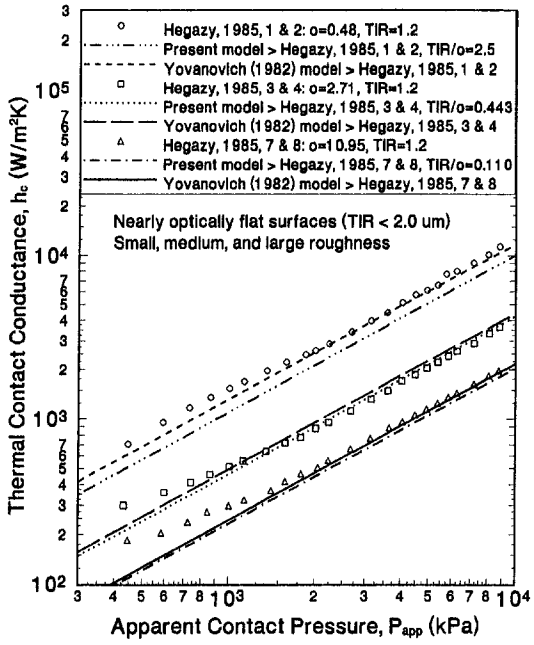

Fig. 7(a) Present model and model by Yovanovich (1982) compared to experimental results by Hegazy (1985) for nearly optically flat (TIR $\leq$ 2.0 μm) stainless steel 304 with small, medium, and large roughness (σ = 0.48, 2.71, and 10.95 μm)

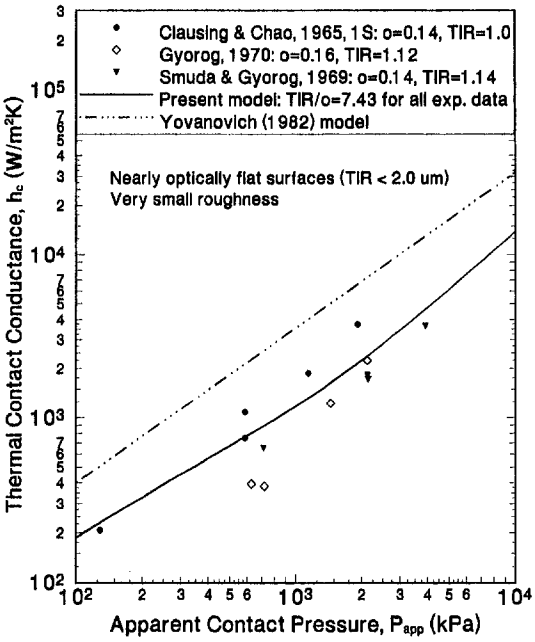

Fig. 7(b) Present model and model by Yovanovich (1982) compared to experimental results by Clausing and Chao (1965), Gyorog (1970), and Smuda and Gyorog (1969) for nearly optically flat (TIR $\leq$ 2.0 μm) stainless steel 303 and 304 with very small roughness (σ = 0.14 to 0.16 μm)

The present model and the model by Yovanovich (1982) are plotted in Fig. 7(c) against experimental results for a slightly nonflat (TIR = 3.8 μm) spherical contact pair with large roughness (σ = 4.83 μm). Both correlations yield nearly identical predictions and agree well with the data. The RMS errors for the present model and the model by Yovanovich (1982) are 26.4 percent and 31.9 percent, respectively.

Both models are graphed in Fig. 7(d) with experimental results for a very smooth (σ = 0.11 μm), slightly nonflat (TIR = 3.75 μm) spherical contact pair. Note that the nonflatness, TIR, for the surfaces in Figs. 7(c) and 7(d) are nearly equal. The present correlation closely approximates the data in Fig.

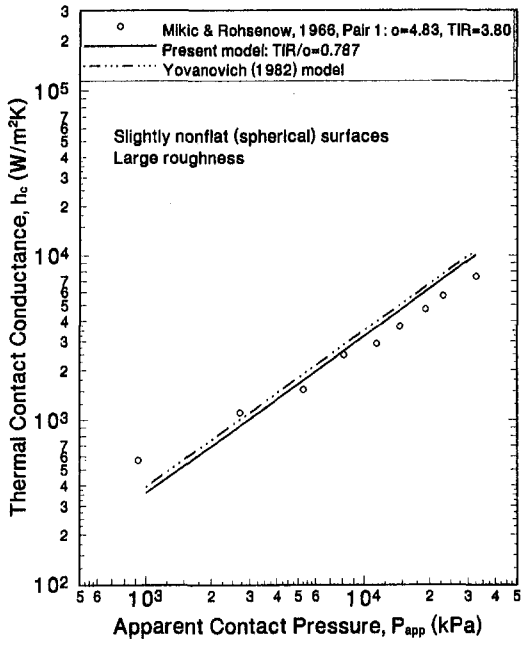

Fig. 7(c) Present model and model by Yovanovich (1982) compared to experimental results by Mikic and Rohsenow (1966) for slightly nonflat (TIR = 3.8 μm), spherical stainless steel 303 with large roughness (σ = 4.83 μm)

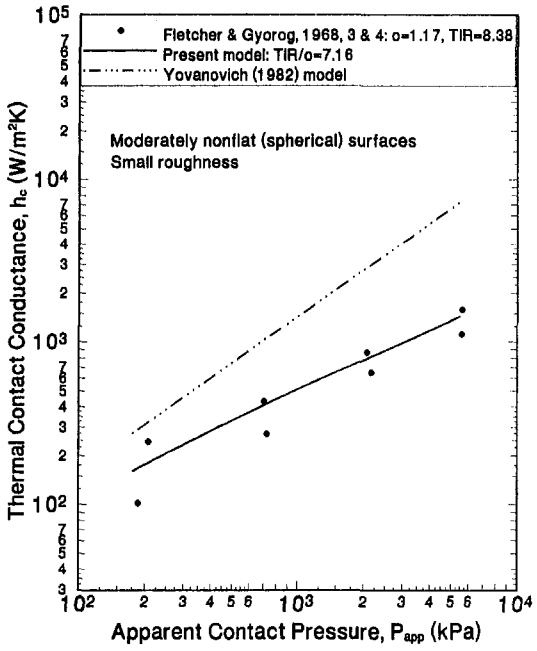

Fig. 7(e) Present model and model by Yovanovich (1982) compared to experimental results by Fletcher and Gyorog (1968) for moderately nonflat (TIR = 8.38 μm), spherical stainless steel 304 with small roughness (σ = 1.17 μm)

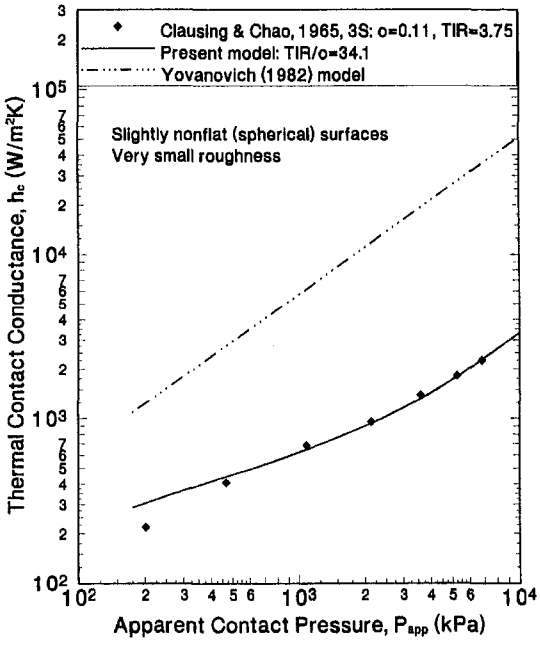

Fig. 7(d) Present model and model by Yovanovich (1982) compared to experimental results by Clausing and Chao (1965) for slightly nonflat (TIR = 3.75 μm), spherical stainless steel 303 with very small roughness (σ = 0.11 μm)

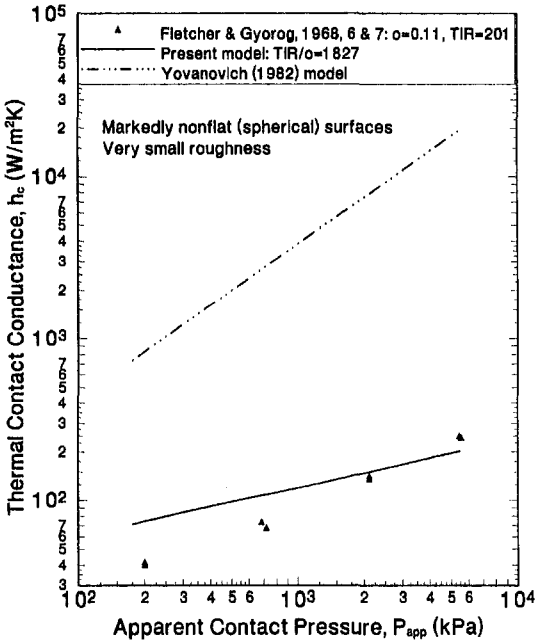

Fig. 7(f) Present model and model by Yovanovich (1982) compared to experimental results by Fletcher and Gyorog (1968) for markedly nonflat (TIR = 201 μm), spherical stainless steel 304 with very small roughness (σ = 0.11 μm)

7(d) (RMS error equals 16.6 percent), while the model by Yovanovich (1982) is over-predictive (RMS errors equals 937 percent, i.e., approximately an order of magnitude). Note that for such a smooth contact pair, the relatively small nonflatness dominates the total (R_S plus R_L) contact resistance. The results in Figs. 7(c) and 7(d) suggest that the model by Yovanovich may be extended to surfaces with nonflatness TIR, double that for optically flat surfaces (TIR $\leq$ 2 μm) for which his model was developed, provided roughness, σ, is approximately equal to or greater than nonflatness TIR.

The present model and the model by Yovanovich (1982) are illustrated in Fig. 7(e) with data for a moderately nonflat (spherical) contact pair (TIR = 8.38 μm) with small roughness (σ = 1.17 μm). The present correlation agrees well with the data (RMS error equals 24.6 percent, while the model by Yovanovich (1982) is over-predictive (RMS error equals 297 percent). Again, this is because R_L is substantially greater than R_S.

Both models are shown in Fig. 7(f) with experimental results for a smooth (σ = 0.11 μm), markedly nonflat (TIR = 201 μm) spherical contact pair. Again, the present model matches the data reasonably well (RMS error equals 47.6 percent), while the model by Yovanovich (1982) is vastly over-predictive (RMS error equals 5210 percent, i.e., about a factor of fifty).

For cases such as this, in which nonflatness is many times greater than roughness, the contact resembles a relatively smooth sphere for which the model by Clausing and Chao (1965) is also appropriate. The discrepancy between the present model and the experimental data at low loads may be due to specimens which are not truly spherical.

5.0 Conclusions

The present model performs quite well for all combinations of nonflatness, TIR, and roughness, σ, as demonstrated in Figs. 7(a–f). The model by Yovanovich (1982) performs well for nearly optically flat surfaces (TIR $\leq$ 2 μm), provided roughness is not much less than, say, 0.45 μm (Figs. 7(a) and 7(b)). His model also performs well for slightly nonflat surfaces (TIR $\leq$ 4 μm), provided $\sigma \geq$ TIR (Figs. 7(c) and 7(d)). The model by Yovanovich (1982) becomes increasingly over-predictive with increasing TIR (Figs. 7(e) and 7(f)), irrespective of roughness.

6.0 Acknowledgments

Support for this work was provided by the Naval Surface Warfare Center in Crane, Indiana under contract number N00164-94-C-0185.

7.0 References

Clausing, A. M., and Chao, B. T., 1965, "Thermal Contact Resistance in a Vacuum Environment," ASME JOURNAL OF HEAT TRANSFER, Vol. 87, No. 3, pp. 243–251.

Cooper, M., Mikic, B. B., and Yovanovich, M. M., 1969, "Thermal Contact Conductance," *Inter. Jour. of Heat and Mass Trans.*, Vol. 12, pp. 279–300.

Fletcher, L. S., and Gyorog, D. A., 1968, *Heat Transfer Between Surfaces in Contact; An Analytical and Experimental Study of Thermal Contact Resistance of Metallic Interfaces,* Report No. ME-TR-033-4, Mechanical Engineering Department, Arizona State University, also AIAA Paper No. 70-852.

Greenwood, J. A., and Tripp, J. H., 1967, "The Elastic Contact of Rough Spheres," *ASME Journal of Applied Mechanics,* Vol. 89, No. 1, pp. 153–159.

Gyorog, D. A., 1970, "Investigation of Thermal Isolation Materials for Contacting Surfaces," AIAA Paper No. 70-13, presented at the AIAA 8th Aerospace Sciences Meeting, New York, Jan. 19–21.

Hegazy, A. A., 1985, "Thermal Joint Conductance of Conforming Rough Surfaces," Ph.D. dissertation, University of Waterloo, Waterloo, Ontario, Canada.

Hertz, H. R., 1896, *Miscellaneous Papers,* english translation, MacMillan and Co., London.

Lambert, M. A., 1995, "Thermal Contact Conductance of Spherical Rough Metals," Ph.D. dissertation, Texas A&M University, College Station, Texas.

Mikic, B. B., 1970, "Thermal Constriction Resistance Due to Nonuniform Surface Conditions: Contact Resistance at Nonuniform Interface Pressure," *Int. Jour. of Heat and Mass Trans.,* Vol. 13, pp. 1497–1500.

Mikic, B. B., 1974, "Thermal Contact Conductance: Theoretical Considerations," *Int. Jour. of Heat and Mass Trans.,* Vol. 17, pp. 205–214.

Mikic, B. B., and Rohsenow, W. M., 1966, *Thermal Contact Conductance,* Technical Report No. 4542-41, Department of Mechanical Engineering, Massachusetts Institute of Technology, Cambridge, Massachusetts, NASA Contract No. NGR 22-009-065.

Nishino, K., Yamashita, S., Torii, K., 1993, "Thermal Contact Conductance Under Low Applied Load in a Vacuum Environment," *Proceedings of the First International Conference of Aerospace Heat Exchanger Technology,* R. K. Shah and A. Hashemi, eds., Palo Alto, California, February 15–17, Elsevier, Amsterdam, pp. 763–788.

Sasajima, K., and Tsukada, T., 1981, "On the Approach Between a Sphere and a Rough Surface: 2nd Report—Critical Condition to Yield Plastic Deformation in Contacting Bodies," Journal of the Japanese Society of Precision Engineering, in Japanese, Vol. 47, No. 6, pp. 694–699.

Smuda, P. A., and Gyorog, D. A., 1969, "Thermal Isolation with Low-Conductance Interstitial Materials Under Compressive Loads," AIAA Paper No. 69-25, AIAA 7th Aerospace Sciences Meeting, New York, Jan. 20–22.

Sridhar, M., and Yovanovich, M. M., 1993, "Critical Review of Elastic and Plastic Thermal Contact Conductance Models and Comparison with Experiment," Paper No. AIAA 93-2776, presented at the AIAA 28th Thermophysics Conference, Orlando, Florida, July 6–9.

Thomas, T. R., and Sayles, R. S., 1974, "Random-Process Analysis of the Effect of Waviness on Thermal Contact Resistance," AIAA Paper No. 74-691, presented at the AIAA/ASME 1974 Thermophysics and Heat Transfer Conference, Boston, Massachusetts, July 15–17.

Tsukada, T., and Anno, Y., 1979, "On the Approach Between a Sphere and a Rough Surface: 1st Report—Analysis of Contact Radius and Interface Pressure," Journal of the Japanese Society of Precision Engineering, in Japanese Vol. 45, No. 4, pp. 473–479.

Yovanovich, M. M., 1982, "Thermal Contact Correlations," Progress in Aeronautics and Astronautics: Spacecraft Radiative Transfer and Temperature Control, T. E. Horton, ed., Vol. 83, pp. 83–95.

Yovanovich, M. M., Burde, S. S., and Thompson, J. C., 1977, "Thermal Constriction Resistance of Arbitrary Planar Contacts with Constant Flux," AIAA Paper No. 76-440.

Yovanovich, M. M., and Burde, S. S., 1978, "Thermal Resistance at Smooth-Sphere/Rough-Flat Contacts: Theoretical Analysis," AIAA Paper No. 78-871, presented at the 2nd AIAA/ASME Thermophysics and Heat Transfer Conference, Palo Alto, California, May 24–26.

Observation and Computation of Vortex and/or Reverse Flow Development in Mixed Convection of Air in a Slightly Inclined Rectangular Duct

W. L. Lin

T. F. Lin

Department of Mechanical Engineering,
National Chiao Tung University,
1001 Ta Hsueh Road,
Hsinchu, Taiwan, R.O.C.

Combined flow visualization and conjugated numerical heat transfer analysis were carried out to study the axial evolution of the buoyancy induced secondary vortex and reverse flow in a mixed convective air flow through a bottom heated, slightly inclined rectangular duct. Results were obtained for the Grashof number Gr ranging from 1.6×10^3 to 2.8×10^5, inclined angle ϕ from -20 deg to 26 deg and the Reynolds number Re below 102 covering the steady and time dependent flows. For the buoyancy-opposing case, at a certain critical buoyancy-to-inertia ratio depending on the Re and ϕ both the experimental and numerical results clearly showed the generation of the longitudinal vortex rolls in the entry half of the duct and a slender reverse flow zone was induced near the exit end of the duct. At a higher buoyancy-to-inertia ratio the stronger reverse flow moves upstream and is in a time periodic snaking motion which is considered to result from the Kelvin-Helmholtz instability associated with the two counter flow streams, namely, the downstream moving longitudinal vortex rolls and the upstream moving reverse flow. Through the viscous shearing effects the strong snaking reverse flow induces a number of eddies moving along it and the longitudinal rolls are pushed towards the duct sides. This strong interaction between the vortex flow and reverse flow leads to an earlier transition to turbulence. A correlation equation was proposed for the penetration length of the reverse flow. However, for buoyancy-assisting flow no reverse flow is induced and the longitudinal vortex rolls prevail for the buoyancy-to-inertia ratio up to 2.8×10^5. Significant conjugated heat transfer effects were noted from the numerical results.

1 Introduction

Buoyancy-induced vortex flow and heat transfer in a mixed convective flow through a heated duct are known to be relatively sensitive to the duct orientation. In a bottom heated horizontal rectangular duct the buoyancy is normal to the forced flow direction and the longitudinal or transverse vortex rolls can be induced at supercritical Grashof numbers depending on the Reynolds number of the flow. When the duct is inclined from the horizontal, the secondary vortex flow is expected to be weaker due to the smaller normal buoyancy component and the forced flow will be accelerated in the aiding situation and decelerated in the opposing situation by the tangential buoyancy component. Thus, the longitudinal and/or transverse rolls and flow reversal can simultaneously exist in an inclined duct. At high buoyancy, the resulting flow will be rather complex and can undergo transition to a time-dependent state. These complicated processes are often encountered in a low Reynolds number flow. Detailed understanding of this buoyancy-induced vortex flow structure is important in fundamental fluid mechanics, heat transfer study, and in various technological processes such as cooling of microelectronic equipment (Incropera, 1988), heat transfer in compact heat exchangers (Kays and London, 1984), growth of single-crystal film through chemical vapor deposition (CVD) (Evans and Greif, 1989) and many others. The literature on the mixed convection in horizontal rectangular ducts was already reviewed in Huang and Lin (1994). In the following, only the literature on the mixed convective flow in inclined ducts is briefly reviewed.

Fukui et al. (1983) experimentally and numerically investigated steady fully developed mixed convective flow in an inclined duct with the Rayleigh number Ra $<$ 9300 and inclined angle measured from the horizontal ϕ below 32.1 deg. In the horizontal flow, the interaction between the vortices was found to be rather small. However, in the inclined flow the neighboring vortices tend to form a vortex pair with a single velocity peak. Experimental data for the local and average Nusselt numbers were provided by Morcos et al. (1986) and Maughan and Incropera (1987). Visualization of recirculating flow in steady aiding and opposing mixed convection at low buoyancy in inclined ducts was recently conducted by Morton et al. (1989), Lavine et al. (1989), and Ingham et al. (1990). The corresponding numerical analysis was performed by Heggs et al. (1990), including heat conduction in the wall. Koizumi and Hosokawa (1993) experimentally demonstrated that a properly designed unsteady mixed convective gas flow is suitable for CVD processes. Recently, the present authors (Lin and Lin, 1996) experimentally showed the vortex and reverse flow structural changes in both aiding and opposing convection of air in a bottom heated inclined rectangular duct. The temporal flow oscillation at increasing buoyancy and the vortex flow near the duct exit were also clearly manifested. But, the axial development of the whole vortex and reverse flow structure in the entire duct remains unexplored.

To complement our earlier study, combined flow visualization and numerical simulation were carried out here to investi-

Contributed by the Heat Transfer Division for publication in the JOURNAL OF HEAT TRANSFER. Manuscript received by the Heat Transfer Division June 26, 1996; revision received June 11, 1997; Keywords: Conjugate Heat Transfer; Flow Instability; Mixed Convection. Associate Technical Editor: A. S. Lavine.

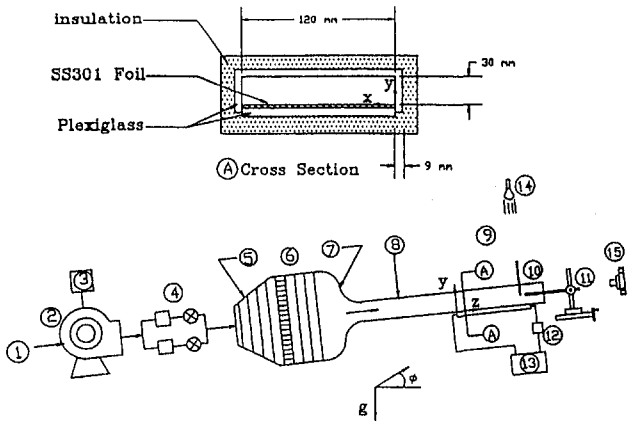

Schematic Diagram of Experimental Apparatus.

1.air flow ; 2.blower ; 3.frequency regulator ; 4.flowmeters and valves ; 5.diffuser with screens ; 6.straightener with honeycomb and screens ; 7.nozzle ; 8.developping channel ; 9.test section ; 10.probes ; 11.three-way traversing device ; 12.ammeter ; 13. D.C. power supply ; 14.lamp ; 15.camera.

Fig. 1 The schematic diagram of the experimental apparatus

gate the axial evolution of the buoyancy-driven secondary flow structure in a mixed convective air flow through a bottom heated rectangular duct slightly inclined from the horizontal. Attention was focused on the effects of the inclined angle and Grashof numbers on the characteristics of air flow in a rectangular duct of a finite aspect ratio ($A = 4$). Specifically, the inclination angle ϕ was varied from -20 deg to 26 deg.

2 Experimental Apparatus and Procedures

2.1 Experimental Apparatus. Figure 1 shows a schematic view of the mixed convective experimental apparatus established in our previous study (Lin and Lin, 1996) that is also used here. The apparatus consists of three parts: wind tunnel, test section, and measuring probes (along with a data acquisition system). The test section is a bottom heated rectangular duct constructed of 9 mm thick plexiglass top and side walls to facilitate flow visualization. The duct is rectangular, 30 mm in height and 120 mm in width, providing an aspect ratio of $A = 4$ and a total length of $l = 800$ mm. The apparatus is described in detail in Lin and Lin (1996).

2.2 Data Reduction for Convective Heat Transfer. The surface energy balance relating the total energy dissipated in the thin heater plate acting as duct bottom due to the resistance heating per unit surface area q''_{tot} to the heat fluxes associated with the convection from the heated surface to the air flow q''_{conv}, radiation heat loss from the surface q''_{rad}, and conduction loss through the insulation q''_{insul} is

$$q''_{tot} = q''_{conv} + q''_{rad} + q''_{insul}. \quad (1)$$

The convective heat flux was therefore determined by measuring the total dissipated heat flux and applying appropriate correlations for the nonconvective components. In view of the low heat transfer in the low Reynolds number mixed convective flow, the radiation loss ranges from 24 to 33 percent and the conduction loss from 14 to 23 percent of the total flux in the present experiment.

Uncertainties in the Grashof number and other parameters were estimated according to the standard procedures proposed by Kline and McClintock (1953). Our analysis indicated that the combination of many measurements, together with the uncertainties in the predicted quantities (radiation and conduction losses), yields the spanwise average Grashof number uncertainties ranging from 10 to 25 percent, which primarily reflects the uncertainty in the convective heat flux. The estimated uncertainty in the Reynolds number was 2 percent. Because of the fluid property variations with the temperature, the Reynolds and Grashof numbers vary with the axial distance. Although the variations in the Reynolds number were small, the Grashof number could vary by as much as 25 percent. For convenience, experiments are identified according to the Reynolds and Grashof numbers based on the inlet conditions and averaged convection heat flux.

3 Mathematic Model and Solution Method

3.1 Geometry. The mathematical model employed to simulate the mixed convective air flow in a bottom heated inclined rectangular duct with finite thickness walls is shown in Fig. 2, along with the chosen coordinate system. An isothermal fully developed forced flow at temperature T_{in} and averaged speed $\bar{w}_{in}$ enters the duct at the far upstream of the heated

Nomenclature

A = aspect ratio, b/d
b, d = width and height of the duct
g = gravitational acceleration
Gr = modified Grashof number, $g\beta q''_{conv} d^4/k\nu^2$
h = local convection heat transfer coefficient
k = thermal conductivity
l, L = dimensional and dimensionless length of the heated plate, l/d
L_p = penetration length
Nu = local Nusselt number, hd/k
p_m, P = dimensional and dimensionless dynamic pressures, $p_m/\rho\bar{w}_{in}^2$
Pr = Prandtl number, ν/α
q''_{conv} = local convective heat flux
q''_{insul} = local conduction heat loss through the insulation
q''_{rad} = local radiation heat loss from the surface
q''_{tot} = the total heat flux in the plate
q''_w = wall heat flux
Re = Reynolds number, $\bar{w}_{in} d/\nu$
t, τ = dimensional and dimensionless time, $t/(d/\bar{w}_{in})$
T, θ = dimensional and dimensionless temperature, $(T - T_{in})/(q''_w d/k)$
u, v, w = velocity components in x, y, z directions
U, V, W = dimensionless velocity components in X, Y, Z directions, $u/\bar{w}_{in}$, $v/\bar{w}_{in}$ and $w/\bar{w}_{in}$
x, y, z = Cartesian coordinates
X, Y, Z = dimensionless Cartesian coordinates, x/d, y/d and z/d
α = thermal diffusivity
β = thermal expansion coefficient
δ = thickness
ν = kinematic viscosity
ρ = density
ϕ = inclined angle measured from horizontal

Subscripts

a = of ambient quantities
fd = fully developed
in = values at the inlet of the test section
lon = of Superlon insulator quantities
s = of plexiglass plate quantities
$s\text{-}f$ = values from plexiglass plate to fluid
w = of heated wall quantities
$w\text{-}f$ = values from heater plate to fluid

Superscripts

$-$ = average value

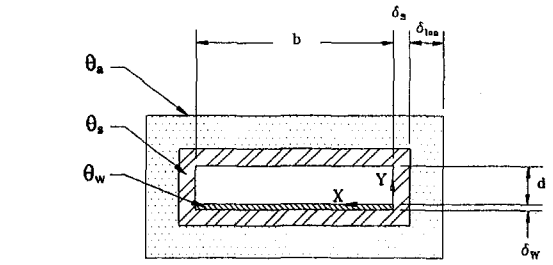

Cross Section of Heating Region

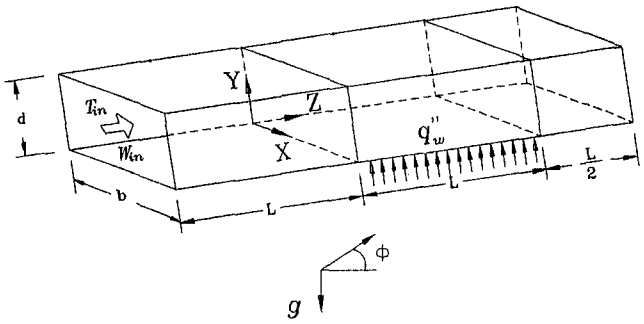

The Physical Model of Numerical Simulation

Fig. 2 The physical system of the numerical model for a mixed convective air flow in a rectangular duct

section. Initially, the flow in the entire duct is isothermal at T_{in}. At a certain instant of time, designated as time $t = 0$, a uniform volumetric heat source $\dot{q}'''$ is suddenly generated by the resistance heating in the thin heater plate and is maintained at this level thereafter. Meanwhile, the entire duct is thermally well insulated by the Superlon insulator. Note that two thermally well insulated sections of length L and $L/2$ are, respectively, added to the upstream and downstream ends of the heated section to facilitate the prescription of the in-flow and out-flow boundary conditions in the present elliptic flow analysis (Huang and Lin, 1994).

3.2 Governing Equations. In view of the thermal conductivity of the plexiglass side and top walls ($k_s \approx 0.21$ W/m°C) is much higher than that of the air ($k_a \approx 0.0263$ W/m°C), heat conduction in the duct walls is expected to exert profound influences on the air convection in the duct. Hence, the conjugate heat transfer effects should be included in the analysis. Basic nondimensional equations describing this unsteady mixed convective flow of a Boussinesq fluid in a bottom heated inclined rectangular duct driven by the interactions of the convection in the duct and conduction in the duct walls are outlined in the following subsections.

(a) Convection Equations for Flow in the Duct.
Continuity equation:

$$\frac{\partial U}{\partial X} + \frac{\partial V}{\partial Y} + \frac{\partial W}{\partial Z} = 0 \tag{2}$$

X-direction momentum equation:

$$\frac{\partial U}{\partial \tau} + U\frac{\partial U}{\partial X} + V\frac{\partial U}{\partial Y} + W\frac{\partial U}{\partial Z} = -\frac{\partial P}{\partial X} + \frac{1}{\mathrm{Re}}\left[\frac{\partial^2 U}{\partial X^2} + \frac{\partial^2 U}{\partial Y^2} + \frac{\partial^2 U}{\partial Z^2}\right] \tag{3}$$

Y-direction momentum equation:

$$\frac{\partial V}{\partial \tau} + U\frac{\partial V}{\partial X} + V\frac{\partial V}{\partial Y} + W\frac{\partial V}{\partial Z} = -\frac{\partial P}{\partial Y} + \frac{1}{\mathrm{Re}}\left[\frac{\partial^2 V}{\partial X^2} + \frac{\partial^2 V}{\partial Y^2} + \frac{\partial^2 V}{\partial Z^2}\right] + \frac{\mathrm{Gr}}{\mathrm{Re}^2}\theta \cdot \cos\phi \tag{4}$$

Z-direction momentum equation:

$$\frac{\partial W}{\partial \tau} + U\frac{\partial W}{\partial X} + V\frac{\partial W}{\partial Y} + W\frac{\partial W}{\partial Z} = -\frac{\partial P}{\partial Z} + \frac{1}{\mathrm{Re}}\left[\frac{\partial^2 W}{\partial X^2} + \frac{\partial^2 W}{\partial Y^2} + \frac{\partial^2 W}{\partial Z^2}\right] + \frac{\mathrm{Gr}}{\mathrm{Re}^2}\theta \cdot \sin\phi \tag{5}$$

Energy equation:

$$\frac{\partial \theta}{\partial \tau} + U\frac{\partial \theta}{\partial X} + V\frac{\partial \theta}{\partial Y} + W\frac{\partial \theta}{\partial Z} = \frac{1}{\mathrm{Re}\cdot\mathrm{Pr}}\left[\frac{\partial^2 \theta}{\partial X^2} + \frac{\partial^2 \theta}{\partial Y^2} + \frac{\partial^2 \theta}{\partial Z^2}\right]. \tag{6}$$

Nondimensional variables used in the above equations are defined as

$$X = x/d \quad Y = y/d \quad Z = Z/d$$
$$U = u/\bar{w}_{in} \quad V = v/\bar{w}_{in} \quad W = w/\bar{w}_{in}$$
$$\tau = t/(d/\bar{w}_{in}) \quad P = p_m/\rho\bar{w}_{in}^2 \quad \theta = (T - T_{in})/(q''_w d/k)$$
$$\mathrm{Gr} = g\beta q''_w d^4/k\nu^2 \quad \mathrm{Pr} = \nu/\alpha \quad \mathrm{Re} = \bar{w}_{in} d/\nu$$
$$A = b/d$$

where q''_w is the wall heat flux considered to be equal to $\bar{q}''_{conv}$, which is determined by averaging the data from the experimental measurement, Eq. (1).

(b) Conduction Equations in the Solid Walls. Considering that the thickness of the duct wall is much smaller than the length and width of the duct, the conduction resistance across the wall is neglected here to facilitate the computation. Thus we have unsteady two-dimensional heat conduction equations for the heater plate:

$$\frac{\partial \theta_w}{\partial \tau} = \left(\frac{\alpha_{rw}}{\mathrm{Pr}\cdot\mathrm{Re}}\right)\left\{\left(\frac{\partial^2 \theta_w}{\partial X^2} + \frac{\partial^2 \theta_w}{\partial Z^2}\right) - \left(\frac{k_{rs}}{k_{rw}}\right)\left(\frac{d}{\delta_w}\right)\left[\frac{\theta_w - \theta_s}{(\delta_w + \delta_s)/2d}\right] + \left(\frac{1}{k_{rw}}\right)\left(\frac{d}{\delta_w}\right)\left(1 + \left.\frac{\partial \theta}{\partial Y}\right|_{w-f}\right)\right\} \tag{7}$$

the plexiglass bottom wall:

$$\frac{\partial \theta_s}{\partial \tau} = \left(\frac{\alpha_{rs}}{\mathrm{Pr}\cdot\mathrm{Re}}\right)\left\{\left(\frac{\partial^2 \theta_s}{\partial X^2} + \frac{\partial^2 \theta_s}{\partial Z^2}\right) - \left(\frac{k_{rlon}}{k_{rs}}\right)\left(\frac{d}{\delta_s}\right)\left(\frac{\theta_s - \theta_a}{\delta_{lon}/d}\right) + \left(\frac{d}{\delta_s}\right)\left[\frac{\theta_w - \theta_s}{(\delta_w + \delta_s)/2d}\right]\right\} \tag{8}$$

the plexiglass right side wall:

$$\frac{\partial \theta_s}{\partial \tau} = \left(\frac{\alpha_{rs}}{\mathrm{Pr}\cdot\mathrm{Re}}\right)\left[\left(\frac{\partial^2\theta_s}{\partial Y^2}+\frac{\partial^2\theta_s}{\partial Z^2}\right)-\left(\frac{1}{k_{rs}}\right)\left(\frac{d}{\delta_s}\right)\left.\frac{\partial\theta}{\partial X}\right|_{s-f} - \left(\frac{k_{rlon}}{k_{rs}}\right)\left(\frac{d}{\delta_s}\right)\left(\frac{\theta_s-\theta_a}{\delta_{lon}/d}\right)\right] \quad (9)$$

the plexiglass left side wall:

$$\frac{\partial \theta_s}{\partial \tau} = \left(\frac{\alpha_{rs}}{\mathrm{Pr}\cdot\mathrm{Re}}\right)\left[\left(\frac{\partial^2\theta_s}{\partial Y^2}+\frac{\partial^2\theta_s}{\partial Z^2}\right)+\left(\frac{1}{k_{rs}}\right)\left(\frac{d}{\delta_s}\right)\left.\frac{\partial\theta}{\partial X}\right|_{s-f} - \left(\frac{k_{rlon}}{k_{rs}}\right)\left(\frac{d}{\delta_s}\right)\left(\frac{\theta_s-\theta_a}{\delta_{lon}/d}\right)\right] \quad (10)$$

and the plexiglass top wall:

$$\frac{\partial \theta_s}{\partial \tau} = \left(\frac{\alpha_{rs}}{\mathrm{Pr}\cdot\mathrm{Re}}\right)\left[\left(\frac{\partial^2\theta_s}{\partial X^2}+\frac{\partial^2\theta_s}{\partial Z^2}\right)-\left(\frac{1}{k_{rs}}\right)\left(\frac{d}{\delta_s}\right)\left.\frac{\partial\theta}{\partial Y}\right|_{s-f} - \left(\frac{k_{rlon}}{k_{rs}}\right)\left(\frac{d}{\delta_s}\right)\left(\frac{\theta_s-\theta_a}{\delta_{lon}/d}\right)\right]. \quad (11)$$

Note that in writing the above equations, the outside surface of the Superlon insulator is assumed to be at the ambient temperature, which is the same as the inlet temperature in the present experiment. It is also noted that the thermal radiative transfer between the heater plate and side walls is approximately treated by considering the radiation loss in the energy balance for the heater plate. Besides, the thermal diffusivity and conductivity ratios and wall thickness are defined and assigned with the values for the present system as

$$\alpha_{rs} = \alpha_s/\alpha \approx 0.00553, \quad \alpha_{rw} = \alpha_w/\alpha \approx 0.187$$

$$k_{rs} = k_s/k \approx 7.622, \quad k_{rw} = k_w/k \approx 571.43,$$

$$k_{rlon} = k_{lon}/k \approx 10$$

$$d/\delta_s \approx 3.333, \quad d/\delta_w \approx 120, \quad \delta_{lon}/d \approx 5.$$

Due to the neglect of the thermal resistance across the thickness of the walls, the solution for the above conduction equations actually acts as the thermal boundary conditions for the flow equations.

(c) Initial and Boundary Conditions. The imposed initial and boundary conditions for the above governing equations are

$$\text{at } \tau \le 0,\ U = V = \theta = \theta_w = \theta_s = 0$$

$$W = W_{fd} = \left(\frac{m+1}{m}\right)\left(\frac{n+1}{n}\right)[1-(|2Y-1|)^n] \times \left[1-\left(\left|\frac{2X}{A}-1\right|\right)^m\right] \quad (12)$$

where the initial velocity is assumed as fully developed with the values of the constants m and n depending on the aspect ratio A (Shah and London, 1978; Holmes and Vermeulen, 1968; Natarajan and Lakshmanan, 1972).

$$\text{At } \tau > 0,\ \text{at } Z = -L,\quad U = V = \theta = \theta_s = 0,\ W = W_{fd} \quad (13)$$

$$\text{at } Z = \frac{3L}{2},\quad \frac{\partial U}{\partial Z} = \frac{\partial V}{\partial Z} = \frac{\partial W}{\partial Z} = \frac{\partial \theta}{\partial Z} = \frac{\partial \theta_s}{\partial Z} = 0 \quad (14)$$

$$\text{at } Z = 0 \text{ and } L,\quad \frac{\partial \theta_w}{\partial Z} = 0 \quad (15)$$

at the fluid-wall interfaces,

$$U = V = W = 0,\ \theta = \theta_s \text{ or } \theta = \theta_w. \quad (16)$$

3.3 Solution Method. In view of the nonlinearity in the inertia terms, the basic equations were solved numerically. In particular, the explicit finite-difference method was used to solve the conduction equations in the solid walls. Meanwhile, the explicit projection method (Peyret and Taylor, 1983) was chosen to integrate the flow equations on a staggered grid system. This fractional step (splitting) method consists of two steps. First, a provisional value is explicitly computed for the velocity field ignoring the pressure gradient. Then, the provisional velocity field is corrected by including the pressure effect and by enforcing the mass conservation. The details of the solution procedures are available from our previous numerical study (Huang and Lin, 1994).

Since only the low Reynolds number flow ($\mathrm{Re} \le 102$) is to be simulated, a uniform grid is placed in the computational domain with $\Delta X = A/I$, $\Delta Y = 1/J$, and $\Delta Z = 2.5L/K$ where I, J, and K are, respectively, the total numbers of nodes used in X, Y, and Z directions. I, J, and K are, respectively, chosen as 61, 22, and 91. The stability of the scheme is limited by the requirement that the Courant number be less than unity (Anderson et al., 1984). To insure the numerical convergence and enhance numerical accuracy, the Courant number is set below 0.05 in the computation.

To verify the proposed numerical scheme, a series of stringent program tests were conducted. First, the predicted results for the flow without considering the wall conduction effects were in qualitative agreement with the results in our experimental results and literature, as was clearly illustrated in our previous numerical study (Huang and Lin, 1994; Lin et al., 1996) for the horizontal duct flow. Then, a space and time grid-independence test and a test of the downstream insulated section length for the inclined duct flow were carried out. Results from such tests for the flow and temperature fields computed by the $61 \times 22 \times 91$ space grid with the downstream insulated section length $L/2$, by the $61 \times 22 \times 137$ and $81 \times 30 \times 121$ grids with the downstream insulated section length L, and with the time intervals selected at Courant number = 0.05 show good agreement. More comparisons will be made later between the present numerical simulation and experimental measurement. Through these program tests, the adopted solution procedures are considered to be suitable for the present study. Finally, it should be mentioned that the computations were performed on the IBM 580 workstations. The CPU times for these unsteady fully three-dimensional cases were about 6–12 days with a 50 percent share of CPU. Due to the limited availability of the computational facilities, grids much finer than those used above were not tested.

4 Results and Discussion

In the following section of the paper, selected results from the present combined experimental and numerical investigation will be presented, mainly to illustrate the axial development of the complex flow structures containing the buoyancy induced vortex flow and/or reverse flow for various Grashof numbers with ϕ varied from -20 deg to 26 deg. Then the conjugated heat transfer effects deduced from the numerical simulation are manifested. A similar study for the horizontal duct ($\phi = 0$ deg) was recently reported by Lin et al. (1996).

4.1 Axial Evolution of Vortex and Reverse Flow. In the first situation to be discussed, the air flows downwards in the duct with the lower plate heated so that the duct inlet is at a higher elevation over the exit end, resulting in an opposing mixed convection ($\phi < 0$ deg). At a low buoyancy-to-inertia ratio ($\mathrm{Gr}/\mathrm{Re}^2$), steady vortex flow prevails after the transient has elapsed when the Grashof number is above the critical value for the onset of secondary flow. To exemplify the axial vortex

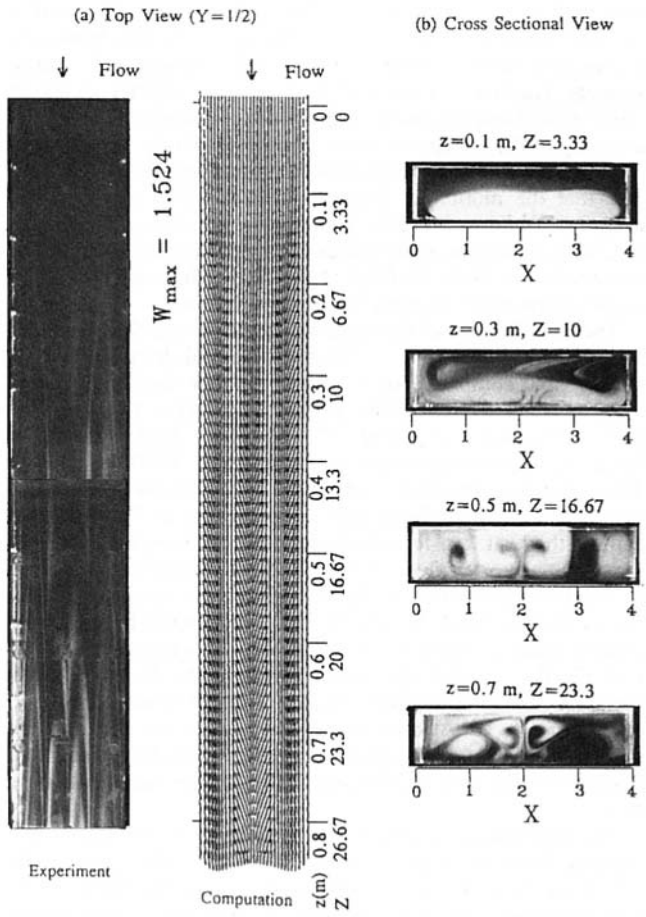

Fig. 3 Comparisons of experimental photos and computed results at τ = 1200 for air flow for Re = 35, Gr/Re^2 = 9.8, and ϕ = −20 deg for (*a*) top view and (*b*) cross section view

flow development in this opposing mixed convection, Fig. 3 shows the photos taken from the top and end views of the steady vortex flow for Re = 35 and Gr/Re^2 = 9.8 (Gr = 1.2 × 10^4) for ϕ = −20 deg. For clear comparison, the corresponding planform of the velocity field predicted from the conjugated heat transfer analysis is also shown in Fig. 3. Note that the vortex flow development visualized from the experiment is in qualitative agreement with that from the numerical simulation. The top view flow photo shows that in the immediate entry of the heated section, the smoke spreads fairly uniformly on the heated plate for $z < 0.2$ m suggesting the dominant laminar two-dimensional forced convection flow there. Then at $z \geq 0.2$ m, two spanwisely symmetric tracer lines with fringes start to appear near the duct sides (top view) and we have the onset of one pair of longitudinal vortices there. This vortex pair is clearly seen from the end view at $z = 0.3$ m ($Z \approx 10$). But near $z = 0.2$ m ($Z \approx 6.67$) the vortex flow is still rather weak and does not touch the upper plate. When the flow moves downstream to the station $z = 0.5$ m ($Z \approx 16.67$), another pair of vortices form in the core region adjacent to the first pair, as evident from the top view. The associated isotherms from the numerical simulation not shown here suggest that these newly formed vortex rolls are driven by the thermals rising from the central portion of the heated plate. Thus, beyond $z = 0.5$ m ($Z \approx 16.67$) we have two pairs of longitudinal vortex rolls in the duct, which are also symmetric with respect to the vertical central plane at $X = 2$. Proceeding downstream, the rolls grow slowly in size and strength, as evident from the top view flow photos and numerical results. This in turn squeezes the rolls near the side walls to cause them to become smaller. In summary, our results suggest that the axial evolution of the vortex flow of the opposing mixed convection at low buoyancy is mainly characterized by the generation of symmetric vortex rolls as the flow moves downstream. No reverse flow was observed at this low Gr/Re^2. Additional results for a higher Gr/Re^2 or lower ϕ indicates that the onset of vortices moves upstream and the vortex intensity is stronger.

Next, the axial development of the opposing mixed convection flow at the buoyancy-to-inertia ratio high enough to reverse the forced flow in the downstream and to cause the flow to become time periodic is examined (Lin and Lin, 1996). Typical results for the snapshots of the complex flow from the top and side views at large τ for Re = 35, ϕ = −20 deg, and Gr/Re^2 = 61.2 (Gr = 7.5 × 10^4) are given in Fig. 4. At this higher buoyancy one can observe the earlier onset of the longitudinal vortices at $z \approx 0.1$ m ($Z \approx 3.33$) and the vortices are stronger and somewhat sinuous. At this higher opposing buoyancy a slender zone of the reverse flow can be seen near the central vertical plane at $X = 2$ for $z > 0.25$ m. The flow reversal starts from the exit end of the heated section and extends towards the duct inlet. It is interesting to observe the cross section of the narrow reverse flow zone varying nearly periodically in the axial direction resulting in the weak, slightly meandering motion of the neighboring longitudinal vortex rolls. This interaction of the upstream moving reverse flow and downstream moving longitudinal vortices causes the flow to become slightly asymmetric and time periodic. The side view of the flow shown in

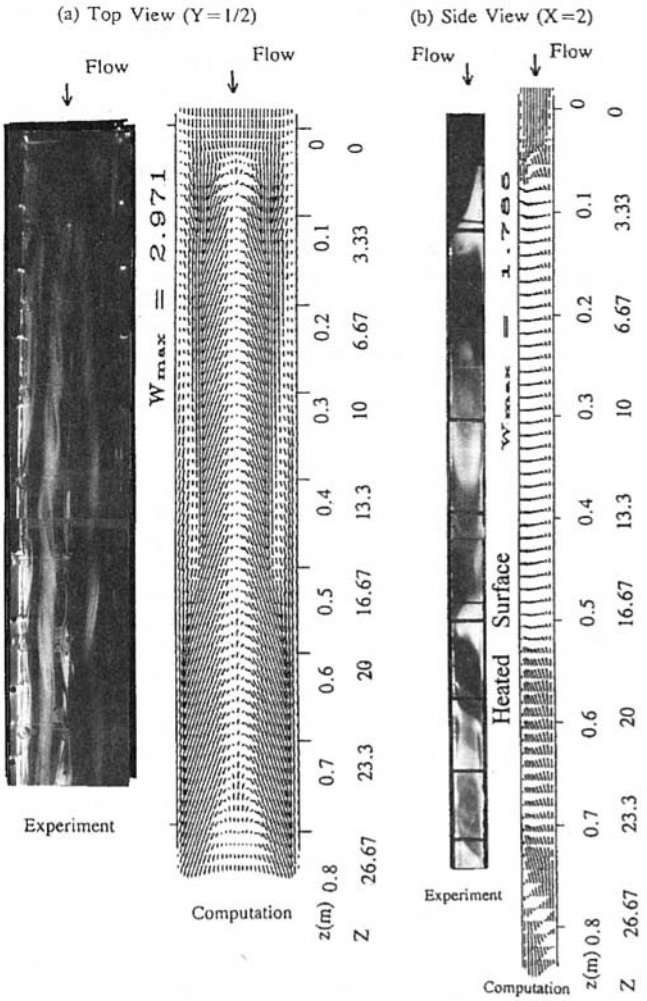

Fig. 4 Comparisons of experimental photos and computed results at τ = 1500 for air flow for Re = 35, Gr/Re^2 = 61.2, and ϕ = −20 deg for (*a*) top view and (*b*) side view

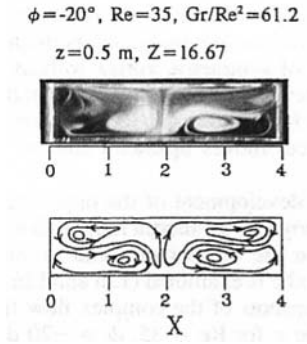

Fig. 5 The instantaneous flow photo and schematically sketched cross plane vortex flow for Re = 35, Gr/Re^2 = 61.2, and $\phi = -20$ deg at z = 0.5 m or Z = 16.7

Fig. 4(b) indicates that the reverse flow is much stronger in the downstream end of the duct. Besides, the slender reverse flow zone also contains weak cross plane recirculation. Thus in the duct core one observes an upstream moving spiral flow. Note that the tilted S-shape smoke tracers in the side view flow photo in Fig. 4(b) are the consequence of this reverse vortex flow. An overview of the experimental flow photos indicates that at this higher buoyancy, aside from the slender reverse flow zone, one pair of forward moving longitudinal vortex rolls have been generated near the side walls in a short distance after the flow entering the heated section ($z \approx 0.1$ m or $Z \approx 3.33$). When the flow moves downstream to $z \approx 0.2$ m ($Z \approx 6.67$), another nearly symmetric pair of forward moving longitudinal vortex rolls are induced by the thermals rising from the central portion of the heated plate for $z \geq 0.2$ m. Further downstream, the rolls in the duct core grow and extend to occupy nearly the entire top half of the cross section, causing the rolls near the duct sides to shrink and to stay near the lower corners of the duct. Thus we have two large rolls on top of the two small rolls in this portion of the duct ($0.4 \text{ m} \leq z \leq 0.7$ m). This interesting flow structure is illustrated in Fig. 5 by the cross plane vortex flow in the cross section z = 0.5 m, which is also slightly asymmetric. Note that the cross plane vortex flow is the secondary flow in the plane normal to the main forced flow direction. Beyond z = 0.7 m ($Z \approx 23.3$) the smaller rolls disappear and we have two-roll structure. It should be mentioned that the numerically predicted flow is spanwisely symmetric. This is due to the absence of the random disturbances in solving the flow equations, except the relatively small errors inherent in the numerical discretization and computation. While in the experiment the turbulence level of the inlet stream is about 0.7 percent.

When the buoyancy-to-inertia ratio is further increased to 122.5, the reverse flow is slightly unstable and can penetrate to the more upstream region, as shown in Fig. 6. Note that the reverse flow moves sinuously upstream. Moreover, one can observe the vortices recirculating along an elongated S-shape interface, which is considered to result from the strong viscous shearing of the strong sinuous reverse flow. This generation of the vortices is very similar to that observed in the interface between two counter flow streams and is due to the Kelvin Helmholtz stability. In addition, the tip of the reverse flow zone at the duct inlet is found to be unsteady and moves up and down both axially and normally. It is further noted that the sinuous interface between the reverse flow and vortices around it is not steady but instead grows and collapses in a periodic manner. The whole reverse flow was found to move slightly upstream and downstream with a period of approximately 25 seconds. In summary, the driven flow at this high buoyancy is characterized by the strong snaking reverse flow in the duct core, a forward moving longitudinal vortex roll near each side wall and a number of irregular vortices in-between.

A similar buoyancy-induced secondary flow structure is observed when the buoyancy is further raised. Results for a typical case with Re = 35, Gr/Re^2 = 155.1 ($Gr = 1.9 \times 10^5$) and $\phi = -20°$ are given in Fig. 7. Note that at this higher buoyancy the snaking motion of the reverse flow is stronger and is more sinuous. Besides, the reverse flow zone is slighter larger in cross section and penetrates slightly more upstream. The vortex intensity of the vortices moving around the slender reverse flow zone is higher. The experimental and numerical results all indicate that the motion of these vortices is rather unstable and irregular. The flow is highly asymmetric. Obviously, some delicate vortical motion of the eddies is not predicted by the numerical simulation. Note also that at this higher buoyancy the flow in the downstream actually becomes turbulent.

The distributions of the local heat transfer coefficient on the bottom heated plate are important in thermal design. Figure 8 presents the computed local Nusselt number distributions, defined as $Nu = hd/k = (d/k) \cdot [q''_w/(T_w - T_{in})] = 1/\theta_w$, for Gr/Re^2 = 9.8, 61.2, 122.5, and 155.1 for $\phi = -20$ deg and Re = 35 at τ, respectively equal to 1200, 1500, 1500, and 1800. These distributions clearly reflect the secondary flow structures discussed above for these cases. Specifically, in Fig. 8(a) we can see the heat transfer enhancement by the buoyancy induced longitudinal vortex flow and the dominated four roll structure in the downstream half of the duct. Since the buoyancy driven vortex flow is weak at low Gr/Re^2, only small heat transfer enhancement is noted at Gr/Re^2 = 9.8. At a higher buoyancy with Gr/Re^2 = 61.2, the results in Fig. 8(b) distinctly show the axial change in the flow structure from the four rolls to two rolls at $z/d \approx 16$. At even higher buoyancies, the distributions in Figs. 8(c) and (d) are clearly in accordance with the intensive vortical motion of the eddies generated by the snaking reverse flow.

The penetration length of the reverse flow defined as the distance from the upstream tip of the reverse flow zone to its tail in the duct exit is relatively important in the study of the high buoyancy opposing mixed convection and is also experi-

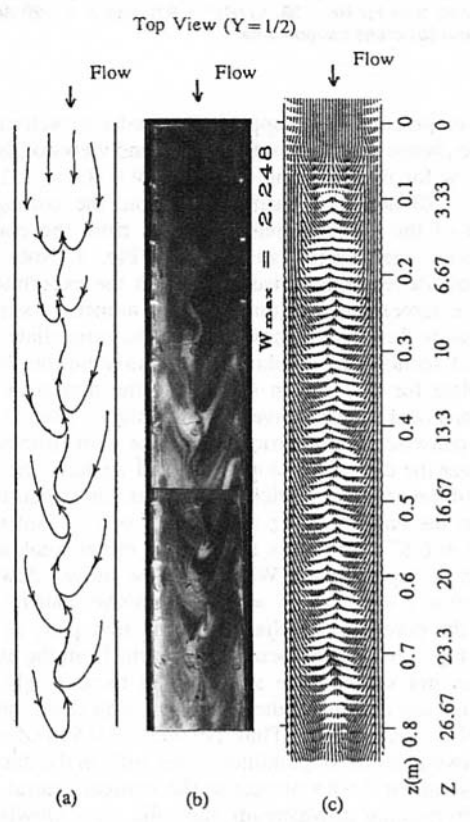

Fig. 6 Comparisons of (a) schematically sketched flow pattern, (b) experimental photos, and (c) computed results at τ = 1500 for air flow for Re = 35, Gr/Re^2 = 122.5 and $\phi = -20$ deg at a selected top view

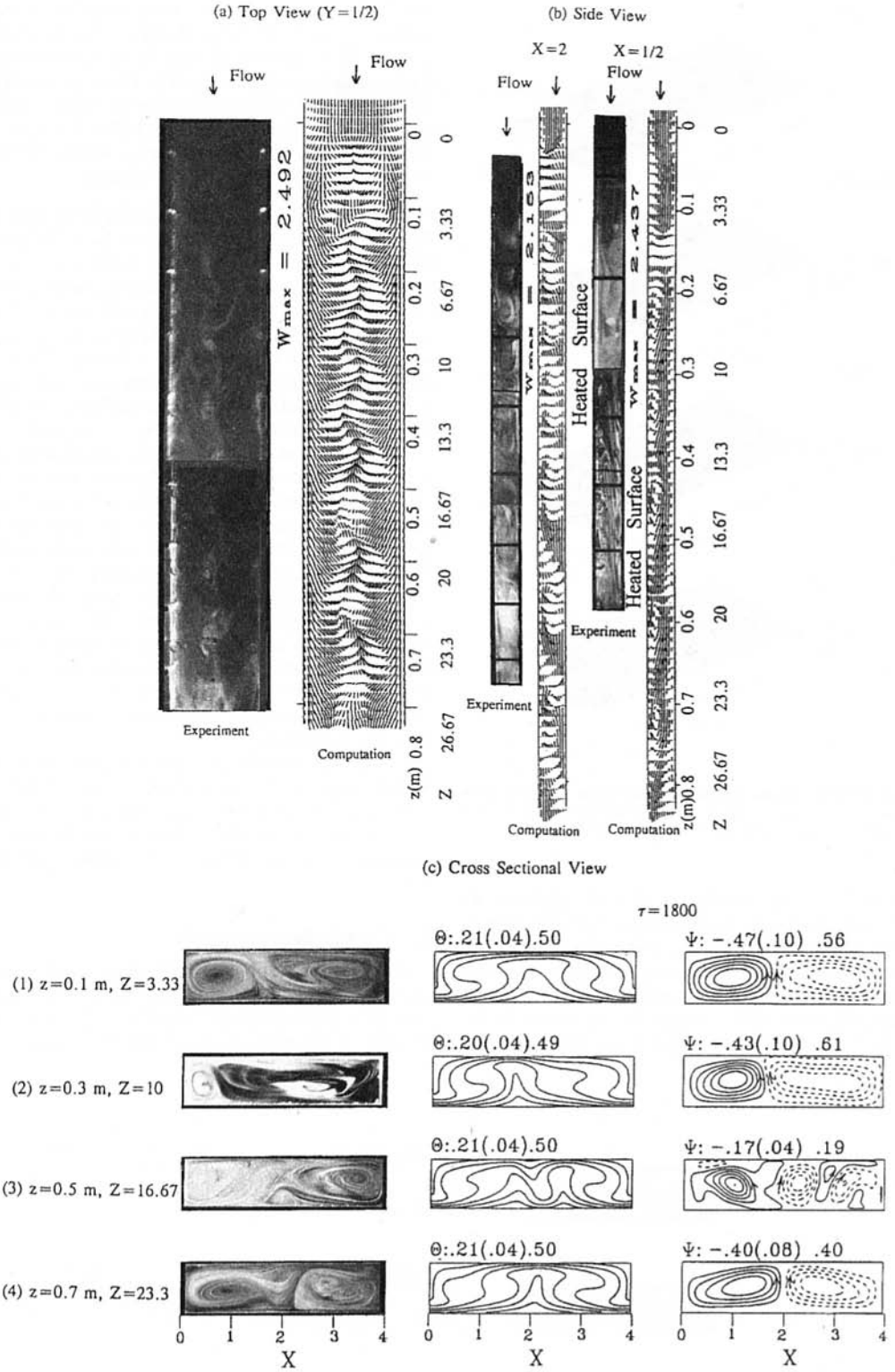

Fig. 7 Comparisons of experimental photos and computed results at τ = 1800 for air flow for Re = 35, Gr/Re^2 = 155.1, and ϕ = −20 deg for (a) top view, (b) side view, and (c) cross section view

mentally measured. Based on the present data, a dimensionless penetration length scaled with the duct height is correlated as

$$L_p = 2.7 \times 10^{-4} \left(\frac{\mathrm{Gr}}{\mathrm{Re}^2}\right)^2 - 1.2 \times 10^{-2} \left(\frac{\mathrm{Gr}}{\mathrm{Re}^2}\right) + 10.7\,(1 - 2\sin\phi) \quad (17)$$

This correlation is within 5 percent of the rms error against the experimental data. It was found that the equation is applicable for $5 \times 10^4 \le \mathrm{Gr} \le 2 \times 10^5$, $20 \le \mathrm{Re} \le 102$, and -20 deg $\le \phi \le -5$ deg.

When the air flows upwards in the duct ($\phi > 0$ deg) for the aiding mixed convection, the normal buoyancy component is prone to induce longitudinal vortices. Meanwhile, the parallel component will accelerate the flow in the axial direction. Figure 9 shows the instantaneous flow pictures taken at large τ at four selected cross sections for the Reynolds number fixed at 35,

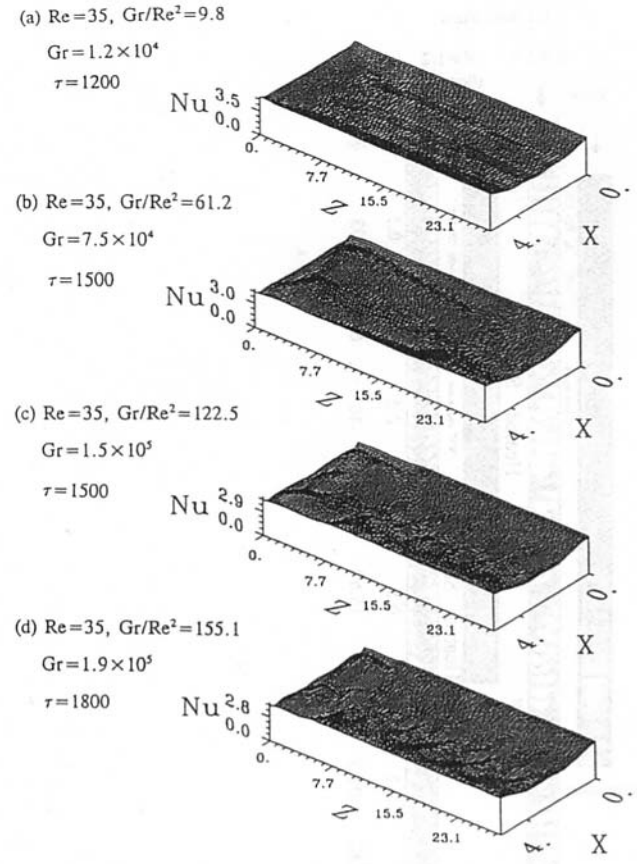

Fig. 8 The predicted local Nusselt number distributions on the heated bottom plate for Re = 35 and $\phi = -20$ deg for (*a*) $Gr/Re^2 = 9.8$, (*b*) $Gr/Re^2 = 61.2$, (*c*) $Gr/Re^2 = 122.5$, and (*d*) $Gr/Re^2 = 155.1$ at large τ

Grashof number at 2.8×10^5 ($Gr/Re^2 = 228.6$), and ϕ at 26 deg. It is of interest to note from the results that one pair of weak longitudinal vortex rolls with the vortex flow ascending along the side walls are induced in the entry region for $z \leq 0.2$ m and downstream another pair of longitudinal rolls are induced but the rolls near the duct sides change the direction of the recirculation with the vortex flow descending near the side walls. Besides, the vortices were found to swing left and right in the spanwise direction. However, for the case of buoyancy-assisted flow, no reverse flow is observed within the range of the buoyancy parameter studied. The numerical predicted vortex flow pattern is found to be in good agreement with that observed in the experiment. Additionally, results not given here indicated that the vortex flow is stronger for higher Gr/Re^2 and smaller ϕ with the earlier onset of the vortices.

4.2 Importance of Conjugated Heat Transfer. Finally, the importance of the interactions between the convection in the flow and conduction in the solid walls on the vortex and reverse flow structure is illustrated by comparing the numerical results for those cases including and excluding the conjugated effects. Figure 10 shows this comparison for the case with Re = 35, $Gr/Re^2 = 61.2$, and $\phi = -20$ deg. These results indicate that there are significant differences in the thermal and flow structures predicted from the two different models. In particular, the nonconjugated analysis (Fig. 10(*b*)) gives larger vortex rolls near the side walls, and they circulate upwards along the side walls in the entry half of the duct. In addition, because the plate temperature results in the bottom corners in the nonconjugated analysis are higher than in other portions of the duct, the reverse flow is induced near the side walls in the downstream. This does not agree with the experimental observation. These unrealistic outcomes are mainly caused by the neglect of the conduction in the plexiglass side walls. Including the side wall conduction, the conjugated analysis predicts the stronger and larger vortex rolls in the duct core and a reverse flow generated near the central vertical plane at $X = 2$, as already shown in Fig. 4(*a*). Besides, the vortex pair always circulates downwards near the duct sides.

The results from the present conjugated heat transfer analysis clearly manifest the importance of the conduction in the solid walls in affecting the buoyancy-induced vortex and reverse flow structure in the air flow. This is simply due to the thermal conductivity of air being much smaller than that of the solid walls.

5 Concluding Remarks

The present combined experimental observation and conjugated heat transfer analysis for the mixed convective air flow through a rectangular duct illustrated the generation of the vortex rolls in the entry region of the duct and the existence of the

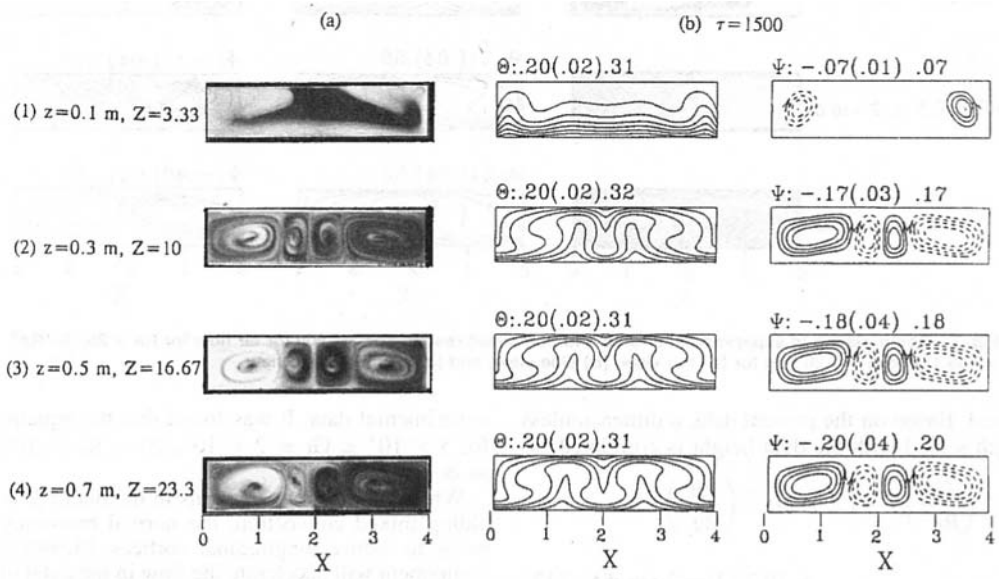

Fig. 9 (*a*) Experimental photos and (*b*) computed results at $\tau = 1500$ for air flow for Re = 35, $Gr/Re^2 = 228.6$, and $\phi = 26$ deg at selected cross sections

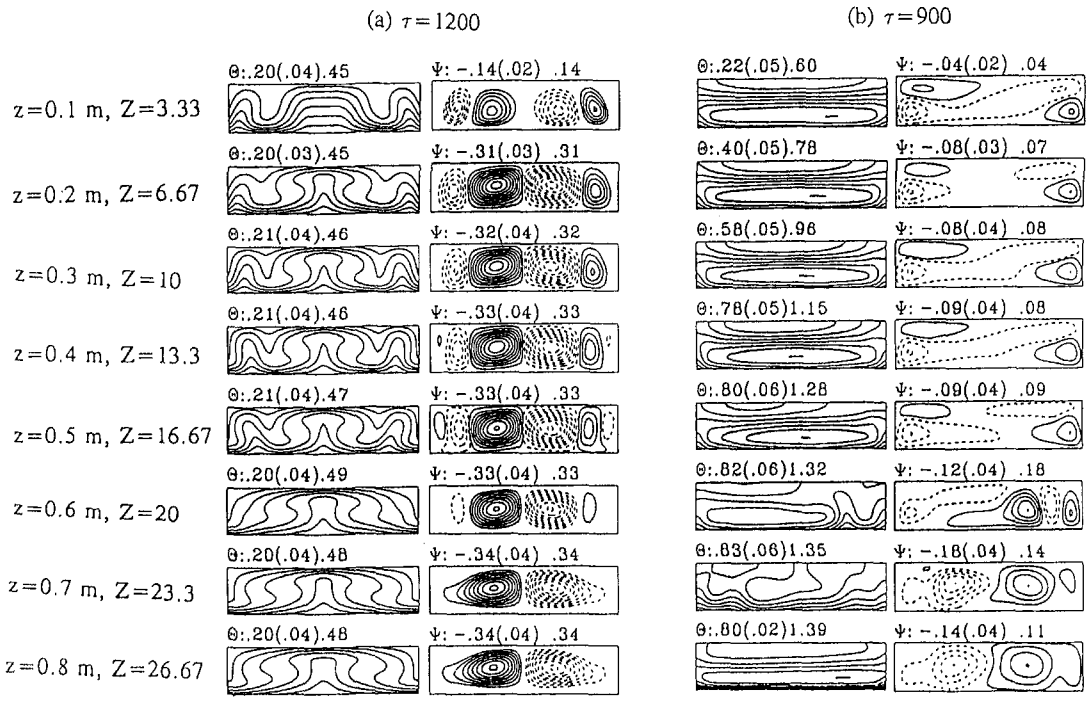

Fig. 10 Comparisons of the cross plane secondary flow from (*a*) conjugated analysis and (*b*) nonconjugated analysis for Re = 35, $Gr/Re^2 = 61.2$, and $\phi = -20$ deg at selected cross sections

slender reverse flow zone in the duct core if the opposing buoyancy force is high enough. At a higher buoyancy, the counter flow streams resulting from the downstream moving longitudinal rolls and the upstream moving reverse flow induce an unsteady snaking motion of the reverse flow, which in turn induces a number of eddies recirculating in the major portion of the duct. These experimentally observed flow structures are in qualitative agreement with the conjugated heat transfer analysis. Moreover, the conjugation of the conduction in the solid walls and the convection in the flow was shown to be rather significant in influencing the flow structure of the air flow and can not be ignored in the analysis.

It should be noted that in application, such as the growth of thin solid film from the chemical vapor deposition processes, the vortex flow should be stabilized and even eliminated to obtain a high quality film. Simple methods to stabilize and eliminate the vortex flow need to be investigated in the future.

Acknowledgment

The financial support of this study by the engineering division of National Science Council of Taiwan, R. O. C. through the contract NSC83-0404-E-009-054 is greatly appreciated. The computations were done on the IBM 580 workstations at the National Center for High-Performance Computing. Their support is also acknowledged.

References

Anderson, D. A., Tannehill, J. C., and Pletcher, R. H., 1984, *Computational Fluid Mechanics and Heat Transfer,* Hemisphere Publishing, Washington D. C., pp. 71–77.

Evans, G., and Geif, R., 1989, "A Study of Traveling Wave Instabilities in a Horizontal Channel Flow with Applications to Chemical Vapor Deposition," *International Journal of Heat and Mass Transfer,* Vol. 32, pp. 895–911.

Fukui, K., Nakajima, M., and Ueda, H., 1983, "The Longitudinal Vortex and its Effects on the Transport Processes in Combined Free and Force Laminar Convection between Horizontal and Inclined Parallel Plates," *International Journal of Heat and Mass Transfer,* Vol. 26, pp. 109–120.

Heggs, P. J., Ingham, D. B., and Keen, D. J., 1990, "The Effects of Heat Conduction in the Wall on the Development of Recirculating Combined Convection Flows in Vertical Tubes," *International Journal of Heat and Mass Transfer,* Vol. 33, pp. 517–528.

Holmes, D. B., and Vermeulen, J. R., 1968, "Velocity Profiles in Ducts with Rectangular Cross Sections," *Chemical Engineering Science,* Vol. 23, pp. 717–722.

Huang, C. C., and Lin, T. F., 1994, "Buoyancy Induced Flow Transition in Mixed Convective Flow of Air through a Bottom Heated Horizontal Rectangular Duct," *International Journal of Heat and Mass Transfer,* Vol. 37, pp. 1235–1255.

Incropera, F. P., 1988, "Convective Heat Transfer in Electronic Equipment Cooling," ASME JOURNAL OF HEAT TRANSFER, Vol. 110, pp. 1097–1111.

Ingham, D. B., Heggs, D. J., and Morton, B. R., 1990, "Recirculating Pipe Flows," *J. Fluid Mech.,* Vol. 213, pp. 443–464.

Kays, W. M., and London, A. L., 1984, *Compact Heat Exchangers,* 3rd ed., McGraw-Hill, New York, NY.

Kline, S. J., and McClintock, F. A., 1953, "Describing Uncertainties in Single-Sample Experiments," *Mechanical Engineering,* Vol. 75, pp. 3–12.

Koizumi, H., and Hosokawa, I., 1993, "Unsteady Behavior and Mass Transfer Performance of the Combined Convective Flow in a Horizontal Rectangular Duct Heated from Below," *International Journal of Heat and Mass Transfer,* Vol. 36, pp. 3937–3947.

Lavine, A. S., Kim, M. Y., and Shores, C. N., 1989, "Flow Reversal in Opposing Mixed Convection Flow in Inclined Pipes," ASME JOURNAL OF HEAT TRANSFER, Vol. 111, pp. 114–120.

Lin, W. L., and Lin, T. F., 1996, "Unstable Aiding and Opposing Mixed Convection of Air in a Bottom Heated Rectangular Duct Slightly Inclined from the Horizontal," ASME JOURNAL OF HEAT TRANSFER, Vol. 118, pp. 47–55.

Lin, W. L., Ker, Y. T., and Lin, T. F., 1996, "Experimental Observation and Conjugated Heat Transfer Analysis of Vortex Flow Development in Mixed Convection of Air in a Horizontal Rectangular Duct," *International Journal of Heat and Mass Transfer,* Vol. 39, pp. 3667–3683.

Maughan, J. R., and Incropera, F. P., 1987, "Experiments on Mixed Convection Heat Transfer for Airflow in a Horizontal and Inclined Channel," *International Journal of Heat and Mass Transfer,* Vol. 30, pp. 1307–1318.

Morcos, S. M., Hilal, M. M., Kamel, M. M., and Soliman, M. S., 1986, "Experimental Investigation of Mixed Laminar Convection in the Entrance Region of Inclined Rectangular Channels," ASME JOURNAL OF HEAT TRANSFER, 108, pp. 574–579.

Morton, B. R., Ingham, D. B., Keen, D. J., and Heggs, P. J., 1989, "Recirculating Combined Convection in Laminar Pipe Flow," ASME JOURNAL OF HEAT TRANSFER, Vol. 111, pp. 106–113.

Natarajan, N. M., and Lakshmanan, S. M., 1972, "Laminar Flow in Rectangular Ducts: Prediction of Velocity Profiles and Friction Factor," *Indian Journal of Technology,* Vol. 10, pp. 435–438.

Peyret, R., and Taylor, T. D., 1983, *Computational Methods for Fluid Flow,* Chap. 6, Springer-Verlag, New York.

Shah, R. K., and London, A. L., 1978, *Laminar Flow Force Convection in Ducts,* Academic Press, New York, pp. 196–198.

Optimal Geometric Arrangement of Staggered Vertical Plates in Natural Convection

G. A. Ledezma
Mem. ASME.

A. Bejan
J. A. Jones Professor.
Fellow ASME.

Department of Mechanical Engineering and Materials Science,
Duke University,
Durham, NC 27708-0300

This paper documents the geometric optimization of an assembly of staggered vertical plates that are installed in a fixed volume. The heat transfer is by laminar natural convection. The objective is to maximize the overall thermal conductance between the assembly of plates and the surrounding fluid. The geometric parameters that vary are the horizontal spacing between adjacent columns of plates, the number of plates mounted in each vertical column, the plate dimensions, and the stagger between columns. The optimization is performed numerically and experimentally in the range $Pr = 0.72$ *and* $10^3 \leq Ra_L \leq 10^6$, *where* Ra_L *is the Rayleigh number based on the vertical dimension of the assembly* (L). *The results for the optimal horizontal spacing are correlated using formulas derived from the theory of the intersection of asymptotes (Bejan, 1984, 1995).*

1 Introduction

A recent trend in heat transfer research is the simultaneous pursuit of fundamental results and optimization results that may have general applicability in design. This combination of fundamentals and design optimization is evident in the research on techniques for cooling electronics. The work is not limited to measuring or predicting the heat transfer performance of a given technique. An integral component of the work is the design aspect, for example, the optimization of the way in which the technique is implemented in a certain class of applications.

In the natural convection cooling of electronic components, it was found that the components can be arranged in an optimal way in the given volume such that the hot-spot temperature is minimal. This geometric-optimization subfield began with the study of natural convection in a space filled with vertical equidistant plates. Bejan (1984) and Bar-Cohen and Rohsenow (1984) showed that the plate-to-plate spacing or the number of plates installed in the volume can be selected optimally. Subsequent studies on stacks of vertical plates have established the spacing optimization as a fundamental feature of thermal design in the cooling of electronics (Peterson and Ortega, 1990; Anand et al., 1992; Kim and Lee, 1996). Similar geometric optima have been developed for forced convection cooling (e.g., Knight et al., 1991; Weisberg et al., 1992; Kim and Anand, 1994a, b).

The objective of the work reported in this paper is to apply the geometric optimization method to another important configuration, i.e., vertical plates (in-line or staggered) installed in a given volume. This configuration is considerably more complicated than the stacks of vertical plates that have been optimized until now. Additional geometric parameters are the number of plates installed in each column, the plate dimensions, and the relative position of adjacent columns (the stagger), e.g., Fig. 1. These geometric complications raise the question of which length scale of the assembly governs the optimal spacing between adjacent columns, the plate height or the height of the assembly? Furthermore, the assembly of staggered plates is a configuration with applications not only in the cooling of electronics, but also in heat exchangers subjected to volume constraints.

The geometric-optimization steps of the present work are made on the ground covered already by a significant body of research dedicated to the heat transfer fundamentals of staggered plates in vertical natural convection (e.g., Prakash and Sparrow, 1980; Sparrow and Faghri, 1980; Guglielmini et al., 1987; Tanda, 1993, 1995). Relative to the existing work, in the present paper we focus on the design optimization problem in a global sense, by maximizing the overall thermal conductance between the given volume (assembly of plates) and the surrounding fluid. We do this by adjusting little by little the geometric features of the assembly, so that we may compare the performances of a large number of similar configurations. In order to execute this voluminous work systematically and efficiently, we perform the optimization numerically and experimentally. The purpose of the numerical work is to generate a large volume of optimal-geometry information, which will be correlated using theory based formulas in the concluding section of the paper. The function of the experimental part is to demonstrate physically the existence of an opportunity to optimize the geometry of the assembly of plates and to show that the numerical optimal-spacing results can be used with confidence in the sizing of actual devices.

2 Geometric and Operational Parameters

The geometric parameters of the space filled with staggered parallel plates are defined in Fig. 1. The total volume occupied by this ensemble is fixed; it has the length L in the direction of gravity, the width H in the horizontal direction perpendicular to the plates, and breadth B in the direction perpendicular to the plane of Fig. 1. The plates are identical: each has a swept length b, thickness t, and breadth B.

The geometric arrangement of the plates has the following four degrees of freedom: the spacing W between two adjacent rows, the number of plates mounted in one row of length L, the plate height b, and the stagger parameter β defined in Fig. 1. The spacing W and plate dimension b can be nondimensionalized as

$$\tilde{W} = \frac{W}{L} \quad A = \frac{Nb}{L} \tag{1}$$

where A is dimensionless and proportional to the heat transfer area that comes in contact with the elemental channel indicated

Contributed by the Heat Transfer Division for publication in the JOURNAL OF HEAT TRANSFER. Manuscript received by the Heat Transfer Division January 21, 1997; revision received June 13, 1997; Keywords: Augmentation and Enhancement; Electronic Equipment; Finned Surfaces. Associate Technical Editor: P. G. Simpkins.

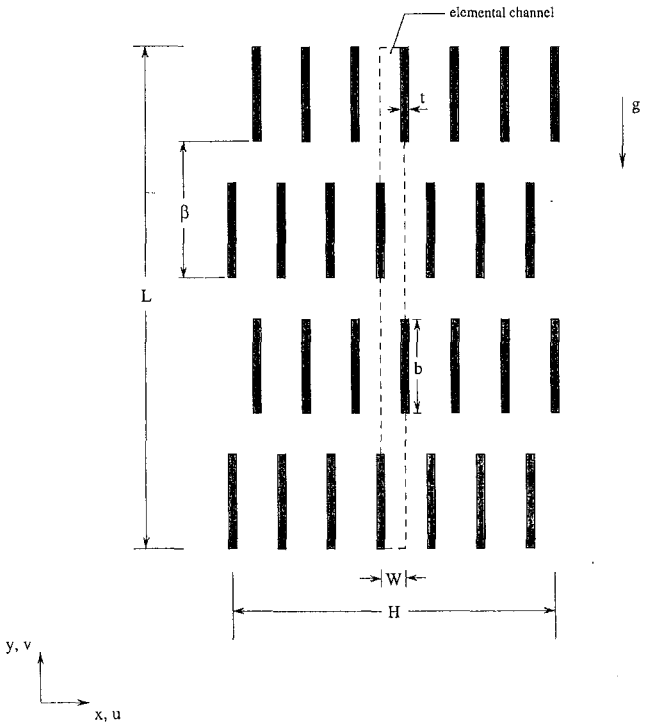

Fig. 1 The geometric parameters of a volume filled with staggered vertical plates

by the dashed lines in Fig. 1. In the A definition, N is the number of plates that are wetted by the flow through a single elemental channel (e.g., $N = 4$ in Fig. 1). According to this definition, $A = 2$ represents the limit where the plate edges touch. The stagger parameter is defined as

$$\tilde{\beta} = \frac{\beta}{\beta_{\max}} \tag{2}$$

where maximal stagger corresponds to $\tilde{\beta} = 1$, and $\beta_{\max} = (L - b)/(N - 1)$. The Rayleigh number is defined based on the height of the volume (L) and the difference between the plate temperature T_w (assumed the same for all the plates) and the ambient temperature, T_∞,

$$\mathrm{Ra}_L = \frac{g\beta(T_w - T_\infty)L^3}{\alpha\nu}. \tag{3}$$

The geometry of the assembly mounted in the volume $L \times H \times B$ can be changed by varying $\tilde{W}$, A, N, or β, or a combination of these parameters. We are interested in the geometric arrangement that maximizes the overall thermal conductance between the plates and the quiescent surrounding fluid. Since the overall dimensions are fixed, to maximize the overall thermal conductance means to maximize the ratio $q/[W(T_w - T_\infty)]$ of the elemental channel. A dimensionless alternative to this ratio, which is suitable for both numerical and experimental investigations described next, is

$$\tilde{q} = \frac{q}{W(T_w - T_\infty)kB/L} \tag{4}$$

where q is the heat transfer rate from a single elemental channel (Fig. 1). The total heat transfer rate from the entire assembly is $Q = qH/W$. Therefore, to maximize Q when the overall volume is fixed (LHB) is equivalent to maximizing $\tilde{q}$.

3 Numerical Method

The numerical simulations were developed in two steps. In the first we set up and tested a robust and reliable solver based on a Galerkin finite element method (FIDAP, 1993). In the second we compared and validated the finite-element solutions against our own finite element code. We assumed that there are enough elemental channels in the bundle ($H \gg W$) such that the flow through a single channel is representative of the flow through the complete bundle, Fig. 1. Consequently, our computational domain is two-dimensional and is represented by one elemental channel ($L \times W$) fitted with an upstream section ($L_u \times W$) and a downstream section ($L_d \times W$), as shown in Fig. 2. The lengths L_u and L_d were chosen based on accuracy tests that are described later in this section. All the simulations were performed for air ($\mathrm{Pr} = 0.72$). Four Ra_L values were used (10^3, 10^4, 10^5, and 5×10^5). In all the cases the flow is laminar because $\mathrm{Ra}_L < 10^9$ Pr, while $\mathrm{Ra}_L \sim 10^9$ Pr would mark the transition to turbulent boundary layer flow. The evidence that the streamlines are steady, nearly straight, and vertical when $\mathrm{Ra}_L < 10^9$ is voluminous, and can be found in the literature reviewed in Bejan and Lage (1990). In our case, the $\mathrm{Ra}_L < 10^9$ criterion is even more conservative because what counts in this criterion is the Rayleigh number (r) based on the height of a single plate and the temperature difference felt by that plate (note that $r < \mathrm{Ra}_L$; in other words, the criterion is $r < 10^9$).

The steady-state conservation equations for mass, momentum, and energy were simplified by assuming nearly constant properties and using the Oberbeck-Boussinesq approximation in the buoyancy term for the vertical momentum equation,

Nomenclature

A = dimensionless contact area, Eq. (1)
b = plate swept length, m (Fig. 1)
B = plate length (bundle width), m
D = spacing between L-long parallel plates
H = bundle thickness, m (Fig. 1)
k = fluid thermal conductivity
L = bundle flow length, m (Fig. 1)
L_d = downstream length, m
L_u = upstream length, m
N = number of plate surfaces facing the elemental channel (Fig. 1)
p = pressure, $\mathrm{N/m^2}$
q = heat transfer rate per elemental channel, W
$\tilde{q}$ = dimensionless overall thermal conductance, Eq. (4)
Q = total heat transfer rate from the bundle
$\mathbf{R}$ = residual vector
Ra_L = Rayleigh number, Eq. (3)
t = plate thickness, m (Fig. 1)
T = temperature, K
T_w = plate temperature, K
$\bar{T}_w$ = average surface temperature, K
T_∞ = ambient temperature, K
$\mathbf{u}$ = solution vector, Eq. (11)
u, v = velocity components, m/s
W = channel spacing, m (Fig. 1)
$\tilde{W}$ = dimensionless channel spacing, Eq. (1)
x, y = cartesian coordinates, m
α = thermal diffusivity, $\mathrm{m^2/s}$
β = stagger parameter, m (Fig. 1)
β = coefficient of volumetric thermal expansion, $\mathrm{K^{-1}}$
$\beta_{\max}$ = maximum stagger parameter
θ = dimensionless temperature, Eq. (10)
λ = kinematic viscosity, $\mathrm{m^2/s}$
$(\ )_{\max}$ = maximal
$(\ )_{\mathrm{opt}}$ = optimal
$\tilde{(\ )}$ = dimensionless variables, Eqs. (9)–(10)

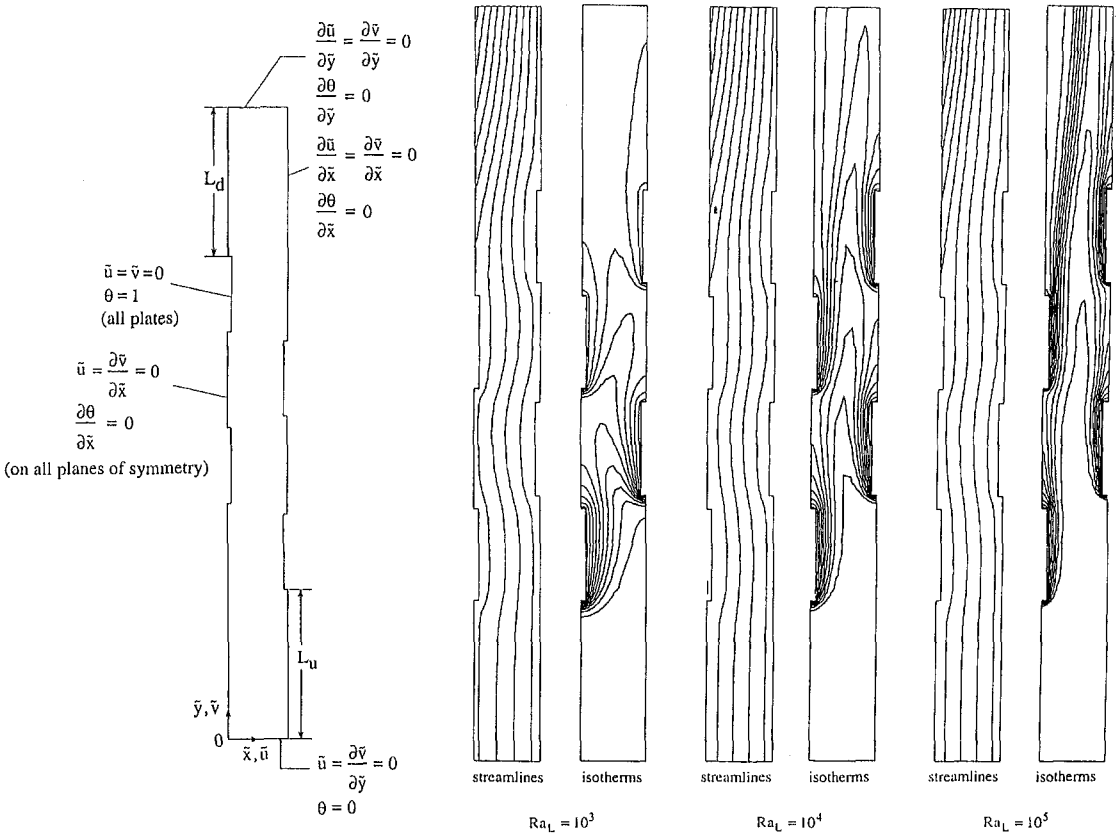

Fig. 2 The computational domain and boundary conditions for the case $A = 0.8$, $N = 4$, and $\tilde{\beta} = 1$, and the Ra_L effect on the flow and temperature field when $A = 0.9$, $N = 4$, $\tilde{W} = 0.16$, and $t/b = 0.1$

$$\frac{\partial u}{\partial x} + \frac{\partial v}{\partial y} = 0 \tag{5}$$

$$u\frac{\partial u}{\partial x} + v\frac{\partial u}{\partial y} = -\frac{1}{\rho}\frac{\partial p}{\partial x} + \nu\nabla^2 u \tag{6}$$

$$u\frac{\partial v}{\partial x} + v\frac{\partial v}{\partial y} = -\frac{1}{\rho}\frac{\partial p}{\partial y} + \nu\nabla^2 v + g\beta(T - T_\infty) \tag{7}$$

$$u\frac{\partial T}{\partial x} + v\frac{\partial T}{\partial y} = \alpha\nabla^2 T \tag{8}$$

where $\nabla^2 = \partial^2/\partial^2 x + \partial^2/\partial^2 y$. The origin of the cartesian frame (x, y), sketched in Fig. 2, is placed in the bottom left corner of the computational domain. The horizontal and vertical velocity components are u and v. The nondimensionalization of the governing equations is achieved by introducing the variables

$$(\tilde{x}, \tilde{y}) = \frac{(x, y)}{L} \quad (\tilde{u}, \tilde{v}) = \frac{(u, v)}{(\alpha/L)\,\mathrm{Ra}_L^{1/2}} \tag{9}$$

$$\theta = \frac{T - T_\infty}{T_w - T_\infty} \quad \tilde{P} = \frac{pL^2}{\mu\alpha\,\mathrm{Ra}_L^{1/2}}. \tag{10}$$

The following flow boundary conditions are indicated in Fig. 2: zero normal stress and vertical flow ($u = 0$) at the inlet to the computational domain ($y = 0$); free slip and no penetration at the fluid interfaces (planes of symmetry) between two consecutive plates; no slip and no penetration at the plate surfaces; and free slip and no penetration on the vertical boundaries of the inlet section. As we discovered in an earlier study (Bejan et al., 1995), we avoided an artificial upward acceleration of the fluid by specifying a zero-stress condition along the side opposite to the topmost plate. By specifying $\partial\tilde{u}/\partial\tilde{x} = 0$ over this portion of the boundary, we allow fluid to flow horizontally through the boundary (Fig. 2) and cancel the unrealistic vertical acceleration (chimney) effect that would have been created had we imposed no-slip on that surface. The temperature boundary conditions were $T = T_w$ on the plate surfaces, and $T = T_\infty$ at the bottom end ($y = 0$) of the computational domain. The remaining portions of the domain were modeled as adiabatic.

Equations (5)–(8) were nondimensionalized, cf. Eqs. (9) and (10), and then solved on a Cray T90. Quadrilateral elements with biquadratic interpolation functions were used. The explicit appearance of the pressure in the momentum equations was eliminated through the penalty function method. In all the simulations the compressibility parameter was 10^{-8}. The nonlinear equations resulting from the Galerkin finite element discretization were solved using successive substitution followed by a quasi-Newton method. The following convergence criteria were used,

$$\frac{\|\mathbf{u}^{(n)} - \mathbf{u}^{(n-1)}\|}{\|\mathbf{u}^n\|} \le 0.001 \quad \text{and} \quad \frac{\|\mathbf{R}(\mathbf{u}^{(n)})\|}{\|\mathbf{R}_0\|} \le 0.001 \tag{11}$$

where $\mathbf{R}(\mathbf{u})$ is the residual vector, and $\mathbf{u}$ is the complete solution vector. The norm $\|\cdot\|$ is an Euclidian norm. The grid was nonuniform in both $\tilde{x}$ and $\tilde{y}$-directions. The grid was double graded in the $\tilde{x}$-direction so as to put more nodes near the plate surfaces to capture the boundary layers. The grid varied from one geometric configuration to the next. The nodes in the $\tilde{x}$-direction were between 27 and 39. In the $\tilde{y}$-direction the nodal points varied from 121 to 145. Tests showed that the results were essentially insensitive to further grid doubling in both $\tilde{x}$ and $\tilde{y}$ (e.g., the changes in the channel heat transfer rate were less than 1 percent). Another set of accuracy tests showed that when $L_u/L = 0.44$ and $L_d/L = 0.5$, the channel heat transfer rate varied less than 0.3 percent after the doubling of the upstream and downstream lengths (L_u, L_d). The appropriateness of these lengths

Table 1 Comparison between the results generated with the FIDAP code and with our own penalty-finite-element code, using a uniform mesh with 100 nodes in the x-direction and 30 nodes in the y-direction ($A = 1$, $N = 4$, $\tilde{W} = 0.2$, $t/b \to 0$).

Ra_L	$\tilde{q}$	
	FIDAP	our code
10^3	16.134	15.192
10^4	30.528	28.942
10^5	52.238	50.187

was verified further through streamline and isotherm visualizations, as shown for three cases in Fig. 2.

The accuracy of the numerical method was further verified by placing a single plate of length $L = 2b$ (case $A = 2$) in the computational domain and calculating the overall Nusselt number $\bar{Nu}_L$ for $Ra_L = 10^3$ and 10^4. These results were compared with two well known results. One is the similarity solution for boundary layer natural convection on a vertical plate with uniform temperature (e.g., Bejan, 1993)

$$\bar{Nu}_L = 0.52\ Ra_L^{1/4}. \tag{12}$$

The other is the experimental correlation (Churchill and Chu, 1975)

$$\bar{Nu}_L = 0.68 + 0.52\ Ra_L^{1/4}. \tag{13}$$

which is particularly good in the low Ra_L limit where the boundary layer approximation loses its accuracy. For $Ra_L = 10^3$ our numerical method yielded $\bar{Nu}_L = 3.256$, while Eq. (13) predicts $\bar{Nu}_L = 3.586$ and Eq. (12) predicts $\bar{Nu}_L = 2.91$. Our numerical results falls within 11 percent between these two predictions. We repeated this comparison for $Ra_L = 10^4$ and found the same type of agreement.

The numerical results developed using FIDAP were validated against our own penalty finite element, which we constructed based on the formulation described by Reddy and Gartling (1994). In our code the penalty terms were evaluated using a reduced integration (1 point Gauss quadrature for the penalty terms and 2×2 Gauss quadrature to evaluate the integrals of the nonpenalty terms). The upwinding scheme described by Hughes (1978) was implemented to ensure convergence and to prevent oscillations when the Rayleigh number was greater than 10^4. The elements used were four-noded quadrilaterals (bilinear interpolation functions). In addition we used a penalty parameter equal to 10^{-8} to be consistent with the FIDAP solution. The finite element equations associated with Eqs. (5)–(8) were solved using a Newton-Raphson scheme. The convergence criteria of our code are based on the norm of the energy in the current iteration,

$$\left| \frac{\mathbf{R}^{(n)} \Delta \mathbf{d}^{(n+1)}}{\mathbf{R}^{(0)} \Delta \mathbf{d}^{(1)}} \right| \leq 10^{-12} \tag{14}$$

where $\mathbf{R}$ is the residual vector at the iteration n, and $\Delta \mathbf{d}$ is the displacement increment vector.

In order to compare the results obtained using the two numerical schemes, we selected the simple case $A = 1$, $N = 4$, $t/b \to 0$, and $\tilde{W} = 0.2$. We discretized the computational domain using a uniform mesh with 100×30 nodes and generated results for three different Rayleigh numbers (10^3, 10^4, and 10^5). The FIDAP results shown in Table 1 were obtained using bilinear interpolation functions in order to make a consistent comparison between FIDAP and our code. Table 1 shows that the agreement between the two methods was always within 6 percent. The fact that our finite element results underestimate the FIDAP results is due to the way in which we calculated the heat fluxes from the plates. In our post-processing phase we calculated the heat fluxes at the Gaussian points, which are not located exactly on the plate surface. In spite of this inconsistency, the nodal solutions for temperature and velocities agree within 1 percent in all the cases tested.

4 Numerical Results

In this section we report the numerical results for the optimal spacing $\tilde{W}$ between two adjacent rows and the optimal dimensionless heat transfer area A. Next, we document systematically the effect of the plate thickness, the effect of the number of plates N in a single channel, and the effect of changing the geometry of the array from perfectly staggered plates to aligned plates.

Figure 3 illustrates the voluminous character of the numerical work and the design optimization objective that guided this work. The results displayed in Fig. 3 correspond only to the case ($N = 4$, $t/b = 0.1$) and show the effect of varying the horizontal spacing $\tilde{W}$, the Rayleigh number, and the contact area per elemental channel (A). The main conclusion is that $\tilde{q}$ has a distinct maximum with respect to $\tilde{W}$. The optimal plate-to-plate spacing ($\tilde{W}_{opt}$) decreases as the Rayleigh number increases, and increases as A increases. These trends are clearer in Fig. 4, which summarizes the $\tilde{W}_{opt}$ values deduced from the series of numerical runs displayed in Fig. 3.

The maximized thermal conductance values that correspond to Fig. 4 are reported in Fig. 5. The $\tilde{q}_{max}$ values decrease as A increases while the number of plates N is held fixed. This behavior is due to the thickening of the boundary layers, which occurs when the plate height b increases. As expected, the maximized thermal conductance increases with the Rayleigh number. These trends are confirmed by experimental measurements (section 5) and correlated in the concluding section of this paper.

The effect of varying the thickness of the plates is documented in Fig. 6. In the range $0 \leq t/b \leq 0.1$, the relative thickness t/b does not change significantly the optimal spacing and corresponding maximal thermal conductance. The effect of t/b is felt only on the small-spacings side ($\tilde{W} < \tilde{W}_{opt}$) of the thermal conductance maximum.

In the results exhibited in Figs. 3–6, the number of plates in contact with one elemental channel was fixed at $N = 4$. The effect of varying N while holding A constant is illustrated in Fig. 7. Note that to increase N while A is fixed means to use more numerous plates that are shorter. The effect of N on the optimal spacing is not negligible, especially when N is small. When N is greater than 10, the use of more plates to install the same area (A) in the elemental channel has practically no effect on $\tilde{W}_{opt}$. This conclusion is strengthened by the corresponding behavior of $\tilde{q}_{max}$: the number of plates per elemental channel does not change $\tilde{q}_{max}$ when $N \geq 4$. There is a slight advantage — a 15 percent increase in $\tilde{q}_{max}$—to installing the smallest number of plates in the channel ($N = 2$).

The stagger parameter $\tilde{\beta}$ has a perceptible effect on the maximized thermal conductance, as illustrated in Fig. 8. The best arrangement is the one with no stagger (plates in line horizontally); the $\tilde{q}_{max}$ value for plates in line ($\tilde{\beta} = 0$) exceeds by 9 percent the $\tilde{q}_{max}$ value of perfectly staggered plates ($\tilde{\beta} = 1$). The effect of $\tilde{\beta}$ on the optimal spacing of the elemental channel is negligible.

5 Experimental Results

For a more definitive demonstration of the geometric optimization principle, we conducted a series of experiments in which we varied the plate-to-plate spacing $\tilde{W}$. The objective in these experiments was to show that W can be selected such that the

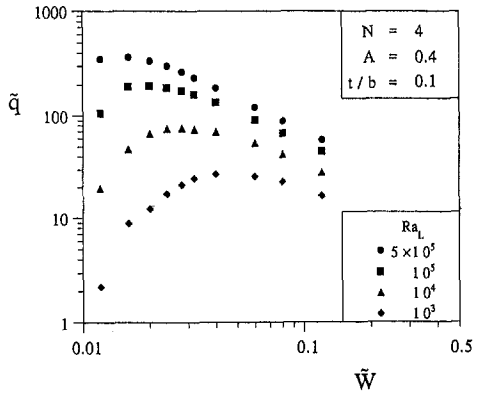

(a)

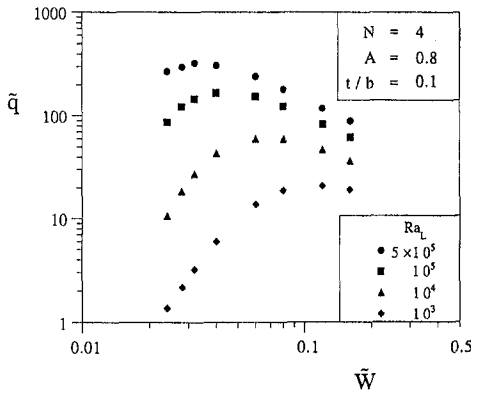

(b)

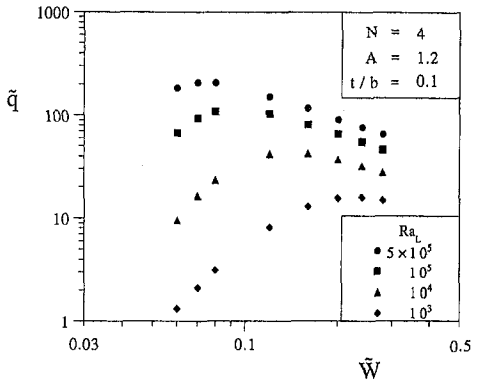

(c)

Fig. 3 Numerical results showing the effects of plate-to-plate spacing, Rayleigh number and heat transfer area per elemental channel

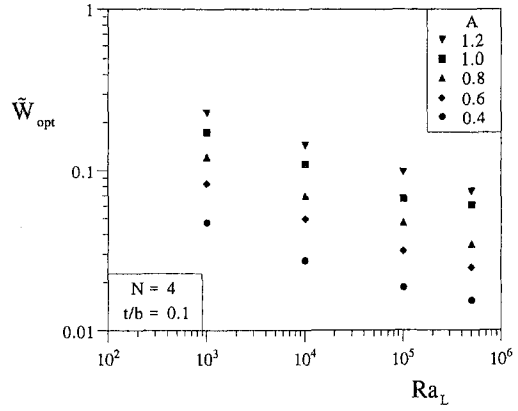

Fig. 4 Effect of the Rayleigh number and the channel heat transfer area on the optimal channel spacing

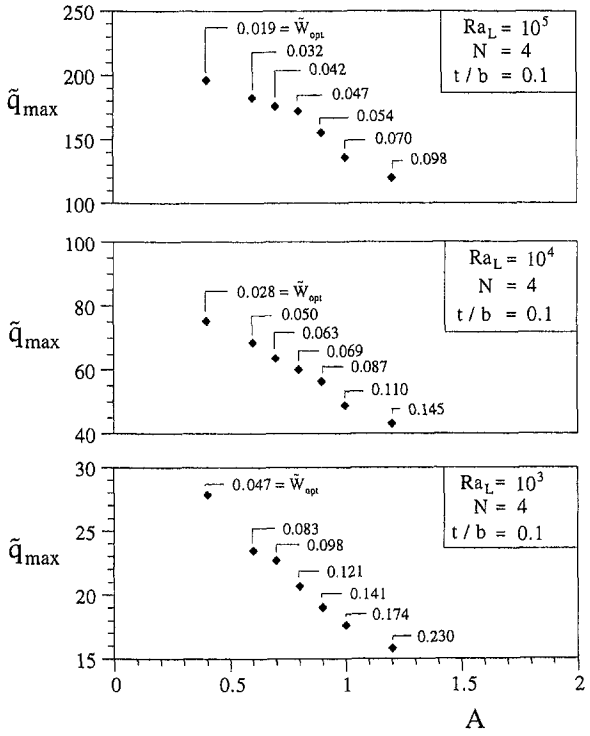

Fig. 5 The effect of the channel heat transfer area on the optimal channel spacing and the corresponding maximum heat transfer rate

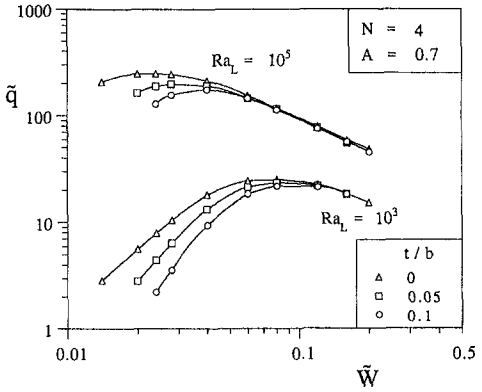

Fig. 6 The effect of the plate thickness on the overall thermal conductance and the optimal channel spacing

overall thermal conductance of the assembly is maximized. The objective was not to reproduce in the laboratory the idealized configurations that were simulated numerically; this would have been impossible in view of the size constraints (e.g., number of plates and elemental channels) of the experimental apparatus. In spite of these difficulties an additional objective of the experimental work was to show that the geometric optimization results developed numerically in section 4 are adequate for engineering

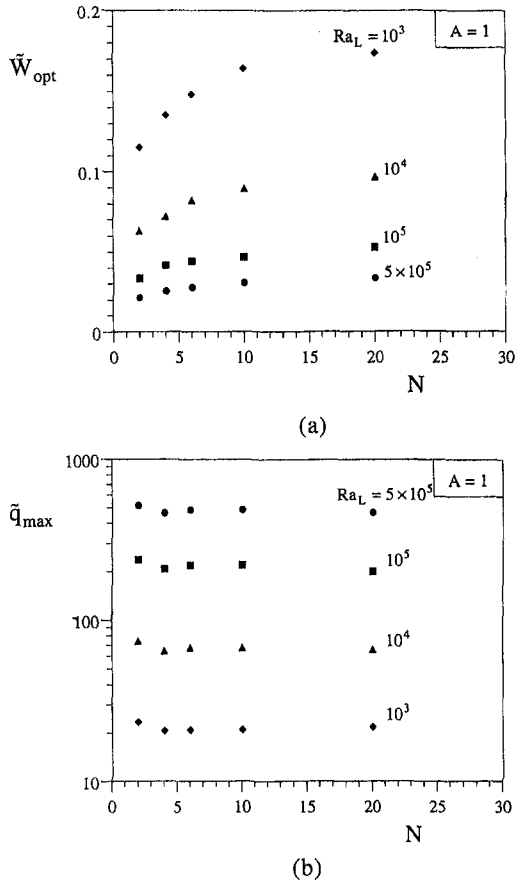

Fig. 7 The effect of the number of plates N on the optimal channel spacing and the maximum heat transfer rate when the heat transfer area per channel is fixed

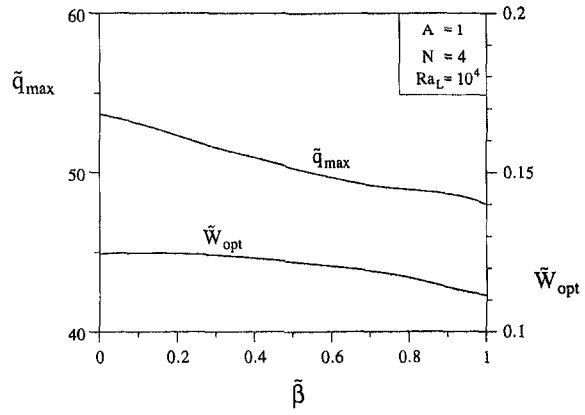

Fig. 8 The effect of the stagger parameter $\tilde{\beta}$ on the optimal channel spacing and the maximal heat transfer rate

design purposes, e.g., for selecting the optimal spacing between vertical plates in actual applications.

The main features of the experimental apparatus are illustrated in Fig. 9. The volume occupied by the plates assembly was the same in all the experiments. Another feature held constant in all the experiments was the heat transfer area per channel, $A = 1.2$. We varied the total number of plates and their arrangement in the assembly. We tested assemblies with 4, 6, 8, 10, and 12 plates, however, in all the assemblies each elemental channel had $N = 4$. The stagger parameter was maximum (β_{max}) in all the experiments. In summary, the geometries tested experimentally had only one degree of freedom, the channel spacing $\tilde{W}$.

The right part of Fig. 9 shows the experimental assembly in which we used six plates. Each plate was a thin thermofoil heater (MINCO HR5334R17.2L12A, resistance 17.2Ω) which was sandwiched between two aluminum strips with a thickness of 0.3 mm. The heater and the strips were bonded tightly using a highly conductive cement (#6 RTV). The plates were heated identically: they were connected in parallel and powered by a variable autotransformer that produced voltages between 0 and 140 volts.

Each assembly was tested inside an enclosure with the dimensions 304 mm × 304 mm × 914 mm. The internal and external surfaces of the enclosure were covered with aluminum foil to minimize the effect of thermal radiation. The top and bottom ends of the enclosure were left open in order to prevent the stagnation and gradual warming of the trapped air.

The temperatures were measured using four precision thermistors (YSI44004, resistance 2250Ω at 25°C), which were calibrated in the laboratory. The bias limit of our temperature measurements was ±0.001 K. It was deduced from the resistance versus temperature response measured during the calibration of each thermistor [$dT/dR = (-1/14)$ K/Ω] and from the 0.01Ω resolution of the HP 3468B ohmmeter with which we read the thermistor resistance.

The central part of Fig. 9 shows the thermistor positions. Two thermistors were attached to the surface of one of the trailing plates in the assembly along the midline of the surface. We selected a trailing plate for this measurement because the highest temperature in vertical natural convection occurs at the trailing end of the configuration. The readings provided by the two thermistors were labeled T_{w1} and T_{w2}. A third thermistor was attached along the midline of an upstream plate. The fourth thermistor was positioned 30 mm upstream of the assembly and 100 mm to the side (in the horizontal direction), for measuring the temperature of the quiescent air.

The experiments were designed for three Rayleigh numbers, $Ra_L = 10^5$, 5×10^5, and 10^6. Each overall thermal conductance was estimated by taking 25 measurements of the power dissipated in all the heaters (q), the maximum temperature (T_{w1}), and the air temperature (T_∞). The $\tilde{q}$ values were calculated using Eq. (4) with T_{w1} in place of T_w. The properties of air were evaluated at the film temperature $(T_w + T_\infty)/2$, where $T_w = (T_{w1} + T_{w2})/2$.

The uncertainties associated with $\tilde{q}$ and Ra_L were estimated based on the method described by Moffat (1988). The bias limit of 0.001 K determined during the calibration of the thermistors agrees with the bias limit reported by Howle et al. (1992) and an instrumentation handbook (Dally et al., 1993). The bias limit for the voltage across the plate heaters and their resistance are 0.001 V and, respectively, 0.86 Ω (i.e., 5 percent of 17.2 Ω). The uncertainty in the tabulated properties of air (μ, k, α, β) was taken as 5 percent. The precision limit of measured quantities such as the temperature and the power dissipated by the heaters was estimated as two times the standard deviation. The precision limit values for temperature were as high as 0.18 K, which made the 0.001 K bias limit negligible. Table 2 shows the experimental uncertainties calculated for $\tilde{q}$ and Ra_L.

An important limitation of the apparatus design is the size (horizontal dimension) of the space in which the assembly is tested. In the example shown on the right side of Fig. 9 there was room for only two of the "elemental channels" that were defined in Fig. 1. In the experiments a portion of the buoyant air flowed around (on the outside) of the two central elemental channels. This by-pass flow distinguishes the experimental configuration from the numerical model ($H \gg W$) constructed in Figs. 1 and 2. To account for this difference and still be able to make a meaningful comparison between the experimental setup and the closest numerical con-

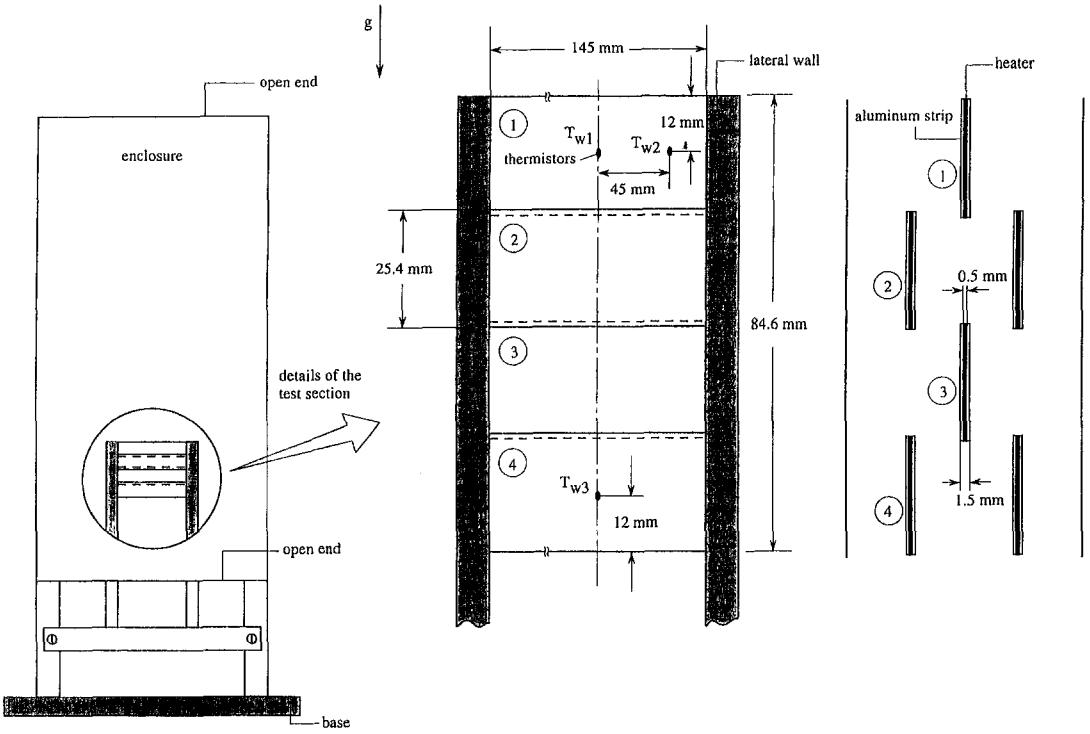

Fig. 9 The experimental apparatus

figuration available in the experiments, we calculated $\tilde{q}$ based only on the heat transfer rate released into the elemental channels, which constituted the volume that was held fixed (see Fig. 10 inset).

Figure 10 shows the experimental results for the effect of channel spacing on the overall thermal conductance of the assembly. An optimal spacing $\tilde{W}$ that maximizes $\tilde{q}$ exists for each of the Rayleigh numbers that we considered. The behavior is similar to what we found in the numerical part of the study (e.g., Fig. 3). The agreement between the experimental and numerical results is quantitative as well. In Table 3 we show the optimal spacings determined experimentally (Fig. 10) next to the numerical results developed for $N = 4$, $A = 1.2$, $\tilde{\beta} = 1$, and $t/b = 0.1$. The agreement is very good, certainly from the point of view of optimizing the geometry of an engineering system. Note that in order to attain a $\tilde{q}$ value close to $\tilde{q}_{max}$ it is sufficient to approximate $\tilde{W}_{opt}$ within 20 or 30 percent. The agreement with respect to optimal spacing is illustrated further in Fig. 11: if the builder uses the $\tilde{W}_{opt}$ value predicted based on numerical simulations, then the device will operate close to the highest $\tilde{q}$ value of which it is capable. The agreement between the experimental and numerical $\tilde{q}_{max}$ values (within 27 percent) is also worth noting, in view of the by-pass air flow and calculation of $\tilde{q}$ during experiments.

Table 2 Experimental uncertainties: the table shows the values of $[U_{\tilde{q}}/\tilde{q}]/[U_{Ra_L}/Ra_L]$.

$\tilde{W}$	$Ra_L = 10^5$	5×10^5	10^6
0.296	0.105 / 0.098	0.026 / 0.077	0.063 / 0.062
0.148	0.126 / 0.137	0.061 / 0.065	0.059 / 0.062
0.099	0.088 / 0.103	0.06 / 0.063	0.058 / 0.06
0.074	0.075 / 0.077	0.065 / 0.062	0.059 / 0.064
0.059	0.061 / 0.057	0.061 / 0.059	0.062 / 0.064

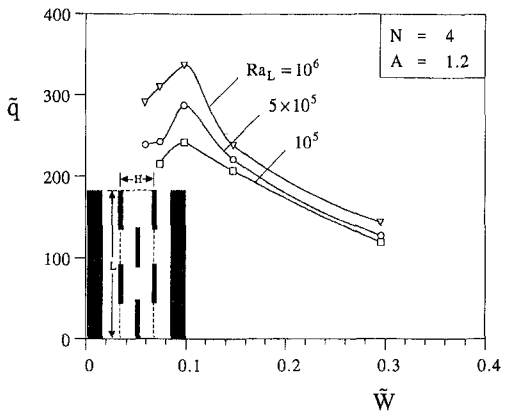

Fig. 10 Experimental results showing the effect of the channel spacing on the overall thermal conductance of the assembly

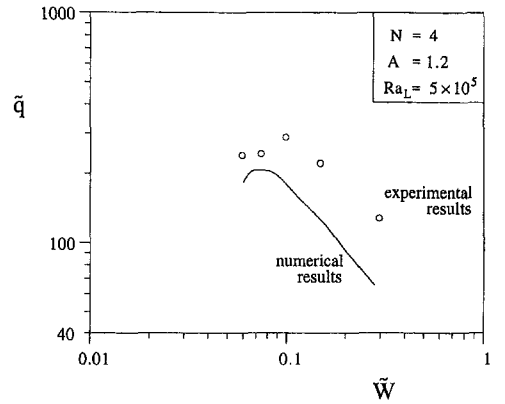

Fig. 11 Comparison between the experimental and the numerical results for the geometric maximization of the overall thermal conductance

6 Discussion

In this paper we showed that the geometric arrangement of vertical staggered plates in a fixed volume can be optimized such that the thermal conductance between the assembly and the surrounding fluid is maximized. We demonstrated this optimization principle numerically and experimentally. The geometric optimum owes its existence to the fact that the vertical natural convection boundary layers that coat the plates have a characteristic thickness, the best way to fill the given space is by selecting spacings that are comparable with the boundary layer thicknesses (e.g., Bejan, 1984; Bar-Cohen and Rohsenow, 1984; Guglielmini et al., 1987; Tanda, 1993, 1995).

This explanation of the optimal geometry is also a way to correlate and condense the present results into compact formulas that have a theoretical basis. The work on constrained volumes filled with parallel continuous plates showed that the optimal plate-to-plate spacing and the maximal thermal conductance of the assembly can be predicted by using a spacing W of the same order as the boundary layer thickness $L\ \mathrm{Ra}_L^{-1/4}$, where L is the height of the assembly. For example, these results are illustrated in closed form by the brief analysis shown in Bejan (1995), which yielded

$$\frac{W_{\text{opt}}}{L} \cong 2.3\ \mathrm{Ra}_L^{-1/4} \tag{15}$$

$$\frac{Q_{\max}}{LHB} \lessapprox 0.45\ \frac{k}{L^2}\ \mathrm{Ra}_L^{1/2}. \tag{16}$$

Equations (15) and (16) are purely theoretical: they represent the trade-off point obtained by intersecting the small and large-spacing asymptotes of the assembly. The overall thermal conductance is maximum at this point, Eq. (16), because in the small-W limit the flow experiences blockage, while in the large-W limit the heat transfer area vanishes. The intersection of the asymptotes method was applied to several configurations in both natural and forced convection, as reviewed in Bejan (1995). Rewritten in the dimensionless notation used in this paper, Eqs. (15) and (16) become

$$\tilde{W}_{\text{opt}} \cong 2.3\ \mathrm{Ra}_L^{-1/4} \tag{17}$$

$$\tilde{q}_{\max} \lessapprox 0.45\ \mathrm{Ra}_L^{1/2}. \tag{18}$$

Equations (17) and (18) serve as a guide in correlating the geometric optimization results reported in this paper. We seek power-law functions of Ra_L and find that our numerical results (in Fig. 3, $10^3 \leq \mathrm{Ra}_L \leq 5 \times 10^5$, $0.4 \leq A \leq 1.2$, $N = 4$, $t/b = 0.1$) are correlated within 6.7 percent and, respectively, 6 percent by

$$\tilde{W}_{\text{opt}} \cong 0.63A^{1.48}\ \mathrm{Ra}_L^{-0.19} \tag{19}$$

$$\tilde{q}_{\max} \cong 1.92e^{-0.7A}\ \mathrm{Ra}_L^{0.43}. \tag{20}$$

Note that the 6 percent deviation represents a very tight correlation in view of the additional geometrical complications (physical differences between competing designs) brought about by the presence of several plates in each vertical column.

The agreement between Eqs. (19) and (20) and Eqs. (17) and (18) is both qualitative and quantitative. For example, when $\mathrm{Ra}_L = 5 \times 10^5$ and $A = 1$, Eq. (19) yields $\tilde{W}_{\text{opt}} = 0.052$, which is only 40 percent smaller than the estimate based on the continuous-plates formula, Eq. (17), (that is, a theory for a different setup), namely $\tilde{W}_{\text{opt}} = 0.086$. On the usefulness of being able to anticipate $\tilde{W}_{\text{opt}}$ approximately and efficiently we commented when we discussed Table 3. For the same (Ra_L, A) case, Eq. (20) yields $\tilde{q}_{\max} \cong 268$, which is 16 percent smaller than (i.e., on the correct side of) the result based on Eq. (18), $\tilde{q}_{\max} \lessapprox 318$.

Table 3 Numerical and experimental optimal spacings for $A = 1.2$ and $N = 4$

Ra_L	$\tilde{W}$ (numerical)	$\tilde{W}$ (experimental)
10^5	0.098	0.109
5×10^5	0.074	0.107
10^6	0.069	0.099

7 Conclusion

This paper demonstrated numerically and experimentally that it is possible to optimize geometrically the internal architecture of a finite-size volume such that its global thermal resistance is minimized. The optimal arrangement of vertical staggered plates in natural convection reported in this paper is only the most recent in a continuing series of geometric optimization results in both natural and forced convection (Bejan, 1995). This geometric approach is important not only in engineering design but also in explaining, in purely theoretical fashion, the origin of the formation of geometry (e.g., shape, structure, and nonuniformities) in nature, in both animate and inanimate systems (Bejan, 1997; Ledezma et al. 1997).

Acknowledgments

This research was supported by the National Science Foundation. The numerical work was supported by a grant from the North Carolina Supercomputing Center. The authors thank Prof. Alex Fowler and Prof. Jose Vargas for their advice during the formulation of the numerical model and method.

References

Anand, N. K., Kim, S. H., and Fletcher, L. S., 1992, "The Effect of Plate Spacing on Free Convection Between Heated Parallel Plates," ASME JOURNAL OF HEAT TRANSFER, Vol. 114, pp. 515–518.

Bar-Cohen, A., and Rohsenow, W. M., 1984, "Thermally Optimum Spacing of Vertical, Natural Convection Cooled, Parallel Plates," ASME JOURNAL OF HEAT TRANSFER, Vol. 106, pp. 116–123.

Bejan, A., 1984, *Convection Heat Transfer*, John Wiley & Sons, Inc., New York, p. 157, problem 11.

Bejan, A., 1993, *Heat Transfer*, John Wiley & Sons, Inc., New York.

Bejan, A., 1995, *Convection Heat Transfer*, 2nd ed., John Wiley & Sons, Inc., New York, pp. 202–205.

Bejan, A., 1997, "Constructal-Theory Network of Conducting Paths for Cooling a Heat Generating Volume," *Int. J. Heat Mass Transfer*, Vol. 40, No. 4, pp. 799–816.

Bejan, A., and Lage, J. L., 1990, "The Prandtl Number Effect on the Transition in Natural Convection Along a Vertical Surface," ASME JOURNAL OF HEAT TRANSFER, Vol. 112, pp. 787–790.

Bejan, A., Fowler, A. J., and Stanescu, G., 1995, "The Optimal Spacing Between Horizontal Cylinders in a Fixed Volume Cooled by Natural Convection," *Int. J. Heat Mass Transfer*, Vol. 38, pp. 2047–2055.

Churchill, S. W., and Chu, H. H. S., 1975, "Correlating Equations for Laminar and Turbulent Free Convection from a Vertical Plate," *Int. J. Heat Mass Transfer*, Vol. 18, pp. 1323–1329.

Dally, J. W., Riley, W. F., and McConnell, K. G., 1993, *Instrumentation for Engineering Measurements*, John Wiley & Sons, Inc., New York, p. 425.

FIDAP Theory Manual, 1993, Fluid Dynamics International, Evanston, IL, V. 7.0.

Guglielmini, G., Nannei, E., and Tanda, G., 1987, "Natural Convection and Radiation Heat Transfer From Staggered Vertical Fins," *Int. J. Heat Mass Transfer*, Vol. 30, pp. 1941–1948.

Howle, L., Georgiadis, J., and Behringer, R., 1992, "Shadowgraphic Visualization of Natural Convection in Rectangular-Grid Porous Layers," *ASME HTD-Vol. 206-1*, pp. 17–24.

Hughes, T. J. R., 1978, "A Simple Scheme for Developing 'Upwind' Finite Elements," *Int. J. Num. Methods in Eng.*, Vol. 12, pp. 1359–1365.

Kim, S. H., and Anand, N. K., 1994a, "Laminar Developing Flow and Heat Transfer Between a Series of Parallel Plates With Surface-Mounted Discrete Heat Sources," *Int. J. Heat Mass Transfer*, Vol. 37, pp. 2231–2244.

Kim, S. H., and Anand, N. K., 1994b, "Turbulent Heat Transfer Between a Series of Parallel Plates With Surface-Mounted Discrete Heat Sources," ASME JOURNAL OF HEAT TRANSFER, Vol. 116, pp. 577–587.

Kim, S. J., and Lee, S. W., 1996, *Air Cooling Technology for Electronic Equipment*, CRC Press, Boca Raton, FL.

Knight, R. W., Goodling, J. S., and Hall, D. J., 1991, "Optimal Thermal Design of Forced Convection Heat Sinks—Analytical," *ASME Journal of Electronic Packaging,* Vol. 113, pp. 313–321.

Ledezma, G. A., Bejan, A., and Errera, M. R., 1997, "Constructal Tree Networks for Heat Transfer," *J. Appl. Phys.,* Vol. 82(1), pp. 89–100.

Moffat, R. J., 1988, "Describing Uncertainties in Experimental Results," *Exp. Thermal Fluid Sci.,* Vol. 1, pp. 3–17.

Peterson, G. P., and Ortega, A., 1990, "Thermal Control of Electronic Equipment and Devices," *Adv. Heat Transfer,* Vol. 20, pp. 181–314.

Prakash, C., and Sparrow, E. M., 1980, "Natural Convection Heat Transfer Performance Evaluations for Discrete- (In-Line or Staggered) and Continuous-Plate Arrays," *Num. Heat Transfer,* Vol. 3, pp. 89–105.

Reddy, J. N., and Gartling, D. K., 1994, *The Finite Element Method in Heat Transfer and Fluid Dynamics,* CRC Press, Boca Raton, pp. 223–226.

Sparrow, E. M., and Faghri, M., 1980, "Natural Convection Heat Transfer from the Upper Plate of a Colinear, Separated Pair of Vertical Plates," ASME JOURNAL OF HEAT TRANSFER, Vol. 102, pp. 623–629.

Tanda, G., 1993, "Natural Convection Heat Transfer From a Staggered Vertical Plate Array," ASME JOURNAL OF HEAT TRANSFER, Vol. 115, pp. 938–945.

Tanda, G., 1995, "Experiments on Natural Convection From Two Staggered Vertical Plates," *Int. J. Heat Mass Transfer,* Vol. 38, pp. 533–543.

Weisberg, A., Bau, H. H., and Zemel, J. N., 1992, "Analysis of Microchannels for Integrated Cooling," *Int. J. Heat Mass Transfer,* Vol. 35, pp. 2465–2474.

Laminar Natural Convection From an Elliptic Tube With Different Orientations

H. M. Badr

Mechanical Engineering Department,
King Fahd University of
Petroleum and Minerals,
Dhahran 31261,
Saudi Arabia
badrhm@dpc.kfupm.edu.sa

The problem of two-dimensional natural convection heat transfer from a straight tube of elliptic cross section is investigated. The tube, which has an isothermal surface, is placed with its axis horizontal in an initially quiescent fluid of infinite extent. The velocity and thermal fields are obtained by studying the time development of these fields following a sudden increase of the tube surface temperature until reaching steady state. The study is based on the solution of the full conservation equations of mass, momentum, and energy with no boundary layer simplifications. The paper focuses on the effects of the tube orientation, axis ratio, and Rayleigh number while keeping the Prandtl number unchanged (Pr = 0.7). The study revealed that the maximum average Nusselt number is obtained when the tube major axis is vertical. Within the range of axis ratios considered (Ar = 0.4 to 0.98), smaller Ar resulted in higher heat transfer rate in most cases. Higher Rayleigh number leads to higher velocities and also higher local and average Nusselt numbers in all cases considered. The details of the steady flow and thermal fields are presented in the form of local Nusselt number and surface vorticity distributions as well as streamline and isotherm patterns for some selected cases.

1 Introduction

Natural convection from cylinders or tubes of elliptic shapes are receiving growing interest since they cover a wide extent of geometries ranging from a flat plate (when the axis ratio Ar = 0) to a circular tube (Ar = 1). This paper deals with the problem of two-dimensional laminar natural convection from an elliptic isothermal tube placed horizontally in an initially static fluid of infinite extent. The variables affecting natural convection are the Rayleigh number, Ra, Prandtl number, Pr, tube axis ratio (minor to major axis ratio), Ar, and tube orientation, represented by the angle of inclination of the major axis, λ. The resulting flow and thermal fields are symmetric about the tube's minor or major axis only when either one is vertical and asymmetric for other orientations.

Interest in studying natural convection from elliptic tubes started in the early 70's when Lin and Chao (1974) reported their results on natural convection from two-dimensional and axisymmetric bodies with circular and elliptic cylinders as special cases. The solution had the drawback of its inapplicability in the buoyant plume region since it was based on the solution of the boundary layer equations with the buoyancy term replaced by a hypothetical outer stream velocity function. No results were reported on the asymmetrical case when the major axis is inclined. Raithby and Hollands (1976) studied the problem of natural convection from an elliptic cylinder with a vertical plate and a horizontal circular cylinder as special cases. The study was limited to the vertical major axis configuration. In their work, a thin layer analysis applicable only to thin boundary layer flows was modified to take into consideration the effect of surface curvature. The average Nusselt numbers were found to be in good agreement with the experimental data for a wide range of Rayleigh numbers. Merkin (1977) studied the symmetrical case of the same problem when either the major axis or the minor axis was vertical. The study was based on the solution of the boundary layer equations, and results were obtained for the entire cylinder surface excluding the buoyant plume region. None of the above researchers considered the low Ra range when boundary layer simplifications are invalid. The most relevant experimental study is that reported by Huang and Mayinger (1984) in which laminar natural convection from elliptic tubes was studied for different orientations and for different axis ratios. The average and local Nusselt numbers were reported together with correlations for $\overline{Nu}$. Badr and Shamsher (1993) solved the problem of free convection from an elliptic cylinder for Rayleigh numbers ranging from 10 to 10^3, and axis ratios ranging from 0.1 to 0.964. The solution covered the entire flow region with no boundary layer approximations. The paper focused on the final steady solution only for the special case of a vertical major axis with no details reported on the transient results.

The two limiting cases of the elliptic tube (namely the flat plate and the circular cylinder) received a considerable attention in the past. The reported work on the limiting case of Ar = 1 include the papers by Pera and Gebhart (1972), Merkin (1976), Kuehn and Golstein (1980), and Farouk and Guceri (1981) which dealt with the analysis of the steady natural convection regime. The same problem was studied by Elliot (1970) and Badr (1987) but with emphasis on the transient phase of the development of the thermal field as it approaches its final steady state. The boundary layer equations were solved by Elliot (1970) while the full equations were considered by Badr (1987). The other limiting case of a flat plate (Ar = 0) was studied by Goldstein and Briggs (1964) who investigated transient free convection from vertical semi-infinite plates and circular cylinders following a change in wall temperature. The problem of steady free convection from finite vertical and horizontal plates was solved by Suriano and Yang (1968) in the Rayleigh number range up to 300. The streamline and temperature contours were plotted for both low Ra conduction regime and moderate Ra convection regime. Hardwick and Levy (1973) focused on the analysis of the wake region above an isothermal vertical plate. The problem was investigated theoretically and experimentally in order to determine the temperature and velocity profiles in the wake for Grashof numbers ranging from 10^4 to 10^5. Correlating equations for laminar and turbulent

Contributed by the Heat Transfer Division for publication in the JOURNAL OF HEAT TRANSFER. Manuscript received by the Heat Transfer Division May 30, 1996; revision received April 14, 1997; Keywords: Natural Convection; Numerical Methods. Associate Technical Editor: K. Vafai.

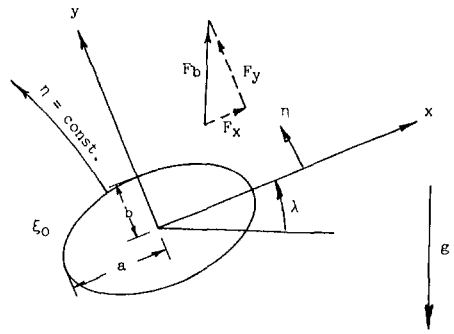

Fig. 1 The elliptic tube geometry and the coordinate system

free convection from a vertical plate were reported by Churchill and Chu (1975) based on the available experimental data and theoretical solutions for Rayleigh numbers ranging from zero to infinity. The spatial development of the wall and free plumes above a heated vertical plate was investigated by Sparrow et al. (1978). The investigation was based on the solution of the laminar boundary layer equations in order to determine the velocity and temperature profiles in the plume which was either developing freely or adjacent to an adiabatic wall. The distances required to reach a fully developed plume were obtained in both cases.

2 Conservation Equations and Method of Solution

Consider a straight tube placed horizontally in an initially quiescent fluid of temperature T_∞. The tube cross section is elliptic with major axis $2a$ and minor axis $2b$. The major axis is inclined to the horizontal with an angle λ, as shown in Fig. 1. The tube surface temperature is suddenly and uniformly increased to T_s, thus creating a buoyancy driven flow. The initial flow is transient but approaching steady state as time increases. The tube is long enough such that the end effects can be neglected and the resulting flow and thermal fields can be considered two-dimensional. Assuming a Boussinesq fluid and neglecting viscous dissipation, the conservation equations of mass, momentum and energy can be expressed as:

$$-\zeta = \nabla^2\psi \tag{1}$$

$$\frac{\partial\zeta}{\partial t} + u\frac{\partial\zeta}{\partial x} + v\frac{\partial\zeta}{\partial y} = \frac{1}{\rho}\left[\frac{\partial F_y}{\partial x} - \frac{\partial F_x}{\partial y}\right] + \nu\nabla^2\zeta \tag{2}$$

$$\frac{\partial T}{\partial t} + u\frac{\partial T}{\partial x} + v\frac{\partial T}{\partial y} = \alpha\nabla^2 T \tag{3}$$

where $\nabla^2 = (\partial^2/\partial x^2) + (\partial^2/\partial y^2)$ and F_x and F_y are the x and y-components of the buoyancy force, F_b, respectively. The defining equations of these components are

$$F_x = F_b \sin\lambda, \quad F_y = F_b \cos\lambda, \quad F_b = \rho g\beta(T - T_\infty).$$

Let us now introduce the dimensionless variables $x' = x/L$, $y' = y/L$, $t' = t\alpha/L^2$, $u' = uL/\alpha$, $v' = vL/\alpha$, $\psi' = \psi/\alpha$, $\zeta' = -\zeta L^2/\alpha$ and $\phi = (T - T_\infty)/(T_s - T_\infty)$ in Eqs. (1–3) and then drop all primes for simplicity. The dimensionless form of the above equations can be written as:

$$\zeta = \nabla^2\psi \tag{4}$$

$$\frac{\partial\zeta}{\partial t} + u\frac{\partial\zeta}{\partial x} + v\frac{\partial\zeta}{\partial y} = -\mathrm{Ra}\,\mathrm{Pr}\left[\frac{\partial\phi}{\partial x}\cos\lambda - \frac{\partial\phi}{\partial y}\sin\lambda\right] + \mathrm{Pr}\nabla^2\zeta \tag{5}$$

$$\frac{\partial\phi}{\partial t} + u\frac{\partial\phi}{\partial x} + v\frac{\partial\phi}{\partial y} = \nabla^2\phi \tag{6}$$

where Ra is the Rayleigh number $(= g\beta L^3(T_S - T_\infty)/\nu\alpha)$.

The boundary conditions are mainly the no-slip and impermeability conditions on the tube surface and the ambient conditions far away from it. These can be expressed as: $u = v = 0$ and $\phi = 1$ on the tube surface, and $u, v, \phi, \zeta \Rightarrow 0$ far away from the surface.

In order to work with coordinates appropriate to the tube geometry, we write Eqs. (4–6) in elliptic coordinates using the transformation

$$x + iy = c\cosh(\xi + i\eta)$$

where c is the dimensionless focal distance $(= (a^2 - b^2)^{1/2}/L)$. Using the above transformation, Eqs. (4–6) can be written as:

$$H\zeta = \nabla^2\psi \tag{7}$$

$$H\frac{\partial\zeta}{\partial t} + \frac{\partial\psi}{\partial\eta}\frac{\partial\zeta}{\partial\xi} - \frac{\partial\psi}{\partial\xi}\frac{\partial\zeta}{\partial\eta} = -\mathrm{Ra}\,\mathrm{Pr}\Big[(\sinh\xi\cos\lambda\cos\eta - \cosh\xi\sin\lambda\sin\eta)\frac{\partial\phi}{\partial\xi} - (\sinh\xi\sin\lambda\cos\eta$$

Nomenclature

Ar = minor to major axis ratio, b/a
a, b = semimajor and minor axes
c = dimensionless focal distance, $(a^2 - b^2)^{1/2}/L$
c_p = fluid specific heat
F_o, f_n, F_n = functions defined in Eq. (11a)
F_b = buoyancy force
g = gravitational acceleration
G_o, g_n, G_n = functions defined in Eq. (11b)
Gr = Grashof number, $g\beta L^3(T_S - T_\infty)/\nu^2$
h = heat transfer coefficient
H_o, h_n, H_n = functions defined in Eq. (11c)
k = fluid conductivity
L = characteristic length, $2a$
Nu, $\overline{\mathrm{Nu}}$ = local and average Nusselt numbers defined in Eq. (17)
P = elliptic section perimeter
Pr = Prandtl number, ν/α
Ra = Rayleigh number, $g\beta L^3(T_S - T_\infty)/\nu\alpha$
t = dimensionless time
T = fluid temperature
u, v = dimensionless x and y-velocity components
x, y = rectilinear coordinates

Greek symbols

α = thermal diffusivity
β = coefficient of volumetric thermal expansion
δ = Kronecker delta
ζ = vorticity
η, ξ = elliptical coordinates
λ = angle between major axis and the horizontal
ν = fluid kinematic viscosity
ρ = fluid density
ϕ = dimensionless temperature
ψ = dimensionless stream function

Subscripts

s = at the surface
∞ = at infinite distance from the surface

Table 1 Comparison between the values of $\overline{Nu}$ obtained in the present study and those obtained by Huang and Mayinger (1984)

Ra	λ	Nu (Present Study) Ar=0.4	Nu (Reference [4]) Ar=0.389	% Difference
10^3	90°	3.59	3.41	5.01%
10^4	0°	4.90	4.98	1.63%
10^4	90°	5.91	6.06	2.54%

$$- \cosh \xi \cos \lambda \sin \eta) \frac{\partial \phi}{\partial \eta} \Bigg] + \mathrm{Pr} \nabla^2 \zeta \quad (8)$$

$$H \frac{\partial \phi}{\partial t} + \frac{\partial \psi}{\partial \eta} \frac{\partial \phi}{\partial \xi} - \frac{\partial \psi}{\partial \xi} \frac{\partial \phi}{\partial \eta} = \nabla^2 \phi \quad (9)$$

where $H = \frac{1}{2} c^2 (\cosh 2\xi - \cos 2\eta)$. The boundary conditions given following Eq. (6) can now be expressed as:

$$\psi = \frac{\partial \psi}{\partial \xi} = \frac{\partial \psi}{\partial \eta} = 0, \quad \phi = 1 \quad \text{at} \quad \xi = \xi_o \quad (10a)$$

$$\psi, \phi, \frac{\partial \psi}{\partial \xi}, \frac{\partial \psi}{\partial \eta}, \quad \zeta \Rightarrow 0 \quad \text{as} \quad \xi \Rightarrow \infty \quad (10b)$$

The initial conditions which apply for $t \leq 0$ are the static conditions and uniform temperature distribution ($\phi = 0$) in the entire field. At the start of computations ($t = 0$), the dimensionless tube surface temperature is suddenly increased to 1.0, and this moment represents the start of the time development of the flow and thermal fields. The main mathematical problem is to predict the details of both fields as time increases. The method adopted here is similar to that used by Badr (1983, 1994). In this method, the dimensionless stream function, vorticity, and temperature are approximated using a finite number of terms in a Fourier series and can be expressed as follows:

$$\psi = \tfrac{1}{2} F_o + \sum_{n=1}^{N} [f_n(\xi, t) \sin n\eta + F_n(\xi, t) \cos n\eta] \quad (11a)$$

$$\zeta = \tfrac{1}{2} G_o + \sum_{n=1}^{N} [g_n(\xi, t) \sin n\eta + G_n(\xi, t) \cos n\eta] \quad (11b)$$

$$\phi = \tfrac{1}{2} H_o + \sum_{n=1}^{N} [h_n(\xi, t) \sin n\eta + H_n(\xi, t) \cos n\eta]. \quad (11c)$$

The use of the above approximations in Eqs. (7–9) results in three sets of differential equations for the Fourier coefficients with each set containing $(2N + 1)$ equations. The first set specifies the differential equations governing the time variation of the Fourier coefficients of vorticity (G_o, g_n, and G_n) and can be expressed as follows:

$$\frac{1}{2} c^2 \left[\cosh 2\xi \frac{\partial G_o}{\partial t} - \frac{\partial G_2}{\partial t} \right] = \mathrm{Pr} \frac{\partial^2 G_o}{\partial \xi^2} + S_o(\xi, t) \quad (12a)$$

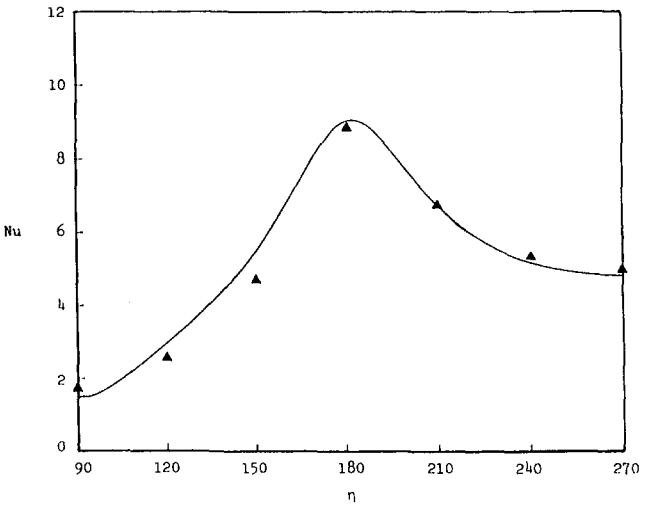

Fig. 2 Comparison between the local Nusselt number distribution obtained in this study for the case of Ra = 10^4, Ar = 0.4, and λ = 0 deg and the experimental results given by Huang and Mayinger (1984) for Ar = 0.389: (——) present study; (▲) Huang and Mayinger

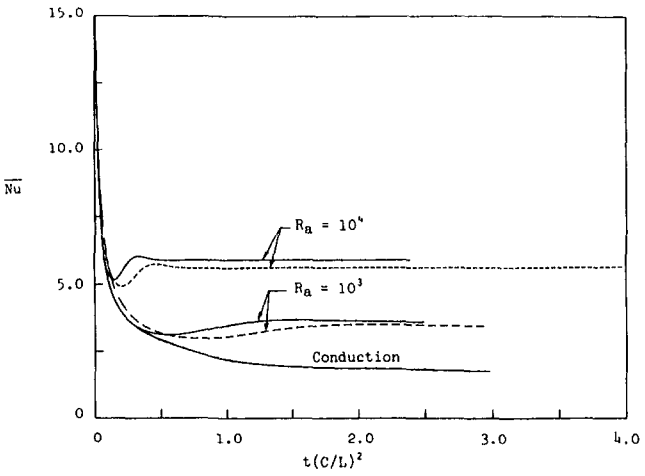

Fig. 3 The time variation of the average Nusselt number for the case of vertical major axis (λ = 90 deg): (——) Ar = 0.4; (-----) Ar = 0.6

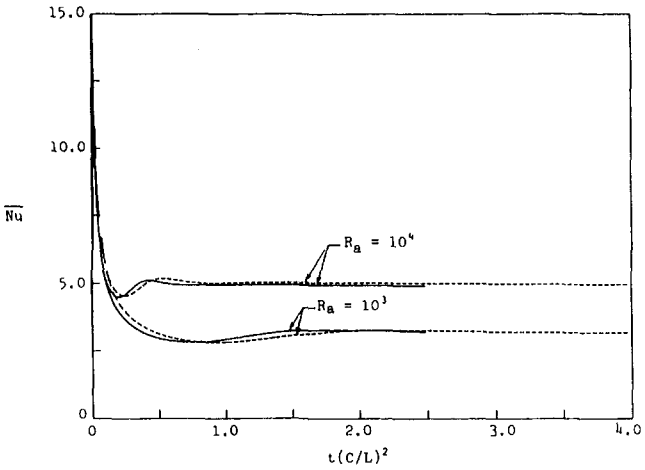

Fig. 4 The time variation of the average Nusselt number following the sudden temperature rise for the case of λ = 0 deg. (——) Ar = 0.4; (-----) Ar = 0.6

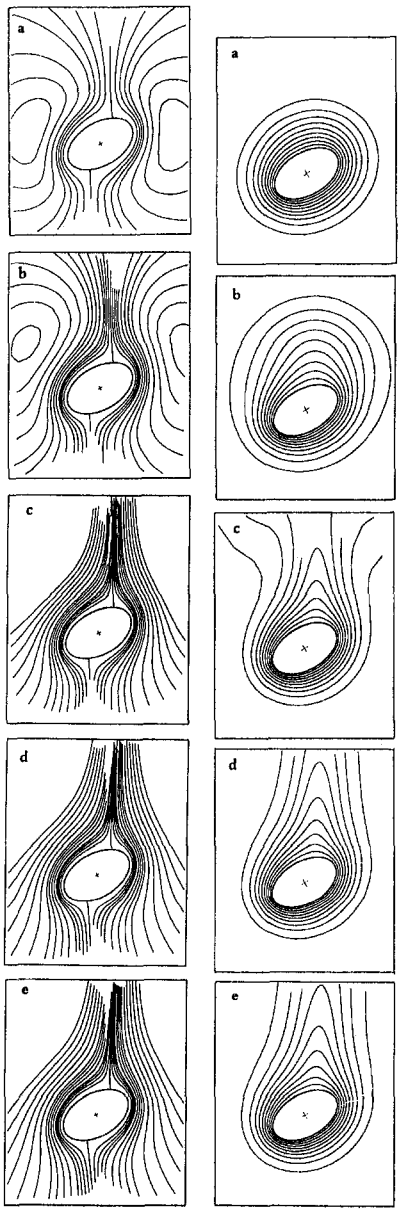

Fig. 5 (left) The streamline patterns for the case of Ra = 10^3, Ar = 0.6, and λ = 30 deg at times (*a*) t^* = 0.5, (*b*) t^* = 1.0, (*c*) t^* = 2.0, (*d*) t^* = 3.0, (*e*) t^* = 4.0. Streamlines plotted are ψ = −9.0(1.0) − 3.0(0.5) − 1.0(0.25)1.0(0.5)3.0(1.0)9.0.

Fig. 6 (right) The isotherm patterns for the case of Ra = 10^3, Ar = 0.6, and λ = 30 deg at times (*a*) t^* = 0.5, (*b*) t^* = 1.0, (*c*) t^* = 2.0, (*d*) t^* = 3.0, (*e*) t^* = 4.0. Isotherms plotted are ϕ = 0.1(0.1)0.9.

$$c^2\left[\cosh 2\xi\,\frac{\partial g_n}{\partial t} - \frac{1}{2}\left\{\operatorname{sgn}(n-2)\,\frac{\partial g_{|n-2|}}{\partial t} + \frac{\partial g_{(n+2)}}{\partial t}\right\}\right] = 2\,\mathrm{Pr}\left[\frac{\partial^2 g_n}{\partial \xi^2} - n^2 g_n\right] + nF_n\,\frac{\partial G_o}{\partial \xi} - nG_n\,\frac{\partial F_o}{\partial \xi} + S_{n1}(\xi, t) \quad (12b)$$

$$c^2\left[\cosh 2\xi\,\frac{\partial G_n}{\partial t} - \frac{1}{2}\left\{\delta_{n2}\,\frac{\partial G_o}{\partial \xi} + \frac{\partial G_{|n-2|}}{\partial t} + \frac{\partial G_{(n+2)}}{\partial t}\right\}\right] = 2\,\mathrm{Pr}\left[\frac{\partial^2 G_n}{\partial \xi^2} - n^2 G_n\right] + ng_n\,\frac{\partial F_o}{\partial \xi} - nf_n\,\frac{\partial G_o}{\partial \xi} + S_{n2}(\xi, t) \quad (12c)$$

where δ_{mn} is the Kronecker delta ($\delta_{mn} = 0$ for $m \neq n$ and $\delta_{mn} = 1$ for $m = n$) and sgn $(n-2)$ represents the sign of the term $(n-2)$. The terms with subscript $|n-2|$ vanish when $n = 2$ and the functions S_o, S_{n1}, and S_{n2} are easily identifiable functions. Equations (12*a*)–(12*c*) are to be integrated in time in order to predict the functions G_o, g_n, and G_n at time level $(t + \Delta t)$, provided that these functions are known at time t.

The second set specifies the differential equations that provide the link between vorticity and stream function. This set results from using the approximations (given in (11)) in the stream function, Eq. (7), which finally gives

$$\frac{\partial^2 F_o}{\partial \xi^2} = \frac{1}{2}\,c^2[\cosh 2\xi G_o - G_2] \quad (13a)$$

$$\frac{\partial^2 f_n}{\partial \xi^2} - n^2 f_n = \tfrac{1}{2}c^2[\cosh 2\xi g_n - \tfrac{1}{2}\{\operatorname{sgn}(n-2)g_{|n-2|} + g_{(n+2)}\}] \quad (13b)$$

$$\frac{\partial^2 F_n}{\partial \xi^2} - n^2 F_n = \tfrac{1}{2}c^2[\cosh 2\xi G_n - \tfrac{1}{2}\{\delta_{n2}G_o + G_{|n-2|} + G_{(n+2)}\}]\,. \quad (13c)$$

The last set of equations governs the time variation of Fourier coefficients of the dimensionless temperature ϕ. This set is obtained by using expressions (11*a*) and (11*c*) in Eq. (9) which results in

$$\frac{1}{2}\,c^2\left[\cosh 2\xi\,\frac{\partial H_o}{\partial t} - \frac{\partial H_2}{\partial t}\right] = \frac{\partial^2 H_o}{\partial \xi^2} + Z_o(\xi, t) \quad (14a)$$

$$c^2\left[\cosh 2\xi\,\frac{\partial h_n}{\partial t} - \frac{1}{2}\left\{\operatorname{sgn}(n-2)\,\frac{\partial h_{|n-2|}}{\partial t} + \frac{\partial h_{(n+2)}}{\partial t}\right\}\right] = 2\left[\frac{\partial^2 h_n}{\partial \xi^2} - n^2 h_n\right] + nF_n\,\frac{\partial H_o}{\partial \xi} - nH_n\,\frac{\partial F_o}{\partial \xi} + Z_{n1}(\xi, t) \quad (14b)$$

Table 2 The effect of axis ratio on the average Nusselt number for the horizontal and vertical major axis configurations

Ra	λ	Ar	$\overline{Nu}$
10^3	0°	0.4	3.20
		0.6	3.16
		0.8	3.11
10^3	90°	0.4	3.59
		0.6	3.44
		0.8	3.23
		0.98	3.09
10^4	0°	0.4	4.90
		0.6	4.96
		0.8	4.93
10^4	90°	0.4	5.91
		0.6	5.63
		0.8	5.36
		0.98	5.05

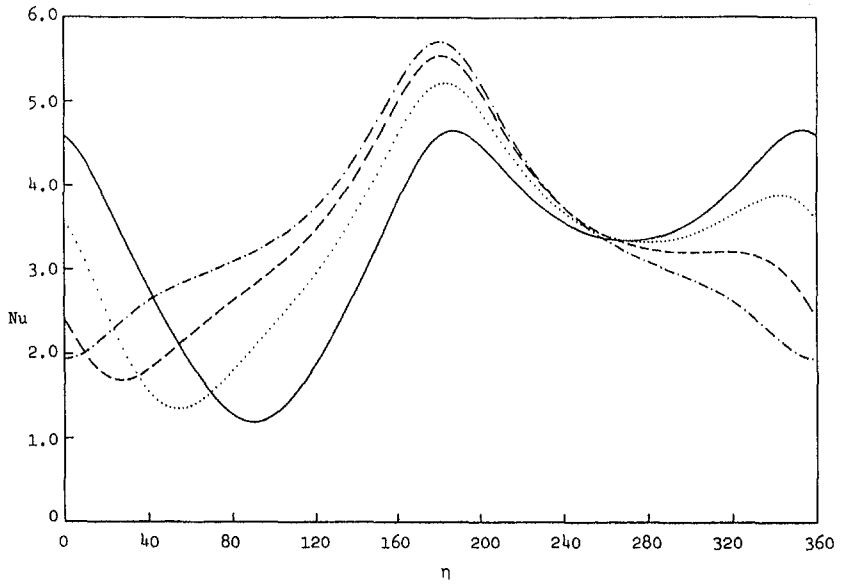

Fig. 7 The effect of tube orientation on the local Nusselt number distribution for the case of Ra = 10^3 and Ar = 0.6: (——) λ = 0 deg; (· · · · · ·) λ = 30 deg; (-----) λ = 60 deg; (– · – · – ·) λ = 90 deg

$$c^2\left[\cosh 2\xi\,\frac{\partial H_n}{\partial t} - \frac{1}{2}\left\{\delta_{n2}\,\frac{\partial H_o}{\partial \xi} + \frac{\partial H_{|n-2|}}{\partial t} + \frac{\partial H_{(n+2)}}{\partial t}\right\}\right]$$

$$= 2\left[\frac{\partial^2 H_n}{\partial \xi^2} - n^2 H_n\right] + n h_n \frac{\partial F_o}{\partial \xi}$$

$$- n f_n \frac{\partial H_o}{\partial \xi} + Z_{n2}(\xi, t) \quad (14c)$$

where the functions Z_o, Z_{n1}, and Z_{n2} can be easily identified.

The boundary conditions given in Eq. (10) provide a source for the boundary conditions of all Fourier coefficients. The Fourier series approximations (given in Eqs. (11*a–c*)) are used in Eqs. (10*a*) and (10*b*) and results in the following conditions:

$$h_n = H_n = F_o = f_n = F_n = \frac{\partial}{\partial \xi}(F_o, f_n, F_n) = 0 \quad \text{and}$$

$$H_o = 2 \quad \text{at} \quad \xi = \xi_o \quad (15a)$$

$$H_o, h_n, H_n, F_o, f_n, F_n, G_o, g_n, G_n, \frac{\partial}{\partial \xi}(F_o, f_n, F_n) \Rightarrow 0$$

$$\text{as} \quad \xi \Rightarrow \infty. \quad (15b)$$

A set of integral conditions is also obtained by integrating Eqs. (13*a*)–(13*c*) with respect to ξ between ξ_o and ∞ and making use of Eqs. (15*a*) and (15*b*). These conditions are

$$\int_o^\infty \frac{c^2}{2}\{\cosh 2\xi G_o - G_2\}\,d\xi = 0 \quad (16a)$$

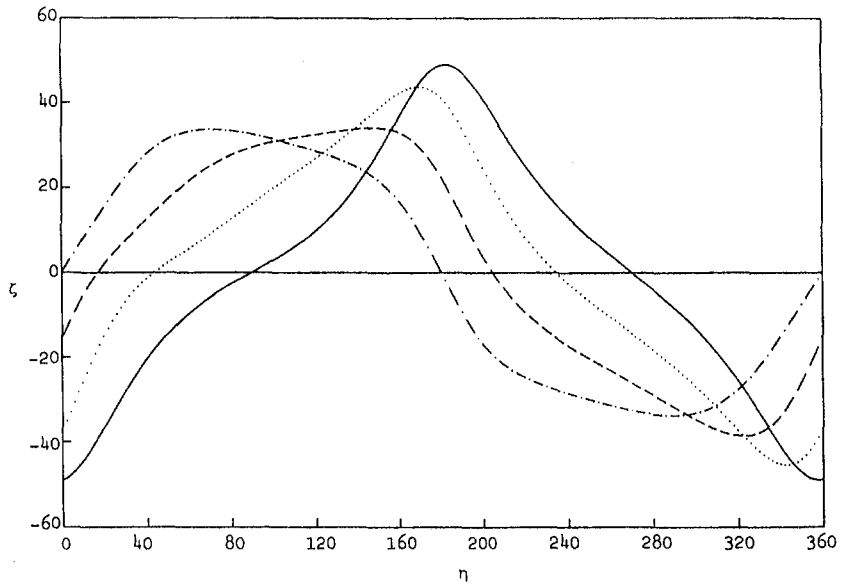

Fig. 8 The effect of tube orientation on the surface vorticity distribution for the case of Ra = 10^3 and Ar = 0.6; (——) λ = 0 deg; (· · · · · ·) λ = 30 deg; (-----) λ = 60 deg; (– · – · –) λ = 90 deg

$$\int_o^\infty \frac{c^2}{2}\left\{\cosh 2\xi g_n - \frac{1}{2}\left[\text{sgn}\,(n-2)g_{|n-2|} + g_{(n+2)}\right]\right\}e^{-n\xi}d\xi = 0 \quad (16b)$$

$$\int_o^\infty \frac{c^2}{2}\left\{\cosh 2\xi G_n - \frac{1}{2}\left[\delta_{n2}G_o + G_{|n-2|} + G_{(n+2)}\right]\right\}e^{-n\xi}d\xi = 0. \quad (16b)$$

The above integral conditions are similar to those deduced by Badr (1994) though not the same. These conditions are important not only for predicting the values of G_o, g_n, and G_n on the tube surface ($\xi = \xi_o$) but also for ensuring the periodicity of pressure (for more details, see Badr, 1994).

The numerical integration of Eqs. (12–14) starts at $t = 0$ by setting $H_o = 2$ at $\xi = \xi_o$ while equating all other Fourier coefficients to zero in the entire domain. This simulates the sudden temperature rise of the tube surface temperature from T_∞ to T_S. The conditions at $\xi = \infty$ are enforced at a distance that can reach a maximum of $\xi_{\max} = \xi_o + 10$, which corresponds to a very large distance away from the tube surface (greater than 11,000 times the focal distance). The actual field boundaries are time dependent, matching the physical behavior of the flow and thermal fields. At small times, the flow and thermal fields are limited to the immediate neighborhood of the tube surface, however, the size of the two fields increases as time increases until reaching steady conditions. The solution procedure follows closely the same procedure described in Badr (1983, 1994) and will not be repeated here.

The local Nusselt number is defined as $\text{Nu} = hL/k$ where h is the local heat transfer coefficient given by

$$h = -k\left[\frac{\partial T}{\partial n}\right]_{\xi_o} /(T_S - T_\infty)$$

and n is the dimensional coordinate normal to the surface. Using the above definitions, one can easily prove that

$$\text{Nu} = \frac{hL}{k} = -\frac{1}{H^{1/2}}\left[\frac{\partial \phi}{\partial \xi}\right]_{\xi_o}. \quad (17a)$$

The average Nusselt number, $\overline{\text{Nu}}$, is calculated using the above expression which is averaged over the elliptic section perimeter and can be written as:

$$\overline{\text{Nu}} = -(2a\pi/P)\left[\frac{\partial H_o}{\partial \xi}\right]_{\xi_o} \quad (17b)$$

where P is the elliptic section perimeter.

3 Verification of the Method of Solution

The accuracy of the method of solution is verified by considering a number of cases for which either experimental or theoretical results are available for comparison. Results for the special case of a circular cylinder reported earlier by Kuehn and Goldstein (1980) are compared with the case of elliptic tube with axis ratio Ar = 0.98 considered in this study. Kuehn and Goldstein reported $\overline{\text{Nu}} = 3.09$ and 4.94 for Rayleigh numbers $\text{Ra} = 10^3$ and 10^4 while the present method predicted $\overline{\text{Nu}} = 3.09$ and 5.05 for the same two Rayleigh numbers. The percentage difference in $\overline{\text{Nu}}$ for the case of $\text{Ra} = 10^4$ is 2.2 percent. The experimental results obtained by Huang and Mayinger (1984) for free convection from elliptic tubes are also compared with the present results. In their work, $\overline{\text{Nu}}$ and Ra were based on the equivalent diameter $D = 4A/P$, where A is the tube cross-sectional area. Furthermore, the value of Ar studied by Huang and Mayinger nearest to the values considered in this work is Ar = 0.389. Table 1 shows a comparison between the values of $\overline{\text{Nu}}$ obtained in the present work for Ar = 0.4 and those reported by Huang and Mayinger for Ar = 0.389, after making the necessary corrections to match the present definitions of Ra and $\overline{\text{Nu}}$. The table shows a percentage difference in $\overline{\text{Nu}}$ ranging from 1.63 percent to 5.01 percent.

A comparison between the local Nusselt number distribution obtained in this study for the case of $\text{Ra} = 10^4$ and Ar = 0.4 when the major axis is horizontal ($\lambda = 0$) and the experimental Nu distribution reported by Huang and Mayinger for the same Ra and λ but for Ar = 0.389 is shown in Fig. 2. The figure shows a good agreement in the neighborhood of the rear and front stagnation points ($\eta = 90$ deg and 270 deg) with reasonable agreement near $\eta = 180$ deg. The differences are attributed to three reasons. The first is due to the difference in the value of Ar considered in the two studies, and the second is due to the accuracy of the experimental prediction of Nu from the interferograms. The third reason is due to curve fitting of experimental data. The point of maximum Nu reported by Huang and Mayinger was at $\eta = 180$ deg, while it is found at $\eta = 182$ deg in the present study. The above comparisons show that the numerical scheme used in this study is highly accurate.

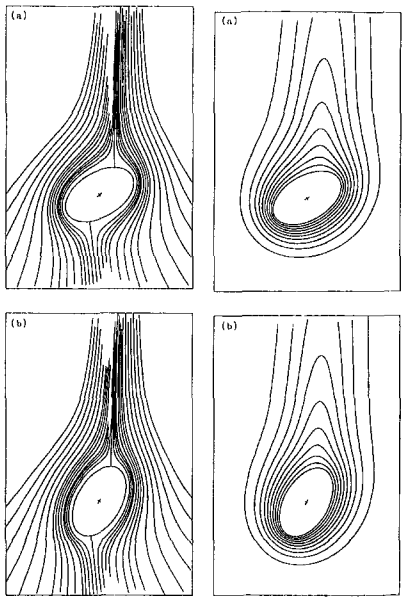

Fig. 9 (left) The streamline patterns for the case of Ra = 10^3, Ar = 0.6, and inclination angles (*a*) λ = 30 deg and (*b*) λ = 60 deg. Streamlines plotted are the same as in Fig. 5.

Fig. 10 (right) The isotherm patterns for the case of Ra = 10^3, Ar = 0.6, and inclination angles (*a*) λ = 30 deg and (*b*) λ = 60 deg. Isotherms plotted are the same as in Fig. 6.

4 Discussion of Results

The problem of natural convection from a horizontal tube of elliptic cross section is studied with special emphasis on the effects of angle of inclination, Rayleigh number, and the tube axis ratio while keeping the Prandtl number unchanged (Pr = 0.7). In all cases, the tube surface temperature, which is assumed isothermal, is suddenly increased and the thermal and momentum boundary layers continue to develop with time until reaching steady conditions. Figure 3 shows the time variation of the average Nusselt number following the sudden temperature rise when the major axis is vertical (λ = 90 deg) for

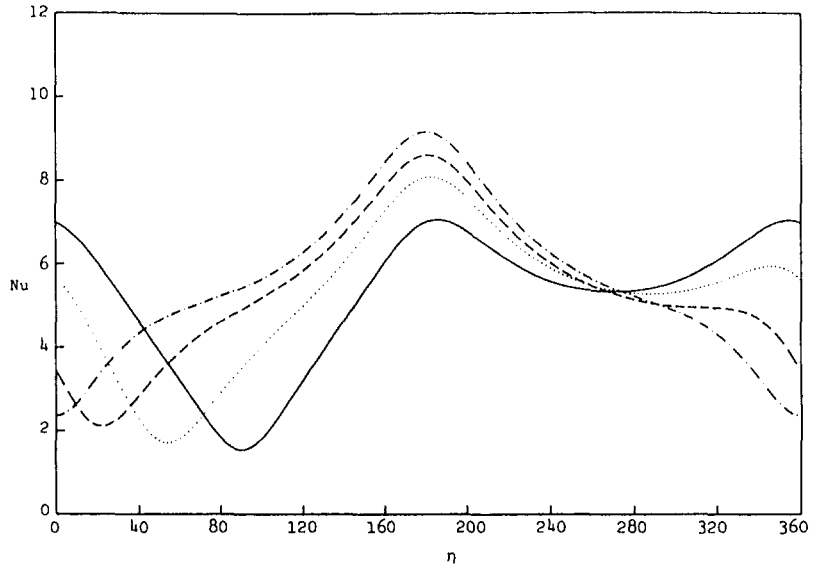

Fig. 11 The local Nusselt number distribution for the case of Ra = 10^4 and Ar = 0.6: (——) λ = 0 deg; (· · · · · ·) λ = 30 deg; (-----) λ = 60 deg; (– · – · –) λ = 90 deg

Rayleigh numbers of 10^3 and 10^4 and axis ratios of Ar = 0.4 and 0.6. As expected, Nu is very high at small times since the thermal boundary layer starts with infinitely small thickness. The sharp decrease in Nu at small times reflects the rapid growth of the thermal boundary layer. The heat transfer regime in this phase is dominated by conduction due to the very small flow velocities prevailing at small times. The case of transient conduction for the same initial conditions is investigated for comparison with the small time results obtained in the present study. The same governing equations and numerical scheme are used with the exception of keeping zero flow velocities at all times. The transient Nu-t curve for the conduction regime is also shown in Fig. 3 for the case of Ra = 10^3 and Ar = 0.4. The comparison shows the close behavior of the conduction and convection regimes at small times. Another interesting phenomenon observed is that the heat transfer overshoot occurs in the intermediate stage between the small time conduction regime and the large time convection regime. Figure 3 shows this phenomenon for the two cases of Ra = 10^3 and 10^4, though more pronounced in the latter case.

The same phenomenon was reported for the case of a circular cylinder in the works by Vest and Lawson (1972), Parsons and Mulligan (1978, 1980) and by Faw et al. (1984). Figure 3 also shows that higher Ra results in higher Nu values while higher axis ratio lead to lower heat transfer rates.

The time development of Nu for the same conditions but with horizontal major axis is shown in Fig. 4. It is clear from the figure that the Nu-t curves at small time (the conduction phase) are exactly the same for different values of Ra but the same axis ratio. Such phenomenon is quite expected based on theoretical grounds since the governing equations (Eqs. (7–9)) reduce to a simplified form of Eq. (9) by eliminating the convection terms. The remaining equation in this case is the transient heat conduction equation

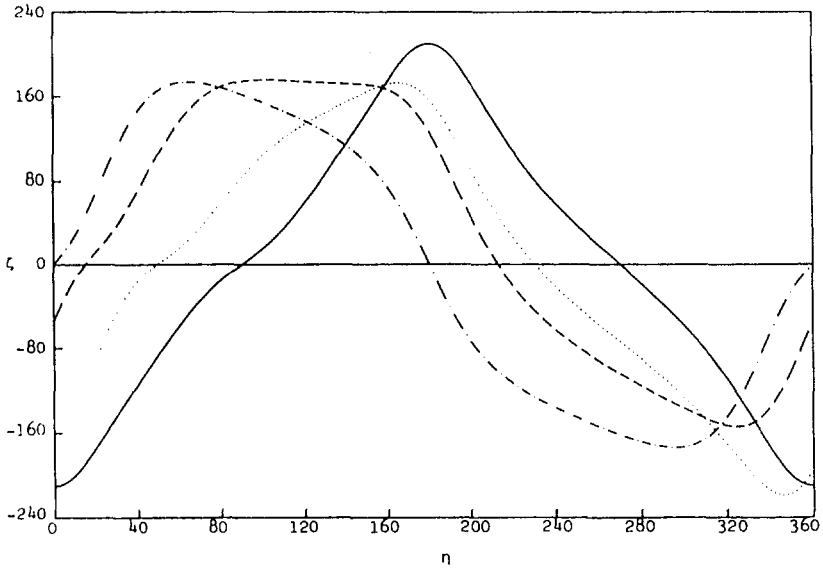

Fig. 12 The surface vorticity distribution for the case of Ra = 10^4 and Ar = 0.6: (——) λ = 0 deg; (· · · · · ·) λ = 30 deg; (-----) λ = 60 deg; (– · – · –) λ = 90 deg

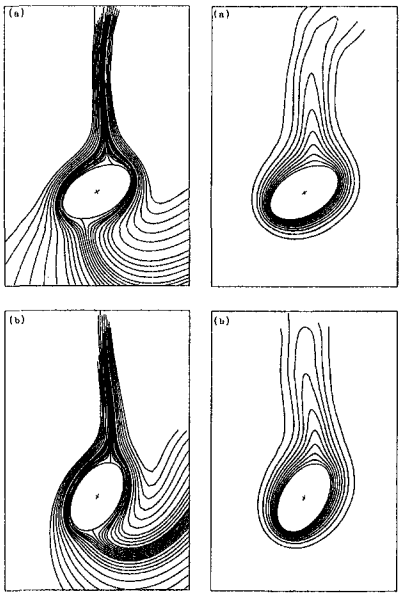

Fig. 13 (left) The streamline patterns for the case of Ra = 10^4, Ar = 0.6, and inclination angles (*a*) λ = 30 deg and (*b*) λ = 60 deg. Streamlines plotted are the same as in Fig. 5.

Fig. 14 (right) The isotherm patterns for the case of Ra = 10^4, Ar = 0.6, and inclination angles (*a*) λ = 30 deg and (*b*) λ = 60 deg. Isotherms plotted are the same as in Fig. 6.

$$H\partial\phi/\partial t = \nabla^2\phi$$

with no role for the Rayleigh number in the heat transfer process. Similar to Fig. 3, the heat transfer overshoot occurs clearly in the case of Ra = 10^4 and with less extent when Ra = 10^3. The time variations of the flow and thermal fields following the sudden temperature rise are shown in Figs. 5 and 6 for the case of Ra = 10^3, Ar = 0.6, and λ = 30 deg. The streamlines and isotherms at small time ($t^* = t(c/L)^2 = 0.5$) shown in Figs. 5*a* and 6*a* indicate low flow velocities in the first and a conduction dominated regime depicted by concentric isotherms in the second. As time increases, the flow velocity increases and convection becomes more dominant until reaching the final steady state (Figs. 5*e* and 6*e*).

The final steady values of $\overline{Nu}$ for the horizontal major axis configuration (λ = 0 deg) are lower than those obtained in the vertical axis case (λ = 90 deg). The numerical values of $\overline{Nu}$ for both cases and for different axis ratios are given in Table 2. The effect of tube orientation on the local Nusselt number distribution is shown in Fig. 7 for the case of Ra = 10^3, Ar = 0.6, and λ = 0 deg, 30 deg, 60 deg, and 90 deg. One interesting phenomenon clearly shown in Fig. 7 is that the maximum local Nusselt number occurs at approximately η = 180 deg in all tube orientations. This point always represents one end of the tube major axis. In the case when the major axis is vertical, the

Table 3 The effect of angle of inclination on the average Nusselt number for the case of Ar = 0.4

Ra	λ	$\overline{Nu}$
10^3	0°	3.16
	30°	3.23
	60°	3.35
	90°	3.44
10^4	0°	4.96
	30°	5.11
	60°	5.34
	90°	5.63

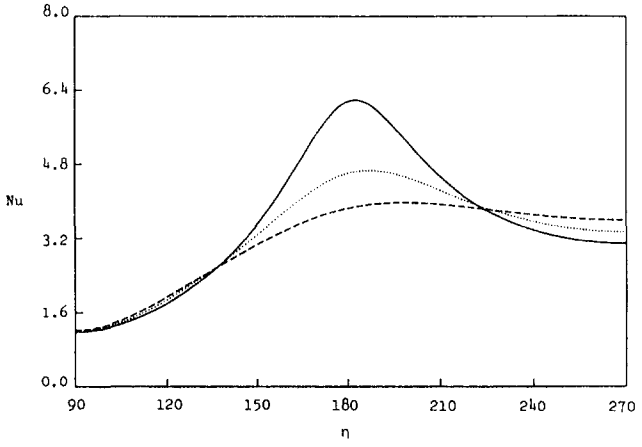

Figure 15a

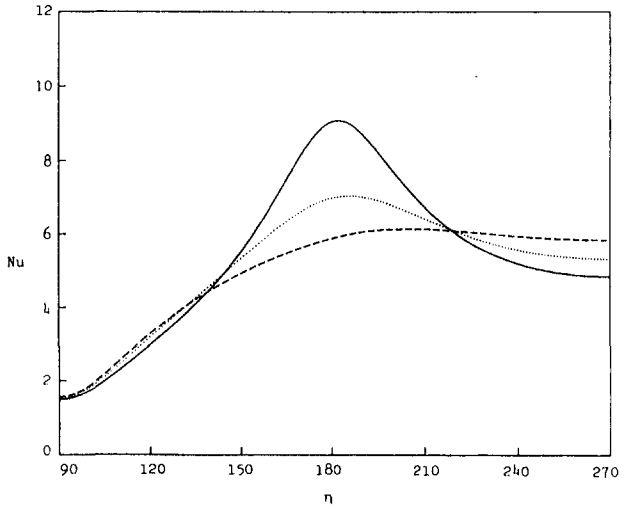

Figure 15b

Fig. 15 The effect of axis ratio on the local Nusselt number distribution when the major axis is horizontal and (*a*) Ra = 10^3, (*b*) Ra = 10^4: (——) Ar = 0.4; (· · · · · ·) Ar = 0.6; (-----) Ar = 0.8

point of maximum Nu is the lowest point on the tube surface (forward stagnation point) while in the case when the major axis is horizontal, the two end points of the major axis (η = 0 deg and η = 180 deg) are very close to the points of maximum Nu. On the other hand, the point of minimum heat transfer moves from η = 90 deg in the case when the major axis is horizontal to η = 0 deg when the major axis is vertical. In both cases, this point is the topmost point on the tube surface (corresponding to the rear stagnation point). Figure 8 shows the surface vorticity distribution for the same cases presented in Fig. 7. The maximum absolute surface vorticity occurs near η = 0 deg and 180 deg in the case of horizontal major axis (λ = 0 deg), which is approximately the same location of maximum local Nusselt number. The two cases of λ = 0 deg and λ = 90 deg show symmetrical absolute surface vorticity and local Nusselt number about minor and major axes, respectively, as shown in Figs. 7 and 8. The streamline and isotherm patterns for the cases of Ra = 10^3, Ar = 0.6, and inclination angles λ = 30 deg and 60 deg are shown in Fig. 9 and 10. The figures show the front and rear stagnation points (these are the points of zero vorticity in Fig. 8) and also show the relative magnitude of the temperature gradient normal to the tube surface. It is clear from the figures that the rear stagnation point in both cases of λ = 30 deg and λ = 60 deg is the point of minimum temperature gradient and accordingly the point of minimum local Nus-

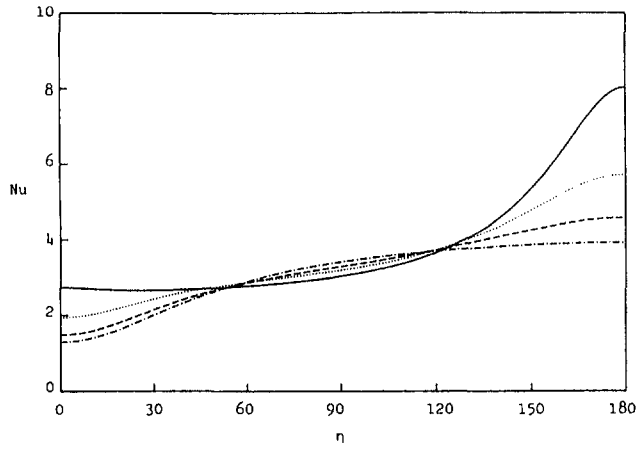

Figure 16a

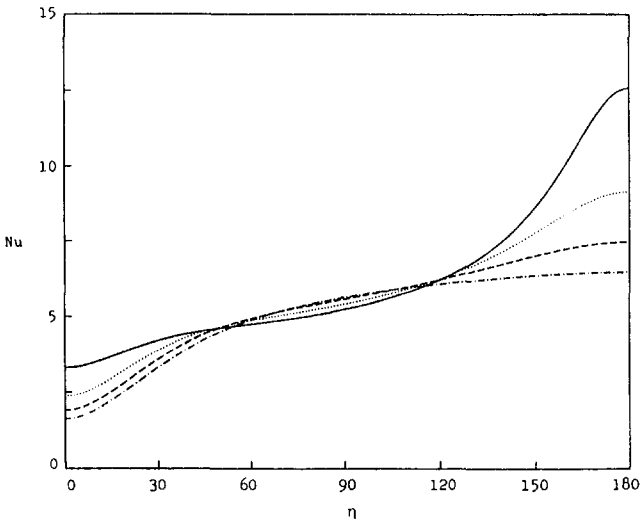

Figure 16b

Fig. 16 The effect of axis ratio on the local Nusselt number distribution when the major axis is vertical and (*a*) Ra = 10^3, (*b*) Ra = 10^4: (——) Ar = 0.4; (· · · · · ·) Ar = 0.6; (- - - - -) Ar = 0.8; (- · - · -) Ar = 0.98

selt number. This criterion also applies to the other two cases of $\lambda = 0$ deg and $\lambda = 90$ deg, as it is clearly shown in Figs. 7 and 8.

The higher Rayleigh number case of Ra = 10^4 is investigated for the same axis ratio (Ar = 0.6) and inclination angles ($\lambda = 0$ deg, 30 deg, 60 deg and 90 deg). The local Nusselt number distributions shown in Fig. 11 indicate that the point of maximum Nu continues to be near $\eta = 180$ deg for all tube orientations, while the point of minimum Nu exists at the rear stagnation point in all cases. The figure also shows that the case of vertical major axis ($\lambda = 90$ deg) possesses higher Nu values over most of the tube surface in comparison with the case of horizontal major axis ($\lambda = 0$ deg). Figure 12 shows the surface vorticity distributions for the same cases presented in Fig. 11. Since no separation exists on the tube surface, the points of zero vorticity represent either the front or the rear stagnation points. By comparing Figs. 8 and 12, one can see that the general shape of the vorticity distribution curves when Ra = 10^4 differs only slightly from those obtained in the case of Ra = 10^3. However, the magnitudes are much higher in Fig. 12. The streamlines and isotherms are shown in Figs. 13 and 14, respectively, for inclination angles of 30 deg and 60 deg. The closer isotherms in Fig. 14 reflect the higher temperature gradient and accordingly higher local Nusselt number. The overall effect of the inclination angle on the average Nusselt number is shown in Table 3. Tubes with vertical major axis result in higher $\overline{Nu}$ values for the Ra values considered.

The effect of tube axis ratio on the local Nusselt number distribution is shown in Figs. 15*a* and 15*b* for the two cases of Ra = 10^3 and 10^4 when the major axis is horizontal ($\lambda = 0$ deg). The general shape of the curves given in the two figures is the same with the only difference being in the numerical values. Tubes with smaller axis ratio have higher Nu values in the range of $\eta = 136$ deg to 220 deg, while the differences are small on the rest of the tube surface. All curves in Figs. 15*a* and 15*b* possess a maximum Nu at $\eta = 180$ deg and two minimums: one absolute minimum at the rear stagnation point ($\eta = 90$ deg) and another minimum at the front stagnation point ($\eta = 270$ deg). The effect of axis ratio is also studied for the vertical major axis configuration ($\lambda = 90$ deg) and the results are shown in Figs. 16*a* and 16*b* for the two cases of Ra = 10^3 and 10^4. The figures show that changing Ar has little effect on Nu between $\eta = 50$ deg and $\eta = 120$ deg with the major effect being in the small region downstream of the front stagnation point ($\eta = 120$ deg to 180 deg). Table 2 shows that tubes of small axis ratio have higher $\overline{Nu}$ values in most cases. The effect of axis ratio on the resulting streamline and isotherm patterns is shown in Figs. 17 and 18 for the vertical axis configuration and in Figs. 19 and 20 for the horizontal axis configuration. Figure 18 shows the minimum temperature gradient occurring at the topmost point on the tube surface ($\eta = 0$) while the maximum temperature gradient occurs at the lowest point ($\eta = 180$ deg). Similar to the vertical major axis configuration, Fig. 20

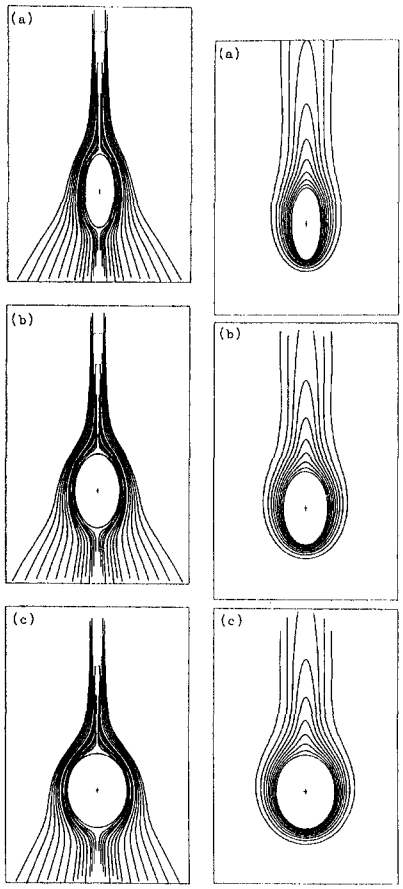

Fig. 17 (left) The streamline patterns for the case of Ra = 10^4, $\lambda = 90$ deg and (*a*) Ar = 0.4, (*b*) Ar = 0.6, (*c*) Ar = 0.8

Fig. 18 (right) The isotherm patterns for the case of Ra = 10^4, $\lambda = 90$ deg and (*a*) Ar = 0.4, (*b*) Ar = 0.6, (*c*) Ar = 0.8

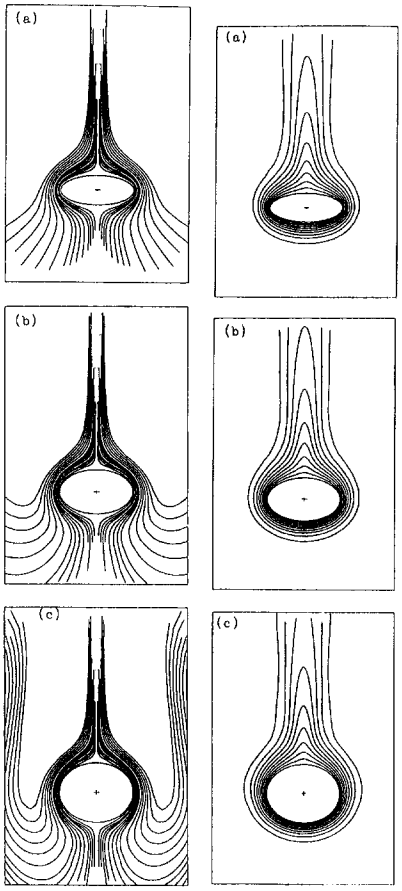

Fig. 19 (left) The streamline patterns for the case of Ra = 10^4, λ = 0 deg and (*a*) Ar = 0.4, (*b*) Ar = 0.6, (*c*) Ar = 0.8

Fig. 20 (right) The isotherm patterns for the case of Ra = 10^4, λ = 0 deg and (*a*) Ar = 0.4, (*b*) Ar = 0.6, (*c*) Ar = 0.8

shows minimum temperature gradient at the topmost point, however, the maximum temperature gradient occurs at the two ends of the tube major axis (η = 0 and 180 deg) where the magnitude of surface vorticity is maximum.

5 Conclusions

The time development of the flow and thermal fields in the neighborhood of a straight tube of elliptic cross section is investigated when the tube is suddenly heated while placed in an initially quiescent fluid of infinite extent. The resulting flow is driven by buoyancy forces, and the heat transfer regime is purely natural convection. The study focused on the effects of tube orientation, axis ratio and Rayleigh number while keeping Prandtl number unchanged. The tube orientation varies from horizontal to vertical major axis while the axis ratio varies from 0.4 to 0.98. Results are obtained for the two Rayleigh numbers Ra = 10^3 and 10^4. The study revealed that the average Nusselt number is maximum when the major axis is vertical. It also revealed that smaller axis ratio results in higher heat transfer rates in most cases. Higher Rayleigh number leads to higher flow velocities and accordingly higher heat transfer rates. The results show that the point of maximum Nu is always at or near η = 180 deg, while the point of minimum Nu is at the rear stagnation point for all cases considered. The details of the flow and thermal fields for some selected cases are presented in the form of surface vorticity and local Nusselt number distributions as well as streamline and isotherm patterns.

Acknowledgments

The author wishes to acknowledge the support received from King Fahd University of Petroleum & Minerals during this study. The work in this paper started during a sabbatical leave spent at the University of Western Ontario (UWO), London, Canada during 1991/92 academic year. The pleasant work environment provided by UWO is very much appreciated.

6 References

Badr, H. M., 1983, "A Theoretical Study of Laminar Mixed Convection From a Horizontal Cylinder in a Cross Stream," *Int. J. Heat Mass Transfer,* Vol. 26, pp. 639–653.

Badr, H. M., 1987, "Heat Transfer in Transient Buoyancy Driven Flow Adjacent to a Horizontal Rod," *Int. J. Heat Mass Transfer,* Vol. 30, pp. 1997–2012.

Badr, H. M., 1994, "Mixed Convection From a Straight Isothermal Tube of Elliptic Cross-Section," *Int. J. Heat Mass Transfer,* Vol. 37, pp. 2343–2365.

Badr, H. M., and Shamsher, K., 1993, "Free Convection From an Elliptic Cylinder With Major Axis Vertical," *Int. J. Heat Mass Transfer,* Vol. 36, pp. 3593–3602.

Churchill, S. W., and Chu, H. H., 1975, "Correlating Equations for Laminar and Turbulent Free Convection From a Vertical Plate," *Int. J. Heat Mass Transfer,* Vol. 18, pp. 1323–1329.

Elliot, L., 1970, "Free Convection on a Two-dimensional or Axisymmetric Body," *Q. J. Mech. Appl. Math.,* Vol. 23, pp. 153–162.

Farouk, B., and Guceri, S. I., 1981, "Natural Convection From a Horizontal Cylinder—Laminar Regime," ASME JOURNAL OF HEAT TRANSFER, Vol. 103, pp. 522–527.

Faw, R. E., Ismuntoyo, R. P. H., and Lester, T. W., 1984, "Transition From Conduction to Convection Around a Horizontal Cylinder Experiencing a Ramp Excursion in Internal Heat Generation," *Int. J. Heat Mass Transfer,* Vol. 27, pp. 1087–1097.

Goldstein, R. J., and Briggs, D. G., 1964, "Transient Free Convection About Vertical Plates and Circular Cylinders," ASME JOURNAL OF HEAT TRANSFER, Vol. 86C, pp. 490–500.

Hardwick, N. E., and Levy, E. K., 1973, "Study of the Laminar Free-Convection Wake Above an Isothermal Vertical Plate," ASME JOURNAL OF HEAT TRANSFER, Vol. 95, pp. 289–294.

Huang, S. Y., and Mayinger, F., 1984, "Heat Transfer With Natural Convection Around Elliptic Tubes," *Warme-Und Stoffubertragung,* Vol. 18, pp. 175–183.

Kuehn, T. H., and Goldstein, R. J., 1980, "Numerical Solution to the Navier-Stokes Equations for Laminar Natural Convection About a Horizontal Isothermal Circular Cylinder," *Int. J. Heat Mass Transfer,* Vol. 23, pp. 971–979.

Lin, F. N., and Chao, B. T., 1974, "Laminar Free Convection Over Two-Dimensional and Axisymmetric Bodies of Arbitrary Contour," ASME JOURNAL OF HEAT TRANSFER, Vol. 96, pp. 435–442.

Merkin, J. H., 1976, "Free Convection on an Isothermal Horizontal Cylinder," ASME Paper No. 76-HT-16.

Merkin, J. H., 1977, "Free Convection Boundary Layers on Cylinders of Elliptic Cross-Section," ASME JOURNAL OF HEAT TRANSFER, Vol. 99, pp. 453–457.

Parsons, J. R., and Mulligan, J. C., 1978, "Transient Free Convection From a Suddenly Heated Horizontal Wire," ASME JOURNAL OF HEAT TRANSFER, Vol. 100, pp. 423–428.

Parsons, J. R., and Mulligan, J. C., 1980, "Onset of Natural Convection From a Suddenly Heated Horizontal Cylinder," ASME JOURNAL OF HEAT TRANSFER, Vol. 102, pp. 636–639.

Pera, L., and Gebhart, B., 1972, "Experimental Observations of Wake Formation Over Cylindrical Surfaces in Natural Convection Flows," *Int. J. Heat Mass Transfer,* Vol. 15, pp. 175–177.

Raithby, G. D., and Hollands, K. G., 1976, "Laminar and Turbulent Free Convection From Elliptic Cylinders with a Vertical Plate and Horizontal Circular Cylinder as Special Cases," ASME JOURNAL OF HEAT TRANSFER, Vol. 98, pp. 72–80.

Sparrow, E. M., Patankar, S. V., and Abdel-Wahed, R. M., 1978, "Development of Wall and Free Plumes Above a Heated Vertical Plate," ASME JOURNAL OF HEAT TRANSFER, Vol. 100, pp. 184–190.

Suriano, F. J., and Yang, K., 1968, "Laminar Free Convection About Vertical and Horizontal Plates at Small and Moderate Grashof Numbers," *Int. J. Heat Mass Transfer,* Vol. 11, pp. 473–490.

Vest, C. M., and Lawson, M. L., 1972, "Onset of Convection Near a Suddenly Heated Horizontal Wire," *Int. J. Heat Mass Transfer,* Vol. 15, pp. 1281–1283.

Wide Band Correlated-k Approach to Thermal Radiative Transport in Nonhomogeneous Media

O. Marin
Research Assistant.

R. O. Buckius
Richard W. Kritzer Professor.
buckius@ux1.cso.uiuc.edu
Fellow ASME.

Department of Mechanical and Industrial Engineering,
University of Illinois at Urbana-Champaign,
140 Mechanical Engineering Building, MC-244,
1206 West Green Street,
Urbana, IL 61801

The correlated-k approach is compared with the exact line-by-line calculations for thermal radiative transport in highly nonhomogeneous media containing water vapor and carbon dioxide. It is shown that the magnitude of the spectral interval over which k-distribution functions are generated can be increased up to approximately 1000 cm^{-1} for water vapor and 500 cm^{-1} for carbon dioxide, with only a slight loss of accuracy. Different solution techniques of the radiative transfer equation in nonhomogeneous media are used and compared. The wide band correlated-k method and a simplified approach to the exponential wide band correlated-k method are shown to provide very good results for the cases considered. The calculations include the entire infrared spectrum of water vapor and carbon dioxide for temperatures up to 2500 K.

Introduction

Thermal radiative transport in absorbing, emitting and scattering media must address the spectral interval under consideration and the physical property variation with position. The spectral intervals include individual wavenumbers by summing the rotational-vibrational line contributions (line-by-line method), narrow spectral intervals with band models (narrow band models), entire rotational-vibrational bands (wide band models), and the entire wavelength spectrum (total models). The use of each of these models in thermal radiative transport calculations has various advantages and disadvantages. Since practical applications include variations of properties with position, the transport must accurately incorporate such variations. Additionally, the computational accuracy and efficiency of the thermal transport methodology is dependent upon the relationship between the spectral interval and position dependence.

The exact method of solving gas radiation problems is the line-by-line method. The method evaluates the absorption coefficient at each spectral location by summing the contributions of all vibrational-rotational absorption lines within neighboring spectral intervals. This approach requires detailed gas information, including the line intensity, linewidth, line center position, transition lower level energy, and quantum identification, which are functions of the local physical characteristics of the gas. The large number of absorption lines within an absorption band can be handled through existing databases, yet significant computational effort and large data storage capacity are required.

An often used database is known by the acronym of HITRAN (Rothman et al., 1992a, b; Rothman 1996), which was originally designed for use in atmospheric analyses and recently extended to include reliable high temperature line-by-line information. The main difficulty in the development of high temperature data is the exponential increase in the number of significant lines with temperature, since the transitions irrelevant at low temperature become important as the temperature increases. Special interest has been placed on the study of water vapor and carbon dioxide at high temperatures due to their importance in combustion applications. Hartmann et al. (1984) and Riviere et al. (1995) developed line-by-line procedures for H_2O hot lines, valid for temperatures up to 1500 K and 2500 K, respectively. Taine (1983) developed a line-by-line calculation for CO_2-CO gas mixtures up to 3000 K, while Scutaru et al. (1994) developed a new high temperature database for CO_2. Hot lines for these molecules are also efficiently generated with the Direct Numerical Diagonalization method (DND), based on the variational method for solving the quantum mechanical equations (Wattson and Rothman, 1986, 1992). Recently, Rothman (1996) released the HITEMP database containing spectral information up to 1000 K for the commonly used gases and up to 1500 K for water vapor. The present investigation uses this spectral information for radiative transport in nonhomogeneous media.

The significant computational burden required by the line-by-line method has necessitated the use of band models designed to approximate the nongray gas behavior over various spectral intervals. The narrow band model replaces spectral properties with averages of the gas radiative properties over a relatively small spectral interval and uses the band average transmissivity or absorptivity as the primary quantity. The most accurate models, termed statistical models, assume randomly positioned lines. Goody (1952) considered a random model, together with an exponential line intensity distribution within the band, while Malkmus (1967) assumed an exponential-tailed inverse line intensity distribution function. A large body of literature has focused on the development and improvement of the narrow band parameters. Ludwig et al. (1973) developed narrow band parameters for many common gases for a wide range of conditions. Bernstein (1980) and Bernstein et al. (1980) generated rotational vibrational lines and calculated narrow band parameters for linear triatomic molecules. Hartmann et al. (1984) and Riviere et al. (1995) updated the band parameters for the H_2O molecule. Soufiani and Taine (1997a) used the Malkmus narrow band model and developed band parameters for water vapor, carbon dioxide, and carbon monoxide up to 2900 K. The present work uses the narrow band parameters (Soufiani and Taine, 1997a, 1997b) for calculations in high temperature nonhomogeneous media.

Narrow band model validation and application in transport equation solutions have received considerable attention. Soufi-

Contributed by the Heat Transfer Division for publication in the JOURNAL OF HEAT TRANSFER. Manuscript received by the Heat Transfer Division September 3, 1996; revision received June 6, 1997; Keywords: Combustion; Radiation; Radiation Interactions. Associate Technical Editor: B. W. Webb.

ani et al. (1985) compared the narrow band model results with line-by-line calculations for both water vapor and carbon dioxide, concluding that the random statistical models give accurate results for transmissivities but introduce errors in emissivity calculations. Wang and Ryan (1983) extended the applicability of the statistical narrow band models to mixtures of absorbing gases. Menart et al. (1993) developed a narrow band formulation to solve for nongray radiative gas problems using the S-N discrete ordinate method. Kritzstein and Soufiani (1993) employed the statistical narrow band model to study the gas radiation in a homogeneously turbulent medium. Liu and Tiwari (1994) apply the Malkmus narrow band model in connection with a Monte Carlo method and investigate the radiative transport of nongray gases in complex geometries. The narrow band models constitute an accurate tool in radiative heat transfer calculations.

Thermal transport analyses require radiative transfer calculations over the entire infrared spectrum. The desire for computational efficiency led to the development of models useful for entire rotational-vibrational bands, termed wide band models. The most popular wide band model assumes that the mean intensity-to-spacing ratio varies exponentially. Edwards and Menard (1964), Edwards and Balakrishnan (1973), Edwards (1976) and Edwards (1981) applied this wide band model together with the statistical narrow band model developed by Goody (1952) and derived simple correlations for the band absorption. Modak (1979) improved the band parameters for the rotational band of water vapor. Wang (1983) developed an analytical solution for the exponential wide band model applied to the Malkmus narrow band model. Considering applications, Soufiani et al. (1985) used the band parameters as derived by Edwards for CO_2 and H_2O with combined conduction-radiation problems and indicated generally good results. The wide band model proves to be a powerful method of solving the radiative transfer equation, yielding accurate results in a wide range of applications.

The methods presented above provide the radiative properties of gases for different spectral intervals—from a single spectral value to an entire band of hundreds of cm^{-1}. Hottel (1954) developed a method termed the "weighed-sum-of-gray-gases" and provides emissivity and absorptivity data that included the entire spectrum of gas radiation. Modest (1991) extended the applicability of the total spectrum approach to any arbitrary solution method, such as the P-N procedure. Although the weighed-sum-of-gray-gas method has some restrictions, the method represents a useful approach for thermal radiative transfer problems, leading to major reductions in computational effort.

The integration of the radiative transfer equation with respect to frequency is very tedious due to the rapid spectral variation of the absorption coefficient. An alternate method, the k-distribution method, replaces the integration over frequency with an integration over the absorption coefficient distribution function. Goody and Yung (1989) presented a thorough analysis of the *k*-distribution method, with particular applicability to atmospheric radiation problems. Goody et al. (1989) generated narrow band absorption coefficient distributions directly from line-by-line calculations and show that the *k*-distribution method is in very good agreement with line-by-line calculations. The *k*-distribution function can also be determined from band models, as an inverse Laplace transform of the transmission function (Domoto, 1974). Lacis and Oinas (1991) developed a closed form solution for the Malkmus model absorption coefficient cumulative distribution function and applied the method to atmospheric calculations. Soufiani and Taine (1997a) employed the *k*-distribution method in connection with the Malkmus narrow band model and provided explicit values for narrow spectral interval absorption coefficients. Wide band intervals can also be employed in connection to the *k*-distribution method. Lee et al. (1996) and Parthasarathy et al. (1996) used a numerical Laplace transform inversion of the effective bandwidth to calculate a reordered spectral distribution of the absorption coefficient. West et al. (1990) developed wide band *k*-distribution functions directly from line-by-line calculations, while Wang and Shi (1988) developed an analytical expression for the distribution function resulting from the Malkmus model and the exponential wide band model. Marin and Buckius (1996) calculated limiting and approximate forms for the cumulative distribution function resulting from the Malkmus model and the Edwards wide band distribution. It is shown that the results provided by the Malkmus and Goody models when used with the Edwards exponential wide band properties are within 12 percent. The present work uses the wide band cumulative distribution function (Marin and Buckius, 1996) and the adjustments to the Edwards band parameters to account for the band absorption differences between models as suggested by Edwards and Balakrishnan (1973).

The application of the *k*-distribution concept to total spectrum calculations requires a suitable choice for the spectral blackbody intensity. Denison and Webb (1993, 1995a, b) introduced a function incorporating the local value of the blackbody distribution function together with the magnitude of the absorption coefficient. Thus a "blackbody distribution function" for the entire radiative spectrum was created, and the equation of transfer is efficiently solved using the weighed-sum-of-gray-gas method.

Nomenclature

A = effective bandwidth, cm^{-1}
b = line halfwidth, cm^{-1}
B = pressure broadening parameter, $B = \pi b/d$
C = coefficient in exponential wide band formulation
d = line spacing, cm^{-1}
f = distribution function
g = cumulative distribution function
i = intensity, W/m^2 sr
k = absorption coefficient, m^2/g
L = layer thickness, m
N = number of elements in summation
R = ratio, $R = s_{max}/s_{min}$
$\bar{s}$ = line intensity, $cm^{-1}/(g - m^{-2})$
s = line intensity divided by line spacing, m^2/g
s_{min} = minimum line intensity, m^2/g
s_{max} = maximum line intensity, m^2/g
T = temperature, K
u = mass path length, g/m^2
w = weight factor for Gaussian integration
W = equivalent bandwidth
x = variable

Greek

α = integrated band intensity, $cm^{-1}/(g - m^{-2})$
ν = wavenumber, cm^{-1}
$\Delta\nu$ = wavenumber interval, cm^{-1}
ρ = density, g/m^3
τ = transmissivity
ω = bandwidth parameter, cm^{-1}

Subscripts

0 = band center or band head
b = blackbody
e = equivalent
G = Goody model
i, i', j, j' = summation parameters
L = layer thickness
M = Malkmus model
max = maximum
min = minimum
q = quadrature
wb = wide band
ν = wavenumber dependent
ν_0 = band center (band head) based

The solution of the equation of transfer is more complex when the medium is nonhomogeneous. The line-by-line method is the exact approach to solve the equation of transfer. The spectral changes in the absorption coefficient along a line of sight must be incorporated, and the transmissivity for a line of sight is then calculated using the multiplicative property. In order to obtain an exact result, the radiative properties have to be calculated at all adjacent locations, which is usually not computationally feasible. In practice, the nonhomogeneous medium is divided in a number of homogeneous layers, each with constant properties.

Scaling techniques accounting for the nonuniform gas properties along a line of sight are popular in transport calculations for nonhomogeneous media. The commonly used narrow band scaling techniques are the Curtis-Godson (CG) (Godson, 1953) and the Lindquist-Simmons (LS) (Lindquist and Simmons, 1972) methods. Both determine equivalent homogeneous parameters for the nonhomogeneous path transmissivity, providing correct dependencies for weak and strong line limits. Young (1975a, b) extended the LS application of Goody and of Malkmus narrow band models to Doppler and combined Lorentz and Doppler lines. Grosshandler (1980) developed a computer program (RADCAL) to solve for the total intensity for a line of sight using the data of Ludwig et al. (1973), the Goody narrow band model and the CG scaling. Edwards and Morizumi (1970) extended the scaling concept to wide band models, providing approximate relations for the band parameters. These scaling methods effectively reduce the transport in nonhomogeneous media to the study of an equivalent homogeneous medium, with important computational savings.

The k-distribution method is an alternate approach to solving nonhomogeneous radiative transfer problems. Distinct k-distributions are evaluated within the nonhomogeneous medium and the integration of the radiative transfer equation is based on the hypothesis that the distributions are spectrally correlated. This means that a certain spectral interval yields the same value for the absorption coefficient cumulative distribution function, regardless of the local gas properties. The correlation of the k-distribution assumption, termed the correlated-k method, has been used for moderate temperature gradients and moderate spectral intervals with good results for narrow band calculations. Goody et al. (1989) and Lacis and Oinas (1991) successfully applied the narrow band correlated-k method for atmospheric nonhomogeneous media. Levi Di Leon and Taine (1986) extended the concept of separating a gas into several "fictitious gases" (Ludwig et al., 1973) to the correlated-k method. For each homogeneous layer, several k-distributions are developed for the fictitious gases characterized by radiative gas transitions with the lower level energy within a certain interval. Although this method proves to be accurate, no major computational reduction, when compared to the line-by-line method, is reported. Denison and Webb (1995c) applied the total blackbody distribution function to calculations in nonhomogeneous media.

The current work attempts to enhance the efficiency of the transport calculations in nonhomogeneous media while maintaining accuracy. The correlated-k method for wide bands is applied to highly nonhomogeneous media for both water vapor and carbon dioxide. The results are compared to line-by-line, scaling and blackbody distribution function methods. The computational efficiency of each method is discussed. This work also presents an efficient and accurate, simplified correlated-k wide band approach.

Solution Methodologies

The solution of the radiative transfer equation for a nonhomogeneous medium with cold boundaries is given by the expression

$$i(L) = \int_{\Delta\nu}\int_{0}^{L} i_{b\nu}(T(L'))\frac{\partial}{\partial L'}\tau_{\nu}(L', L)dL'd\nu \quad (1)$$

where $i(L)$ is the emitted intensity at location L, $\tau_\nu(L', L)$ is the spectral transmissivity between locations L' and L, and $i_{b\nu}$ is the spectral blackbody intensity. With the nonhomogeneous medium discretized into a series of homogeneous layers and the spectral domain into a series of finite intervals, Eq. (1) can be rewritten as

$$i(L) = \sum_{i=1}^{N_\nu}\{\sum_{j=1}^{N_L} i_{b\nu,i}(T(L_j'))[\tau_{\nu,i}(L_{j+1}', L) - \tau_{\nu,i}(L_j', L)]\}\Delta\nu_i \quad (2)$$

where N_ν is the number of spectral intervals and N_L is the number of homogeneous layers in the medium. The blackbody intensity function is considered to be constant on the spectral interval $\Delta\nu_i$. The absorption coefficient, considered constant over small spectral intervals $\Delta\nu_i$, is calculated as a sum of the neighboring rotational-vibrational transition effects. This approach is termed the line-by-line method and it is exact in the limit as the spectral interval goes to zero. The line-by-line procedure is computationally expensive since the transmissivity results from the expression

$$\tau_\nu(L', L) = \exp(-\sum_{L'}^{L} k_{j'}u_{j'}) \quad (3)$$

where the absorption coefficient $k_{j'}$ has to be calculated as a summation of the rotational-vibrational absorption line contributions within the spectral domain for each j' homogeneous layer. $u_{j'} = \rho_{j'}L_{j'}$ is the mass path length for the jth layer.

From the data available in literature and extensive calculations performed using the detailed spectral information (Rothman, 1996), it is concluded that the absorption coefficient may be considered constant for intervals of $\Delta\nu = 0.01$ cm^{-1}. The infrared water vapor spectrum of 8000 cm^{-1} necessitated the calculation of 800,000 values of the absorption coefficient, each resulting from the summation of many neighboring absorption lines. Within a nonhomogeneous medium, the evaluation of the spectral absorption coefficient has to be repeated for each set of temperatures, pressures, and concentrations. These considerations show the computational burden of the line-by-line method and justify the effort directed towards the development of more efficient algorithms to solve transport problems, such as band models. Different methodologies to be applied in nonhomogeneous media are briefly reviewed below.

Narrow Band Scaling. Narrow band models replace the spectral absorption coefficient with an equivalent absorption over a spectral interval, generally of the order of several cm^{-1}. The transmissivity for a homogeneous layer is defined as

$$\tau = \exp(-W) \quad (4)$$

where W is termed the equivalent bandwidth (equivalent width for a single absorption line as defined by Malkmus (1967)), expressed as a function of the mass path length u, the mean line intensity-to-spacing parameter $s = \bar{s}/d$, and the pressure broadening parameter $B = \pi b/d$. Among the different models developed the most accurate prove to be the statistical models that assume a random position of the rotational-vibrational lines within the band. The differences between various statistical models reside in the line intensity distribution within the band. The Goody narrow band model assumes an exponential distribution of the line intensity yielding an equivalent band width of

$$W_G = \frac{su}{\sqrt{1 + \frac{su}{B}}} \quad (5a)$$

while the Malkmus narrow band model, assuming an inverse-tailed exponential distribution, yields

$$W_M = \frac{B}{2}\left[\sqrt{1 + 4\frac{su}{B}} - 1\right]. \quad (5b)$$

The narrow band models are used to solve for the radiative transfer equation in nonhomogeneous media combined with the concept of scaling. The scaling replaces a nonhomogeneous medium with an equivalent homogeneous medium with modified band parameters. The scaling method employed here is the CG technique, designed to determine equivalent band parameters that satisfy the weak and strong line limits and correctly approximate the other cases. The equivalent parameters are defined as

$$(su)_e(L', L) = \int_{L'}^{L} s\rho dL'' = \sum_{L'}^{L} s_{j'}u_{j'} \quad (6a)$$

and

$$B_e(L', L) = \frac{\int_{L'}^{L} sB\rho dL''}{\int_{L'}^{L} s\rho dL''} = \frac{\sum_{L'}^{L} s_{j'}B_{j'}u_{j'}}{\sum_{L'}^{L} s_{j'}u_{j'}}. \quad (6b)$$

Grosshandler (1980) develops a computer code (RADCAL) designed to solve nonhomogeneous gas radiative problems by applying the CG technique and band model parameters provided by Ludwig et al. (1973). This work uses RADCAL and compares the results with different methods. The narrow band model database (Soufiani and Taine, 1997a, b) using the Malkmus model is also used in connection to the correlated-k method, as shown below.

Wide Band Models. Equation (1) can be solved with less computational effort by using larger spectral intervals involving entire rotational-vibrational bands. In this case, the solution uses the wide band method with the effective bandwidth A defined as

$$A = \int_{\Delta\nu_{wb}} [1 - \exp(-W(\nu))]d\nu, \quad (7)$$

where $\Delta\nu_{wb}$ represents the wide band spectral interval. Edwards and co-workers assume an exponential variation of the mean line intensity-to-spacing parameter s as

$$s = s_{\max}\exp\left(-\frac{C|\nu - \nu_0|}{\omega}\right) \quad (8)$$

where $s_{\max} = \alpha/\omega$ represents the maximum mean line intensity-to-spacing value, α is the integrated band intensity, and ω is the bandwidth parameter. ν_0 is either the band center ($C = 2$), or the band head ($C = 1$), depending on the band profile.

The wide band model can be used to solve for emitted band intensity from a nonhomogeneous medium, $i_{wb}(L)$ as

$$i_{wb}(L) = \sum_{j=1}^{N_L} i_{b\nu_0}(T(L_j'))[A(L_j', L) - A(L_{j+1}', L)] \quad (9)$$

where $A(L_i', L)$ represents the effective bandwidth for an equivalent homogeneous layer between the locations L_i' and L, and $i_{b\nu_0}$ is the blackbody intensity at the band center or band head. The total intensity is the sum of the individual band intensities. The effective bandwidth $A(L', L)$ is calculated using scaled parameters of the form

$$\alpha_e(L', L) = \frac{\int_{L'}^{L} \rho_a\alpha dL''}{\int_{L'}^{L} \rho_a dL''} = \frac{\sum_{L'}^{L} \alpha_{j'}u_{j'}}{\sum_{L'}^{L} u_{j'}} \quad (10a)$$

$$\omega_e(L', L) = \frac{\int_{L'}^{L} \rho_a\alpha\omega dL''}{\int_{L'}^{L} \rho_a\alpha dL''} = \frac{\sum_{L'}^{L} \alpha_{j'}\omega_{j'}u_{j'}}{\sum_{L'}^{L} \alpha_{j'}u_{j'}} \quad (10b)$$

and

$$B_e(L', L) = \frac{\int_{L'}^{L} \rho_a\alpha\omega B dL''}{\int_{L'}^{L} \rho_a\alpha\omega dL''} = \frac{\sum_{L'}^{L} \alpha_{j'}\omega_{j'}B_{j'}u_{j'}}{\sum_{L'}^{L} \alpha_{j'}\omega_{j'}u_{j'}} \quad (10c)$$

as developed by Edwards and Morizumi (1970). The wide band scaling method is applied in this work, and the results are compared with other methods.

Correlated-k Method. General radiative transport phenomena in an absorbing, emitting, and scattering medium requires explicit values of the absorption coefficient. The information regarding the magnitude of k is lost in the band methods presented above, and replaced with average transmission values over different spectral intervals. The k-distribution method removes this impediment. A spectral interval and a given state is characterized by a k-distribution function $f(k)$ and by a cumulative distribution function $g(k)$. The average transmissivity is calculated as

$$\tau = \frac{1}{\Delta\nu}\int_{\Delta\nu} e^{-k(\nu)u}d\nu = \int_0^\infty e^{-ku}f(k)dk = \int_0^1 e^{-ku}dg \quad (11)$$

where the first equality denotes the direct method to calculate the transmissivity τ over the spectral integral $\Delta\nu$. The subsequent equalities apply the k-distribution concept by replacing the integral over the spectral interval with an integral over the distribution function $f(k)$ and over the cumulative distribution function $g(k)$, respectively. $g(k)$ can also be used to solve the radiative transfer equation in nonhomogeneous media. For a wide band spectral interval, Eq. (1) becomes

$$i_{wb}(L) = \Delta\nu_{wb}\int_0^1\int_0^L i_{b\nu_0}(T(L'))\frac{\partial}{\partial L'}\tau(L', L)dL'dg. \quad (12a)$$

The integration process in Eq. (12a) uses the assumption that all the different cumulative distribution functions within the medium are spectrally correlated. This means that for each spectral location, all different conditions yield the same magnitude of the cumulative distribution function. This assumption is termed the correlated-k method. Equation (12a) is generally numerically integrated as

$$i_{wb}(L) = \Delta\nu_{wb}\sum_{i=1}^{N_q}\{\sum_{j=1}^{N_L} i_{b\nu_0}(T(L_j'))[\tau_i(L_{j+1}', L) - \tau_i(L_j', L)]\}w_i \quad (12b)$$

where N_q is the number of quadratures in the summation and w_i are the weight factors in the numerical integration. The transmissivity $\tau_i(L_j', L)$ for a specific abscissa i is

$$\tau_i(L_j', L) = \exp(-\sum_{L_j'}^{L} k_{i,j'}u_{j'}) \quad (13)$$

where j' is the summation parameter over distinct homogeneous layers between the locations L_j' and L. The absorption coefficient $k_{i,j'}$ is obtained from the cumulative distribution function corresponding to the state in layer $L_{j'}$ and to the quadrature number i.

This work generates all cumulative distribution functions from line-by-line calculations for spectral intervals of 25 (320 distribution functions for the entire spectrum), 50, 125, 250, 500, 1000, 2000, 4000 cm^{-1} and the entire infrared interval of approximately 8000 cm^{-1} (a single distribution required). The application of the correlated-k approach in connection with narrow band models is extensively studied in the literature with good results in highly nonhomogeneous media. This work applies this method using the Malkmus narrow band model database (Soufiani and Taine, 1997a, b) and compares it with line-by-line results. The excellent agreement between these methods permits the use of the narrow band model database as a benchmark for high temperature calculations, where accurate line-by-line information is not available. The cumulative distribution functions are also generated from the exponential wide band model as developed by Marin and Buckius (1996). The present work also applies the blackbody distribution function approach. The method calculates only one distribution function for the entire infrared spectrum, for a given gas and state, by incorporating the variation of the Planck function together with the absorption coefficient distribution. The results of the blackbody distribution function applied to nonhomogeneous media (Denison and Webb, 1995c) are presented in the next section. The blackbody distribution function method uses between 35 and 45 gases for all the cases presented in this work, following the prescriptions of Denison and Webb (1995c).

In addition to the use of these relatively complicated forms of the cumulative distribution functions, a simplified approach is developed based upon the pressure broadened limit. As the temperature of the medium increases, the pressure broadening parameter B increases for all bands of CO_2 and H_2O, with the exception of the rotational band of H_2O. In the large pressure limit, the Malkmus and Goody narrow band models provide a step function of the absorption coefficient cumulative distribution function for a value of the absorption coefficient equal to the average line intensity-to-spacing ratio within the narrow band (Lacis and Oinas, 1991). This corresponds to an analytical expression of the exponential wide band cumulative distribution function

$$g(k) = \frac{\ln (k/s_{\min})}{\ln (R)}, \qquad (14)$$

with k in the interval $[s_{\min}, s_{\max}]$ and $R = s_{\max}/s_{\min}$ (Marin and Buckius, 1996). Since this work is directed towards the investigation of efficient computational approaches for high temperature transport phenomena, the use of Eq. (14) in highly nonhomogeneous media is considered. The exponential model as described by Eq. (8) indicates that the mean intensity-to-spacing ratio is spectrally monotonic within the wide band, decreasing exponentially from the band center (band head) towards the band wings. In the pressure broadened limit, the monotonic decrease in mean-intensity-to-spacing ratio yields a monotonic decrease of the absorption coefficient. In nonhomogeneous media, Goody et al. (1989) prove that k-distribution functions that yield a monotonic variation in the absorption coefficient are strictly correlated. Therefore, by using the cumulative distribution function from Eq. (14), it is expected that the errors introduced by the pressure broadening approximation are reduced by the increased accuracy of the strict correlation in nonhomogeneous calculations. Equation (14) is not only simple, but it has the advantage of being analytically invertible. In order to solve the radiative transfer equation expressed in Eq. (1), the relationship $k = k(g)$ is sought. Generally, the existing expressions of the cumulative distribution function are not analytically invertible, requiring a rather expensive numerical inversion process. Consequently, the use of Eq. (14) further simplifies the calculations and reduces the computational burden.

Results and Discussion

The calculations presented in this section include the infrared spectra of water vapor and carbon dioxide and replicate conditions related to combustion applications. The radiant intensity is calculated using the exact, line-by-line method, as well as approximate methods and models. Unless otherwise specified, 48 quadrature locations and weights have been selected for all applicable numerical integrations. Present calculations and the results of other researchers confirm that 48 quadratures or less are sufficient to accurately quantify the phenomena, and a constant number for all methods permits a relative comparison of the computational efficiency.

The radiative transfer equation described by Eq. (1) is solved using a spectral and spatial differencing scheme. The infrared spectrum is divided into a number of subintervals, which depend upon the particular solution method considered. The spectral absorption coefficient or the cumulative distribution function is then calculated for each spectral interval. Then the nonhomogeneous medium is discretized into several homogeneous layers and the local absorption coefficient is calculated for the temperature, pressure, and concentration at the center of the homogeneous layer.

Line-by-line Results. One set of calculations considers a mixture of water vapor and nitrogen for a line of sight with total length L, composed of three adjacent isothermal layers with $T_1 = 500$ K, $T_2 = 1000$ K, and $T_3 = 1500$ K. The partial pressures of the components are maintained equal $P_{H_2O} = P_{N_2} = 0.5$ atm, since results in the literature suggest that the pressure gradients are less important than the temperature gradient contributions. The radiant intensity leaving the medium is calculated at both the high temperature and low temperature sides of the medium and presented in Fig. 1(a).

The second set of calculations considers a mixture of carbon dioxide and nitrogen for a line of sight with total length L, composed of three adjacent isothermal layers with $T_1 = 500$ K, $T_2 = 750$ K, and $T_3 = 1000$ K. The partial pressures of the components are the same as above, $P_{CO_2} = P_{N_2} = 0.5$ atm. The radiant intensity leaving the medium is calculated at both the high and low-temperature sides of the medium and presented in Fig. 2(a).

The third set of results considers a mixture of water vapor and nitrogen for a line of sight over a wide range of lengths. The pressure is maintained constant, $P_{H_2O} = P_{N_2} = 0.5$ atm. The medium is described by a parabolic temperature variation, between 500 K and 1500 K, and is divided into 20 equal-thickness homogeneous layers. The emitted intensity is calculated for both the hot boundaries (1500 K)-cold medium (500 K at the center) case and the cold boundaries (500 K)-hot medium (1500 K at the center) case and presented in Fig. 3(a).

The line-by-line results are compared to the correlated-k method. The distribution functions are obtained from a line-by-line data base (Rothman, 1996) using different spectral intervals, varying from 25 cm^{-1} to the entire infrared spectrum (8000 cm^{-1}). The spectral intervals are chosen from the band center, or head, and proceeded to smaller and larger spectral values. It is noted that the spectral locations of the different spectral intervals do not significantly affect the magnitude of the results. The Planck function is calculated in the center of each spectral interval for which $g(k)$ functions are created. The differences introduced by the approximate methods are defined as

$$\text{Difference} = \frac{i_{\text{line-by-line}} - i_{\text{approximate method}}}{i_{\text{line-by-line}}} 100 \text{ (percent)}. \qquad (15)$$

Figures 1(a) through 3(a) show the variation of the radiant intensity leaving the medium with respect to the medium thickness, based upon the line-by-line calculations (bold lines). The

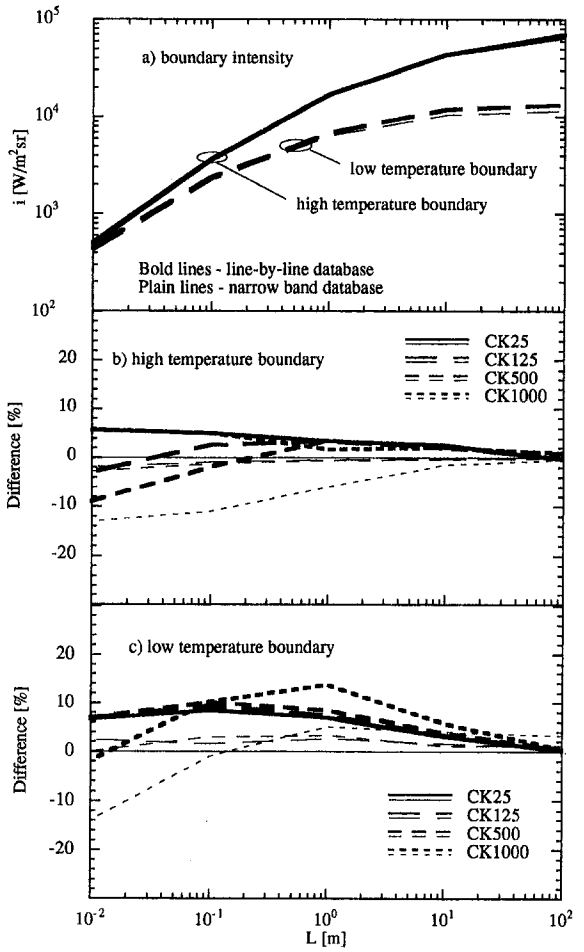

Fig. 1 Three isothermal layers (T_1 = 500 K, T_2 = 1000 K, T_3 = 1500 K) of H_2O-N_2 with partial pressures P_{H_2O} = 0.5 atm and P_{N_2} = 0.5 atm. The bold lines show the results obtained with the line-by-line database (Rothman, 1996), the plain lines show the results obtained with the narrow band model database (Soufiani and Taine, 1997a): (*a*)—emitted intensity at the high and low temperature sides; (*b*) and (*c*)—differences introduced by the correlated-*k* method (CK25-CK1000) at the high temperature boundary (*b*) and at the low temperature boundary (*c*).

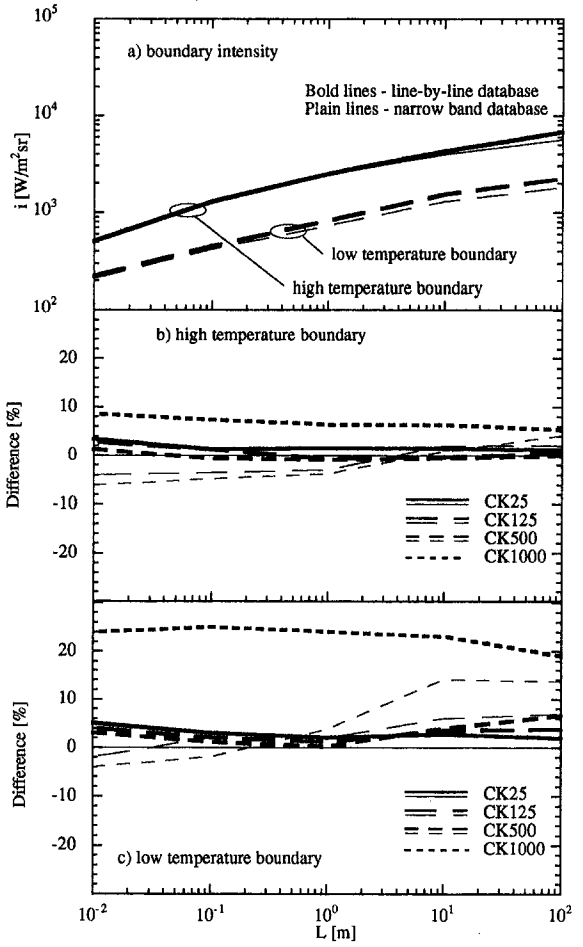

Fig. 2 Three isothermal layers (T_1 = 500 K, T_2 = 750 K, T_3 = 1000 K) of a CO_2-N_2 mixture with partial pressures P_{CO_2} = 0.5 atm and P_{N_2} = 0.5 atm. The bold lines show the results obtained with the line-by-line database (Rothman, 1996), the plain lines show the results obtained with the narrow band model database (Soufiani and Taine, 1997a): (*a*)—emitted intensity at the high and low temperature sides; (*b*) and (*c*)—differences introduced by the same methods as in Fig. 1 at the high temperature boundary (*b*) and at the low temperature boundary (*c*).

notations CK25 through CK1000 in Figs. 1 through 3 refer to the correlated-*k* method (the number represents the magnitude of the interval over which the cumulative distribution functions have been developed, in cm^{-1}). Although additional calculations have been performed for the spectral intervals noted above, Figs. 1 through 3 show only four correlated-*k* cases for clarity. The differences introduced by the correlated-*k* method originating from intervals larger than 1000 cm^{-1} have not been plotted. For such intervals, the assumption of a constant Planck function becomes inaccurate and the errors become much larger than those reported.

Figure 1 shows the results obtained for the three isothermal layer case of the water vapor-nitrogen mixture. The differences introduced by the correlated-*k* at the high temperature and low temperature boundary are presented in Figs. 1(*b*) and 1(*c*), respectively. It is observed that for both boundaries the differences introduced by the correlated-*k* method are generally within 10 percent of the line-by-line results (bold lines), relatively independent on the correlation spectral interval. At the same time, the differences observed at the low temperature boundary (Fig. 1(*c*)) are slightly larger than the differences obtained at the high temperature boundary (Fig. 1(*b*)).

Figure 2 follows the same format as Fig. 1 for the three layer geometry of carbon dioxide between 500 K and 1000 K. Figure 2(*b*) shows that, for the high temperature boundary case, the correlated-*k* method up to 1000 cm^{-1} yields good results, with differences no larger than 9 percent. The differences are higher at the low temperature boundary (Fig. 2(*c*)) for CK1000. It is important to note that the carbon dioxide vibrational-rotational bands are of the order of 500 cm^{-1}, for which the correlated-*k* method yields excellent results. Also, calculations with triangular and trapezoid temperature profiles (not shown) with similar pressure, temperatures, and lengths have been studied with no significant differences from those indicated above.

Figure 3 presents the results obtained when using a parabolic temperature profile, between 500 K and 1500 K, with a mixture of water vapor and nitrogen. The bold lines in Fig. 3(*a*) show the emitted intensity for both the cold medium-hot boundary and the hot medium-cold boundary cases using the line-by-line calculations. Figures 3(*b*) and 3(*c*) show the differences introduced by the correlated-*k* (bold lines). In both cases the maximum differences introduced by the correlated-*k* method are below 10 percent for spectral intervals up to 1000 cm^{-1}. It is noted that as the slab thickness increases, the differences decrease.

The results presented in Figs. 1 through 3 show that the correlated-*k* method can be accurately used for intervals up to 1000 cm^{-1} for water vapor in highly nonhomogeneous media. For correlation intervals of 1000 cm^{-1}, the maximum error introduced by the correlated-*k* method for the cases investigated

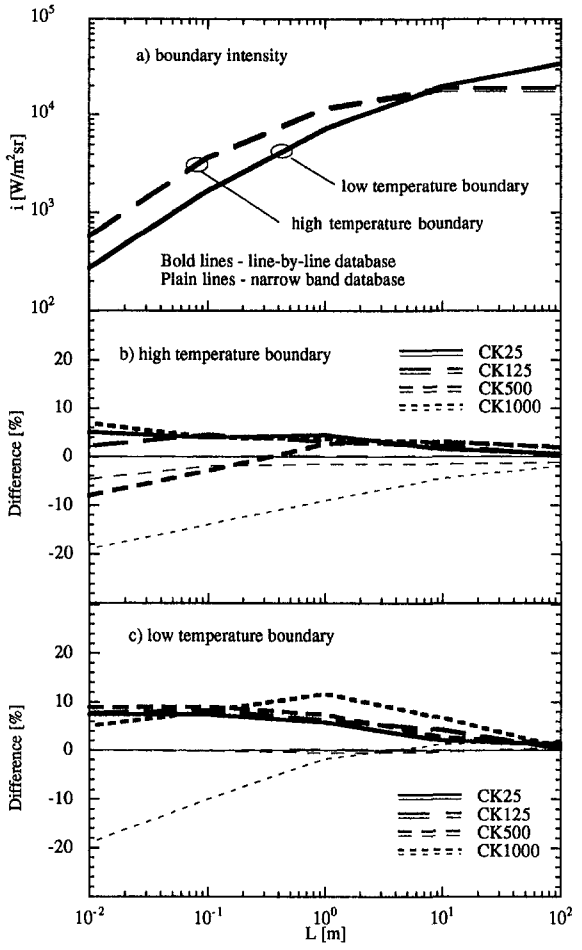

Fig. 3 Parabolic temperature profile of a H_2O-N_2 mixture with partial pressures P_{H_2O} = 0.5 atm and P_{N_2} = 0.5 atm. The bold lines show the results obtained with the line-by-line database (Rothman, 1996), the plain lines show the results obtained with the narrow band model database (Soufiani and Taine, 1997a). (*a*)—emitted intensity by the high temperature medium-low temperature boundary and by the low temperature medium-high temperature boundary cases; (*b*) and (*c*)—differences introduced by the correlated-*k* method (CK25-CK1000) and the same methods as in Figs. 1 and 2 for the cold medium-hot boundary case (*b*) and hot medium-cold boundary case (*c*).

is 13.6 percent, while the root mean square error is 6.1 percent. The correlation of the cumulative distribution functions is somewhat less accurate for the carbon dioxide, but very good results are obtained with intervals of correlation up to 500 cm^{-1}. For this correlation interval, the maximum error introduced by the correlated-*k* method is 6.6 percent, while the root mean square error is 2.7 percent for the cases investigated. The results show that when a high temperature medium radiates into a low temperature medium, the errors obtained with the correlated-*k* method increase. The spectral intervals for which the correlated-*k* method yields good results correspond to a spectral interval similar to a rotational-vibrational band interval. This fact implies that the wide band model, specifically the exponential wide band model, should be the attractive alternative to the study of transport phenomena in nonhomogeneous media.

Model Based Methods. This section compares the results obtained with various methodologies that are widely used in engineering applications. The two narrow band approaches are the correlated-*k* method using the database developed by Soufiani and Taine (1997a) and the scaling method using the RADCAL code (Grosshandler, 1980). The latter approach uses band parameters based upon the database of Ludwig et al. (1973). The wide band approaches presented below use the exponential wide band model with wide band scaling (Edwards and Morizumi, 1970) and with the correlated-*k* method. These wide band methods use the same band parameters as developed by Edwards (1981). Finally, the blackbody distribution function approach is applied using the prescriptions of Denison and Webb (1993, 1995a) with the nonhomogeneous approach presented by Denison and Webb (1995c). It is noted that each approach is based on different band parameters, originating from different databases. Thus, the differences presented below result from approximations introduced by each method and the differences in the origin of the band parameters.

Figures 1 through 3 present the results (plain lines) obtained for the same cases as above, using the narrow band model database of Soufiani and Taine (1997a, b). The gas intensities presented in Figs. 1(*a*), 2(*a*), and 3(*a*) are calculated using a correlated-*k* approach over 25 cm^{-1} intervals together with the Malkmus cumulative distribution function formulation and the database band parameters. Figs. 1(*a*) through 3(*a*) show that the results obtained with the narrow band database are in very good agreement with the line-by-line results, with an average difference between methods of approximately 4 percent. The largest differences are observed for large values of the thickness at the low temperature boundary case of carbon dioxide in Fig. 2(*a*). The application of the correlated-*k* method using the narrow band database is extended to larger spectral intervals of up to 1000 cm^{-1} for water vapor and 500 cm^{-1} for carbon dioxide and compared to the results obtained for intervals of 25 cm^{-1}. Note that the differences (plain lines in Figs. 1 through 3) compare the CK25 results to the other correlated intervals (and not the line-by-line results as indicated in Eq. (15)). The plain lines in Figs. 1(*b*) and 1(*c*), 2(*b*) and 2(*c*), and 3(*b*) and 3(*c*) show that the differences between CK25 (considered as a reference so the difference is always zero) and CK125 through CK1000 (CK500 for carbon dioxide, in Figs. 2(*b*) and 2(*c*)), although higher than for the line-by-line calculations, are generally of the same order of magnitude as the line-by-line-based correlated-*k* results. The only notable differences are observed for small slab thicknesses, where the differences between CK25 and CK1000 can reach values of 18 percent for the parabolic case in Figs. 3(*b*) and 3(*c*). It is concluded that the narrow band database is a very reliable alternative to line-by-line calculations. The availability of narrow band parameters for a wide range of conditions, together with the computational efficiency of the method, suggest the use of this database and the correlated-*k* method over intervals of 25 cm^{-1} as a benchmark for high temperature calculations. Such cases are presented below.

Figures 4 through 6 compare the line-by-line results with scaling models, wide band correlated-*k* method, and blackbody distribution function approach. The differences between each approach and the line-by-line results are calculated with Eq. (15) and plotted in Figs. 4 through 6. The scaling approaches use the CG narrow band scaling (NBS) in RADCAL (Grosshandler, 1980), and the wide band scaling (WBS) of Edwards and Morizumi (1970). The wide band correlated-*k* distributions (CKWB) as developed by Marin and Buckius (1996) using Edwards wide band parameters, together with the recommendations in Edwards and Balakhrishnan (1973), are employed. Thus, the integrated band intensity α and the bandwidth parameter ω are adjusted to compensate the differences between the Edwards correlations and the effective bandwidth calculated with the cumulative distribution function of Marin and Buckius (1996). The simplified wide band correlated-*k* method (CKPB) is also presented, where the cumulative distribution function $g(k)$ is the simple logarithmic expression (Eq. 14), regardless of the local magnitude of the pressure broadening parameter. The CKPB method uses the original wide band parameters developed by Edwards (1976). Finally, the blackbody distribution function method (BB) is presented as prescribed by Denison and Webb (1993, 1995a, c).

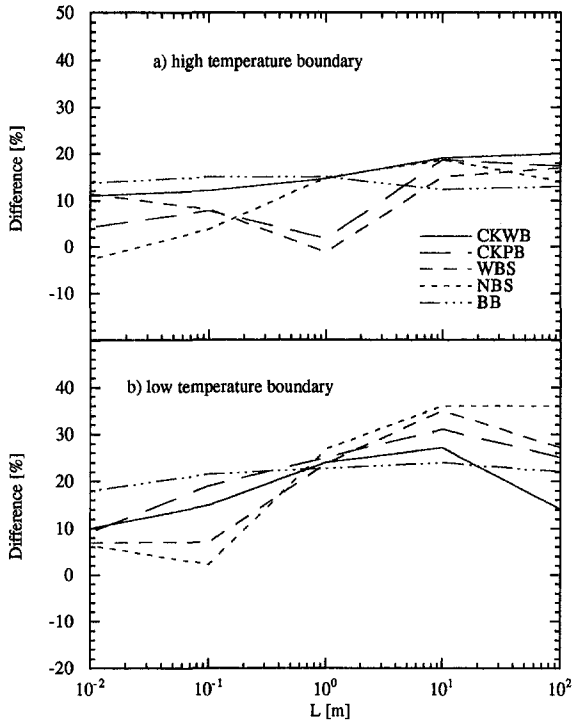

Fig. 4 Three isothermal layers (T_1 = 500 K, T_2 = 1000 K, T_3 = 1500 K) of a H_2O-N_2 mixture with partial pressures P_{H_2O} = 0.5 atm and P_{N_2} = 0.5 atm. Differences introduced at the high temperature boundary (*a*) and the low temperature boundary (*b*) by the wide band correlated-*k* (CKWB) method, the pressure broadened limit of the wide band correlated-*k* (CKPB) method, the wide band scaling (WBS) method, the narrow band scaling (NBS) method, and the blackbody distribution function method (BB), all compared to line-by-line results.

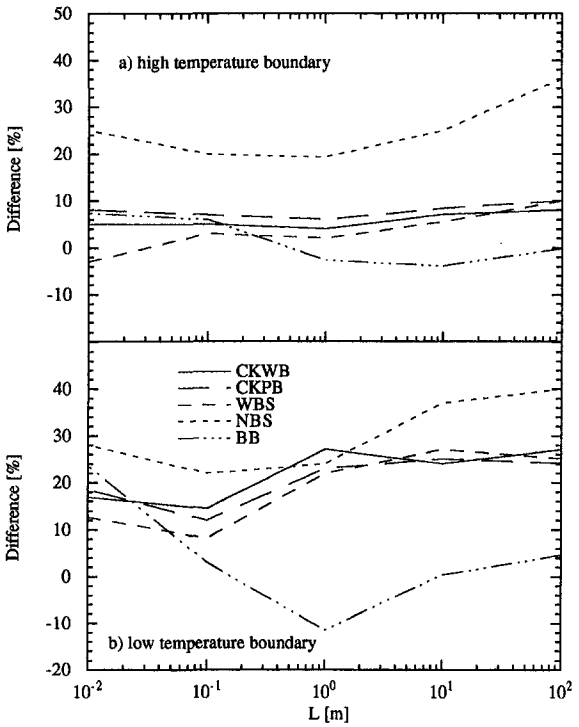

Fig. 5 Three isothermal layers (T_1 = 500 K, T_2 = 750 K, T_3 = 1000 K) of a CO_2-N_2 mixture with partial pressures P_{CO_2} = 0.5 atm and P_{N_2} = 0.5 atm. Differences introduced at the high temperature boundary (*a*) and at the low temperature boundary (*b*) by the same models as noted in Fig. 4.

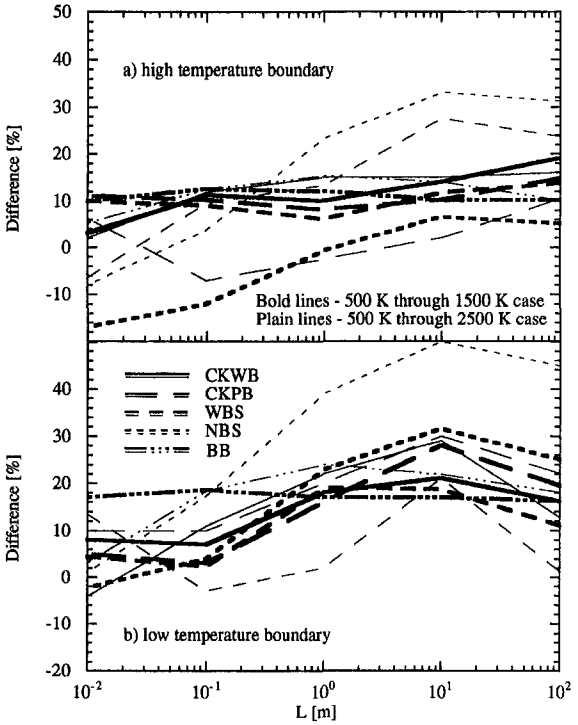

Fig. 6 Parabolic temperature profiles between 500 K and 1500 K (bold lines) and between 500 K and 2500 K (plain lines) of a H_2O-N_2 mixture with partial pressures P_{H_2O} = 0.5 atm and P_{N_2} = 0.5 atm. Differences in the emitted intensity introduced by the same models as in Figs. 4 and 5, for (*a*) the cold medium-hot boundary case, and (*b*) the hot medium-cold boundary case.

The differences in intensity for H_2O (Fig. 4) and CO_2 (Fig. 5) for the three-layer cases are presented. For the water vapor case, it is observed that the differences at the high temperature boundary (Fig. 4(*a*)) are all within 20 percent, generally the approximate methods underpredicting the outbound intensity. The differences are slightly higher at the low temperature boundary (Fig. 4(*b*)), the maximum difference of approximately 35 percent being obtained with the narrow band scaling (NBS) method for large values of the optical thickness. The approximate methods yield the same range of differences and systematically underpredict the radiant intensity at the low temperature boundary. The same general observations are valid for the carbon dioxide results in Fig. 5. The only notable difference is that the narrow band scaling at the low temperature boundary (Fig. 5(*b*)) yields an average difference that is larger than the water vapor case, with a maximum value of approximately 40 percent for large values of the slab thickness.

Figure 6 presents the differences introduced by various methods compared to the line-by-line results (bold lines) for the parabolic temperature profile of the water vapor-nitrogen mixture between 500 K and 1500 K shown in Fig. 3. Figure 6(*a*) shows the differences for the high temperature boundary and low temperature medium case. The NBS method overpredicts the emitted intensity for small and medium values of the thickness and is accurate for large values L. Figure 6(*b*) presents the differences in the cold boundary and hot medium case for the same range of optical thicknesses. Similar trends are observed for all the investigated methods, with the highest differences occurring for the narrow band scaling method. For these cases, the correlated-k wide band calculations and all other methods yield differences close to 13 percent, increasing to a maximum of 26 percent. Figure 6 (plain lines) presents the differences between the modeling methods and the correlated-k results obtained with the narrow band model database (Soufiani and Taine, 1997a) for high temperature calculations. A line

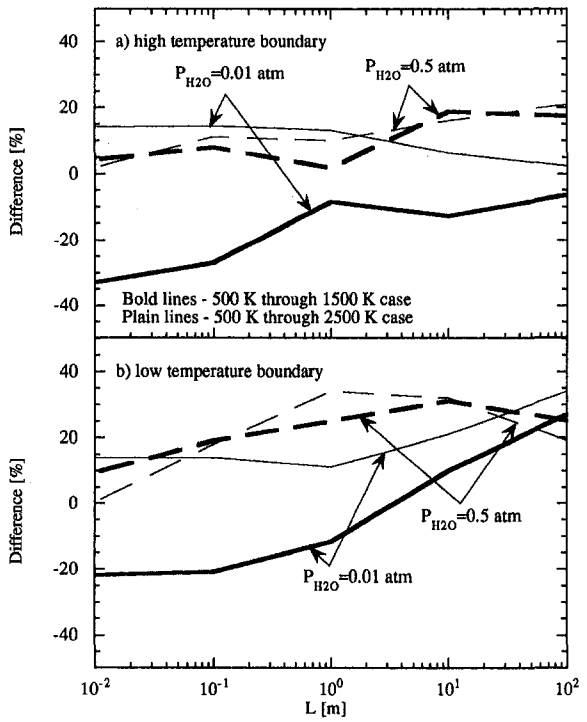

Fig. 7 Three isothermal layers with T_1 = 500 K, T_2 = 1000 K, T_3 = 1500 K (bold lines) and with T_1 = 500 K, T_2 = 1500 K, T_3 = 2500 K (plain lines) of H_2O-N_2 mixtures with partial pressures P_{H_2O} = 0.5 atm and P_{H_2O} = 0.01 atm, respectively, and a total pressure P_{tot} = 1 atm. Differences between the pressure broadened limit of the wide band correlated-k method (CKPB) and line-by-line (bold lines) and between CKPB and narrow band model database (plain lines) for (a) the high temperature boundary, and (b) the low temperature boundary emitted intensity.

of sight of length L with a mixture of water vapor and nitrogen with $P_{H_2O} = P_{N_2} = 0.5$ atm and a parabolic temperature profile between 500 K and 2500 K is investigated. The results in Fig. 6 show that the narrow band scaling introduces the largest differences, particularly for large values of the slab thickness at the low temperature boundary case (Fig. 6(b)). The correlated-k wide band calculations and all other methods yield differences close to 14 percent and up to a maximum of 28 percent. For all the approximate methods, the differences are slightly larger for the 500 K through 2500 K case than for the 500 K through 1500 K case.

Wide Band Correlated-k Accuracy. The CKWB and CKPB prove to accurately describe the emitted gas intensity in highly nonhomogeneous media. The differences between these wide band formulations (WBS included) and benchmark calculations are generally of the same order of magnitude as the original wide band model (Edwards, 1976). The CKWB and CKPB methods have the advantage of being applicable in scattering media. The CKPB approach yields accurate results for the cases investigated, even when the pressure broadening parameter is less than 1. This reasonable accuracy of the CKPB approach results from the competing contributions of the decrease in accuracy by assuming the gas to be in pressure broadened limit and the increase in accuracy due to the strict correlation of a monotonic absorption coefficient in this limit.

Figure 7 considers the application of CKPB for lower pressures. The investigation includes a water vapor-nitrogen mixture with $P_{H_2O} = 0.01$ atm and $P_{N_2} = 0.99$ atm, and the line of sight case considered in Fig. 1. Figure 7(a) shows the results obtained at the high temperature boundary case, while Fig. 7(b) refers to the low temperature boundary case. The low pressure results are plotted together with the previous case (P_{H_2O} = P_{N_2} = 0.5 atm), and it is observed that the differences increase as the pressure decreases for the hot boundary case. Differences of up to approximately 30 percent occur for small values of the medium thickness (larger for the high temperature boundary) where the CKPB method overpredicts the emitted intensity. The differences are within 10 to 15 percent for intermediate values of the medium thickness. The differences in emitted intensity at the low temperature boundary are lower than those for the high temperature boundary. Figure 7 (plain lines) presents the differences between the CKPB method and the narrow band correlated-k method (Soufiani and Taine, 1997a) for a three layer case with temperatures of 500 K, 1500 K, and 2500 K and the same pressures as above. The results at the high temperature boundary are on average within 20 percent difference, while the results at the low temperature boundary generally underpredict the emitted intensity by a maximum of 35 percent. The overprediction introduced by approximating the gas properties as those in the pressure broadened limit is compensated by the underprediction introduced by the correlated-k method. It can be concluded that the pressure broadened correlated-k method applied to wide band intervals is a reasonably accurate approach to such highly nonhomogeneous media for carbon dioxide and water vapor.

Computational Effort. The CPU time required by each method for the three layer case has been recorded and analyzed. It is noted that the programs have not been optimized and enhancements in CPU time are surely possible. Thus, the results are only comparative. The CKWB method is taken as the base case, and all the other methods are compared to the CKWB method. As previously noted, the number of quadratures, where applicable and if not otherwise specified, is 48.

The most efficient algorithms are the WBS method, about two orders of magnitude faster than the CKWB method. The CKPB method follows with about one order of magnitude faster than the CKWB method, due to the simplicity of the cumulative distribution function and the analytical inversion of $k = k(g)$. The NBS method is approximately as efficient as the CKPB method, while the BB method is comparable to the CKWB method, primarily due to the fact that the distribution functions in both cases are not explicitly invertible. The Malkmus narrow band model correlated-k method is less efficient than the CKWB (about two orders of magnitude higher) due to an increased number of distribution functions required. In addition, the cumulative distribution function describing the Malkmus narrow band model (Lacis and Oinas, 1991) is not invertible. The line-by-line approach proves to be the most inefficient, four orders of magnitude slower than the CKWB approach, yet the most accurate.

Conclusions

This work presents methods to solve the radiative transfer equation in highly nonhomogeneous media for various spectral resolutions. Each method is compared to the exact results provided by the line-by-line approach. The correlated-k method is applied for different intervals over which the absorption coefficient distribution functions are generated, varying from 25 cm^{-1} to the entire infrared spectrum. It is shown that, for the cases analyzed, the accuracy of the correlated-k method is very good for intervals up to approximately 1000 cm^{-1} for water vapor and 500 cm^{-1} for carbon dioxide. This conclusion substantially improves the computational efficiency of such calculations, while preserving the accuracy. Since the intervals generally coincide with the rotational-vibrational bands for the two gases discussed, these findings indicate that the wide band models and the correlated-k method provide an efficient and accurate approach to solve thermal radiation transport phenomena in nonhomogeneous media.

The line-by-line calculations (Rothman, 1996) are compared to the narrow band model database (Soufiani and Taine, 1997a,

b), and very good agreement between methods is found. This conclusion permits the use of the narrow band model database as an alternative benchmark. The results reported throughout this work compare several methods with the line-by-line calculations for the temperature range where this data is available and with the narrow band model database calculations for high temperature calculations where line-by-line data is not available.

The band models investigated use different approaches to nonhomogeneous calculations, namely, the scaling method, the correlated-k method, and the blackbody distribution function method. Band scaling methods introduce differences that vary with conditions and optical depth. Both narrow band and wide band scaling methods are considered—with relatively large differences when compared to line-by-line calculations. The correlated-k method is also applied to both narrow band models and wide band models. As mentioned above, the narrow band model database of Soufiani and Taine (1997a) is used to generate narrow band cumulative distribution functions. The correlated-k method combined with the exponential wide band model is studied using the cumulative distribution function developed by Marin and Buckius (1996). The results are in good agreement with the line-by-line calculations for the cases considered. The wide band correlated-k method introduces differences of the same order of magnitude as the differences introduced by the wide band model applied to a homogeneous medium. A simplified approach of the correlated-k method, using the limiting form of the cumulative distribution function that is exact in the pressure broadening limit, is extrapolated to a large range of pressures. The simple logarithmic form and the analytical inversion of this function decreased the computational time by one order of magnitude when compared to the wide band correlated-k method, without a major loss in accuracy.

This work suggests the need for the development of improved wide band cumulative distribution functions in order to more accurately and efficiently predict transport phenomena. The calculations presented here show that the wide band correlated-k approach is useful in highly nonhomogeneous media transport analysis. The development of simple yet accurate functions to account for wide band intervals can improve radiative heat transfer analyses in such nonhomogeneous media.

Acknowledgments

This research was supported, in part, by the Richard W. Kritzer Fund. We thank Dr. Denison for his assistance with the blackbody distribution function calculations.

References

Bernstein, L. S., 1980, "Band Model Parameters for the Parallel Bands of Linear Triatomic Molecules—I. Theory," *Journal of Quantitative Spectroscopy and Radiative Transfer,* Vol. 23, pp. 157–167.

Bernstein, L. S., Robertson, D. C., and Conant, J. A., 1980, "Band Model Parameters for the 4.3 μm CO_2 Band for 200 to 3000K—II. Prediction, Comparison to Experiment, and Application to Plume Emission-Absorption Calculations," *Journal of Quantitative Spectroscopy and Radiative Transfer,* Vol. 23, pp. 169–185.

Denison, M. K., and Webb, B. W., 1993, "An Absorption-Line Blackbody Distribution Function for Efficient Calculation of Total Gas Radiative Transfer," *Journal of Quantitative Spectroscopy and Radiative Transfer,* Vol. 50, pp. 499–510.

Denison, M. K., and Webb, B. W., 1995a, "Development and Application of an Absorption-Line Blackbody Distribution Function for CO_2," *International Journal of Heat and Mass Transfer,* Vol. 38, pp. 1813–1821.

Denison, M. K., and Webb, B. W., 1995b, "The Spectral-Line Weighed-Sum-of-Gray-Gases Model for H_2O/CO_2 Mixtures," ASME JOURNAL OF HEAT TRANSFER, Vol. 117, pp. 788–792.

Denison, M. K., and Webb, B. W., 1995c, "The Spectral Line-Based Weighed-Sum-of-Gray-Gases Model in Nonisothermal Nonhomogeneous Media," ASME JOURNAL OF HEAT TRANSFER, Vol. 117, pp. 359–365.

Domoto, G. A., 1974, "Frequency Integration for Radiative Transfer Problems Involving Homogeneous Non-Gray Gases: The Inverse Transmission Function," *Journal of Quantitative Spectroscopy and Radiative Transfer,* Vol. 14, No. 9, pp. 935–942.

Edwards, D. K., 1976, "Molecular Gas Band Radiation," *Advances in Heat Transfer,* Vol. 12, pp. 115–194.

Edwards, D. K., and Balakrishnan, A., 1973, "Thermal Radiation by Combustion Gases," *International Journal of Heat and Mass Transfer,* Vol. 16, No. 1, pp. 25–40.

Edwards, D. K., 1981, *Radiation Heat Transfer Notes,* Hemisphere Publishing Co., New York.

Edwards, D. K., and Menard, W. A., 1964, "Comparison of Models for Correlation of Total Band Absorption," *Applied Optics,* Vol. 3, No. 5, pp. 621–626.

Edwards, D. K., and Morizumi, S. J., 1970, "Scaling of Vibration-Rotation Band Parameters for Nonhomogeneous Gas Radiation," *Journal of Quantitative Spectroscopy and Radiative Transfer,* Vol. 10, pp. 175–188.

Godson, W. L., 1953, "The Evaluation of Infra-Red Radiative Fluxes due to Atmospheric Water Vapour," *Journal of the Royal Meteorological Society,* Vol. 79, pp. 367–379.

Goody, R. M., 1952, "A Statistical Model for Water-Vapor Absorption," *Quarterly Journal of the Royal Meteorological Society,* Vol. 78, No. 2, pp. 165–169.

Goody, R. M., and Yung, Y. L., 1989, *Atmosphere Radiation. Theoretical Basis,* Oxford University Press, New York.

Goody, R. M., West, R., Chen, L., and Crisp, D., 1989, "The Correlated-k Method for Radiation Calculations in Nonhomogeneous Atmospheres," *Journal of Quantitative Spectroscopy and Radiative Transfer,* Vol. 42, pp. 539–550.

Grosshandler, W. L., 1980, "Radiative Heat Transfer in Non-Homogeneous Gases: A Simplified Approach," *International Journal of Heat and Mass Transfer,* Vol. 23, pp. 1447–1459.

Hartmann, J. M., Levi Di Leon, R., and Taine, J., 1984, "Line-by-Line and Narrow-Band Statistical Model Calculations for H_2O," *Journal of Quantitative Spectroscopy and Radiative Transfer,* Vol. 32, pp. 119–127.

Hottel, H. C., 1954, *Radiant Heat Transmission,* chap. 4, in *Heat Transmission,* W. H. McAdams, ed., McGraw-Hill, New York.

Kritzstein, F., and Soufiani, A., 1993, "Infrared Gas Radiation from a Homogeneously Turbulent Medium," *International Journal of Heat and Mass Transfer,* Vol. 36, pp. 1749–1762.

Lacis, A. A., and Oinas, V., 1991, "A Description of the Correlated-k Distribution Method for Modeling Nongray Gaseous Absorption, Thermal Emission, and Multiple Scattering in Vertically Inhomogeneous Atmospheres," *Journal of Geophysical Research,* Vol. 96, pp. 9027–9063.

Lee, P. Y. C., Hollands, K. G. T., and Raithby, G. D., 1996, "Reordering the Absorption Coefficient Within the Wide Band for Predicting Gaseous Radiant Exchange," ASME JOURNAL OF HEAT TRANSFER, Vol. 118, pp. 394–400.

Levi Di Leon, R., and Taine, J., 1986, "A Fictive Gas-Method for Accurate Computations of Low-Resolution IR Gas Transmissivities: Application to the 4.3 μm CO_2 Band," *Revue de Physique Appliquee,* Vol. 21, pp. 825–831.

Lindquist, G. H., and Simmons, F. S., 1972, "A Band Model Formulation for Very Nonuniform Paths," *Journal of Quantitative Spectroscopy and Radiative Transfer,* Vol. 12, pp. 807–820.

Liu, J., and Tiwari, S. N., 1994, "Investigation of Radiative Transfer in Nongray Gases Using a Narrow Band Model and Monte Carlo Simulation," ASME JOURNAL OF HEAT TRANSFER, Vol. 116, pp. 160–166.

Ludwig, C. B., Malkmus, W., Reardon, J. E., and Thompson, J. A. L., 1973, *Handbook of Infrared Radiation from Combustion Gases,* NASA SP-3080.

Malkmus, W., 1967, "Random Lorentz Band Model with Exponential-Tailed S^{-1} Line-Intensity Distribution Function," *Journal of the Optical Society of America,* Vol. 57, No. 3, pp. 323–329.

Marin, O., and Buckius, R. O., 1996, "WideBand Correlated-k Method Applied to Absorbing, Emitting and Scattering Media," *AIAA Journal of Thermophysics and Heat Transfer,* Vol. 10, pp. 364–371.

Menart, J. A., Lee, H. S., and Kim, T. K., 1993, "Discrete Ordinates Solutions of Nongray Radiative Transfer With Diffusely Reflecting Walls," ASME JOURNAL OF HEAT TRANSFER, Vol. 115, pp. 184–193.

Modak, A. T., 1979, "Exponential Wide Band Parameters for the Pure Rotational Band of Water Vapor," *Journal of Quantitative Spectroscopy and Radiative Transfer,* Vol. 21, pp. 131–142.

Modest, M. F., 1991, "The Weighted-Sum-of-Gray-Gases Model for Arbitrary Solution Methods in Radiative Transfer," ASME JOURNAL OF HEAT TRANSFER, Vol. 113, pp. 650–656.

Parthasarathy, G., Chai, J. C., and Raithby, G. D., 1996, "A Simple Approach to Non-Gray Gas Modeling," *Numerical Heat Transfer,* Part B, Vol. 29, pp. 394–400.

Pierrot, L., Soufiani, A., and Taine, J., 1996, "Accuracy of Various Gas IR Radiative Property Models Applied to Radiative Transfer in Planar Media," *Radiative Transfer—I: Proceedings of the International Symposium on Radiative Transfer,* M. P. Menguc, ed., Begell House, New York, pp. 228–238.

Riviere, Ph., Langlois, S., Soufiani, A., and Taine, J., 1995, "An Approximate Data Base of H_2O Infrared Lines for High Temperature Applications at Low Resolution: Statistical Narrow-Band Model Parameters," *Journal of Quantitative Spectroscopy and Radiative Transfer,* Vol. 53, pp. 221–234.

Rothman, L. S., 1996, *HITRAN Newsletter,* Phillips Laboratory/Geophysics Directorite, No. 5, pp. 1–4.

Rothman, L. S., Gamache, R. R., Tipping, R. H., Rinsland, W. W., Smith, M. A. H., Chris Benner, D., Malathy Devi, V., Flaud, J.-M., Camy-Peyret, C., Perrin, A., Goldman, A., Massie, S. T., Brown, L. R., Toth, R. A., 1992a, "The HITRAN Molecular Database: Editions of 1991 and 1992," *Journal of Quantitative Spectroscopy and Radiative Transfer,* Vol. 48, pp. 469–507.

Rothman, L. S., Hawkins, R. L., Wattson, R. B., and Gamache, R. R., 1992b, "Energy Levels, Intensities, and Linewidths of Atmospheric Carbon Dioxide

Bands," *Journal of Quantitative Spectroscopy and Radiative Transfer,* Vol. 48, pp. 537–566.

Scutaru, D., Rosenmann, L., and Taine, J., 1994, "Approximate Intensities for CO_2 Hot Bands at 2.7, 4.3, and 12 μm for High Temperature and Medium Resolution Applications," *Journal of Quantitative Spectroscopy and Radiative Transfer,* Vol. 52, pp. 765–781.

Soufiani, A., and Taine, J., 1997a, "High Temperature Gas Radiative Property Parameters of Statistical Narrow-Band Model for H_2O, CO_2, and CO, and Correlated-k Model for H_2O and CO_2," *International Journal of Heat and Mass Transfer,* Vol. 40, pp. 987–991.

Soufiani, A., and Taine, J., 1997b, Private communication.

Soufiani, A., Hartmann, J. M., and Taine, J., 1985, "Validity of Band-Model Calculations for CO_2 and H_2O Applied to Radiative Properties and Conductive-Radiative Transfer," *Journal of Quantitative Spectroscopy and Radiative Transfer,* Vol. 33, pp. 243–257.

Taine, J., 1983, "A Line-by-Line Calculation of Low-Resolution Radiative Properties of CO_2-CO-Transparent Nonisothermal Gases Mixtures up to 3000 K," *Journal of Quantitative Spectroscopy and Radiative Transfer,* Vol. 30, pp. 371–379.

Wang, W.-C., 1983, "An Analytical Expression for the Total Band Absorptance of Infrared-Radiating Gases," *Journal of Quantitative Spectroscopy and Radiative Transfer,* Vol. 29, pp. 279–281.

Wang, W.-C. and Ryan, P. B., 1983, "Overlapping Effect of Atmospheric H_2O, CO_2, and O_3 on the CO_2 Radiative Effect," *Tellus,* Vol. 35B, pp. 81–91.

Wang, W.-C., and Shi, G.-Y., 1988, "Total Band Absorptance and k-distribution Function for Atmospheric Gases," *Journal of Quantitative Spectroscopy and Radiative Transfer,* Vol. 39, No. 5, pp. 387–397.

Wattson, R. L., and Rothman, L. S., 1986, "Determination of Vibrational Energy Levels and Parallel Band Intensities of CO_2 by Direct Numerical Diagonalization," *Journal of Molecular Spectroscopy,* Vol. 119, pp. 83–100.

Wattson, R. L., and Rothman, L. S., 1992, "Direct Numerical Diagonalization: Wave of the Future," *Journal of Quantitative Spectroscopy and Radiative Transfer,* Vol. 48, pp. 763–780.

West, R., Crisp, D., and Chen, L., 1990, "Mapping Transformations for Broadband Atmospheric Radiation Calculations," *Journal of Quantitative Spectroscopy and Radiative Transfer,* Vol. 43, pp. 191–199.

Young, S. J., 1975a, "Band Model Formulation for Inhomogeneous Optical Paths," *Journal of Quantitative Spectroscopy and Radiative Transfer,* Vol. 15, pp. 483–501.

Young, S. J., 1975b, "Addendum to: Band Model Formulation for Inhomogeneous Optical Paths," *Journal of Quantitative Spectroscopy and Radiative Transfer,* Vol. 15, pp. 1137–1140.

Schemes and Applications of First and Second-Order Discrete Ordinates Interpolation Methods to Irregular Two-Dimensional Geometries

H.-M. Koo
Graduate Research Assistant.

K.-B. Cheong
Graduate Research Assistant.

T.-H. Song
Associate Professor.
thsong@sorak.kaist.uc.kr
Mem. ASME.

Department of Mechanical Engineering,
Korea Advanced Institute
of Science and Technology,
Kusong-dong 373-1, Yusong-ku,
Taejon, Korea

This paper presents numerical schemes and comparison of predictions of radiative heat transfer for the first and the second order discrete ordinates methods (DOM1 and DOM2) using an interpolation scheme. The formulations are followed by derivation of numerical schemes for two-dimensional body fitted grids. With varying the optical depths and the numbers of grids and ordinates, radiative wall heat fluxes by DOM1 and DOM2 are calculated to compare with the exact solutions for three kinds of two-dimensional enclosures (square, quadrilateral, and J-shaped) containing absorbing/emitting and nonscattering media of known temperature with cold black walls. Emissive power and radiative wall heat fluxes by DOM1 and DOM2 are calculated to compare with zonal results for two-dimensional square enclosure containing absorbing/emitting and isotropically scattering medium of known uniform heat source with cold black walls. The results of DOM1 and DOM2 are in good agreement with the exact solutions or the zonal results. DOM1 gives more accurate results than DOM2 for most of the tested optical depths and the numbers of grids and ordinates. These methods appear as powerful candidates of very versatile radiation analysis tool. Their grid and ordinate dependencies are also discussed in depth.

1 Introduction

Among the many numerical methods of solving radiative transfer equation (RTE), the discrete ordinates method (DOM or S_N-method) is considered a potential and very promising tool. Many variations of the DOM have been suggested in the literature. Since the application of the S_N method to engineering radiative heat transfer problems, notably by Hyde and Truelove (1977), it has been implemented more and more widely (Fiveland, 1984; Truelove, 1987; Jamaluddin and Smith, 1988; Kim, 1990). The finite volume method (FVM) proposed by Raithby and Chui (1990) is another kind of the DOM together with the FVM of Chai et al. (1994) that discretized angular domains into a set of discrete directions over the entire sphere, where all variables were assumed constant within each discrete angle. In fact, the conventional DOM (hereafter referred to as CDOM) and the FVM differ only in the way the angular discretization of the RTE is performed. The FVM and the CDOM using control volume-based spatial discretization have been successfully extended to general nonorthogonal coordinates (Chui and Raithby, 1993; Chai et al., 1995; Fiveland and Jessee, 1995; Giridharan et al., 1995).

Song and Park (1992) derived second order simultaneous differential equations from the conventional discrete ordinates equations including the general scattering term, which is named here "second order discrete ordinates method (DOM2)." The conventional DOM is called here "first order discrete ordinates method (DOM1)" since it is a set of first order simultaneous integro-differential equations. The DOM2 decreases the number of governing equations to half of DOM1 and the resulting equations of the DOM2 are the second order parabolic differential equations. Cheong and Song (1995, 1996) developed and critically examined various solution schemes for the DOM2; they recommended the exponential scheme with cubic interpolation method (or simply interpolation method, IM) considering numerical accuracy and grid dependence. The IM can also be developed for the conventional discrete ordinates equations (DOM1), and it allows discrete ordinates methods (both DOM1 and DOM2) to be extended to irregular geometries, such as the above mentioned FVM and CDOM can handle.

The IM is a conceptually simple scheme to apply to multidimensional problems using not only nonrectangular grids but also unstructured grids.

This paper presents the discretization equations of the DOM1 and the DOM2 with IM for general two-dimensional geometries. In addition, comparisons of the DOM1 and the DOM2 results are made. Radiative wall heat fluxes are calculated for three test enclosures (square, quadrilateral, and J-shaped) with absorbing/emitting and nonscattering media of known temperature. Emissive power and radiative wall heat flux are calculated for a square enclosure with an absorbing/emitting and an isotropically scattering medium of a known uniform heat source. The results are compared with the exact solutions or zonal results. Their grid and ordinate dependency and other related topics are investigated and discussed in depth.

2 Discrete Ordinates Formulations

The formulations of the first order and the second order discrete ordinates methods are briefly given here.

2.1 First Order Discrete Ordinates Formulation (DOM1). The RTE is replaced by a set of equations for a finite number of ordinate directions $\tilde{\mathbf{s}}_i$, $i = 1, 2, \ldots, M$, and

Contributed by the Heat Transfer Division for publication in the JOURNAL OF HEAT TRANSFER. Manuscript received by the Heat Transfer Division September 23, 1997; revision received August 4, 1997; Keywords: Furnaces & Combustors; Numerical Methods; Radiation. Associate Technical Editor: B. W. Webb.

the scattering term integral is replaced by a quadrature of order M with appropriate angular weights W_i as

$$\frac{1}{\beta}\frac{dI_i}{ds_i} = -I_i + \dot{S}_i \tag{1}$$

where

$$\dot{S}_i = (1-\omega)I_b + \frac{\omega}{4\pi}\sum_{j=1}^{M} I_j \Phi(\vec{\mathbf{s}}_j, \vec{\mathbf{s}}_i) W_j \tag{2}$$

and where I_i is the intensity at a position $\vec{\mathbf{r}}$ for a direction $\vec{\mathbf{s}}_i$; β $(=\kappa + \sigma_s)$ is the extinction coefficient; κ and σ_s are the absorption and the scattering coefficients; ω is the scattering albedo; and $\Phi(\vec{\mathbf{s}}_j, \vec{\mathbf{s}}_i)$ is the scattering phase function of intensity entering from $\vec{\mathbf{s}}_j$ and leaving to $\vec{\mathbf{s}}_i$. The boundary condition at a diffuse wall is given by

$$I_i = \epsilon I_{bw} + \frac{1-\epsilon}{\pi}\sum_{\vec{\mathbf{n}}\cdot\vec{\mathbf{s}}_j<0} |\vec{\mathbf{n}}\cdot\vec{\mathbf{s}}_j| I_j W_j, \quad \vec{\mathbf{n}}\cdot\vec{\mathbf{s}}_i > 0 \tag{3}$$

where ϵ is the wall emissivity, I_{bw} is the blackbody intensity of the wall, and $\vec{\mathbf{n}}$ is the unit inward normal vector from the wall. The governing equation is first order, requiring only one boundary condition for the emanating intensity for $\vec{\mathbf{n}}\cdot\vec{\mathbf{s}}_i > 0$. Eq. (1), together with the boundary condition (3), constitutes a set of M simultaneous, first order, linear differential equations.

The ordinate $\vec{\mathbf{s}}_i$ and angular weight W_i can be arbitrarily obtained (Truelove, 1987). Among them, the conventional method using Gaussian quadrature (Kim, 1990) is employed in this study.

The local medium temperature may be obtained, when it is not known, from the pointwise energy balance equation iteratively as

$$\sum_{i=1}^{M} \kappa I_i W_i - 4\pi\kappa I_b + \dot{q} = 0 \tag{4}$$

where $\dot{q}$ is the radiative strength of the heat source per unit volume. Also, the radiative heat flux at a wall can be found by

$$q_w'' = \sum_{i=1}^{M} (\vec{\mathbf{n}}\cdot\vec{\mathbf{s}}_i) I_i W_i. \tag{5}$$

2.2 Second Order Discrete Ordinates Formulation (DOM2). The second order discrete ordinates equation for an absorbing, emitting, and anisotropic scattering medium have been reformulated from the first order RTE as (Song and Park, 1992; Cheong and Song, 1995)

$$\frac{1}{\beta}\frac{\partial}{\partial s_i}\left(\frac{1}{\beta}\frac{\partial F_i}{\partial s_i}\right) = F_i - \dot{P}_i \tag{6}$$

where $\dot{P}_i$ is the source term given as

$$\dot{P}_i = 2(1-\omega)I_b + \sum_{j=1}^{M/2}\left(\frac{\omega}{4\pi}A_{ij}F_j + \frac{1}{\beta}\frac{\partial}{\partial s_i}\frac{C_{ij}}{\beta}\frac{\partial F_j}{\partial s_j}\right). \tag{7}$$

In the above equations, the variable F_i is defined as

$$F_i = I_i^+ + I_i^- \tag{8}$$

where I_i^+ and I_i^- denote the intensities to the positive and the negative ordinate directions, respectively. While the first order DOM solves for M discrete ordinates, the second order DOM solves for $M/2$ ordinates. The set of discrete ordinates is made by taking one out of every even-parity pair of ordinates (the opposite-direction pairs). The number of equations is reduced to half, while the order of them is increased to the second. The A_{ij} and C_{ij} have been defined as follows:

$$[A_{ij}] = [A^o(\vec{\mathbf{s}}_j, \vec{\mathbf{s}}_i)W_j], \tag{9}$$

$$[C_{ij}] = [T_{ij} - \delta_{ij}] \tag{10}$$

where the sum of weights W_j over j is 2π; δ_{ij} is the Kronecker delta, ω is the scattering albedo, T_{ij} is the entry of $[\delta_{ij} - (\omega/4\pi)B_{ij}]^{-1}$ and $[B_{ij}]$ is $[B^o(\vec{\mathbf{s}}_j, \vec{\mathbf{s}}_i)W_j]$. The quantities A^o and B^o express scattering quantities and are defined as

$$A^o(\vec{\mathbf{s}}_j, \vec{\mathbf{s}}_i) = \Phi(\vec{\mathbf{s}}_j, \vec{\mathbf{s}}_i) + \Phi(\vec{\mathbf{s}}_j, -\vec{\mathbf{s}}_i), \tag{11}$$

$$B^o(\vec{\mathbf{s}}_j, \vec{\mathbf{s}}_i) = \Phi(\vec{\mathbf{s}}_j, \vec{\mathbf{s}}_i) - \Phi(\vec{\mathbf{s}}_j, -\vec{\mathbf{s}}_i). \tag{12}$$

Nomenclature

A, B, C = matrices appearing in the formulation of DOM2 (Eqs. (9) and (10))
A^o, B^o = scattering quantities defined by Eqs. (11) and (12)
D = width of square, m
E_b = blackbody emissive power, W/m^2
E_b^* = nondimensional emissive power of the medium along a centerline (x = 0.5 m) for square enclosure, $E_b/\dot{q}D$
F = sum of opposite-direction intensities, $I^+ + I^-$, W/(m$^2\cdot$Sr)
G = difference between opposite-direction intensities, $I^+ - I^-$, W/(m$^2\cdot$Sr)
I = radiative intensity, W/(m$^2\cdot$Sr)
I_b = blackbody radiative intensity, W/(m$^2\cdot$Sr)
L_n = Lagrange polynomial bases
M = total number of ordinate directions
$\vec{\mathbf{n}}$ = inward unit normal vector at the wall
$\dot{P}$ = source term for DOM2, W/(m$^2\cdot$Sr)
q_w'' = wall heat flux, W/m^2
$\dot{q}$ = strength of radiative heat source per unit volume, W/m^3
$\vec{\mathbf{r}}$ = position vector, m
$\dot{S}$ = source term for DOM1, W/(m$^2\cdot$Sr)
s = spatial coordinate along a line of sight, m
$\vec{\mathbf{s}}$ = unit vector into a given direction
T = a matrix appearing in the formulation of DOM2
W_i = angular weights ($i = 1, \ldots, M$)
x, y, z = spatial coordinates, m
β = extinction coefficient, m^{-1}
δ_{ij} = Kronecker delta (1 when $i = j$, 0 otherwise)
ϵ = wall emissivity
θ = polar angle measured from the positive z-axis
κ = absorption coefficient, m^{-1}
μ, ξ, η = direction cosines with x, y, and z-axis, respectively
σ = Stefan-Boltzmann constant, W/(m^{2}K^4)
σ_s = scattering coefficient, m^{-1}
τ = optical path, $\int_0^s \beta(s)ds$
ϕ = azimuthal angle measured from the positive x-axis
Φ = scattering phase function
ω = scattering albedo

Subscripts

B = boundary node
i, j, k = index for ordinate directions
IN = interpolation point
P = center node
w = wall

Superscripts

$+$ = positive direction
$-$ = negative direction

A variable G_i, defined as $I_i^+ - I_i^-$, can be expressed using F_i as

$$G_i = -\sum_{j=1}^{M/2} T_{ij} \frac{1}{\beta} \frac{\partial F_j}{\partial s_j}. \quad (13)$$

When the wall is diffuse, the boundary condition for F_i is

$$F_i - \text{sign}\,(\vec{\mathbf{n}}\cdot\vec{\mathbf{s}}_i) \sum_{j=1}^{M/2} (\delta_{ij} + C_{ij}) \frac{1}{\beta} \frac{\partial F_j}{\partial s_j}$$
$$= 2\epsilon I_{bw} + \frac{1-\epsilon}{\pi} \sum_{j=1}^{M/2} |\vec{\mathbf{n}}\cdot\vec{\mathbf{s}}_j| \Bigg[F_j + \text{sign}\,(\vec{\mathbf{n}}\cdot\vec{\mathbf{s}}_j)$$
$$\times \sum_{k=1}^{M/2} (\delta_{jk} + C_{jk}) \frac{1}{\beta} \frac{\partial F_k}{\partial s_k} \Bigg] W_j \quad (14)$$

where the function sign denotes the sign of the argument. Note that for nonscattering medium Eqs. (7) and (14) become much simpler since $\omega = C_{ij} = 0$.

The local medium temperature and radiative heat flux from the wall can be obtained by

$$\sum_{i=1}^{M/2} \kappa F_i W_i - 4\pi\kappa I_b + \dot{q} = 0, \quad (15)$$

$$q_w'' = \sum_{i=1}^{M/2} (\vec{\mathbf{n}}\cdot\vec{\mathbf{s}}_i) G_i W_i. \quad (16)$$

3 The Interpolation Scheme

3.1 Discretization Equations for DOM1. Consider a line of sight in direction $\vec{\mathbf{s}}$ passing through a nodal-point P as shown in Fig. 1 (for simplicity, subscript i for the ordinate is omitted hereafter). Eq. (1) is rewritten as

$$\frac{dI}{ds} + \beta I = \beta \dot{S}. \quad (17)$$

The source term $\dot{S}$ is approximated by the first two terms of a Taylor series expansion about point P as follows (Raithby and Chui, 1990):

$$\dot{S} = \dot{S}(s) = \dot{S}_P + \left(\frac{d\dot{S}}{ds}\right)_P (s - \Delta s). \quad (18)$$

Given the boundary values I_{IN}, Eq. (17) can be exactly solved for I_P for constant β, i.e.,

$$I_P = I_{IN} e^{-\beta\Delta s} + \dot{S}_P (1 - e^{-\beta\Delta s}) - \frac{1}{\beta} \cdot \left(\frac{d\dot{S}}{ds}\right)_P$$
$$\times [1 - e^{-\beta\Delta s}(1 + \beta\Delta s)] \quad (19)$$

where I_{IN} is a nongrid value interpolated with its neighboring values of I by a linear or higher order polynomial. Derivation of Eq. (19) is similar to the finite volume formulation of Raithby and Chui (1990). However, I_{IN} is correlated in a different way here. For the ordinate direction $\vec{\mathbf{s}}$ as shown in Fig. 1, linearly interpolated I_{IN} is expressed as

$$I_{IN} = \sum_{n=0}^{1} L_n I(l - 1 + n, m - 1) \quad (20)$$

and cubically interpolated I_{IN} is expressed as

$$I_{IN} = \sum_{n=0}^{3} L_n I(l - 2 + n, m - 1) \quad (21)$$

where $L_n's$ ($n = 0, 1, \ldots$) are the Lagrange's polynomial bases (Press et al., 1986) and $I(l, m)$ is the intensity for the nodal point P. Higher order interpolation is also possible, however, it is recommended to use an odd-order scheme to equally treat the right and the left grids. In the cubic interpolation method, the interpolation uses two neighboring grid values to its left (and right too) marked with circles along the line marked $m - 1$ (see Fig. 1) when they are available. However, when it is shifted to the left boundary and only one left grid is available for the cubic interpolation, it uses one left grid and three right grids for the interpolation, and vice versa. As an example, the Lagrange's polynomial bases of linear interpolation (in Eq. (20)) in the situation shown in Fig. 1 are expressed as

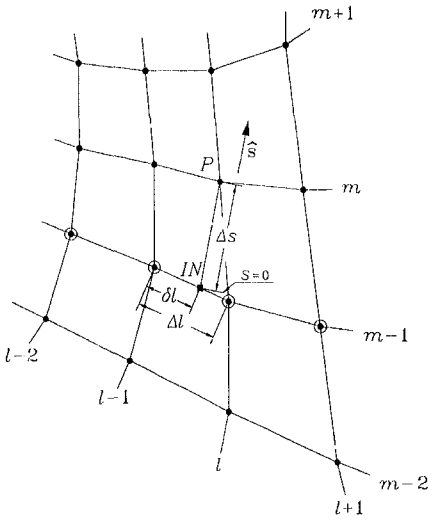

Fig. 1 Grid notation for discretization equation of DOM1

$$L_0 = \frac{\Delta l - \delta l}{\Delta l}, \quad (22a)$$

$$L_1 = \frac{\delta l}{\Delta l}. \quad (22b)$$

The gradient of $\dot{S}$ in Eq. (18) can be obtained from the following discretization equation:

$$\left(\frac{d\dot{S}}{ds}\right)_P = \frac{\dot{S}_P - \dot{S}_{IN}}{\Delta s} \quad (23)$$

where $\dot{S}_{IN}$ is interpolated in the same way as I_{IN}.

Expression for I_P in terms of its neighboring values of I and $\dot{S}$ is obtained when Eq. (20) (or (21)) and Eq. (23) are introduced to Eq. (19). For instance, when linear interpolation is used, the discretization equation for I_P reads

$$I_P = a_{l-1,m-1} I_{l-1,m-1} + a_{l,m-1} I_{l,m-1} + b \quad (24)$$

where

$$a_{l-1,m-1} = \frac{\Delta l - \delta l}{\Delta l} e^{-\beta\Delta s}, \quad (25a)$$

$$a_{l,m-1} = \frac{\delta l}{\Delta l} e^{-\beta\Delta s}, \quad (25b)$$

$$b = \dot{S}_P (1 - e^{-\beta\Delta s}) - \frac{1}{\beta} \frac{1}{\Delta s} \Bigg[\dot{S}_P - \frac{\Delta l - \delta l}{\Delta l} \dot{S}_{l-1,m-1}$$
$$- \frac{\delta l}{\Delta l} \dot{S}_{l,m-1} \Bigg] \times [1 - e^{-\beta\Delta s}(1 + \beta\Delta s)]. \quad (25c)$$

It is noteworthy that the linear or any other interpolated and

discretized equations resume the original RTE when Δs is infinitesimally small. It means that the error due to spatial finite gridding can be indefinitely decreased by taking finer grid. In the DOM2, however, linear interpolation may not have this property while higher order interpolation warrants it (Cheong and Song, 1995).

If any, this scheme (called "first order discrete ordinates interpolation method" and abbreviated as DOM1 with IM or simply as DOM1) may be alternatively termed as "finite line" or "finite angle method" since the photon balance is taken along a segment of line and angle in contrast to the volume balance taken in the finite volume method of Raithby and Chui (1990).

3.2 Discretization Equations for DOM2. The governing equation (Eq. (6)) and the boundary condition (Eq. (14)) in direction $\vec{s}$ as shown in Fig. 2 can be written as,

$$\frac{\partial^2 F}{\partial \tau^2} = F - \dot{P}, \tag{26}$$

$$\frac{\partial F}{\partial \tau} = \text{sign}\,(\vec{n}\cdot\vec{s})(F - S_w) \tag{27}$$

where $\tau = \int_0^s \beta(s)ds$ and

$$S_w = 2\epsilon I_{bw} + \frac{1-\epsilon}{\pi}\sum_{j=1}^{M/2}|\vec{n}\cdot\vec{s}_j| \times\left[F_j + \text{sign}\,(\vec{n}\cdot\vec{s}_j)\sum_{k=1}^{M/2}(\delta_{jk} + C_{jk})\cdot\frac{1}{\beta}\frac{\partial F_k}{\partial s_k}\right]W_j + \text{sign}\,(\vec{n}\cdot\vec{s})\sum_{j=1}^{M/2} C_{ij}\frac{1}{\beta}\frac{\partial F_j}{\partial s_j}. \tag{28}$$

Various solution methods for DOM2 have been examined by Cheong and Song (1995, 1996). Among them the control line approach (1996) has been adopted in this study since it can be readily extended to irregular geometries.

Assuming a uniform source term $\dot{P}$ and constant extinction coefficient β, integration of Eq. (26) over a control line (from *is* to *in*) as shown in Fig. 2(*a*) gives

$$\left.\frac{\partial F}{\partial \tau}\right)_{in} - \left.\frac{\partial F}{\partial \tau}\right)_{is} - F_P\Delta\tau + \dot{P}\Delta\tau = 0 \tag{29}$$

where $\Delta\tau = \beta\Delta s = \beta(\Delta s_1/2 + \Delta s_2/2) = (\Delta\tau_1 + \Delta\tau_2)/2$. Given two boundary values F_{IN} (or F_{IS}) and F_P, we can get the exact solution of Eq. (26) and the exact gradient at the interface *in* (or *is*) which is located at the midpoint. The obtained exact gradients are introduced into Eq. (29), then the discretization equation is given as

$$a_P F_P = \sinh\left(\frac{\Delta\tau_1}{2}\right)F_{IN} + \sinh\left(\frac{\Delta\tau_2}{2}\right)F_{IS} + \dot{P}(\Delta\tau_1 + \Delta\tau_2)\sinh\left(\frac{\Delta\tau_1}{2}\right)\sinh\left(\frac{\Delta\tau_2}{2}\right) \tag{30}$$

where

$$a_P = \sinh\left(\frac{\Delta\tau_1}{2}\right) + \sinh\left(\frac{\Delta\tau_2}{2}\right) + (\Delta\tau_1 + \Delta\tau_2)\sinh\left(\frac{\Delta\tau_1}{2}\right)\sinh\left(\frac{\Delta\tau_2}{2}\right). \tag{31}$$

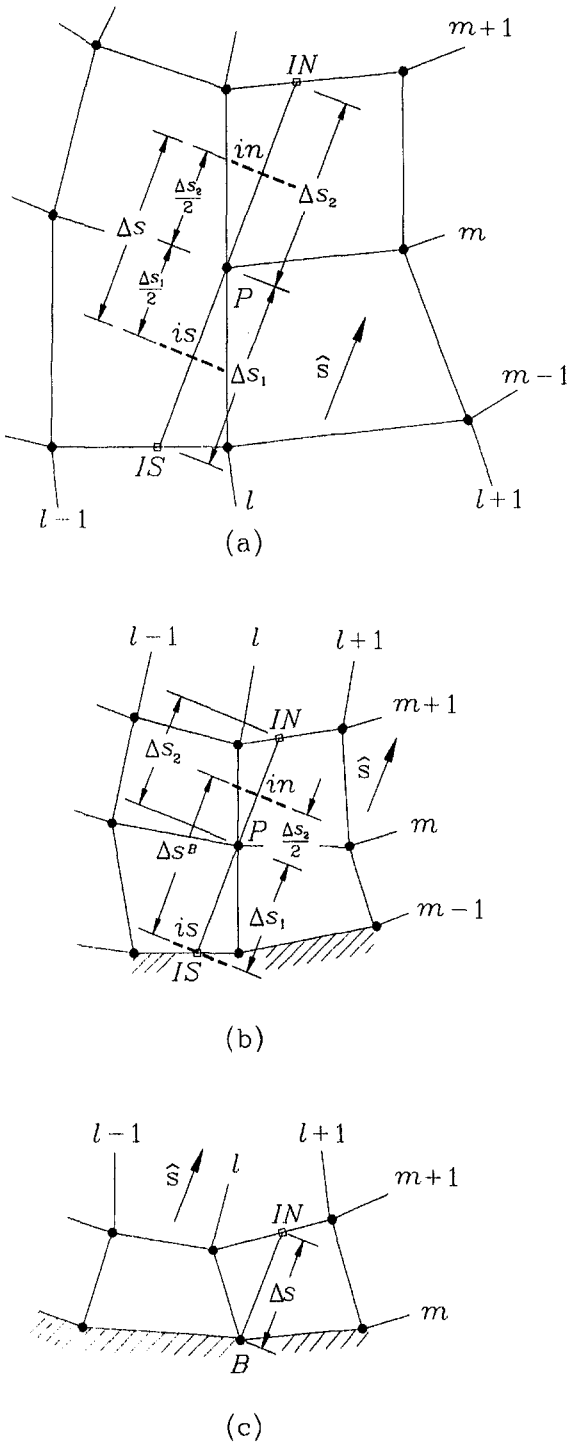

Fig. 2 Grid notation for discretization equation of DOM2 for: (*a*) internal nodes except near-boundary nodes; (*b*) near-boundary nodes; and (*c*) boundary nodes

The values of F_{IN} and F_{IS} are interpolated in the same way as I_{IN} with a third order polynomial (see Eq. (21)).

In the meanwhile, when the intergrid point *IS* (or *IN*) lies on a wall, the control line for the internal grid points just near a wall (see Fig. 2(*b*)) is increased to $\Delta\tau_1 + \Delta\tau_2/2$, and the exact gradient at the wall is obtained as

$$\left.\frac{\partial F}{\partial \tau}\right)_{is} = \frac{F_P - \dot{P} - (F_{IS} - \dot{P})\cosh(\Delta\tau_1)}{\sinh(\Delta\tau_1)}. \tag{32}$$

In a similar manner to obtain Eq. (30), we can get F_P for Fig. 2(b) as follows:

$$a_P^B F_P = \sinh(\Delta\tau_1) F_{IN} + 2\sinh\left(\frac{\Delta\tau_2}{2}\right)[\dot{P} + (F_{IS} - \dot{P})\cosh(\Delta\tau_1)] + 2\dot{P}\Delta\tau^B \sinh(\Delta\tau_1)\sinh\left(\frac{\Delta\tau_2}{2}\right) \quad (33)$$

where

$$\Delta\tau^B = \beta\Delta s^B = \beta\left(\Delta s_1 + \frac{\Delta s_2}{2}\right), \quad (34a)$$

$$a_P^B = \sinh(\Delta\tau_1) + 2\sinh\left(\frac{\Delta\tau_2}{2}\right) + 2\Delta\tau^B \sinh(\Delta\tau_1)\sinh\left(\frac{\Delta\tau_2}{2}\right). \quad (34b)$$

For the boundary point B in Fig. 2(c), Eq. (32) is introduced to the boundary condition (27) with subscripts IS and P in Eq. (32) replaced by B and IN and the expression for F_B is obtained as

$$a_B F_B = F_{IN} + \dot{P}[\cosh(\Delta\tau) - 1] + S_w \sinh(\Delta\tau) \quad (35)$$

where

$$a_B = \cosh(\Delta\tau) + \sinh(\Delta\tau). \quad (36)$$

This scheme is named "second order discrete ordinates interpolation method" and abbreviated as DOM2 with IM or simply as DOM2.

4 Results and Discussions

First, three two-dimensional (infinite in the direction normal to paper) test enclosures as shown in Fig. 3 are considered to compare the DOM1/IM and the DOM2/IM results with the exact solutions; they are (a) square, (b) quadrilateral, and (c) J-shaped infinite cylinders. All the media are absorbing/emitting and nonscattering, and are maintained at a constant temperature T_g and all the walls are cold black. Since the medium temperature is known, the exact intensity at any location is given by

$$I(s) = I_{bw} e^{-\kappa s} + I_b(1 - e^{-\kappa s}) \quad (37)$$

where I_{bw} is the blackbody intensity of the wall from which the path length s is measured, and $I_b = \sigma T_g^4/\pi$ is the blackbody intensity of the medium. The exact radiant heat fluxes on the walls are calculated using Eq. (37) and Gaussian quadrature numerical integration.

The relative average error of radiant heat fluxes on a wall is considered for comparison, which is defined as

$$\text{Error} = \sum_{\text{node}} \frac{|q_w'' - q_{\text{true}}''|/q_{\text{true}}''}{\text{Number of wall nodes}} \quad (38)$$

where q_w'' is the calculated value and q_{true}'' is the exact value.

The optical depth τ_D, defined as κD where $D = 1m$, is varied as 0.1, 1.0, and 10. The S_4, S_6, and S_8 methods are tried using linear and cubic IM's for DOM1 and cubic IM for DOM2 (linear IM for DOM2 is not recommended because of an inherent error; Cheong and Song, 1995).

Table 1 and Table 2 show the relative average errors of wall heat fluxes with DOM1 and DOM2 (Eq. (38)) for the square and the quadrilateral enclosures, respectively, and Table 3 shows it on wall 1-1, wall 1-2 and wall 1-3 for the J-shaped enclosure, with varying the optical depths and the numbers of ordinates and grids.

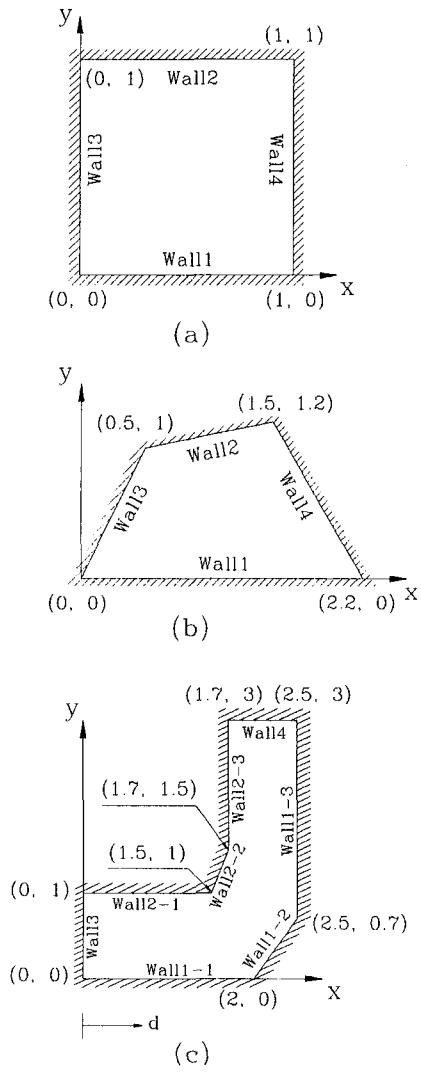

Fig. 3 Test enclosures containing absorbing-emitting media at constant temperature (coordinates in meter): (*a*) square; (*b*) quadrilateral; and (*c*) J-shaped

On the whole, both of DOM1 and DOM2 results agree well with the exact solutions, and DOM1 gives more accurate results than DOM2 for most of the tested enclosures, the optical depths, and the numbers of grids and ordinates. Improvement of accuracy from DOM2 to DOM1 is prominent when the optical depth is increased. When the optical depth is small, however, the error is large for both of DOM1 and DOM2, and the difference between them is not large. Note that the error is at most less than 10 percent in the most complex geometry, i.e., J-shaped enclosure. For most of them the error is usually a few percent or even smaller.

In Tables 1 through 3, for the given number of grids, the errors of DOM1 and DOM2 are generally reduced as the number of ordinates is increased for all the optical depths. Some exceptions to this finding are shown in Table 2 (quadrilateral enclosure). When the optical depth is 10.0 and the number of grids is 11×11 and 21×21, the errors of DOM1 and DOM2 are increased to some degree as the number of ordinates is increased although the magnitude of error is as small as 0.1 to 3 percent. The results of DOM1 are in general more sensitive to the number of ordinates than those of DOM2.

Table 1 Comparison of the relative average error of DOM1 with that of DOM2, with varying the optical depths and the numbers of grids and ordinates for square enclosure

Optical depth	No. of grids	S_N	DOM1 (with linear IM)	DOM1 (with cubic IM)	DOM2 (with cubic IM)
0.1	5 x 5	S_4	0.07647	0.02671	0.02843
		S_6	0.07152	0.02372	0.02649
		S_8	0.05242	0.00709	0.02315
	11 x 11	S_4	0.05009	0.03076	0.02326
		S_6	0.04466	0.02173	0.02732
		S_8	0.02472	0.00959	0.05460
	21 x 21	S_4	0.03952	0.03154	0.03219
		S_6	0.03397	0.02352	0.02536
		S_8	0.01377	0.01471	0.02849
1.0	5 x 5	S_4	0.05204	0.01975	0.03242
		S_6	0.04888	0.01490	0.03380
		S_8	0.04093	0.00909	0.02424
	11 x 11	S_4	0.03761	0.02995	0.02967
		S_6	0.03258	0.01606	0.01781
		S_8	0.02210	0.00960	0.01420
	21 x 21	S_4	0.03458	0.03411	0.03275
		S_6	0.02497	0.01884	0.01808
		S_8	0.01357	0.01305	0.01309
10.0	5 x 5	S_4	0.00454	0.00292	0.01187
		S_6	0.00304	0.00202	0.00952
		S_8	0.00299	0.00195	0.00969
	11 x 11	S_4	0.00763	0.00334	0.03812
		S_6	0.00667	0.00325	0.04045
		S_8	0.00590	0.00262	0.03905
	21 x 21	S_4	0.00757	0.00349	0.03227
		S_6	0.00693	0.00255	0.03644
		S_8	0.00540	0.00170	0.03499

Table 2 Comparison of the relative average error of DOM1 with that of DOM2, with varying the optical depths and the numbers of grids and ordinates for quadrilateral enclosure

Optical depth	No. of grids	S_N	DOM1 (with linear IM)	DOM1 (with cubic IM)	DOM2 (with cubic IM)
0.1	5 x 5	S_4	0.01842	0.02298	0.03826
		S_6	0.02743	0.01583	0.03057
		S_8	0.02745	0.01705	0.03028
	11 x 11	S_4	0.02371	0.03277	0.07824
		S_6	0.01346	0.02013	0.05233
		S_8	0.01154	0.01362	0.04576
	21 x 21	S_4	0.02641	0.03886	0.05341
		S_6	0.01368	0.02186	0.02879
		S_8	0.00686	0.01455	0.02001
1.0	5 x 5	S_4	0.02736	0.00829	0.01498
		S_6	0.03039	0.00548	0.01316
		S_8	0.03417	0.00195	0.01446
	11 x 11	S_4	0.01291	0.01364	0.01555
		S_6	0.01541	0.00775	0.01034
		S_8	0.02370	0.00326	0.00683
	21 x 21	S_4	0.01133	0.01758	0.01918
		S_6	0.00897	0.01028	0.01141
		S_8	0.01659	0.00740	0.00655
10.0	5 x 5	S_4	0.00296	0.00162	0.00493
		S_6	0.00279	0.00165	0.00460
		S_8	0.00288	0.00169	0.00477
	11 x 11	S_4	0.00759	0.00352	0.02402
		S_6	0.00822	0.00387	0.02653
		S_8	0.00882	0.00414	0.02790
	21 x 21	S_4	0.00778	0.00204	0.02494
		S_6	0.00859	0.00241	0.02819
		S_8	0.00926	0.00286	0.03083

Table 3 Comparison of the relative average error of DOM1 with that of DOM2, with varying the optical depths and the numbers of grids and ordinates for J-shaped enclosure

Optical depth	No. of grids	S_N	DOM1 (with linear IM)	DOM1 (with cubic IM)	DOM2 (with cubic IM)
0.1	11 x 5	S_4	0.06309	0.08812	0.09440
		S_6	0.04215	0.06021	0.08341
		S_8	0.02764	0.03363	0.07428
	25 x 10	S_4	0.06665	0.08894	0.09040
		S_6	0.04269	0.05984	0.08401
		S_8	0.02131	0.02972	0.07090
	50 x 20	S_4	0.07349	0.09133	0.09332
		S_6	0.04546	0.06471	0.08046
		S_8	0.01941	0.03416	0.07052
1.0	11 x 5	S_4	0.02771	0.02624	0.02867
		S_6	0.02251	0.01843	0.02811
		S_8	0.01661	0.00992	0.02810
	25 x 10	S_4	0.02370	0.02627	0.02639
		S_6	0.01902	0.01834	0.02570
		S_8	0.01316	0.00686	0.02451
	50 x 20	S_4	0.02460	0.02966	0.03201
		S_6	0.01806	0.02162	0.02877
		S_8	0.01045	0.01140	0.02686
10.0	11 x 5	S_4	0.00513	0.00471	0.01147
		S_6	0.00362	0.00326	0.00970
		S_8	0.00110	0.00076	0.00757
	25 x 10	S_4	0.00708	0.00575	0.02810
		S_6	0.00557	0.00423	0.02927
		S_8	0.00282	0.00157	0.02803
	50 x 20	S_4	0.00907	0.00704	0.03034
		S_6	0.00701	0.00487	0.03024
		S_8	0.00342	0.00142	0.02871

Even for a coarse grid (5×5 for the square and the quadrilateral enclosures and 11×5 for the J-shaped enclosure), DOM1 and DOM2 yield the good results for all the optical depths; however, for the given number of ordinates, increasing the number of grids does not always exert a favorable influence on the reduction of errors for all the optical depths in DOM1 and DOM2. This unexpected phenomenon calls for further explanation as follows.

Figs. 4 through 6 show the obtained nondimensional heat fluxes along wall 1 for square and quadrilateral enclosures with 21×21 grids and along wall 1-1, wall 1-2 and wall 1-3 for a J-shaped enclosure with 50×20 grids, using S_8 method. The wall heat fluxes are nondimensionalized with σT_g^4 (T_g is constant here). The solid lines denote exact wall heat fluxes. For all the tested cases, the coarser grids are not useful in expressing the rapid change of radiative heat flux near the corners where the heat flux decreases sharply due to the two neighboring cold side walls. When the number of grids is increased, the sharp change near the corners is predicted very well. This may adversely affect the magnitude of error, i.e., when the wall heat flux is underestimated with coarser grid, finer grid with sharper drop of heat flux may further increase the error. This explains the aforementioned phenomenon.

If we turn to the results of DOM1 in Tables 1 through 3, it is observed that increasing the order of interpolation does not always decrease errors. This phenomenon occurs more clearly as the enclosure is more complex and the optical depth is smaller. When the optical depth is small, intensity at a position hardly affects that at another position which is not on the same line of sight. Therefore, when the optical depth is small, increasing the order of interpolation, which relates the neighboring intensities more strongly, may give additional errors.

All the computational tests were performed on a CRAY YMP C916/16512 machine with partial vectorization. DOM1 re-

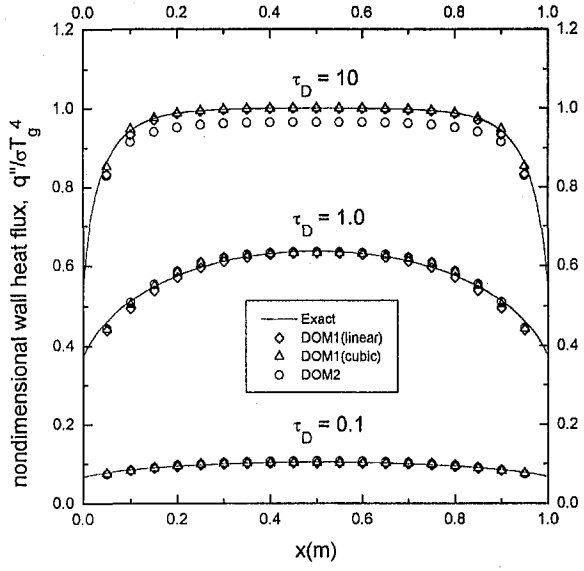

Fig. 4 Nondimensional wall heat fluxes along the wall 1 using S_8 with 21 × 21 grids for square enclosure

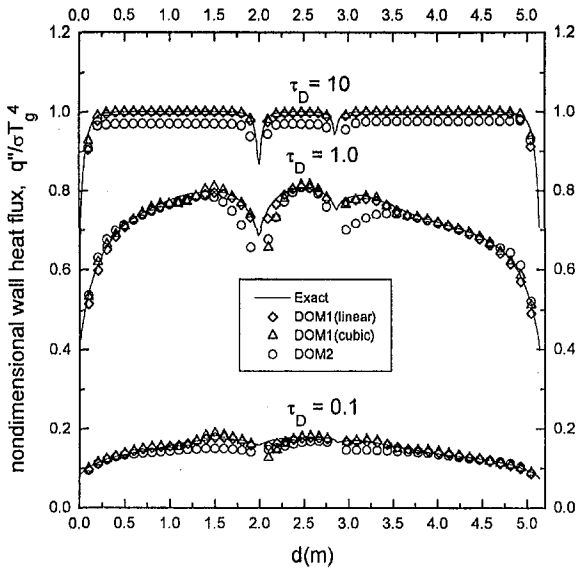

Fig. 6 Nondimensional wall heat fluxes along the wall 1-1, wall 1-2, and wall 1-3 using S_8 with 50 × 20 grids for J-shaped enclosure ('d' is measured from the lower left corner along the wall 1-1, wall 1-2, and wall 1-3 of the enclosure)

quired about 19 s of CPU time for both of the square and the quadrilateral enclosures with 21 × 21 grids using S_8 method, and about 54 s for the J-shaped enclosure with 50 × 20 grids using S_8 method. The order of interpolation schemes did not affect the computation time very much. On the other hand, DOM2 needed about 9 s of CPU time for both of the square and the quadrilateral enclosures, and about 64 s for the J-shaped enclosure for the same conditions as DOM1. The solution time of DOM2 appeared to be more dependent on the number of grids than that of DOM1. This was because the direct matrix inversion method instead of the iteration method was used in DOM2 to attain well balanced solution time for all the optical depths. From this, we can state that both of DOM1 and DOM2 have comparable computation speed. The computation time is reasonably short already. For application to more complicated grids such as unstructured grids, more advanced and efficient matrix operation schemes are expected to further reduce the computation time.

Secondly, to briefly demonstrate the capability of handling scattering, an isotropically scattering problem is solved. Square enclosure, as shown in Fig. 3(*a*), containing absorbing/emitting and isotropically scattering medium (κ = 1.0 m^{-1} and σ_s = 1.0 m^{-1}) of known uniform heat source ($\dot{q}$ = 1.0 W/m^3) with cold black walls is considered to compare the DOM1 with IM and the DOM2 with IM results with zonal ones.

Figures 7 and 8 show nondimensional emissive power along a centerline (x = 0.5 m) and nondimensional wall heat flux ($q''_w/\dot{q}D$) along wall 1, respectively. Zonal results are for 31 × 31 uniform control volumes and the others are for 31 × 31 uniform grid spacings and S_6 method is tried. The results of DOM1 and DOM2 are in good agreement with zonal results. And this confirms the applicability of current schemes to scattering problems.

Mostly the cases of uniform temperature are tried here and further complications are anticipated by introducing inhomoge-

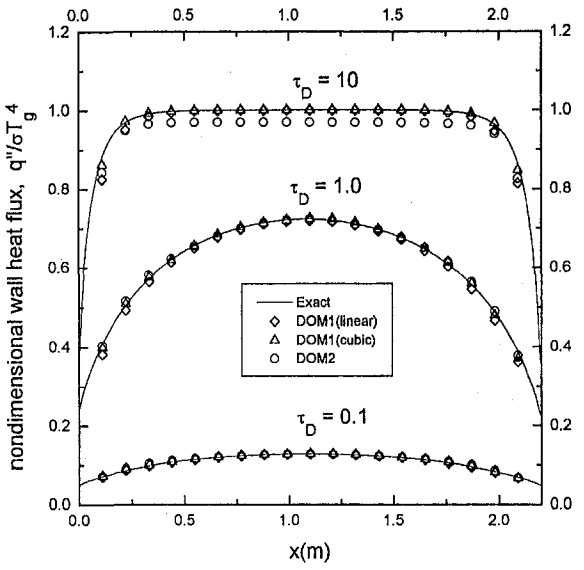

Fig. 5 Nondimensional wall heat fluxes along the wall 1 using S_8 with 21 × 21 grids for quadrilateral enclosure

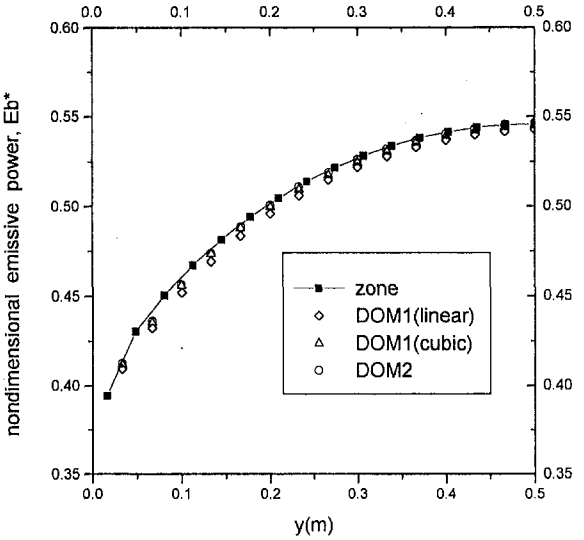

Fig. 7 Nondimensional emissive power of the medium along a centerline (x = 0.5 m) using S_6 for square enclosure containing absorbing/emitting and isotropically scattering medium with $\dot{q}$ = 1.0 W/m^3, κ = 1.0 m^{-1}, and σ_s = 1.0 m^{-1}

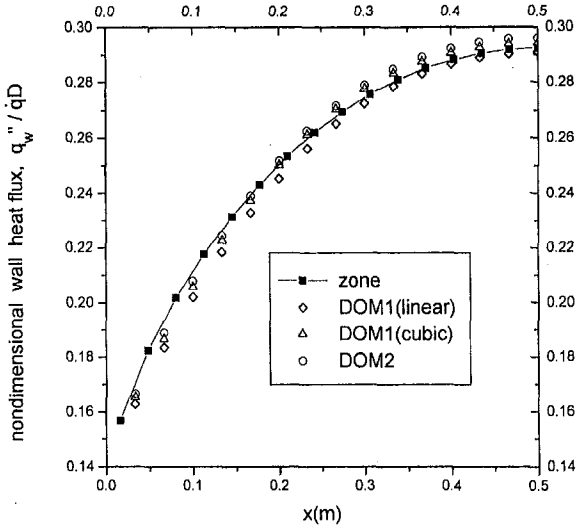

Fig. 8 Nondimensional wall heat fluxes along the wall 1 using S_6 for square enclosure containing absorbing/emitting and isotropically scattering medium with $\dot{q}$ = 1.0 W/m^3, κ = 1.0 m^{-1}, and σ_s = 1.0 m^{-1}

neity of temperature, existence of heat source and more complex geometries. However, it is very promising that both of DOM1 and DOM2 predict very accurately in the tested problems, and the current schemes call for further application to more complicated problems. While DOM2 is slightly more complicated than DOM1, the current schemes are simple, easy, and accurate. And this is why the simple idea, especially DOM1, can be extended to more complex problems with a reasonable amount of effort.

5 Concluding Remarks

Formulations of DOM1 and DOM2 with IM are described. Their discretization equations are derived for irregular two-dimensional coordinate. Sample computations for three test enclosures (square, quadrilateral, and J-shaped) containing absorbing/emitting media of known temperature with cold black walls have been made. Radiative wall heat fluxes for DOM1 and DOM2 are calculated to compare with the exact solutions for various optical depths and numbers of grids and ordinates. The results of DOM1 and DOM2 agree well with the exact solutions, and DOM1 gives better results than DOM2 for most of the tested optical depths and the numbers of grids and ordinates. The maximum error is smaller than 10 percent for 1000 grids or less, S_4 ordinates, and almost-transparent cases. When the optical depth is greater than 1, the errors are roughly less than 1 percent for all the tested cases. Complex geometry causes greater error. The results of DOM1 and DOM2 are generally more accurate as the number of ordinates is increased; DOM1 is more sensitive to the number of ordinates than DOM2. The difference between the results of DOM1 is not large although DOM1 with cubic IM gives the best results. The solution time for both of DOM1 and DOM2 has been presented and the result shows that both of them are computationally efficient.

Another sample computation for square enclosure containing absorbing/emitting and isotropically scattering medium of known uniform radiative heat source with cold black walls has been made. Emissive powers and radiative wall heat fluxes for DOM1 and DOM2 are calculated to compare with zonal results. The results of DOM1 and DOM2 agree well with zonal ones, and this proves the possibility of handling scattering problems with current schemes.

The two proposed methods are proved to be very reliable and accurate candidates of future radiation analysis tool. With DOM2 being more sophisticated than DOM1, DOM1 and DOM2 are simple and easy to extend to more complicated and multidimensional problems. More tests for nonuniform and complicated effects are called for.

References

Chai, J. C., Lee, H. S., and Patankar, S. V., 1994, "Finite Volume Method for Radiation Heat Transfer," *Journal of Thermophysics and Heat Transfer,* Vol. 8, No. 3, pp. 419–425.

Chai, J. C., Parthasarathy, G., Lee, H. S., and Patankar, S. V., 1995, "Finite Volume Radiative Heat Transfer Procedure for Irregular Geometries," *Journal of Thermophysics and Heat Transfer,* Vol. 9, No. 3, pp. 410–415.

Cheong, K. B., and Song, T. H., 1995, "Examination of Solution Methods for the Second Order Discrete Ordinate Formulation," *Numerical Heat Transfer, Part B,* Vol. 27, No. 2, pp. 155–173.

Cheong, K. B., and Song, T. H., 1996, "Application of the Second Order Discrete Ordinate Method to a Radiation Problem in a Square Geometry," in *Radiative Transfer-1, Proceedings of the First International Symposium on Radiation Transfer,* M. P. Menguc, ed., Begel House, New York, pp. 75–91.

Chui, E. H., and Raithby, G. D., 1993, "Computation of Radiant Heat Transfer on a Nonorthogonal Mesh Using the Finite-Volume Method," *Numerical Heat Transfer, Part B,* Vol. 23, pp. 269–288.

Fiveland, W. A., 1984, "Discrete-Ordinates Solutions of the Radiative Transport Equation for Rectangular Enclosures," ASME JOURNAL OF HEAT TRANSFER, Vol. 106, pp. 699–706.

Fiveland, W. A., and Jessee, J. P., 1995, "Comparison of Discrete Ordinates Formulations for Radiative Heat Transfer in Multidimensional Geometries," *Journal of Thermophysics and Heat Transfer,* Vol. 9, No. 1, pp. 47–54.

Giridharan, M. G., Lowry, S., and Krishnan, A., 1995, "A Multi-block, BFC Radiation Model for Complex Geometries," AIAA-95-2020, 30th AIAA Thermophysics Conference.

Hyde, D. J., and Truelove, J. S., 1977, "HTFS RS189: The Discrete Ordinate Approximation for Multidimensional Radiant Heat Transfer in Furnaces," HTFS Report No. AERE-R8502.

Jamaluddin, A. S., and Smith, P. J., 1988, "Predicting Radiative Transfer in Rectangular Enclosures Using the Discrete Ordinates Method," *Combustion Science and Technology,* Vol. 59, pp. 321–340.

Kim, T. K., 1990, "Radiation and Combined Mode Heat Transfer Analyses in Absorbing, Emitting, and Mie-Anisotropic Scattering Media Using the S-N Discrete Ordinates Method," Ph.D. thesis, University of Minnesota, MN.

Press, W. H., Flannery, B. P., Teukolsky, S. A., and Vetterling, W. T., 1986, *Numerical Recipes,* Cambridge University Press, NY, pp. 121–130.

Raithby, G. D., and Chui, E. H., 1990, "A Finite-Volume Method for Predicting a Radiant Heat Transfer in Enclosures with Participating Media," ASME JOURNAL OF HEAT TRANSFER, Vol. 112, pp. 415–423.

Song, T. H., and Park, C. W., 1992, "Formulation and Application of the Second Order Discrete Ordinate Method," *Proceedings 5th ISTP in Thermal Engineering,* pp. 833–841, Beijing.

Truelove, J. S., 1987, "Discrete-Ordinate Solutions of the Radiation Transport Equation," ASME JOURNAL OF HEAT TRANSFER, Vol. 109, pp. 1048–1051.

An Approximate Solution to Radiative Transfer in Two-Dimensional Rectangular Enclosures

J. B. Pessoa-Filho

S. T. Thynell
umt@psu.edu

Department of Mechanical Engineering,
Penn State University,
University Park, PA 16802

The application of a new approximate technique for treating radiative transfer in absorbing, emitting, anisotropically scattering media in two-dimensional rectangular enclosures is presented. In its development the discontinuous nature of the radiation intensity, stability of the iterative solution procedure, and selection of quadrature points have been addressed. As a result, false scattering is eliminated. The spatial discretization can be formed without considering the chosen discrete directions, permitting a complete compatibility with the discretization of the conservation equations of mass, momentum, and energy. The effects of anisotropic scattering, wall emission, and gray-diffuse surfaces are considered for comparison with results available in the literature. The computed numerical results are in excellent agreement with those obtained by other numerical approaches.

Introduction

Radiative heat transfer is an important mode of energy transfer in many different applications. Examples of such applications include, among others, pulverized-coal combustion, solid-propellant and liquid-fueled rocket motors, gas turbines, and diesel engines (Viskanta and Mengüç, 1987; Parry and Brewster, 1991). Recently, analysis of liquid-droplet radiators for use in space (Siegel, 1987), modeling of heat transfer from highly porous ceramic foam inserts in combustion systems (Yoshizawa et al., 1988), and determination of medium temperature distributions and radiative properties via inverse techniques (Subramaniam and Mengüç, 1991) indicate a continued growth in the areas of application. Accompanying this growth, however, is the need to develop more computationally efficient solution techniques to the radiation problem.

To model radiative heat transfer, many different aspects must be considered. These include: (1) the effects of multidimensional enclosures, anisotropic scattering, nonuniform and spectrally dependent properties; (2) the compatibility with grid-generation routines for conservation equations of mass, momentum, and energy as well as mass diffusion; and (3) the ability to effectively use vector and parallel-processing techniques. It is also well known that the coupling of radiation with other modes of energy transport leads to extremely stiff problems, requiring the use of sophisticated numerical techniques for accelerating the convergence of the solution. Based on these aspects, which have been discussed by Howell (1988), only a few mathematical techniques appear to be attractive for dealing with complex radiation problems. A large portion of recent research efforts on modeling of radiative heat transfer has been on the use of the P_N-approximation (Mengüç and Viskanta, 1986), the Monte-Carlo method (Howell, 1968), the discrete-ordinates technique (Lathrop and Carlson, 1967; Fiveland, 1987), or the finite-volume methods (Raithby and Chui, 1990; Chai et al., 1994). The elliptic nature, overall complexity, and relative inaccuracy have curtailed the use of the P_3-approximation—the P_1-approximation is often used in interaction problems. The Monte-Carlo method is computationally very intensive, which has limited its application primarily to problems with a specified temperature distribution within the medium. The discrete-ordinates method has been applied to a wide variety of multidimensional (Kim and Lee, 1988, 1990) and nongray problems (Kim et al., 1991). However, the use of a large set of ordinates may be computationally intensive in order to satisfy stability criteria. The finite-volume techniques have shown to give results of similar accuracy to that achievable by the discrete-ordinates method. Both the discrete-ordinates and the finite-volume techniques suffer from ray effects and false scattering, as stated by Chai et al. (1994, p. 424).

Ray Effects and False Scattering

Chai et al. (1993) have presented an excellent discussion on ray effects and false scattering associated with the discrete-ordinates method. Ray effects occur as a result of discretization of the radiation intensity in a finite number of directions; these effects are independent of the employed spatial discretization practice. As shown by Chandrasekhar (1960, p. 75, 83) for a one-dimensional problem, it may be possible to eliminate ray effects by utilizing the formal solution of the intensity. It appears, however, that such an approach may not be attractive for multidimensional problems. The use of the formal solution requires an interpolation of the extinction coefficient and the source function across the computational domain.

False scattering or numerical diffusion is caused by the spatial discretization practice. As discussed by Chai et al. (1993), its elimination is difficult to achieve. False scattering occurs once the spatial discretization is performed over domains where the intensity or its slope is discontinuous; that is, a fraction of the radiant intensity in one direction at one spatial location falsely propagates into the radiant intensity in the same direction at another spatial location. As a result, several investigators have employed the Fredholm integral form of the equation of transfer (Crosbie and Schrenker, 1984; Thynell and Özisik, 1986, 1987). However, a complete elimination of the discontinuity may not be achieved by using the Fredholm integral equation because its solution often requires an evaluation of a singular kernel; hence, ray effects or false scattering may occur (Lathrop, 1971). It is thus evident that one should consider the discontinu-

Contributed by the Heat Transfer Division for publication in the JOURNAL OF HEAT TRANSFER. Manuscript received by the Heat Transfer Division February 21, 1997; revision received July 14, 1997; Keywords: Numerical Methods; Radiation; Radiation Interactions. Associate Technical Editor: B. W. Webb.

ous nature of the radiation intensity in order to eliminate false scattering, which is the objective of our work.

Approach

In this work, a recently established method is applied for treating radiative transfer within two-dimensional rectangular enclosures. This approach has been employed to solve radiation problems in one-dimensional slabs, spheres, and cylinders (Pessoa-Filho and Thynell, 1994, 1995a), and two-dimensional cylinders (Pessoa-Filho and Thynell, 1995b). The formulation of the solution considers three aspects. First and foremost, a careful account is made for the discontinuous nature of the radiation intensity. Second, since the radiative transfer problem is first order, an integration along the line of sight of the equation of transfer is utilized. By exploiting this feature, stability problems inherent in many numerical schemes are eliminated. Third and finally, the set of discrete ordinates is defined by Gauss-Legendre quadratures, which are used to evaluate solid-angle integrals that define quantities of practical interest—namely, incident radiation and radiative heat fluxes. In general, the choice of quadratures is arbitrary (Modest, 1993).

Analysis

Mathematical Formulation. The applicability of the proposed approximate technique is considered for a rectangular enclosure containing absorbing, emitting, anisotropically scattering constituents distributed nonuniformly throughout the enclosure as shown in Fig. 1. The boundaries are opaque and diffuse. The temperature of the medium and bounding surfaces are known or specified via an overall conservation of energy. For simplicity, we assume that specular reflections effects are negligible and that the scattering phase function can be represented by a finite series in terms of Legendre polynomials. The mathematical description of the radiation problem is then specified as (Özisik, 1973)

$$\left[\sin\theta\cos\phi\,\frac{\partial}{\partial y}+\cos\theta\,\frac{\partial}{\partial z}+(\kappa+\sigma_p)\right]I(y,z,\theta,\phi)=(\kappa+\sigma_p)S(y,z,\theta,\phi),\quad(1)$$

with boundary conditions given by

$$I^+(y,0,\theta,\phi)=\epsilon_1 I_b[T(y,0)]+(1-\epsilon_1)q_z^-(y,0)/\pi,\quad(2a)$$

$$I^+(0,z,\theta,\phi)=\epsilon_2 I_b[T(0,z)]+(1-\epsilon_2)q_y^-(0,z)/\pi,\quad(2b)$$

$$I^-(y,L_z,\theta,\phi)=\epsilon_3 I_b[T(y,L_z)]+(1-\epsilon_3)q_z^+(y,L_z)/\pi,\quad(2c)$$

$$I^-(L_y,z,\theta,\phi)=\epsilon_4 I_b[T(L_y,z)]+(1-\epsilon_4)q_y^+(L_y,z)/\pi.\quad(2d)$$

The source function $S(y, z, \theta, \phi)$ for anisotropic scattering is

$$S(y,z,\theta,\phi)=(1-\omega)I_b[T(y,z)]+\frac{\omega}{4\pi}\sum_{j=0}^{N_s}a_j\int_0^{2\pi}\int_0^{\pi}P_j[\cos\theta\cos\theta'+\sin\theta\sin\theta'\cos(\phi'-\phi)]I(y,z,\theta',\phi')\times\sin\theta'd\theta'd\phi'.\quad(3)$$

The various terms specified in Eqs. (1)–(3) are defined in the nomenclature.

Formulation of Approximate Solution. Detailed development of the approximate solution commences by examining Fig. 2. In this figure, the radiant energy streaming towards the point located at (y, z) is split into eight solid-angle regions. In each of these regions, the intensity is continuous and its derivative with respect to either the polar or azimuth-angle is continuous. The use of eight different regions is chosen such that the

Nomenclature

a_j = anisotropic-scattering coefficient in phase function
B1, B2 = backward scattering phase functions of Kim and Lee (1988)
F1, F2 = forward scattering phase functions of Kim and Lee (1988)
$G(y, z) = \int_0^{2\pi}\int_0^{\pi} I(y, z, \theta, \phi) \times \sin\theta d\theta d\phi$, incident radiation
$I(y, z, \theta, \phi)$ = radiation intensity
I_b = blackbody intensity
I_{B1} = intensity in direction from corner at ($y = 0$, $z = 0$), see Fig. 5
I_{N1} = intensity in direction normal to surface at $z = 0$, see Fig. 5
L_y = width of enclosure
L_z = height of enclosure
N_s = order of scattering phase function
N_y, N_z = number of nodes in y and z-directions
N_θ, N_ϕ = number of discrete ordinates over polar and azimuth angles
P_j = Legendre polynomial of order j
$q_y(y, z) = \int_0^{2\pi}\int_0^{\pi} I(y, z, \theta, \phi) \times \cos\phi \sin^2\theta d\theta d\phi$, net heat flux in y-direction
$q_z(y, z) = \int_0^{2\pi}\int_0^{\pi} I(y, z, \theta, \phi) \times \cos\theta \sin\theta d\theta d\phi$, net heat flux in z-direction
$S(y, z, \theta, \phi)$ = source function
T = temperature of medium
T_i = surface temperature of wall, see Fig. 1
w_m, w_n = weights in quadrature
y = physical coordinate in y-direction
z = physical coordinate in z-direction
β = extinction coefficient
δ_y, δ_z = distance defined in Fig. 4 and 5, respectively
$\Delta y = L_y/(N_y - 1)$, cell width in Figs. 4 and 5
$\Delta z = L_z/(N_z - 1)$, cell height in Figs. 4 and 5
$\Delta\mu_{kn}$ = angle defined by Eq. (9d)
ϵ = emissivity
θ = polar angle
κ = absorption coefficient
$\mu = \cos\theta$
$\mu_{kn}^* \equiv \cos\theta_{kn}^*$, defined for $k = 1$ in Fig. 3
ξ_m = mth zero of Legendre polynomial
σ_p = scattering coefficient
ϕ = azimuth angle
ω = scattering albedo, σ_p/β

Subscripts

i, j = spatial indices
k = contribution from kth region of Fig. 2
m, n = solid-angle indices
y = y-direction
z = z-direction
1, 2, 3, or 4 = quantity of bounding wall

Subscripts

$\pm$ = forward (+) and backward (−) directions
$\tilde{}$ = angularly interpolated quantity
$\bar{}$ = spatially interpolated quantity

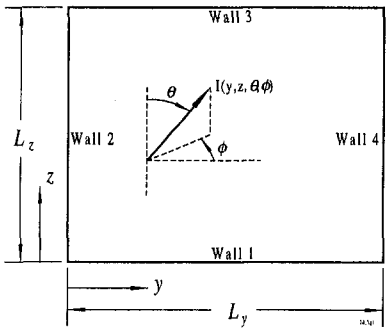

Fig. 1 Schematic diagram of system considered

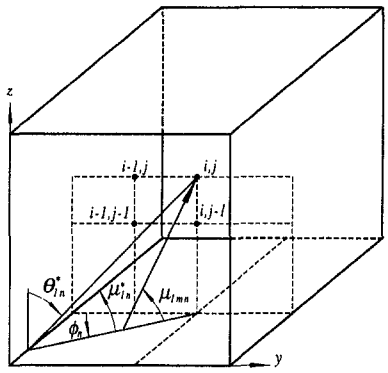

Fig. 3 Specification of various angles employed in region 1 of Fig. 2. Node (i, j), shown above, corresponds to position (y, z) in Fig. 2.

forward and backward heat fluxes can be determined within the medium. If the net heat fluxes are needed only along the bounding surfaces, then it is possible to employ four different regions by collapsing each of regions 1 and 8, 2 and 3, 4 and 5, and 6 and 7 into one region, respectively. Continuity in the intensity is required in order to accurately perform numerical solid-angle integrations of the incident radiation and the net radiant heat fluxes as well as the forward and backward radiant heat fluxes. Therefore, the temperature and radiative properties must be continuous along each surface and within the medium, and the medium must not contain line or point sources, which could be the case in the corresponding neutron transport problems. To limit the formulation, a detailed development is presented for only region 1 shown in Fig. 2. In this, as well as in the other seven regions, N_θ polar angles are specified as $\cos\theta_m = \mu_m$, $m = 1, \ldots, N_\theta$, and N_ϕ different azimuth angles ϕ_n, $n = 1, \ldots, N_\phi$ are specified. Such a specification requires the use of an N_θ-point quadrature for the polar angle integration, and an N_ϕ-point quadrature for the azimuth-angle integration. These points are selected based on the zeros of the Legendre polynomials, ξ_m, which are subsequently shifted onto these angular intervals following standard procedures (Abramowitz and Stegun, 1972). Figure 3 shows the specification of the angles involved for a single direction of the intensity. For region 1, the angular directions are specified by

$$\phi_n = \pi(1 + \xi_n)/4, \quad \mu_{mn} = (1 + \xi_m)(1 - \mu^*_{1n})/2 \quad (4a, b)$$

$$\mu^*_{1n} = \cos\,[\tan^{-1}\,(y/z\,\cos\,\phi_n)]. \quad (4c)$$

That is, $0 \le \phi \le \pi/2$ and $\mu^*_{1n} \le \mu \le 1$. Overall, there are $N_\theta \times N_\phi$ discrete directions in each region for a total of $8N_\theta \times N_\phi$ discrete directions at each point within the medium. Furthermore, these directions are different at each point within the medium as well as along the bounding surfaces. The reason for using Gaussian quadratures over other numerical integration techniques, such as project-invariance techniques, is related to the fact that for single integrals they will exactly integrate a polynomial with the least number of points.

The next step is to solve Eq. (1) over a discretized domain. Figure 4 shows four nodes of Fig. 3 in the ϕ-plane. Equation (1) is integrated along the line of sight within this discretized domain in a direction specified by the polar and azimuth angles (Lathrop and Carlson, 1967). By considering this discretized domain, rather than an integration all the way from the wall to the point at (y, z), one should be able to reduce the computational effort. The solution to this integration may be approximated as

$$I_{ijmn} = \exp(-\bar{\beta}_{ij}\Delta s_{mn})\tilde{I}_{ijmn} + \bar{S}_{ijmn}[1 - \exp(-\bar{\beta}_{ij}\Delta s_{mn})]. \quad (5)$$

However, the integration yielded an unknown intensity $\tilde{I}_{ijmn}$ and an unknown source function $\bar{S}_{ijmn}$. $\tilde{I}_{ijmn}$ must be approximated over both the spatial and directional domains (in the direction of I_{ijmn}), whereas $\bar{S}_{ijmn}$ requires only a spatial approximation. First, we outline the spatial approximations.

Spatial Interpolation. If the intensity $\tilde{I}_{ijmn}$ is located between $(i - 1, j - 1)$ and $(i, j - 1)$, as shown in Fig. 4, then the spatial interpolation is straightforward and represented by

$$\bar{\beta}_{ij} = [\beta_{ij} + (1 - \delta_y)\beta_{i-1,j-1} + \delta_y\beta_{i,j-1}]/2 \quad (6a)$$

$$\bar{S}_{ijmn} = [S_{ijmn} + (1 - \delta_y)S_{i-1,j-1,mn} + \delta_y S_{i,j-1,mn}]/2 \quad (6b)$$

$$\tilde{\bar{I}}_{ijmn} = (1 - \delta_y)\tilde{I}_{i-1,j-1,mn} + \delta_y\tilde{I}_{i,j-1,mn} \quad (6c)$$

$$\Delta s_{mn} = \Delta z/\mu_{mn}, \quad (6d)$$

$$\delta_y = 1 - \frac{\Delta y}{\Delta z}\frac{(1 - \mu^2_{mn})^{1/2}}{\mu_{mn}\cos\,\phi_n}. \quad (6e)$$

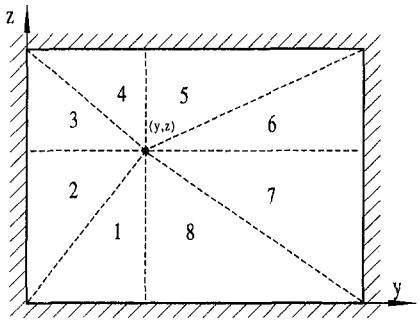

Fig. 2 Definition of the eight angular regions

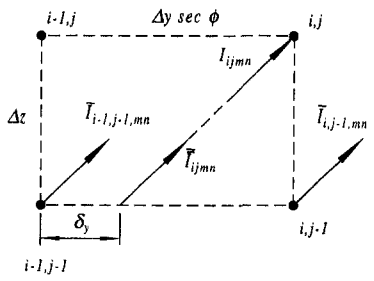

Fig. 4 Spatial interpolation of the intensity $\tilde{\bar{I}}_{ijmn}$ in terms of the intensities $\tilde{I}_{i-1,j-1,mn}$ and $\tilde{I}_{i,j-1,mn}$

If the intensity $\tilde{I}_{ijmn}$ intersects the vertical line between nodes $(i-1,j)$ and $(i-1,j-1)$, shown in Fig. 5, then the intensity at node $(i-1,j)$ may not be defined in the direction of I_{ijmn} (at node (i,j)). This may occur for the larger values of the polar angle. As discussed by Pessoa-Filho and Thynell (1995b), interpolation is the preferred approximate technique for the evaluating of $\tilde{I}_{ijmn}$, but it must then be replaced by an extrapolation resulting in a loss of accuracy. Namely, the intensity at node $(i-1,j)$ is extrapolated into an angular interval for which it is not defined. To avoid extrapolation in this work, a bounding intensity I_{B1} is calculated. The bounding intensity of region 1 is determined by integrating Eq. (1) from the lower-left corner to the position specified in Fig. 5 along the line of sight. Although the employed expressions are not included here, they involve a summation of spatially interpolated values of the source function. This is clearly an added complexity, but it is needed to avoid extrapolation. Equivalent expressions to those specified by Eqs. (6) are developed and utilized in the interpolation; they are not defined here.

Angular Interpolation. In addition to interpolation over the spatial domain, angular interpolation is also performed to increase the accuracy of the results. For example, the interpolation over the angular domain is required to specify the intensities at nodes $(i-1,j-1)$ and $(i,j-1)$, shown in Fig. 4, in the direction of the intensity I_{ijmn} at node (i,j). Such an interpolation is performed using a quadratic polynomial. To obtain the bounding intensity I_{B1} in direction of I_{ijmn} at node (i,j), a normal intensity I_{N1} is introduced. It is computed by solving Eq. (1) from the bounding wall to the point specified in Fig. 5 along the spatial grid with $\theta = 0$. Finally, a linear interpolation involving I_{B1} and I_{N1} are used to obtain an approximate value of the bounding intensity in direction of I_{ijmn} at node (i,j).

Inspection of Eq. (5) reveals the following. First, an iterative use of Eq. (5), coupled with the corresponding equations for the other seven angular intervals, must be performed. The use of these equations does not require a need for satisfying a stability criterion. All the terms appearing on the right-hand side are positive. Thus, it is possible to select the physical dimensions of each cell independent of the discrete directions given by (μ_{mn}, ϕ_n) and it offers an improved compatibility with grid-generation routines for solving the conservation equations of mass, momentum, and energy. Second, the use of mean beam lengths are not required. Instead, actual physical paths are employed. Third, the approximations of the intensity $\tilde{I}_{ijmn}$ and source function $\tilde{S}_{ijmn}$ do account for differences in the direction as a result of the variation in the polar and azimuth angles with position.

Solution Procedure. In order to obtain a solution to the intensity, an iterative scheme must be employed. In this work a marching procedure is utilized. For intensities within regions 1 and 8, I_1 and I_8, respectively, it starts at the bottom surface by neglecting the incident intensities $(q_z^-(y,0) = 0)$. The next step is to solve for the intensities along the plane $j = 2$, and then continues until the incident intensities are solved for along the top surface. Simultaneously, the intensities within the other six regions are computed and the source function is updated. The iterative scheme continues until convergence is established. In this work, it is specified when

$$\sum_{ijmn} \delta I_{ijmn}/I_{ijmn} < 10^{-6}, \tag{7}$$

where δI represents the change in the intensity from one iteration to the next iteration. Once the convergence is established, the incident radiation and net heat fluxes are, respectively, computed from

$$G_{ij} = \sum_{k=1}^{8} G_{kij}, \tag{8a}$$

$$q_{y,ij} = \sum_{k=1}^{4} q_{y,kij} - \sum_{k=5}^{8} q_{y,kij} \tag{8b}$$

$$q_{z,ij} = \sum_{k=1,2,7,8} q_{z,kij} - \sum_{k=3}^{6} q_{z,kij}, \tag{8c}$$

where

$$G_{kij} = \frac{\pi}{4} \sum_{n=1}^{N_\phi} w_n \Delta\mu_{kn} \sum_{m=1}^{N_\theta} w_m I_{kijmn}, \tag{9a}$$

$$q_{y,kij} = \frac{\pi}{4} \sum_{n=1}^{N_\phi} w_n \Delta\mu_{kn} \sum_{m=1}^{N_\theta} w_m I_{kijmn} (1 - \mu_{kijmn}^2)^{1/2} \cos\phi_m, \tag{9b}$$

$$q_{z,kij} = \frac{\pi}{4} \sum_{n=1}^{N_\phi} w_n \Delta\mu_{kn} \sum_{m=1}^{N_\theta} w_m I_{kijmn} \mu_{kijmn}, \tag{9c}$$

$$\Delta\mu_{kn} = \begin{cases} (1 - \mu_{kn}^*)/2, & k = 1, 4, 5, 8 \\ \mu_{kn}^*/2, & k = 2, 3, 6, 7 \end{cases}. \tag{9d}$$

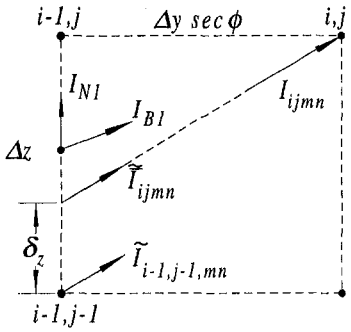

Fig. 5 Definition of intensities used in the spatial interpolation along the vertical direction of a cell

Discussion of Results

To assess the accuracy of the above outlined approximation, several different cases are considered. The first case illustrates the angular variation of the radiation intensity in cases of both isotropic and anisotropic scattering. The second case considers a cold, purely absorbing medium contained in a rectangular enclosure whose bottom surface emits radiant energy, whereas the other surfaces are nonemitting. The third case deals with effects of scattering, including both isotropic and anisotropic scattering. The fourth and final situation involves the effects of surface reflection of the walls and an anisotropically scattering medium. In the following discussion, F1 and F2 denote forward whereas B1 and B2 represent backward scattering phase functions with coefficients a_j, $j = 0, \ldots, N_s$, listed by Kim and Lee (1988); they are not reproduced here. F1 involves thirteen coefficients ($N_s = 12$ in Eq. (3)), F2 involves nine coefficients, B1 involves six coefficients, and B2 involves three coefficients in the expansion of the scattering phase function. The considered cases were executed using single precision in FORTRAN.

Figure 6 illustrates the angular variation of the radiation intensity at three selected points along the vertical line at $y = L_y/2$. In this case, emission occurs along the bottom surface ($I_{b1} = 1$), whereas all other surfaces are nonemitting. The optical dimensions are $\beta L_y = \beta L_z = 1$, the medium is purely scattering ($\omega = 1$), and all surfaces are black. This situation was solved by using a uniform spatial discretization of $N_y \times N_z = 5 \times 5$ and an angular discretization of $N_\theta \times N_\phi = 6 \times 6$. Inspection of the results shown in these figures reveals that first, the intensity distributions possess discontinuities at all three spatial locations. For example, in Fig. 6(*a*), which shows the distribution at the bottom surface, there is a sharp discontinuity in the plane where

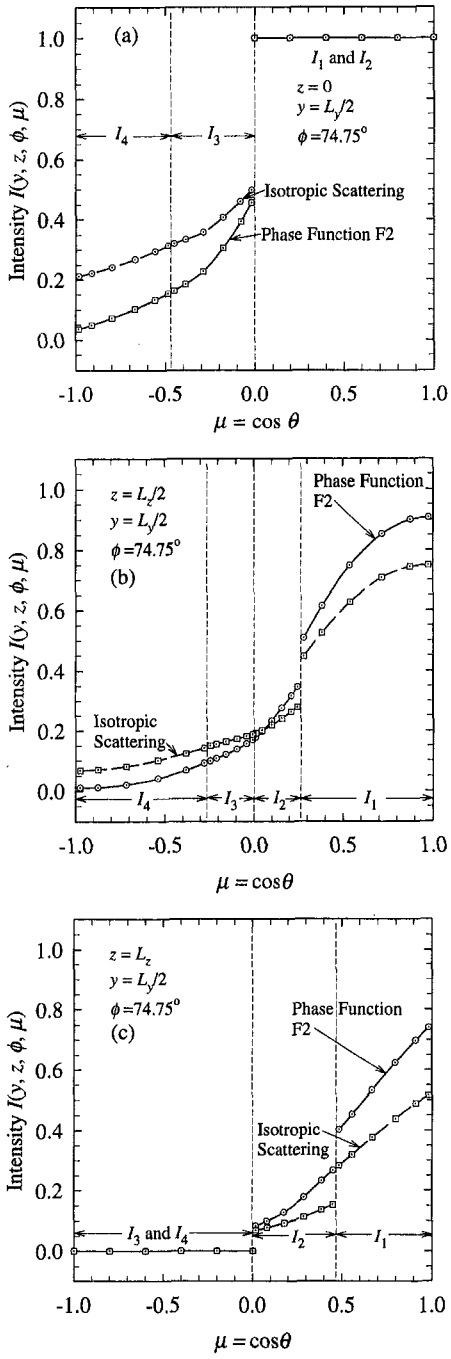

Fig. 6 Angular distribution of the radiation intensity at $y = L_y/2$, ϕ = 74.75° and three vertical points: (*a*) $z = 0$, (*b*) $z = L_z/2$, and (*c*) $z = L_z$. Emission occurs from the bottom surface, whereas the other surfaces are cold ($\epsilon = 1$, $\omega = 1$, $\beta L_y = \beta L_z = 1$).

$\mu = 0$. In Fig. 6(c), the discontinuity between I_1 and I_2 near μ = 0.47 is caused by differences in the specified boundary condition along the bottom wall ($y = 0$) and the left wall ($z = 0$). The corner at $y = 0$, $z = L_z$ does not cause a discontinuity in the distributions between I_3 and I_4. Second, in Fig. 6(a) and Fig. 6(c), the forward intensities I_1 and I_2 and backward intensities I_3 and I_4 are, respectively, uniform, as required by the assumed diffuse surfaces. Third, although the optical dimensions are only in the intermediate range, back scattering is readily observed and it produces the contribution to the intensities I_3 and I_4 in Figs. 6(a) and (b). Fourth, differences in the assumed scattering phase functions are noticed both in the forward and backward directions of the intensity. Finally, in the cases shown it appears that the intensity within each region is a smoothly varying function. However, the use of second-order interpolating polynomials may be inadequate in some cases; for example, the slope of the intensity I_1 in Fig. 6(b) varies considerably in both cases of isotropic and anistropic scattering. In addition, higher-order discretizations in both spatial and angular domains were utilized but the predicted changes were only minimal.

Table 1 shows the convergence of the incident radiation at several selected points within and at the boundary of a purely absorbing medium with unit optical width and height ($\beta L_y = \beta L_z = 1$). The bottom wall has a uniform temperature with $I_{b1} = 1$, whereas the other walls are at a zero temperature. The four bounding walls are black. This case is considered for two reasons. First and foremost, it is the most difficult case to determine accurately since the solution depends to a large extent on interpolated intensities. That is, there are no sources of radiant energy within the medium and the intensity is a highly discontinuous function. Second, highly accurate results of the incident radiation can be generated from a direct numerical integration of the solution to the intensity. The "exact" results shown in the bottom row of Table 1 were generated by integrating the solution to the radiation intensity using a 20 point Gauss-Legendre quadrature. The convergence of the results was assessed using a uniform spatial discretization involving either 5 × 5, 11 × 11, or 15 × 15 nodes in the horizontal and vertical directions ($N_y \times N_z$). Similarly, the number of nodes in the polar (N_θ) and azimuth (N_ϕ) directions within each of the eight regions defined in Fig. 2 was varied from 2 × 2 to 12 × 12. Hence, the largest system involved approximately 259,000 unknown intensities. In the case of a 3 × 3 directional discretization, there are 72 unknown intensities at each grid point within the medium in addition to the required bounding and normal intensities I_{Bi} and I_{Ni}, respectively, defined in Fig. 5. Examination of Table 1 is first performed with respect to the number of angular directions considered. Clearly, as the number of angular directions is nearly doubled from 8 × 8 to 12 × 12 in each angular region of Fig. 2, the numerical results of the incident radiation changed only in the third or the fourth decimal place. The largest change occurred, as expected, when the number of angular directions increased from 2 × 2 to 3 × 3. In the case of 3 × 3 angular directions, results within about 1 percent of the "exact" results can be obtained.

However, increasing the number of spatial nodes does not imply that the results should converge towards the "exact" results. In fact, the case involving 5 × 5 spatial nodes is in better agreement with the "exact" results than those obtained

Table 1 Convergence of incident radiation at selected points for a cold, absorbing medium with $\beta L_y = \beta L_z = 1$ and bounded by black boundaries. Emission occurs along the bottom wall, $I_{b1} = 1$, and all other walls are at zero emissive power.

$N_y = N_z$	$N_\theta = N_\phi$	$G/4\pi$			
		$(0.5L_y, 0.5L_z)$	$(0.5L_y, L_z)$	$(0, L_z/2)$	$(0, L_z)$
5	2	0.11231	0.03749	0.07121	0.02858
	3	0.11646	0.03858	0.07362	0.02953
	4	0.11812	0.03830	0.07521	0.03015
	8	0.11743	0.03828	0.07504	0.02978
	12	0.11747	0.03829	0.07507	0.02981
11	2	0.11225	0.03730	0.06901	0.02852
	3	0.11666	0.03837	0.07303	0.02981
	4	0.11853	0.03803	0.07490	0.03033
	8	0.11746	0.03800	0.07408	0.02966
	12	0.11791	0.03801	0.07414	0.02990
15	2	0.11224	0.03720	0.06825	0.02850
	3	0.11665	0.03833	0.07300	0.02981
	4	0.11867	0.03798	0.07473	0.03037
	8	0.11779	0.03796	0.07338	0.02975
	12	0.11815	0.03796	0.07344	0.02991
"Exact" Solution		0.11753	0.03863	0.07525	0.02986

in the case of 15 × 15 spatial nodes. This finding may not be intuitive and needs further explanation. By increasing the number of grid points, the distance between the emitting surface and the first node within the medium decreases. Because of this decreased distance, the interpolation of intensities over the polar angle at this first node spans polar angles over the range $0 < \theta < \pi/2$. Over such a large angular variation, the intensity also varies considerably. In particular, as $\phi \to \pi/2$, the optical distances become very large and the intensity is considerably attenuated, whereas for $\phi \to 0$, the extent of attenuation is quite limited. The accuracy of the linear interpolation involving the bounding and normal intensities I_{Bi} and I_{Ni} over the polar angle then decreases; hence, the results for the 5 × 5 spatial discretization are slightly more accurate than the case involving 15 × 15 spatial discretization. Increased accuracy in the results can only be achieved if this part of the overall interpolation process is improved. In addition, the approach outlined in this work does not utilize rebalance factors (Kim and Lee, 1988) to assure a correct energy balance at each control volume.

Table 2 shows the convergence of the incident radiation in the case of a purely isotropically scattering medium. The physical situation under consideration is identical to the one described previously, except that the medium contains purely scattering particles rather than purely absorbing particles. In this case, the calculation of highly accurate results is much less difficult since scattering produces a much more smoothly varying intensity; that is, scattering tends to reduce the magnitude of discontinuities in the radiation intensity. Results from Crosbie and Schrenker (1984), Kim and Lee (1988), and Thynell and Özisik (1987) are included for comparison purposes. Crosbie and Schrenker (1984) solved the integral form of the equation of transfer using a numerical integration technique; their results are accurate to at least three significant digits. Kim and Lee (1988) used the *S*-14 method but did not show the convergence of their results. Thynell and Özisik (1987) also solved the integral form of the equation of radiative transfer by employing the Galerkin method, and the results are believed to be accurate to within the number of digits shown. Inspection of the results reveals that the method described in this work produces results which are in close agreement with those obtained by either Crosbie and Schrenker (1984) or Thynell and Özisik (1987). It should be noted that Kim and Lee (1988) only presented *S*-14 results of the incident radiation along the vertical line at $y = L_y/2$ using a spatial discretization of $N_y \times N_z = 26 \times 26$; their results of the incident radiation at the boundary differ by more than 2 percent compared to those obtained by either Crosbie and Schrenker (1984) or Thynell and Özisik (1987). Using the approach described in this work, results of similar accuracy to that obtained by the *S*-14 method involving 112 directions are achieved here by using 8 × 2 × 2 = 32 directions. However, results from lower-order *S*-*N* solutions are not shown by Kim and Lee (1988).

Table 2 Convergence of incident radiation at selected points for a purely isotropically scattering medium with $\beta L_y = \beta L_z = 1$ and bounded by black boundaries. Emission occurs along the bottom wall, $I_{b1} = 1$, and all other walls are at zero emissive power.

$N_y = N_z$	$N_\theta = N_\phi$	$G/4\pi$ $(0.5L_y, 0.5L_z)$	$(0.5L_y, L_z)$	$(0, L_z/2)$	$(0, L_z)$
5	2	0.24457	0.08453	0.13943	0.05727
	3	0.24880	0.08617	0.14137	0.05809
	4	0.25053	0.08638	0.14260	0.05910
	8	0.24980	0.08619	0.14242	0.05857
	12	0.24981	0.08618	0.14243	0.05859
11	2	0.24463	0.08536	0.13792	0.05715
	3	0.24896	0.08650	0.14060	0.05832
	4	0.25079	0.08688	0.14192	0.05909
	8	0.24953	0.08692	0.14145	0.05832
	12	0.25038	0.08701	0.14151	0.05873
15	2	0.24472	0.08573	0.13769	0.05729
	3	0.24904	0.08673	0.14069	0.05842
	4	0.25082	0.08720	0.14190	0.05922
	8	0.24984	0.08740	0.14113	0.05862
	12	0.25065	0.08749	0.14118	0.05895
Crosbie&Schrenker, 1984		0.2500	0.0863	0.1422	0.0587
Kim & Lee, 1988		0.24999	0.08836	-	-
Thynell & Özisik, 1987		0.250	0.086	0.142	0.059

Table 3 Convergence of net vertical heat flux, $q_z(y, z)/\pi$, at bottom-center and top-center position for a purely scattering medium with $\beta L_y = \beta L_z = 1$ and bounded by black boundaries. Emission occurs along the bottom wall, $I_{b1} = 1$, and all other walls are at zero emissive power.

y	$N_\theta = N_\phi$	Isotropic	F1	F2	B1	B2
0	2	0.76064	0.93879	0.91161	0.71857	0.67930
	4	0.76195	0.95027	0.91438	0.72194	0.68298
	8	0.76219	0.95090	0.91457	0.72186	0.68288
	12	0.76222	0.95091	0.91453	0.72186	0.68289
Kim & Lee, 1988		0.76696	0.95681	0.92383	0.72657	0.68718
Crosbie&Schrenker, 1984		0.7636	-	-	-	-
L_y	2	0.24480	0.40775	0.36826	0.23340	0.21435
	4	0.24391	0.39770	0.35387	0.22386	0.20546
	8	0.24375	0.40149	0.35644	0.22486	0.20631
	12	0.24378	0.40184	0.35668	0.22490	0.20633
Kim & Lee, 1988		0.24712	0.40798	0.35732	0.22862	0.21069
Crosbie&Schrenker, 1984		0.2439	-	-	-	-

Table 3 illustrates the convergence of the net vertical heat flux, $q_z(y, z)/\pi$, at $(y = L_y/2, z = 0)$ and at $(y = L_y/2, z = L_z)$ in the case of a square, purely scattering medium with $\beta L_y = \beta L_z = 1$. The physical situation is identical to the one described previously, except that the medium also may scatter the radiation anisotropically. The results were computed by using a spatially uniform 5 × 5 discretization and increasing orders of the angular discretization, whereas the *S*-14 method used a 26 × 26 spatial discretization. Examination of the results shown in Table 3 reveals that the net vertical heat flux indeed is in very good agreement with results available in the literature. In the case of isotropic scattering, the results from Crosbie and Schrenker (1984) are in excellent agreement with those obtained by the method outlined in this work. However, results obtained by the *S*-14 method in the case of isotropic scattering appear to deviate slightly more from the exact results compared to the results obtained by the method described in this work. In the case of anisotropic scattering, the differences in the results between the *S*-14 method and our approach are similar in magnitude to those shown for isotropic scattering.

Figure 7 shows the net radiant heat flux in the z-direction along the centerline for a square enclosure with several different

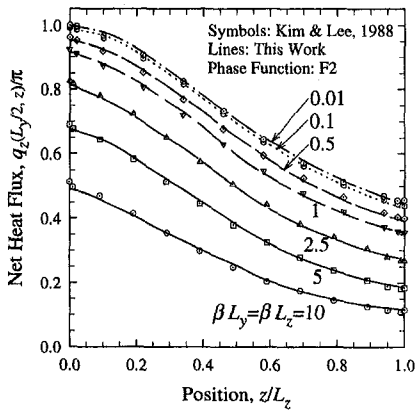

Fig. 7 Comparison of results of net radiant heat flux along the centerline between the discrete-ordinates method and the method outlined in this work using scattering phase F2 with different optical dimensions of the square enclosure ($\epsilon = 1$, $\omega = 1$).

optical dimensions and scattering phase function F2. The physical situation considers a medium bounded by black walls and a bottom surface with unit emissive power ($I_{b1} = 1$), whereas the other three surfaces are cold. Our calculations utilized a uniform grid with $N_y \times N_z = 11 \times 11$ and $N_\theta \times N_\phi = 4 \times 4$, except in the case with $\beta L_y = \beta L_z = 10$ in which we utilized $N_y \times N_z = 21 \times 21$ and $N_\theta \times N_\phi = 3 \times 3$. Our results were curve-fitted in order to more easily compare with the *S*-14 method. The inclusion of results from Kim and Lee (1988) involves some uncertainty since the reading from their Fig. 8 was difficult. The *S*-14 method of Kim and Lee (1988) utilized $N_y \times N_z = 26 \times 26$ for $\beta L_y = \beta L_z \leq 1$, and $N_y \times N_z = 52 \times 52$ for $\beta L_y = \beta L_z > 1$; it appears, however that one additional node was inserted near the bounding surfaces. Inspection of the results reveals that our method is capable of handling both optically thin and thick cases, since the results are in very good agreement with those of Kim and Lee (1988). It is also noted that the *S*-14 method predicts a spurious rapid decrease and a rapid increase in the flux near the bottom and top walls, respectively. Such rapid changes appear to be nonphysical in nature and are not predicted by the method outlined in this work.

Figure 8 illustrates a comparison of the results of the normalized net heat flux along the centerline for scattering phase function F2. The *S*-14 results of Kim and Lee (1988) were taken from their Fig. 7 (the reading of which involved some uncertainty) and utilized $N_y \times N_z = 26 \times 26$. The considered physical situation is identical to the one described previously, except that the four bounding walls are nonblack with identical emissivity of the four bounding surfaces. The numerical method described in this work utilized a uniform 11×11 spatial discretization ($N_y \times N_z$), and a 4×4 polar-azimuth discretization ($N_\theta \times N_\phi$). Examination of this figure reveals once again that an excellent agreement is produced in all cases considered. As the emissivity decreases, the intensity becomes increasingly an angularly uniform function and the role of discontinuities diminishes. Furthermore, as the intensity becomes more angularly uniform, the role of the scattering phase function decreases. The intensity, however, is nonetheless discontinuous. As expected from the results shown in Table 3, the largest relative differences between those computed by the present method and those of discrete-ordinates method (Kim and Lee, 1988) occurred in cases for which $\epsilon \to 1$.

Finally, Table 4 shows the number of iterations required for reaching the specified convergence criterion of 10^{-6} according to Eq. (7). These results, as well as others, were obtained on a Pentium P5 equipped with a 66 MHz CPU and 16MB of RAM using Lahey FORTRAN and single precision. The CPU time does not include compiling, which required about 20 s. The situation considered involves a purely isotropically scattering medium bounded by black boundaries. Emission occurs along the bottom wall, $I_{b1} = 1$, and all other walls are at zero emissive power. These results show that the number of iterations is quite insensitive to the order of the angular quadrature, whereas they are much more sensitive to the optical dimensions. An increased number of iterations is required as the optical dimensions increase because radiation transfer takes on a diffusion-like character. In other words, the radiant intensity at a point within the medium is controlled by multiple scattering rather than the direct contribution from wall emission. The case with $N_y = N_z = 15$, and $N_\theta \times N_\phi = 8 \times 8$ involves approximately 115,000 unknowns; in the optically thick case it requires about 5 s per iteration and a total of 528 s to reach the specified convergence criterion of 10^{-6}. In the optically intermediate case $L_y = L_z = 1$, the number of iterations ranged from 17 to 47, which, on the average, is quite similar to that required for a three-dimensional case considered by Chai et al. (1994) (who also used a convergence criterion of 10^{-6}).

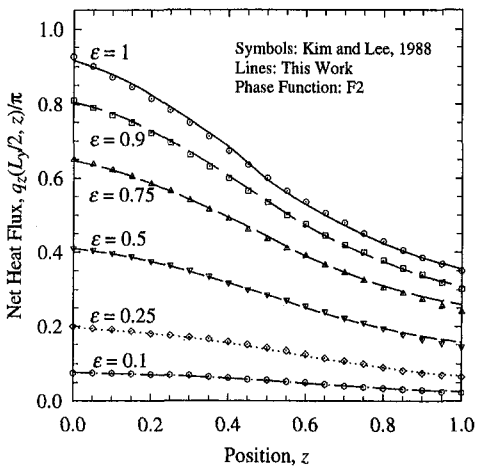

Fig. 8 Comparison of results of net radiant heat flux along the centerline between the discrete-ordinates method and the method outlined in this work using scattering phase *F2* and different surface emissivities of the four bounding walls ($\omega = 1$, $\beta L_y = \beta L_z = 1$)

Table 4 The required number of iterations and corresponding CPU time (s) to reach convergence of the solution. The situation considered involves a purely scattering medium bounded by black boundaries. Emission occurs along the bottom wall, $I_{b1} = 1$, and all other walls are at zero emissive power.

$\beta L_y = \beta L_z$	$N_y = N_z$	$N_\theta \times N_\phi = 2\times2$		$N_\theta \times N_\phi = 4\times4$		$N_\theta \times N_\phi = 8\times8$	
		Iter.	CPU	Iter.	CPU	Iter.	CPU
0.1	5	11	3	13	4.5	15	11
	10	20	7	22	18	28	71
	15	30	24	32	65	37	223
1	5	18	2.5	17	5	17	13
	10	27	9	33	25	35	87
	15	36	28	45	89	47	288
5	5	57	4.5	57	9	57	34
	10	84	22	83	57	83	196
	15	92	68	89	171	88	528

Conclusions

An approximate method of analysis for treating radiative heat transfer in a two-dimensional rectangular medium containing absorbing, emitting, and anisotropically scattering particles bounded by emitting and diffusely reflecting surfaces is described. The method utilizes interpolated intensities at each grid point to obtain the indicated accuracy of the results. It is shown that results obtained for the case of an absorbing and isotropic scattering medium are in excellent agreement with those obtained by a direct numerical integration technique of the integral form of the equation of transfer. In the case of an absorbing and anisotropic scattering medium, the produced results are in very good agreement with those obtained by the discrete-ordinates method. To further improve the accuracy of the method, linear interpolation involving the bounding and normal intensities I_{Bi} and I_{Ni} needs to be replaced by higher-order approaches.

Acknowledgments

This work was partially performed under Contract DAAH04-95-1-0268 with Dr. D. M. Mann, U.S. Army Research Office, Research Triangle Park, North Carolina, serving as the Program Manager. It should be noted that the content of the information contained in this work does not necessarily reflect the position or the policy of the government and no official endorsement should be inferred.

References

Abramowitz, M., and Stegun, I. A., 1972, *Handbook of Mathematical Functions*, Dover, New York.

Chai, J. C., Lee, H. S., and Patankar, S. V., 1993, "Ray Effect and False Scattering in the Discrete Ordinates Method," *Num. Heat Transfer,* Part B, Vol. 24, pp. 373–389.

Chai, J. C., Lee, H. S., and Patankar, S. V., 1994, "Finite Volume Method for Radiation Heat Transfer," *Journal of Thermophysics and Heat Transfer,* Vol. 8, No. 3, pp. 419–425.

Chandrasekhar, S., 1960, *Radiative Transfer,* Dover, New York.

Crosbie, A. L., and Schrenker, R. G., 1984, "Radiative Transfer in a Two-Dimensional Rectangular Medium Exposed to Diffuse Radiation," *J. Quant. Spectrosc. Radiat. Transfer,* Vol. 31, No. 4, pp. 339–372.

Duderstadt, J. J., and Martin, W. R., 1979, *Transport Theory,* Wiley, New York.

Fiveland, W. A., 1987, "Discrete Ordinate Methods for Radiative Transfer in Isotropically and Anisotropically Scattering Media," ASME JOURNAL OF HEAT TRANSFER, Vol. 109, No. 3, pp. 809–812.

Fiveland, W. A., 1991, "The Selection of Discrete Ordinate Quadrature Sets for Anisotropic Scattering," *Fundamentals of Radiation Heat Transfer,* ASME HTD-Vol. 160, pp. 89–96.

Howell, J. R., 1968, "Application of Monte Carlo to Heat Transfer Problems," *Advances in Heat Transfer,* Vol. 5, Academic Press, New York.

Howell, J. R., 1988, "Thermal Radiation in Participating Media: The Past, the Present, and Some Possible Futures," ASME JOURNAL OF HEAT TRANSFER, Vol. 110, No. 4, pp. 1220–1229.

Kim, T.-K., and Lee, H., S., 1988, "Effect of Anisotropic Scattering on Radiative Transfer in Two-Dimensional Rectangular Enclosures," *Int. J. Heat Mass Transfer,* Vol. 31, No. 8, pp. 1711–1721.

Kim, T.-K., and Lee, H., S., 1990, "Modified δ-M Scaling Results for Mie-Anisotropic Scattering Media," ASME JOURNAL OF HEAT TRANSFER, Vol. 112, No. 4, pp. 988–994.

Kim, T.-K., Menart, J. A., and Lee, H., S. 1991, "Nongray Radiative Gas Analyses Using the S-N Discrete Ordinates Method," ASME JOURNAL OF HEAT TRANSFER, Vol. 113, No. 4, pp. 946–952.

Lathrop, K. D., 1971, "Remedies for Ray Effects," *Nucl. Sci. Eng.,* Vol. 45, pp. 255–268.

Lathrop, K., and Carlson, B., 1967, "Numerical Solution of the Boltzmann Transport Equation," *Journal of Computational Physics,* Vol. 2, pp. 173–197.

Mengüç, M. P., and Viskanta, R., 1986, "Radiative Transfer in Axisymmetric, Finite Cylindrical Enclosures," ASME JOURNAL OF HEAT TRANSFER, Vol. 108, No. 2, pp. 271–276.

Modest, M. F., 1993, *Radiative Heat Transfer,* McGraw-Hill, New York.

Özisik, M. N., 1973, *Radiative Transfer and Interactions with Conduction and Convection,* John Wiley and Sons, Inc., New York.

Parry, D. L., and Brewster, M. Q., 1991, "Optical Constants of Al_2O_3 Smoke in Propellant Flames," *Journal of Thermophysics and Heat Transfer,* Vol. 5, No. 2, pp. 142–149.

Pessoa-Filho, J., and Thynell, S. T., 1994, "Development of Approximate Solutions to Radiative Transfer in Slabs and Spheres," *J. Quant. Spectrosc. Radiat. Transfer,* Vol. 52, No. 1, pp. 59–73.

Pessoa-Filho, J., and Thynell, S. T., 1995a, "Approximate Solution to the Equation of Radiative Transfer in Cylindrical Participating Media," *J. Quant. Spectrosc. Radiat. Transfer,* Vol. 53, No. 5, pp. 533–547.

Pessoa-Filho, J., and Thynell, S. T., 1995b, "An Approximate Solution to Radiant Heat Transfer in Two-Dimensional Cylindrical Geometry," *Advances in Computational Methods for Heat Transfer,* ASME HTD-Vol. 311, pp. 83–94.

Raithby, G. D., and Chui, E. H., 1990, "A Finite-Volume Method for Predicting Radiant Heat Transfer in Enclosures with Participating Media," ASME JOURNAL OF HEAT TRANSFER, Vol. 112, No. 2, pp. 415–423.

Siegel, R., 1987, "Transient Radiative Cooling of a Droplet-Filled Layer," ASME JOURNAL OF HEAT TRANSFER, Vol. 109, No. 1, pp. 159–164.

Subramaniam, S., and Mengüç, M. P., 1991, "Solution of the Inverse Radiation Problem for Inhomogeneous and Anisotropically Scattering Media Using Monte Carlo Technique," *Int. J. Heat Mass Transfer,* Vol. 34, pp. 253–266.

Thynell, S. T., and Özisik, M. N., 1986, "Use of Eigenfunctions for Solving Radiation Transfer in Anisotropically Scattering, Plane-Parallel Media," *J. Appl. Phys.,* Vol. 60, No. 2, pp. 541–551.

Thynell, S. T., and Özisik, M. N., 1987, "Radiation Transfer in Isotropically Scattering, Rectangular Enclosures," *Journal of Thermophysics and Heat Transfer,* Vol. 1, No. 1, pp. 69–76.

Viskanta, R., and Mengüç, M. P., 1987, "Radiation Heat Transfer in Combustion Systems," *Progress in Energy and Combustion Science,* Vol. 13, pp. 97–160.

Weston, K. C., and Drago, D. W., 1975, "Discontinuities in Radiative Transfer Analysis Using Quadrature Formulas," ASME JOURNAL OF HEAT TRANSFER, Vol. 103, No. 1, pp. 149–151.

Yoshizawa, Y., Sasaki, K., and Echigo, R., 1988, "Analytical Study of the Structure of Radiation Controlled Flame," *Int. J. Heat Mass Transfer,* Vol. 31, No. 2, pp. 311–319.

A Method for Modeling the Mitigation of Hazardous Fire Thermal Radiation by Water Spray Curtains

S. Dembele

A. Delmas
agnes.delmas@cethil.insa-lyon.fr

J. F. Sacadura
Centre de Thermique de l'Insa de Lyon
(CETHIL),
UPRESA CNRS Q5008,
Bâtiment 404,
20 Avenue Albert Einstein,
69621 Villeurbanne Cedex, France

A radiative transfer model describing the interactions between hazardous fire thermal radiation and water sprays is presented. Both the liquid (water droplets) and gaseous (mainly water vapor and carbon dioxide) phases of the spray are considered in the present work. Radiative properties of the polydisperse water droplets are derived from Mie theory. The gaseous phase behavior is handled by the correlated-k distribution method, where the k-distribution function is evaluated for Malkmus narrow-band statistical model. The radiative transfer equation, in its integral form, is solved by a discrete ordinates method. After a general description of the radiative model developed and the experimental task to validate it, some results are discussed on its accuracy and CPU time. A deeper analysis is also carried out to point out the influence of the main parameters involved in the problem.

1 Introduction

Recently, water sprays have been widely used for the mitigation of industrial hazards. The reasons for such an interest are twofold: on one hand, these sprays offer high ability of mechanical dispersion of accidental toxic releases; on the other hand, they are an efficient means of shielding the thermal radiation of fires. In fire mitigation applications, the spray barriers are interposed between the source of radiation (fire) and the target to be protected (petrochemical storage tanks, buildings, fire brigade, etc.). In order to know with confidence the behavior of this technique of attenuation, a common European research project ASTRRE has been initiated by the Centre de Thermique de Lyon (CETHIL), the Institut des Technologies Chimiques de Lyon (ITC), and the Von Karman Institute for Fluid Dynamics (VKI-Belgium).

Water spray is a two-phase semitransparent medium constituted by polydisperse liquid drops and participating gases (water vapor and possibly carbon dioxide emanating from the fire). Extensive works have been performed in the past on the analysis of using such media for fire radiation attenuation; Ravigururajan and Beltran (1989) and Stephenson and Coward (1986) among others. The common features between most of these approaches, with regard to radiative transfer modeling, are of the following two orders:

(1) They do not take into account the gaseous phase contribution in the total attenuation of the spray, and only water droplets are considered. Then, the attenuation ability of the spray is underestimated (Section 4.5) by a factor depending on the temperature, molar fractions of participating gases, and also on the nature of the fire emission spectrum (function of the type of fuel and its ratio to the air).

(2) These works are mostly based on Beer-Lambert law or Schuster-Schwarzchild approximation (two-flux model), which may lead to inaccurate results depending on the optical thickness and the scattering pattern of the investigated spray.

Contributed by the Heat Transfer Division for publication in the JOURNAL OF HEAT TRANSFER. Manuscript received by the Heat Transfer Division July 25, 1996; revision received May 7, 1997; Keywords: Modeling & Scaling; Radiation; Sprays/Droplets. Associate Technical Editor: B. W. Webb.

Approaches including the two phases have been developed in studying radiative transfer through plane parallel atmospheres (water clouds and water vapor). Hunt and Grant (1969) used the exponential-sum-fitting of transmissions (ESFT) method with the discrete space technique, while the same method (ESFT) was associated to Chandrasekhar's principle of invariance by Yamamoto et al. (1970) to describe radiative transfer through water clouds in the infrared region. Recently, Lacis and Oinas (1991) reported a detailed testing of the correlated-k (CK) method, associated with the doubling and adding technique, for modeling nongray gaseous absorption in multiple scattering inhomogeneous atmospheres.

El Wakil and Sacadura (1992) improved a technique for solving the radiative transfer equation (RTE) in its integral form by using a discrete ordinates method, thereby avoiding some numerical abberations of the classical differential form. This was achieved for gray participating media.

The same approach was then extended to nongray gaseous but nonscattering media by Borges De Miranda and Sacadura (1996). In the present study, the effect of scattering is included in the analysis with a CK procedure to describe fire radiation transfer through the two phases of water sprays.

Thus, the main objective of the work presented in this paper is to develop a numerical tool based on the best submodels from the literature that is more rigorous and accurate and offering a good computational efficiency for fire engineering applications.

2 Statement of the Problem

2.1 Radiative Properties of Water Droplets.

Mie Theory. Details concerning this theory may be found in the literature (Van De Hulst, 1957). For the sake of clarity, some major definitions are briefly recalled here.

Mie theory describes the scattering of a plane wave by a single homogeneous sphere. The initial step is the calculation of coefficients a_n and b_n, used to represent the scattered wave outside the spherical particle (water droplet here), and written as follows:

$$a_n = \frac{[D_n(y)/m + n/x]\, R_e[\xi_n(x)] - R_e[\xi_{n-1}(x)]}{[D_n(y)/m + n/x]\xi_n(x) - \xi_{n-1}(x)}, \quad (1)$$

$$b_n = \frac{[mDn(y) + n/x]R_e[\xi_n(x)] - R_e[\xi_{n-1}(x)]}{[mDn(y) + n/x]\xi_n(x) - \xi_{n-1}(x)}. \quad (2)$$

The Riccati-Bessel function $\xi_n(x)$ and the logarithmic derivative $D_n(y)$ appearing in Eqs. (1) and (2), are calculated by recurrence relations given in the literature.

From a_n and b_n values, calculation of the efficiency factors is then achieved with the following relations:

$$Q_{ext}(x, m) = \frac{2}{x^2} \sum_{n=1}^{N_{max}} (2n + 1)R_e(a_n + b_n) \quad (3)$$

$$Q_{sca}(x, m) = \frac{2}{x^2} \sum_{n=1}^{N_{max}} (2n + 1)(|a_n|^2 + |b_n|^2) \quad (4)$$

$$Q_{abs}(x, m) = Q_{ext}(x, m) - Q_{sca}(x, m). \quad (5)$$

Where $|a_n|$ represents the modulus of the complex coefficient a_n. The number of terms in the summation is given by

$$N_{max} = x + 4x^{1/3} + 2. \quad (6)$$

The asymmetry factor of a single water droplet is expressed as follows:

$$g(x, m) = \frac{4}{x^2 Q_{sca}} \sum_{n=1}^{N_{max}} \left[\frac{n(n+2)}{n+1} \mathrm{Re}(a_n a_{n+1}^* + b_n b_{n+1}^*) + \frac{2n+1}{n(n+1)} \mathrm{Re}(a_n b_n^*) \right]. \quad (7)$$

Using Results From Mie Calculations in the RTE. In the RTE (Section 2.3), parameters needed for the polydisperse liquid phase of the spray are the coefficients $\beta_{\nu l}$, $\sigma_{\nu l}$, $K_{\nu l}$ and the phase function (that of Henyey-Greenstein $P_{\nu HG}$ here). For droplet polydispersion, these coefficients are given by the following relations:

$$\beta_{\nu l} = \int_0^\infty \pi r^2 N(r) Q_{ext}(x, m) dr \quad (8)$$

$$\sigma_{\nu l} = \int_0^\infty \pi r^2 N(r) Q_{sca}(x, m) dr \quad (9)$$

and

$$K_{\nu l} = \beta_{\nu l} - \sigma_{\nu l}. \quad (10)$$

The asymmetry factor for this polydispersion is given by the following:

$$\langle \cos\theta \rangle = \frac{1}{\sigma_{\nu l}} \int_0^\infty \pi r^2 N(r) Q_{sca}(x, m) g(x, m) dr \quad (11)$$

where $g(x, m)$ is given by Eq. (7).

For our practical computations, the exact Mie phase function, involving heavy calculations, is approximated by the Henyey-Greenstein phase function. For the type of medium considered here, it has been shown that this approximate phase function yields results consistent with those obtained by using the exact Mie phase function (Hansen, 1969; Goody and Yung, 1989).

The Henyey-Greenstein phase function is given by:

$$P_{\nu HG}(\langle \cos\theta \rangle, \mu) = \frac{1 - \langle \cos\theta \rangle^2}{(1 + \langle \cos\theta \rangle^2 - 2\langle \cos\theta \rangle \mu)^{3/2}}. \quad (12)$$

Results from our Mie computational program (double precision FORTRAN), have been successfully compared to those of many works from the literature. For the purpose of model predictions comparison with the laboratory experimental data for the sprayer TG 03 (Section 4.3), the droplet size and the number density $N(r)$ distribution have been determined experimentally

Nomenclature

a_n = complex Mie coefficient
b_n = complex Mie coefficient
$\langle \cos\theta \rangle$ = asymmetry factor for droplet polydispersion
d = $2r$, water droplet diameter
Dc = $4\rho_l N(r)\pi r^3/3$, droplet concentration (or mass loading)
D_{32} = $2\int_0^\infty r^3 N(r)dr / \int_0^\infty r^2 N(r)dr$, mean Sauter diameter
$f(k)$ = k-distribution function
g_j = jth g-quadrature point in CK method
$g(k)$ = cumulative distribution function
$g(x, m)$ = droplet asymmetry factor
$I_{b\nu}$ = blackbody spectral intensity
I_ν = spectral intensity
$k(g)$ = $g^{-1}(k)$, inverse of the cumulative distribution function
$K_{\nu l}$ = spray droplet polydispersion absorption coefficient
$K_{\nu g}$ = spray gaseous phase absorption coefficient
k_l = imaginary part of the droplet refraction index
L = thickness of a participating medium
m = droplet relative index of refraction ($=m_1/m_2$) or discrete direction in Section 2.3
m_l = $n_l - ik_l$, droplet refraction index
m_2 = refraction index of the medium surrounding the droplet
M = number of directions in discrete ordinates method
n = series term in Mie calculations
n_l = real part of the droplet refraction index
$N(r)$ = number of droplets of r radius per unit volume (number density)
Pr = spray nozzle feeding relative pressure
$P_{\nu HG}$ = Henyey-Greenstein phase function
Q = efficiency factor in Mie calculations
r = water droplet radius
R_e = real part of a complex number
s = space coordinate
Δs = crossed path in a control volume
T_g = temperature of the spray gaseous phase
T_l = temperature of the spray liquid phase
$\overline{T_\nu}$ = narrow-band averaged transmission function
w_m = weight associated to a discrete direction, m
x = $2\pi r m_2/\lambda$, size parameter
X = space coordinate
y = mx

Greek symbols

$\beta_{\nu l}$ = droplet polydispersion extinction coefficient
θ = angle between incident and scattering directions
λ = wavelength
μ = $\cos\theta$
ν = frequency
Δ_ν = narrow frequency band
ρ = wall reflectivity
ρ_l = liquid phase density
$\sigma_{\nu l}$ = droplet polydispersion scattering coefficient
ω_j = jth g-quadrature weighting coefficients in CK method
Ω = solid angle

Subscripts

abs = absorption
ext = extinction
sca = scattering

Superscripts

$-$ = averaged over Δ_ν
$*$ = complex conjugate

Abbreviations

CK = Correlated-K
DOM = Discrete Ordinates Method
NBS = Narrow-Band Statistical
RTE = Radiative Transfer Equation

with a Phase Doppler Particle Analyser (PDPA) by the Von Karman Institute.

2.2 The Correlated-k (CK) Distribution Method for the Spray Gaseous Phase Analysis. The reader may refer to Goody and Yung (1989) and Riviere et al. (1992) for more informations about the K and CK distribution methods. Some useful definitions are recalled here.

Spectral radiative properties of droplets inside water sprays, described in Section 2.1, slightly vary over frequency, while in the same narrow spectral interval, the gaseous phase may have hundreds of major absorption lines (Menart et al., 1993). One way of accurately modeling this complex phenomenon with reasonable computational time is to use narrow-band models that provide averaged transmissivities over specified spectral intervals Δ_ν. However, it is difficult to apply narrow-band models to problems involving scattering since averaged transmissivity values cannot easily be used in the RTE for such media. Therefore, treatment of the RTE through the two phases of an absorbing, emitting, and scattering water spray is problematic since the RTE should be integrated over Δ_ν. In fact, this may be achieved through line-by-line calculations, but this method is very time consuming. An alternative way of carrying out this frequency integration is to use the k-distribution technique for homogeneous gaseous media and the CK distribution method for inhomogeneous ones.

The k-Distribution Technique. The k-distribution method consists in transforming a frequency integration into an integration over the absorption coefficient $K_{\nu g}$ for a homogeneous non-gray gas (Goody and Yung, 1989; Domoto, 1974). Then, in general, for any function $G[K_{\nu g}(\nu)]$, its averaged value over Δ_ν, defined as

$$\overline{G[K_{\nu g}(\nu)]} = \frac{1}{\Delta\nu}\int_{\Delta\nu} G[K_{\nu g}(\nu)]d\nu \tag{13}$$

is transformed into

$$\overline{G[K_{\nu g}(\nu)]} = \int_0^\infty G(k)f(k)dk \tag{14}$$

where $K_{\nu g}(\nu) = k$ is the gas absorption coefficient, and $f(k)$ is the normalised k-distribution function.

In particular, the averaged transmissivity of a homogeneous and isothermal column of length Δs given by

$$\overline{T_\nu}(\Delta s) = \frac{1}{\Delta\nu}\int_{\Delta\nu} \exp[-K_{\nu g}(\nu)\Delta s]d\nu \tag{15}$$

may be rewritten, using the property of Eq. (14), as

$$\overline{T_\nu}(\Delta s) = \int_0^\infty \exp(-k\Delta s)f(k)dk. \tag{16}$$

Domoto (1974) pointed out that from Eq. (16), $f(k)$ can be interpreted as the inverse Laplace transform of $\overline{T_\nu}(\Delta s)$ and that this property allows the calculation of $f(k)$ from narrow-band statistical (NBS) models.

In the present work, $\overline{T_\nu}(\Delta s)$ is calculated from the Malkmus NBS model with exponential-tailed-inverse line strength distribution (Malkmus, 1967; Young, 1977). The expression for this averaged transmissivity for a given molar fraction of absorbing species f_m through an isothermal and homogeneous path length Δs, under a total pressure P, is

$$\overline{T_\nu}(\Delta s) = \exp\left[-\frac{\overline{\beta_\nu}}{\pi}\left(\sqrt{1+\frac{2\pi f_m P\Delta s\,\overline{K_\nu}}{\overline{\beta_\nu}}}-1\right)\right] \tag{17}$$

where $\overline{\beta_\nu} = 2\pi\overline{\gamma_\nu}/\overline{\delta_\nu}$. Then, $f(k)$ obtained by inversion of $\overline{T_\nu}(\Delta s)$ in Eq. (17) (Goody and Yung, 1989; Domoto, 1974) is

$$f(k) = \frac{1}{k}\sqrt{\frac{\overline{k_\nu\cdot\gamma_\nu}}{\pi k\overline{\delta_\nu}}}\exp\left[\frac{\overline{\gamma_\nu}}{\overline{\delta_\nu}}(2 - k/\overline{k_\nu} - \overline{k_\nu}/k)\right]. \tag{18}$$

$\overline{k_\nu}$ and $\overline{\delta_\nu}$ are spectral parameters for H_2O and CO_2 obtained by Soufiani et al. (1985) from line-by-line calculations. The mean half width γ_ν for these species are obtained from the general expression given by Zang et al. (1988):

$$\overline{\gamma_{\nu H_2O}} = 0.066\frac{P}{Ps}\left\{7.0\,f_{H_2O}\frac{Ts}{T} + [1.2\,(f_{H_2O}+f_{N_2}) + 0.8\,f_{O_2} + 1.6\,f_{CO_2}]\sqrt{\frac{Ts}{T}}\right\}, \tag{19}$$

$$\overline{\gamma_{\nu CO_2}} = \frac{P}{Ps}\left(\frac{Ts}{T}\right)^{0.7} \times [0.07\,f_{CO_2} + 0.058\,(f_{N_2}+f_{O_2}) + 0.15\,f_{H_2O}]. \tag{20}$$

Parameters f_m and P are, respectively, the molar fraction of the absorbing species m and total pressure, Ps and Ts designate standard pressure and temperature (1 atm, 296 K). All parameters are averaged over $\Delta_\nu = 25\ \text{cm}^{-1}$.

The Correlated-*k* Distribution Method. The CK method employs the cumulative distribution function given by the following:

$$g(k) = \int_0^k f(k')dk' \tag{21}$$

with $f(k)$ given by Eq. (18). $g(k)$ is a growing monotonic function, from $0 \le k < \infty$ to $0 \le g < 1$, with an inverse function $k(g) = g^{-1}(k)$. Therefore, using the previous definition of the cumulative distribution function g, Eq. (14) is rewritten as

$$\overline{G[K_{\nu g}(\nu)]} = \int_0^1 G[k(g)]dg. \tag{22}$$

One advantage of using Eq. (22) instead of Eq. (13) lies in the fact that only a few quadrature points are needed to approximate the former since variations versus g are smooth, whereas evaluation of Eq. (13) requires a very fine integration steps because of strong variations of $K_{\nu g}$ with respect to ν. The major difficulties for CK method practical use, are the choice of the best quadrature formula to use in Eq. (22), and the calculation of $k(g)$ values since no explicit analytical expression exists. Riviere et al. (1992) in their CK procedure used a seven Gaussian-Lobatto quadrature to approximate the integral term in Eq. (22) according to the following expression:

$$\overline{G[K_{\nu g}(\nu)]} = \int_0^1 G[k(g)]dg \cong \sum_{j=1}^{7}\omega_j G[k(g_j)]. \tag{23}$$

These authors performed $k(g)$ calculations from a line-by-line fitting procedure under 26 temperature and pressure conditions; the quadrature points g_j (j = 1 to 7) are 0.0, 0.155405848, 0.45, 0.744594152, 0.9, 0.935505103, and 0.984494897. The weights ω_j associated with the points are, respectively, 0.045, 0.245, 0.32, 0.245, 0.0561111111, 0.051248583, and 0.037640306.

The formulation used in this work is a hybrid approach since it is based on the seven known g-points and weights above mentioned from Riviere et al. (1992) (these few g-points considerably reduce the computational time), but $k(g)$ calculation is based on Malkmus NBS model technique (Lacis and Oinas,

1991). This technique is attractive because, provided that the band model parameters $\overline{k_\nu}$ and $\overline{\delta_\nu}$ are known, $k(g)$ calculation is easily achieved with a numerical Newton-Raphson procedure (Lacis and Oinas, 1991).

2.3 Spectrally Averaged Radiative Transfer Equation.

Averaged Intensity. The radiative transfer equation (RTE) applied to a water spray is expressed as

$$\frac{dI_\nu(s, \Omega)}{ds} + (K_{\nu l} + K_{\nu g} + \sigma_{\nu l})I_\nu(s, \Omega) = K_{\nu l}I_{b\nu}[T_l] + K_{\nu g}I_{b\nu}[T_g] + \frac{\sigma_{\nu l}(s)}{4\pi}\int_{\Omega'=4\pi} I_\nu(s, \Omega')P_{\nu HG}(\Omega' \to \Omega)d\Omega'. \quad (24)$$

To obtain the spectrally averaged intensity $\overline{I_\nu}$, the RTE is averaged over a narrow spectral interval Δ_ν. Applying the operator $(1/\Delta\nu)\int_{\Delta\nu}(\ldots\ldots)d\nu$ to both sides of Eq. (24) and using properties from CK procedure given by Eq. (23), we deduce the following expression:

$$\frac{dI_i(s, \Omega)}{ds} + \beta_i I_i(s, \Omega) = S_i(s, \Omega) \quad (25)$$

with

$$\beta_i = K_{\nu l} + k(g_i) + \sigma_{\nu l}, \quad (26)$$

and the index i varying from 1 to 7.

The source term is given by the following:

$$S_i(s, \Omega) = K_{\nu l}I_{b\nu}[T_l] + k(g_i)I_{b\nu}[T_g] + \frac{\sigma_{\nu l}(s)}{4\pi}\int_{\Omega'=4\pi} I_i(s, \Omega')P_{\nu HG}(\Omega' \to \Omega)d\Omega'. \quad (27)$$

Integral formulation of a discrete ordinates method is used to solve Eq. (25) and the averaged intensity is then deduced from I_i values by:

$$\overline{I_\nu} = \frac{1}{\Delta\nu}\int_{\Delta\nu} I_\nu d\nu = \sum_{i=1}^{7} \omega_i I_i. \quad (28)$$

Integral Formulation of the Discrete Ordinates Method. Equation (25) is solved by the integral approach of a DOM (El Wakil and Sacadura, 1992), using the control volume technique. Integration of this equation along the physical path from $s = 0$ to s gives the following:

$$I_i(s, \Omega) = I_i(0, \Omega)\exp(-\beta_{iS}) + \int_0^s S_i(s', \Omega)\exp[-\beta_i(s - s')]ds' \quad (29)$$

where $I_i(0, \Omega)$ is the intensity at $s = 0$ for a direction Ω.

Using a discrete ordinates method, Eq. (29) is expressed for a discrete direction m as follows:

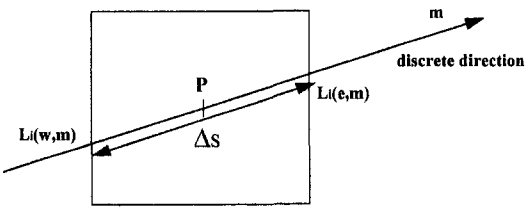

Fig. 1 Arbitrary control-volume

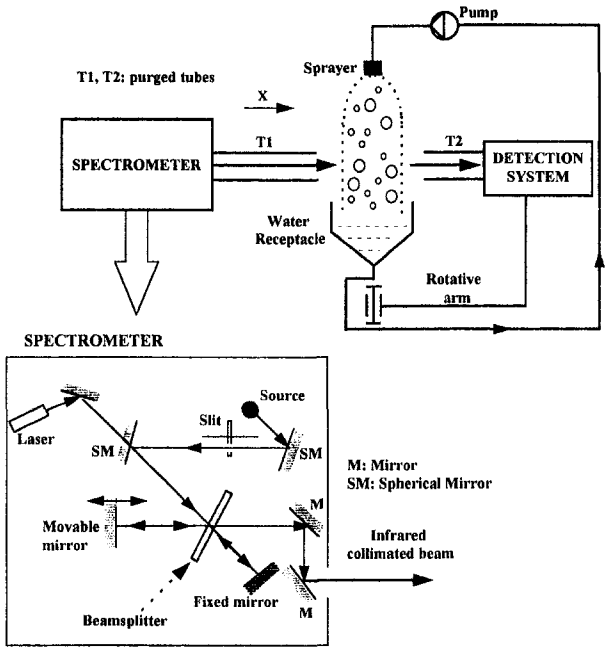

Fig. 2 Simplified view of the laboratory water spray facility

$$I_i(s, m) = I_i(0, m)\exp(-\beta_{iS}) + \int_0^S S_i(s', m)\exp[-\beta_i(s - s')]ds' \quad (30)$$

with

$$S_i(s', m) = K_{\nu l}I_{b\nu}[T_l] + k(g_i)I_{b\nu}[T_g] + \frac{\sigma_{\nu l}(s')}{4\pi}\sum_{m'=1}^{M} w_{m'}I_i(s', m')P_{\nu HG}(m' \to m). \quad (31)$$

Index m varies from 1 to M.

The integrated Eq. (30) is applied to a control volume (Fig. 1) with the assumptions that the source term $S_i(s', m)$ is constant in the control volume and intensities are uniform on both of its sides. Then, the resulting intensity is expressed as follows:

$$L_i(e, m) = L_i(w, m)\exp(-\beta_i\Delta_s) + \frac{S_i(P, m)}{\beta_i}[1 - \exp(-\beta_i\Delta s)]. \quad (32)$$

$S_i(P, m)$ represents the source term evaluated at the center of the control volume, and Δs represents the path crossed between the in and out sides.

3 Experimental Set Up

Instrumentation. The experimental arrangement used in the CETHIL laboratory to investigate water sprays attenuation ability is schematically shown in Fig. 2. The objective is to determine the fraction of the infrared incident collimated beam transmitted through the spray (the range 1.5–12 μm of wavelength region is considered). The spectrometer is a FTS 60 A (Bio-Rad, Inc.)-type, based on Fourier transform spectroscopy. The source of radiation, characterised by a blackbody emission spectrum at 1300°C, is a tungsten filament inside a silica tube. An entrance slit with four movable holes (1.2, 2.7, 4, and 7 mm diameter) determines the solid angle of the infrared collimated beam. [The Michelson interferometer principle is used, so that the exit infrared beam can be measured by a detector, as a function of path difference between the fixed and movable mirrors (Fig. 2).] The detection system, composed of a spherical

mirror collecting the beams and concentrating them on a quantic detector HgCdTe (1.5–12 μm), is mounted on a goniometer arm to allow bidirectional transmission measurements and detection of scattered radiation. Both the spectrometer and the detection system are purged with dry air and connected to a data acquisition system. The incident collimated beam and the beam transmitted through the spray, cross-purged tubes T1 and T2, to prevent any absorption from the surrounding atmosphere so that the measured attenuation is only due to the spray. Water sprays that we investigated are generated by different type of industrial sprayers from Spraying Systems Co. The sprayer is movable in vertical direction, and the measurements are parameterized in function of the vertical distance from the spray nozzle exit and the feeding pressure.

Measurement Procedure. The experimental arrangement presented above allows measurement of spectral transmittances. For a given sprayer and feeding pressure, two measurements are carried out: one without the spray (to know the incident energy), and the other with the spray (transmitted energy). The ratio between the transmitted and incident energies provides the transmittance of the water spray.

4 Results and Discussion

4.1 Comparisons Between Model Predictions and Previous Works for a Water Vapor Slab Bounded by Diffusely Reflecting Walls. The aim of this part is to check the accuracy and computational time of the model presented in Section 2 through a comparison with published work (Menart et al., 1993) for a one-dimensional transfer. The studied configuration is that presented by Menart et al. (1993) and consists of pure water vapor at 1 atm in a plane parallel slab bounded by gray, diffusely reflecting walls. The slab temperature profile is either uniform (1000 K), with both walls at 0 K, or a parabolic type, with a temperature range lying from 400 K (at $X = 0$ and $X = L$) to 1100 K (at $X = L/2$) (Zhang et al., 1988). The slab thickness is divided into 20 uniform sublayers, and results are presented in terms of total volumetric radiative source distribution ($-dq/dx$). Calculations are carried out for our model with a S20 Gaussian quadrature scheme in DOM, and the following spectral absorption bands of water vapor are considered: 150–2325 cm^{-1}, 2900–4725 cm^{-1}, and 4900–5675 cm^{-1}. Figure 3 presents the radiative source distribution for the uniform temperature profile with $L = 0.5$ m, $\rho(X = 0) = 0.9$, and $\rho(X = L) = 0.0$. Results of our model are compared to those of Menart et al. (1993) using what these authors call "first-degree closure" formulation, in which spectral correlations are accounted for and wall reflections explicitly treated. A maximum relative deviation of about 20 percent at $X/L = 0.825$ is observed, where our approach underestimates the radiative source. For the major part of the spatial domain, our predictions are nearly close to their solution. The CPU time required in our work for this case is 9.21 s on a IBM RISC System/6000 3 AT computer. Figure 4 shows the comparison for the parabolic temperature profile with both reflecting walls for $L = 0.1$ m, $\rho(X = 0) = 0.9$ and $\rho(X = L) = 0.9$; small discrepancies are observed between the two curves. It is worth noting that the CPU time required in our approach for this last case is 40.59 s on a IBM RISC computer, whereas the solution by Menart et al. (1993), for such highly reflecting walls, requires 10,000 s on a CRAY-2 super computer.

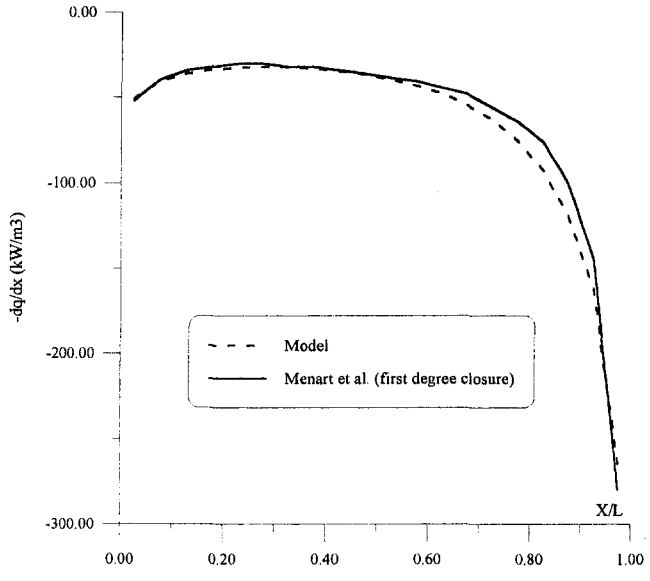

Fig. 3 Radiative source distribution for the uniform temperature profile [$L = 0.5$ m, $\rho(X = 0) = 0.9$, $\rho(X = L) = 0.0$]

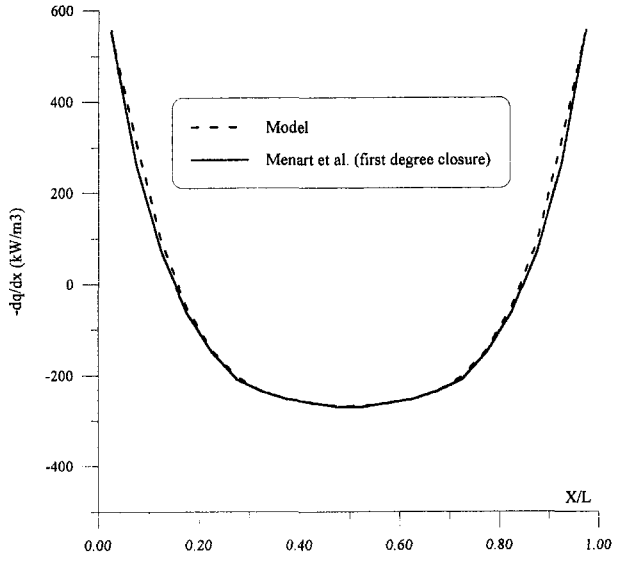

Fig. 4 Radiative source distribution for the parabolic temperature profile [$L = 0.1$ m, $\rho(X = 0) = 0.9$, $\rho(X = L) = 0.9$]

4.2 Experimental Spectral Transmittances of a Water Spray: Influence of Droplet Size and Concentration. The objective of this section is to show, experimentally, the influence of the two main parameters controlling the spray liquid phase attenuation: the droplet size and concentration. Results are presented for the sprayer TG 03 at 250 mm vertically from the nozzle in the incident direction. The spectrometer spectral resolution is 8 cm^{-1}, and the transmittance curves are presented in Fig. 5, for three pressures: Pr = 1, 3, and 5 bars, corresponding to a spray thickness of about 0.24 m and mean Sauter diameters of 105, 100, and 90 μm, respectively. An integration of measured spectral transmittances from 1.5 to 12 μm leads to the following values: 0.90, 0.80, and 0.68, respectively, for the three previous pressures. Figure 5 clearly shows that an increase in pressure (and flow rate) improves the spray attenuation ability. This behavior arises from the fact that increasing the nozzle pressure involves two main effects: first a larger break-up of the liquid drops, inducing production of much smaller droplets, and second an increase in the droplets density (and concentration). Thus, the concentration varies from 0.009 kg/m^3 at 1 bar to 0.05 kg/m^3 at 5 bars. Moreover, an analysis of the scattering diagrams given by Mie theory shows that small droplets scatter more radiation outside the incident and forward direction, with an important backscattering fraction in some situations (contrary to large drops scattering mainly in the forward direction); this contributes to their higher attenuation power. The combined

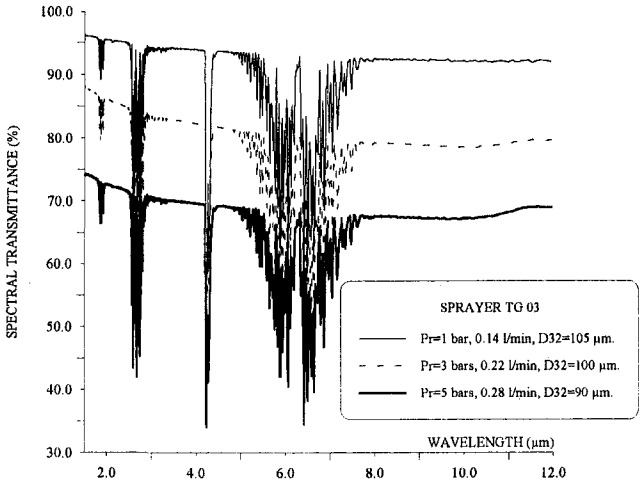

Fig. 5 Experimental spectral transmittances of a sprayer TG 03: influence of droplet size and concentration. Pr = 1 bar (Dc = 0.009 kg/m^3), Pr = 3 bars (Dc = 0.026 kg/m^3), Pr = 5 bars (Dc = 0.05 kg/m^3).

effect of small droplets and high concentration on attenuation, observed from the experimental curves in Fig. 5, can also be explained from the extinction coefficient expression

$$\beta_{\nu l} = 3Q_{\text{ext}}Dc/(2\rho_l d). \tag{33}$$

From Eq. (33), increasing the droplet concentration and decreasing its diameter leads to higher values of the extinction coefficient. The experimental results presented in this section are also in good agreement with the model parametric study carried out in Section 4.5 to investigate a large range of drop sizes and concentrations.

4.3 Model Validation With Experimental Spectral Transmittances of a Water Spray (With Both Phases Participating). The experimental results presented in Section 4.2 are compared to predictions from our water spray model. Comparison results are presented in Figs. 6 and 7, respectively, for 1 and 5 bars pressures, with a respective mean standard deviation of 1 and 2 percent on experimental transmittances. The calculated spectral transmittance is the ratio of transmitted and

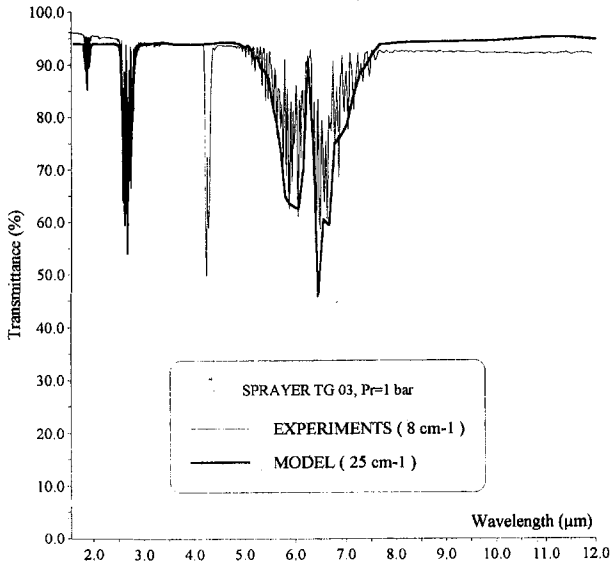

Fig. 6 Comparison between experimental and model predicted transmittances for a sprayer TG 03, Pr = 1 bar (D_{32} = 105 μm, Dc = 0.009 kg/m^3, L = 0.24 m)

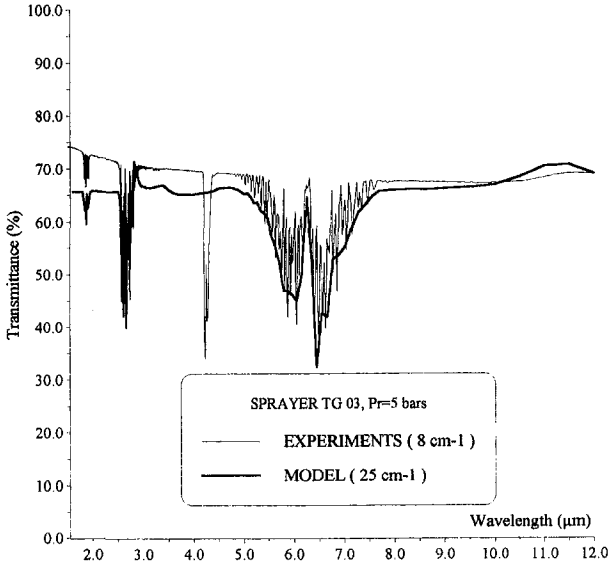

Fig. 7 Comparison between experimental and model predicted transmittances for a sprayer TG 03, Pr = 5 bars (D_{32} = 90 μm, Dc = 0.05 kg/m^3, L = 0.24 m)

incident intensities when considering the incident normal direction. A S20 Gaussian quadrature in DOM, with 20 uniform sublayers, are used for a one-dimensional transfer. Temperature and relative humidity of the spray (measured by the Institut des Technologies Chimiques) are, respectively, 25°C and 80 percent, and these parameters are used in gas model calculations. The two phases of the spray are included in the analysis and water vapor is the main participating specie of the gaseous phase (H_2O-N_2-O_2-CO_2 mixture) that is considered, the other species are accounted for in broadening. The resolution for the experimental spectrum is 8 cm^{-1}, while CK calculations are performed with a 25 cm^{-1} resolution that is determined by the data $\overline{k}_\nu$ and $\overline{\delta}_\nu$ provided by Soufiani et al. (1985) for this resolution. Although carbon dioxide has no significant molar fraction in the considered spray (0.00029) with a negligible contribution to the total attenuation, a 4.3 μm absorption band is observed for the 8 cm^{-1} experimental curve. Including CO_2 as a participating species, predictions of our 25 cm^{-1} model for this 4.3 μm region results in no significant difference with model predictions presented in Figs. 6 and 7. Since the target to be protected receives total or integrated fluxes, comparison between model and experimental data are carried out in terms of total transmitted intensities (1.5–12 μm).

A good agreement is observed between the spectral experimental and model-predicted transmittances. The gaseous phase behavior is well suited by the model. For Pr = 1 bar (Fig. 6), a relative error between experimental and model transmitted intensities of 1.55 percent is observed with a CPU time (IBM RISC) of 38.49 s. The corresponding quantities for Pr = 5 bars (Fig. 7) are, respectively, 6.6 percent and 70 s. A similar relative error model-experiments (2.5 percent) is observed for Pr = 3 bars. One reason of the relatively larger spectral deviation for small wavelengths in Fig. 7 (Pr = 5 bars) is that the experimental curves show higher standard deviation for this spectral range when the sprayer pressure increases.

According to these previous comparisons, the developed model shows a good agreement with experimental curves and offers an efficient computational time.

4.4 Total Transmissivities of Water Droplets: Influence of Size and Mass Loading. In order to check the effect of droplet size and concentration on the attenuation ability of water sprays, a simulation has been performed with our code (version without gas) for a wide range of droplet sizes and concentra-

tions. A droplet monodispersion is assumed. Figure 8 shows the results for a water spray of length $L = 30$ cm. The wavelength range for spectral integration is 0.8–20 μm, and a-S20 quadrature scheme with 20 uniform sublayers is used. It is well shown that small droplets with high concentration are extremely efficient in radiation attenuation (this behavior has been experimentally shown in Section 4.2). In contrast, large drops are poorly efficient even at high loadings. The reason is that for a given concentration, decreasing the size of the droplets leads to an increase of the total surface facing radiation. Although performances of a water spray curtain are improved by small droplets with high concentration, a compromise must be found for industrial applications. Such sprays with fine drops have shorter reach and are more susceptible to wind effect. Moreover, nozzles producing them are easily obstructed. A compromise solution may be a "sandwiching" of fine sprays between a large droplets arrangment for wind stabilization.

4.5 Effect of the Gaseous Phase Temperature and Molar Fraction on the Total Attenuation of a Spray. The aim of this section is to show the effect of gaseous phase on the attenuation power of a water spray. The configuration simulated here is a spray barrier of length $L = 0.2$ m, constituted with monodisperse droplets of diameter 100 μm and concentration $Dc = 0.1$ kg/m^3, providing a mean total attenuation of about 50 percent (see Fig. 8). The gaseous phase considered here is water vapor, and the spray temperature and relative humidity are varying, respectively, in the range 27–70°C and 60–100 percent. All the above-mentioned simulation parameters are consistent with realistic configurations. The incident radiation spectrum is that of a blackbody at 1300°C and, this spectrum may be compared to emission spectra of hydrocarbon fires. A comparison is made, in the incident direction, between the integrated transmitted intensity (0.8–20 μm, significant wavelength range) when taking into account the two phases of the spray (so called "complete" solution) and when neglecting the gas contribution. Figure 9 shows tendencies for the simulated configuration. Neglecting the gaseous phase overestimates the total transmitted intensity (or underestimates the attenuation ability of the spray). The relative error on Fig. 9 is defined as:

Error = |"Complete" solution—Integrated transmitted intensity without gas |/"Complete" solution.

It is well shown that an increase in temperature and relative humidity of the spray leads to a larger underestimation of its total mitigation power. An error of about 16 percent is observed at 70°C with a relative humidity of 100 percent. Although these conclusions are relative to the simulated configuration, they prove the importance of taking into account the gas when modeling interactions between water spray and fire radiation.

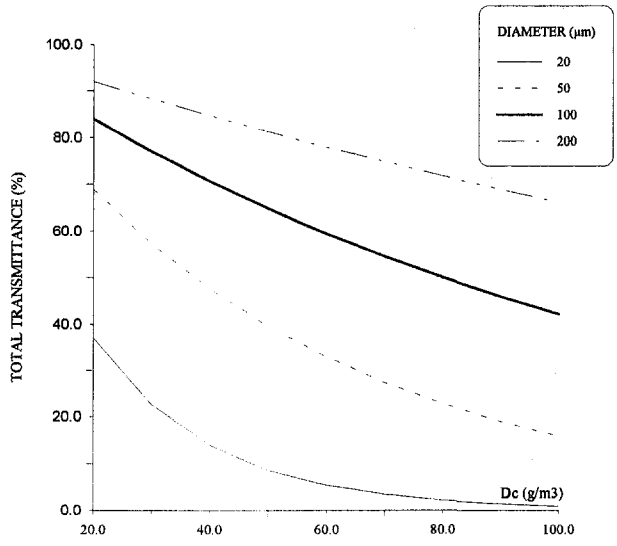

Fig. 8 Influence of droplet diameter and concentration on total attenuation of the liquid phase of a water spray ($L = 0.3$ m)

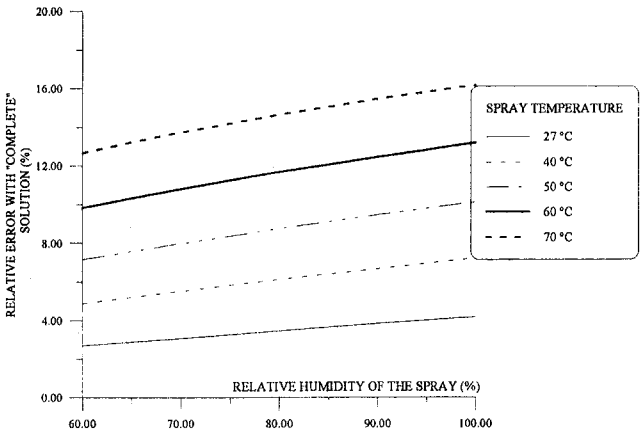

Fig. 9 Influence of the gaseous phase parameters (temperature, relative humidity) on the transmitted intensities for a given water spray [$L = 0.2$ m, $Dc = 0.1$ kg/m^3, $d = 100$ μm]

5 Conclusions

This study has presented a method for modeling fire radiation transfer through water sprays for fire engineering applications. Our approach, more rigorous than previous works available in the literature, includes the two phases (liquid and gaseous) of the spray in the analysis by combining the best submodels from the literature: the Mie theory for droplet properties, the correlated-k method to handle the gaseous phase contribution, and the integral formulation of the discrete ordinates method to solve the radiative transfer equation. The good accuracy and computational efficiency of this model have been shown with comparison to some results from Menart et al. (1993) for a one-dimensional transfer. A comparison with the laboratory experimental data for a sprayer TG 03 also shows a good agreement, with computational times consistent with an industrial use. This work has also provided new and useful information regarding the experimental spectral behavior of water sprays and the influence of the main parameters controlling the spray attenuation ability: droplet size and concentration and water vapor molar fraction.

Acknowledgments

This work is supported by the European Union and co-sponsored by French industrial partners: Gaz de France, Elf Aquitaine and Total R.D.

References

Borges De Miranda, A., and Sacadura, J. F., 1996, "An Alternative Formulation of the S-N Discrete Ordinates for Predicting Radiative Transfer in Nongray Gases," ASME JOURNAL OF HEAT TRANSFER, Vol. 118, No. 3, pp. 650–653.

Domoto, G. A., 1974, "Frequency Integration for Radiative Transfer Problems Involving Homogeneous Nongray Gases: The Inverse Transmission Function," *Journal of Quantitative Spectroscopy and Radiative Transfer,* Vol. 14, pp. 935–942.

El Wakil, N., and Sacadura, J. F., 1992, "Some Improvements of the Discrete Ordinates Method for the Solution of the Radiative Transport Equation in Multidimensional Anisotropically Scattering Media," *Developments in Radiative Heat Transfer,* S. T. Thynell et al., eds., ASME HTD, Vol. 203, pp. 119–127.

Goody, R. M., and Yung, Y. L., 1989, *Atmospheric Radiation,* Oxford Univ. Press, New York.

Hansen, J. E., 1969, "Exact and Approximate Solutions for Multiple Scattering by Cloudy and Hazy Planetary Atmospheres," *Journal of the Atmospheric Sciences,* Vol. 26, pp. 478–487.

Hunt, G. E., and Grant, I. P., 1969, "Discrete Space Theory of Radiative Transfer and its Application to Problems in Planetary Atmospheres," *Journal of the Atmospheric Sciences,* Vol. 26, pp. 963–971.

Lacis, A. A., and Oinas, V., 1991, "A Description of the Correlated-*k* Distribution Method for Modeling Nongray Gaseous Absorption, Thermal Emission, and Multiple Scattering in Vertically Inhomogeneous Atmospheres," *Journal of Geophysical Research,* Vol. 96, No. D5, pp. 9027–9063.

Malkmus, W., 1967, "Random Lorentz Band Model With Exponential-Tailed S^{-1} Line-Intensity Distribution Function," *Journal of the Optical Society of America,* Vol. 57, No. 3, pp. 323–329.

Menart, J. A., Lee, H. S, and Kim, T. K., 1993, "Discrete Ordinates Solutions of Nongray Radiative Transfer With Diffusely Reflecting Walls," ASME JOURNAL OF HEAT TRANSFER, Vol. 115, pp. 184–193.

Ravigururajan, T. S., and Beltran, M. R., 1989, "A Model for Attenuation of Fire Radiation Through Water Droplets," *Fire Safety Journal,* Vol. 15, pp. 171–181.

Riviere, Ph., Soufiani, A., and Taine, J., 1992, "Correlated-*k* and Fictitious Gas Methods for H_2O Near 2.7 μm," *Journal of Quantitative Spectroscopy and Radiative Transfer,* Vol. 48, No. 2, pp. 187–203.

Soufiani, A., Hartmann, J. M., and Taine, J., 1985, "Validity of Band-Model Calculations for CO_2 and H_2O Applied to Radiative Properties and Conductive-Radiative Transfer," *Journal of Quantitative Spectroscopy and Radiative Transfer,* Vol. 33, No. 3, pp. 243–257.

Stephenson, S., and Coward, M. J., 1986, "Attenuation of Radiant Heat on LNG/LPG Carriers With Freestanding Water Curtains," *Gastech 86 LNG/LPG Conference,* Hamburg, pp. 157–168.

Van De Hulst, H. C., 1957, *Light Scattering by Small Particles,* John Wiley & Sons, Inc., New York.

Yamamoto, G., Tanaka, M., and Asano, S., 1970, "Radiative Transfer in Water Clouds in the Infrared Region," *Journal of the Atmospheric Sciences,* Vol. 27, pp. 282–292.

Young, S. J., 1977, "Nonisothermal Band Model Theory," *Journal of Quantitative Spectroscopy and Radiative Transfer,* Vol. 18, pp. 1–28.

Zang, L., Soufiani, A., and Taine, J., 1988, "Spectral Correlated and Non-Correlated Radiative Transfer in Finite Axisymmetric System Containing an Absorbing and Emitting Real Gas-Particle Mixture," *International Journal of Heat and Mass Transfer,* Vol. 31, No. 11, pp. 2261–2272.

Velocity Field in Turbulent Subcooled Boiling Flow

R. P. Roy
Professor.
roy@asu.edu

V. Velidandla

S. P. Kalra

Department of Mechanical and Aerospace Engineering,
Box 876106,
Arizona State University,
Tempe, AZ 85287-6106

The velocity field was measured in turbulent subcooled boiling flow of Refrigerant-113 through a vertical annular channel whose inner wall was heated. A two-component laser Doppler velocimeter was used. Measurements are reported in the boiling layer adjacent to the inner wall as well as in the outer all-liquid layer for two fluid mass velocities and four wall heat fluxes. The turbulence was found to be inhomogeneous and anisotropic and the turbulent kinetic energy significantly higher than in single-phase liquid flow at the same mass velocity. A marked shift toward the inner wall was observed of the zero location of the axial Reynolds shear stress in the liquid phase, and the magnitude of the shear stress increased sharply close to the inner wall. The near-wall liquid velocity field was quite different from that in single-phase liquid flow at a similar Reynolds number. Comparison of the measurements with the predictions of a three-dimensional two-fluid model of turbulent subcooled boiling flow show reasonably good agreement for some quantities and a need for further development of certain aspects of the model.

Introduction

Turbulent subcooled boiling flow is found in many types of equipment of engineering interest—for example, nuclear reactors, steam generators, and refrigeration systems. In this flow, discrete vapor bubbles flow with a liquid continuum. Among the many aspects of turbulent subcooled boiling flow about which little is known are: (i) the turbulence characteristics of the liquid and vapor phases, (ii) spatial distribution of vapor-liquid interfacial area, and (iii) interfacial transport rates of mass, momentum, and thermal energy.

We are collaborating with Electricité de France (EDF) in a study of the aforementioned aspects of turbulent subcooled boiling flow. The study includes experiments as well as model development. In an earlier effort we had measured velocity and temperature fields in the all-liquid layer (region I, Fig. 1) by three-sensor hot-film anemometry, Roy et al. (1993). Possible discrepancies in some of these measurements will be pointed out in the present paper. In another paper, Roy et al. (1994), a method for obtaining the interfacial area concentration distribution was described. Measurement of the temperature field in the boiling layer was also presented. Mention should be made here of the temperature field measurements reported by Hino and Ueda (1985a, b).

In this paper we report measurements of some of the important velocity field quantities in turbulent subcooled boiling flow through an annular channel with heated inner wall. Measurements were made in the boiling layer (region II, Fig. 1) and in the adjacent all-liquid layer (region I) at one axial plane of the channel. Our goals were to obtain from these measurements a clear idea of the structure of turbulence and help in model development. The liquid-phase velocity field is compared with that of single-phase liquid flow, both heated and unheated, in the same channel and the same Reynolds number based on liquid properties at the channel inlet. The measurements are also compared to the predictions of a computational code based on three-dimensional two-fluid model of turbulent subcooled boiling flow which is under development at EDF, Briere et al. (1995).

While no previous measurements could be found of the velocity field in the two-phase region of turbulent subcooled boiling flow, the open literature contains many experimental studies of the velocity field in isothermal bubbly gas-liquid flow. For brevity, we will refer to only a few.

Serizawa et al. (1975a, b, c) performed experiments and modeling in a study of turbulent bubbly air-water flow through a vertical pipe. A two-sensor electrical resistivity probe was used to measure the local bubble velocity, gas fraction, and bubble passage rate. The water velocity distribution was measured by constant temperature hot-film anemometry. Radial and axial temperature distributions due to a heated line source were measured by thermocouples. Transport quantities such as turbulent shear stress and turbulent thermal diffusivity were reported.

Theofanous and Sullivan (1982) conducted laser Doppler velocimeter (LDV) measurements of the liquid velocity field in turbulent bubbly nitrogen-water flow through a vertical glass pipe. Distributions of the liquid mean axial velocity and axial and tangential intensities were reported. A simple theory for predicting the liquid turbulent intensity was proposed.

Marié (1982) employed LDV to measure the rising velocity of bubbles and the normal Reynolds stresses in the liquid phase of air-water bubbly flow through a vertical square channel. The measurements were made in the uniform mean flow region of the channel. The data indicated significant increases in the normal Reynolds stresses in the liquid.

Wang et al. (1987) used single and multi-sensor hot-film anemometry to measure the gas-phase distribution and liquid-phase turbulence in bubbly air-water up and down-flow through a pipe. Reynolds normal and shear stresses in the liquid were found to increase in the presence of air bubbles.

Vassallo et al. (1993) conducted LDV measurement of the time-mean gas bubble and liquid velocities in turbulent air-water flow through a vertical rectangular channel. A combination of back-scattered and reflected forward-scattered (retro-reflect) light collection techniques was used.

Grossetête (1995) carried out optical fiber probe measurements in isothermal bubbly gas-liquid flow through a vertical pipe. The objective was to explore issues such as interphase momentum transfer and coalescence/fragmentation of bubbles.

Velidandla et al. (1996a) measured the velocity field in isothermal, turbulent bubbly gas-liquid flow through a vertical pipe by laser Doppler velocimetry. The gas-phase distribution was also measured—by an optical fiber probe.

The Experimental Apparata

The Test Section. The 3.66 m long vertical concentric annular test section featured a heated inner wall and an outer wall

Contributed by the Heat Transfer Division for publication in the JOURNAL OF HEAT TRANSFER. Manuscript received by the Heat Transfer Division May 6, 1996; revision received May 30, 1997; Keywords: Boiling; Multiphase Flows; Turbulence. Associate Technical Editor: R. D. Boyd.

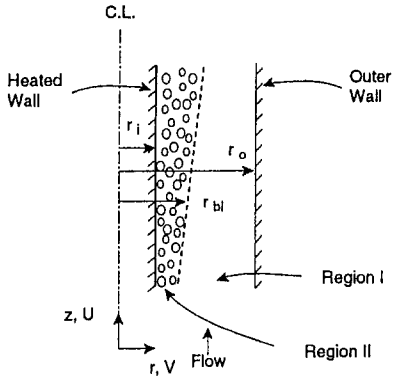

Fig. 1 Subcooled boiling flow in an annular channel—boiling layer and adjacent all-liquid layer

insulated all along its length except for a 15 cm portion of the 0.521 m long measurement section shown in Fig. 2. The inner tube of the test section was of 304 stainless steel (i.d. = 14.6 mm, o.d. = 15.8 mm). The outer tube was of transparent pyrex glass (i.d. = 38.1 mm, o.d. = 47.0 mm) except for the measurement section which was of optical quality quartz (i.d. = 37.9 mm or 38.0 mm[1], o.d. = 41.8 mm). Refrigerant-113 (R-113) was the working fluid. An anodized aluminum box with quartz front, side, and back windows served as a jacket around the aforementioned 15 cm length of the quartz tube. This box was filled with liquid R-113 to alleviate laser beam refraction at the outer wall of the quartz tube.

The upper 2.75 m length of the stainless steel tube could be resistively heated by direct current. The lower 0.91 m length of the test section served as the hydrodynamic entrance length. The stainless steel tube was equipped with four surface thermocouples on its inner wall (all located in the measurement section) and filled with aluminum oxide powder insulation. The temperature of the tube outer wall (this being the annulus inner wall) could be calculated from the measured tube inner wall temperature and the known wall heat generation rate by a steady-state heat conduction analysis. The heating power to the test section was calculated as the product of the magnitude of direct current from a D.C. power supply (Rapid Technologies; 40 volts, 1500 amperes maximum) and the voltage differential across the heater tube.

[1] Two quartz sections were used in the course of these experiments. Although they were prescribed to be of the same i.d., measurement revealed a difference of about 0.1 mm.

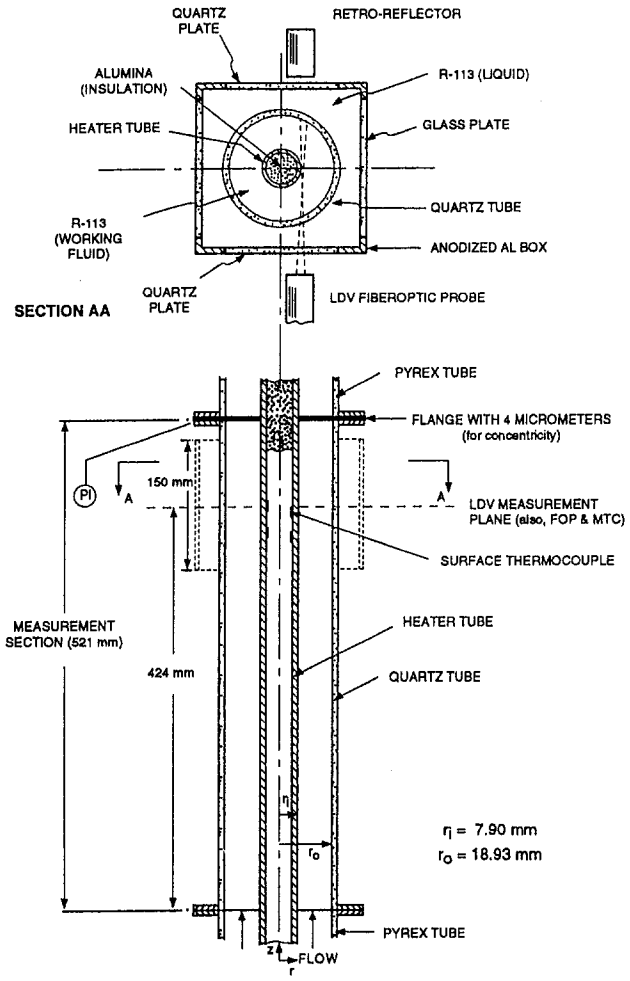

Fig. 2 The measurement section

The measurement plane (m.p.) was 0.424 m (≈19 hydraulic diameters) downstream of the measurement section entrance, this entrance being, in turn, 1.562 m downstream of the beginning of the channel heated length. Effect of the slight mismatch (≲0.2 mm) between the inner diameters of the quartz tube and the upstream pyrex tube on the fluid velocity field at the m.p. was assumed to be negligible.

The measurement section shown schematically in Fig. 2 was not equipped with a mounting block for the microthermocouple.

Nomenclature

$\bar{a}_i$ = local, time-averaged interfacial area concentration
$\bar{D}_b$ = mean vapor bubble diameter
k_L = liquid phase turbulent kinetic energy per unit liquid mass
q''_w = inner wall heat flux
r = radial coordinate
r_{bl} = radius of boiling layer outer edge
r_i = annulus inner wall radius
r_o = annulus outer wall radius
R^* = nondimensional radial coordinate $= (r - r_i)/(r_o - r_i)$
$\bar{T}$ = time-mean temperature
t' = temperature fluctuation intensity
U_τ = friction velocity $= \sqrt{\tau_w/\rho_L}$
$\bar{U}_G$ = time-mean vapor bubble axial velocity
$\bar{U}_L$ = time-mean liquid axial velocity
u'_G = vapor bubble axial velocity fluctuation intensity
u'_L, v'_L = liquid axial velocity fluctuation intensity, radial velocity fluctuation intensity
u^+ = nondimensional mean axial velocity $= \bar{U}/U_\tau$
u_s = interfacial energy per unit area
$(\overline{uv})_L$ = single-point cross-correlation between liquid axial and radial velocity fluctuations
$\bar{V}_L$ = time-mean liquid radial velocity
y^+ = nondimensional coordinate normal to wall $= yU_\tau/\nu_L$
z = axial coordinate

Greek symbols

α_G, α_L = vapor residence time fraction, liquid residence time fraction
ν_L = liquid kinematic viscosity
ρ_L = liquid density
ρ_M = density of vapor-liquid mixture
σ = surface tension
τ = Reynolds stress tensor
τ_w = wall shear stress
ϵ_L = turbulent energy dissipation rate in liquid per unit liquid mass

A second section (quartz tube i.d. = 38.0 mm) was provided with a mounting block a few mm downstream of the LDV m.p. where a microthermocouple was installed to measure fluid temperature distribution at the LDV m.p..

Measurement Instrumentation. A two-component laser Doppler velocimeter (LDV) system (TSI) was used to measure the fluid velocity field in the annular measurement section. The system featured a 100 mW argon-ion laser and an 83 mm diameter 250 mm focal length fiber-optic probe with a back-scatter light detector. The LDV system included a fiber detector that could be placed in any light scattering direction (for example, at 90 degrees to the direction of laser beam incidence) as well as a retro-reflector. The retro-reflector consisted of a reflecting prism and a focusing lens and directed the forward-scattered light back to the backscatter detector.[2] The probe, the fiber detector, and the retro-reflector were mounted on independent three-dimensional traverse mechanisms, each mechanism also containing a rotational stage. All velocity data reported in this paper were obtained in the backscatter mode. White nylon particles of 3–7 μm size were used to seed the flow.

There is a significant difference between the refractive indices of liquid R-113 and quartz; for example at 31.2°C, the refractive index of liquid R-113 is 1.351 and that of quartz 1.458. So, refractive index mismatch existed at the inner and outer walls of the quartz tube. Furthermore, in the heated flow experiments, the time-mean liquid refractive index varied spatially in the annulus due to variation of the mean liquid temperature. There was also some (albeit much less) spatial variation of the time-mean refractive index in the aluminum box liquid. To compensate for these and locate the LDV measuring volume (m.v.) at desired positions in the annulus, a beam tracing algorithm and a beam steering module were used, Velidandla et al. (1994).

One other refractive index-related issue required attention. It involved the cumulative (along the laser beam path) effect of the random fluctuations in the liquid refractive index, due to turbulent temperature fluctuations, on the crossing of the beams and the movement of fringes in the m.v. (Buchhave et al., 1979). Further comments are made on this issue in the section on LDV calibration.

In isothermal flow of liquid R-113, the LDV probe volume was calculated to be an ellipsoid with minor axes (in the r-z plane) about 0.1 mm long and major axis (perpendicular to the r-z plane) about 1.0 mm long. The actual measuring volume is more difficult to determine and was assumed to coincide with the probe volume. In the arrangement shown in Fig. 2, the minor axes defined the radial and axial positions of measurement in the test section.

Measurement of liquid velocity in bubbly boiling flow is further complicated by refraction and reflection of the laser beams by the bubbles. On the other hand, light reflected by the bubbles, under proper conditions, enables measurement of bubble velocity. A bubble could only be "seen" by the backscatter detector ($\approx$250 mm away) when the reflected light was within the 11 degree cone angle subtended at the location of reflection by the detector lens. Furthermore, a burst signal was generated only when reflected light due to both laser beams of a particular color interfered at the detector. Such interference will typically occur for a duration significantly shorter than that due to a seed particle in the liquid.

To measure liquid velocity, the LDV signal must be processed so as to discriminate between the Doppler bursts due to the seed particles in the liquid and those due to bubbles. Now, as the bubbles are much larger in size than the seed particles, the amplitude of the Doppler signal pedestals, due to bubbles passing through the central region of the m.v., would usually be considerably higher than the pedestal amplitude due to seed particles passing through the same region. Bubbles travelling through the edges of the m.v. may, however, give rise to pedestal amplitudes comparable to those due to seed particles passing through the central region of the m.v. Distorted and unsteady shape of the larger bubbles may also reduce the pedestal amplitude, as noted by Sheng and Irons (1991). Hence, the potential for "cross-talk" between liquid (seed particle) and bubble signals remains.

Two factors rendered this cross-talk small during our liquid velocity measurement. First, an electronic discrimination circuit was installed between one of the two PMTs and the LDV signal processor. The bursts with pedestal amplitude higher than a chosen threshold voltage were tagged by the circuit as being due to bubbles and removed from both PMT output signals prior to their analysis. Second, the data rate due to bubbles (established separately) was typically two orders of magnitude lower than that due to seed particles in the liquid.[3] As such, bias imparted to the liquid velocity data by bursts due to vapor bubbles that escaped removal by the discrimination circuit would be very small.

The velocity of vapor bubbles was measured separately in the backscatter mode. This measurement depends on the fringes produced at the detector by laser beam light reflected from a bubble surface as it moves through the measurement volume. This reflected light reaches the detector only when it is within the solid angle subtended by the detector at the measurement volume. Furthermore, the number of fringe crossings must be sufficient for signal validation.

In the bubble velocity measurement experiments, first, the seed particles were removed from the liquid by filtration. Next, the PMT excitation voltage was lowered below the voltage required by the seed particles to generate Doppler burst signals, thus ensuring that no bursts resulted from any remaining seed particles. At the same time, a much larger frequency shift compared to that used for measuring liquid velocity (500 kHz compared to 100 kHz) was introduced so that sufficient number of cycles would be contained in at least some of the bubble-generated Doppler bursts to allow validation of data. One problem caused by this large frequency shift was that for about one-third of the validated data, two velocity samples were gathered from a single bubble. For the remainder, one sample was obtained per burst. We analyzed some of these signals in two ways: (i) the second sample was removed from the appropriate data and the signal so conditioned was analyzed for velocity; and (ii) the original (unconditioned) signal was analyzed for velocity. In all cases, the difference between the mean bubble axial velocities obtained by the two procedures was within 1 percent. The difference between the bubble axial velocity fluctuation intensities was within 5 percent. These biases have been incorporated in the uncertainty estimates of the mean bubble axial velocity and axial fluctuation intensity. The uncertainty estimates are reported later in this paper.

To determine the extent of statistical bias in the liquid velocity data, some of the isothermal and heated liquid flow experiments were repeated in the retro-reflect light collection mode. Because of the much higher data rate that become available in this mode, the signal processor could be operated as a controlled processor and bias essentially eliminated. Statistical bias in the backscatter data was found to be insignificant (Velidandla et al., 1996b).

To determine whether the cumulative effect, along the beam paths, of the random fluctuations in the liquid refractive index was significant, the backscatter data for several heated single-phase liquid flow experiments were compared with the corresponding retro-reflect data.[4] Results indicated that the velocity

[2] The data rate in this mode was usually much higher than in the backscatter light collection mode. However, the retro-reflect mode was an option in single-phase flow measurement only.

[3] This was the case even in regions where the bubble passage rate was large because only a few generated validated burst signals.

[4] Note that the scattered light travels approximately thrice the distance in the annulus liquid in the retro-reflect mode compared with the backscatter mode.

Table 1 Range of parameters and their uncertainties*—subcooled boiling flow experiments

Parameter	Range	Uncertainty
Inner wall heat flux	79400–126000 W/m^2	±200 W/m^2
Mass velocity	565–785 kg/m^2 s	±3 kg/m^2 s
R-113 partial pressure at measurement plane/ sat. temp.	269 kPa/80.5°C	±0.7 kPa/±0.2°C
Mean liquid temperature at test section inlet	42.7–50.2°C	±0.1°C

* The uncertainty estimates are for 95 percent confidence.

measurements were not significantly affected by the random fluctuations in the liquid refractive index (Velidandla et al., 1996b).

CTA measurement comparisons encompassed measurements in single-phase liquid flow through the measurement section, both heated and unheated. The LDV data were compared with data obtained in an almost identical measurement section (the outer tube was of 304 stainless steel rather than quartz) by constant temperature hot-film anemometry (CTA), (see Hasan et al., 1992).[5] While good agreement was generally obtained for isothermal flows, distortions became apparent in the CTA data for heated flows (Velidandla et al., 1996b). It appears that the CTA turbulence measurements in heated flow were affected not only by the large dimensions of the intrusive probe (this was a factor in isothermal flow as well) but also by inadequate temperature compensation of the velocity signals. It is our view that the LDV measurements are considerably more accurate than our earlier CTA measurements.

Other System Measurements. Other measurements included: (1) the dissolved air content, (2) pressure, (3) flow rate, and (4) the dual-sensor optical fiber probe (FOP) and microthermocouple (MTC). Air is highly soluble in liquid R-113 and the influence of dissolved air can be significant in boiling flow experiments. Careful degassing of the rig R-113 inventory was therefore performed and the residual air content measured (by an Aire-Ometer, Seaton-Wilson) prior to each experiment. For the experiments reported here, the residual air partial pressure was about 8 kPa out of a total pressure of 277 kPa at the measurement plane. This corresponds to a reduction in the R-113 saturation temperature from 81.6°C to 80.5°C. The pressure at the measurement plane was monitored by a test gauge (Omega, O-1200 kPa range, 1.4 kPa resolution). The volumetric flow rate of liquid at the test section inlet was measured by a turbine flow meter (EG & G Flow Technology). The FOP and MTC were used, respectively, to measure vapor bubble-related quantitites and vapor/liquid temperatures and have been described by Roy et al. (1994).

The Experiments and Measurement Uncertainties

Experiments. Table 1 contains the range of parameters, over which the measurements were performed, and the associated uncertainties. In Table 1 and in the remainder of the paper, the term "mean" of a quantity implies its "time-mean". Also, "vapor residence time fraction" has often been abbreviated as "vapor fraction".

Test section heat balance experiments were performed at the outset with single-phase liquid flow. About 2 percent of the supplied power was found to be lost to the ambient.

Subcooled boiling flow experiments were carried out at seven different conditions as defined by the inner wall heat flux, fluid mass velocity, measurement plane pressure, and liquid temperature at the test section inlet (Velidandla, 1997). Each experiment was repeated at least once. The results of experiments at four conditions, Table 2, will be given in this paper.

To be able to quantitatively examine the changes that occurred in the velocity field upon transition from single-phase liquid flow to subcooled boiling flow, two single-phase liquid flow experiments were performed at each "mass velocity-inlet liquid temperature" combination (565 kg/m^{2}s-42.7°C; 785 kg/m^{2}s-50.2°C). One of the two was an isothermal experiment and the other heated (inner wall heat flux = 16000 W/m^2).

Table 3 contains the quantitites for which radial distributions were measured at the measurement plane (m.p., see Fig. 2). Appropriate single-phase liquid flow data have been included for comparison in the figures which follow.

Measurement Uncertainties. A discussion of the statistical bias in our velocity data (mean Reynolds stresses) for unheated and heated single-phase liquid flows was presented by Velidandla et al. (1996b). Statistical bias was judged not to be of significance in these flows. The uncertainty in the location of the LDV measurement volume due to uncertainty in the mean liquid temperature (and hence, the refractive index) distribution was also estimated to be insignificant.

In the case of boiling flow, the issue of measurement uncertainty assumes greater importance. In the following paragraphs we present our estimates of uncertainty for the various measured quantities.

The uncertainty in the vapor local residence time fraction is ±1 percent for $\alpha_G < 0.1$ and ±2 percent for $0.1 < \alpha_G \lesssim 0.5$. The uncertainty in the location of the boiling fluid layer outer edge (Roy et al., 1994) is shown in Figs. 3(a) and 6(a).

The uncertainty in the mean liquid temperature at the m.p. is ±0.3°C and that in the heated wall temperature, ±0.4°C.

The uncertainty in the liquid mean axial velocity due to the radial gradient of the velocity across the LDV m.v. is ±3 percent for $R^* < 0.3$ and ±1 percent for $R^* > 0.3$. When combined with the estimated statistical bias for the relatively high turbulence intensity flow (3 percent for $R^* < 0.2$, 1 percent for $R^* > 0.2$), the overall uncertainty becomes ±4 percent near the wall ($R^* < 0.2$) and ±2 percent away from the wall ($R^* > 0.3$).

The uncertainties in the Reynolds stresses in the liquid phase were estimated solely from the variance about the sample mean as calculated from multiple measurements at each location. The uncertainty in the axial velocity intensity is ±3 percent and that in the radial velocity intensity ±4 percent. The uncertainty in the axial Reynolds shear stress is ±10 percent.

For the vapor bubble mean axial velocity measured by LDV, the following three contributions to the uncertainty were considered: the random error found from the variance about the sample mean (±3 percent), bias due to multiple bursts from some of the bubbles (±1 percent), and m.v. location uncertainty (±3 percent near the inner wall, ±1 percent away from the wall). These combine to give uncertainty estimates of approximately ±5 percent near the inner wall and ±4 percent away from the wall.

For the vapor bubble interface mean axial velocity as measured by FOP, the uncertainty due to the limited resolution of the cross-correlation peak (Roy et al., 1994) was estimated to be ±10 percent. Possible bias due to some of the small bubbles flowing around the sensors was not considered.

The uncertainty in the vapor bubble axial velocity intensity was estimated by combining the random error found from the variance about the sample mean (±7 percent) and the multiple burst bias (±5 percent). This yields an overall uncertainty of about ±9 percent.

Experimental Results

Figures 3(a)–(i) contain the measurements of experiment 1. In Fig. 3(a), the radial distribution of vapor fraction at the

[5] Measurements could be made much closer to the inner wall of the annular channel by LDV compared to by CTA.

Table 2 Conditions for four experiments

Parameter	Experiment 1	Experiment 2	Experiment 3	Experiment 4
Inner wall heat flux (W/m^2)	79380	94960	115680	125920
Fluid mass velocity (kg/m^2 s)/Re_{in}	565/22580	785/34300	785/34300	785/34300
R-113 pressure at m.p. (kPa)	269	269	269	269
Mean liquid temperature at test section inlet (°C)	42.7	50.2	50.2	50.2

m.p. is shown. The radial location of the boiling layer outer edge is also shown along with its uncertainty. The criterion for determining the boiling layer outer edge was described by Roy et al. (1994).

Figures 3(b) and (c) show, respectively, the radial profiles of mean fluid and liquid temperatures and the corresponding temperature fluctuation intensities. The method of obtaining vapor and liquid temperatures from the measured fluid temperature has been described by Roy et al. (1994). The mean vapor phase temperature was very close to the local saturation temperature (80.5°C) across the boiling layer. The liquid remained significantly subcooled (in the mean sense) to at least $R^* \approx 0.04$ (our closest approach to the inner wall). The liquid temperature fluctuation intensity was substantial in the boiling layer. The mean liquid temperature distribution, in addition to being an important state property, is vital to the tracing of the beam paths in LDV measurement. The liquid temperature fluctuation intensity is not only an important turbulence parameter but also an indicator of the liquid refractive index fluctuation intensity.

Figure 3(d) shows the radial distribution of liquid mean axial velocity for experiment 1. Also shown are the corresponding distributions for isothermal and heated single-phase liquid flows.[6] The effect of buoyancy on the latter profile has been discussed by Velidandla et al. (1996b). Boiling brought about significant changes in the distribution. First, the mean liquid axial velocity inside the boiling layer increased with a concomitant decrease in the velocity outside the boiling layer.[7] Second, there was a marked shift of the maximum liquid axial velocity location toward the heated wall. It is useful to view these trends in conjunction with the vapor bubble mean axial velocity profile, Fig. 3(e). Both FOP and LDV measurements are shown in this figure. The FOP measurements used the cross-correlation technique (Roy et al., 1994) and the differences observable between these and the LDV measurement will be discussed shortly. It is evident that the vapor bubbles as well as the liquid inside the boiling layer flowed downstream with higher axial velocity than the liquid in nonboiling condition. The liquid mean axial velocity in the boiling flow case did not remain higher than the liquid velocity in nonboiling condition much beyond the boiling layer edge (this finding does not agree with our earlier CTA measurement (Roy et al., 1993)) and eventually became lower. One would expect the three profiles to merge as the annulus outer wall is approached. It is also worth noting that for both the LDV and the FOP measurements, the mean axial velocity peak was farther away from the wall than the highest vapor fraction location. Also, the FOP measurements were typically higher than the LDV measurements in the outer two-thirds of the boiling layer. Possible explanations for this difference in measured velocity are the following: (1) some of the smaller bubbles can be expected to flow around the FOP sensor; and (2) the smaller bubbles move slower than the larger ones.

The radial profile of the liquid mean radial velocity is shown in Fig. 3(f). The profiles for the corresponding isothermal and heated single-phase liquid flows are also shown. In all cases, the radial velocity was only about 1 percent of the mean axial velocity in magnitude.

Figures 3(g) and (h) contain, respectively, the radial distributions of liquid axial velocity fluctuation intensity and radial velocity fluctuation intensity for the subcooled boiling, heated single-phase liquid, and isothermal liquid flows. Buoyancy effects which led to differences between the intensity distributions in the latter two flows have been discussed by Velidandla et al. (1996b). In the case of subcooled boiling flow, dramatic increases in both axial and radial intensities were observed within the boiling layer, especially as the heated wall was approached. The radial intensity remained significantly lower than the axial intensity as in single-phase liquid flow. In turbulent single-phase flow, the radial intensity reaches its peak farther from the wall than does axial intensity—a well-known feature that is readily seen in these two figures. No such characteristic could be discerned in the boiling flow case, at least up to our measurement location closest to the heated wall.[8] The minima in the axial and radial intensity profiles were near the boiling layer edge, although the flat distributions here made the locations of the minima somewhat uncertain. It should also be noted that both the intensities remained high well into the all-liquid region. We expect the intensity profiles for the boiling and single-phase liquid flows to merge sufficiently close to the outer wall.

Figure 3(i) shows the radial distribution of $(\overline{uv})_L$, ~ axial Reynolds shear stress in the liquid phase of the subcooled boiling flow, heated single-phase liquid flow, and isothermal liquid flow. The characteristics of the two single-phase liquid flow distributions have been discussed by Velidandla et al. (1996b). In the case of subcooled boiling flow, a dramatic shift of the zero shear stress location toward the heated wall can be seen. This location is well inside the boiling layer and near the location of maximum liquid mean axial velocity, Fig. 3(d). The magnitude of $(\overline{uv})_L$ increased sharply close to the inner wall. There may well have been an increase in the wall shear stress, notwithstanding the decrease in liquid density in the vicinity of the wall because of higher temperature, although a definite conclusion can not be made due to data scatter.

A measure of the degree of correlation between u and v is given by

$$C_{(uv)_L} \equiv \frac{(\overline{uv})_L}{u'_L v'_L}. \quad (1)$$

Figure 4 shows plots of this correlation coefficient for the subcooled boiling flow as well as the two single-phase liquid flows. There occurred some reduction in the magnitude of $C_{(uv)_L}$ in the heated liquid flow compared to the isothermal liquid flow over

[6] Measurements were not made in these flows beyond $R^* \approx 0.82$ because of the relatively severe laser beam refraction in the tube wall.

[7] Mass balances for the three experiments (subcooled boiling flow and the two single-phase liquid flows) based on the liquid mean axial velocity and density profiles (along with the vapor fraction and vapor mean axial velocity profiles in the boiling flow case) agreed to within 1 percent. Beyond $R^* \approx 0.82$, it was necessary to extrapolate the axial velocity profile to the outer wall. This was done on the basis of (1) an isothermal liquid flow experiment conducted later in which we were able to measure, by considerable steering of the beams, the mean axial velocity up to $R^* \approx 0.9$ and (2) the Brighton and Jones (1964) measurements.

[8] It was not possible in boiling flow to measure the liquid velocity as close to the inner wall as in single-phase liquid flow because of a substantial reduction in LDV data rate. This reduction is due to the reflection and refraction of incident and scattered light by vapor bubbles in their paths, as well as thermophoresis of the seed particles.

Table 3 Quantities for which radial distributions were measured at the measurement plane

Flow Regime	
Single-phase liquid flow	Subcooled boiling flow
—	Vapor fraction
Mean temperature	Mean temperature—fluid*, liquid
Temperature fluctuation intensity	Temperature fluctuation intensity—fluid, liquid
Mean axial velocity	Mean axial velocity—liquid, vapor
Mean radial velocity	Mean radial velocity—liquid
Axial velocity fluctuation intensity	Axial velocity fluctuation intensity—liquid, vapor
Radial velocity fluctuation intensity	Radial velocity fluctuation intensity—liquid
Single-point cross-correlation $\overline{uv}$ (~axial Reynolds shear stress)	$\overline{uv}$—liquid

* By the term *fluid* we mean *liquid* when in the all-liquid layer and *liquid and vapor* when in the boiling layer.

the inner half of the annulus. The reduction in the magnitude of $C_{(uv)_L}$ inside the boiling layer is, however, more dramatic.

Scrutiny of the liquid velocity data suggests that the near-wall region velocity field undergoes significant changes when boiling occurs. The wall laws for isothermal liquid flow (Velidandla et al., 1996b) and heated single-phase liquid flow (Zarate et al., 1997) are no longer valid. Preliminary calculations also indicate that a general wall law may not exist in subcooled boiling flow.

We now briefly discuss some of the physical implications of the subcooled boiling flow velocity field measurements shown in Fig. 3. The liquid velocity field is discussed first.

The turbulence was found to be inhomogeneous and anistropic, which is to be expected. The azimuthal velocity fluctuation was not measured but, as in single-phase flow, the axial velocity fluctuation intensity was generally much higher than the radial velocity fluctuation intensity. This suggests that as in single-phase flow, turbulent energy is produced primarily in the axial fluctuation mode.

It has been suggested that two-phase flow turbulence is the result of nonlinear interaction between wall turbulence and bubble-induced pseudo-turbulence, the latter being perturbations due to random stirring of the liquid by the bubbles (Lance and Bataille, 1991) and deformation of their surface. It has been conjectured that these perturbations are proportional to the local vapor fraction and the square of the vapor bubble velocity relative to the liquid, and that they contribute directly to the normal Reynolds stresses only. Through dynamic interactions, they contribute to the Reynolds shear stresses.

The sign and magnitude of the radial gradient of the liquid mean axial velocity (i.e., the mean strain rate) in conjunction with the sign and magnitude of the axial Reynolds shear stress in the liquid have important implications vis-á-vis the production of turbulence. In experiment 1, these signs were such that production of turbulence could be expected across the annulus at the m.p. The axial Reynolds shear stress magnitude increased sharply near the inner wall where the vapor fraction was high, as was the radial gradient of liquid mean axial velocity. The turbulence energy production rate per unit fluid volume is

$$-\rho_L \alpha_L (\overline{uv})_L \frac{\partial \bar{U}_L}{\partial r}. \tag{2}$$

The high vapor fraction served to diminish the production rate, whereas the high Reynolds shear stress and mean strain rate augmented the production rate in the wall vicinity.

(a)

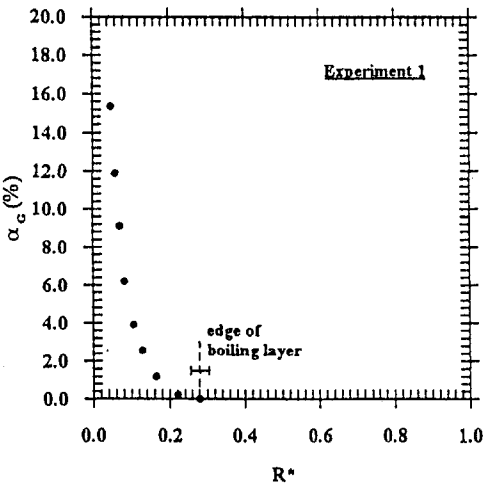

(b)

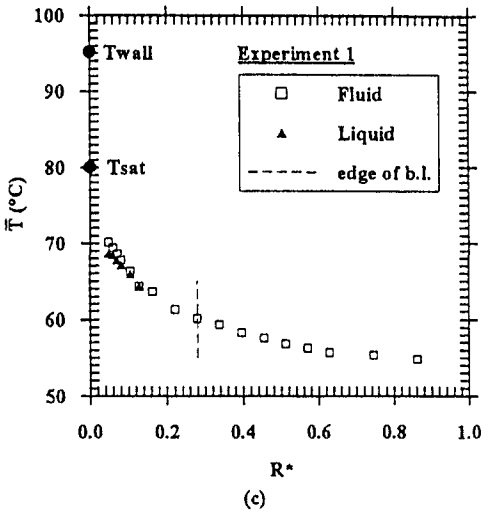

(c)

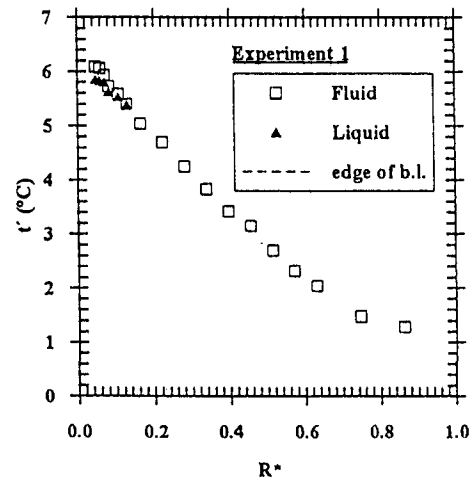

The turbulent energy dissipation rate would also be expected to increase near the inner wall. Invoking the analogy with single-phase flow, an estimate of the dissipation rate in the liquid per unit liquid mass may be obtained by (Tennekes and Lumley, 1972)

$$\epsilon_L \approx \frac{u_L'^3}{l} \tag{3}$$

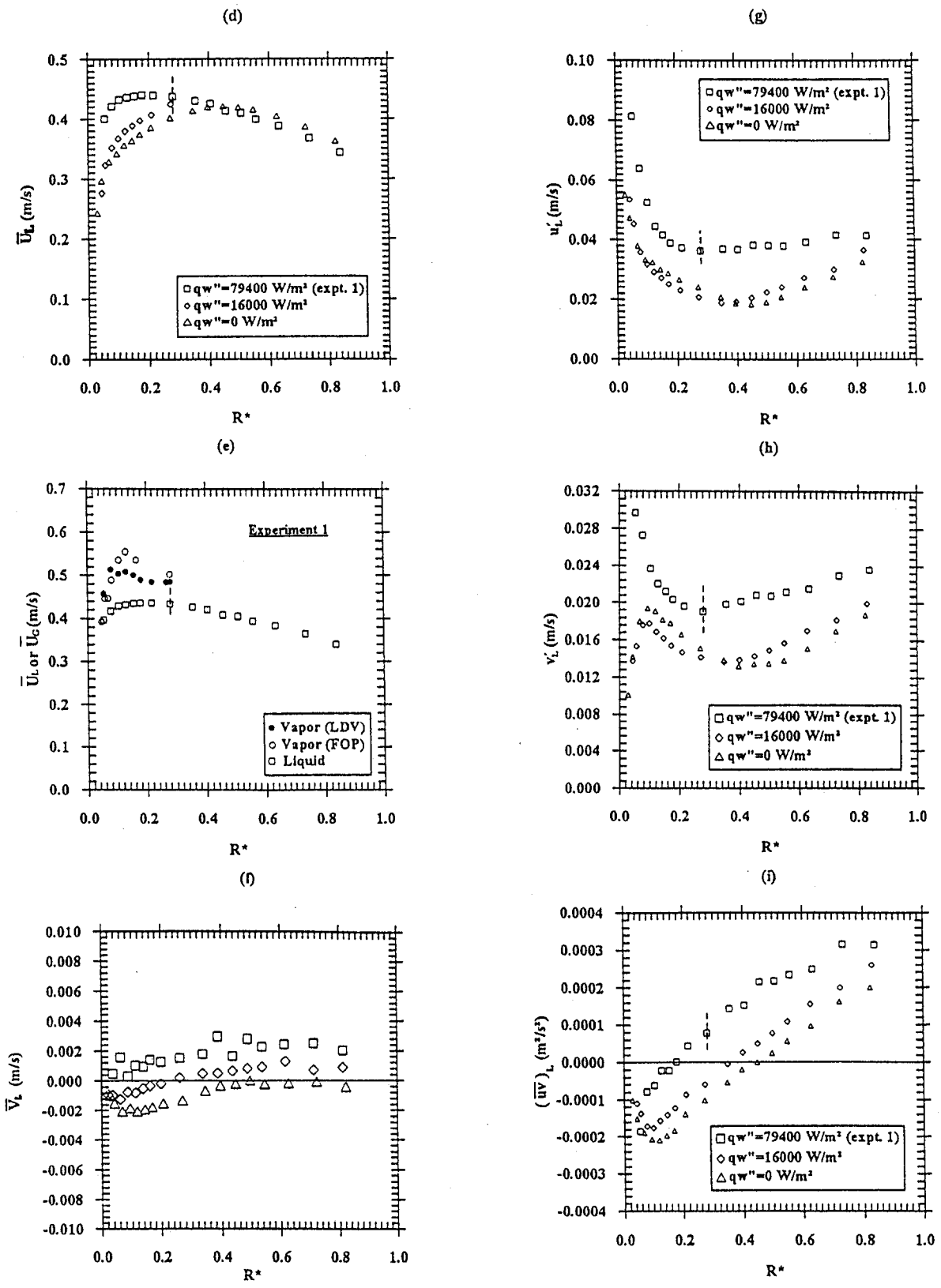

Fig. 3 Measurements—Experiment 1

where l represents the largest length scale of turbulence. Higher dissipation rates can thus be associated with the larger values of u'_L observed.

In the absence of azimuthal velocity fluctuation intensity measurement, the liquid turbulent kinetic energy per unit liquid mass may be estimated by assuming $w'^2_L \approx \frac{3}{2} v'^2_L$ (based on the isothermal air flow data of Brighton and Jones, 1964):

$$k_L \approx \frac{1}{2}(u'^2_L + 2.5\, v'^2_L). \tag{4}$$

An estimate of the characteristic turbulence length scale in the liquid may be obtained from (Wilcox, 1993)

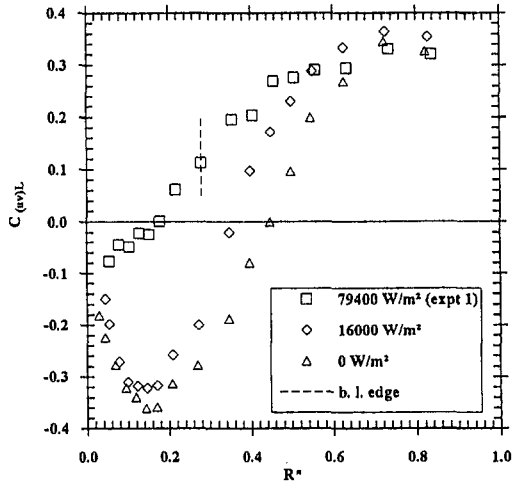

Fig. 4 Correlation coefficient $C_{(uv)_L}$—Experiment 1 and two single-phase liquid flows

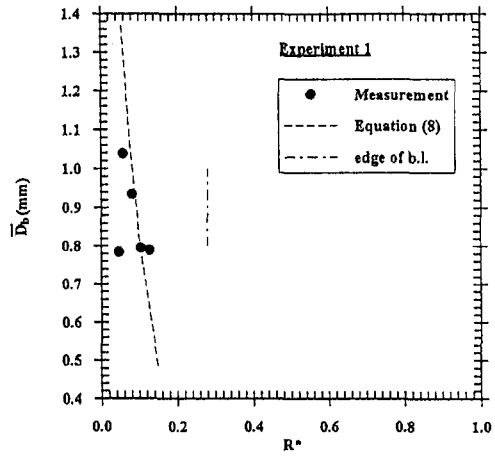

Fig. 5 Mean vapor bubble diameter—Experiment 1 and theoretical estimate

$$\Lambda_L \approx 0.09 \frac{k_L^{3/2}}{\epsilon_L}. \tag{5}$$

In the boiling layer, Λ_L was found to be of the order of 0.5 mm. The Kolmogorov length scale (Tennekes and Lumley, 1972)

$$\eta_L \approx \left(\frac{\nu_L^3}{\epsilon_L}\right)^{1/4} \tag{6}$$

was estimated to be of the order of 0.05 mm.[9] The latter length scale was smaller compared to that in the heated and unheated single-phase liquid flows. As such, turbulent energy would be expected to be present to higher frequencies in the boiling region and in at least portions of the all-liquid region. This has been demonstrated in air-water bubbly flow—for example, Lance and Bataille (1991).

The turbulence energy per unit volume of the fluid (vapor and liquid) may be approximated by

$$[\rho_L \alpha_L k_L + u_s \bar{a}_i] \tag{7}$$

neglecting the turbulent kinetic energy of the vapor phase. The first term in the above expression represents the turbulent kinetic energy of the liquid, and the second term the interfacial (bubble surface) energy (Serizawa and Kataoka, 1990). One may envision interchange between these two forms of energy. For instance, turbulent kinetic energy would be transferred to surface energy as a result of either bubble surface distortion or bubble splitting.

Herringe and Davis (1976) suggested a simple method of estimating the expected mean bubble diameter in isothermal gas-liquid flow in which it is assumed that the turbulence energy of the two-phase mixture is partitioned equally between the turbulent kinetic energy of the liquid and the interfacial energy. On this basis, one obtains

$$\bar{D}_b \approx \frac{6\sigma\alpha_G}{\rho_M k_L}. \tag{8}$$

We must keep in mind, however, that the situation is more complicated in boiling flow because of wall nucleation and evaporation/condensation at bubble surface. Nevertheless, it is interesting to compare the estimate obtained from Eq. (8) with the mean bubble diameter calculated from the measured probability density function of the diameter.[10] Figure 5 shows this comparison for experiment 1. While the agreement is reasonable in part of the boiling layer, the feature of smaller bubble diameter in the wall proximity found in our experiment is not captured by Eq. (8). Statistically meaningful bubble diameters could not be measured in the outer part of the boiling layer because the bubble passage rate was too low. As such, data for this region does not appear in Fig. 5.

In the remainder of this paper, measurements at the same m.p. are presented for experiments 2 through 4. The measurements have the same qualitative features as those of experiment 1. The radial distributions of liquid mean temperature, temperature fluctuation intensity, and mean radial velocity have not been included for reasons of brevity.

Figure 6(*a*) contains the vapor fraction radial profile for the three experiments.[11] This is followed by Fig. 6(*b*) in which the radial profile of liquid mean axial velocity is shown for five experiments: the three subcooled boiling flows; heated single-phase liquid flow at the same mass velocity, inlet temperature, and wall heat flux of 16,000 W/m^2; and isothermal liquid flow, also at the same mass velocity and inlet temperature.[12] The changes in the velocity profile brought about by boiling are qualitatively similar to those in experiment 1, Fig. 3(*d*). In the subcooled boiling flows, the liquid mean axial velocity within the boiling layer increased slightly as the extent of boiling increased at higher wall heat flux. Near the heated wall, the radial gradient of liquid mean axial velocity increased with increases in local vapor fraction. However, the location of maximum axial velocity did not change significantly in the three boiling flows. It is useful to view these liquid axial velocity profiles in conjunction with the corresponding vapor bubble mean axial velocity profiles, Figs. 6(*c*)–(*e*).

Examination of the vapor mean axial velocity distribution in Figs. 6(*c*)–(*e*) indicates that the maximum vapor axial velocity progressively increases with increases in wall heat flux (i.e., with increased vapor fraction in the boiling layer). However, the radial location of the maximum velocity did not change significantly.

Radial distributions of liquid axial velocity fluctuation intensity for experiments 2 through 4 are contained in Fig. 6(*f*). Also shown are the intensity distributions for the corresponding heated and isothermal single-phase liquid flows. The trends are generally similar to those in experiment 1, Fig. 3(*g*). Three

[9] The Kolmogorov length scale was not resolved in our LDV measurements.

[10] The mean bubble diameter is defined here to be the probability density function-weighted linear sum of all diameter values.

[11] These profiles were also given in Roy et al. (1994). They are included here for completeness of presentation.

[12] Mass balances for these five experiments were to within 1 percent.

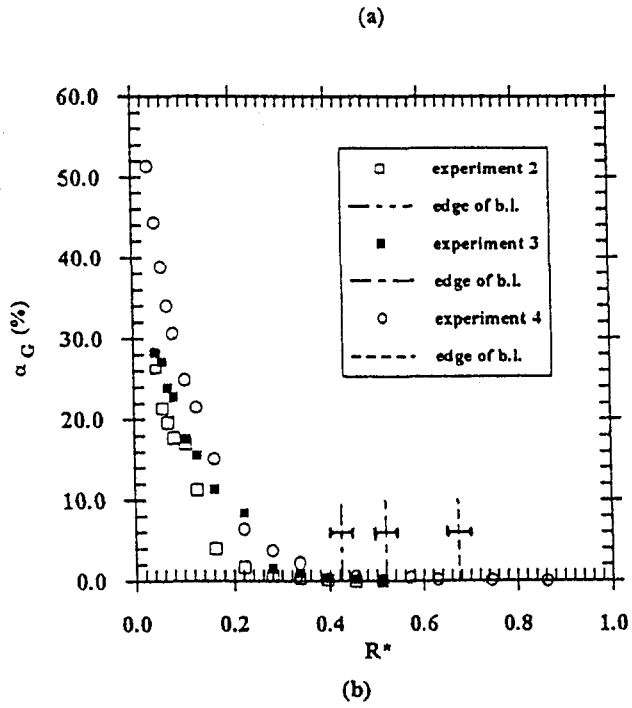

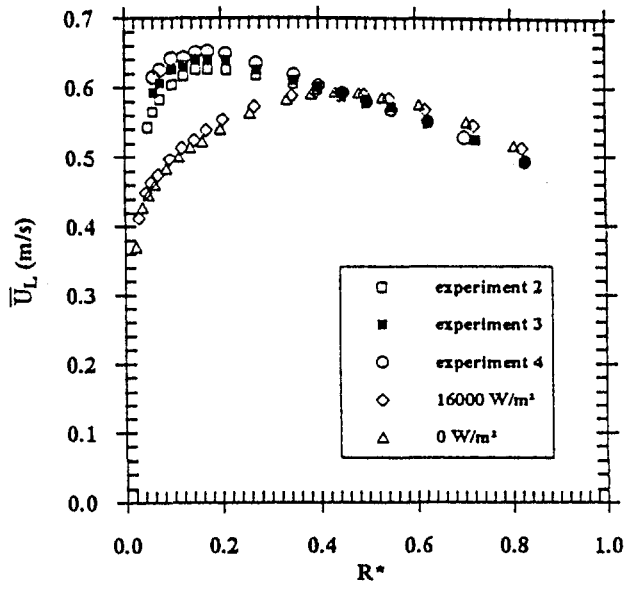

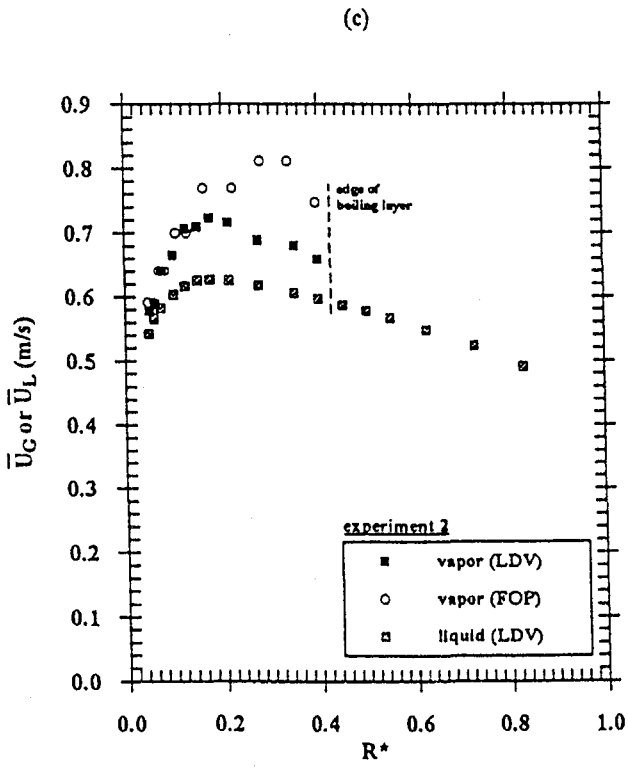

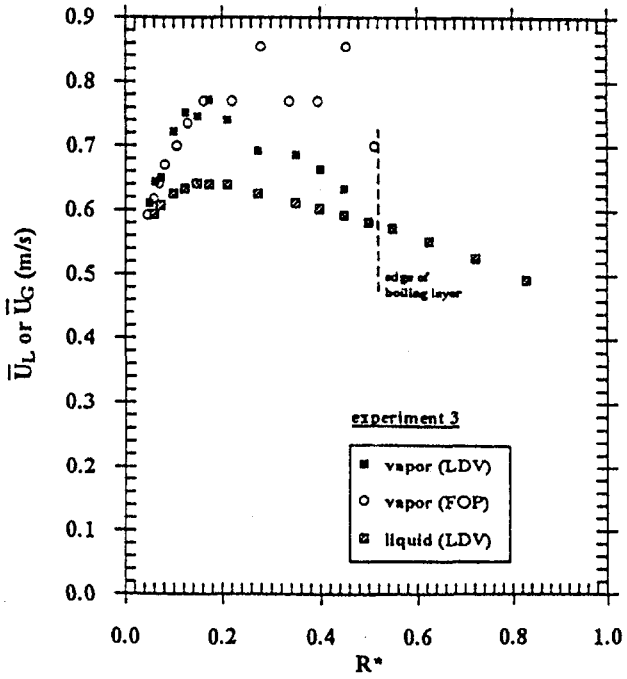

additional features should be pointed out: first, the intensity level increased from experiment 2 through experiment 4 across the boiling layer; second, the intensity became more uniform radially from experiment 2 through experiment 4; and third, the intensity profiles for the three experiments merged close to the heated wall.

In Figures 6(*g*)–(*i*) we present the radial profiles of vapor bubble axial velocity fluctuation intensity for experiments 2–4, respectively. The corresponding liquid axial velocity intensity profiles are shown for comparison. It is apparent that the vapor axial velocity intensity was significantly higher than the corresponding liquid velocity intensity. This is not surprising in view of the low inertia of the bubbles. The vapor velocity intensity was especially high in the higher vapor fraction region of the boiling layer, and increased with wall heat flux (i.e., with vapor fraction) in this region. The vapor velocity intensity approached the liquid intensity near the boiling layer edge. Local information on vapor bubble mean axial velocity, axial fluctuation intensity, and bubble passage frequency can be used to estimate the local, time-averaged interfacial area concentration $\bar{a}_i$ (Kataoka et al., 1986; Roy et al., 1994).

Figure 6(*j*) contains the radial profile of liquid radial velocity fluctuation intensity for the three subcooled boiling flows, the heated liquid flow, and the isothermal liquid flow. The radial intensity remained significantly lower than the axial intensity in each of these experiments. The three features pointed out earlier in the context of the liquid axial velocity intensity distribution, Fig. 6(*f*), are observable here as well.

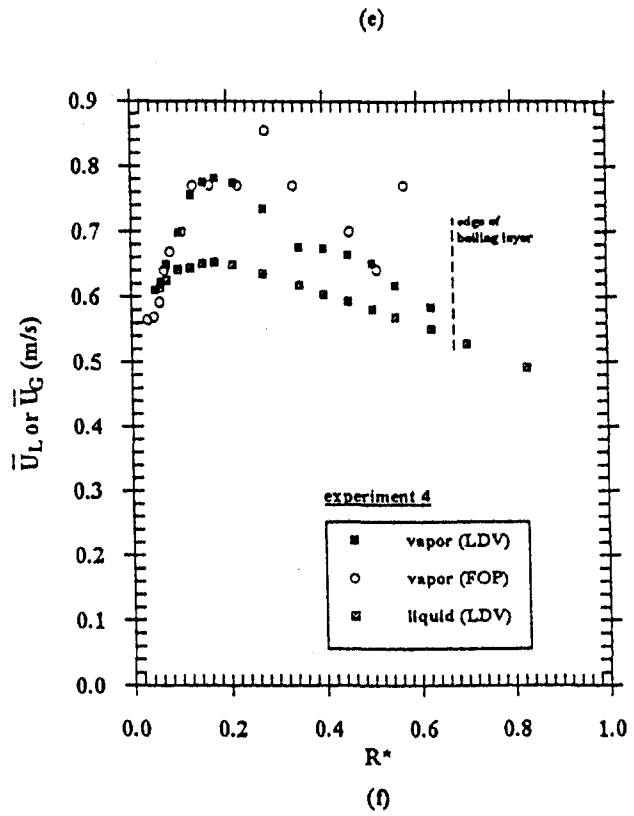

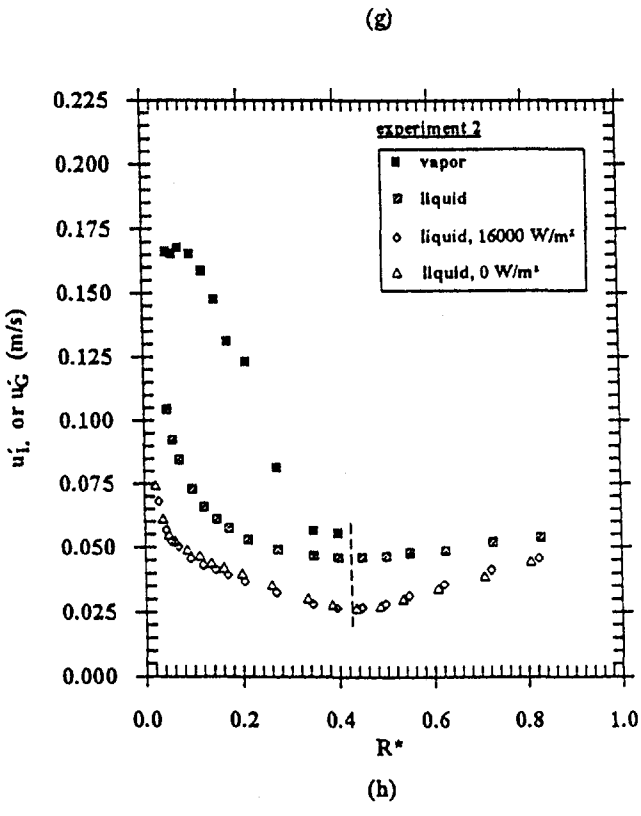

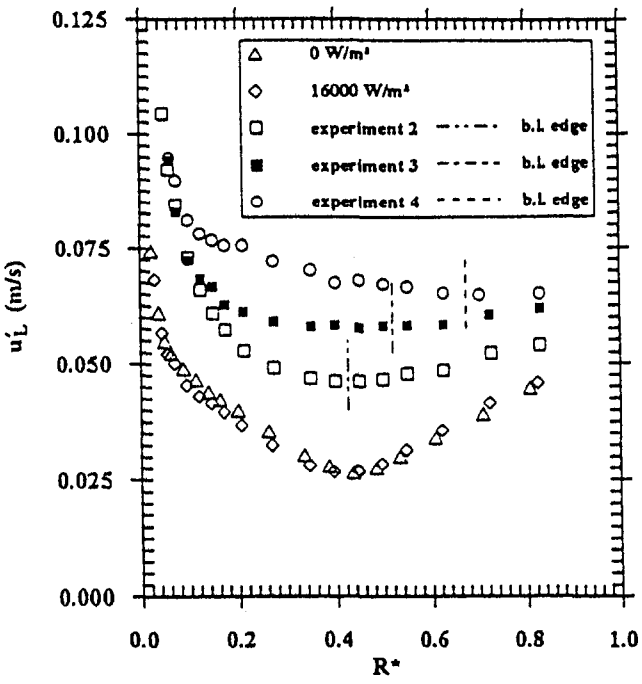

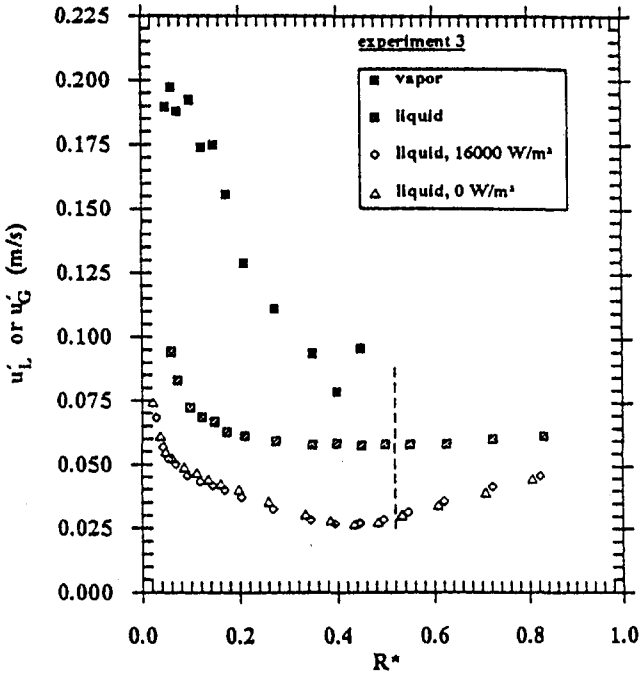

Figure 6(k) shows the radial distribution of $(\overline{uv})_L$ for experiments 2–4, the heated liquid flow, and the isothermal liquid flow. The main characteristics of the profiles for the three boiling flows are similar to those of experiment 1, Fig. 3(i). As the wall heat flux was increased, the zero shear stress location moved closer to the inner wall. The radial gradient of $(\overline{uv})_L$ became larger (i.e., the increase in the magnitude of $(\overline{uv})_L$ became sharper) near the inner wall and became progressively larger as the vapor fraction in this region increased with wall heat flux. The magnitude of $(\overline{uv})_L$ became higher in the region outside the zero shear stress location as the wall heat flux increased and the radial extent of the boiling layer became larger.

Comparison With the Calculations of a Multidimensional Two-Fluid Model

The experimental results have been compared with the calculations of a three-dimensional two-fluid model of turbulent subcooled boiling flow incorporated in the computer code ASTRID (Briere et al., 1995). This code has been under development

(i)

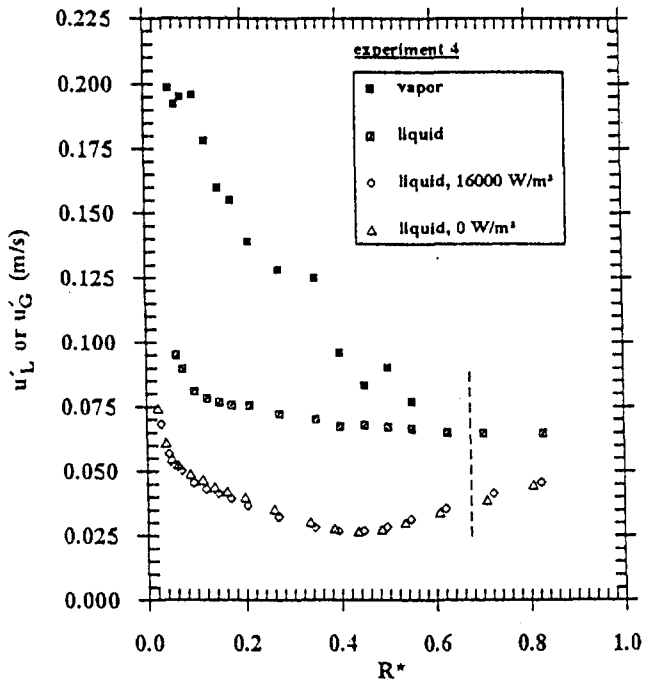

(j)

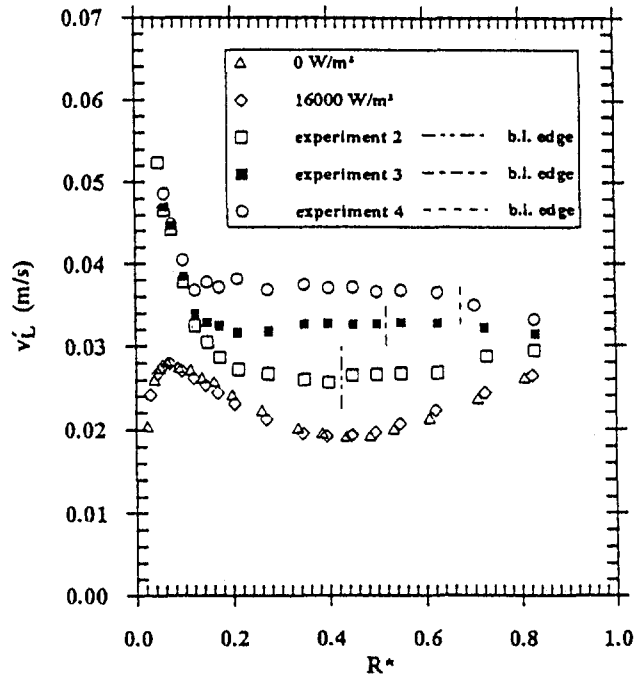

(k)

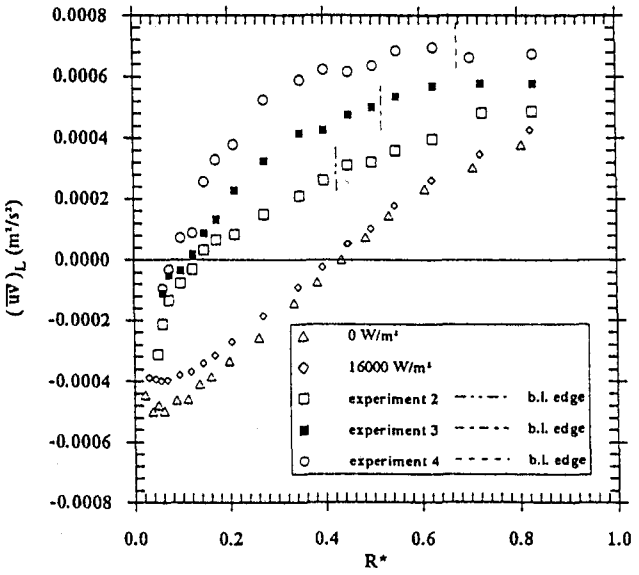

Fig. 6 Measurements—Experiments 2, 3, and 4

in the Two-Phase Flow Research Group of Electricité de France (EDF) during the past several years.

In the model, the averaged local field equations (mass, momentum, thermal energy) for each phase (vapor, liquid) are derived from the corresponding instantaneous local equations by density-weighted averaging (Ishii, 1975; Drew, 1983). These are complemented by the local interfacial balance equations for mass, momentum, and thermal energy. Closure relations are provided for the interfacial transfer rates of mass, momentum, and thermal energy as well as the turbulence terms in the field equations. The equations and closure relations can be found in Simonin and Viollet (1989), Thai Van et al. (1994), and Briere et al. (1995).

The model for the liquid phase turbulence is comprised of the transport equations for the per unit liquid mass turbulent kinetic energy (k_L) and kinetic energy dissipation rate ($\in_L$) in conjunction with the eddy diffusivity concept. Each transport equation is modified from the corresponding single-phase form of the equation by provision of an additional source term which embodies the influence of the vapor bubbles. The fluctuating motion of the bubbles is simulated by extending Tchen's theory of particle dispersion in turbulent flow.

The near-wall region is treated by the wall function approach. For the calculations reported here, a wall law concocted from our isothermal single-phase liquid flow data for the same annular channel (Velidandla et al., 1996b) is used at the inner wall proximity in lieu of one, as yet undetermined, which may be more appropriate for subcooled boiling flow:

$$u^+ = 2.63 \ln y^+ + 5.9. \quad (9)$$

This wall law corresponds to a Von Karman constant of 0.38. At the outer wall of the annulus, the standard wall law for pipe flow with Von Karman constant of 0.40 is adopted. The wall heat transfer model follows the approach of Kurul and Podowski (1991).

Space discretization follows a structured mesh with a collocated arrangement of velocity components. Either finite difference or finite volume method can be used in this code to obtain the discretized equations. The former method was chosen for the calculations reported here.

In our application, the flow through the annular channel is assumed to be a two-dimensional (r, z) mean flow.

Care needed to be taken in constructing the computational grid such that along any coordinate the ratio between consecutive grid sizes is in the 0.7–1.3 range. Also, the ratio between two grid sizes orthogonal to each other and sharing a node was no larger than 15. Furthermore, since a wall function is used, the normal distance between the wall and the first node in the fluid should be such that the corresponding $y+$ would be greater than 30. These criteria were met in our calculations and the results did not change perceptibly upon further grid refinement.

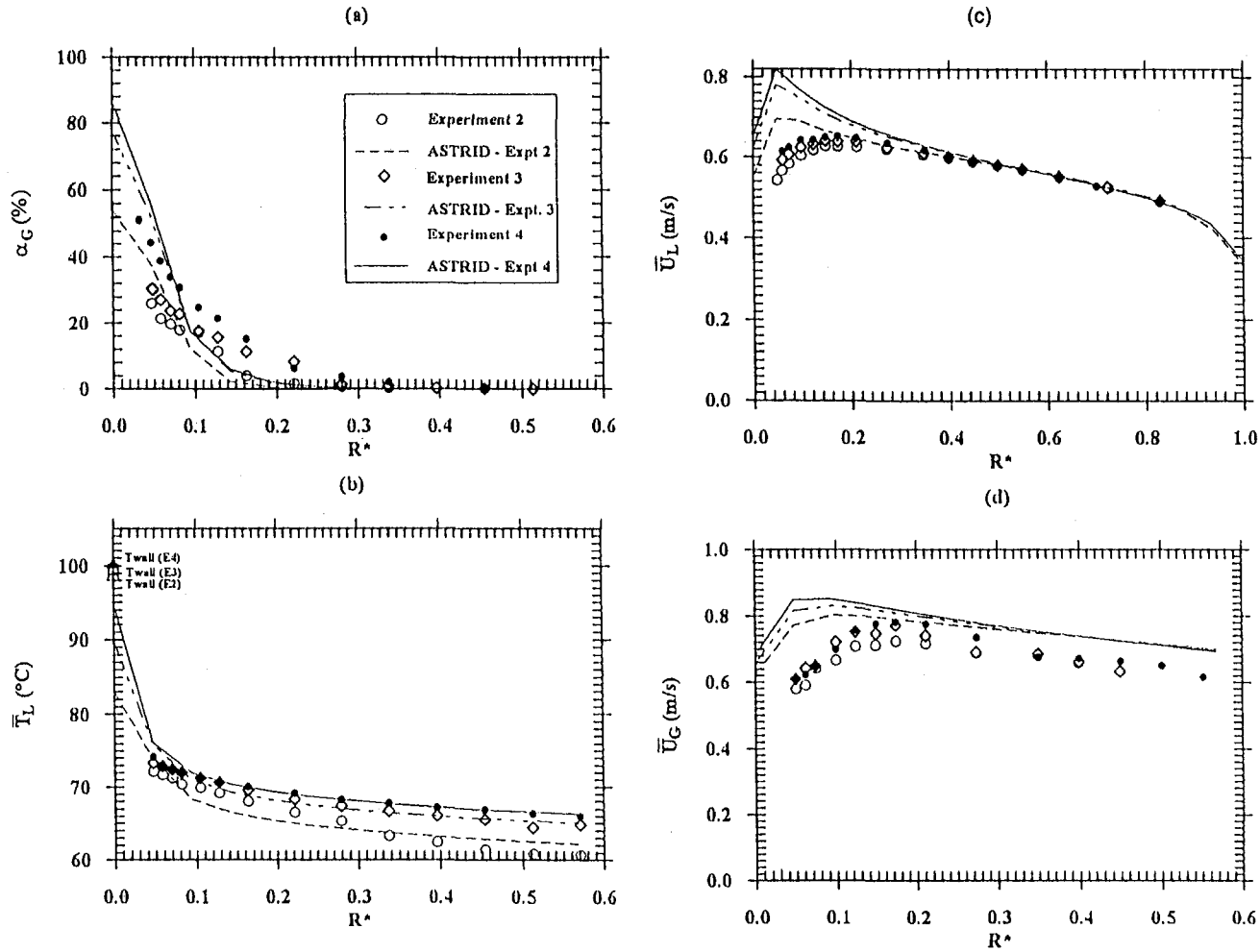

Fig. 7 Comparison of model calculations with measurements—Experiments 2, 3, and 4

For experiments 2, 3, and 4, Figs. 7(*a*)–(*d*) show, respectively, comparisons of vapor fraction, time-mean liquid and wall temperatures, liquid mean axial velocity, and vapor mean axial velocity calculations using ASTRID with our measurements. The agreement is reasonable away from the inner wall, but further work clearly remains to be done in modeling the near-wall velocity field and wall heat transfer.

Concluding Remarks

The measurements and calculations reported in this paper are one part of a continuing study of turbulent subcooled boiling flow. The study is motivated by the realization that a correct model for such flow can be developed only when its many complex features are properly understood.

Our measurements in a vertical annular channel indicate that the liquid velocity field in turbulent subcooled boiling flow is significantly different from the velocity field in turbulent single-phase liquid flow, heated or unheated, at comparable mass velocity. The mean axial velocity distribution is different and the turbulent kinetic energy is much higher in subcooled boiling flow. The zero crossing of the axial Reynolds shear stress occurs much closer to the heated inner wall and the shear stress magnitude increases sharply near the wall. Higher rates of turbulent energy production and dissipation would be expected in this region.

The liquid phase turbulence is inhomogeneous and anisotropic as in all turbulent shear flows. While bubble-induced pseudo-turbulence contributes to the overall turbulence measured, it is unclear how this contribution can be isolated.

Characterization of the near-wall distribution of the liquid-phase velocity field will require further study. It appears at this time that a wall law for the mean axial velocity akin to turbulent single-phase flow does not exist.

Numerical simulation of the subcooled boiling flow experiments by the multidimensional two-fluid code ASTRID (under development at EDF) yielded reasonable agreement with our measurements, except close to the heated inner wall. Further modeling work is in progress.

Acknowledgments

This research was partially funded by the National Science Foundation, Thermal Transport and Thermal Processing Program, Chemical and Thermal Systems Division under Grant No. CTS-9411898. Funding from the Electric Power Research Institute and Electricité de France is also gratefully acknowledged. Contributions were made to the experimental and numerical work by M. Capizzani and A. Zarate, graduate research assistants. Discussions regarding ASTRID models with Drs. E. Briere and D. Larrauri of EDF were most helpful.

References

Briere, E., Larrauri, D., and Olive, J., 1995, "ASTRID: A 3D Eulerian Software for Subcooled Boiling Flow Modeling—Comparison with Experimental Results in Tubes and Annuli," *Proceedings of Seventh International Topical Meeting on Nuclear Reactors Thermal-Hydraulics (NURETH-7)*, NURETH/CP-0142, Saratoga Springs, NY, Vol. 1, pp. 736–749.

Brighton, J. A., and Jones, J. B., 1964, "Fully Developed Turbulent Flow in Annuli," *ASME Journal of Basic Engineering*, Vol. 86, pp. 835–844.

Buchhave, P., George, W. K., and Lumley, J. L., 1979, "The Measurement of Turbulence with Laser-Doppler Anemometer," *Annual Review of Fluid Mechanics*, Vol. 11, pp. 443–503.

Drew, D. A., 1983, "Mathematical Modeling of Two-Phase Flow," *Annual Review of Fluid Mechanics,* Vol. 15, pp. 261–291.

Grossetête, C., 1995, "Experimental Investigation and Preliminary Numerical Simulation of Void Profile Development in a Vertical Cylindrical Pipe," *Multiphase Flow Conference,* Vol. 2, Kyoto, Japan, A. Serizawa, et al., eds., IF1.

Hasan, A., Roy, R. P., and Kalra, S. P., 1992, "Velocity and Temperature Fields in Turbulent Liquid Flow Through a Vertical Concentric Annular Channel," *International Journal of Heat and Mass Transfer,* Vol. 35, No. 6, pp. 1455–1467.

Herringe, R. A., and Davis, M. R., 1976, "Structural Development of Gas-Liquid Mixture Flows," *Journal of Fluid Mechanics,* Vol. 73, No. 1, pp. 97–123.

Hino, R., and Ueda, T., 1985a, "Studies on Heat Transfer and Flow Characteristics in Subcooled Flow Boiling—Part 1. Boiling Characteristics," *International Journal of Multiphase Flow,* Vol. 11, No. 3, pp. 269–281.

Hino, R., and Ueda, T., 1985b, "Studies on Heat Transfer and Flow Characteristics in Subcooled Flow Boiling—Part 2. Flow Characteristics," *International Journal of Multiphase Flow,* Vol. 11, No. 3, pp. 283–297.

Ishii, M., 1975, *Thermo-Fluid Dynamic Theory of Two-Phase Flow,* Eyrolles, Paris.

Kataoka, I., Ishii, M., and Serizawa, A., 1986, "Local Formulation and Measurements of Interfacial Area Concentration in Two-Phase Flow," *International Journal of Multiphase Flow,* Vol. 12, No. 4, pp. 505–529.

Kurul, N., and Podowski, M. Z., 1991, "On the Modeling of Multidimensional Effects in Boiling Channels," *ANS Proceedings,* Vol. 5, National Heat Transfer Conference, Minneapolis, MN, pp. 30–40.

Lance, M., and Bataille, J., 1991, "Turbulence in the Liquid Phase of the Uniform Bubbly Air-Water Flow, *Journal of Fluid Mechanics,* Vol. 222, pp. 95–118.

Marié, J. L., 1982, "Investigation of Two-Phase Bubbly Flows Using Laser-Doppler Anemometry," *PhysioChemical Hydrodynamics,* Vol. 4, No. 2, pp. 103–118.

Roy, R. P., Hasan, A., and Kalra, S. P., 1993, "Temperature and Velocity Fields in Turbulent Liquid Flow Adjacent to a Bubbly Boiling Layer," *International Journal of Multiphase Flow,* Vol. 19, No. 5, pp. 765–795.

Roy, R. P., Velidandla, V., Kalra, S. P., and Peturaud, P., 1994, "Local Measurements in the Two-Phase Region of Turbulent Subcooled Boiling Flow," ASME JOURNAL OF HEAT TRANSFER, Vol. 116, No. 3, pp. 660–669.

Serizawa, A., Kataoka, I., and Michiyoshi, I., 1975a, "Turbulence Structure of Air-Water Bubbly Flow—I. Measuring Techniques," *International Journal of Multiphase Flow,* Vol. 2, pp. 221–233.

Serizawa, A., Kataoka, I., and Michiyoshi, I., 1975b, "Turbulence Structure of Air-Water Bubbly Flow—II. Local Properties," *International Journal of Multiphase Flow,* Vol. 2, pp. 235–246.

Serizawa, A., Kataoka, I., and Michiyoshi, I., 1975c, "Turbulence Structure of Air-Water Bubbly Flow—III. Transport Properties," *International Journal of Multiphase Flow,* Vol. 2, pp. 247–259.

Serizawa, A., and Kataoka, I., 1990, "Turbulence Suppression in Bubbly Flow," *Nuclear Engineering and Design,* Vol. 122, pp. 1–16.

Sheng, Y. Y., and Irons, G. A., 1991, "A Combined Laser Doppler Anemometry and Electrical Probe Diagnostic for Bubbly Two-Phase Flow," *International Journal of Multiphase Flow,* Vol. 17, No. 5, pp. 585–598.

Simonin, O., and Viollet, P. L., 1989, "Numerical Study in Phase Dispersion Mechanisms in Turbulent Bubbly Flows," *International Conference on Mechanics of Two-Phase Flows,* Taipei, Taiwan (also, EDF Report HE 44/89-20).

Tennekes, H., and Lumley, J. L., 1972, *A First Course in Turbulence,* MIT Press, Boston, MA.

Thai Van, D., Minier, J. P., Simonin, O., Fredier, P., and Olive, J., 1994, "Multidimensional Two-Fluid Model Computation of Turbulent Dispersed Two-Phase Flows," *Proceedings of ASME FED Summer Meeting,* Lake Tahoe, NV, pp. 277–290.

Theofanous, T. G., and Sullivan, J., 1982, "Turbulence in Two-Phase Flows," *Journal of Fluid Mechanics,* Vol. 116, pp. 343–362.

Vassallo, P. F., Trabold, T. A., Moore, W. E., and Kirouac, G. J., 1993, "Measurement of Velocities in Gas-Liquid Two-Phase Flow Using Laser Doppler Velocimetry," *Experiments in Fluids,* Vol. 15, pp. 227–230.

Velidandla, V., Putta, S., and Roy, R. P., 1994, "LDV Measurement of Turbulent Liquid Velocity Field in Channels with Curved Walls," *International Communications in Heat and Mass Transfer,* Vol. 21, No. 6, pp. 765–773.

Velidandla, V., Putta, S., and Roy, R. P., 1996a, "Velocity Field in Isothermal Turbulent Bubbly Gas-Liquid Flow Through a Pipe," *Experiments in Fluids,* Vol. 21, pp. 347–356.

Velidandla, V., Putta, S., and Roy, R. P., 1996b, "Velocity Field in Isothermal and Heated Turbulent Liquid Flow Through a Vertical Annular Channel," *International Journal of Heat and Mass Transfer,* Vol. 39, No. 16, pp. 3333–3346.

Velidandla, V., 1997, "A Study of Turbulent Subcooled Bubbly Boiling Flow Using Laser Doppler Velocimetry," Ph.D. thesis, Arizona State University, Tempe, AZ.

Wang, S. K., Lee, S. J., Jones, Jr., O. C., and Lahey, Jr., R. T., 1987, "3-D Turbulence Structure and Phase Distribution Measurements in Bubbly Two-Phase Flow," *International Journal of Multiphase Flow,* Vol. 13, No. 3, pp. 327–343.

Wilcox, D. C., 1993, *Turbulence Modeling for CFD,* DCW Industries Inc.

Zarate, J. A., Capizzani, M., and Roy, R. P., 1997, "On Velocity and Temperature Wall Laws in a Vertical Concentric Annular Channel," *International Journal of Heat and Mass Transfer,* in press.

S. H. Najibi

H. Müller-Steinhagen
hms@surrey.ac.uk

Department of Chemical and Process Engineering, University of Surrey, Guildford, GU2 5XH, England

M. Jamialahmadi
University of Petroleum Industry, Ahwaz, Iran

Calcium Carbonate Scale Formation During Subcooled Flow Boiling

Scale deposition on the heat transfer surfaces from water containing dissolved salts considerably reduces fuel economy and performance of the heat transfer equipment. In general, this problem is more serious during nucleate boiling due to the mechanisms of bubble formation and detachment. In this study, a large number of experiments were performed to determine the effect of fluid velocity, initial surface temperature, and bulk concentration on the rate of calcium carbonate deposition on heat transfer surfaces during subcooled flow boiling. A physically sound prediction model for the deposition process under these operating conditions has been developed which predicts the experimental data with good accuracy. Two previously published models are also discussed and used to predict the experimental data.

Introduction

Evaporation of water containing dissolved salts is common practice in most concentration, crystallization and separation processes. In many desalination plants for the production of fresh water, sea water with high dissolved electrolyte content is evaporated. Fouling is one of the most expensive problems in these desalting units. This problem causes the efficiency of the evaporator to decrease drastically and limits the widespread production of large quantities of fresh water. Scaling can typically degrade the performance of heat exchangers by as much as 80 percent and can sometimes cause complete failure, as stated by O'Callaghan (1986). Therefore, it is important for designers and users of heat transfer equipment to understand the fundamental processes and parameters that affect the rate of fouling in heat exchangers.

Fouling is a function of time starting from zero and proceeding along some pseudoasymptotic or linear relationship. Using a constant value for the fouling resistance at the design stage, which is a common practice in designing heat exchangers, can predict what will happen to the heat exchanger performance but not when it will happen (Müller-Steinhagen, 1993). Thus, it is likely that the equipment will have to be taken out of service for cleaning at an inconvenient and economically undesirable time. Rational design procedures for a heat exchanger subject to fouling should allow not only the forecasting of how much fouling deposit will build up, but also the time and the extent to which this will happen (Sanatgar and Somerscale, 1991).

Calcium is the most common metal ion present in water. It exists in varying concentrations in virtually all natural waters (Wiechers et al., 1975) but is particularly evident in underground and surface waters derived from dolomitic areas and often in effluent from domestic and industrial areas. The presence of anions such as CO_3^{-2} in these waters will cause the formation of solid $CaCO_3$ if the ionic product $[Ca^{+2}].[CO_3^{-2}]$ exceeds the solubility product K_{SP}. Calcium carbonate has an inverse solubility in water and hence preferably crystallizes on heat transfer surfaces. The calcium carbonate layer imposes an additional barrier to heat transfer, i.e., a fouling resistance.

The main objective of this investigation was to study systematically the $CaCO_3$ fouling during subcooled flow boiling by measuring the overall heat transfer coefficient over a wide range of flow velocities, bulk, and initial heat transfer surface temperatures and fluid bulk concentrations. After clarification of the effect of these parameters on the deposition process, a predictive model for $CaCO_3$ fouling rates under subcooled flow boiling has been developed.

Contributed by the Heat Transfer Division for publication in the JOURNAL OF HEAT TRANSFER. Manuscript received by the Heat Transfer Division September 13, 1996; revision received February 24, 1997; Keywords: Boiling; Evaporation; Forced Convection; Fouling; Heat Exchangers; Multiphase Flows; Phase-Change Phenomena. Associate Technical Editor: S. H. Chan.

Previous Works

Several investigators have studied deposition mechanisms during forced convective heat transfer, but hardly any information is available on fouling during subcooled flow boiling. Oufer and Knudsen (1993) and Fetissoff (1982) investigated fouling during subcooled flow boiling of organic fluids. However, their results did not lead to any generalized conclusions and can not be applied for scale formation from aqueous solutions. Subcooled boiling can occur over a considerable length of the evaporator tubes and may represent up to 50 percent of the total heat duty (Wenzel, 1992). In this mode of heat transfer, vapour bubbles are generated at the heat transfer surface, while the bulk temperature of the liquid is still below the saturation temperature of the solution. Bubbles detaching from the heat transfer surface collapse and condense in the subcooled liquid bulk.

Hasson and Perl (1981) and Gazit and Hasson (1975) analyzed the mechanism of $CaCO_3$ scale deposition from a laminar falling film under evaporative nonboiling conditions. They presented theoretical models, taking into account the effects of water composition and hydrodynamic conditions. Based on the analysis of the experimental results they concluded that diffusional effects can be of importance even in thin-film flow.

Hasson et al. (1968) investigated calcium carbonate scale deposition on the surface of an annular constant heat flux exchanger. They examined the effect of parameters such as flow velocity, scale surface temperature, and water composition on scale growth by measuring the scale deposition rates and concluded that in the range of experimental parameters of their investigation, $CaCO_3$ deposition is mainly controlled by the diffusion of Ca^{+2} and HCO_3^- ions.

Chan and Ghassemi (1991) used conservation equations and surface reaction kinetics to model scaling of heat transfer surfaces by calcium carbonate. They conclude that using multispecies crystallization reaction rates in conjunction with their model predicts the calcium carbonate fouling rates with good accuracy.

Sheikholeslami and Watkinson (1986) studied the scaling of calcium carbonate on the surfaces of plain copper and mild steel heat exchanger tubes and on an externally finned mild steel tube.

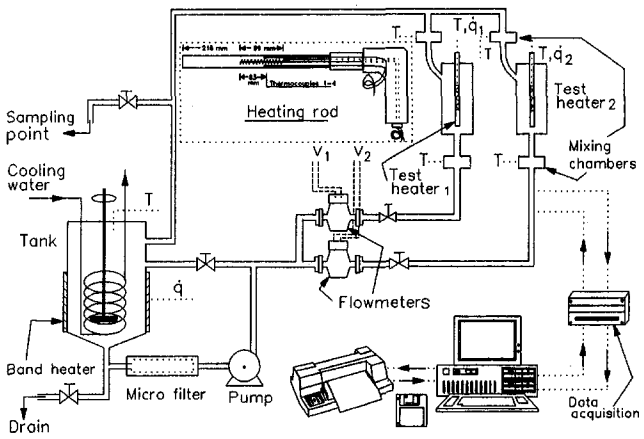

Fig. 1 Schematic drawing of test apparatus

In most of their experiments they observed a linear increase in R_f values with time under constant heat flux. It was found that the deposition rate is clearly higher on the plain tube at equal velocity and that for both steel tubes the rate generally decreases with increasing velocity for $V > 0.3$ m/s. They also mentioned that falling scaling rates with increasing velocity are commonly found where particulate fouling dominates or where deposits are fragile. Nevertheless, they used Hasson's ionic diffusion model to predict their experimental results, even though this model predicts increasing scaling rates with increasing velocity.

Watkinson and Martinez (1975) studied the effects of flow velocity and bulk temperature on calcium carbonate scaling on copper heat exchanger tubes under constant wall temperature conditions. They found that with increasing flow velocity, the fouling resistance first increases, then passes through a maximum, and finally decreases. At constant inlet temperature, tube diameter was found to have a weak effect on fouling resistance due to the difference in average liquid temperature as the diameter is changed. They used a model based on the models by Reitzer (1964) and Kern and Seaton (1959) and added a removal term to correlate their results.

Experiments

Test Rig. Measurements were performed in a flow boiling apparatus as shown in Fig. 1. A detailed description of the test rig is given by Wenzel (1992). To prevent corrosion, all wetted parts were manufactured from stainless steel. Boiling occurred at the outside of the heater rods with the following dimensions:

diameter of heating rod	1.067 cm
annular gap	1.473 cm
length of heating rod	40.0 cm
length of heating section	10.0 cm

Each test heater consists of two concentric tubes with close tolerances. A miniature stainless-steel sheathed resistance heater is fitted into the center of the inner tube. Four stainless-steel sheathed E-type thermocouples are embedded along the circumference of the inner tube. Boiling measurements with distilled water reproduced published data within ±7 percent.

A microcomputer-controlled data acquisition system was used to measure pressure, flow velocity, heat flux, and temperatures at given time intervals. The power supplied to the test heaters is calculated from the measured current and voltage drop. The average of five readings was used to determine the difference between the wall and bulk temperature for each thermocouple. The temperature drop between the location of the wall thermocouples and the heat transfer surface was deducted from the measured temperature differences according to

$$T_s - T_b = (T_{TC} - T_b) - \frac{S}{\lambda}\dot{q}. \tag{1}$$

The average wall superheat was the arithmetic average for three thermocouple locations. The remaining wall thermocouple was used for control purposes. The heat transfer coefficient α was then calculated from

$$\alpha = \frac{\dot{q}}{T_s - T_b}. \tag{2}$$

The temperature measurements were accurate within ±0.2K and error involved in the heat flux measurement was ±2 percent. Based on the definition of the fouling resistance (Eq. 7), this means that its uncertainty varies between infinity at the beginning of the experiment and about 7 percent at the end, if the ASME procedures for error analysis are used.

Experimental Procedure. A 55 litre charge of calcium carbonate solution with predetermined concentration was placed in the supply tank. The pump was switched on and the test rig

Nomenclature

C = concentration, kg/m^3
d = diameter, m
D = diffusivity, m^2/s
E = activation energy, J/mole
f = friction factor
F = coefficient in Chen model
K = specific reaction rate constant
k = radius ratio of rod heater to outer tube
km = Von Karman constant (=0.418) in Eqs. (22) and (23)
K_{sp} = solubility product mol^2/ltr^2
n = rate of mass deposited, kg/m^2.s
n = exponent in the Eq. (8)
NBF = nucleate boiling fraction defined in Eq. (10)
q = heat flux, W/m^2
R = universal gas constant J/mol.K
R_A = reaction in bulk of liquid
R = radius of annulus, m
Re = Reynolds number
R_f = fouling resistance, m^{2}K/W
S = suppression factor in Chen model
s = distance between thermocouple location and heat transfer surface, m
Sc = Schmidt number
T = temperature, K
t = time, s
V = fluid velocity, m/s

Greek symbols

α = heat transfer coefficient, W/m^2.K
β = mass transfer coefficient, m/s
γ = concentration effect in Eq. (15)
λ = thermal conductivity, W/m.K
λ = zero shear stress location in annulus, defined in Eq. (24)
ρ = density, kg/m^3
τ = shear stress, N/m^2

Subscripts/Superscripts

aq = aqueous bulk
bub = bubble
d = deposit
eq = equivalent
f = fouling
fb = flow boiling
fc = forced convective
g = gas
i = interphase
nb = nucleate boiling
S = solid
S = surface
TC = thermocouple
* = saturation

Table 1 Range of operating parameters

Velocity m/s	Bulk temperature °C	Initial Surface temperature °C	Solution $[Ca^{++}]$ mol/l	pH
0.6-1.8	80	105-120	0.0035 - 0.0075	7.2-7.7

left to equilibrate at a selected bulk temperature and flow velocity. After steady-state conditions were reached, a sample of the solution was taken. Then the selected heat flux, initial surface temperature, or difference between bulk and initial surface temperature were adjusted, and the experiment started. All temperatures and flow velocities were recorded with a personal computer in connection with a data acquisition system. For safety reasons, the fouling runs were terminated once the surface temperature of the heater exceeded 170°C. The concentration of calcium ions, the total alkalinity, and the pH of the solution were measured at the beginning and at the end of each run, and the average values were used for the calculations. Total alkalinity was measured by titration with a dilute solution of hydrochloric acid, and the calcium concentration was determined by EDTA titration (Skoog et al., 1992). All chemicals used in this investigation had a purity above 99 percent. Solutions were prepared for each run by dissolving the respective salts in distilled water and allowing it to stand for about 12 hours. The range of the experimental parameters is given in Table 1.

Test solutions. In this investigation, calcium carbonate was used as solute. Due to the hardness and adhesion characteristic of $CaCO_3$, it is expected that any removal of deposit would be insignificant (Hasson et al., 1968). Calcium carbonate crystals exist in three forms: aragonite, calcite, and vaterite. All three forms of this salt have an inverse solubility with temperature, as shown in Fig. 2 (Plummer and Busenberg, 1982). Therefore, the saturation concentration will decrease near the heated surface. If the concentration of the solution exceeds the equilibrium concentration, crystallization will occur.

Since calcium carbonate crystals do not dissolve easily in water, calcium nitrate $Ca(NO_3)_2.4H_2O$ and sodium carbonate Na_2CO_3 were dissolved in water, resulting in calcium carbonate crystallizing on the heat transfer surface. The dissociation of the various ionic species of sodium carbonate in water are quite sensitive to the pH of the solution. In the present analysis, pH of the solutions were low (i.e., pH < 8.5) so that most of the dissolved carbonate ions are in the form of bicarbonate HCO_3^- (Wahl, 1977). The bicarbonate ions undergo the following equilibrium reaction in the vicinity of the heated surface (Hasson et al., 1968):

$$2HCO_3^- \rightarrow H_2O + CO_2(aq) + CO_3^{-2}. \quad (3)$$

The CO_3^{-2} species produced in this reaction react with Ca^{+2},

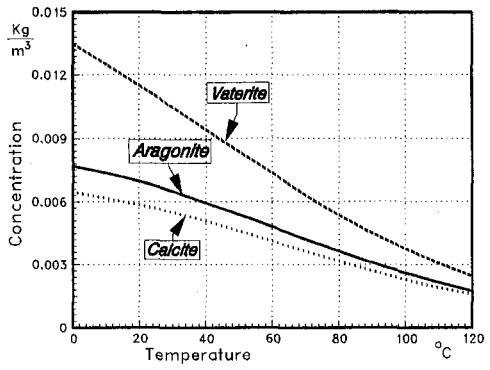

Fig. 2 Solubility of calcium carbonate in water as a function of temperature

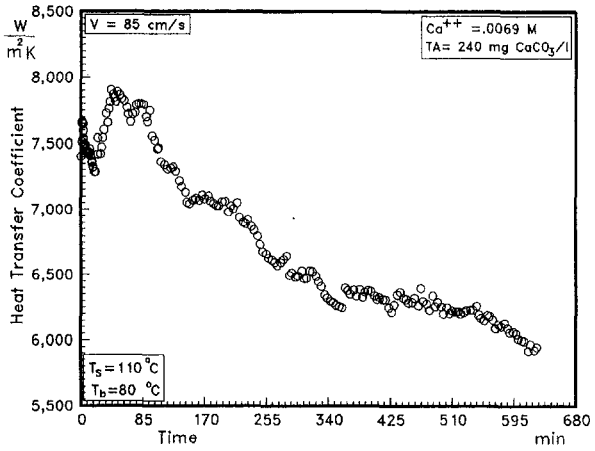

Fig. 3 Typical variation of heat transfer coefficient with time

which has been transported to the surface, to form a $CaCO_3(s)$ deposit on the heat transfer surface.

In studies of $CaCO_3$ deposition, the equilibrium of the H_2O-CO_2 system is usually considered (Chan and Ghassemi, 1991). Knowing the pH of the solution, total alkalinity and the dissociation constants for carbonic acid, the concentration of CO_3^{-2} can be calculated from the following equation:

$$[CO_3]^{-2} = \frac{\text{T.A.} - [OH^-] + [H^+]}{\left[2 + \frac{[H^+]}{K_2}\right]} \quad (4)$$

where T.A. is the total alkalinity of the solution which is defined as

$$\text{T.A.} = [HCO_3^-] + 2[CO_3^{-2}] + [OH^-] - [H^+]. \quad (5)$$

K_2 is the second dissociation constant of CO_2 in water, defined by the following equation:

$$K_2 = \frac{[CO_3^{-2}][H^+]}{[HCO_3^-]}. \quad (6)$$

Experimental Results

A series of experiments was designed to investigate the effect of operating parameters such as fluid velocity, initial surface temperature, and bulk concentration on fouling rates during subcooled flow boiling. The overall heat transfer coefficient was measured in each run for time periods up to 10 hours. Figure 3 shows typical measurements as a function of time. The shape of the measured heat transfer coefficient versus time curve is characterized by a sharp decrease in heat transfer coefficient at the beginning of the operating time, followed by steep increase and subsequent gradual decrease. The increase in heat transfer coefficient at the early stage of fouling is thought to be due to the increase in the number of bubble nucleation sites generated by the deposit (Jamialahmadi and Müller-Steinhagen, 1993). Additional nucleation sites increase the turbulence level in the zone near the heat transfer surface and, therefore, improve the heat transfer coefficient until the insulation effect of the growing deposit becomes dominant. A fouling curve shows the relationship between the thermal resistance of the fouling deposit and the time. The shape of the fouling curves is indicative of the phenomena occurring during the fouling process. A typical measured fouling curve in the subcooled flow boiling regime is shown in Fig. 4. The fouling resistances were calculated from the heat transfer coefficients at the beginning of each experiment and the actual heat transfer coefficients after a certain operational period, according to the following equation:

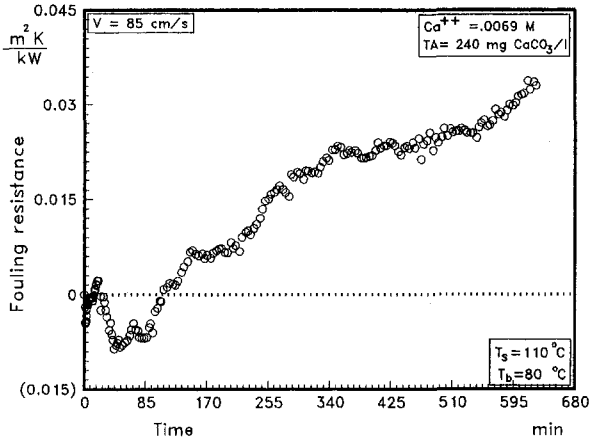

Fig. 4 Typical variation of fouling resistance with time

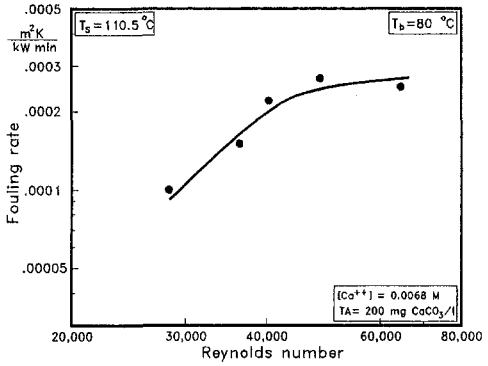

Fig. 6 Fouling rates as a function of Reynolds number

$$R_f = \frac{1}{\alpha(t)} - \frac{1}{\alpha(t=0)}. \quad (7)$$

After a slight improvement at the beginning of some runs, almost all curves show a linear increase in fouling resistance with time. A linear relationship is characteristic for adherent deposits and indicates that the deposition rate is constant and that there is no removal.

Effect of Flow Velocity on Fouling. Many studies have attempted to determine the effect of flow velocity on scale formation during forced convective heat transfer. The laminar sublayer which forms next to the heat transfer surface has a strong effect on the fouling characteristics. The thickness of this layer is strongly affected by flow velocity; temperature and degree of supersaturation are different from those in the fluid bulk. The mechanism of fouling on the heat transfer surface can be controlled either by molecular diffusion within this film or by chemical reaction at the heat transfer surface, or by both mechanisms. It is generally believed that if fouling is not influenced by diffusional mass transfer, the fouling rate should be independent of the flow velocity if the fouling surface temperature remains constant. According to the work of Hasson et al. (1968) crystallization fouling of calcium carbonate under forced convective conditions is mass transfer controlled.

The effect of fluid velocity on the fouling resistance is shown in Fig. 5 for constant initial surface and bulk temperature. For all velocities, the fouling curves show an almost linear increase in fouling after the initial period of the experiments when surface nucleation effects are dominant. To determine the controlling mechanism, the effect of velocity on scale growth rate was evaluated over the range of 70 to 160 cm/s for constant supersaturation and constant bulk and initial surface temperatures. The results are plotted as a function of Reynolds numbers in Fig. 6. At low fluid velocities, the mass transfer boundary layer thickness is still large and, therefore, molecular diffusion has a significant effect on the fouling rate. As the fluid velocity is increased, the boundary layer thickness is decreased and the mass transfer across the boundary layer no longer affects the fouling rate, which means the fouling process is more controlled by the chemical reaction at the surface.

The above considerations apply for convective, single-phase heat transfer. During subcooled flow boiling, parts of the heat transfer surface are covered with growing vapor bubbles, depending on the surface temperature or heat flux. It can be assumed that the fouling process in the vicinity of these emerging bubbles is reaction controlled due to the agitation of the liquid layer close to the heat transfer surface by the vapor bubbles.

Effect of Fouling Surface Temperature. The variation in fouling resistance with initial surface temperature at constant bulk temperature and concentration is shown in Figs. 7 and 8 for two different liquid velocities. The heat transfer surface temperature has only a small effect on the fouling rate at 90 cm/s, but a significant effect at 140 cm/s. This is in agreement with the conclusions about the controlling mechanisms discussed in the previous section. Reaction-controlled fouling (high flow velocities and/or high bubble densities) is strongly affected by the surface temperature. Diffusion-controlled fouling (low flow velocities and low bubble densities) also increases with surfaces temperature as a result of the decreasing solubility of $CaCO_3$ and the increasing mass transfer coefficients, but this effect is considerably less pronounced.

Effect of Bulk Concentration. The primary cause of fouling is supersaturation. When the solubility product of Ca^{2+} and CO_3^{-2} ions exceeds its solubility value, $CaCO_3$ precipitates and

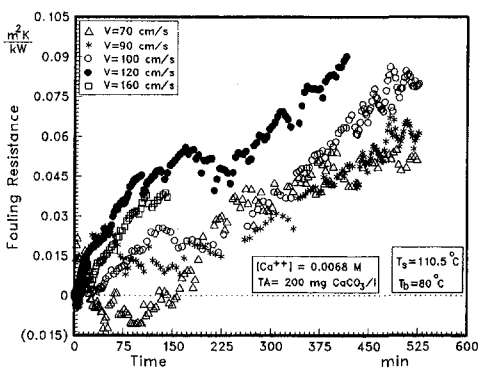

Fig. 5 Effect of flow velocity on the fouling resistance

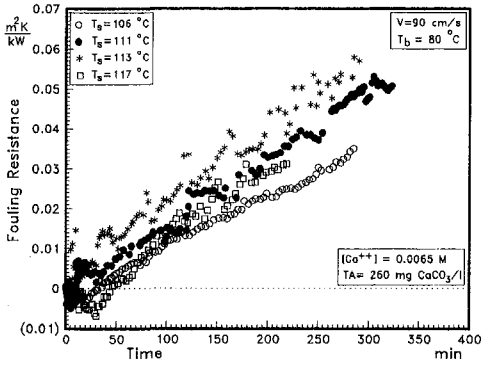

Fig. 7 Fouling resistances as a function of time showing the effect of surface temperature at lower velocities

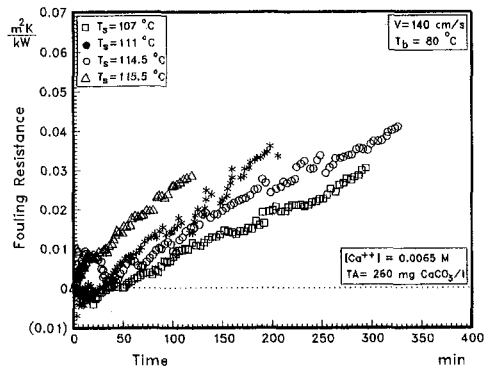

Fig. 8 Fouling resistances as a function of time showing the effect of surface temperature at higher velocities

forms scale. When the removal rate can be ignored, the rate of deposition is usually expressed in the following form:

$$\dot{m} = k(C_b - C^*)^n. \tag{8}$$

For diffusion-controlled fouling, n is equal to 1, for reaction-controlled fouling, n is reported to be equal to 2 (Hasson and Perl, 1981; Hasson et al., 1968). Equation (8) shows that regardless of the mechanism of fouling, the effect of concentration is strong and it should be more pronounced under reaction-controlled condition. The effect of $CaCO_3$ bulk concentration at constant bulk and initial surface temperature is shown in Fig. 9.

Correlation of Data

Most boiling heat transfer models divide the total heat transfer surface into two parts (Lorenz et al., 1974; Mikic and Rohsenow, 1969; Shoukri and Judd, 1987); namely, the area affected by active nucleation sites, and the remaining heat transfer area which is controlled by the forced convective heat transfer mechanism. Chen (1966) suggested an additive correlation combining the convective and nucleate boiling contributions to flow boiling heat transfer that has been accepted as one of the best available correlations for pure fluids and mixtures. In its basic form, it is expressed as

$$\alpha_{fb} = \alpha_{fc}F + \alpha_{nb}S \tag{9}$$

where α_{fc} is the convective heat transfer coefficient which would be found for the liquid phase flowing alone, and α_{pb} is the nucleate pool boiling heat transfer coefficient depending on the wall superheat. In Eq. (9), S is a "suppression factor" to account for the decrease in nucleate boiling as forced convective effect are increased. The parameter F accounts for the effective increase in liquid velocity due to the presence of the vapour

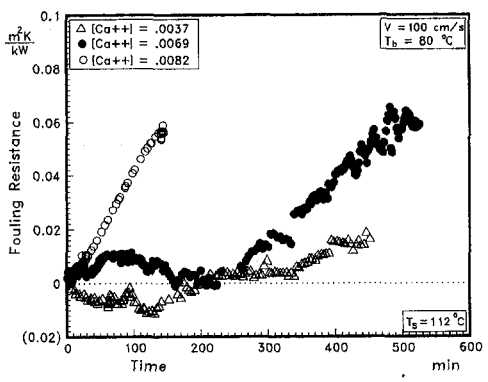

Fig. 9 Effect of $CaCO_3$ bulk concentration on fouling resistance

Table 2 Operating conditions in some of the fouling experiments

Run ID	Initial Surface Temp.°C	Bulk Conc. mol/l	Velocity cm/s	NBF (10)	ß·10⁵ m/s (36)
171	111	.0064	70	13	11.03
172	111.8	.0069	100	8.9	15.09
173	110.4	.0069	120	5.5	17.31
174	110	.0072	160	0.6	21.99
175	109.16	.0069	140	1.5	19.42
176	112.25	.0068	90	5.5	13.88
177	112.4	.0065	90	9	13.91
179	119	.0054	90	16.4	15.10
1710	113.12	.0069	120	4.2	17.92
1711	111	.004	120	4.9	17.44
1712	111.1	.0037	100	8.9	14.96
182	110	.0069	90	12.5	13.48
184	111.6	.0072	70	7.1	11.12
186	113.18	.0068	140	4.1	20.45
187	110.14	.0065	140	1.9	19.67
188	107	.0071	140	0.2	18.88
189	114	.0054	140	4.3	20.66
1810	116	.0069	140	5.3	21.19
1811	109.4	.004	70	6	10.81

phase and is a function of the Martinelli parameter (Chen, 1966). The complete set of equations as applicable for the prediction of local subcooled flow boiling heat transfer coefficients is given by Collier (1984). This calculation procedure has been generally accepted as one of the best available for pure fluids under saturated and subcooled conditions. It has been shown recently that it can also be used to predict heat transfer coefficients for subcooled liquid mixtures (Wenzel, 1992). The Gnielinski (1986) equation is used to calculate α_{fc}, and the Gorenflo (1988) correlation to calculate α_{nb}. The Chen (1966) model is used in this investigation to develop a model for prediction of fouling rates. The fraction of heat transferred by nucleate boiling as predicted by this model is defined by Branch (1991) as

$$\text{NBF} = \frac{\alpha_{nb}S}{\alpha_{fb}} \tag{10}$$

This parameter may be interpreted as a measure of the percentage of the heat transfer area affected by nucleate boiling. The calculated values for this parameter for some of the present fouling runs are given in Table 2.

Fouling of the heat transfer surface during subcooled flow boiling is a combination of the following two mechanisms:

1 In the area which is affected by the vapour bubbles, fouling occurs mainly due to the mechanism of bubble formation and microlayer evaporation.
2 In the remaining area fouling takes places by forced convective mechanisms.

As shown by Han and Griffith (1965), the area from which the superheated layers is pumped away by a bubble is πd_b^2. As shown in Fig. 10, both of the above mechanisms occur in parallel in separate zones of the heat transfer surface. Therefore, the overall fouling rate can be presented by the following equation:

$$\frac{\partial R_f}{\partial t}(\rho_d \lambda_d) = \text{NBF} \cdot \dot{m}_{nb} + (1 - \text{NBF}) \cdot \dot{m}_{fc}. \tag{11}$$

Where NBF is the nucleate boiling fraction, which can be calculated from Eq. (10) in conjunction with the Chen model. As the heat flux increases, the number of active nucleation sites

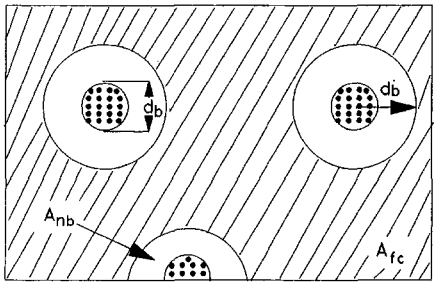

Fig. 10 Areas affected by nucleate boiling and forced convection

increases and Eq. (11) predicts that the fouling caused by the boiling mechanism will increase.

Prediction of $\dot{m}_{nb}$. In the boiling zones, vapour bubbles emerge from distinct nucleation sites and their number increases with heat flux. Because of the high level of turbulence created by the departure of the vapour bubbles from the nucleation sites and the rapid evaporation of liquid beneath the vapour bubbles, it seems reasonable to assume that the deposition reaction is rate controlling in the boiling zones. The reaction controlled scaling rate of calcium carbonate is usually correlated by a second order reaction as follows:

$$\dot{m}_{nb} = K_1([Ca^{++}]_{bub} - [Ca^{++}]^*)^2. \quad (12)$$

Where $[Ca^{++}]_{bub}$ is the concentration of the calcium ions beneath the bubbles, and the temperature dependence of the reaction rate constant follows an Arrhenius type equation:

$$K_1 = K_{1,0}e^{-E/RT_s}. \quad (13)$$

Electron Scanning Microscopy revealed that more than 99 percent of the deposited calcium carbonate found in this investigation was in the form of aragonite, the solubility of which was studied in detail by Plummer and Busenberg (1982) and other investigators (Rau, 1982; Wiechers et al., 1975). The equilibrium concentration of calcium, $[Ca^{++}]^*$, is given by the square root of the solubility product, K_{sp}, of aragonite, which is given by the following equation (Plummer and Busenberg, 1982):

$$\log(K_{sp}) = -171.9773 - 0.077993*T + \frac{2903.293}{T} + 71.595*\log T \quad (14)$$

where K_{sp} is in molar units, and T is the absolute temperature in degree Kelvin.

Concentration Beneath the Vapour Bubbles. Figure 11 shows a bubble growing from a nucleation site on the heat transfer surface. Heat transfer to the boiling liquid occurs by three mechanisms (Jamialahmadi et al., 1989): forced convection to the liquid; conduction through and evaporation of a liquid microlayer between bubble and heat transfer surface; and heat transfer from the superheated liquid boundary layer to the vapour bubble. Of these mechanisms, only microlayer evaporation can cause a significant increase in the foulant concentration beneath the bubble. Therefore, the concentration of ions beneath the bubbles can be written in terms of bulk concentration as

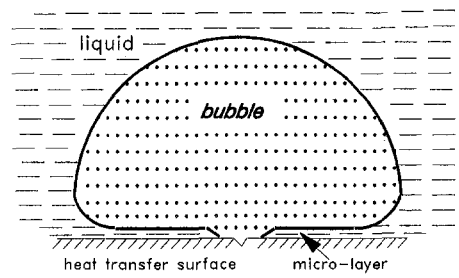

Fig. 11 Bubble growing at heat transfer surface

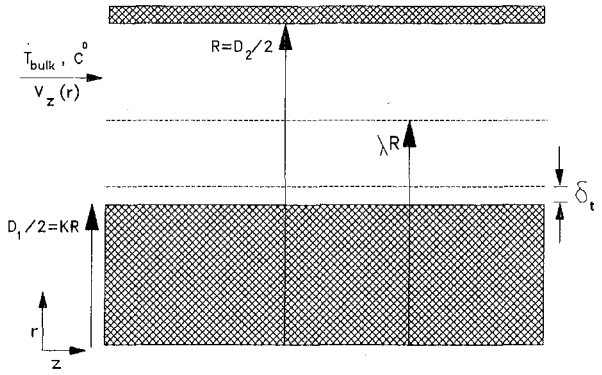

Fig. 12 Geometry of the annular test section

$$C_{bub} = \gamma C \quad (15)$$

Where γ is the concentration effect in the microlayer, which is difficult to predict exactly. An estimation for the concentration of ions in the microlayer can be made by assuming that all the vapour is supplied to the bubble by the vaporization of liquid from the microlayer. Al-Hayes and Winterton (1981) and Wenzel (1992) measured the bubble departure diameter in subcooled flow boiling of water and reported that it does not exceed 3 mm. Using this value for the bubble departure diameter and 2 μm for the thickness of the microlayer, which was reported by Moore and Mesler (1961) for a hemispherical bubble, the concentration multiplier γ is 1.48. A value of 1.5 was therefore used in the following analysis. Substituting this value, and Eq. (13) into Eq. (12), the final form for the deposition rate in the area affected by the vapour bubbles becomes

$$\dot{m}_{nb} = K_{1,0}e^{-E/RT_s}(1.5[Ca^{++}] - [Ca^{++}]^*)^2. \quad (16)$$

Prediction of $\dot{m}_{fc}$. As shown in Table 2, most of the heat transfer in the present investigation occurred by forced convection. Therefore, one would expect that these zones contribute significantly to the total deposition process. Several investigators (Hasson and Perl, 1981; Gazit and Hasson, 1975; Hasson et al., 1968; Chan and Ghassemi, 1991; Sheikholeslami and Watkinson, 1986; Watkinson and Martinez, 1975) have attempted to correlate the calcium carbonate scaling rates during convective, nonboiling heat transfer. In this investigation, two of these models have been used to predict the convective contribution to the total fouling rate. A third method has been developed to predict the convective part by combining the diffusion and reaction terms. The agreement between predicted and experimental values is satisfactory if the model by Chan and Ghassemi (1991) and the present model are used. However, there are considerable deviations between experimental and predicted results using Hasson's Ionic Diffusion Model for prediction of the convective component of fouling.

Chan and Ghassemi Model. This model is based on the solution of the continuity equation. Figure 12 shows a cross section of the annular test heater. A constant flow of water with predetermined concentration of calcium carbonate is maintained in the gap between the heater rod and the outer tube. Heat transfer occurs with a constant heat flux, and calcium carbonate deposition occurs on the surface of the heater rod. The continuity equation for a multicomponent system with constant diffusivity and density becomes

$$\frac{\partial C_i}{\partial t} + (v \cdot \nabla C_i) = D_{i_{eff}} \cdot \nabla^2 C_i + R_A \quad (17)$$

At steady state and with no reaction in the bulk of the solution, this equation reduces to

$$v \cdot \nabla C_i = D_{i_{eff}} \nabla^2 C_i \tag{18}$$

and with cylindrical coordinates:

$$v_r \frac{\partial C_i}{\partial r} + v_\theta \frac{1}{r} \frac{\partial C_i}{\partial \theta} + v_z \frac{\partial C_i}{\partial z} = D_{i_{eff}} \left[\frac{1}{r} \frac{\partial}{\partial r} \left(r \frac{\partial C_i}{\partial r} \right) + \frac{1}{r^2} \frac{\partial^2 C_i}{\partial \theta^2} + \frac{\partial^2 C_i}{\partial z^2} \right]. \tag{19}$$

For the flow geometry in this study, v_r and v_θ are zero. We also can assume that there is no significant amount of diffusive mass flux in comparison to bulk convection in the z-direction due to the low concentration of the solution. Consequently, Eq. (19) reduces to

$$v_z(r) \frac{\partial C_i}{\partial z} = D_{i_{eff}} \left[\frac{1}{r} \frac{\partial}{\partial r} \left(r \frac{\partial C_i}{\partial r} \right) \right]. \tag{20}$$

This equation is to be solved with the following boundary conditions:

$$@r = kR \quad D_i \frac{\partial C_i}{\partial r} = K_r([Ca^{+2}] - [Ca^{+2}]^*)^2 \tag{21}$$

$$@r = R \quad \frac{\partial C_i}{\partial r} = 0$$

$$@z = 0 \quad C_i = C_i^0.$$

Where kR is the heater rod radius. For a fully developed profile ($v_z = v_z(r)$), the mean turbulent velocity distribution in annuli can be approximated by

$$v_{z,max} - v_z = \frac{1}{km} \left(\frac{\tau_0}{\rho} \frac{\lambda^2 - k^2}{k} \right)^{1/2} \ln \frac{(\lambda - k)R}{r - kR} \quad \text{for} \quad r < \lambda R \tag{22}$$

$$v_{z,max} - v_z = \frac{1}{km} \left[\frac{\tau_0}{\rho} (1 - \lambda^2) \right]^{1/2} \ln \frac{R - \lambda R}{R - r} \quad \text{for} \quad r > \lambda R \tag{23}$$

according to Bird et al. (1960), where

$$\lambda^2 = \frac{1 - k}{2 \ln \left(\frac{1}{k} \right)}. \tag{24}$$

The shear stress at the wall, τ_0, can be obtained if the friction factor for the inner wall is known. This factor, f_1, for annuli has been correlated to the flow Reynolds number by Perry and Chilton (1984) as

$$f_1 = f_2 \frac{(\lambda^2 - 2k^2)}{k(1 - \lambda^2)} \tag{25}$$

where f_2, the outer wall friction factor, is

$$f_2 = \frac{0.0791}{[Re_f(1 - \lambda^2)]^{1/4}}. \tag{26}$$

Then, the wall shear stress may be calculated using

$$\tau_0 = f_1 \rho \langle v_z \rangle^2. \tag{27}$$

A Fortran program was written to solve Eq. (20) based on a finite difference method for appropriate boundary conditions.

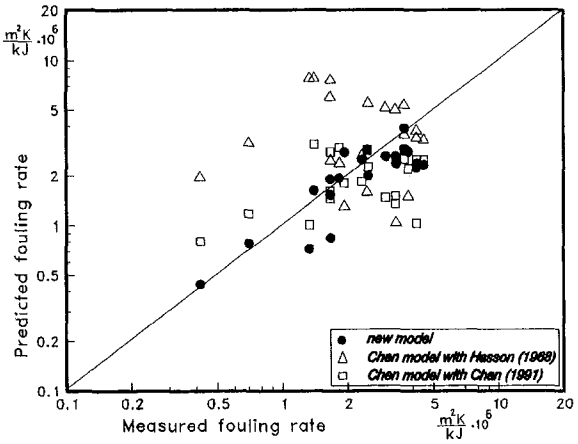

Fig. 13 Measured and predicted fouling rates for three models

The convective contribution to the fouling rate $\dot{m}_{fc}$ was calculated using the solution of Eq. (20) as follows:

$$\dot{m}_{fc} = D_{i_{eff}} \left(\frac{\partial C_i}{\partial r} \right). \tag{28}$$

The total fouling rate was calculated by using Eq. (28) in conjunction with Eq. (11). A comparison between predicted fouling rates and experimental data is shown in Fig. 13. The average absolute error is 44 percent, which is quite reasonable for fouling predictions.

Hasson's Ionic Diffusion Model. Hasson et al. (1968) developed a model for predicting calcium carbonate scaling rates, which is based on diffusion of calcium and carbonate ions from the fluid bulk followed by crystallization of $CaCO_3$ on the hot wall. The deposition rate is given by

$$\dot{m}_{fc} = K_r([Ca^{++}]_i[CO_3^{--}]_i - K_{sp}). \tag{29}$$

The concentrations of calcium and carbonate at the interface are eliminated using the mass transfer expressions

$$\dot{m}_{fc} = \beta([Ca^{++}] - [Ca^{++}]_i) = \beta([CO_2] - [CO_2]_i) = 0.5\beta([HCO_3^-] - [HCO_3^-]_i) \tag{30}$$

and the deposition rate at pH < 8.5 (similar to the present case) is found by solution of the following equation:

$$K_1 \left(\frac{\dot{m}_{fc}}{K_r} + K_{sp} \right) \left(\frac{\dot{m}_{fc}}{\beta} + y \right) = 4K_2 x^2 \left(1 - \frac{\dot{m}_{fc}}{\beta x} \right) \left(\frac{z}{2} - \frac{\dot{m}_{fc}}{\beta} \right)^2 \tag{31}$$

where $x = [Ca^{++}]$, $y = [CO_2]$, $z = [HCO_3^-]$, and K_1 and K_2 are the first and second dissociation constants of CO_2. If $[Ca^{++}] \gg [CO_3^-]$, this equation reduces to

$$\dot{m}_{fc} = \frac{0.5\beta x b \left(\left(1 + \frac{4ac}{b^2} \right)^{1/2} - 1 \right)}{a} \tag{32}$$

with

$$a = 1 - \frac{4K_2K_r x}{K_1 \beta} \tag{33}$$

$$b = \frac{y}{x} + \frac{4K_2K_r z}{K_1 \beta} + \frac{K_{sp}K_r}{\beta x} \tag{34}$$

$$c = \frac{K_2K_r z^2}{K_1 \beta x} - \frac{K_{sp}K_r y}{\beta x^2}. \tag{35}$$

The mass transfer coefficient β was calculated using the equation developed by Dittus and Bölter (1930):

$$\beta = 0.023\ \mathrm{Re}^{0.85}\ \mathrm{Sc}^{0.33}\ \frac{D}{d_{eq}}. \qquad (36)$$

The fouling rate in this model is calculated using Eqs. (32) and (11). If, pH, total alkalinity and $[Ca^{++}]$ are known, variables a, b, and c can be determined to find the fouling rate. In this model, removal of existing deposit is not considered. Figure 13 shows that there are considerable differences between the predictions of this model and the experimental data. The prediction of this model is very sensitive to the value of total alkalinity. During the experiments, this value was not constant and for prediction purposes the average value of total alkalinity was used. This may have been the cause of the discrepancy between experimental and predicted results. Another possibility is that the agreement between experimental and predicted fouling rates for this model is not good for fouling rates higher than 10^{-6} m^2K kJ^{-1}, as mentioned by Sheikholeslami and Watkinson (1986).

Proposed Model. It is generally assumed that the deposition of calcium carbonate on the heat transfer surface during convective heat transfer takes place by a two-step mechanism. Due to the concentration gradient, Ca^{++} and HCO_3^- will be transported from the bulk of the liquid to the heated surface. At the liquid-solid interface (and in the bulk), HCO_3^- undergoes the following equilibrium reaction (Hasson et al., 1968):

$$2HCO_3^- \rightarrow H_2O + CO_{2(aq)} + CO_3^{--}. \qquad (37)$$

The CO_2 formed from this reaction is transported through the liquid and desorbed at the liquid-gas interface. The CO_3^{-2} species produced in the same reaction reacts with Ca^{++}, which has been transported to the surface, to form $CaCO_3(s)$.

$$Ca^{++} + CO_3^{--} \rightarrow CaCO_3(s) \qquad (38)$$

This completes the precipitation of $CaCO_3$ scale on the heat transfer surface. Reactions in Eqs. (37) and (38) are combined in the following form (Hasson and Perl, 1981):

$$Ca^{++} + 2HCO_3^- \rightarrow CaCO_{3(s)} + CO_{2(g)} + H_2O. \qquad (39)$$

The above processes can be summarized into two steps. In the first step, calcium and bicarbonate ions are transported to the heat transfer surface by diffusion through the boundary layer which is formed between the scale and the solution, according to the following equation:

$$\dot{m}_{fc} = \beta([Ca^{++}] - [Ca^{++}]_i). \qquad (40)$$

In the second step, these ions react at the surface to form the solid phase of calcium carbonate. This surface reaction can be described by

$$\dot{m}_{fc} = K_1([Ca^{++}]_i - [Ca^{++}]^*)^2. \qquad (41)$$

In these equations, $[Ca^{++}]$, $[Ca^{++}]^*$, and $[Ca^{++}]_i$ are the bulk, saturation, and interface concentrations of calcium ions, respectively, and K_1 is the reaction rate constant defined in Eq. (13). By the combination of Eqs. (40) and (41) and elimination of the interface concentration, the deposition rate for the forced convective part becomes

Table 3 Parameters and physical properties used in this investigation

$K_{1,0}$ $m^4/kg.s$	E J/mole	λ_d W/m.K	ρ_d kg/m^3
$9.8x10^{11}$	122150	1.942	2705

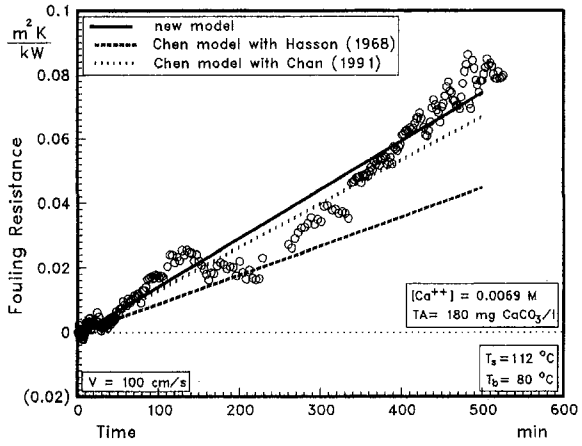

Fig. 14 Comparison of measured and predicted fouling resistances for three models

$$\dot{m}_{fc} = \beta\left[\frac{1}{2}\left[\frac{\beta}{K_1}\right] + (C - C^*) - \sqrt{\frac{1}{4}\left[\frac{\beta}{K_1}\right]^2 + \left[\frac{\beta}{K_1}\right](C - C^*)}\right] \qquad (42)$$

Therefore, the overall fouling rate under subcooled flow boiling can be calculated with Eq. (42) in conjunction with Eqs. (11) and (13).

The reaction rate constant and the activation energy in Eq. (13) are obtained from nonlinear regression analysis of the experimental data and are summarized in Table 3.

The values of 2705 kg/m^3 and 1.942 kW/(m.K) for density and thermal conductivity of calcium carbonate deposits are the average values reported by Hasson and Perl (1981) and Sheikholeslami and Watkinson (1986). The mass transfer coefficients used in these calculations are predicted using Eq. (36), with the diffusivities of Ca^{++} and HCO_3^- calculated according to Reid et al. (1988). Based on this procedure, a value of 1.016275 E-9 m^2/s at 298 K temperature was calculated for the diffusivity of Ca^{++} and HCO_3^- ions and extrapolated for different temperatures using the approximate relation (Bird et al., 1960):

$$D_{T_2} = D_{T_1}(T_2/T_1)\cdot\exp[3.8T_b(1/T_1 - 1/T_2)] \qquad (43)$$

where T_b denotes the boiling temperature of the liquid, and T_1 and T_2 are two arbitrary temperatures. The calculated mass transfer coefficients for some of the fouling runs are presented in Table 2.

Comparison With Experimental Data

A comparison between predicted fouling resistances using Eq. (11) in conjunction with the three above convective deposition models and experimental data is shown in Figs. 14 and 15. The predicted results are in good agreement with the experimental data for the proposed model and the model incorporating the Chan and Ghassemi (1991) model for the prediction of the forced convective contribution to the total fouling rate. However, there are considerable differences between experimental data and prediction of the model using Hasson's ionic diffusion model (Hasson et al., 1968) for the forced convective component. The fundamental assumptions for the derivation of the three models are the same. The major difference between the second model (using Hasson's ionic diffusion mode) and the two others is that in the first, the diffusion of both Ca^{++} and CO_3^- is considered and the interdependency of these two causes the model to be very sensitive to total alkalinity. Accurate pre-

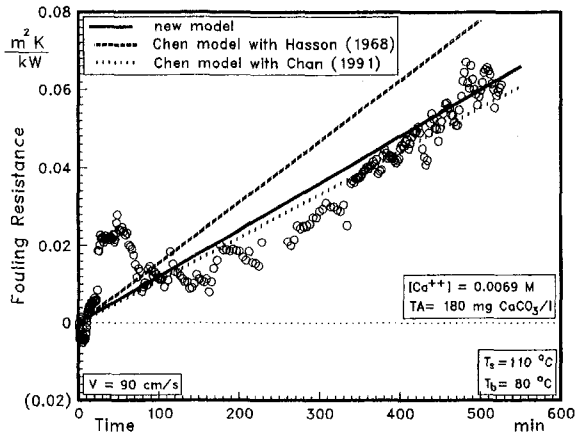

Fig. 15 Comparison of measured and predicted fouling resistances for three models

diction with the model of Hasson et al. (1968) requires accurate values of total alkalinity and the diffusivities of the species. In the two other models only the concentration of Ca^{++} is considered. A comparison between all experimental and predicted fouling rates for the three prediction procedures is shown in Fig. 13. The root mean square error of 5 percent and average absolute error of 22 percent between predicted and experimental data illustrates the applicability of the model incorporating Eq. (42). However, it is important to note that independent of the selected model for the mass transfer controlled deposition component, the suggested subcooled flow boiling fouling model predicts the qualitative effects of flow velocity, bulk temperature, heat flux, and $CaCO_3$ concentration correctly.

References

Al-Hayes, R. A. M. and Winterton, R. H. S., 1981, "Bubble Diameter on Detachment in Flowing Liquids," *Int. J. Heat Mass Transfer,* Vol. 24, pp. 223–230.

Bird, R. B., Stewart, W. E., and Lightfoot, E. N., 1960, *Transport Phenomena,* John Wiley & Sons, Inc., New York.

Branch, C. A. 1991, "Heat Transfer and Heat Transfer Fouling in Evaporators With Kraft Pulp Black Liquor, Ph.D. thesis, University of Auckland, New Zealand.

Chan, S. H., and Ghassemi, K. F., 1991, "Analytical Modelling of Calcium Carbonate Deposition for Laminar Falling Films and Turbulent Flow in Annuli: Part II—Multispecies Model," ASME JOURNAL OF HEAT TRANSFER, Vol. 113, pp. 741–746.

Chen, J. C., 1966, "Correlation for Boiling Heat Transfer to Saturated Fluids in Convective Flow," *Ind. Eng. Chem. Process Design and Development,* Vol. 5, pp. 322–329.

Collier, J. G., 1984, *Heat Exchanger Design Handbook,* Hemisphere Pub. Corp. Bristol, PA.

Dittus, F. W., and Bölter, L. M. K., 1930, *Heat Transfer in Automobile Radiators of the Tubular Type,* Vol. 2, No. 13, Univ. California Press, Berkeley, CA. (1930).

Fetissoff, P. E., 1982, "Comparison of Two Fouling Probes," M.Sc. thesis, University of British Columbia, Vancouver B.C., Canada.

Gazit, E., and Hasson, D., 1975, "Scale Deposition From an Evaporating Falling-Film," *Desalination,* Vol. 17, pp. 339.

Gnielinski, V., 1986, *Wärmeübertragung in Rohren, VDI-Wärmeatlas,* 5th ed., VDI-Verlag, Düsseldorf.

Gorenflo, D., 1988, *Pool Boiling,* 5th ed., VDI-Wärmeatlas VDI-Verlag, Düsseldorf.

Hasson, D., Avriel, M., Resnick, W., Rozenman, T., and Winderich, S., 1968, "Mechanism of Calcium Carbonate Scale Deposition on Heat Transfer Surfaces," *I & EC Fundamentals,* Vol. 7, pp. 59–65.

Hasson, D., and Perl, I., 1981, "Scale Deposition in a Laminar Falling-Film System," *Desalination,* Vol. 37, pp. 279–292.

Jamialahmadi, M., Blöchl, R., and Müller-Steinhagen, H., 1989, "Bubble Dynamics and Scale Formation During Boiling of Aqueous Calcium Sulphate Solutions," *Chem. Eng. Process.,* Vol. 26, pp. 15–26.

Jamialahmadi, M., and Müller-Steinhagen, H., 1993, "Scale Formation During Nucleate Boiling—A review," *Corrosion Reviews,* Vol. 11, pp. 25–54.

Kern, D. Q., Seaton, R. E., 1959, "A Theoretical Analysis of Thermal Surface Fouling," *Br. Chem. Eng.,* Vol. 4, pp. 258–262.

Lorenz, J. J., Mikic, B. B., and Rohsenow, W. M., 1974, "The Effect of Surface Conditions on Boiling Characteristics," *Proceedings of the fifth Int. Heat Transfer Conference,* Tokyo, Vol. 4, pp. 35–39.

Mikic, B. B., and Rohsenow, W. M., 1969, "A New Correlation of Pool Boiling Data Including the Effect of Heat Surface Characteristics," ASME JOURNAL OF HEAT TRANSFER, Vol. 5, pp. 245–250.

Moore, F. D., and Mesler, R. B., 1961, "The Measurement of Rapid Surface Temperature Fluctuations During Nucleate Boiling of Water," *A.I.Ch.E. Journal,* Vol. 7, pp. 620–624.

Müller-Steinhagen, H., 1993, "Fouling—The Ultimate Challenge for Heat Exchanger Design," *6th Int. Symp. on Transport Phenomena in Thermal Eng.,* South Korea, pp. 1–13.

O'Callaghan, M. G., 1986, *Heat Exchanger Sourcebook,* Hemisphere Publishing, Washington, DC.

Oufer, L., and Knudsen, J. G., 1993, "Modelling Chemical Reaction Fouling Under Subcooled Boiling Conditions," *AICHE Symp. Ser., Heat Transfer,* Atlanta, Vol. 89, pp. 308–313.

Perry, R. H., and Chilton, C. H., 1984, *Chemical Engineers' Handbook,* 5th ed., McGraw-Hill Book Company, New York.

Plummer, L. N., and Busenberg, E., 1982, "The Solubilities of Calcite, Aragonite, and Vaterite in CO_2-H_2O Solutions Between 0 and 90°C and an Evaluation of the Aqueous Model for the System $CaCO_3$-CO_2-H_2O," *Geochimica et cosmochimica acta,* Vol. 46, pp. 1011–1040.

Rau, H., 1982, "Modelling of Calcium Carbonate and Silica Deposition in Geothermal Energy Systems," M.S. thesis, Department of Mechanical Engineering, University of Wisconsin, Milwaukee, WI.

Reid, R., Prausnitz, J. M., and Poling, B. E., 1988, *The Properties of Gases and Liquids,* McGraw-Hill Book Company, New York.

Reitzer, B. J., 1964, "Rate of Scale Formation in Tubular Heat Exchangers," *I&EC Process Design Develop.,* Vol. 3, pp. 345.

Sanatgar, H., and Somerscale, E. F. C., 1991, "Account for Fouling in Heat Exchanger Design," *Chem. Eng. Process,* December, pp. 53–59.

Sheikholeslami, R., and Watkinson, A. P., 1986, "Scaling of Plain and Externally Finned Heat Exchanger Tubes," ASME JOURNAL OF HEAT TRANSFER, Vol. 108, pp. 147–152.

Shoukri, M., and Judd, R. L., 1987, "On the Influence of Surface Conditions in Nucleate Boiling—the Concept of Bubble Flux Density," ASME JOURNAL OF HEAT TRANSFER, Vol. 100, pp. 618–623.

Skoog, D. A., West, D. A., and Holler, F. J., 1992, *Analytical Chemistry,* 6th ed., Saunders College Publishing, Philadelphia, PA.

Wahl, E. F., 1977, *Geothermal Energy Utilization,* John Wiley & Sons, Inc., New York.

Watkinson, A. P., and Martinez, O., 1975, "Scaling of Heat Exchanger Tubes by Calcium Carbonate," ASME JOURNAL OF HEAT TRANSFER, pp. 504–508.

Wenzel, U., 1992, "Saturated Pool Boiling and Subcooled Flow Boiling of Mixtures," Ph.D. thesis, University of Auckland, New Zealand.

Wiechers, H. N. S., Sturrock, P., and Marias, G. V. R., 1975, "Calcium Carbonate Crystallization Kinetics," *Water Research,* Vol. 9, pp. 835–845.

A Predictive Model for Condensation in Small Hydraulic Diameter Tubes Having Axial Micro-Fins

C.-Y. Yang
Department of Mechanical Engineering,
National Central University,
Chung-Li 32054, Taiwan,
Republic of China

R. L. Webb
r5w@psu.edu
Department of Mechanical Engineering,
The Pennsylvania State University,
University Park, PA 16802

A semiempirical model is proposed to predict the condensation coefficient inside small hydraulic diameter extruded aluminum tubes having microgrooves. The model accounts for the effects of vapor shear and surface tension forces. Surface tension force is effective in enhancing the condensation coefficient as long as the fin tips are not flooded by condensate. This enhancement increases as mass velocity is reduced. At high mass velocity the flow is vapor shear controlled and the surface tension contribution is very small. The surface tension effect is strongly affected by the fin geometry. A smaller fin tip radius provides a higher surface tension drainage force. A large cross sectional area in the interfin region will allow the surface tension enhancement to occur at lower vapor quality. Separate models are developed for the surface tension and vapor shear controlled regimes and the models are combined in the form of an asymptotic equation. The vapor shear model is based on use of an equivalent mass velocity and the heat-momentum transfer analogy. The surface tension model is analytically based. The model is validated by predicting the authors' data for two tube geometries using R-12 and R-134a, and the model predicts 95 percent of the condensation data within ±16 percent.

Introduction

Tube-side condensation is important in the refrigeration, automotive, and process industries. The refrigeration industry has developed the "micro-fin" tube, which is used in virtually all residential, refrigerant evaporators and condensers. It provides a heat transfer coefficient two to three times that of a plain tube. Figure 1(a) shows the single helix micro-fin tube having 0.3 mm groove depth. The Fig. 1(a) copper tube is made in diameters between 4 and 16 mm, and is formed by drawing a seamless tube over a grooved, floating internal plug. The manufacture of small diameter micro-fin tubes (4.0–5.0 mm diameter) is a recent development and is reported by Morita et al. (1993) and Tsuchida (1993). The same basic enhancement geometry is also used in brazed aluminum, automotive refrigerant condensers. However, the extruded aluminum tube is made in a quite small hydraulic diameter, as compared to the Fig. 1(a) tubes (e.g., 1–3 mm). Figure 1(b) shows a flat extruded aluminum tube (3.0 mm minor diameter) having internal membranes that is used in such automotive refrigerant condensers. The wall and membrane thickness is typically 0.3–0.5 mm. The internal membranes provide strength to support high internal pressure. The Fig. 1(b) tube has 0.20 mm high internal micro-fins. Other than the hydraulic diameter, the only key difference between the Fig. 1(a) copper micro-fin tube and the Fig. 1(b) extruded aluminum tube is that the micro-fins in the Fig. 1(b) tube are axial.

Chapter 14 of Webb (1994) discusses the advances that have been made in the Fig. 1 tubes used for condensation. Many studies have reported heat transfer data (evaporation and condensation) and pressure drop characteristics for the round, Fig. 1(a) "micro-fin" tubes. Khanpara et al. (1986) and Morita et al. (1993) provide qualitative discussion concerning the effect of fin tip shape, valley shape, fin height, number of fins, and spiral angle. However, no significant work has been done to develop either a correlation or a theoretically based predictive model to predict the heat transfer or pressure drop in any of the Fig. 1 micro-fin tubes. Webb and Yang (1995) have reported R-12 and R-134a condensing coefficients for the Fig. 1(b) and Fig. 1(d) tubes.

As the technology of enhanced heat transfer advances, increased interest exists in understanding the enhancement mechanism of the various enhancement possibilities. This paper explains the heat transfer mechanism of condensation in micro-fin tubes of Fig. 1(b) and Fig. 1(c) and proposes a model to predict the condensation coefficient.

Condensation in Micro-Fin Tubes

Yang and Webb (1996a, b) reported heat transfer (condensation and single-phase) and friction data for R-12 in the Fig. 1(b) and Fig. 1(d). Webb and Yang (1995) extended the work to include R-134a. Yang (1994) provides R-12 and R-134a data on two additional geometries. These data were used for development and validation of the predictive model presented in this work. The geometries of the 1(b), 1(c), 1(d), and 1(e) tubes are given in Table 1.

Figure 2 shows the R-12 condensation data for the Fig. 1(b) and 1(d) tubes. The condensation coefficient is defined in terms of the total micro-fin internal surface area. The ability of existing correlations to predict the data for the Fig. 1(d) plain tube. These correlations are shown on Fig. 2 as the Shah (1979) and the Akers et al. (1959) correlations. The tube hydraulic diameter is used in these correlations. The Shah correlation substantially over predicts the plain tube data. However, the Akers et al. correlation provides excellent prediction of the Fig. 1(d) plain tube. Akers et al. proposed that the condensation coefficient is equal to that for an equivalent all liquid flow having the same wall shear stress as that of the condensing flow. Akers et al. proposed that the mass velocity for the equiva-

Contributed by the Heat Transfer Division for publication in the JOURNAL OF HEAT TRANSFER. Manuscript received by the Heat Transfer Division November 12, 1996; revision received July 21, 1997; Keywords: Augmentation and Enhancement; Condensation; Heat Exchangers. Associate Technical Editor: T. J. Rabas.

lent all-liquid flow that gives the same wall shear stress as the condensing flow is given by

$$G_{eq} = G\left[(1 - x) + x\left(\frac{\rho_l}{\rho_v}\right)^{1/2}\right]. \quad (1)$$

The equivalent all-liquid Reynolds corresponding to G_{eq} is given by

$$\mathrm{Re}_{eq} = \frac{G_{eq} D_h}{\mu_l}. \quad (2)$$

The average condensation coefficient for condensation between $x_1 \le x \le x_2$ is based on G_{eq} evaluated at the average vapor quality in the tube. One may obtain a given G_{eq} by operating at low x and high G, or at high x and low G.

Figure 2 shows that, at the same Re_{eq}, the condensation coefficient for the micro-fin tube is greater than that for the plain tube. For single-phase flow, Yang and Webb (1996a) found that $h_m/h_p \approx A_{im}/A_{ip}$ at the same Re_L. However, Fig. 2 shows that with condensation, $h_m/h_p > A_{im}/A_{ip}$. If only surface shear is responsible for fixing the condensing coefficient, one would expect that $h_m/h_p = A_{im}/A_{ip}$ for both single-phase flow and condensation. The Fig. 2 comparison suggests that factors other than surface shear cause enhancement in the micro-fin tube. Understanding of the enhancement is facilitated by Fig. 3, which shows the same data as on Fig. 2, except the ordinate is the Nusselt number (hD_h/k) based on hydraulic diameter. At high mass velocity or low mass velocity and low vapor quality, the Nusselt numbers for the plain and micro-fin tubes are nearly equal. The most dramatic difference occurs at low mass velocity and vapor qualities greater than 0.5. The Nusselt number sharply increases with increasing vapor quality. We will show that surface tension enhancement is responsible for the additional enhancement.

For vapor qualities greater than 0.5 the condensate film is sufficiently thin that part of the fin height penetrates into the vapor region. Thus, it is not flooded by condensate as shown in Fig. 4(a). A surface tension, induced pressure gradient acts to drain condensate from the small radius fin tip into the concave channel at the base of and between the fins. The knowledge that surface tension force can enhance condensate on a finned surface was proposed by Gregorig (1954). The condensation coefficient is given by $h = k_l/\delta$ for a laminar condensate film, where δ is the condensate film thickness. Surface tension force acts to maintain a smaller film thickness on the micro-fins than would exist for vapor shear force acting alone. Hence, surface tension force will enhance the condensation coefficient if the fins are not flooded. However, the magnitude of the enhancement will depend on the magnitude of the vapor shear stress.

At low vapor quality the micro-fins are flooded by the condensate (Fig. 4(b)), so little or no fin surface is exposed on which surface tension drainage can act. Then, only vapor shear force is important. In this case the heat transfer mechanism is the same as for a plain tube.

Surface tension drainage force provides an additional enhancement, which adds to the effect produced by vapor shear. This effect is significant at low mass velocity (400 kg/m^2-s) for vapor qualities greater than 0.5. At high mass velocity (1000 kg/m^2-s) this effect is not as strong because the vapor shear force is much higher at the high vapor qualities.

Proposed Condensation Model

Figure 5 shows a sketch of a typical round micro-fin tube having triangular micro-fins. Variation of the geometric parame-

Nomenclature

A = heat transfer surface, m^2
A_c = cross sectional flow area, m^2
$A_{c,f}$ = cross sectional area of condensate film, m^2
A_e = core flow area based on D_e, m^2
A_f = flooded surface area, m^2
A_u = unflooded surface area, m^2
b = tube minor dimension, m
d_e = diameter over fins of internally finned tube, m
D_h = hydraulic diameter of flow passages, $4LA_c/A$, m
e = fin height, m
f = friction factor, dimensionless
$f(\gamma)$ = a function of the fin apex angle defined in Eq. (7)
g = acceleration due to gravity, m/s^2
G = mass velocity in tube, kg/m^2-s
$G_{eq} = G[(1 - x) + x(\rho_l/\rho_v)^{1/2}]$, kg/m^2-s
h = heat transfer coefficient, h_L (total mass rate flowing as a liquid), h_p (plain tube), h_m (micro-fin), h (average), W/m^2-K
J = Colburn J-factor, dimension less
k = thermal conductivity, W/m-K
L = tube length, m
Nu = Nusselt number, hD/k_l, dimension less
p = fin pitch, m
Pr = Prandtl number, dimensionless
r = local radius, rad
r_0 = fin tip radius, rad
r_b = fin base radius, rad
Re = Reynolds number, defined where used, dimensionless
Re_{Dh} = Reynolds number, based on hydraulic diameter, dimensionless
Re_{eq} = equivalent Reynolds number defined by Eq. (1), dimensionless
Re_L = Reynolds number, total mass flowing as liquid, dimensionless
s = coordinate distance along curved condensing profile, m
S_b = fin geometry defined by Fig. 6, m
S_f = length of flooded region, m
S_{fb} = fin geometry defined by Fig. 6, m
S_m = length of fin profile, m
S_u = length of unflooded region, m
St = Stanton number, dimensionless
t = thickness of tube wall fin, m
T = temperature: T_W (wall), T_{sat} (saturation), K
u = liquid film flow velocity, m/s
w = tube major dimension, m
We = Weber number defined by Eq. (28), dimensionless
x = vapor quality, dimensionless
y = coordinate distance perpendicular to condensing surface, m

Greek Symbols

α = void fraction, dimensionless
β = helix angle relative to tube axis, rad or deg
γ = apex angle of fins, rad or deg
δ = condensate film thickness, m
η = coordinate distance perpendicular to condensing surface, m
μ = dynamic viscosity μ_l (of liquid), μ_v (of vapor), kg/m-s
ν = kinematic viscosity, m^2/s
ρ = density: ρ_l (of liquid), ρ_v (of vapor), kg/m^3
σ = surface tension, N/m
τ_i = liquid-vapor interfacial shear stress, N/m^2
τ_s = wall shear stress in s-direction (Fig. 7), N/m^2
τ_w = wall shear stress based on pressure drop, N/m^2
τ_z = wall shear stress in z-direction (Fig. 7), N/m^2

Subscripts

exp = measured value
f = flooded
i = designates inner surface of tube
l = liquid phase
L = total mass rate flowing as liquid
m = micro-fin tube
p = plain tube
pre = predicted value
sat = saturation condition
sh = vapor shear
st = surface tension
u = unflooded
v = vapor phase
w = at tube wall

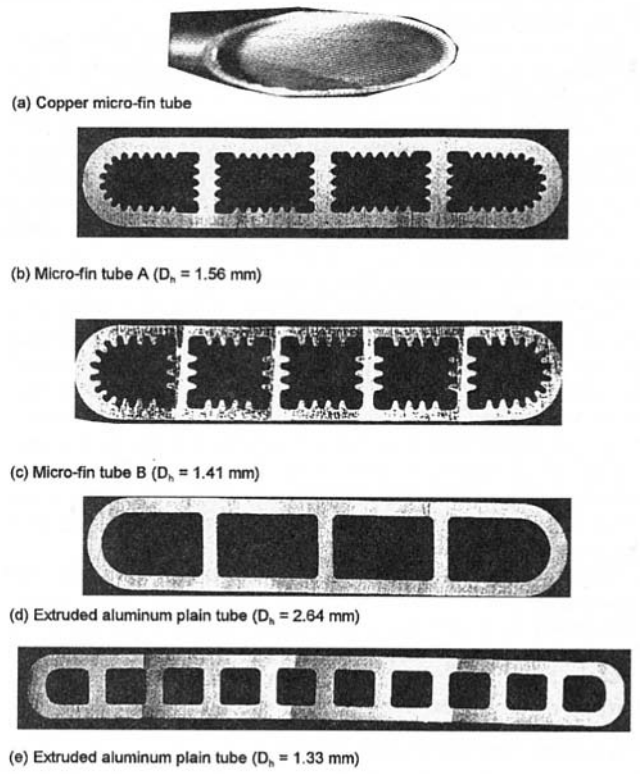

Fig. 1 Micro-fin and plain tubes

ters can affect the tube's performance. The key dimensions of the fins include fin pitch (p), fin height (e), tip radius (r_0), base radius (r_b), apex angle (γ), and helix angle (β) along the tube axis. The core diameter d_e is defined as the diameter measured at the fin tips; A_c is the tube cross section area; and A_e is the flow core area which is defined as $A_e = \pi d_e^2/4$.

Figure 6 illustrates a cross section of liquid film between two micro-fins. When refrigerant is condensed in micro-fin tubes, surface tension force pulls the condensate to the base of the fin. At high vapor qualities the condensate film is very thin, especially near the tip of the fins, and the heat transfer coefficient is very high on the part of the fins exposed to the vapor. At low vapor quality the void fraction $\alpha < A_e/A_c$, and the micro-fins are flooded by the condensate. The curvature of the condensate-vapor interface is nearly constant (Fig. 4(b)), so no surface tension effect exists there.

Because the entire fin perimeter is wetted and acted upon by vapor shear, one may consider prediction of the vapor shear component of the condensation coefficient by use of existing condensation correlations for plain tubes. However, one would use the hydraulic diameter in the place of the plain tube diameter. Applicable correlations include Carpenter and Colburn (1951), Akers et al. (1959), Cavallini and Zecchin (1974), and Shah (1979). As previously noted the Akers et al. (1959) appears to give the best correlation for the small hydraulic diameter extruded aluminum tubes of the present interest.

When the fin tips are not flooded (e.g., when $\alpha > A_e/A_c$), other vapor shear and surface tension forces are important. The resulting heat transfer coefficients averaged over the total surface area can be calculated as

$$h = h_u \frac{A_u}{A} + h_f \frac{A_f}{A}, \qquad (3)$$

where A is the total heat transfer surface area, A_u is the unflooded area, A_f is the flooded area, and h_u and h_f are the heat transfer

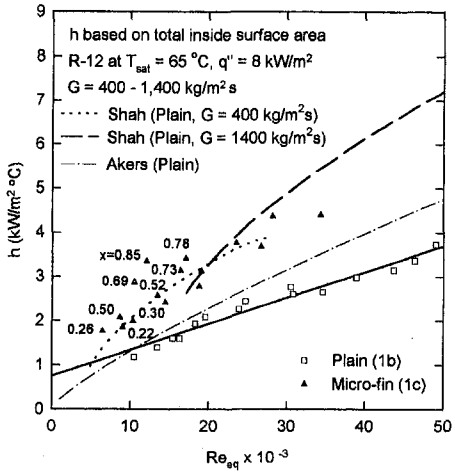

Fig. 2 Comparison of condensation coefficient in plain and micro-fin tubes

coefficients in the unflooded region and flooded region, respectively.

At the limiting condition, $A_u \to 0$, the condensation heat transfer coefficient for the flooded area (h_f) is equal to the total heat transfer coefficient (h) at low vapor quality condition. Hence, the vapor shear dominated equations may again be used to calculate the flooded area condensation heat transfer coefficient, h_f.

Calculation of Flooded Area Fraction A_f/A. Figure 6 shows the liquid film maintained by capillary force within a microgroove having base angle γ. It is assumed that the liquid-vapor interface is a circular arc. Figure 6(a) shows the fin base radius (r_b) and the condensate film surface radius (r_f) between the fins which are given by

Table 1 Tube geometries tested by Yang (1994)

		Micro-fin A	Micro-fin B	Plain A	Plain B
Tube	Figure	1b	1c	1d	1e
	No. ports	4	5	4	10
	w (mm)	16	16	16	20
	b (mm)	3.0	3.0	3.0	2.0
	A_c (mm²)	22.68	26.60	27.27	16.08
	A_e (mm²)	18.49	22.75		
	A_e/A_c	0.815	0.855		
	A_f/L (mm)	57.99	75.33	41.36	48.38
	D_h (mm)	1.56	1.41	2.64	1.33
	t (mm)	0.50	0.40	0.50	0.40
Fin	e (mm)	0.20	0.30		
	p (mm)	0.40	0.45		
	γ (deg)	40	40		
	r_0 (mm)	0.013	0.060		
	r_b (mm)	0.15	0.060		
	S_s (mm)	0.56	0.10		
	S_b (mm)	0.41	0.30		

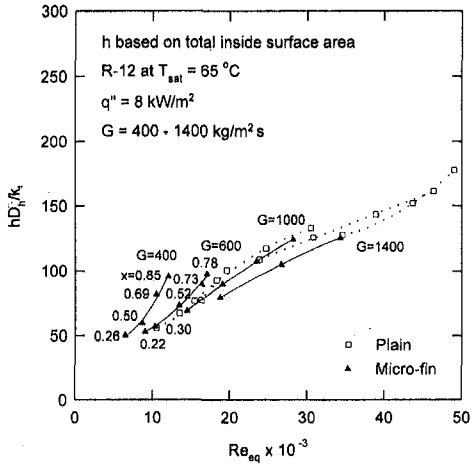

Fig. 3 Comparison of condensation Nusselt number in plain and micro-fin tubes

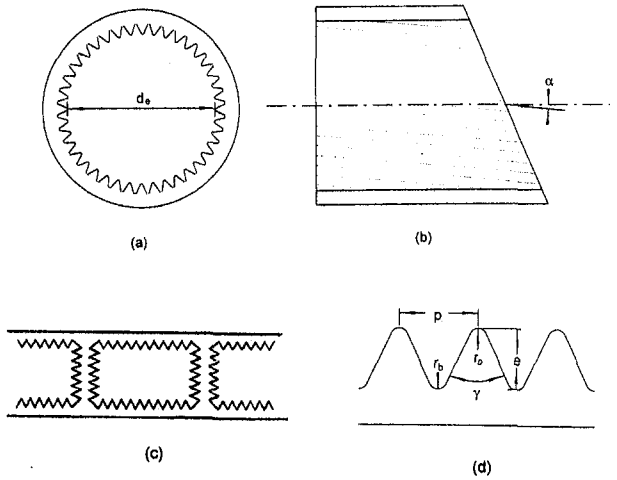

Fig. 5 (*a*) End view of round micro-fin tube, (*b*) side view of round micro-fin tube, (*c*) end view of flat, extruded aluminum micro-fin tube, and (*d*) detail of micro-fin geometry

$$r_b = S_b \cdot \tan\frac{\gamma}{2} \tag{4}$$

$$r_f = S_{fb} \cdot \tan\frac{\gamma}{2}, \tag{5}$$

where S_b and S_{fb} are the perimeters shown in Fig. 6(a). From Fig. 6(b), the cross sectional area ($A_{c,f}$) of the condensate film surface between the fins is equal to the curved area enclosed by points ABDE; that is, equal to the difference of the area of the quadrangle OABC minus the area of the sector OAB and the quadrangle PDEC minus the area of the sector PDE. Thus, area $A_{c,f}$ is given by

$$A_{c,f} = 2\left(\frac{1}{2}\cdot S_{fb}\cdot S_{fb}\tan\frac{\gamma}{2}\right) - \frac{\pi-\gamma}{2\pi}\pi r_f^2$$

$$- 2\left(\frac{1}{2}\cdot S_b\cdot S_b\tan\frac{\gamma}{2}\right) + \frac{\pi-\gamma}{2\pi}\pi r_b^2. \tag{6}$$

Substituting Eqs. (4) and (5) for r_b and r_f into Eq. (6), the cross section area $A_{c,f}$ becomes

$$A_{c,f} = S_{fb}^2\left(\tan\frac{\gamma}{2} - \frac{\pi-\gamma}{2}\tan^2\frac{\gamma}{2}\right)$$

$$- S_b^2\left(\tan\frac{\gamma}{2} - \frac{\pi-\gamma}{2}\tan^2\frac{\gamma}{2}\right)$$

$$= (S_{fb}^2 - S_b^2)\cdot f(\gamma) \tag{7}$$

where the terms in the parenthesis of the RHS can be expressed as $f(y)$ which is a function of fin base angle only.

Assuming the film thickness in the unflooded region is very thin compared to that in the flooded region, the fraction of the total tube cross section area that is liquid filled, $A_{c,f}/A_c$, is approximately equal to the liquid volume fraction in the flow, $1 - \alpha$. The line S_{fb} is given by

$$S_{fb} = \left[\frac{A_{c,f}}{f(\gamma)} + S_b^2\right]^{1/2} \approx \left[\frac{A_c(1-\alpha)}{f(\gamma)} + S_b^2\right]^{1/2}, \tag{8}$$

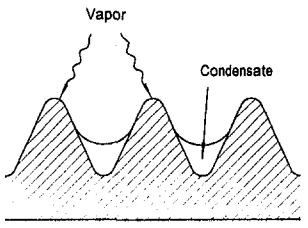

(a) High vapor quality

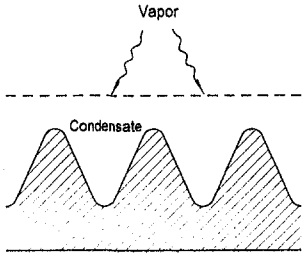

(b) Low vapor quality

Fig. 4 Cross section through the wall of a micro-fin tube

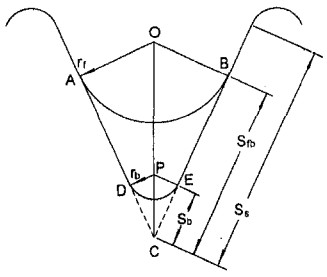

(a)

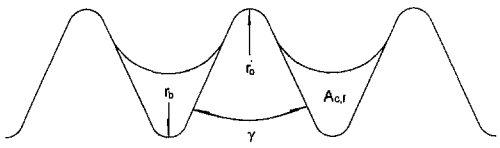

(b)

Fig. 6 (*a*) Cross section geometry of liquid film (*b*) liquid maintained within a micro-groove

where S_b is defined by the fin geometry, and the void fraction α can be obtained from the Zivi (1964) correlation at the known vapor quality.

The flooded and unflooded perimeters (S_f and S_u) can be calculated by

$$S_f = 2(S_{fb} - S_b) + r_b(\pi - \gamma) \tag{9}$$

$$S_u = 2(S_s - S_{fb}) + r_0(\pi - \gamma). \tag{10}$$

The length S_s is also known for the fin geometry. The total length of the fin profile $S_m = S_f + S_u$. The flooded and unflooded fractions then can be obtained by

$$\frac{A_f}{A} = \frac{S_f}{S_m} \tag{11}$$

$$\frac{A_u}{A} = \frac{S_u}{S_m}. \tag{12}$$

Prediction of Flooded Area Heat Transfer Coefficient h_f. When the fin are flooded there is no surface tension contribution. The present model assumes an annular flow, hence vapor shear dominated condensation. The wall shear stress is related to the heat transfer coefficient for the equivalent single-phase flow (h_L) as proposed by Akers et al. (1959). The mass velocity (G_{eq}) associated with this equivalent liquid flow is defined by Eq. (2). The all liquid heat transfer coefficient is written in terms of the wall shear stress using the heat-momentum transfer analogy ($\mathrm{St}\,\mathrm{Pr}^{2/3} = f/2$) with $f = T_W/[(G_{eq})^2/2\rho)]$. The result is

$$h_L = T_W \frac{k_l}{D_h} \mathrm{Re}_L \,\mathrm{Pr}_l^{1/3} \frac{\rho_l}{G_{eq}^2}. \tag{13}$$

Yang and Webb (1996a) have shown that the single-phase heat transfer coefficient in the Fig. 1(b) and 1(d) tubes is well predicted using an appropriate equation for turbulent flow in tubes based on hydraulic diameter. Akers et al. (1959) used Eq. (13) with the Seider and Tate (1936) equation to obtain

$$h_{\mathrm{Akers}} = 0.0265 \frac{k_l}{D_h} \mathrm{Re}_{eq}^{0.8} \,\mathrm{Pr}_l^{1/3}, \tag{14}$$

where Re_{eq} is defined by Eq. (1). The present model uses $h_f = h_{\mathrm{Akers}}$.

Prediction of Unflooded Area Heat Transfer Coefficient h_u. Figure 7 illustrates the vapor flow parallel to axial microfins. The condensate film is assumed to be laminar. Coordinate direction z is in the flow direction. The coordinate direction along the fin surface (normal to the flow) and normal to the fin are s and η, respectively. The condensate film (thickness δ) is drained by both vapor shear and surface tension at velocity $u(\eta)$. The pressure gradients (in the condensate film) in the z-direction (dp/dz) and s-direction (dp/ds) are caused by the fluid flow and surface tension drainage, respectively.

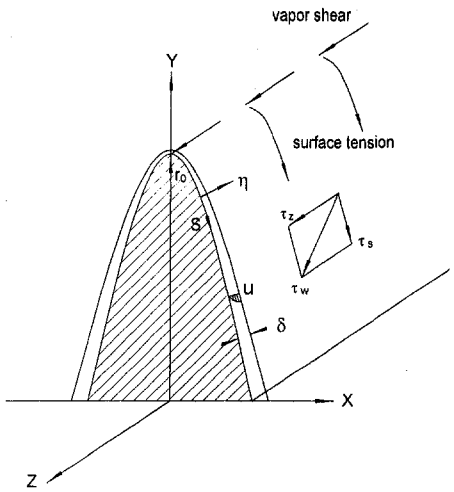

Fig. 7 Vapor shear and surface tension effects on a fin

Assuming $dp/ds \gg (\rho_l - \rho_v)g$, the momentum equations in the z and s direction with the boundary layer approximations are

$$-\frac{dp}{dz} + \mu_l \frac{\partial^2 u}{\partial \eta^2} = 0 \tag{15}$$

$$-\frac{dp}{ds} + \mu_l \frac{\partial^2 u}{\partial \eta^2} = 0. \tag{16}$$

The boundary conditions are $T_s = 0$ at $\eta = \delta$) and $T_z = T_i$ (T_i is the interfacial shear stress) at $\eta = \delta$.

Integrating Eqs. (15) and (16), and assuming dp/dz and dp/ds are independent of η, we obtain the z and s-direction wall shear stress components as

$$\mu_l \left(\frac{\partial u}{\partial \eta}\right)_{z,\eta=\delta} - \mu_l \left(\frac{\partial u}{\partial \eta}\right)_{z,\eta=0} = T_i - T_z = \int_0^\delta \frac{dp}{dz} d\eta = \delta \frac{dp}{dz}. \tag{17}$$

The corrected equation is

$$\mu_l \left(\frac{\partial u}{\partial \eta}\right)_{s,\eta=\delta} - \mu_l \left(\frac{\partial u}{\partial \eta}\right)_{s,\eta=0} = 0 - T_s = \int_0^\delta \frac{dp}{ds} d\eta = \frac{dp}{ds} \int_0^\delta d\eta = \delta \frac{dp}{ds}, \tag{18}$$

where T_s is the s-direction shear stress at the wall. The s-direction interfacial shear stress is zero.

Because the shear stress in the z-direction and the s-direction are perpendicular, the resultant shear stress at the wall (T_W) is

$$T_W = \left[\tau_z^2 + (\tau_z - \tau_i)^2 \left(\frac{dp/ds}{dp/dz}\right)^2\right]^{1/2}. \tag{19}$$

Substituting Eqs. (17) and (18) into Eq. (19) and eliminating the unknown film thickness (δ), the resultant wall shear stress can be written in terms of the z-direction shear stress (τ_z), the interfacial shear stress (τ_i), and pressure gradients.

The wall shear stress in Eq. (19) is related to the heat transfer coefficient for the equivalent single-phase flow (h_L) as defined by Eq. (14). Substituting Eq. (19) for the wall shear stress T_W into Eq. (18) we may solve for the composite heat transfer coefficient, h_u.

$$h_u = \left[\tau_z^2 + (\tau_z - \tau_i)^2 \left(\frac{dp/ds}{dp/dz}\right)^2\right]^{1/2} \frac{k_l}{D_h} \mathrm{Re}_{eq} \,\mathrm{Pr}_l^{1/3} \frac{\rho_l}{G_{eq}^2} \tag{20}$$

Expanding Eq. (19) into two terms on the right hand side gives

$$h_u^2 = \left(\tau_z \frac{k_l}{D_h} \mathrm{Re}_{eq} \,\mathrm{Pr}_l^{1/3} \frac{\rho_l}{G_{eq}^2}\right)^2 + \left[(\tau_z - \tau_i)\left(\frac{dp/ds}{dp/dz}\right) \frac{k_l}{D_h} \mathrm{Re}_{eq} \,\mathrm{Pr}_l^{1/3} \frac{\rho_l}{G_{eq}^2}\right]^2. \tag{21}$$

The first and second terms in RHS of Eq. (20) are the contribution due to vapor shear and surface tension, respectively. Thus, we may define

$$h_{sh} = \tau_z \frac{k_l}{D_h} \mathrm{Re}_{eq} \mathrm{Pr}_l^{1/3} \frac{\rho_l}{G_{eq}^2} \tag{22}$$

$$h_{st} = (\tau_z - \tau_i)\left(\frac{dp/ds}{dp/dz}\right) \frac{k_l}{D_h} \mathrm{Re}_{eq} \mathrm{Pr}_l^{1/3} \frac{\rho_l}{G_{eq}^2}. \tag{23}$$

Using the definitions of Eqs. (22) and (23), Eq. (21) may be written as

$$h_u^2 = h_{sh}^2 + h_{st}^2. \tag{24}$$

The Akers et al. (1959) correlation given by Eq. (14) is used to predict the vapor shear term h_{sh}.

The surface-tension-drained pressure gradient dp/ds in Eq. (24) can be obtained by the equation, which assumes linear surface tension drainage force.

$$\frac{dp}{ds} = \sigma \frac{d(1/r)}{ds} = \sigma \frac{(1/r_b - 1/r_o)}{S_m}. \tag{25}$$

Using Eq. (25) and the definition of Weber number as follows:

$$\mathrm{We} = \frac{G_{eq}^2 D_h}{\rho_l \sigma} \tag{26}$$

Eq. (23) results in

$$h_{st} = \frac{\tau_z - \tau_i}{dp/dz} k_l \frac{d(1/r)}{ds} \frac{\mathrm{Re}_{eq} \mathrm{Pr}_l^{1/3}}{\mathrm{We}}. \tag{27}$$

The terms τ_z, τ_i, and dp/dz can be obtained from measured single-phase and two-phase flow pressure drop data. The interfacial shear stress is obtained using the Blasius friction factor for the vapor core. An empirical constant C may be used in Eq. (27) to obtain a best fit of the experimental data. Including the constant, Eq. (27) is re-written as

$$h_{st} = C \frac{\tau_z - \tau_i}{dp/dz} k_l \frac{d(1/r)}{ds} \frac{\mathrm{Re}_{eq} \mathrm{Pr}_l^{1/3}}{\mathrm{We}} \tag{28}$$

Using Eq. (24) to predict the condensation coefficient inside micro-fin tubes is easy and asymptotic to vapor shear or surface tension dominated conditions.

Comparison of Theoretical Model to Experimental Results

Yang (1994) measured the single-phase and the condensing heat transfer coefficient of R-12 and R-134a inside two plain tubes (Fig. 1(*d*) and 1(*e*)) and two micro-fin tubes (Fig. 1(*b*), and 1(*c*)). Yang and Webb (1996a) also provide R-12 data for the Fig. 1(*b*) and 1(*d*) tubes. The geometry details are given in Table 1.

Yang (1994) provided an empirical correlation for the single-phase heat transfer coefficient in the form

$$\mathrm{Nu}_{Dh} = C\, \mathrm{Re}_{Dh}^m \mathrm{Pr}_l^{1/3}. \tag{29}$$

For the plain tubes $C = 0.052$ and $m = 0.73$, and for the micro-fin tubes $C = 0.10$ and $m = 0.64$.

Equation (29) was applied in place of h_{Akers} (Eq. (14)) to calculate h_f and h_u for the present micro-fin geometries. Equation (28) was used to predict the surface tension term (h_{st}). Substituting these equations into Eq. (3) we predicted the composite condensation coefficient in the two micro-fin tubes. Use of empirical constant $C = 0.0703$ in Eq. (28) provided the minimum error in correlation of the Fig. 8 data. The ratio of predicted-to-experimental heat transfer coefficients is shown on Fig. 8. This figure shows that all of the data for both refrigerants (R-12 and R-134a) are predicted within ±20 percent, or 95 percent of the data are within ±16 percent, which is within the experimental uncertainty range.

Figure 9 shows $h_{st}A_u/hA$ (the fraction of composite heat transfer conductance due to surface tension) plotted versus vapor quality. At low vapor qualities ($x < 0.5$) the total fin height is flooded by condensate so no surface tension effect exists. When the vapor quality is higher than approximately 0.5, the unflooded area increases so the surface tension contribution fraction increases. At the lowest mass velocity ($G = 400$ kg/m^{2}s) and the highest vapor quality condition the surface tension fraction is greater than 0.5. The surface tension drainage force is larger than vapor shear force at high vapor quality and low mass velocity. As shown by the theoretical model the surface tension effect decreases with increasing mass velocity. At $G = 1400$ kg/m^{2}s the surface tension fraction is very small. At this condition the condensation mechanism is controlled by vapor shear.

Figure 9 also compares the surface tension effect on different fin geometries. The parameters which can affect the surface tension effect are the fin height (e), tin tip radius (r_0), apex angle (γ), and the ratio A_e/A_c (ratio of the core area-to-actual cross section area). The most important parameter that affects the surface tension force is the fin tip radius. A smaller fin tip radius provides a higher surface tension drainage force. Referring to Table 1, the fin tip radius of micro-fin tube A is only 20 percent that of tube B. This is the principal reason why the surface tension effect in tube B is not as strong as that for tube A at the same mass velocity and vapor quality. The other parameter is the A_e/A_c ratio. Referring to Eqs. (4)–(10), a higher A_e/A_c ratio will allow the fin tip to be unflooded at lower vapor quality. The fin height e and A_e/A_c ratio of tube B are greater than that of tube A. When the vapor quality increases, the fin tip of tube B is unflooded at lower vapor quality than that in tube A. The surface tension effect is first present in tube B at lower vapor quality than that in tube A.

In comparing the surface tension effect of different refrigerants, the surface tension of R-12 is 30 percent higher than that of R-134a at tested condition, $T_{\mathrm{sat}} = 65$°C. This is why the surface tension contribution for R-12 is higher than that for R-134a at same mass velocity and vapor quality (Fig. 9).

Yang and Webb, 1996b provide a method to predict the friction pressure drop in the Fig. 1(*b*) through 1(*e*) tubes.

Conclusions

The Akers et al. (1959) correlation reasonably predicts the condensation coefficient in the small hydraulic diameter plain

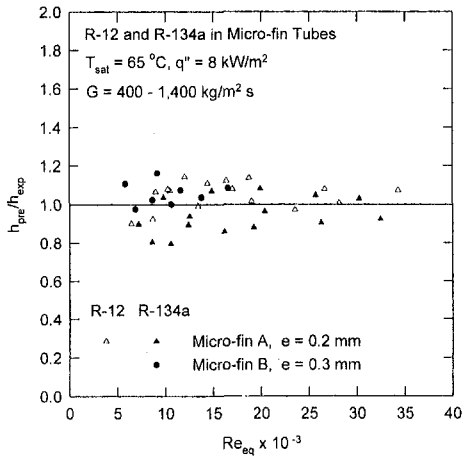

Fig. 8 Ratio of predicted-to-experimental heat transfer coefficient

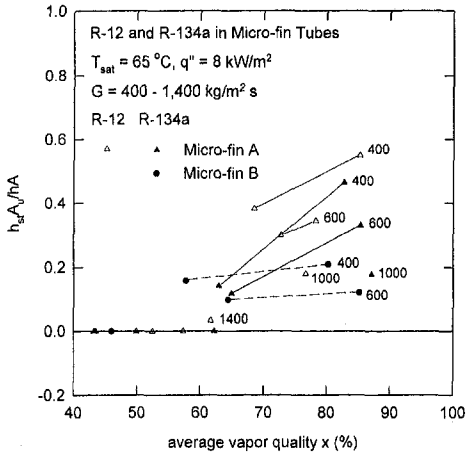

Fig. 9 Fraction of composite heat transfer coefficient due to surface tension

tubes. However, the Shah (1979) correlation substantially over predicts.

In micro-fin tubes, surface tension force is effective in enhancing the condensation coefficient, especially at low mass velocity and high vapor qualities. At low mass velocity and high vapor quality the surface tension effect can be as high, or higher than, the vapor shear controlled condensation coefficient. The surface tension effect is also strongly affected by the fin geometry. A smaller fin tip radius provides a higher surface tension drainage force. A large cross sectional area in the interfin region will allow the surface tension enhancement to occur at lower vapor quality.

Based on the equivalent mass velocity of Akers et al. (1959), and the analogy between momentum and heat transfer, a new semiempirical model is proposed for predicting the heat transfer coefficient of flow condensing inside horizontal micro-fin tubes. The model accounts for the effects of vapor shear and surface tension forces. The predictive model is an asymptotic type equation. The condensation coefficient is obtained from separate correlations for the vapor shear or surface tension dominated flow. The proposed semiempirical model predicts 95 percent of the condensation data within ±16 percent.

Acknowledgment

The extruded aluminum tubes tested were provided by Showa Aluminum Co. We are also grateful for the financial support of Showa Aluminum Co.

References

Akers, W. W., Deans, H. A., and Crosser, O. K., 1959, "Condensation Heat Transfer Within Horizontal Tubes," *Chem. Eng. Prog. Symp. Ser.*, Vol. 55, No. 29, pp. 171–176.

Carpenter, F. G., and Colburn, A. P., 1951, "The Effect of Vapor Velocity on Condensation Inside Tubes," *Proceedings of the General Discussion of Heat Transfer*, The Institute of Mechanical Engineers and the ASME, pp. 20–26.

Cavallini, A., and Zecchin, R., 1974, "A Dimensionless Correlation for Heat Transfer in Forced Convection Condensation," *Proceedings of the Fifth International Heat Transfer Conference*, Vol. 3, ASME, NY, pp. 309–313.

Gregorig, R., 1954, "Film Condensation on Finely Rippled Surface with Condensation of Surface Tension," *Zeitschrift fur Angewandte Mathematik und Physik*, Vol. V, pp. 36–49, (quoted in Webb (1994)).

Khanpara, J. C., Bergles, A. E., and Pate, M. B., 1986, "Augmentation of R-113 In-Tube Condensation with Micro-Fin Tubes," *Heat Transfer in Air Conditioning and Refrigeration Equipment*, ASME, NY.

Morita, H., Kito, Y., and Satoh, Y., 1993, "Recent Improvements in Small Bore Inner Grooved Copper Tube," *Tube & Pipe Technology*, November/December, pp. 53–57.

Seider, E. N., and Tate, C. E., 1936, "Heat Transfer and Pressure Drop of Liquids in Tubes," *Ind. Eng. Chem.*, Vol. 28, p. 1429.

Shah, M. M., 1979, "A General Correlation for Heat Transfer During Film Condensation in Tubes," *Int. Jour. of Heat and Mass Transfer*, Vol. 22, No. 4, pp. 547–556.

Tsuchida, T., 1993, "Internal Heat Transfer Characteristics and Workability of Narrow THERMOFIN Tubes," *Hitachi Cable Review*, No. 12, pp. 59–64.

Webb, R. L., 1994, chap. 14 in *Principles of Enhanced Heat Transfer*, Wiley Interscience.

Webb, R. L., and Yang, C.-Y., 1995, "Condensation of R-12 and R-134a in Brazed Aluminum Automotive Heat Exchangers," *1995 Vehicle Thermal Management Systems*, Society of Automotive Engineers, Warrendale, PA, pp. 77–85.

Yang, C.-Y., 1994, "A Theoretical and Experimental Study of Condensation in Flat Extruded Micro-fin Tubes," Ph.D. thesis, The Pennsylvania State University, PA.

Yang, C.-Y., and Webb, R. L., 1996a, "Condensation of R-12 in Small Hydraulic Diameter Extruded Aluminum Tubes With and Without Micro-fins," *Int. Jour. of Heat and Mass Transfer*, Vol. 39, No. 4, pp. 791–800.

Yang, C.-Y., and Webb, R. L., 1996b, "Friction Pressure Drop of R-12 in Small Hydraulic Diameter Extruded Aluminum Tubes With and Without Micro-fins," *Int. Jour. Heat and Mass Transfer*, Vol. 39, No 4, pp. 801–809.

Zivi, S. M., 1964, "Estimation of Steady State Steam Void-Fraction by Means of Principle of Minimum Entropy Production," ASME JOURNAL OF HEAT TRANSFER, Vol. 86, pp. 237–252.

Experimental Validation of Continuum Mixture Model for Binary Alloy Solidification

M. J. M. Krane
Assistant Professor,
School of Materials Engineering.
krane@ecn.purdue.edu
Assoc. Mem. ASME

F. P. Incropera
Professor,
School of Mechanical Engineering.
Fellow ASME

Heat Transfer Laboratory,
Purdue University,
West Lafayette, IN 47907

Experiments were performed with binary metal alloys to validate a continuum mixture model for alloy solidification. Ingots of two compositions, Pb-20%Sn and Pb-40%Sn, were cast in a permanent mold, and the solidification process was simulated. Temperature histories were measured during casting, and composition profiles were found in the solidified ingot. Dendritic arm spacings were found from optical micrographs of the alloy microstructure and used to determine a constant in the Blake-Kozeny submodel for the mushy zone permeability in the liquid-solid interaction term of the momentum equations. Scaling analysis from a previous work and a large uncertainty in the permeability constant suggested that predictions of the composition are extremely sensitive to the choice of a permeability model. Three simulations of each casting were performed using the permeability constant as a parameter, and measured temperatures and compositions were compared with predictions based on different model constants. In the region of the liquidus interface, where all of the significant advection of solute takes place, the results suggest that the Blake-Kozeny model based on measured dendritic arm spacings significantly underpredicts the resistance of the dendritic array to fluid flow.

Introduction

Macrosegregation, the nonuniform macroscopic distribution of the components of an alloy during solidification, is a defect which can occur in real metal processing systems. These nonuniformities, especially when they form high compositional gradients, can be areas of high stress concentration, which cause cracking when an aluminum or steel billet is extruded or forged or when an as-cast piece, such as a turbine blade, is severely loaded in service. Macrosegregation studies in binary systems have become quite common since the introduction of single-domain numerical models. These models feature one set of conservation equations and one set of boundary conditions for an entire, fixed computational domain, which might contain solid, liquid, and multiphase regions simultaneously. They are well established and have been successful in predicting irregular solidification fronts, channel development, double-diffusive flow cells in the melt region, and general macrosegregation patterns. A more complete review is found in Prescott and Incropera (1996).

Although there has been a great proliferation of numerical studies of the macroscopic heat and mass transfer during alloy solidification using these single domain models, there has been much less effort expended in gathering quantitative data to which these predictions can be compared. Most of the experimental work has been performed using aqueous salt solutions (Prescott and Incropera, 1996). These metal analogues have been useful in qualitatively observing flow patterns in the transparent melt and the interaction of that flow with the mushy region. They also are relatively easy to use due to low liquidus temperatures. While flow visualization and temperature data have been obtained for these systems, measuring composition in the final casting is very difficult because of the low melting points. The saltwater solutions also have much higher Prandtl numbers than metals and, compared to most commercial metal alloys, have relatively little primary solidification before the onset of a eutectic reaction. However, there are very few studies comparing experimental results taken during metal casting to predictions of macroscopic heat and mass transfer made with advanced numerical models.

The first study was by Shahani et al. (1992), who solidified two different Sn-Pb alloys, one on each side of the eutectic composition. Rectangular ingots of these alloys were cast horizontally and unidirectionally. The measured wall temperatures were used as boundary conditions in the numerical model, which was based on the work of Hills et al. (1983). No temperature histories were reported, but the composition was measured by wet chemical analysis at discrete points in each ingot and compared to the calculated results. Reasonable agreement was found in the trends of the composition profiles, although the local experimental compositions differed from the predictions by up to 4 wt% in the Sn-rich case and up to 7 wt% in the Pb-rich ingot. Also, due to limited spatial resolution in the measurements, the *A*-segregation which the code predicted in the Pb-rich case was not seen in the experiments.

Prescott et al. (1994) performed experiments to validate a continuum mixture model (Bennon and Incropera, 1987a; Prescott et al., 1991), which they applied to an axisymmetric Pb-19 wt%Sn ingot. While the model did not account for nonequilibrium effects such as undercooling and recalescence, the predicted transient temperature histories were very similar to the experimental trends. However, agreement between the composition measurements, made with atomic absorption spectrophotometry at 10 mm radial intervals and three different heights, and the corresponding predictions were not as good. While some general trends in the experimental macrosegregation patterns were predicted by the model, there was considerable scatter in the data, which was attributed to a lack of axisymmetry in the cast ingot.

The purpose of this paper is to present experimental results for two binary metal alloys and to compare them directly to calculations performed using a continuum mixture transport model similar to that described in Bennon and Incropera (1987a) and Prescott et al. (1991). Particular attention is paid to the effect of the large uncertainty in the value of the perme-

Contributed by the Heat Transfer Division for publication in the JOURNAL OF HEAT TRANSFER. Manuscript received by the Heat Transfer Division March 24, 1997; revision received September 3, 1997; Keywords: Materials Processing and Manufacturing Process; Modeling and Scaling; Phase-Change Phenomena. Associate Technical Editor: M. Kaviany.

ability function in the mushy zone near the liquidus interface. Ingots of Pb-20%Sn and Pb-40%Sn were cast, and temperature and composition measurements were made. In each case micrographs of the microstructure were taken to provide dendritic arm spacing measurements and to provide qualitative data for comparison to the numerical predictions.

Experimental Methods

Test Cell. Casting experiments were performed in a rectangular stainless-steel (type 304) mold heated by electrical resistance heaters and chilled by water-cooled heat exchangers. A cutaway view of this test cell is found in Fig. 1. The four side walls, the bottom plate, and the top flange are welded together. The two cooled side walls are 89 mm wide, while the adjoining, longer side walls, which are 19 mm thick, each contains two embedded 600 W, 120 V Watlow Firerod cartridge heaters. The lid is bolted to the flange and has holes for the introduction of thermocouples and nitrogen gas. This gas is used to purge the atmosphere above the molten ingot so as to reduce oxidation, to which lead is particularly susceptible.

Two stainless-steel water cooled heat exchangers were mounted on the 89 mm wide side walls. The air gap between the mold walls and the heat exchangers, which was fixed at approximately 0.5 mm, was maintained by wing nuts on threaded rods embedded in the mold. This gap kept the effective heat transfer coefficient between the cold plates and the mold wall low enough to allow solidification of the ingot to occur over a time long enough for significant buoyancy induced flow and the consequent macrosegregation to occur. The relatively high thermal resistance across this gap also prevented continuous steam generation in the cold plates during cooling (a small amount is generated in the first few seconds of cooling) and maintained a relatively isothermal heat sink for the mold. Although exact values were not measured, the overall heat transfer coefficient between the heat exchanger and the mold wall was estimated to be in the range from 85 to 100 W/m^2K (Krane, 1996). While others have measured the heat transfer coefficient to obtain a boundary condition for their numerical simulations (Prescott, 1992; Prescott et al., 1994), the boundary conditions for the simulations in this study came from measured wall temperatures during solidification (cf. Shahani et al., 1992). The thermal resistance of an air gap between the mold and the solidified ingot was neglected, as the experimental results taken in a similar configuration by Reddy and Beckermann (1993) suggest that this resistance is negligible compared to that through the mold.

Metal Alloys. The first ingot cast was a Pb-40%Sn alloy. The ingot was composed of 2.95 kg lead and 1.97 kg tin, stood 80 mm, and had a freezing range (≈50°C) about half that of the 20%Sn ingot. Because this composition is much larger than the maximum solid solubility of tin in lead, it has a much more significant eutectic reaction. The second alloy (Pb-20%Sn) was selected because the Pb-Sn phase diagram shows a large difference between the solidus and liquidus temperatures at that composition. Larger freezing ranges have been shown in many cases to result in higher levels of macrosegregation, which is desirable for comparing experimental and numerical results. The Pb-20%Sn ingot was composed of 1 kg tin and 4 kg lead and, after solidification in the test cell, stood 75 mm tall.

Temperature Measurements. Type E thermocouples were used to measure temperatures in the ingot and in the mold walls during solidification. The ingot and side wall temperatures and their positions are shown in Fig. 1. Voltages were measured using an HP 3497A controller and an HP 3456A digital voltmeter from an HP 3054A Automatic Data Acquisition and Control unit. The HP 3497A unit was controlled by a graphical program written with LABVIEW software and run on an IBM PC/Value Point with an Intel 486DX central processing unit and a 33 MHZ clock. The voltages relative to an electronic ice reference point were converted into temperatures using a ninth order polynomial resident in the LABVIEW software. The standard limit of uncertainty of type E thermocouples is ±1.7°C, while the reference junctions in the multiplexers have an uncertainty of ±0.3°C. Auxiliary experiments using pure lead and pure tin showed that the thermocouples in the ingot gave temperatures within ±0.4°C of the tabulated melting points of those metals.

Six thermocouple probes purchased from Omega Engineering were fashioned into a rake, which was inserted into the test cell as shown in Fig. 1. One thermocouple was placed along the centerline of the ingot, and all were mounted 9.53 mm apart. The 0.25 mm wires inside the probes were protected by magnesium oxide insulation and a 1.6 mm diameter stainless steel sheath. The sheath protected the thermocouple tip from contact with the liquid metal, but the tip was in good thermal contact with the sheath, giving a time constant of approximately 1 s. The mold wall thermocouples were in 1.5 mm diameter stainless steel sheaths, but had exposed beads.

Casting Procedure. After spraying the inside of the test cell with a light coat of graphite mold-release, the solid metal charge was placed in the mold, the air was purged with nitrogen, and the mold was heated to a temperature near 350°C. Once all of the solid metal melted, the lid was removed and the liquid was vigorously stirred. The lid was replaced and the atmosphere was purged again with nitrogen. The heaters were controlled manually to achieve initial mold temperatures of approximately 350°C, and then the test cell was allowed to cool naturally through the insulation. Because heat transfer paths inside the test cell had much lower resistances than the insulation, the mold and melt became nearly isothermal quickly, compared to the overall cooling period. When the test cell cooled to the desired start temperature and all of the mold and melt temperatures were within 2°C of each other, the water flow was initiated to begin the quenching process.

For each ingot, three runs were made. During the first run temperatures were recorded inside the melt, using the thermocouple rake, and in the chill walls. When all of the temperatures in the melt fell below 150°C, which is well below the lowest possible temperature at which liquid could exist, the cooling water was turned off. The second experiment was performed by turning the heaters on, bringing the mold and ingot to well

Nomenclature

B = specific buoyancy force (m/s^2)
c = specific heat (J/kg K)
DAS = dendritic arm spacing (μm)
D_l = liquid mass diffusion coefficient (m^2/s)
f = mass fraction
g = volume fraction
h = enthalpy (J)
k = thermal conductivity (W/m K)
K = permeability (m^2)
P = pressure (N/m^2)
t = time (s)
u = x-velocity (m/s)
U = overall heat transfer coefficient (W/m^2K)
v = y-velocity (m/s)
V = velocity vector (m/s)
x, y = Cartesian coordinates (m)

Greek Symbols

κ_o = permeability constant (m^2)
μ = dynamic viscosity (kg/s m)
ρ = density (kg/m^3)

Subscripts

l = liquid
s = solid

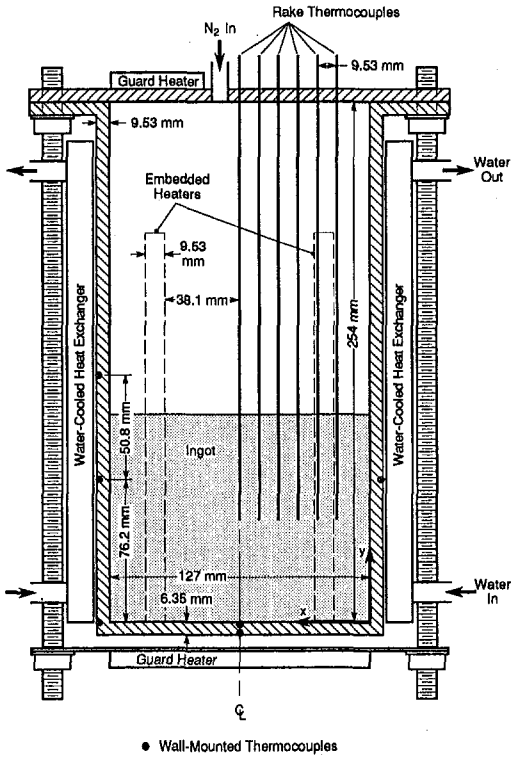

Fig. 1 Vertical section of test cell

above the liquidus temperature, and repeating the cooling process. This experiment was performed to confirm repeatability of the cooling curves. The heating and cooling processes were performed a third time, with the rake thermocouples removed, to obtain a casting for composition measurements and metallography. More details of the casting procedure and test cell are in Krane (1996).

Composition Measurements. Once the test cell cooled to below about 50°C, the insulation and the lid were removed, and the extracted ingot was cut with a band saw to expose a plane corresponding to the two-dimensional numerical calculations. Composition measurements were made in this plane, which was also examined under a microscope to determine microstructural features. Before the measurements were made, the surface was flattened by flycutting with a very sharp, well-rounded tool.

Composition measurements were made by extracting small samples from 2— 3 mm deep holes drilled in the plane using a $\frac{1}{16}''$ bit. The ribbon of metal and other fragments produced by drilling were weighed and, depending on the depth of cut and the composition, ranged in mass from 60 to 125 mg (±0.1 mg). After weighing each sample was dissolved in nitric acid, followed by dilute hydrochloric acid, and finally was diluted with deionized water to a lead concentration between 10 and 20 ppm. Standards were made in the same fashion with known amounts of the pure lead. The concentrations of the final solutions were measured using a Perkin Elmer model 3090 atomic absorption spectrophotometer. The uncertainty analysis used to obtain the error bars on the experimental composition profiles is the same as that used by Prescott (1992). Because the time-consuming nature of this process made measurement of entire macrosegregation fields impractical, several composition profiles were taken across the ingot.

Metallography. Examination of the microstructure of the cast ingots was performed in order to estimate the permeability of the mushy zones and to detect the presence of *A*-segregates. The sectioned ingot provides a surface parallel to that from which the composition measurements were made. This surface was flycut and sawed into four pieces, each approximately 30–40 mm by 30 mm. These smaller specimens were first polished by using a 4–6 μm diamond abrasive with an oil lubricant on a nylon cloth. After carefully cleaning the surface with deionized water and acetone, the polishing was completed with a 0.05 μm alumina abrasive on a Leco B soft cloth. With sufficient polishing no etching was necessary to see the microstructure with an optical microscope. A Leco 300 Metallograph microscope was used to view the samples, and photographs were taken on Polaroid type 55 film.

Numerical Model

The numerical model used to simulate mass, momentum, heat, and species transport during the solidification of a binary alloy was originally developed by Bennon and Incropera (1987a, b) and refined by Prescott et al. (1991). A scaling analysis of that model, which systematically eliminated terms which are negligible everywhere (Krane and Incropera, 1996), resulted in the following model equations:

$$\frac{\partial \rho}{\partial t} + \nabla \cdot (\rho \mathbf{V}) = 0 \tag{1}$$

$$\frac{\partial}{\partial t}(\rho u) + \nabla \cdot (\rho \mathbf{V} u) = \nabla \cdot \mu_l \nabla u - \frac{\mu_l}{K} u + \rho_l B_{lx} - \frac{\partial P}{\partial x} \tag{2}$$

$$\frac{\partial}{\partial t}(\rho v) + \nabla \cdot (\rho \mathbf{V} v) = \nabla \cdot \mu_l \nabla v - \frac{\mu_l}{K} v + \rho_l B_{ly} - \frac{\partial P}{\partial y} \tag{3}$$

$$\frac{\partial}{\partial t}(\rho h) + \nabla \cdot (\rho \mathbf{V} h) = \nabla \cdot \frac{k}{c_s} \nabla h + \nabla \cdot \frac{k}{c_s} \nabla (h_s - h) - \nabla \cdot (f_s \rho (\mathbf{V} - \mathbf{V}_s)(h_l - h_s)) \tag{4}$$

$$\frac{\partial}{\partial t}(\rho f^A) + \nabla \cdot (\rho \mathbf{V} f^A) = \nabla \cdot \rho D^A \nabla f^A + \nabla \cdot \rho D^A \nabla (f_l^A - f^A) - \nabla \cdot (f_s \rho (\mathbf{V} - \mathbf{V}_s)(f_l^A - f_s^A)). \tag{5}$$

The solid is assumed to be rigid and stationary and the flow to be two-dimensional and laminar. The laminar approximation is doubtful only at times before solidification begins, when the Grashof number based on the ingot height and wall-bulk liquid temperature difference is $O(10^9)$, which is in the transition region. As the liquidus front progresses and the bulk superheat is extinguished, the circulation is weakened to the point that the laminar assumption is valid.

The transport Eqs. (1)–(5) are not a closed system, as they require knowledge of the local temperatures, phase fractions, and phase compositions. To obtain these quantities, a linearized Pb-Sn equilibrium phase diagram is employed, using a method first described in Bennon and Incropera (1987b). This method is based on the equilibrium lever law, which gives macrosegregation results similar to the nonequilibrium Scheil formulation (Schneider and Beckermann, 1995).

Because the truly anisotropic nature of a developing mushy zone is not well understood, isotropic permeability has been assumed (Bennon and Incropera, 1987b). The Blake-Kozeny model is of the following form:

$$K_x = K_y = K = \kappa_o \frac{g_l^3}{(1 - g_l)^2}, \tag{6}$$

where the permeability constant is evaluated from the secondary dendrite arm spacing (Asai and Muchi, 1978).

$$\kappa_o = \frac{\mathrm{DAS}^2}{180} \tag{7}$$

Because the purpose of the experiments is to provide data to assess the continuum mixture model for binary solidification, it is desirable to match the boundary and initial conditions of the calculations to those of the experiments as closely as possible. The computational domains for simulating the two ingots have 75 × 88 control volumes for the 40 percent Sn and 75 × 82 for the 20 percent Sn and have the same dimensions as the mold shown in Fig. 1. The domains were truncated at the top of the experimental ingot (75 mm from the bottom of the cavity for 20 percent Sn and 80 mm for 40 percent Sn) and at the midplane of the mold, which is treated as a plane of symmetry. This symmetry was checked by measuring temperatures in both chilled walls, which were consistently within 1.5°C of each other. Because the heat transfer path from the mold directly to the ingot has a resistance several orders of magnitude less than that of radiation and convection between the upper mold wall and the top of the ingot, the top of the numerical domain is modeled as a free surface which does not transfer heat or mass. The stainless steel mold is included in the calculations and it is assumed that the mold and the ingot maintain perfect contact. While the bottom of the mold is assumed to be insulated, the vertical mold wall is chilled by the water cooled heat exchangers. To simulate this cooling the vertical wall temperatures measured during the experiments were used as the boundary condition for the computations by linearly interpolating between the top and bottom temperatures at each time step. Further computational details and thermophysical property values are provided by Krane (1996).

Comparison of Experimental and Numerical Results

In this section, experimental data from solidification of the two alloys are compared to several numerical simulations. Because close similarities exist in the temperature histories, macrosegregation patterns and solidification behavior of the two alloys, most of the results presented are taken from the 40%Sn ingot. The ingots were melted and solidified, and temperature measurements were made in the mold wall next to the water-cooled heat exchangers and in the ingot itself. The position of these thermocouples is found in Fig. 1. For 40%Sn, Fig. 2 shows measured temperature histories of the thermocouples embedded in the left mold wall in Fig. 1 at y = 0.0 mm and y = 76.2 mm. The initial temperature of the mold and liquid is approximately 239°C (±1°C). Because it is measured very close to the outer surface of the mold, the temperature drops rapidly in the short time after cooling begins. As the thermal penetration depth increases and the heat is extracted from a larger volume, the cooling rate at the wall slows. As solidification begins the temperature near the top of the ingot (y = 76.2 mm) begins to fall faster than the temperature in the bottom corner of the mold (y = 0.0 mm). The corner region of the mold is less affected by

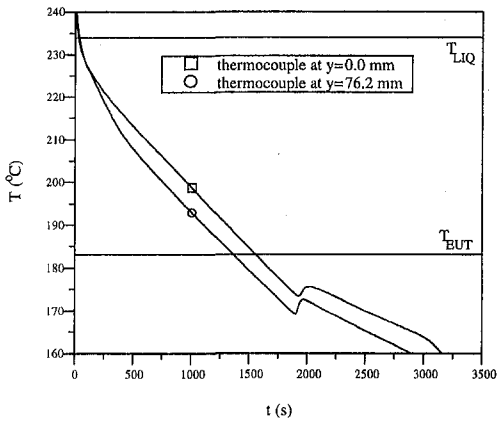

Fig. 2 Measured mold wall temperatures, Pb-40%Sn

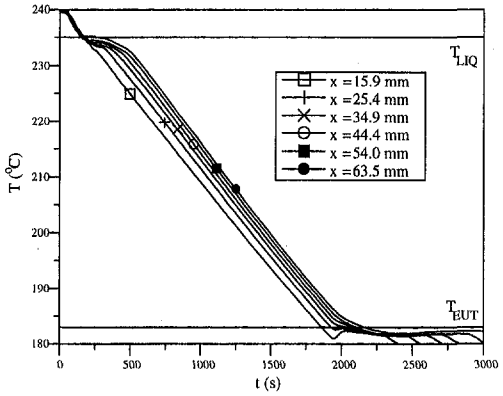

Fig. 3 Measured ingot temperatures, Pb-40%Sn

the onset of freezing and stays warmer longer because the mold bottom has a larger thermal capacity and thermal resistance than the ingot. After freezing begins the two temperatures decrease at approximately the same rate (≈2°C/min). The bottom temperature lags behind that of the top due to the resistance to heat transfer through the bottom of the mold, which remains the warmest part of the system throughout the freezing process. Eutectic freezing begins at $t \approx 1900$ s and is indicated by a sharp rebound in the temperature caused by the sudden release of latent heat which occurs in the rapid eutectic reaction. During the subsequent secondary freezing, the cooling rate is slower than during the primary solidification, but increases at $t \approx 3000$ s when the entire ingot has solidified.

The temperatures measured along the midheight of the ingot (y = 40.0 mm) during solidification are plotted in Fig. 3. After the sensible cooling of the liquid, solidification begins at $t \approx$ 200 s with less than 1°C of undercooling. After a 400 to 500 s period, during which the mushy zone spreads across the ingot, cooling rates at the six thermocouple locations become nearly constant and almost equal. At 1940 s the thermocouple closest to the chilled wall begins to measure a slight increase in temperature from a minimum of 181°C. This increase is a recalescence effect due to the onset of eutectic solidification, which spreads across the ingot and lasts between 350 and 800 s, with the reaction lasting longer at locations further from the mold wall. This lower eutectic freezing period is due to an increase in tin concentration and a decrease in local cooling rates with increasing distance from the cold wall. The first thermocouple (x = 15.9 mm) has complete solidification at 2250 s, and the midplane is totally solidified 750 s later.

After the ingot was cooled, removed from the mold, and sectioned, micrographs were taken along the top of the ingot and are shown in Fig. 4. Figure 4(a) is the top corner at the chilled wall, and the center of Fig. 4(b) is 15 mm from the mold. In these pictures the lighter areas are the eutectic material and the darker regions are the primary phase. Both of these micrographs show a region of eutectic material just below the top surface of the ingot. In Fig. 4(a), an A-segregate ascends from the right chilled wall. This segregate, which solidified after the surrounding dendritic array, was a preferred path for tin-rich liquid flowing out of the mush and along the top of the ingot. Further from the chilled wall there is less eutectic material and the top layer includes some primary phase dendrites, suggesting a lower concentration of tin.

Visual inspection of the surfaces near the mold wall shows several small regions of mostly eutectic material. These A-segregates are approximately 1 mm wide and most range from 5 to 10 mm long. One segregate, which begins 50 mm from the bottom of the ingot, is almost 30 mm long. All begin within a few millimeters of the chilled surface and extend into the ingot at a roughly 45 deg angle. Figure 5 reveals two such segregates, which are the lighter shaded regions extending from near the

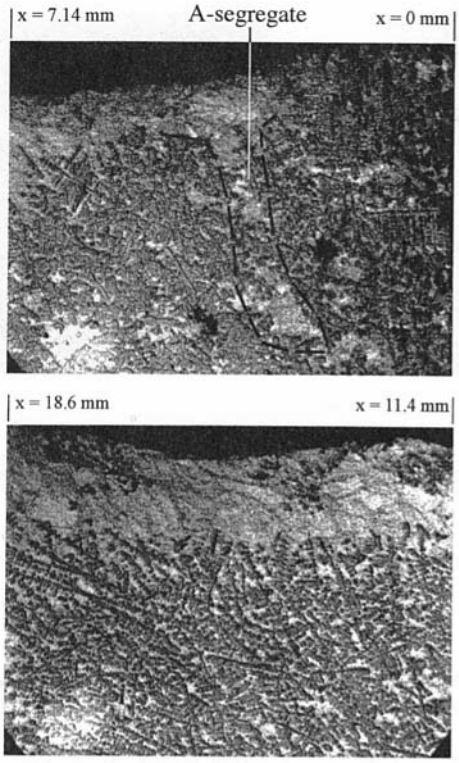

Fig. 4 Microstructure along top of Pb-40%Sn ingot: (*a*) top corner at mold wall; (*b*) 15 mm from mold wall

chilled wall ($x = 0$ mm) into the ingot. These regions do not seem to be continuous, as one might expect. One plausible reason is that dendrites of the primary solid might grow into the fluid of the channel, which is relatively stagnant once the solid volume fraction of the surrounding dendritic array exceeds approximately 10 percent. Several segregates also appear in a region between 50 and 70 mm from the bottom and 20 to 30 mm from the chilled wall.

Having cast the ingots, measured the cooling curves, and examined the microstructure, numerical simulations were performed. Other than the change in composition, the use of different measured wall cooling curves as a thermal boundary condition, and different domain heights, calculations for the two alloys were performed for equivalent conditions. Both sets of simulations were conducted using the permeability constant, κ_o, as a parameter, with $\kappa_o = 2.8 \times 10^{-11}$ m^2, $\kappa_o = 1.0 \times 10^{-11}$ m^2, and $\kappa_o = 5.0 \times 10^{-12}$ m^2. These values were chosen to show the effect of permeability on macrosegregation. While there is some uncertainty in the other thermophysical properties used in this study, the uncertainty in the permeability is much larger than that of any other parameter. While the thermophysical properties are certainly known to within an order of magnitude, the same claim cannot be made for the permeability, K. Over the entire mushy zone, K varies over several orders of magnitude and its variation with solid volume fraction is not well characterized near the liquidus. Because the interdendritic velocity, a measure of the vigor of the flow driving macrosegregation, varies linearly with K (Krane and Incropera, 1996), the much larger uncertainty in the permeability will have the most significant effect on the predictions of the composition field in the cast ingot.

In Fig. 6, measured temperature histories for the 40 percent Sn ingot are compared at three thermocouple locations to predictions for $\kappa_o = 2.8 \times 10^{-11}$ m^2. It should be noted that the liquidus temperature for this alloy calculated with a linearized phase diagram is approximately 1°C lower than that found from the actual liquidus line. The predicted temperatures decrease faster than the measured values, especially in the fully liquid regime at early times, primarily due to the added thermal capacity of the side walls in the experiment. The experimental curves also have longer periods of eutectic solidification. This effect

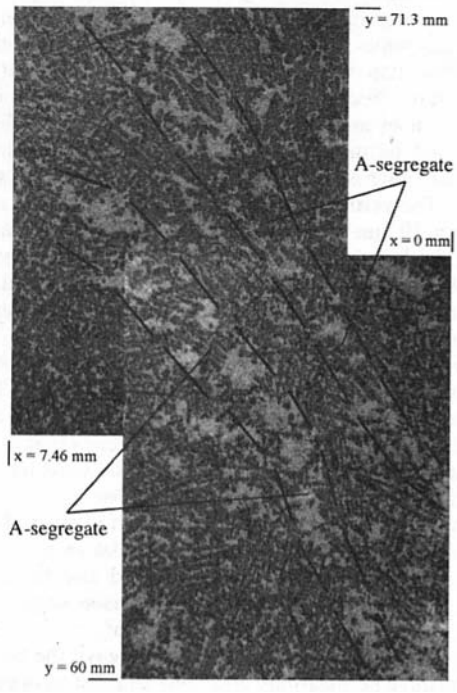

Fig. 5 Micrograph of two channels extending into the Pb-40%Sn ingot from mold wall on right

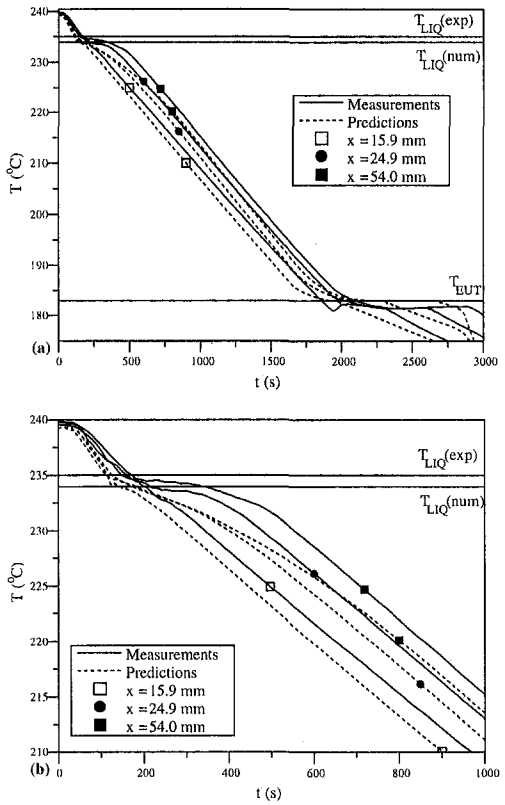

Fig. 6 Comparison of measured and predicted ($\kappa_o = 2.8 \times 10^{-11}$ m^2) ingot temperature histories for Pb-40%Sn: (*a*) complete histories; (*b*) at early times

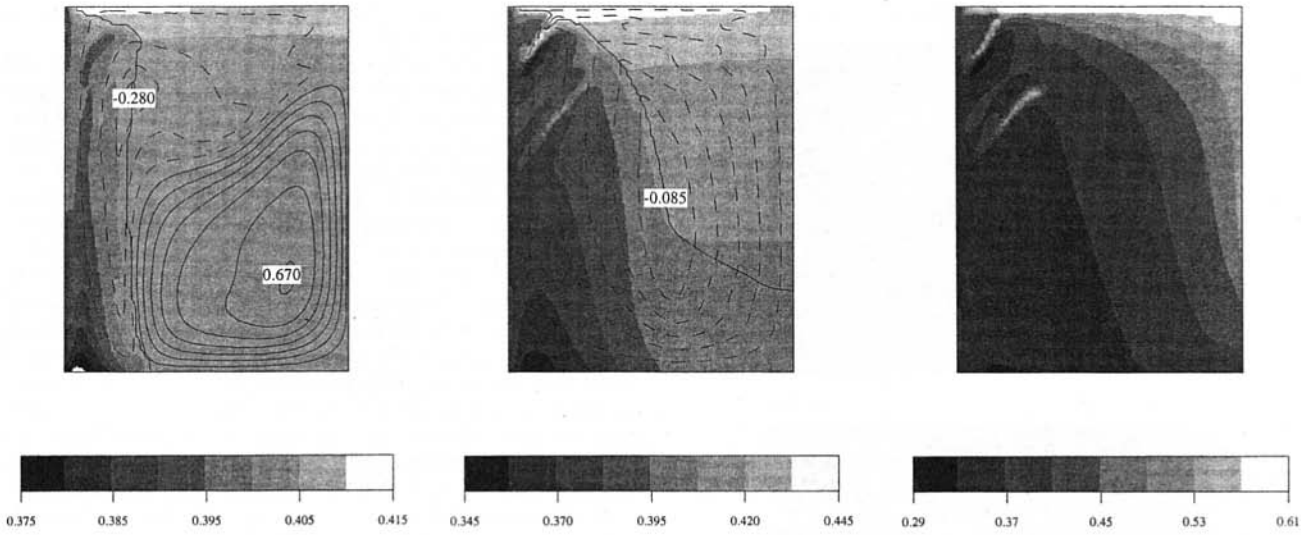

Fig. 7 Predicted macrosegregation and streamline plots for Pb-40%Sn and $\kappa_o = 2.8 \times 10^{-11}$ m^2: (*a*) f^{Sn} at 150 s; (*b*) f^{Sn} at 300 s; and (*c*) f^{Sn} in solid ingot. (Solid and dashed streamlines depict CCW and CW cells, respectively.)

is due primarily to use of the equilibrium lever law in the calculations, rather than the Scheil formulation, which correctly predicts more eutectic formation. While there are some minor discrepancies in the temperature histories, the overall agreement is good, in spite of the assumption of no mold-ingot gap. In fact, no measurable gap developed in the cast ingots, which is explained by the fact that there was some liquid at the mold wall until the onset of eutectic freezing very late in the overall process. Exudation, liquid leaking into any gap which might form by the differential thermal contraction of the steel mold and the lead-tin melt, would help to maintain a good thermal contact.

Progression of the solidification front, solute redistribution, and flow patterns for $\kappa_o = 2.8 \times 10^{-11}$ m^2 are shown in Fig. 7. At 150 s, Fig. 7(*a*), the mushy zone begins to develop and is accompanied by opposing counterclockwise thermal and clockwise solutal flow cells. In Fig. 7(*b*), at 300 s, the thermal cell has dissipated due to the extinction of the melt superheat, and the solutal cell, although weakened, dominates the flow. One smaller and two larger tin-rich segregates are visible in the final macrosegregation pattern of Figure 7(*c*), and there is a strip at the top of the domain which is very tin-rich. Calculations of the redistribution of solute with $\kappa_o = 1.0 \times 10^{-11}$ m^2 and $\kappa_o = 5.0 \times 10^{-12}$ m^2 predict fewer and smaller segregates, a smaller tin-rich region along the top and a decrease in the overall solute redistribution levels with decreasing κ_o.

These results can be qualitatively compared with inspection of the polished surface, which showed only one large (over 10 mm long) *A*-segregate, as well as several smaller segregates along the chilled wall. The numerical grid is not fine enough to resolve the smaller segregates next to the wall, but the absence of larger segregates in the ingot further from the mold wall suggests that the actual permeability is lower than that used for the calculations. The calculated extent of the tin-rich band along the top of the ingot increases with permeability and, in the experimental ingot, is similar to predictions made with a lower permeability.

A quantitative comparison of calculated and measured composition fields is provided by the one vertical and three horizontal profiles of Figs. 8(*a*)–(*d*). The horizontal profiles span the distance from the mold wall ($x = 0.0$ mm) to the ingot centerline ($x = 62.5$ mm), while the vertical profile extends over the entire height of the ingot. The profiles at $y = 15$ mm, Fig. 8(*a*), suggest that the permeability constant is equal to or less than 5.0×10^{-12} m^2, as the data fall fairly close to the corresponding prediction near the chilled wall and below it further out. Similar results are found in Fig. 8(*b*) but, apart from the datum at $x = 11$ mm, the experimental results best match the predicted composition profile for a slightly higher value of κ_o in the region closer to the chilled wall. The composition at $x = 11$ mm may be due to the influence of a local *A*-segregate ascending through the $y = 39$ mm plane. The comparison at $y = 69$ mm, Fig. 8(*c*), is more equivocal. Near the plane of symmetry at $x = 62.5$ mm, the data are in better agreement with predictions based on the lower values of κ_o, while in the middle of the domain the measurements are in better agreement with simulations based on the largest permeability constant. It must be noted, however, that the uncertainty in some of these measurements exceeds the variation in predictions among the three values of κ_o, which differ by only 2 wt%Sn in the middle of the domain. Near the chilled wall ($x < 25$ mm), the measurements do not exhibit the sharp spikes seen in the predictions. This difference could be because the actual permeability, especially at early times when dendrites are forming near the wall, is much less than values used in the simulations. It is also possible that it is because the calculations are a two-dimensional approximation of an inherently three-dimensional effect. This finding would be in agreement with visual inspections of the experimental microstructure, which reveal primarily small *A*-segregates. The vertical composition profiles of Fig. 8(*d*) correspond to $x = 19$ mm with predictions for the lowest permeability providing the best agreement with the data. This agreement is found in the comparison of numerical and experimental composition values and in the apparent lack of severe *A*-segregates near the top of the domain.

Composition profiles were measured at three different heights ($y = 15$ mm, 37 mm, and 57 mm) in the 20 percent Sn ingot. These results, with the corresponding predictions for all three permeabilities, are plotted in Fig. 9, and at each height the best agreement with the data corresponds to predictions for the lowest permeability ($\kappa_o = 5.0 \times 10^{-12}$ m^2). One could attempt to find the value of κ_o which gives a best fit to the data, but given the size of the experimental uncertainty relative to the change in the profiles with κ_o such a result would also be extremely uncertain. However, the foregoing comparison suggests a permeability constant less than 1.0×10^{-11} m^2.

Having noted that $\kappa_o = 5.0 \times 10^{-12}$ m^2 gave the best agreement of the three permeability constants and that an upper bound on κ_o is probably not more than twice that value, it is interesting to compare the presumed dendritic arm spacing from Eq. (7),

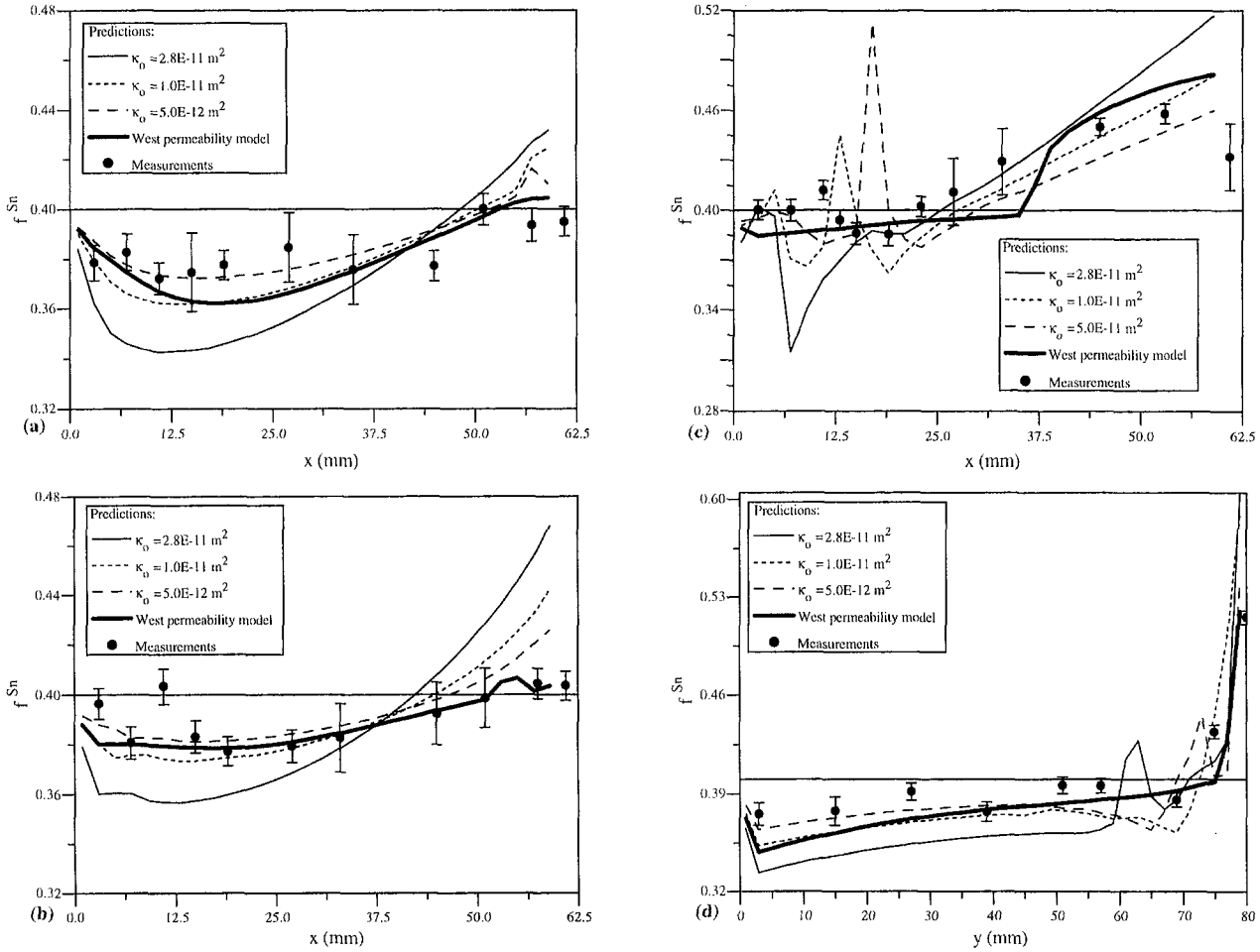

Fig. 8 Composition profiles for Pb-40%Sn: (*a*) y = 15 mm; (*b*) y = 39 mm; (*c*) y = 69 mm; and (*d*) x = 19 mm

DAS = 30 μm, with the measured value in the cast ingot. The experimental dendritic arm spacings are averages of 25 measurements made using the random intercept method at several locations in the ingots. The measured spacing for the 40 percent Sn ingot is 174 μm $\pm$ 21 μm, giving a permeability constant (κ_o = 1.7 $\times$ 10^{-10} m^2 $\pm$ 0.4 $\times$ 10^{-10} m^2) which is an order of magnitude larger than the predicted upper bound. Similarly, the 20 percent Sn ingot has a DAS of 189 μm $\pm$ 20 μm, or κ_o = 2.0 $\times$ 10^{-10} m^2 $\pm$ 0.4 $\times$ 10^{-10} m^2. These discrepancies raise serious questions about the Blake-Kozeny permeability model. While the trends in the experimental and numerical results exhibit qualitative agreement in this and other studies (Shahani et al., 1992; Prescott and Incropera, 1994), the levels of macrosegregation clearly are not predicted by the current model if the permeability constant is calculated by Eq. (7) using measured DAS from the actual casting.

The Blake-Kozeny model of the permeability function used in the foregoing calculations is derived for laminar flow through a "bundle of tangled tubes of weird cross section," as described by Bird et al. (1960). This description certainly fits many dendritic arrays found in metal castings, but Bird et al. also state that the model is only valid for $g_s > 0.5$. Given this restriction it is reasonable to use this model to predict flow deep in the mushy zone. Unfortunately, the scaling analysis of the momentum equations (Krane and Incropera, 1996) shows that only flows very near the liquidus interface are vigorous enough to affect macrosegregation over the time scale of the solidification process. There are no experimental data to support the use of the Blake-Kozeny model for small g_s, and it is possible that related predictions of the permeability are inaccurate.

Another model for the permeability of the mushy zone was developed by West (1985) who fit his model to measurements in an Al-4.5%Cu mushy zone (Piwonka and Flemings, 1966) and showed that it is reasonable for very low solid fractions. Because West fit his model to only one set of data with no method of generalizing the results to other systems, the model cannot be used to simulate the flow in mushy zones of different alloys or for different casting conditions. However, it is instructive to examine the behavior of both models in the near liquidus region. The West model and the Blake-Kozeny model, Eq. (6) with several values of κ_o, are plotted in Fig. 10.

While both the West and the Blake-Kozeny models are valid at higher solid fractions, they predict significantly different behavior as $g_s \Rightarrow 0$. As the liquid fraction increases and the flow resistance decreases, the liquid velocity in the mushy zone becomes more vigorous and advection begins to have a significant effect on the solute redistribution. However, the Blake-Kozeny function increases much more rapidly than the West model, which is fitted to experimental data from a metal alloy mushy zone. While both models yield an infinite permeability as g_s goes to zero, permeabilities based on the West model increase rapidly only very close to the liquidus interface ($g_s < 0.01$). This generally slow rise in K with decreasing g_s yields values of permeability near the liquidus ($g_s < 0.15$) comparable to those given by the Blake-Kozeny model for 1.0 $\times$ 10^{-11} m^2 > κ_o > 1.0 $\times$ 10^{-12} m^2. This range gives the best agreement between the experimental and predicted composition profiles in Figs. 8 and 9.

Calculations were performed for both ingots using the West model for the permeability function in Eqs. (2) and (3), and

the resulting composition profiles are plotted in Figs. 8 and 9. In most cases the West permeability function provides better agreement with the measurements than predictions which used the Blake-Kozeny model with the measured dendritic arm spacings. However, it is noted again that the dendritic structure from which West's function was developed is not characterized well enough in the original work by Piwonka and Flemings (1966) to draw definitive conclusions about its applicability. The form of West's function is based on flow over spherical particles, while Piwonka and Fleming's microstructure was most likely columnar. Pressure drop experiments would have to be performed on the mushy zone of the alloys in this study to determine the correct constants for West's model. However, the curves in Figs. 8–10 suggest that this function might model the behavior of permeability of the dendritic array in the most important region, near the liquidus, much better than the Blake-Kozeny model.

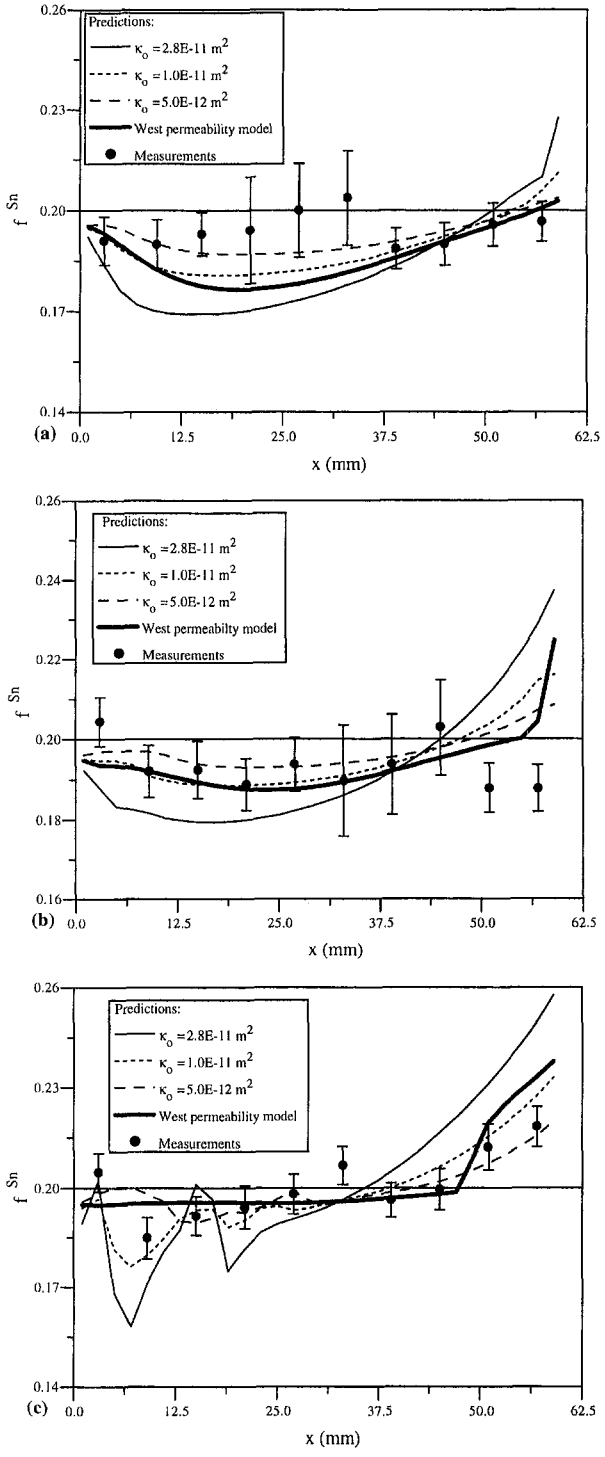

Fig. 9 Composition profiles for Pb-20%Sn: (*a*) y = 15 mm; (*b*) y = 37 mm; and (*c*) y = 57 mm

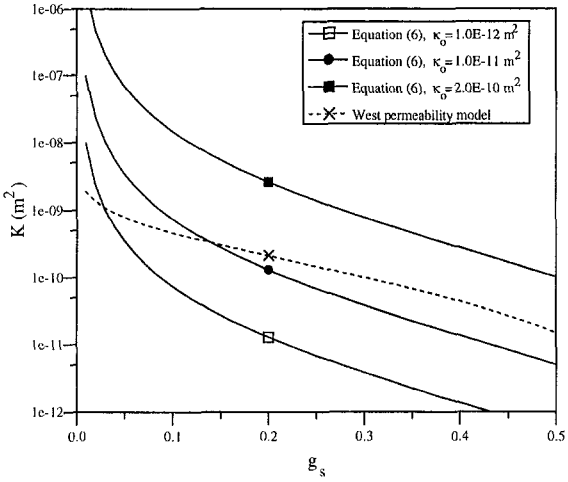

Fig. 10 Permeability as a function of solid volume fraction

In addition to the importance of the behavior of the permeability function when $g_s \Rightarrow 0$, another reason the predictions suggest that the actual DAS is much smaller than that measured could be dendritic coarsening during solidification (Flemings, 1974). Using the results of an analysis found in that reference, the time until complete coarsening in the present experiments was found to be on the order of 4000 s or greater. While the total solidification time was 1500–2000 s shorter than that time, some significant coarsening might have occurred, thus increasing the measured DAS. It is not likely, however, that this effect would account for all of the large discrepancies found between measured and calculated arm spacings.

Summary

In order to gather experimental data to assess the applicability of solidification simulations using the continuum mixture model and equilibrium phase diagrams for binary systems, two metal ingots (Pb-20%Sn and Pb-40%Sn) were cast. Using experimentally measured chill wall temperatures as a thermal boundary condition, numerical simulations of the experiments were performed and comparisons were made to measurements of temperature and composition. Measured temperature histories were generally in good agreement with the predictions, with deviations attributable to nonequilibrium effects and uncertainty in the thermophysical properties.

Composition measurements made at several discrete locations in both ingots did not exhibit consistently good agreement with the simulations. The macroscopic composition fields are determined entirely by the advection of species and the dominant parameter influencing the fluid velocity in the mushy zone is the permeability function. Because of this influence and the very large uncertainty in the permeability, the constant (κ_o) in the Blake-Kozeny model was used as a parameter in the calculations. Overall, experimental trends in the species mass fraction distributions were similar to those of the predictions. However, using values of κ_o derived from measured dendritic arm spacings for these two ingots, the local macrosegregation was overpredicted in all cases. It was concluded that the actual permeability near the liquidus interface is much lower than that predicted by the Blake-Kozeny model, due possibly to the unrealistically rapid rise of the permeability near the liquidus

surface or to the coarsening of the dendritic structure between nucleation and final solidification.

Acknowledgments

This work was funded by the United States Department of Energy through Award Number DE-FG02-87ER13759.

References

Asai, S., and Muchi, I., 1978, "Theoretical Analysis and Model Experiments on the Formation Mechanism of Channel-Type Segregation," *Trans. ISIJ,* Vol. 18, pp. 90–98.

Bennon, W. D., and Incropera, F. P., 1987a, "A Continuum Model for Momentum, Heat and Species Transport in a Binary Solid-Liquid Phase Change System: I. Model Formulation," *Int. J. Heat Mass Trans.,* Vol. 30, pp. 2161–2170.

Bennon, W. D., and Incropera, F. P., 1987b, "A Continuum Model for Momentum, Heat and Species Transport in a Binary Solid-Liquid Phase Change System: II. Application to Solidification in a Rectangular Cavity," *Int. J. Heat Mass Trans.,* Vol. 30, pp. 2171–2187.

Bird, R. B., Stewart, W. E., and Lightfoot, E. N., 1960, *Transport Phenomena,* John Wiley & Sons Inc., New York.

Flemings, M. C., 1974, *Solidification Processing,* McGraw-Hill Inc., New York.

Hills, R. N., Loper, D. E., and Roberts, P. H., 1983, "A Thermodynamically Consistent Model of a Mushy Zone," *Q. J. Mech. Appl. Math.,* Vol. 36, pp. 505–539.

Krane, M. J. M., 1996, "Transport Phenomena During the Solidification of Binary and Ternary Metal Alloys," Ph.D. dissertation, School of Mechanical Engineering, Purdue University, West Lafayette, IN.

Krane, M. J. M., and Incropera, F. P., 1996, "A Scaling Analysis of the Unidirectional Solidification of a Binary Alloy," *Int. J. Heat Mass Trans.,* Vol. 39, pp. 3567–3579.

Piwonka, T. S., and Flemings, M. C., 1966, "Pore Formation in Solidification," *Trans. Met. Soc. AIME,* Vol. 236, pp. 1157–1165.

Prescott, P. J., 1992, "Convective Transport Phenomena During Solidification of Binary Metal Alloys and the Effect of Magnetic Fields," Ph.D. dissertation, School of Mechanical Engineering, Purdue University, West Lafayette, IN.

Prescott, P. J., and Incropera, F. P., 1996, "Convection Heat and Mass Transfer in Alloy Solidification," *Advances in Heat Transfer,* J. P. Hartnett, T. Irvine, Jr., Y. I. Cho, and G. A. Green, eds., Vol. 28, Academic Press, New York, pp. 231–338.

Prescott, P. J., Incropera, F. P., and Bennon, W. D., 1991, "Modelling of Dendritic Solidification Systems: Reassessment of the Continuum Momentum Equation," *Int. J. Heat Mass Trans.,* Vol. 34, pp. 2351–2359.

Prescott, P. J., Incropera, F. P., and Gaskell, D. R., 1994, "Convective Transport Phenomena and Macrosegregation During Solidification of a Binary Metal Alloy: II—Experiments and Comparisons With Numerical Predictions," ASME JOURNAL OF HEAT TRANSFER, Vol. 116, pp. 742–749.

Reddy, A. V., and Beckermann, C., 1993, "Measurements of Metal-Mold Interfacial Solidification of Sn and Sn-Pb Alloys," *Exp. Heat Transfer,* Vol. 6, pp. 111–129.

Schneider, M. C., and Beckermann, C., 1995, "A Numerical Study of the Combined Effects of Microsegregation, Mushy Zone Permeability and Flow, Caused by Volume Contraction and Thermosolutal Convection, on Macrosegregation and Eutectic Formation in Binary Alloy Solidification," *Int. J. Heat Mass Trans.,* Vol. 38, pp. 3455–3473.

Shahani, H., Amberg G., and Fredriksson, H., 1992, "On the Formation of Macrosegregations in Unidirectional Solidified Sn-Pb and Pb-Sn Alloys," *Met. Trans. A,* Vol. 23 A, pp. 2301–2311.

West, R., 1985, "On the Permeability of the Two-Phase Zone During Solidification of Alloys," *Met. Trans. A.,* Vol. 16A, p. 693.

Three-Dimensional Free Convection Boundary Layers in Porous Media Induced by a Heated Surface With Spanwise Temperature Variations

D. A. S. Rees
Department of Mechanical Engineering,
University of Bath,
Claverton Down,
Bath BA2 7AY,
United Kingdom
ensdasr@bath.ac.uk

In this paper we consider the effect of a nonuniform surface temperature distribution on the steady laminar free convection boundary layer flow induced by a vertical plate embedded in a fluid-saturated porous medium. The surface temperature profile exhibits sinusoidal variations in the spanwise (horizontal) direction, but the minimum temperature remains above or equal to that of the ambient medium. The resulting boundary layer flow is three-dimensional, and the governing equations are solved using a combination of a spanwise spectral decomposition and the Keller-box method. Detailed results in terms of the evolution of the rates of heat transfer and the developing thermal field are presented. The numerical work is supplemented by an asymptotic analysis valid far downstream where it is found that the effect of nonuniform heating becomes confined to a thin layer of uniform thickness embedded within the main growing boundary layer.

1 Introduction

The study of free convection heat transfer from uniform surfaces embedded in a saturated porous medium has attracted a great deal of interest from many investigators over the last two decades; see Nield and Bejan (1992) for a comprehensive review of this topic. Studies have centered on those cases where the thermal boundary conditions allow the use of similarity transformations to reduce the governing equations to a system of ordinary differential equations. In general, this means that the heated surface is plane and that the imposed temperature or surface heat flux satisfies a power-law distribution. However, in practice, surfaces are sometimes roughened intentionally in order to enhance the heat transfer. Roughened surfaces are encountered in several heat transfer devices such as flat-plate solar collectors and flat-plate condensers in refrigerators. Larger-scale surface nonuniformities are encountered in cavity wall insulating systems and grain storage containers. Similarly, nonuniformities in the boundary conditions in a plane surface may be obtained by the presence of a nonuniform heat source located nearby.

There is a growing body of literature devoted to this type of generic problem. There are now many papers dealing with boundary nonuniformities in porous channels: Riahi (1993, 1995, 1996) and Rees and Riley (1989a, b) and Rees (1990). But the first papers to study the effects of such nonuniformities on thermal boundary layer flow of a Newtonian (clear) fluid are those of Yao (1983) and Moulic and Yao (1989a, b). More recently, Chiu and Chou (1993) have extended this work to micropolar fluids, and Hossain et al. (1996) to a study of magnetohydrodynamic flow of a highly electrically-conducting fluid. In the area of convection in a porous medium, Rees and Pop (1994a, b, 1995a, b) have considered the effect of wavy surfaces on the otherwise self-similar free convection boundary layer flows. When a uniformly heated vertical surface exhibits surface waves, the resulting flow does in fact remain self-similar (Rees and Pop, 1994a), but when inertia effects are included, this property is lost (Rees and Pop, 1995a). However, when a vertical surface with a uniform heat flux has steady surface waves, the flow immediately becomes nonsimilar even in the absence of inertia effects (Rees and Pop, 1995b). In Rees and Pop (1994b) we considered very small amplitude undulations in a uniformly heated horizontal surface; in this case there exists the possibility of separated flow in the lee of the undulations and conditions were presented to indicate whether or not this would occur for any particular case.

All the papers quoted so far have been concerned with transverse nonuniformities where the boundary conditions are independent of the spanwise direction and, therefore, the resulting flow is two-dimensional. A more recent paper has considered the case of longitudinal surface waves (spanwise variations) on free convection from a vertical surface in a porous medium (Rees and Pop, 1996). Under a wide range of boundary conditions, the flow remains self-similar, but the authors showed that this is only true when the boundary layer thickness is asymptotically smaller than the spanwise wavelength of the nonuniformity. In particular, when the surface temperature is uniform, this means that nonsimilarity is first obtained at an $O(R)$ distance from the leading edge, where R is the porous medium Rayleigh number. In the present paper, we consider a uniform surface with an imposed surface temperature distribution which varies sinusoidally in the spanwise direction. Such a configuration could be supposed to model the presence of a hot water pipe immediately adjacent to a porous insulating cavity such as a double-skin wall of a house packed with a porous insulant, although we are unaware of experimental data against which to compare the present analyses. The resulting flow is three-dimensional, and we study the boundary layer flow using both numerical and asymptotic methods.

The formulation of the problem is given in Section 2, while the detailed description of the numerical method is contained in Section 3. The numerical results are presented in Section 4. Section 5 contains the asymptotic analysis for large distances from the leading edge where we show that the boundary layer

Contributed by the Heat Transfer Division for publication in the JOURNAL OF HEAT TRANSFER. Manuscript received by the Heat Transfer Division September 3, 1996; revision received April 11, 1997; Keywords: Flow Nonuniformity; Natural Convection; Porous Media. Associate Technical Editor: K. Vafai.

splits into a two-layer structure. This type of behavior, where the main boundary layer has a constant thickness near-wall layer embedded within it, also arises in other contexts. Another example of such a two-layer structure arises in the study of the influence of boundary (Brinkman) effects on the vertical free convection boundary layer in a porous medium, as discussed by Kim and Vafai (1989). Finally, the results are discussed briefly in Section 6.

2 Formulation of the Problem

We consider the laminar free-convection boundary layer flow induced by a vertical heated semi-infinite surface embedded in a fluid-saturated porous medium. Attention is given to the case where the surface temperature exhibits sinusoidal variations in a spanwise direction about a mean value which is above the temperature of the ambient medium. The resulting flow is three-dimensional and nonsimilar.

In this paper dealing with three-dimensional boundary layer flows, we assume that the porous medium is isotropic, uniform, and nondeformable, that the fluid and the porous matrix are in local thermal equilibrium, and that inertia, boundary, and dispersion effects are absent. All of these assumptions may be relaxed in future work. Additionally, the flow is laminar and steady; this is a very reasonable assumption given the recent papers by Rees (1993) and Lewis et al. (1995) which show that the vertical free convection boundary layer induced by a uniformly heated surface in a porous medium is stable. It is possible that boundary effects may modify this qualitative behavior, for in the analagous problem of convection in a vertical channel with sidewall heating (the Darcy-Bénard problem rotated through 90 deg), Kwok and Chen (1987) showed that uniform Darcy-Brinkman flow is susceptible to instability, whereas the pure Darcy-flow case is stable (see Gill, 1969 and Lewis et al., 1995).

The nondimensional equations of motion governing steady Darcy-Boussinesq free convection flow for this problem are

$$\frac{\partial u}{\partial x} + \frac{\partial v}{\partial y} + \frac{\partial w}{\partial z} = 0 \tag{1a}$$

$$u = -\frac{\partial p}{\partial x} + R\theta \tag{1b}$$

$$v = -\frac{\partial p}{\partial y}, \quad w = -\frac{\partial p}{\partial z} \tag{1c, d}$$

$$\nabla^2\theta = u\frac{\partial \theta}{\partial x} + v\frac{\partial \theta}{\partial y} + w\frac{\partial \theta}{\partial z} \tag{1e}$$

where we have used the same nondimensionalisation as Rees and Pop (1994a). In (1), x, y, and z are Cartesian coordinates corresponding, respectively, to the streamwise (i.e., upwards), cross stream (i.e., normal), and spanwise directions. The corresponding velocity fluxes are (u, v, w). In Eqs. (1), p is the pressure, θ is the temperature, and ∇^2 is the three-dimensional Laplacian operator. The porous medium Rayleigh number, R, is defined as

$$R = \frac{\rho g \beta d K \Delta T}{\mu \kappa} \tag{2}$$

where ρ is a reference density, g is gravity, β is the coefficient of cubical expansion, μ is the fluid viscosity, and κ is the thermal diffusivity of the saturated medium. In (2), ΔT is the difference between the mean surface temperature and the ambient temperature, K is the permeability, and d is a lengthscale associated with the surface variations, and is such that one full thermal wavelength is precisely $2\pi d$. The boundary conditions required to complete the specification of the problem are

$$v = 0, \quad \theta = 1 + a\cos z \quad \text{at} \quad y = 0, \tag{3a}$$

$$v \to 0, \quad \theta \to 0 \quad \text{as} \quad y \to \infty, \tag{3b}$$

where a is the amplitude of the surface wave. The three velocity components in (1) may be eliminated to obtain the pressure/temperature formulation

$$\nabla^2 p = R\frac{\partial \theta}{\partial x}, \quad \nabla^2\theta = R\theta\frac{\partial \theta}{\partial x} - \nabla p \cdot \nabla\theta \tag{4a, b}$$

subject to the boundary conditions

$$\frac{\partial p}{\partial y} = 0, \quad \theta = 1 + a\cos z \quad \text{at} \quad y = 0, \tag{4c}$$

$$\frac{\partial^2 p}{\partial y^2} \to 0, \quad \theta \to 0 \quad \text{as} \quad y \to \infty. \tag{4d}$$

Without the spanwise surface temperature variation, we recover the well-known Cheng and Minkowycz (1977) similarity solution for free convection from a uniformly heated vertical surface in a porous medium. Cheng and Minkowycz (1977) developed their solution in terms of a local Rayleigh number, a standard method of analysis since there is no natural length scale in the problem they considered. In the present analysis, the surface temperature wavelength provides such a length scale and, therefore, it proves most convenient to work in terms of the Rayleigh number based on this lengthscale. Thus, we can take the Cheng and Minkowycz similarity variable in the form

$$\eta = \frac{yR^{1/2}}{x^{1/2}}. \tag{5a}$$

Nomenclature

a = wave amplitude
d = spanwise dimensional lengthscale
f = similarity solution in (7)
g = gravitational acceleration
h = function defined in (7)
n = subscript
N = truncation level
j = subscript
p = pressure
P = near-wall pressure in asymptotic analysis
$R = \rho g \beta d K \Delta T/\mu\kappa$ = porous medium Rayleigh number
ΔT = reference temperature drop
u = streamwise flux velocity
v = cross-stream flux velocity
w = spanwise flux velocity
x = vertical or streamwise coordinate
y = horizontal or cross-stream coordinate
z = horizontal or spanwise coordinate
β = coefficient of thermal expansion
$\gamma = f''(0)$ in the solution of Eqs. (7)
η = similarity variable
θ = temperature
Θ = near-wall temperature in asymptotic analysis
λ = unknown coefficient
μ = dynamic viscosity
κ = effective thermal diffusivity
ρ = reference fluid density
σ = eigensolution exponent
ξ = scaled streamwise coordinate

The boundary layer is confined to regions where $\eta = O(1)$, and from both this observation and the definition of η in (5a), we see that when $x = O(1)$ the boundary layer thickness in terms of y is of magnitude $O(R^{-1/2})$. However, we are interested in how the spanwise variations affect the boundary layer flow. It is important, therefore, that the cross stream and spanwise diffusion effects balance in terms of their orders of magnitude. Since $z = O(1)$, we must have $y = O(1)$, and hence, from (5a), $\eta = O(1)$ implies that $x = O(R)$. Therefore, we define a new streamwise coordinate, ξ, using

$$\xi = \left(\frac{x}{R}\right)^{1/2} \tag{5b}$$

and introduce both this and (5a) into Eq. (4). As R is assumed to be asymptotically large, we retain only the leading order terms in each equation to obtain the following boundary layer equations:

$$\frac{\partial^2 p}{\partial \eta^2} + \xi^2 \frac{\partial^2 p}{\partial z^2} + \frac{1}{2}\eta \frac{\partial \theta}{\partial \eta} - \frac{1}{2}\xi \frac{\partial \theta}{\partial \xi} = 0, \tag{6a}$$

$$\frac{\partial^2 \theta}{\partial \eta^2} + \xi^2 \frac{\partial^2 \theta}{\partial z^2} + \frac{1}{2}\eta\theta \frac{\partial \theta}{\partial \eta} + \frac{\partial p}{\partial \eta}\frac{\partial \theta}{\partial \eta} + \xi^2 \frac{\partial p}{\partial z}\frac{\partial \theta}{\partial z} - \frac{1}{2}\xi\theta \frac{\partial \theta}{\partial \xi} = 0. \tag{6b}$$

We note in passing that the Cheng and Minkowycz (1977) similarity solution, which forms the solution of (6) when $a = 0$, may be written in the form

$$p = \int_0^\eta f(\alpha)d\alpha - \frac{1}{2}\eta f(\eta) \equiv h(\eta), \quad \theta = f'(\eta) \tag{7a,b}$$

where f is given by the equation

$$f''' + \tfrac{1}{2}ff'' = 0 \tag{7c}$$

subject to

$$f(0) = 0, \quad f'(0) = 1, \quad \text{and} \quad f'(\eta) \to 0 \quad \text{as} \quad \eta \to \infty. \tag{7d}$$

Here, primes denote differentiation with respect to η, and (7a) defines the function $h(\eta)$.

3 Numerical Solution Procedure

Equations (6) are parabolic in ξ, but at $\xi = 0$ they form a pair of ordinary differential equations. Without z-variations the most common approach to solving such parabolic systems in boundary layer flows is to use the Keller-box method (see Keller and Cebeci, 1971). The extra spatial dimension which is present here yields additional difficulties but there are at least three possible methods which could be used to solve Eqs. (6): (i) a full finite difference discretization with an implicit or semi-implicit discretization in ξ which is solved using Gauss-Seidel with multigrid acceleration at each value of ξ (such a scheme is not too great a modification from that used by Rees and Bassom (1993) to investigate boundary layer instabilities in porous media); (ii) a full finite difference discretization solved using multidimensional Newton-Raphson iteration by means of the block tri-diagonal (or Thomas) algorithm; or (iii) a spectral decomposition in the spanwise direction followed by the standard Keller-box method. Of these, the first and second methods are likely to be the least accurate unless very fine grids are used, and although the size of the problem obtained using (iii) is much larger than is usual for Keller-box applications, it was chosen as being the quickest to develop and, given the ease-of-use of nonuniform grids, potentially both the most accurate and the fastest to run. However, we also used method (i) with a large number of grid points to validate our Keller-box computations at the leading edge.

We expanded the solutions in the form

$$p = p_0(\xi, \eta) + 2\sum_{n=1}^{N} p_n(\xi, \eta)\cos nz,$$

$$\theta = \theta_0(\xi, \eta) + 2\sum_{n=1}^{N} \theta_n(\xi, \eta)\cos nz, \tag{8a,b}$$

where N is the truncation level. Substitution of (8) into (6) yields the following equations:

$$\frac{\partial^2 p_n}{\partial \eta^2} - n^2\xi^2 p_n = -\frac{1}{2}\eta \frac{\partial \theta_n}{\partial \eta} + \frac{1}{2}\xi \frac{\partial \theta_n}{\partial \xi}, \quad (n = 0, 1, \ldots, N) \tag{9a}$$

$$\frac{\partial^2 \theta_0}{\partial \eta^2} = -\frac{\partial p_0}{\partial \eta}\frac{\partial \theta_0}{\partial \eta} - \frac{1}{2}\eta\theta_0 \frac{\partial \theta_0}{\partial \eta} + \frac{1}{2}\xi\theta_0 \frac{\partial \theta_0}{\partial \xi} - 2\sum_{j=1}^{N}\left[\frac{\partial p_j}{\partial \eta}\frac{\partial \theta_j}{\partial \eta} + \frac{1}{2}\eta\theta_j \frac{\partial \theta_j}{\partial \eta} - \frac{1}{2}\xi\theta_j \frac{\partial \theta_j}{\partial \xi}\right] - 2\xi^2 \sum_{j=1}^{N} j^2 p_j \theta_j, \tag{9b}$$

$$\frac{\partial^2 \theta_n}{\partial \eta^2} - n^2\xi^2\theta_n = \sum_{j=0}^{N-n}\left[-\frac{1}{2}\eta\left(\theta_j \frac{\partial \theta_{j+n}}{\partial \eta} + \theta_{j+n}\frac{\partial \theta_j}{\partial \eta}\right) - \left(\frac{\partial p_j}{\partial \eta}\frac{\partial \theta_{j+n}}{\partial \eta} + \frac{\partial p_{j+n}}{\partial \eta}\frac{\partial \theta_j}{\partial \eta}\right)\right] + \sum_{j=0}^{N-n}\frac{1}{2}\xi\left(\theta_j \frac{\partial \theta_{j+n}}{\partial \xi} + \theta_{j+n}\frac{\partial \theta_j}{\partial \xi}\right) - \sum_{j=1}^{N-n} j(j+n)\xi^2(p_j\theta_{j+n} + p_{j+n}\theta_j) + \sum_{j=1}^{n-1}\left[j(n-j)\xi^2 p_j\theta_{n-j} - \frac{\partial p_j}{\partial \eta}\frac{\partial \theta_{n-j}}{\partial \eta} - \frac{1}{2}\eta\theta_j \frac{\partial \theta_{n-j}}{\partial \eta} + \frac{1}{2}\xi\theta_j \frac{\partial \theta_{n-j}}{\partial \xi}\right], \quad (n = 1, 2, \ldots, N) \tag{9c}$$

where the final summation in (9c) only applies when the "upper" limit of the sum is not less than the "lower" limit.

Equations (9) form an arbitrarily large system of partial differential equations which can be discretized in the usual Keller-box style by first assigning grids in both the η and ξ directions. The η-grid used was nonuniform and consisted of 61 points lying between 0 and 20 with points concentrated near $\eta = 0$ to allow for the development of a near-wall layer. On the other hand, the ξ-grid was uniform and consisted of 1601 equally spaced points between 0 and 10. Equations (9) were reduced to first-order form in η, yielding a system of $4N + 4$ equations, and these were discretised using central differences based halfway between the η-gridpoints. Apart from at $\xi = 0$, where (9) forms a set of ordinary differential equations, a backward difference discretization in ξ was used; this was deemed necessary since central differences in ξ were found to yield pointwise oscillations reminiscent of those of the Crank-Nicholson method when the steplength is too large. These oscillations could be reduced in size by a very substantial decrease in the streamwise steplength, but the backward difference scheme, though for-

mally of first-order accuracy, yielded sufficiently accurate results and the solutions were free of oscillations.

If we include the boundary conditions in the reckoning, the discretized form of (9) has been transformed into a set of $(4N + 4)M$, nonlinear algebraic equations where M is the number of η-gridpoints. When the equations are arranged suitably, a multidimensional Newton-Raphson iteration scheme can be used to solve the resulting block tri-diagonal matrix/vector iteration equations. The specification of the iteration matrix, the Frechét derivative of the vector of algebraic equations, is exceedingly complicated, and should even one entry be in error, then it is highly likely to degrade seriously the performance of the Newton-Raphson method. Normally, this specification is given explicitly by the programmer. A safer and much quicker specification (though slightly slower computationally) is obtained using numerical differentiation. This technique has been used successfully very recently in another large-scale Keller-box analysis, that of boundary layer flow in a layered porous medium (Rees, 1996). Forward differences were used to obtain the iteration matrix, although high accuracy is not of great concern for this part of the solution methodology. Convergence of the Newton-Raphson procedure was deemed to have taken place when the maximum pointwise correction taken over all variables was less than 10^{-8}.

It is essential at this point to mention how the pressure boundary conditions at $\eta = \eta_{\max}$ were defined. Although $(4d)$ states that the second derivative of p must become zero, thereby allowing p to vary linearly at sufficiently large values of η, we find that this can be relaxed by setting $p = 0$ at $\eta_{\max}$. Referring to Eq. $(9a)$, the right-hand side tends to zero when η is large, and therefore the large-η asymptotic behavior of p_n is that it must be proportional to $e^{-n\xi}$. Thus, when $n \geq 1$, the boundary condition $p_n = 0$ is appropriate. When $n = 0$, a linear variation in p_0 can be allowed, but given the facts (i) that there is also a derivative boundary condition at $\eta = 0$, and (ii) that no ξ-derivatives in p appear in the boundary layer equations, we can impose $p_0 = 0$ at $\eta_{\max}$ with no effect on the overall solution except that the absolute pressure at each value of ξ is unknown. Thus, we compute the pressure relative to its absolute value at the edge of the boundary layer. Further, we have no need to know the absolute pressure, for the computation of v and w rely solely on pressure differences, and the streamwise velocity, u, is equal to $R\theta$ at leading order in R.

Initially, eleven Fourier modes were taken ($N = 10$ in (8)), but it was found that $N = 5$ gave almost indistinguishable results for all cases considered and also a much enhanced computational speed. Thus, we solved a 24th-order system, rather than a 44th-order system. Furthermore, we checked the accuracy of the solution at $\xi = 0$ by comparing directly with a finite difference solution of (6) at $\xi = 0$ using a suitably modified version of the code used by Rees and Bassom (1993). It is essential to note that, although z-derivatives are absent from the governing equations at $\xi = 0$, the surface temperature distribution, in conjunction with the nonlinear terms, serves to make the solution a function of z.

4 Numerical Results

Figure 1 shows the solution at $\xi = 0$ in the form of isotherms for various values of a, the surface temperature wave amplitude. It is important to note that since the velocities and pressure gradients (v, w, $\partial p/\partial y$ and $\partial p/\partial z$) must all balance in magnitude for large values of R, then $u = R\theta + o(R)$. Therefore, Fig. 1 also corresponds to vertical isovels. The aim of Fig. 1 is to display the way the wave amplitude, a, affects the temperature distribution at the leading edge. The main effect of having local hot spots is to cause the local thinning of the boundary layer, and vice versa. A close examination of Fig. 1 for the larger wave amplitudes appears, at first glance, to suggest that increasing the value of a causes the boundary layer to become thinner locally near a cold spot. However, this appearance is deceptive; for isotherm curves corresponding to, say, $\theta = 0.01$ and $\theta = 0.001$, they still indicate that the boundary layer is much thicker at the cold spot, but that it is also quite weak there because of the relatively small excess of the coldest surface temperature above that of the ambient medium.

The variation of the flow as ξ increases is presented in two forms. Firstly, in Fig. 2 we show how the isotherm field evolves at increasing distances from the leading edge. Secondly, the results of further computations are summarised in Fig. 3 in the form of the rates of heat transfer of the individual Fourier modes. Figure 2 shows isotherm plots for $a = 1.0$ at selected values of ξ. As ξ increases from zero, spanwise diffusion becomes increasingly important as the coefficients of the z-derivative terms in (6) are proportional to ξ^2. This has the effect of modifying the temperature field, and, in particular, of reducing the thickness of the boundary layer locally at the cold spots. Once more it is necessary to point out that isotherms corresponding to $\theta = 0.01$ and $\theta = 0.001$ show that the boundary layer is thicker at the cold spots than elsewhere. We find that by the time ξ takes the value 0.5, the boundary layer has essentially a uniform thickness as z varies and z-variations modify the profile only well within the boundary layer. In fact, we see that z-variations become confined to a decreasingly thin region close to the heated surface as ξ increases. Note that the expression "decreasingly thin" refers to the thickness of the near-wall layer in terms of η, but that the near-wall layer actually attains a uniform thickness in terms of y; this observation paves the way for the asymptotic analysis presented in the next section.

In Fig. 3 we show how the surface rate of heat transfer evolves downstream by considering the individual Fourier modes. Figure $3(a)$ shows how the value of $\theta_{0\eta}$ ($\eta = 0$) varies with ξ for various values of the wave amplitude. Here we see that the curves converge fairly quickly onto the value -0.444, which corresponds to an isothermal vertical surface (Cheng and Minkowycz, 1977). Much of the essential evolution, from the leading edge z-dependent solution to what is effectively the isothermal surface similarity solution (save for values of η close to zero), takes place in the interval $0 \leq \xi \leq 4$. The graph of $\theta_{1\eta}$ ($\eta = 0$) shown in Fig. $3(b)$ shows that, at large ξ, the variation of heat transfer is linear; this behavior is explained in the next section. Figures $3(c)$ and $3(d)$ show the evolution of the rate of heat transfer for the second and third modes, respectively. Both sets of curves display well-defined variations in $0 \leq \xi \leq 4$ although their amplitudes are smaller than those for modes 0 and 1. When $\xi > 4$, the rate of heat transfer has decayed very rapidly towards zero. Corresponding heat transfer curves for increasingly higher modes have decreasing maximum value, thereby justifying the choice of $N = 5$ mentioned earlier.

5 Asymptotic Analysis for Large Values of ξ

In this section, we present a brief analysis of the flow at large distances from the leading edge of the heated surface. Figure 2 has shown that the boundary layer splits into two very distinct regions: a main layer where $\eta = O(1)$ and there is no discernable z-variation, and a near-wall layer where $\eta \ll 1$ and z-variations are very evident. The near-wall layer may be shown to have a constant thickness (in terms of y) and it means that $\eta = O(\xi^{-1})$ in this region. Given that $\eta = y/\xi$, it is a simple matter to reduce Eqs. (6) to ones involving only y, z, and ξ. In the near-wall region we shall use P and Θ as the notation for pressure and temperature, respectively, and in both regions we expand the solution as an inverse power series in ξ. Let

$$\begin{pmatrix} p \\ \theta \end{pmatrix} = \begin{pmatrix} p^{(0)}(\eta) \\ \theta^{(0)}(\eta) \end{pmatrix} + \xi^{-1}\begin{pmatrix} p^{(1)}(\eta) \\ \theta^{(1)}(\eta) \end{pmatrix} + \xi^{-2}\begin{pmatrix} p^{(2)}(\eta) \\ \theta^{(2)}(\eta) \end{pmatrix} + \ldots, \quad (10a)$$

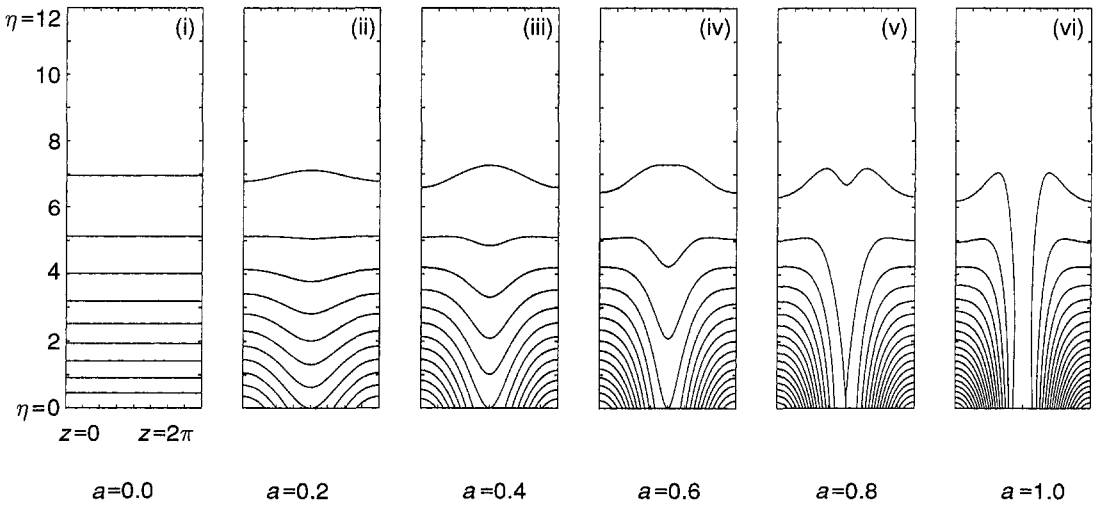

Fig. 1 The isotherms at $\xi = 0$ corresponding to various surface temperature wave amplitudes: (i) $a = 0$; (ii) $a = 0.2$; (iii) $a = 0.4$; (iv) $a = 0.6$; (v) $a = 0.8$; (vi) $a = 1.0$. All isotherm plots in this paper have the isotherms plotted at intervals of 0.1.

$$\begin{pmatrix} P \\ \Theta \end{pmatrix} = \begin{pmatrix} P^{(0)}(y) \\ \Theta^{(0)}(y) \end{pmatrix} + \xi^{-1}\begin{pmatrix} P^{(1)}(y) \\ \Theta^{(1)}(y) \end{pmatrix} + \xi^{-2}\begin{pmatrix} P^{(2)}(y) \\ \Theta^{(2)}(y) \end{pmatrix} + \ldots . \quad (10b)$$

The equations governing P and Θ into which $(10b)$ will be substituted are

$$\frac{\partial^2 P}{\partial y^2} + \frac{\partial^2 P}{\partial z^2} - \frac{1}{2\xi}\frac{\partial \Theta}{\partial \xi} = 0, \quad (11a)$$

$$\frac{\partial^2 \Theta}{\partial y^2} + \frac{\partial^2 \Theta}{\partial z^2} + \frac{\partial P}{\partial y}\frac{\partial \Theta}{\partial y} + \frac{\partial P}{\partial z}\frac{\partial \Theta}{\partial z} - \frac{1}{2\xi}\Theta\frac{\partial \Theta}{\partial \xi} = 0. \quad (11b)$$

At large values of ξ, the flow in the main part of the boundary layer is generated by the mean temperature drop between the surface and the ambient medium, and it is easily shown that the solutions for $p^{(0)}$ and $\theta^{(0)}$ are given by the expressions for p and θ in (7). In the near-wall layer we find that

$$P^{(0)} = 0 \quad \text{and} \quad \Theta^{(0)} = 1 + ae^{-y}\cos z. \quad (12a, b)$$

The solution methodology proceeds by returning to the next order in the main layer, solving the resulting equations, obtaining the asymptotic matching conditions for the near-wall solution as $y \to \infty$, and finally, by solving the associated near-wall equations. The detailed analysis is straightforward but increasingly lengthy as successive terms are obtained. Before the results of our analysis are presented, however, it is important to note that the equations for the $O(\xi^{-2})$ terms in the main layer, i.e.,

$$\frac{d^2 p^{(2)}}{d\eta^2} + \frac{\eta}{2}\frac{d\theta^{(2)}}{d\eta} + \theta^{(2)} = 0, \quad (13a)$$

$$\frac{d^2\theta^{(2)}}{d\eta^2} + \frac{\eta}{2}\frac{d}{dy}(\theta^{(0)}\theta^{(2)}) + \left(\frac{dp^{(0)}}{dy}\frac{d\theta^{(2)}}{dy} + \frac{dp^{(2)}}{dy}\frac{d\theta^{(0)}}{dy}\right) + \theta^{(0)}\theta^{(2)} = 0, \quad (13b)$$

are homogeneous, but admit the eigensolutions

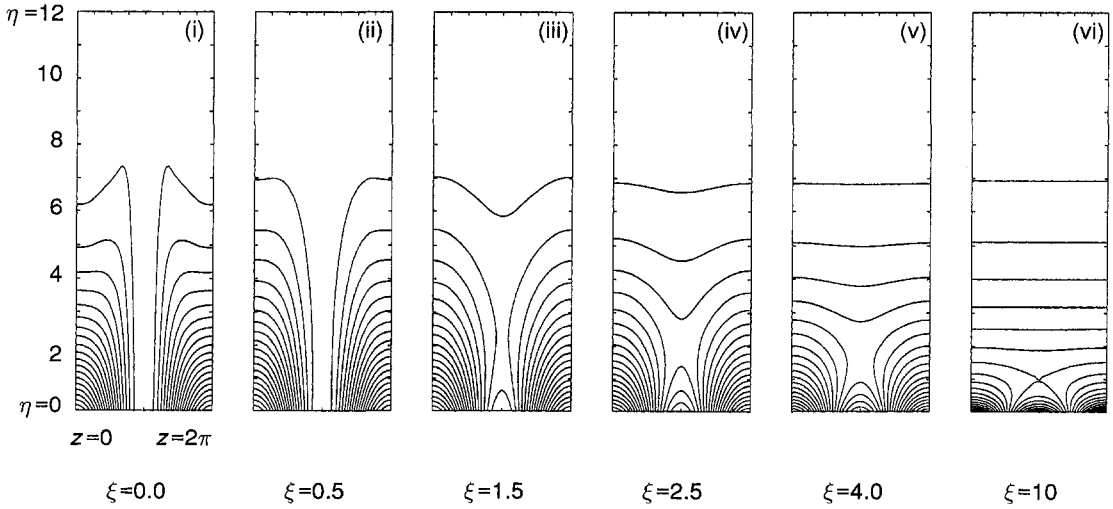

Fig. 2 The isotherms at various values of ξ corresponding to the surface temperature wave amplitude $a = 1.0$: (i) $\xi = 0$; (ii) $\xi = 0.5$; (iii) $\xi = 1.5$; (iv) $\xi = 2.5$; (v) $\xi = 4$; (vi) $\xi = 10$.

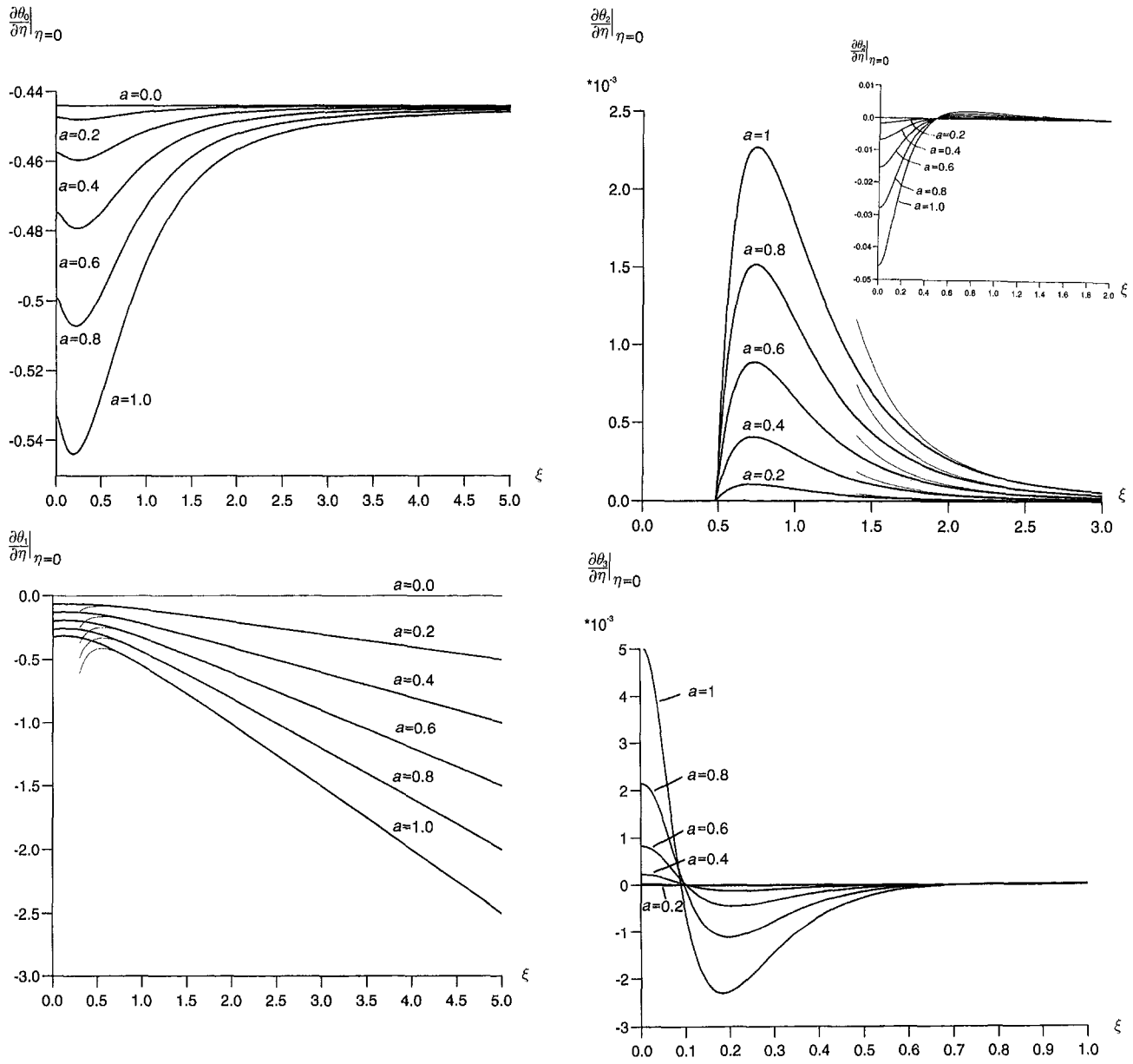

Fig. 3 The variation of the rate of heat transfer for the first few Fourier modes as functions of ξ for various surface temperature wave amplitudes: (*a*) zeroth mode; (*b*) first mode; (*c*) second mode; (*d*) third mode. The $a = 0$ curve for the zeroth mode is also the asymptotic curve for the other values of a. The asymptotic curves for the first and second modes are depicted as thin lines.

$$p^{(2)} = \tfrac{1}{2}\lambda(\eta f - \eta^2 f') \quad \text{and} \quad \theta^{(2)} = \lambda\eta f'' \qquad (14)$$

where λ is an unknown coefficient. Clearly, this means that successive terms in the asymptotic series will contain parts of the solution with arbitrary coefficients. However, it remains possible to obtain exact leading-order solutions for the functions multiplying cos 2*z* and so on, even though they first appear at $O(\xi^{-5})$. We also note, in passing, that the main-layer equations admit other eigensolutions. If eigensolutions appear at $O(\xi^{-\sigma})$ in the expansion, then the first six eigensolutions correspond to the following values of σ: 2.0000, 7.6558, 17.8220, 32.5048, 51.7049, and 75.4225; these values were obtained using a fourth-order accurate Runge-Kutta shooting method code, and the values are correct to four decimal places.

Using the procedure outlined above, we find that the main-region solutions take the following forms:

$$p = h(\eta) + \xi^{-2}[\tfrac{1}{2}\lambda(\eta f - \eta^2 f')] + O(\xi^{-4}), \qquad (15a)$$

$$\theta = f'(\eta) + \xi^{-2}[\lambda\eta f''] + O(\xi^{-4}), \qquad (15b)$$

while the near-wall solutions are

$$P = -\xi^{-3}\left(\frac{\gamma y^3}{12}\right) + \xi^{-5}\left[-\frac{\gamma\lambda y^3}{4} + \frac{\gamma y^5}{160} + \frac{a\gamma}{128}(y^4 + 8y^3 + 21y^2 + 21y + 21)e^{-y}\cos z\right] + o(\xi^{-5}), \qquad (16a)$$

$$\Theta = (1 + ae^{-y}\cos z) + \xi^{-1}(\gamma y) + \xi^{-3}\left[\gamma\left(\lambda y - \frac{y^3}{12}\right) + \frac{a\gamma}{48}(2y^3 + 9y^2 + 9y)e^{-y}\cos z\right] - \xi^{-4}\left(\frac{\gamma^2 y^4}{48}\right) + \xi^{-5}\left[\frac{a^2\gamma}{8192}(8y^4 + 40y^3 + 6y^2 - 165y)e^{-2y}\cos 2z\right] + O(\xi^{-5}). \qquad (16b)$$

In these expressions, it is to be understood that $\gamma = f''(0) \simeq -0.444$ (see (7)), the $O(\xi^{-4})$ terms in (15) are proportional to λ^2, and the $O(\xi^{-5})$ term in (16*b*) contains terms independent of z and others that are proportional to cos z. It is clear that our assumption that the main layer is independent of z is well-justified a posteriori by the inner layer results where all z-dependent terms decay exponentially into the main layer.

The above results may be used to obtain heat transfer data. In order to compare with Figs. 3, we need to obtain the η-derivative of the inner layer solutions. Thus, we find that

$$\left.\frac{\partial \Theta}{\partial \eta}\right|_{\eta=0} = (-a\cos z)\xi + \gamma + \left(\gamma\lambda + \frac{3}{16}\gamma a\cos z\right)\xi^{-2} - \left(\frac{165}{8192}\gamma a^2\cos 2z\right)\xi^{-4} + O(\xi^{-4}). \quad (17)$$

Again, the $O(\xi^{-4})$ terms in (17) contain z-independent terms and terms proportional to cos z.

Using (17) we are able to write down the asymptotic behavior of the rate of heat transfer corresponding to the various Fourier modes defined in Eq. (8*b*):

$$\left.\frac{\partial \theta_0}{\partial \eta}\right|_{\eta=0} = \gamma + (\gamma\lambda)\xi^{-2} + O(\xi^{-4}) \quad (18a)$$

$$\left.\frac{\partial \theta_1}{\partial \eta}\right|_{\eta=0} = -\frac{1}{2}a\xi + \frac{3}{32}\gamma a\xi^{-2} + O(\xi^{-4}) \quad (18b)$$

$$\left.\frac{\partial \theta_2}{\partial \eta}\right|_{\eta=0} = -\frac{165}{16384}\gamma a^2\xi^{-4} + O(\xi^{-6}) \quad (18c)$$

$$\left.\frac{\partial \theta_3}{\partial \eta}\right|_{\eta=0} = O(\xi^{-6}). \quad (18d)$$

By considering the interaction of the nonlinear terms in Eqs. (11), it is straightforward to show that the heat transfer corresponding to mode n, the term proportional to cos nz, is of $O(\xi^{-2n})$ when $n > 1$. The expressions in (18*b*, *c*) are also shown in Figs. 3(*b*, *c*) and give very accurate comparisons with the numerical values obtained from solving the full boundary layer equations. We note that only the leading term in (18*a*) is known with certainty since λ can only be determined by a direct comparison with the full numerical solution of (9).

6 Discussion

In this paper, we have considered how the presence of longitudinal surface temperature variations affects the flow and heat transfer from a vertical heated surface in a porous medium. This is, to our knowledge, the first time a nonsimilar three-dimensional, boundary layer flow in a porous medium has been studied. The pressure and temperature fields have been determined by a combination of numerical methods and an asymptotic analysis. We have found that the flow, even for seemingly very large surface temperature waves, may be described accurately with a surprisingly small number of spanwise Fourier modes. At large distances from the leading edge, the flow is essentially the standard Cheng and Minkowycz (1977) vertical profile with only the first Fourier mode giving substantial changes from this in a near-wall layer adjacent to the heated surface. The numerical and asymptotic analyses compare very favorably, even for values of ξ as small as 3, and this lends support to the accuracy of both types of analysis.

References

Cheng, P., and Minkowycz, W. J., 1977, "Free Convection About a Vertical Flat Plate Imbedded in a Porous Medium With Application to Heat Transfer From a Dike," *J. Geophys. Res.*, Vol. 82, pp. 2040–2044.

Chiu, C.-P., and Chou, H.-M., 1993, "Free Convection in the Boundary Layer Flow of a Micropolar Fluid Along a Vertical Wavy Surface," *Acta Mechanica*, Vol. 101, pp. 161–174.

Gill, A. E., 1969, "A Proof That Convection in a Porous Vertical Slab is Stable," *J. Fluid Mech.*, Vol. 35, pp. 545–547.

Hossain, M. A., Alam, K. C. A., and Pop, I., 1996, "MHD Free Convection Flow Along a Vertical Wavy Surface With Uniform Surface Temperature," submitted for publication.

Keller, H. B., and Cebeci, T., 1971, "Accurate Numerical Methods for Boundary Layer Flows 1: Two-Dimensional Flows," *Proc. Int. Conf. Numerical Methods in Fluid Dynamics*, Lecture Notes in Physics, Springer, New York.

Kim, S. J., and Vafai, K., 1989, "Analysis of Natural Convection About a Vertical Surface Embedded in a Porous Medium," *Int. J. Heat Mass Transf.*, Vol. 32, pp. 665–677.

Kwok, L. P., and Chen, C. F., 1987, "Stability of Thermal Convection in a Vertical Porous Layer," ASME JOURNAL OF HEAT TRANSFER, Vol. 109, pp. 889–893.

Lewis, S., Bassom, A. P., and Rees, D. A. S., 1995, "The Stability of Vertical Thermal Boundary Layer Flow in a Porous Medium," *European Journal of Mechanics B: Fluids*, Vol. 14, pp. 395–408.

Moulic, S. G., and Yao, L. S., 1989a, "Mixed Convection Along a Wavy Surface," ASME JOURNAL OF HEAT TRANSFER, Vol. 111, pp. 974–979.

Moulic, S. G., and Yao, L. S., 1989b, "Natural Convection Along a Vertical Wavy Surface With Uniform Heat Flux," ASME JOURNAL OF HEAT TRANSFER, Vol. 111, pp. 1106–1108.

Nield, D. A., and Bejan, A., 1992, *Convection in Porous Media*, Springer, New York.

Rees, D. A. S., 1990, "The Effect of Long-Wavelength Thermal Modulations on the Onset of Convection in an Infinite Porous Layer Heated From Below," *Q. J. Mech. Appl. Math.*, Vol. 43, pp. 189–214.

Rees, D. A. S., 1993, "Nonlinear Wave Stability of Vertical Thermal Boundary Layer Flow in a Porous Medium," *Journal of Applied Mathematics and Physics (Z.A.M.P.)*, Vol. 44, pp. 306–313.

Rees, D. A. S., 1996, "The Effect of Layering on Free Convection From a Vertical Heated Surface in a Porous Medium," *Proc. Int. Conf. on Porous Media and their Applications in Science, Engineering, and Industry*, Kona, Hawaii, pp. 71–84.

Rees, D. A. S., and Bassom, A. P., 1993, "The Nonlinear Nonparallel Wave Instability of Free Convection Induced by a Horizontal Heated Surface in Fluid-Saturated Porous Media," *J. Fluid Mech.*, Vol. 253, pp. 267–296.

Rees, D. A. S., and Pop, I., 1994a, "A Note on Free Convection Along a Vertical Wavy Surface in a Porous Medium," ASME JOURNAL OF HEAT TRANSFER, Vol. 116, pp. 505–508.

Rees, D. A. S., and Pop, I., 1994b, "Free Convection Induced by a Horizontal Wavy Surface in a Porous Medium," *Fluid Dynamics Research*, Vol. 14, pp. 151–166.

Rees, D. A. S., and Pop, I., 1995a, "Free Convection Induced by a Vertical Wavy Surface With Uniform Heat Flux in a Porous Medium," ASME JOURNAL OF HEAT TRANSFER, Vol. 117, pp. 547–550.

Rees, D. A. S., and Pop, I., 1995b, "Non-Darcy Natural Convection From a Vertical Wavy Surface in a Porous Medium," *Transport in Porous Media*, Vol. 20, pp. 223–234.

Rees, D. A. S., and Pop, I., 1996, "The Effect of Longitudinal Surface Waves on Free Convection From Vertical Surfaces in Porous Media," *Int. Comm. Heat Mass Transf.*, in press.

Rees, D. A. S., and Riley, D. S., 1989a, "The Effects of Boundary Imperfections on Convection in a Saturated Porous Layer: Near-Resonant Wavelength Excitation," *J. Fluid Mech.*, Vol. 199, pp. 133–154.

Rees, D. A. S., and Riley, D. S., 1989b, "The Effects of Boundary Imperfections on Convection in a Saturated Porous Layer: Non-Resonant Wavelength Excitation," *Proc. Roy. Soc.*, Vol. A421, pp. 303–339.

Riahi, D. N., 1993, "Preferred Pattern of Convection in a Porous Layer With a Spatially Nonuniform Boundary Temperature," *J. Fluid Mech.*, Vol. 246, pp. 529–543.

Riahi, D. N., 1995, "Finite-Amplitude Thermal Convection With Spatially Modulated Boundary Temperatures," *Proc. Roy. Soc.*, Vol. A449, pp. 459–478.

Riahi, D. N., 1996, "Modal Package Convection in a Porous Layer With Boundary Imperfections," *J. Fluid Mech.*, Vol. 318, pp. 107–128.

Yao, L. S., 1983, "Natural Convection Along a Vertical Wavy Surface," ASME JOURNAL OF HEAT TRANSFER, Vol. 105, pp. 465–468.

Unsteady Non-Darcian Forced Convection Analysis in an Annulus Partially Filled With a Porous Material

M. A. Al-Nimr
malnimr@just.edu

M. K. Alkam

Mechanical Engineering Department,
Jordan University of Science
and Technology,
Irbid, Jordan

Numerical solutions are presented for the problem of transient, developing, forced-convection flow in concentric annuli partially filled with porous substrates. The porous substrate is attached either to the inner cylinder (case I), or to the outer cylinder (case O). In both cases, the boundary in contact with the porous substrate is exposed to a sudden change in its temperature while the other boundary is kept adiabatic. Including the macroscopic inertial term, the Brinkman-Forchheimer-extended Darcy model is used to model the flow inside the porous domain. The effects of different parameters regarding the geometry, the solid matrix, and the fluid on the hydrodynamic and thermal behavior are investigated. It is shown that porous substrates may improve Nusselt number by 1200 percent keeping other flow and geometrical parameters fixed. Also, it is found that there is an optimum thickness for the porous substrate beyond which there is no significant improvement in Nusselt number. In the present work, the dimensionless hydrodynamic entrance length Z_{en} varies within the range 2–45 and it has significant effect on the fully developed Nusselt number at steady-state conditions. As a result, the macroscopic inertial term in the porous domain momentum equation should not be neglected.

Introduction

The existence of a fluid layer adjacent to a layer of porous medium saturated with fluid has many industrial, geophysical, biomedical, engineering, and environmental applications (Kakac et al., 1991). These applications include the following: porous journal bearing, blood flow in lungs or in arteries, nuclear reactors, porous-flat plate collectors, packed bed thermal storage, solidification of concentrated alloys, fibrous and granular insulation where the insulation occupies only part of the space separating the heated and cooled walls, heat transfer from hair covered skin, grain storage and drying, and paper drying and food storage. In addition, the use of porous substrates to improve forced convection heat transfer in channels, which is considered as a composite of fluid and porous layers, finds applications in heat exchangers, electronic cooling, heat pipes, filtration and chemical reactors, etc. In these applications, engineers avoid filling the entire channel with a solid matrix to reduce the pressure drop.

In a recent survey conducted by Vafai and Kim (1990), there appears to be very limited research on the problem of forced convection in composite fluid and porous layers. The fluid mechanics at the interface between a fluid layer and a porous medium over a flat plate was first investigated by Beavers and Joseph (1967). Vafai and Thiyagaraja (1987) obtained an analytical approximate solution for the same problem based on matched asymptotic expansions for the velocity and temperature distributions. The same problem was revisited by Vafai and Kim (1990) who presented an exact solution. Closed form analytical solutions for parallel plates and circular pipes partially filled with porous materials were obtained by Poulikakos and Kazmierczak (1987) for constant wall heat flux, while numerical results were computed for constant wall temperature. Using Darcy-Brinkman-Forchheimer model, the problem of forced convection in a parallel plate channel partially filled with a porous medium was numerically investigated by Jang and Chen (1992). The same problem was investigated by Rudraiah (1985) using the Darcy-Brinkman model. Also, using the Darcy-Brinkman model, analytical solutions were obtained by Chikh et al. (1995a) for the problem of forced convection in an annular duct partially filled with a porous medium. The same problem was investigated numerically by the same group (1995b) using the Darcy-Brinkman-Forchheimer model.

The above mentioned investigations consider forced convection problems in different composite geometries under steady-state operating conditions. Also, in these works, the macroscopic inertial force was dropped from the momentum governing equations according to the assumption of fully developed hydrodynamics behavior. However, and as reported by Vafai and Kim (1995), the macroscopic inertial term has significant effects, especially on the thermal behavior in channels partially filled with porous material. The appearance of the macroscopic inertial term is essential to ensure the matching between the flow development in the clear fluid and in the fluid-saturated porous layer.

The aim of this work is to present a numerical investigation for the transient forced convection problem in channels partially filled with porous materials. The unsteadiness in the thermal behavior of the channel results from a sudden change in temperature at one of the boundaries. The flow is assumed to be steady but in developing situations. As reported by Vafai and Kim (1995), a porous medium/clear fluid interface is best dealt with by the Darcy-Brinkman-Forchheimer formulation and the continuity of velocity and stresses at the interface. The effects of different parameters, such as the porous layer thickness, the system configuration, and Forchheimer coefficient are investigated. Attention is focused on the transient behavior of the channel and on the importance of the macroscopic inertial term and its effect on Nusselt number, entrance length, and steady-state time.

Contributed by the Heat Transfer Division for publication in the JOURNAL OF HEAT TRANSFER. Manuscript received by the Heat Transfer Division September 27, 1996; revision received June 27, 1997; Keywords: Forced Convection; Porous Media; Transient and Unsteady Heat Transfer. Associate Technical Editor: K. Vafai.

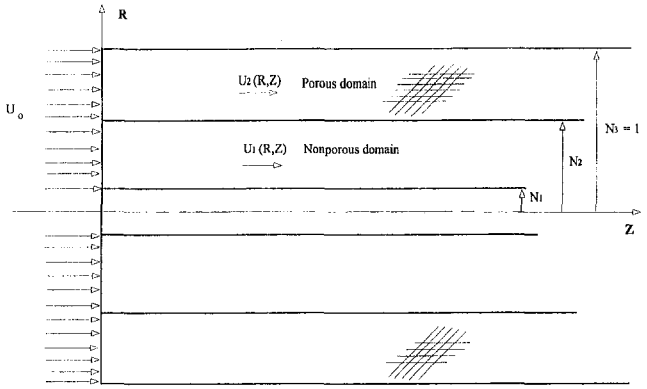

Fig. 1 Schematic diagram for case O

Mathematical Formulation

The flow, as shown in Figs. 1 and 2, is between two concentric cylinders. A porous substrate is deposited either at the inner cylinder (case I) or at the outer cylinder (case O). In both cases, the heating (or cooling) process, which is in the form of a sudden change in the boundary temperature, occurs at the cylinder wall which is in contact with the porous substrate. Both the fluid and the solid matrix have constant physical properties, and the fluid enters the annular passage with a uniform velocity distribution, u_o, which is independent of time. Prior to the start of the time varying heating (or cooling) process, the fluid may either be in a thermal steady state as a result of some steady heating process, or alternately, the fluid and the annulus walls may be at the same uniform temperature. The transient forced convection process starts by imposing (at $\tau > 0$) a sudden change in the temperature at one of the annulus walls while the other wall is kept adiabatic.

The current investigation has been carried out assuming axisymmetric, laminar, boundary-layer flow with no internal heat generation, and neglecting viscous dissipation and axial conduction of heat. Also, it is assumed that the porous medium is homogeneous, isotropic, and saturated with a single phase. The fluid is in local thermal equilibrium with the solid matrix. Using the dimensionless parameters given in the nomenclature, the equations of continuity, motion, and energy, for both fluid and porous domains, reduce to the following nondimensional equations, respectively:

$$\frac{\partial U_1}{\partial Z} + \frac{1}{R}\frac{(R\partial V_1)}{\partial R} = 0 \tag{1}$$

$$\frac{\partial U_2}{\partial Z} + \frac{1}{R}\frac{(R\partial V_2)}{\partial R} = 0 \tag{2}$$

$$U_1\frac{\partial U_1}{\partial Z} + V_1\frac{\partial U_1}{\partial R} = -\frac{\partial P}{\partial Z} + \frac{1}{R}\frac{\partial}{\partial R}\left[R\frac{\partial U_1}{\partial R}\right] \tag{3}$$

$$U_2\frac{\partial U_2}{\partial Z} + V_2\frac{\partial U_2}{\partial R} = -\frac{1}{\rho_R}\frac{\partial P}{\partial Z} + \frac{\nu_{R,e}}{R}\frac{\partial}{\partial R}\left[R\frac{\partial U_2}{\partial R}\right] - \frac{1}{\rho_R \mathrm{Da}}U_2 - AU_2^2 \tag{4}$$

$$\frac{\partial \theta_1}{\partial \tau} + U_1\frac{\partial \theta_1}{\partial Z} + V_1\frac{\partial \theta_1}{\partial R} = \frac{1}{\mathrm{Pr}_1}\frac{1}{R}\frac{\partial}{\partial R}\left[R\frac{\partial \theta_1}{\partial R}\right] \tag{5}$$

$$C_R\frac{\partial \theta_2}{\partial \tau} + U_2\frac{\partial \theta_2}{\partial Z} + V_2\frac{\partial \theta_2}{\partial R} = \frac{k_R}{\mathrm{Pr}_1}\frac{1}{R}\frac{\partial}{\partial R}\left[R\frac{\partial \theta_2}{\partial R}\right]. \tag{6}$$

Nomenclature

A = coefficient of the microscopic inertia term, $\epsilon Fr_3/\rho_R\sqrt{K}$
c = specific heat
c_R = heat capacity ratio, $\rho_2 c_2/\rho_1 c_1 = \epsilon + (1-\epsilon)\rho_s c_s/\rho_f c_f$
Da = Darcy number, K/r_3^2
F = Forchheimer coefficient
k = thermal conductivity
k_R = thermal conductivity ratio, k_2/k_1
K = permeability of the porous substrate
N_1 = dimensionless radius of the inner cylinder, r_1/r_3
N_2 = dimensionless radius radio, r_1/r_3
$N_3 = 1$ = dimensionless radius of the outer cylinder, r_3/r_3
Nu = local Nusselt number, $hr_3/k_2 = (\partial\theta_2/\partial R)/(\theta_m - 1)$ for case O, and $hr_3/k_2 = -(\partial\theta_2/\partial R)/(\theta_m - 1)$ for case I.
p = pressure
P = dimensionless pressure, $pr_3^2/\rho_1\nu_1^2$
Pr_1 = Prandtl number of the fluid, $c_1\mu_1/k_1$
r = radial coordinate
r_1, r_2, r_3 = inner, interface, and outer radii of annulus
R = dimensionless radial coordinate, r/r_3
t = time
t_{ss} = steady-state time
T = temperature at any point
T_i = initial temperature
T_m = mixing cup temperature over any cross section, $= (\int_{r_1}^{r_2} ru_2T_2dr + \int_{r_2}^{r_3} ru_1T_1dr)/\int_{r_1}^{r_2} ru_2dr + \int_{r_2}^{r_3} ru_1dr)$ for case I, and $= (\int_{r_1}^{r_2} ru_1T_1dr + \int_{r_2}^{r_3} ru_2T_2dr)/\int_{r_1}^{r_2} ru_1dr + \int_{r_2}^{r_3} ru_2dr)$ for case O
T_o = temperature of heat transfer boundary
u = axial velocity
u_o = inlet axial velocity
U = dimensionless volume averaged axial velocity, ur_3/ν_1
U_o = dimensionless inlet axial velocity, $u_o r_3/\nu_1$
v = radial velocity
V = dimensionless radial velocity, vr_3/ν_1
z = axial coordinate
z_{en} = hydrodynamic entrance length
Z = dimensionless axial coordinate, z/r_3
Z_{en} = dimensionless hydrodynamic entrance length, z_{en}/r_3

Greek Symbols

ϵ = porosity
θ = dimensionless temperature, $(T - T_i)/(T_o - T_i)$
θ_m = dimensionless mixing cup temperature, $(T_m - T_i)/(T_o - T_i)$
μ = dynamic viscosity
μ_2 = effective dynamic viscosity of the porous domain
μ_R = dynamic viscosity ratio, μ_2/μ_1
ν = kinematic viscosity
ν_R = kinematic viscosity ratio, ν_2/ν_1
ρ = density
ρ_R = density ratio, ρ_2/ρ_1
τ = dimensionless time, $t\nu_1/r_3^2$
τ_{ss} = dimensionless steady-state time, $t_{ss}\nu_1/r_3^2$

Subscripts

1 or f = fluid domain properties
2 = porous domain properties
I = case I, heating (or cooling) at the inner cylinder
O = case O, heating (or cooling) at the outer cylinder
R = ratio
s = solid matrix properties
ss = steady state

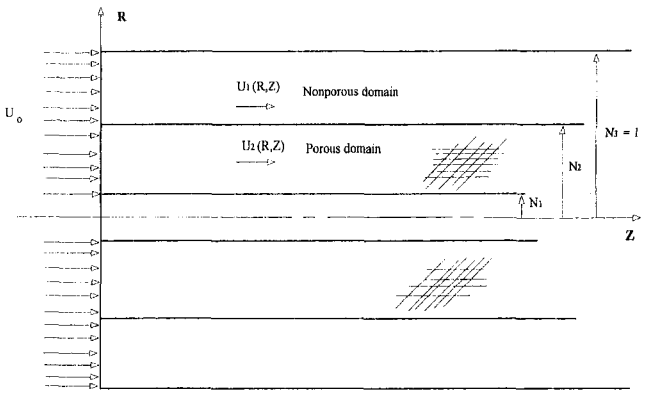

Fig. 2 Schematic diagram for case I

In Eqs. (1–6), subscripts 1 and 2 refer to the clear fluid and porous substrate, respectively. It should be pointed out that it is uncertain what one should use for the effective viscosity ratio $\mu_{R,e}$. Although the suitable value of $\mu_{R,e}$ is far from being settled, the viscosity ratio is taken as either unity or $1/\epsilon$ in the heat transfer literature (Kakac et al., 1991). In fact, $\mu_{R,e} = 1$ is a good approximation in the range $0.7 \leq \epsilon \leq 1$. For lower porosity, the use of Einstein equation for the viscosity of dilute suspension leads to a value of effective viscosity greater than the fluid viscosity. Also, it is noteworthy that the radial momentum equation has been eliminated due to the boundary layer simplifications. However, it is possible, under the linearized numerical scheme of Bodoia and Osterle (1961), to compensate for the lack of such an equation by using the following dimensionless integral continuity equation. For case O,

$$\int_{N_1}^{N_2} U_1 R dR + \int_{N_2}^{1} U_2 R dR = \frac{U_o}{2}(1 - N_1^2)$$

and for case I

$$\int_{N_1}^{N_2} U_2 R dR + \int_{N_2}^{1} U_1 R dR = \frac{U_o}{2}(1 - N_1^2). \quad (7)$$

In the cases under consideration, the momentum equations assume the following boundary conditions:

at $Z = 0$ and $N_1 < R < 1$,

$$U_1 = U_2 = U_o, \quad \text{and} \quad V_1 = V_2 = 0,$$

for $Z > 0$ and $R = N_1$ or $R = 1$,

$$U_1 = U_2 = V_1 = V_2 = 0,$$

for $Z > 0$ and $R = N_2$,

$$U_1 = U_2, \quad \frac{\partial U_1}{\partial R} = \mu_{R,e} \frac{\partial U_2}{\partial R}. \quad (8)$$

For both cases, the energy equations have the following initial conditions:

$$\text{at} \quad \tau = 0 \quad \theta_1 = \theta_2 = 0. \quad (9)$$

For $\tau > 0$, the thermal boundary conditions for the two cases are as follows:

$$\text{case O, At } R = N_1, \quad \frac{\partial \theta_1}{\partial R} = 0; \quad \text{at} \quad R = 1, \quad \theta_2 = 1$$

$$\text{case I, At } R = N_1, \quad \theta_2 = 1; \quad \text{at} \quad R = 1, \quad \frac{\partial \theta_1}{\partial R} = 0. \quad (10)$$

Both cases I and O have the same thermal conditions at the duct inlet and at the interface between the fluid and the porous domains. These conditions are as follows:

$$\text{at } Z = 0, N_1 < R < 1, \quad \theta_1 = \theta_2 = 0,$$

$$\text{at } Z > 0, R = N_2, \quad \theta_1 = \theta_2, \quad \text{and} \quad \frac{\partial \theta_1}{\partial R} = k_R \frac{\partial \theta_2}{\partial R}. \quad (11)$$

Numerical Method of Solution

In the present work, there are three independent variables: R, Z, and τ. A three-dimensional parallel-piped grid in R, Z, and τ has been imposed on half of the annular flow field due to symmetry about the Z-axis. The nondimensional time, τ, is simulated as a third coordinate, normal to the $R-Z$ plane. The linearized implicit finite difference equations are derived using second order central difference scheme for the radial derivatives, and first order backward scheme for both the axial and time derivatives. The consistency and stability of the discretized governing equations have been checked, and it is found that the derived forms are consistent and stable as long as the downstream axial velocities U_1 and U_2 are non-negative, i.e., there is no flow reversal within the domain of the solution.

The method discussed by Bodoia and Osterle (1961) is used to solve the finite difference equations that simulate the flow hydrodynamics at steady-state conditions. Having obtained the values of U_1, U_2, V_1, and V_2 over the flow field, the discritized energy equations are solved by marching in time. The solution procedure in time is carried out until steady-state conditions are practically achieved. The steady-state conditions are declared when the summation of the residue over the cross section reaches a value less than 1×10^{-4}. The residue is defined as the absolute difference in temperature between a grid point and the previous one in time direction.

In order to obtain a solution independent of the grid size, several runs were performed to obtain the optimum step sizes in R, Z, and τ directions. The optimization procedure of the grid size includes computing the radial temperature distribution at an arbitrary location, employing a given number of grid points in both the radial and axial directions. After that the number of grid points is increased gradually, and each time a computer run is performed to compute the temperature profile. A residue is defined as the absolute difference in temperature between the computed temperature distribution and the one obtained in the previous run. The procedure is continued until the residue approaches a value less than 1×10^{-4}. At this point the spacial grid size is fixed. A similar procedure is followed to choose the optimum time step. The optimum choice was $\Delta R = 0.02$, $\Delta Z = 0.1$, and $\Delta\tau = 0.01$.

Results and Discussion

The computations are carried out for the following values of the flow and geometry parameters:

$$N_1 = 0.5, \quad \text{Pr}_1 = 0.7, \quad k_R = 5, \quad \mu_R = 1,$$

$$\rho_R = 2, \quad c_R = 1, \quad U_o = 1000.$$

In order to validate the present code, a special computer run was made in which $\text{Da} \to \infty$, $A \to 0$, and $N_2 \to 1$ for case O. These operating conditions represents the flow of a clear fluid in the developing region of an annulus. Also, in this special case, the inner wall was considered isothermal while the outer wall was kept adiabatic. This was done for the sake of matching the boundary conditions considered by El-Shaarawi and Alkam (1992). The obtained radial temperature profiles are compared with these of El-Shaarawi and Alkam (1992), as shown in Fig. 3. The figure shows an acceptable match between the present work and the results of El-Shaarawi and Alkam (1992).

Figures 4 and 5 show the axial velocity distribution in the radial direction at different axial locations, Z, for both cases I and O, respectively. These figures show that the mean fluid velocity in the porous domain is lower than that in the clear domain. This is due to the additional retardation of the flow

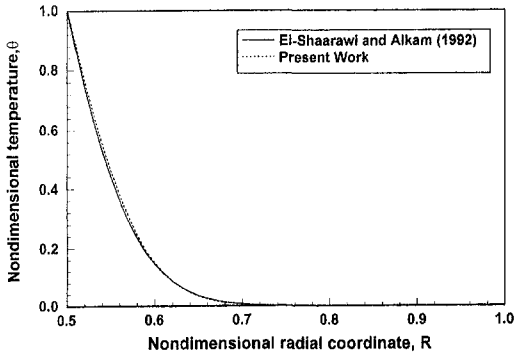

Fig. 3 Nondimensional radial temperature distribution. Case O with Da = 1.0e10, A = 1.0e − 10, $N2$ = 0.98, and modified boundary conditions to match the boundary conditions considered by El-Shaarawi and Alkam (1992). τ = 1.8e − 3 and Z = 6.

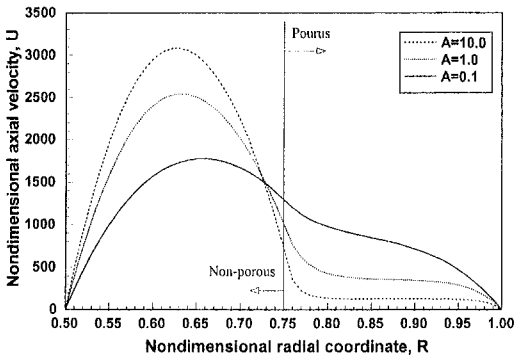

Fig. 6 Nondimensional axial velocity distribution in the radial direction for different values of Forchheimer number for case O. Z = 10, $N2$ = 0.75, and Da = 0.1.

caused by the microscopic inertial and viscous forces generated by the porous solid matrix. Also, the fluid mean velocity in the porous domain decreases as one marches downstream. The drafted fluid from the porous region enhances the fluid flow in the clear domain and causes an increase in its maximum velocity and a simultaneous shift in the location of the maximum velocity towards the porous layer which is the source of the drafted fluid.

The effect of the microscopic inertial term (A) on the axial-velocity radial distribution is shown in Fig. 6. Increasing A implies an increase in the microscopic inertial retardation forces in the porous domain, and consequently, the fluid mean flow in the porous substrate decreases. On the other hand, the drafted fluid resulted from this retardation feeds the clear region and increases its mean velocity. Figure 7 shows the dynamic variation in the radial temperature distribution. The figure suggests

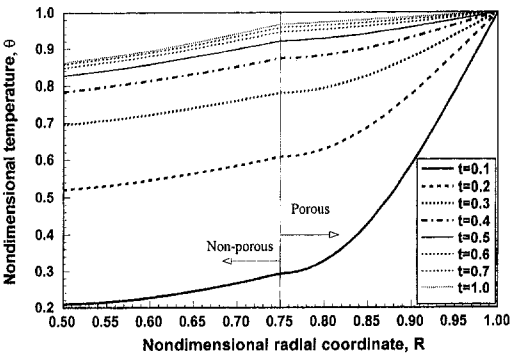

Fig. 7 Nondimensional temperature distribution in the radial direction for different times, at Z = 160 for case O. $N2$ = 0.75, A = 10, and Da = 0.1.

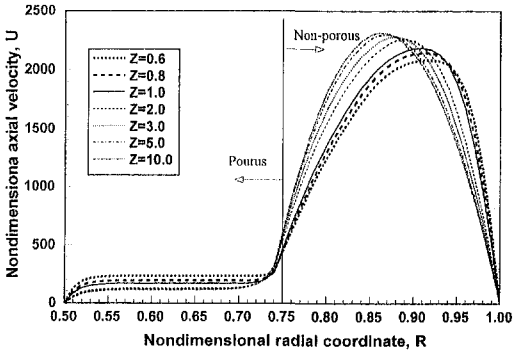

Fig. 4 Nondimensional axial velocity distribution in the radial direction at different axial locations for case I. $N2$ = 0.75, A = 10, and Da = 0.01.

that external heating, which is applied on the outer cylinder, has more effective penetration in the porous substrate than that in the clear fluid domain. This is due to the improvement in Nusselt number, as will be shown later. Figure 8 shows a comparison of the axial variation in Nusselt number between cases I and O. It is observed that inserting the porous substrate at the inner cylinder causes more improvement in Nu number than that in case O. The same observation may be detected in clear annulus which does not contain any porous substrate. Due to its larger surface area, the outer wall drifts more fluid towards the inner wall. This causes the maximum velocity to be shifted towards the inner wall, and consequently the hydrodynamic boundary layer thickness on the inner cylinder is much thinner than that on the outer cylinder; this enhances Nu number at the inner wall. However, case O transfers more heat to the fluid than case I due to its larger surface area.

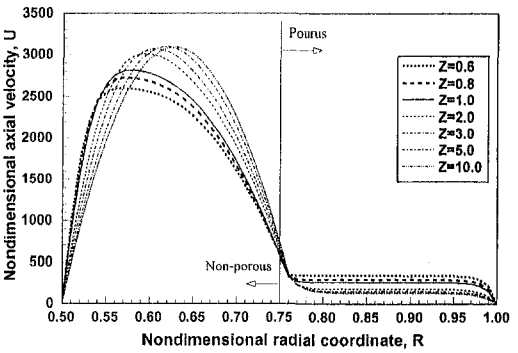

Fig. 5 Nondimensional axial velocity distribution in the radial direction at different axial locations for case O. $N2$ = 0.75, A = 10, and Da = 0.01.

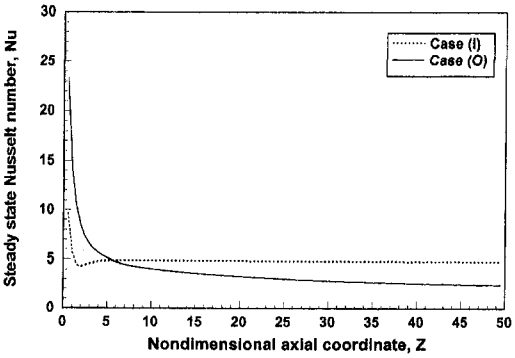

Fig. 8 Axial variation of the steady-state Nusselt number. Comparison between cases I and O with A = 10, Da = 0.01, and $N2$ = 0.75.

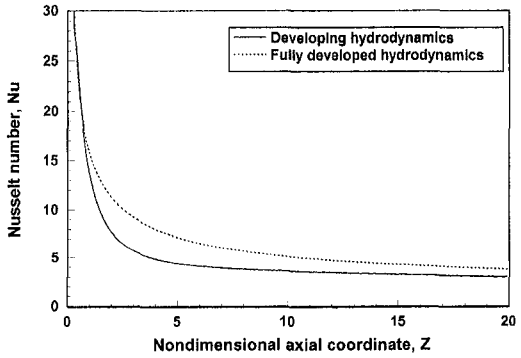

Fig. 9 Effect of the hydrodynamic entrance length on Nusselt number for case O. $N2$ = 0.75, Da = 0.1, and A = 10.

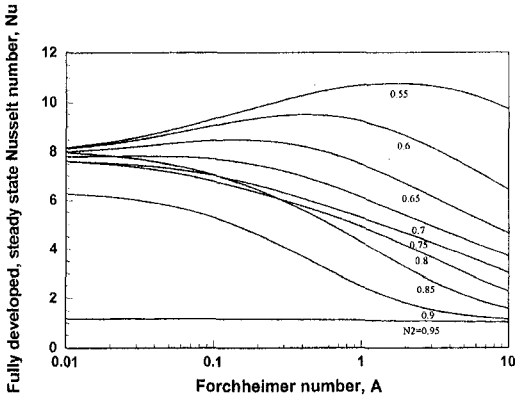

Fig. 11 Effect of Forchheimer number on the fully developed, steady-state Nusselt number for different values of $N2$. Case O with Da = 0.1.

Figure 9 reflects the substantial importance of the macroscopic inertial term. Neglecting this term in both porous and clear domains implies a fully developed hydrodynamics behavior. In Fig. 9, Nu is evaluated under the assumption of fully developed hydrodynamics and it is compared to the corresponding value considering the development of the flow. The assumption that the flow is hydrodynamically fully developed overestimates Nu up to 40 percent. The results of Fig. 9 are computed for $N_2 = 0.75$.

The effect of the porous substrate thickness on the fully developed Nu under steady-state conditions, for case O, is shown in Fig. 10. Increasing the porous substrate thickness (decreasing N_2) causes a substantial increase in Nu, especially at higher values of A. The improvement in Nu due to the porous substrate is caused by: (1) the substrate role in enhancing the mixing mechanism between the fluid and the wall; (2) increasing the fluid effective thermal conductivity; and (3) producing a thinner hydrodynamic boundary layer (low thermal resistance). Also, it is clear from the same figure that for small A, there is an optimum substrate thickness beyond which there is no substantial increase in Nu. As an example, and for $A = 0.01$, increasing the thickness of the porous substrate from 0 ($N_2 = 1$) to 0.11 ($N_2 = 0.89$) improves Nu from 1 to 8, but increasing the thickness from 0.11 ($N_2 = 0.89$) to 0.5 ($N_2 = 0.5$) does not add any significant improvement. This is an important conclusion because in practical situations, one tries to avoid filling the entire channel with the porous substrate in order to reduce the pressure drop, and consequently, the cost of the pumping force within the channel. The figure shows that the value of A plays a major role in choosing the optimum thickness of the porous material as far as Nu number. In other words, upon using porous substrates with high values of A ($\sim$10), optimum values of Nu are achieved by filling the whole domain with porous material. However, if the porous substrate has low A ($\sim$0.01), the optimum Nu number is obtained without having to fill the whole domain with the porous material, and therefore, one can reduce the pumping force needed without sacrificing Nu. The results of Fig. 10 are replotted from another point of view in Fig. 11. It is shown that A has no significant effects on Nu for $N_2 = 0.95$. This is because using very thin substrate does not affect Nu regardless of the value of A. However, for $0.7 < N_2 < 0.9$, increasing A decreases Nu. This is because the microscopic inertial force has a retardation effect on the flow which implies a thicker hydrodynamic boundary layer, and this reduces the local Nusselt number. For $N_2 < 0.7$, increasing A enhances Nu up to a certain point, and then it starts to decrease. Also, it is clear from this figure that the effect of the microscopic inertial term on Nu is more pronounced at higher values of A. The fact that A is multiplied by a nonlinear squared term in the momentum equation clearifies this behavior. In most practical applications, the porosity varies in the range of 0.7–1. In this range, the permeability K has very large values, and as a result, the coefficient of the microscopic inertial term A is very small. As concluded before, any variation within this small range of A brings no significant variation on Nu.

The effect of the porous substrate thickness (case O) on the hydrodynamic entrance length is shown in Fig. 12 for different values of A. As clear from this figure, channels completely filled with porous substrate ($N_2 \rightarrow 0.5$) have very short hydrodynamic entrance length. However, as the porous substrate thickness is reduced, the hydrodynamic entrance length increases considerably. The variation in the entrance length becomes more significant at larger values of A. This is understood, since small changes in the thickness of high-A porous substrates brings significant effects on the hydrodynamic entrance length. On the other hand, in channels with thin porous substrates ($N_2 \rightarrow 1$), the inertial term has no significant effect on the entrance length, especially for small and moderate values of A. Channels having

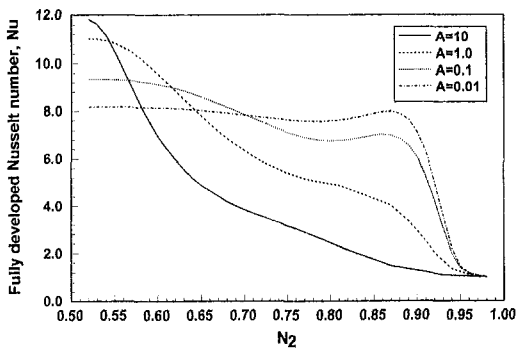

Fig. 10 Effect of the porous substrate thickness on the fully developed Nusselt number under steady-state conditions for case O. Da = 0.1.

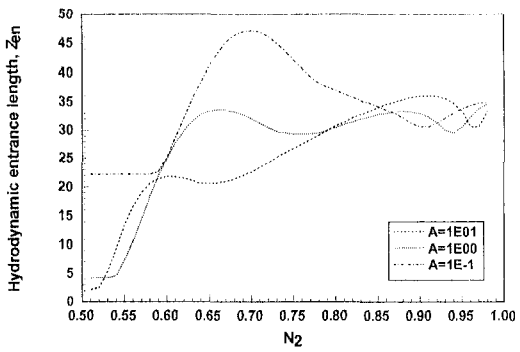

Fig. 12 Effect of the porous substrate thickness on the hydrodynamic entrance length for case O. Da = 0.1.

($N_2 \rightarrow 1$) imply that there is no porous substrate and as a result, A has nothing to do with the hydrodynamic entrance length. Figure 12 leads to the conclusion that one should not drop the macroscopic inertial effect from the momentum equations for channels partially filled with porous materials. For example, inserting a porous substrate having $A = 10$ results in a dimensionless entrance length of 2 at $N_2 = 0.5$, and it goes up to about 35 for $N_2 = 0.95$.

The axial variation in the steady-state time, τ_{ss}, which is the time required to attain the steady-state thermal behavior at a given axial location, is shown in Fig. 13 for both cases I and O. It is obvious that τ_{ss} increases in the downstream direction. Also, and due to its higher Nu, the inner wall heats (or cools) the flow much faster than the outer wall. As a result, case I has lower τ_{ss} than case O.

The effect of the Da number on the axial distribution of the Nu number is shown in Fig. 14. As clear from this figure, increasing the Da number improves the Nu number. Small Da numbers imply substrates of small permeability. This means that the substrate behaves nearly as a complete solid layer that does not contain any voids, and hence the convection effect of heat transfer is retarded. Also, Fig. 14 shows that increasing the Da number beyond a certain limit has insignificant effect on the Nu number. Since the Da number appears in the denominator of the microscopic viscous term, the sensitivity of the solution to the value of the Da number becomes very low for relatively high values of the Da number ($\mathrm{Da} \geq 1 \times 10^{-2}$).

Conclusions

Numerical solutions are presented for the problem of transient developing forced convection flow in concentric annuli partially filled with porous substrates. Including the macroscopic inertial term, the Brinkman-Forchheimer extended Darcy model is used to model the flow inside the porous domain. The effects of different parameters regarding the geometry, the solid matrix, and the fluid on the hydrodynamic and thermal behavior are investigated.

It is found that assuming fully developed hydrodynamic behavior overestimates Nu up to 40 percent for $N_2 = 0.75$, and yet, the overestimation increases for thicker porous substrates. Also, it is concluded that porous substrates may improve the Nusselt number by 1200 percent. The results show that there is an optimum thickness for the porous material, for small A ($A < 0.1$), beyond which there is no significant improvement in the Nusselt number. Also, the dimensionless hydrodynamic entrance length varies within the range 2–45, and it has significant effect on the Nusselt number. As a result, the macroscopic inertial term in the porous domain momentum equation should not be neglected.

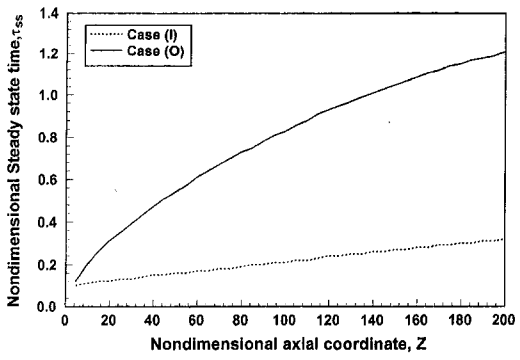

Fig. 13 A comparison of the steady-state time between cases I and O. A = 10, Da = 0.1, and $N2$ = 0.75.

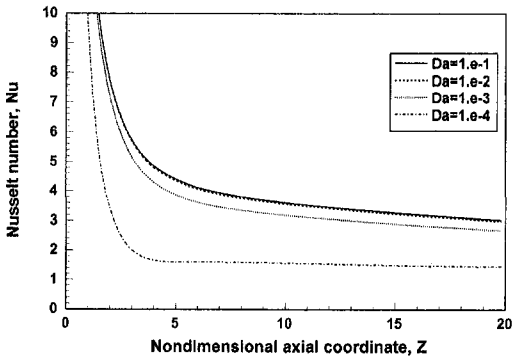

Fig. 14 Effect of Da on Nusselt number for case O. $N2$ = 0.75 and A = 10.

The effect of the microscopic inertial term, A, on the Nu number is dictated by the value of the porous substrate thickness. For large values of A ($A > 0.1$), increasing the porous substrate thickness improves the Nu number. On the other hand, for substrates with ($A < 0.1$), the Nu number has an optimum value for $N_2 = 0.85$, and any further increase in the porous substrate thickness has an insignificant effect on the Nu number. Also, the effect of the microscopic inertial term on Nu is more pronounced at higher values of A.

As the thickness of the porous substrate decreases, the hydrodynamic entrance length increases and it reaches a maximum value after which a moderate reduction in the entrance length is observed. The variation in the entrance length becomes more significant at larger values of A.

A comparison is conducted between cases I and O, where it is found that case I has a higher Nusselt number and lower steady-state time than case O.

References

Beavers, G. S., and Joseph, D. D., 1967, "Boundary Conditions at a Naturally Permeable Wall," *J. Fluid Mech.*, Vol. 13, pp. 197–207.

Bodoia, J. R., and Osterle, J. F., 1961, "Finite-Difference Analysis of Plane Poiseuille and Couette Flow Developments," *Apll. Sci. Res.*, Vol. A10, pp. 265–276.

Chikh, S., Boumedien, A., Bouhadef, K., and Lauriat, G., 1995a, "Analytical Solution of Non-Darcian Forced Convection in an Annular Duct Partially Filled with a Porous Medium," *Int. J. Heat and Mass Transfer,* Vol. 38, pp. 1543–1551.

Chikh, S., Boumedien, A., Bouhadef, K., and Lauriat, G., 1995b, "Non-Darcian Forced Convection Analysis in an Annular Partially Filled with a Porous Material," *Numerical Heat Transfer A,* Vol. 28, pp. 707–722.

El-Shaarawi, M. A., and Alkam, M., 1992, "Transient Forced Convection in the Entrance Region of Concentric Annuli," *Int. J. Heat Mass Transfer,* Vol. 35, pp. 3335–3344.

Jang, J. Y., and Chen, J. L., 1992, "Forced Convection in a Parallel Plate Channel Partially Filled with a High Porosity Medium," *Int. Comm. Heat Mass Transfer,* Vol. 19, pp. 263–273.

Kakac, S., Kilkis, B., Kulacki, F., and Arinc, F., 1991, *Convective Heat and Mass Transfer in Porous Media,* Kluwer Academic Publishers, The Netherlands, pp. 563–615.

Poulikakos, D., and Kazmierczak, M., 1987, "Forced Convection in a Duct Partially Filled with a Porous Material," ASME JOURNAL OF HEAT TRANSFER, Vol. 109, pp. 653–662.

Rudraiah, N., 1985, "Forced Convection in a Parallel Plate Channel Partially Filled with a Porous Material," ASME JOURNAL OF HEAT TRANSFER, Vol. 107, pp. 322–331.

Vafai, K., and Kim, S. J., 1990, "Fluid Mechanics of the Interface Region Between a Porous Medium and a Fluid Layer-An Exact Solution," *Int. J. Heat and Fluid Flow,* Vol. 11, pp. 254–256.

Vafai, K., and Kim, S. J., 1995, "On the Limitations of the Brinkman-Forchheimer-extended Darcy Equation," *Int. J. Heat and Fluid Flow,* Vol. 16, pp. 11–15.

Vafai, K., and Thiyagaraja, R., 1987, "Analysis of Flow and Heat Transfer at the Interface Region of a Porous Medium," *Int. J. Heat and Mass Transfer,* Vol. 30, pp. 1391–1405.

EHD Enhanced Convective Boiling of R-134a in Grooved Channels—Application to Subcompact Heat Exchangers

M. Salehi

M. M. Ohadi
ohadi@eng.umd.edu

S. Dessiatoun

Heat Transfer Enhancement Laboratory,
Center for Environmental
Energy Engineering,
Department of Mechanical Engineering,
University of Maryland,
College Park, MD 20742

Electrohydrodynamically (EHD) enhanced flow boiling of refrigerant R-134a inside grooved channels of approximately 1-mm hydraulic diameter was investigated with the objective of addressing the applicability of the EHD technique in highly compact heat exchangers. Two sets of experiments were performed. The first set included experiments in a channel with a smooth heat transfer wall, whereas in the second set a corrugated (enhanced) surface was used. In each case experiments were conducted as a function of the applied electrical field strength, electric field polarity, flow Reynolds number, inlet test section vapor quality, and flow direction (upward, downward, or horizontal). It is demonstrated that in all cases the EHD effect can substantially increase the heat transfer coefficient particularly at low Reynolds numbers and when applied over the enhanced heat transfer wall.

Introduction

Electrohydrodynamics (EHD) is an emerging promising technique for heat transfer enhancement of both single-phase and phase-change processes. It utilizes the effect of secondary motions to yield substantially higher heat transfer coefficients. The driving force behind electrically induced secondary motions responsible for the heat transfer enhancement is the electric (EHD) body force. For a dielectric fluid medium of permittivity ϵ, density ρ, and temperature T subjected to an electric field strength $\bar{E}$, the body force can be expressed as (Melcher, 1981)

$$\bar{f}_e = \rho_c \bar{E} - \frac{1}{2}\bar{E}^2 \nabla \epsilon + \frac{1}{2}\nabla\left[\bar{E}^2 \rho \left(\frac{\partial \epsilon}{\partial \rho}\right)_T\right] \quad (1)$$

where ρ_c is the electric field space charge density. The first term on the right hand side of Eq. (1) represents the force on the free charges within the fluid medium and is called the Coulomb force. For two-phase flow processes in dielectric fluids, the EHD current discharge is insignificant and therefore the Coulomb's force effect is minimal. The Clausius-Mossoti law (Glasstone, 1946; Kittel, 1956; Jackson, 1962) relates the dielectric constant of the fluid medium to the mass density as

$$\frac{\kappa - 1}{\kappa + 2} = C\rho \quad (2)$$

Utilizing Eq. (2) and neglecting the first term in Eq. (1), an alternative form for the electric body force is given as (Singh, 1995)

$$\bar{f}_e = \frac{\epsilon_0(\kappa - 1)(\kappa + 2)}{6}\nabla \bar{E}^2 + \frac{\epsilon_0 \rho C \bar{E}^2(\kappa + 2)}{3}\nabla \kappa \quad (3)$$

where C is a constant given as $N_o\alpha/(3M)$. κ is the dielectric constant ($\epsilon = \kappa\epsilon_0$) defined as the ratio of the dielectric permittivity of the medium to that of vacuum.

Thus, in a phase-change process the electric field applied to a pure dielectric fluid will produce forces within the fluid medium due to two effects: the nonuniformity of the electric field, and the nonuniformity in the dielectric permittivity of the fluid. Nonuniformity in the electric field can be promoted by applying the field, for example, over an enhanced heat transfer surface (e.g., corrugated surface in the present study), whereas the presence of a vapor-liquid interface gives rise to nonuniformity in the dielectric permittivity of the fluid medium. For example, κ for vapor R-134a varies from 1.2 to 1.3 in the range of 4 to 27°C, respectively. For liquid R-134a, κ varies from 13.9 to 9.8 in the range of −17°C to 30°C, respectively. As a result, the EHD technique is most effective in two-phase flow processes when used in conjunction with an enhanced (non-smooth) heat transfer surface.

Applicability of the EHD technique to the external and in-tube boiling heat transfer enhancement of refrigerants has already been investigated (Yabe, 1991; Ohadi et al., 1992; Singh et al., 1993; Ohadi et al., 1994; Seyed-Yagoobi et al., 1996). However, the literature search failed to identify any previous work on EHD enhanced in-tube boiling of R-134a in a highly compact flow channel geometry of the type studied here.

The present study addresses the applicability of the EHD technique for flow boiling enhancement of R-134a in grooved channels with a hydraulic diameter of less than 1 mm. Two sets of experiments were performed. In the first set the EHD effect was applied in a channel with a smooth heat transfer surface, whereas in the second set a corrugated (enhanced) surface was used. In addition to investigating the effect of parameters such as applied electric field potential, flow Reynolds number, average test section vapor quality, and flow direction (upward or downward), the effect of electric field polarity was also investigated.

Experimental Apparatus and Procedure

The essential features of the experimental apparatus and procedure are given in this section, with additional details documented in Ohadi et al. (1994). As shown in Fig. 1, the boiling loop consisted of a condensation and a subcooling loop, a pump, a preheater, and the test section. Energy supply to both the preheater and the test section heater was via resistive heating. The test section, as shown in Figs. 2 and 3, was an 11.43 cm (4.5 in.) annulus with ID of 9.5 mm (0.37 in.) and OD of 11.56 mm (0.455 in.). These test section dimensions were chosen

Contributed by the Heat Transfer Division for publication in the JOURNAL OF HEAT TRANSFER. Manuscript received by the Heat Transfer Division March 25, 1996; revision received July 15, 1997; Keywords: Augmentation and Enhancement, Boiling, Phase-Change Phenomena. Associate Technical Editor: T. J. Rabas.

to reflect the type of compact geometry considered without compromising accuracy of the measurements. Two heat transfer surfaces were tested—a smooth channel wall and a corrugated wall with helix angle of 18° and 60 internal ridges with ridge height of 0.25 mm (0.010 in.). To facilitate variation of quality at the test section inlet, a 45.7 cm (18 in.) of preheater tube section was heated utilizing fiberglass insulated nichrom wire. To decrease axial thermal conduction effects, the preheater and heater were connected to the boiling loop through stainless steel (type 316 L SS) piping. The test section was designed in such a way that it could be tilted to any desired angle between horizontal to 90° (vertical) position, therefore providing the ability to quantify the effect of flow direction (or gravity induced buoyancy effect) on the EHD enhanced boiling coefficients.

Fluid flow to the test section was through a series of small channels formed by the heat transfer wall, the inner surface (rod), and the electrically insulating spacers (Teflon type material), as shown in Fig. 3. Combination of the inner surface (rod) and the heat transfer surface provided flow channels that simulated the geometry/dimensions of those encountered in sub-compact heat exchangers. When the electric field was applied (positive polarity), the rod served as the charged surface (electrode) and the heat transfer wall as the receiving surface (electrode). The hydraulic diameter of each of the channels was on the order of 1 mm or less. Boiling took place on the outer channel wall, here designated as the heat transfer wall, which also served as the receiving (ground) electrode. The channels, as shown in Fig. 3, were completely sealed off from each other by spacers which were inserted mechanically into the grooves made on the rod. The rod with the spacers then were inserted by some pressure into the test section tube. This reduced the chance of flow mixing between channels and also the heat transfer. The field was applied to the inner wall, designated as the electrode wall in the figure. Copper-Constantan (type T) thermocouples were mounted along the outside heating wall of the channel to measure the average wall temperature. The vapor R-134a leaving the test section was condensed in a shell-and-tube condenser before entering the subcooler. Chilled water for the condenser was provided by a water chiller (12 kW capacity at $\Delta T = 5°C$).

The subcooler was a vapor compression loop. As shown in Fig. 1, the subcooled refrigerant entered a magnetic driven gear pump where it was pumped through the mass flow meter (Coriolis type, equipped with a transmitter that indicated the mass flow through an LCD screen) before entering the control valve and the preheater. The electrical power supply to the heater and the preheater was through a 240 V, 1.7 kW power supply.

The wall temperatures were measured by four thermocouples circumferentially placed (90° apart) at three equally spaced axial locations. The soldering point of the thermocouples to the tube wall was less than 1 mm in diameter. Thermocouples were calibrated before assembling the test section by inserting all of them at once in an ice bath. Maximum deviation of 0.1°C was seen among the thermocouples readings. Measurement of the pressure in the test section was by a 0–100 psi capacitance type pressure transducer. The EHD voltage and current were measured by a general purpose multimeter. A pressure port for measuring the system pressure was installed 30.98 cm (1 ft) upstream of the test section.

A typical experimental run began by first turning on the refrigerant pump and setting the mass flux or mass flow rate at the desired level. Next, the preheater and the heater, depending on the specific test conducted, were turned on and adjusted to provide the desired heat flux and inlet quality to the test section. The chiller was then turned on and the water flow rate was controlled such that the capacity of the cooling and subcooling loops became approximately equal to the heat released by the heater and the preheater. The system was allowed to reach the steady-state condition, which normally took two hours before any data were taken. The steady-state condition was specified as the point when fluctuations in pressure or mass flux were less than 1 percent.

Data Reduction

The average heat transfer coefficient was calculated using the defining equation

$$h = \frac{Q_h}{A[T_{w,i} - T_{\text{sat}}]} \tag{3}$$

in which Q_h was determined by

$$Q_h = \frac{V^2}{R} \tag{4}$$

in which V is the voltage, and R is the resistance of the heater wires. The test section was well insulated and any heat loss to the surroundings were assumed negligible. The inside tube wall temperature $T_{w,i}$ was calculated by the following equation (assuming one-dimensional heat conduction from the outside to the inside of the test section tube wall):

$$T_{w,i} = T_{w,o} - \frac{Q_h \ln\left(\frac{R_o}{R_i}\right)}{2\pi kL}. \tag{5}$$

Since $\ln(R_o/R_i)$ was very small in the present experiments and since the conductivity of copper is very high, the resulting

Nomenclature

A = heat transfer surface area
C = a constant
e_{ap} = specific enthalpy of refrigerant at the preheater exit
e_{bp} = specific enthalpy of refrigerant before the preheater
f_e = electric body force
E = electric field strength
G = refrigerant mass flow rate
h = heat transfer coefficient
h_o = heat transfer coefficient in the absence of electric field (base case)
h/ho = enhancement ratio
HF = heat flux
ID = inside diameter
IQ = inlet quality to the test section
k = thermal conductivity of the test section tube material
L = the test section length
M = molecular mass of dielectric medium
N_0 = number of molecules per mole
OD = outside diameter
p = absolute pressure in the test section
Γ = perimeter of the channel
Q_h = test section heat transfer rate
Q_{ph} = preheater heat transfer rate
R_i = inner radius of the test section tube
R_o = outer radius of the test section tube
T_{bp} = temperature of refrigerant before the preheater
Q_{ph} = heat provided by the preheater
T_{liq} = liquid phase temperature of the refrigerant
$T_{w,i}$ = inner test section tube wall temperature
$T_{w,o}$ = outer test section tube wall temperature
X = refrigerant quality
α = polarization factor
ϵ = dielectric permittivity for a medium
ϵ_0 = dielectric permittivity for vacuum
ρ = mass density of the fluid
ρ_c = electrical charge density
κ = dielectric constant
η = heat transfer enhancement factor
μ = dynamic viscosity of the fluid

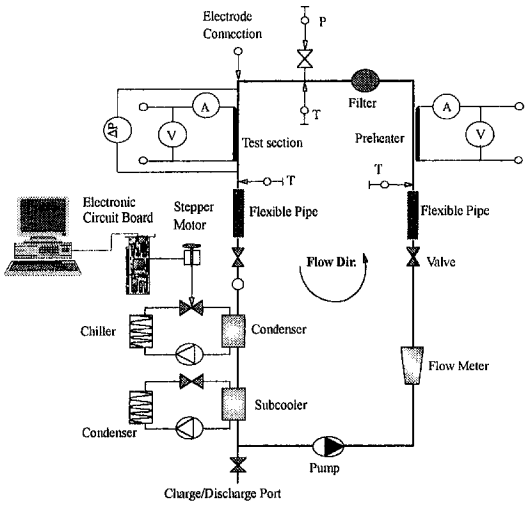

Fig. 1 Schematic diagram of the experimental setup

temperature difference ($T_{w,i} - T_{w,o}$) was insignificant (about 0.03°C) for the range of parameters studied.

The inlet quality to the test section X_{ap} was calculated using the energy balance equations on the test section and the preheater as

$$X_{ap} = f(p, e_{ap}) \tag{6}$$

and

$$e_{ap} = e_{bp} + \frac{Q_{ph}}{\dot{G}} \tag{7}$$

where e_{bp} and e_{ap} are the specific enthalpy of refrigerant before and after the preheater, respectively. e_{bp} can be found from thermodynamics property tables for R-134a for the temperature and pressure conditions at the inlet to the preheater. A liquid phase flow was always maintained upstream of the preheater.

The heat transfer enhancement factor (η) was calculated as

$$\eta = \frac{h}{h_o} \tag{8}$$

where h_o and h are the heat transfer coefficient for the base case (absence of the EHD effect) and in the presence of the EHD effect, respectively.

The ratio of EHD power consumption to the total heat exchange in the test section can be calculated as

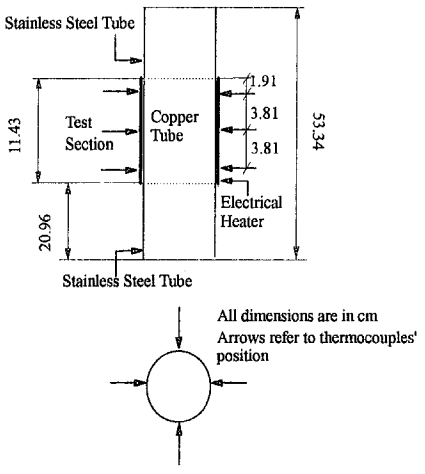

Fig. 2 Thermocouple position along the test section

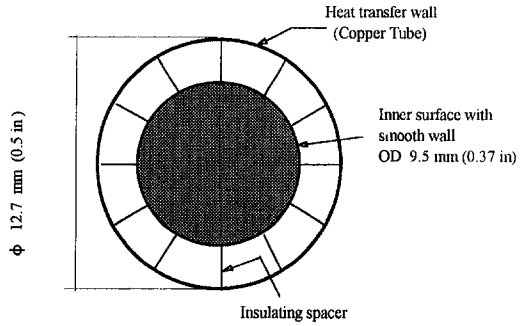

Fig. 3 The channel geometries

$$\frac{Q_{\text{EHD}}}{Q_{\text{Total}}} = \frac{Q_{\text{EHD}}}{Q_h + Q_{\text{EHD}}}. \tag{9}$$

Finally, the Reynolds number was calculated based on the hydraulic diameter of the channel utilizing the mass flow rate measured by the mass flow meter with the working fluid in single-phase (liquid) condition

$$\text{Re} = \frac{4\dot{m}}{\Gamma\mu} \tag{10}$$

in which $\dot{m}$ is the refrigerant mass flow rate (kg/s) in the channel and Γ is the channel perimeter.

Experimental Uncertainty Calculations. The uncertainty calculations were based on the defining equation for differential variation of a function of several variables. In the present experiments, a manufacturer calibrated temperature indicator with resolution of 0.01°C and accuracy of ±0.2°C was employed. This resulted in a value of 0.03°C for ΔT_w. The error in measurement of ΔT_{sat} was calculated from variation of pressure in the test section and resulted in ±0.2°C. The error in measurement of the voltage and resistance (dV and dR) was $\pm 0.7V$ and $\pm 0.1\Omega$, respectively. Accordingly, the uncertainty of Q_h was found to be ±0.51 percent which was for the case when the lowest heat flux (5000 W/m^2) was applied. In addition, by writing an energy balance, taking the test section as the control volume, it was found that about 5 percent of heat input to the test section from the electrical heater was lost to the surroundings. Using the root sum squares technique, uncertainty of heat transfer coefficient (h) was found to be in the range of ±3 percent to ±30 percent (for heat flux range of 5 to 40 kW/m^2), where the highest uncertainty was associated with the lowest heat flux (5 kW/m^2), due to the very small temperature differences at lower mass flow rates. The uncertainty for the heat flux of 25 kW/m^2 was ±12 percent.

Results and Discussion

Presentation of the results begins with reference to Fig. 4, where comparison of the heat transfer coefficient as a function of applied electric field potential is depicted for the smooth and enhanced heat transfer surfaces for a downward flow direction. From an overall inspection of Fig. 4, several observations can be made. First, it is seen that for the smooth surface the increase in the applied electric potential results in a direct increase in the enhancement factor. This is consistent with Eq. (1), where the magnitude of the EHD body force is shown to strongly depend on the applied electric field strength, particularly for processes involving phase change. Second, for the enhanced surface the increase in the applied electric field potential increases the h to a certain level, beyond which additional increase in the field potential causes a reduction in h. This phenomena can be attributed to the fact that at excessively high applied potentials the bubbles are pressed against the heat transfer sur-

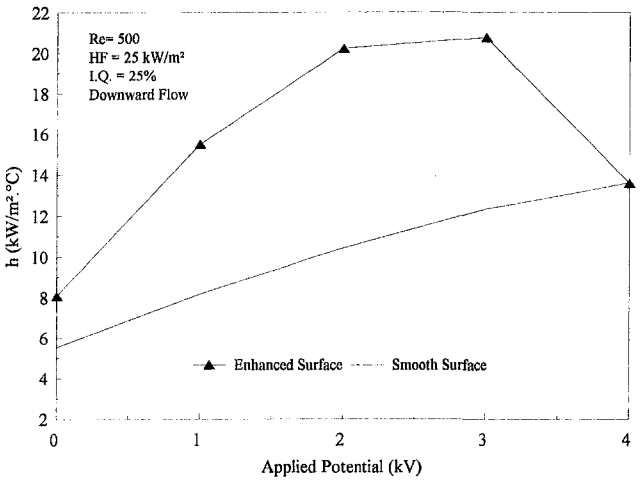

Fig. 4 *h* versus applied potential for two wall surfaces at Re = 500

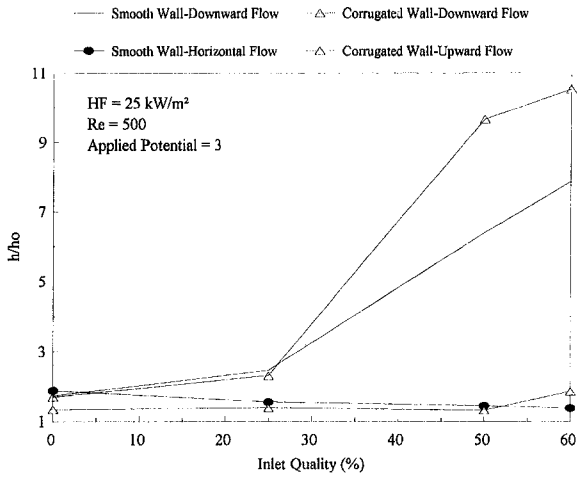

Fig. 6 Enhancement factor versus I.Q. for different flow directions

face and their entrapment in turn causes additional thermal resistance on the heat transfer surface and therefore reduced heat transfer coefficients (Cheung et al., 1995). The third observation in Fig. 4 is that the enhanced surface for the most part exhibits a better performance when compared to the smooth surface. This is because the nonuniformities on the heat transfer wall give rise to the nonuniformities in the electric field distribution, which according to Eq. (1), yields a stronger electric body force and hence higher enhancements.

Attention is next drawn to Fig. 5 where comparison of heat transfer coefficients for enhanced and smooth wall channels in a downward flow condition are depicted for Reynolds numbers of 500 and 1000 at a heat flux of 25 kW/m^2 and inlet quality of 25 percent. It is seen that although the absolute value of the heat transfer coefficient for the lower Re is lower, higher enhancements are associated with the lower Reynolds numbers. This is because at higher Reynolds numbers the EHD effects are much less dominant when compared to the strong momentum diffusivity effects. From Fig. 5 it is seen that at Re = 500, for the enhanced wall channel after a certain voltage, the enhancement starts to decline. This is consistent with the trend observed in Fig. 4 as described above. For smooth wall surfaces this effect does not take place due to the weaker electric body force associated with a smooth surface.

Figure 6 provides comparison of the enhancement factor as a function of test section inlet quality for a smooth and enhanced channel wall under different flow directions. It is seen that the downward flow gives higher enhancements over the entire range of the vapor qualities tested. The instability caused by gravity force in a direction opposite to that of the main flow, as well as the instability caused by the applied potential at the liquid-vapor interface, contribute to more effective flow agitation and result in higher heat transfer coefficients for a downward flow. For horizontal flow and smooth surface, increasing the vapor quality has negligible effect on the heat transfer coefficient. This can be due to the fact that for the tested mass flow rate, a possibility exists that with increased quality in the upper channels in the test section there is not a sufficient liquid flow rate. This in turn causes a decrease in heat transfer coefficient of the upper channels, while the EHD body force helps in increasing the heat transfer coefficients at the lower channel walls.

In all of the experiments discussed so far the electrode was charged with positive polarity. To address the effect of field polarity on the EHD enhancement factor, attention is next drawn to Fig. 7, where a comparison of positive and negative field polarities is depicted for the smooth and enhanced surfaces for a downward flow orientation. Examination of the data in Fig. 7 suggests two observations. First, with increasing inlet quality the increased vapor velocity causes an increase in the heat transfer coefficient, while EHD helps to maintain a wet surface condition and postpones partial dry out. Second, for a given surface-

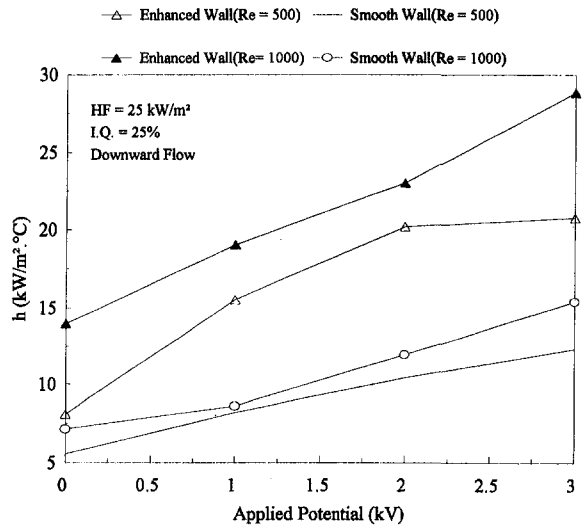

Fig. 5 *h* versus applied potential for different flow directions

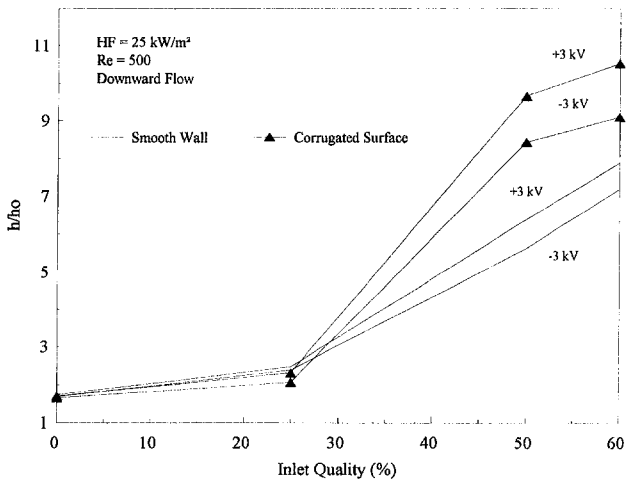

Fig. 7 Effect of polarity on enhancement factor

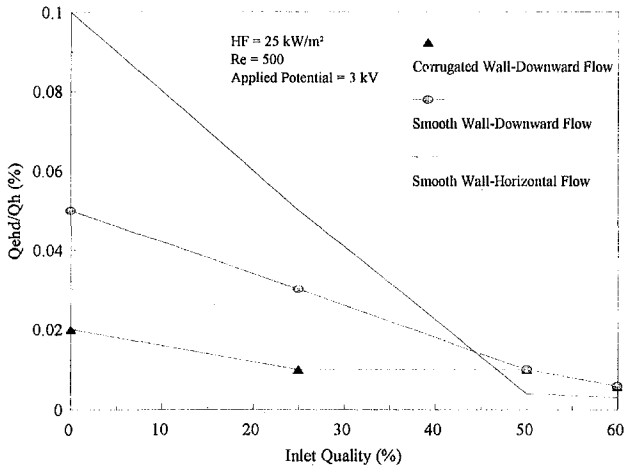

Fig. 8 Power consumption versus inlet quality for various flow direction

electrode combination, the field polarity plays a minimal role. The differences observed between the positive and negative field polarity data can be attributed to two factors. First, to the type of free charges in fluid media including potential impurities in the refrigerant, and second, due to the uncertainties in measuring the temperature and other quantities.

Cost-effective utilization of the EHD enhancement process requires negligible electric power consumption for the electrode(s). Figure 8 demonstrates the electric power consumption for three representative cases. With increasing quality, the amount of vapor in the test section increases, and since the vapor has a lower electrical conductivity than liquid, the EHD power consumption decreases with increasing quality. For smooth tube and horizontal flow, liquid tends to accumulate along the lower channel wall, leading to reduced electrical resistance across the wall, resulting in higher power consumptions. For upward and downward flow directions, the tendency for liquid accumulation is less, and therefore, when compared to horizontal flow, the EHD power consumption is reduced. However, in all three cases the EHD power consumption relative to the test section heat transfer rate is negligible.

Conclusions

This paper presented results of an experimental study on EHD enhanced convective boiling heat transfer of R-134a in circumferentially grooved channels, representing conditions in a subcompact heat exchanger. Experiments addressed the effect of test section inlet vapor quality, test section heat transfer wall (smooth or enhanced), applied electric field strength and polarity, flow Reynolds number, and flow direction (upward, downward, or horizontal). It was demonstrated that the technique is highly effective at lower Reynolds numbers. Up to a 10 fold increase in the boiling heat transfer coefficient was obtained at a Re of 500 when a 3 kV potential was applied over the channels with corrugated heat transfer surface in a downward flow position.

For the downward flow condition with increasing test section vapor quality, the heat transfer coefficient decreased, while the opposite effect took place for the upward flow condition at low vapor qualities. At lower test section vapor qualities the electric field polarity had minimal effect on the heat transfer enhancement factor. The EHD power consumption decreased with increasing the average test section vapor quality. However, at maximum it was only 0.1 percent of the heat transfer rate in the test section.

Acknowledgments

The financial support for this work was provided in part by a consortium of participating member companies. Special thanks are due Dr. Y. Kim (AlliedSignal Aerospace Co.) for the many technical contributions to this project. Corrugated surface used in the experiments was provided by Wolverine Tube, Inc. The assistance of Mr. Peter Thors and James Bogart (both from Wolverine Tube, Inc.) in this regard is gratefully acknowledged.

References

Cheung, K. H., Ohadi, M. M., Dessiatoun, S., and Singh, A., 1997, "EHD Enhanced Pool Boiling Heat Transfer Coefficients and Visualization of R-134a over Enhanced Tubes," ASME *Journal of Heat Transfer,* Vol. 119, No. 2, pp. 332–338.

Glasstone, S., 1946, *Textbook of Physical Chemistry,* 2nd ed., D. Van Nostrand Company Inc., Princeton, NJ, pp. 534–537.

Jackson, J. D., 1962, *Classical Electrodynamics,* John Wiley & Sons Inc., NY, pp. 116–119.

Kittel, C., 1956, *Introduction to Solid State Physics,* 2nd ed., John Wiley & Sons Inc, NY.

Melcher, J. R., 1981, *Continuum Electromechanics,* MIT Press, Cambridge, MA, pp. 3–18.

Ohadi, M. M., 1991, "Electrohydrodynamic Enhancement of Single-Phase and Phase-Change Heat Transfer in Heat Exchangers," *ASHRAE Journal,* Vol. 33, No. 12, pp. 42–48.

Ohadi, M. M., Papar, R. A., Kumar, A., and Ansari, A. I., 1992, "Some Observation on EHD Enhanced Boiling of R-123 in the Presence of Oil Contamination," *Proceedings of the Engineering Foundation Conference on Pool and External Flow Boiling,* ASME, NY.

Ohadi, M. M., Dessiatoun, S., Singh, A., Cheung, K. H., Salehi, M., and Blanford, M., 1994, "EHD Enhancement of Boiling/Condensation Heat Transfer of Alternate Refrigerants," Progress Report No. 5, Heat Transfer Enhancement Lab, University of MD, College Park, MD.

Pohl, H. A., 1958, "Some Effects of Non-Uniform Fields on Dielectrics," *Journal of Applied Physics,* Vol. 29, p. 1182–1189.

Seyed-Yagoobi, J., Geppert, C. A., and Geppert, L. M., 1996, "Electrohydrodynamically Enhanced Heat Transfer in Pool Boiling," ASME JOURNAL OF HEAT TRANSFER, Vol. 118, No. 2, pp. 233–237.

Seyed-Yagoobi, J., 1997, private communications on electrical properties of R-134a.

Singh, A., Kumar, A., Dessiatoun, S., Faani, M. A., Ohadi, M. M., and Ansari, A. I., 1993, "Compound EHD-Enhanced Pool-Boiling of R-123 in a Liquid-to-Refrigerant Heat Exchanger," ASME Paper No. 93-WA/HT-40.

Singh, A., Ohadi, M. M., Dessiatoun, S., and Chu, W., 1995, "In-Tube Boiling Heat Transfer Coefficients of R-123 and Their Enhancement Utilizing the EHD Technique," *J. of Enhanced Heat Transfer,* Vol. 2, No. 4, pp. 431–437.

Singh, A., 1995, Electrohydrodynamic (EHD) Enhancement of In-Tube Boiling and Condensation of Alternate (NON-CFC) Refrigerants, Ph.D. dissertation, University of Maryland, College Park, MD.

Yabe, A., 1991, "Active Heat Transfer Enhancement by Applying Electric Fields," Proceedings of the ASME/JSME Thermal Engineering Joint Conference, Vol. 3, ASME, NY, pp 15–23.

Impingement Cooling Flow and Heat Transfer Under Acoustic Excitations

C. Gau
Professor.
fh26gauc@mail.iaa.ncku.edu.tw

W. Y. Sheu

C. H. Shen

Institute of Aeronautics and Astronautics,
National Cheng Kung University,
Tainan, Taiwan 70101,
Republic of China

Experiments are performed to study (a) slot air jet impingement cooling flow and (b) the heat transfer under acoustic excitations. Both flow visualization and spectral energy evolution measurements along the shear layer are made. The acoustic excitation at either inherent or noninherent frequencies can make the upstream shift for both the most unstable waves and the resulting vortex formation and its subsequent pairing processes. At inherent frequencies the most unstable wave can be amplified, which increases the turbulence intensity in both the shear layer and the core and enhances the heat transfer. Both the turbulence intensity and the heat transfer increase with increasing excitation pressure levels S_{pl} until partial breakdown of the vortex occurs. At noninherent frequencies, however, the most unstable wave can be suppressed, which reduces the turbulence intensity and decreases the heat transfer. Both the turbulence intensity and the heat transfer decreases with increasing S_{pl}, but increases with increasing S_{pl} when the excitation frequency becomes dominant. For excitation at high Reynolds number with either inherent or noninherent frequency, a greater excitation pressure level is needed to cause the enhancement or the reduction in heat transfer. During the experiments, the inherent frequencies selected for excitation are $F_o/2$ and $F_o/4$, the noninherent frequencies are 0.71 F_o, 0.75 F_o, and 0.8 F_o, the acoustic pressure level varies from 70 dB to 100 dB, and the Reynolds number varies from 5500 to 22,000.

1 Introduction

Impingement cooling heat transfer has been studied extensively in the past due to its wide application in cooling the walls of high temperature thermal systems. The air-jet normally impinging on the wall can remove a large amount of heat over a relatively small surface area. It has frequently been used in cooling the hottest section of a combustion chamber or a turbine blade. Good review articles on the study of impingement cooling flow and heat transfer are available (Becko, 1976; Martin, 1977). The impingement cooling for a jet from a single rectangular or round nozzle, or an array of nozzles, over a heated surface has been well studied (Baughn and Shimizu, 1989; Gardon and Akeirat, 1966; Goldstein and Timmers, 1982; Hrycak, 1983). Correlations of stagnation point and local and average Nusselt numbers, in terms of relevant nondimensional parameters, have been obtained.

Studies in the past have considered only the ideal case of a laboratory controlled jet that impinges normally on a heated wall. However, the heat transfer data or correlations obtained from this kind of ideal jet may not be used in a practical situation where the impingement cooling is under a noisy environment. There is no report in the literature to answer if acoustic excitation could affect the heat transfer. It has been noted recently, however, in the field of the fluid mechanics (Crighton, 1981; Mankbadi, 1985; Zaman and Hussain, 1980) that due to the unstable nature of the shear layer in the jet, the shear layer flow structure can be significantly altered by the acoustic excitation. Therefore, one can expect that the altered flow structure in the shear layer will significantly change the wall heat transfer.

However, the selection of the excitation frequency is important since different excitation frequencies can lead to different flow structures. For a free jet, Ho and Huang (1982) have successfully proposed a subharmonic evolution model in which the vortex formation and the pairing process between two neighboring vortices are the result of the evolution of its fundamental and subharmonic instabilities. The vortex formation is developed from the initial most unstable wave at fundamental frequency, F_o. The first pairing process of the vortex is developed from the most amplified wave that occurred later, at the first subharmonic, $F_o/2$; the second pairing process is developed from the most amplified wave that occurred at the second subharmonic, $F_o/4$. A similar process will proceed downstream until the vortex structure becomes disorganized and dissipative. Excitation at all these frequencies is defined as the inherent frequency excitation, while excitation at other frequencies is referred as the noninherent frequency excitation. The inherent frequencies selected and used for excitation in the present experiment are $F_o/2$ and $F_o/4$. The noninherent frequencies selected are 0.71 F_o, 0.75 F_o, and 0.8 F_o. These excitation frequencies have been shown to be able to effectively alter the flow structure in the shear layer of a round jet (Han, 1991).

Therefore, the objective of the present experiments is to study the impingement cooling flow structure and heat transfer under acoustic excitation at either inherent or noninherent frequencies.

2 Experimental Apparatus and Procedures

The impinging air jet issued from the nozzle is supplied with a high pressure blower system which can furnish a maximum air flow of 10 m^3/min. To ensure air quality, a settling chamber with a honeycomb and different sizes of meshes is made and used to reduce the turbulence intensity and maintain a uniform air flow at the exit. The nozzle is made convergent and curved smoothly, which allows rapid acceleration of fluid without the occurrence of flow separation and generation of turbulence. Therefore, uniform velocity profile associated with a relatively low turbulence intensity across the nozzle width at the exit is obtained. The streamwise turbulence intensity at the nozzle exit is measured with a hot wire anemometer and is found to be less than 0.7 percent for a Reynolds number ranging from 2750 to

Contributed by the Heat Transfer Division for publication in the JOURNAL OF HEAT TRANSFER. Manuscript received by the Heat Transfer Division September 6, 1996; revision received May 19, 1997; Keywords: Augmentation and Enhancement; Electronic Equipment; Jets. Associate Technical Editor: B. W. Webb.

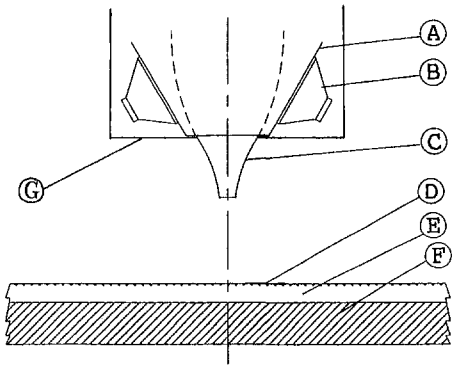

Fig. 1 Schematic of apparatus: (*A*) sound resonant chamber, (*B*) speaker, (*C*) nozzle, (*D*) foil heater, (*E*) Plexiglas plate, (*F*) insulations, and (*G*) wood box.

22,000. The jet velocity is measured with a Pitot tube. The nozzle is rectangular and is 2 cm in width and 15 cm in length. This is to ensure that the second dimension of the nozzle slot does not affect the slot-jet flow.

The excitation system consists of two low frequency range speakers which are mounted on both sides of the sound resonant chamber, as shown in Fig. 1. This chamber is mounted on the outside of the nozzle. The speakers are driven by a function generator which provides sin wave signals at desired frequencies. The sin wave signals are monitored with an oscilloscope and are amplified at desired levels before entering into the speakers. The acoustic wave generated by the two speakers can propagate into the air flow in the wind tunnel, pass through the nozzle, and propagate into the shear layer of the exiting jet. The sound pressure at the nozzle exit is measured with a sound level meter made by B&K Co. and is controlled at desired levels by the amplifier. The meter has an accuracy within +0.5 dB. To reduce the sound pressure level in the laboratory, a wood box enclosing the sound resonant chamber is made. The background noise level is maintained near 43 dB in the current study.

The flat plate is made of 1 cm thick Plexiglas plate which has a dimension of 63 cm × 20 cm. The surface is adhered with 0.015 mm thick, thin stainless steel foil which can be heated by passing it through electric current. Since the steel foil is so thin and the Plexiglas wall has a very low thermal conductivity, the heat conduction along the wall is negligibly small. To reduce heat loss to the ambient, the heated surface is well insulated on the back. To account for the additional radiation heat loss directly from the steel foil, the total heat loss to the ambient is estimated at less than 3 percent.

To measure the temperature distribution along the heated wall, a total of 50 thermocouples are individually inserted into equally spaced small holes drilled in the wall in order that the thermocouple junction can attach to the heated steel foil. One additional thermocouple is used to measure the jet temperature at the slot exit. All the temperature signals are acquired with a data logger and sent into a PC for data processing and plotting. Before the experiments all the thermocouples are calibrated in a constant temperature bath to ensure the measurement accuracy of +0.1°C.

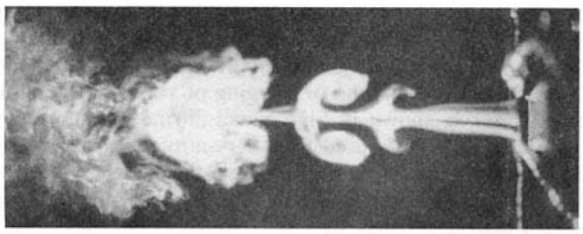

Fig. 2 Vortex flow structure of a free jet for Re = 2750

To ensure that the stainless-steel foil is heated uniformly, the entire foil is cut into a number of long strips. Each strip is heated individually with an equal amount of dc power. With the desired voltage V and current I passing through the thin strip, the heat flux along the surface can be calculated and is equal to VI/A, where A is the area of the strip. The local heat transfer coefficient can be determined with the following equation:

$$h = q/(T_w - T_a) \tag{1}$$

The uncertainty of the experimental data is determined according to the procedure proposed by Kline and McClintock (1953). The maximum uncertainty of local Nusselt number is 5.6 percent, the Reynolds number is 6.2 percent, and the turbulence intensity is 3.25 percent.

3 Results and Discussion

3.1 Flow Visualization. Flow visualization is made at a very low jet velocity (the system has a Reynolds number of 2750) in which the flow structure of smoke can be clearly visualized. We will consider the case of free jet, as shown in Fig. 2, without acoustic excitation. In general, the jet structure can be separated into three different regimes (i.e., the potential core, the mixing region, and the fully developed turbulent region). The mixing of jet flow with ambient air can produce a shear layer which can become unstable, due to Kelvin Helmholtz instability, and cause formation of a vortex, the first vortex occurring near the nozzle exit is shown in Fig. 2. The formation of a vortex is attributed to the most amplified frequency of the small disturbance which grows exponentially and rolls up into discrete vortices (Michalke, 1965). The most amplified frequency is shown to be the fundamental frequency of the jet. It has also been shown (Ho and Huang, 1982; Sheu, 1993) that the location for the vortex formation has the maximum spectral energy with fundamental frequency. As the spectral energy is

Nomenclature

A = area of a heat strip
B = slot width
c_p = specific heat
F_e = excitation frequency
F_i = ratio of excitation frequency versus fundamental frequency
F_o = fundamental frequency of the jet
h = convective heat transfer coefficient
k = thermal conductivity
Nu = Nusselt number, hB/k
Pr = Prandtl number, $c_p\mu/k$
q = heat flux
Re = Reynolds number, U_jB/ν
S_{pl} = sound pressure level
T = temperature
Tu = turbulence intensity
U = streamwise velocity
V = voltage
x = lateral distance from the stagnation point
Z = slot-to-plate spacing or the axial distance of the jet from the nozzle exit

Greek Symbols

α = thermal diffusivity
μ = viscosity
ν = kinematic viscosity

Subscripts

a = refer to ambient air
j = refer to jet flow at slot exit
o = refer to stagnation point
w = refer to wall

consumed and used for the vortex formation it decreases monotonically. At the same time, the spectral energy of the first subharmonic wave $F_o/2$ increases until a maximum is reached. At this location, the pairing or merging of vortices occurs, this second vortex is shown in Fig. 2, and all the spectral energy accumulated at $F_o/2$ is used for the occurrence of the pairing process. After the first pairing process, the vortex which may stretch, distort, and become a self-rotating vortex core can ungo a second pairing process, this third vortex is shown in Fig. 2. At the location of the second pairing process, the spectral energy of the second subharmonic wave $F_o/4$ reaches maximum and is used for the occurrence of the second pairing process. It is noted that the structure and the pairing of these vortices are responsible for the spreading, the momentum transfer, and the generation of turbulence in a mixing layer. After the second pairing process, the large scale vortex breaks down into small eddies; in addition, mixing of the flow is promoted. It is expected that the mean velocity decreases rapidly and the velocity fluctuation intensity increases.

For jet flow with acoustic excitation at the inherent frequency, the occurrence of the vortex formation and the first and the second pairing process move upstream, as shown in Fig. 3(*a*). It appears that the excitation energy at the first or the second subharmonic frequency can transfer into the vortex not only at this subharmonic frequency but also at the fundamental or other subharmonic frequencies, and cause the vortex formation and pairing processes to occur at an earlier stage. The increase of the excitation level increases the effect of upstream shifting, as shown in Figs. 3(*b*) and 3(*c*). At the same time, the transfer of excitation energy into the third vortex becomes so large that the vortex structure can not be maintained but broken down, as shown in Fig. 3(*b*). As the excitation level increases further, all the vortices twist, distort, and finally break down, as shown in Figs. 3(*c*) and 3(*d*). The above phenomenon also occurs for jet flow with acoustic excitation at the noninherent frequencies, as shown in Figs. 4(*a*), 4(*b*), 4(*c*), and 4(*d*).

The spectral energy evolution along the shear layer also indicates the upstream shift of the spectral energy or the most unstable waves in the jet excited with either inherent or noninherent frequencies (Sheu, 1993). For the inherent frequency, the excitation can amplify the most unstable wave and increase

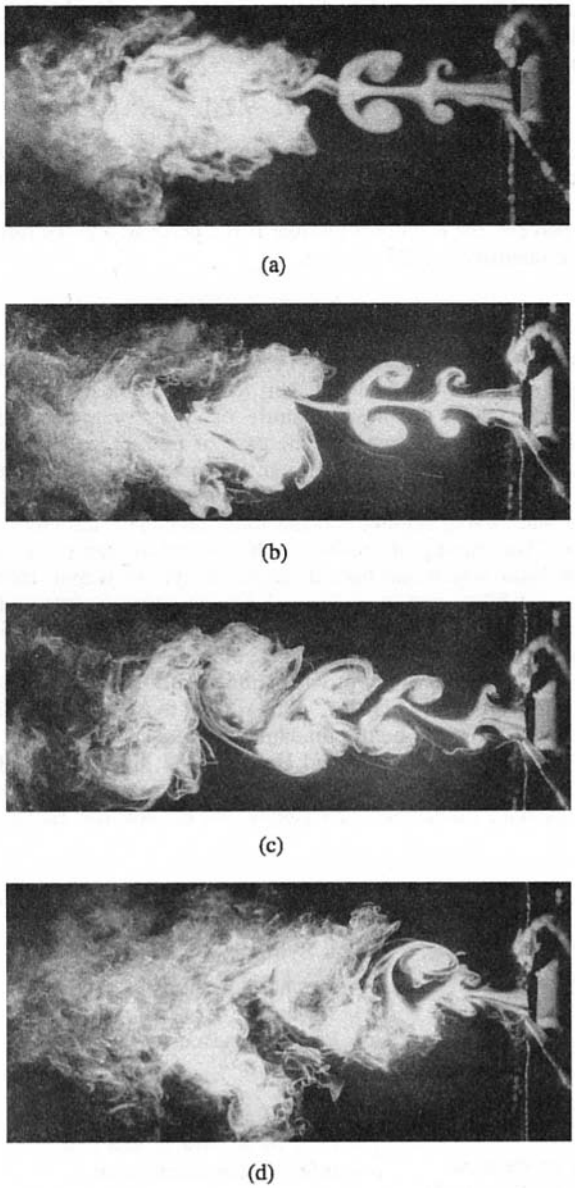

Fig. 3 Vortex flow structure of an excited jet at $F_i = \frac{1}{4}$ and (*a*) S_{pl} = 70 dB, (*b*) S_{pl} = 80 dB, (*c*) S_{pl} = 90 dB, and (*d*) S_{pl} = 94 dB for Re = 2750

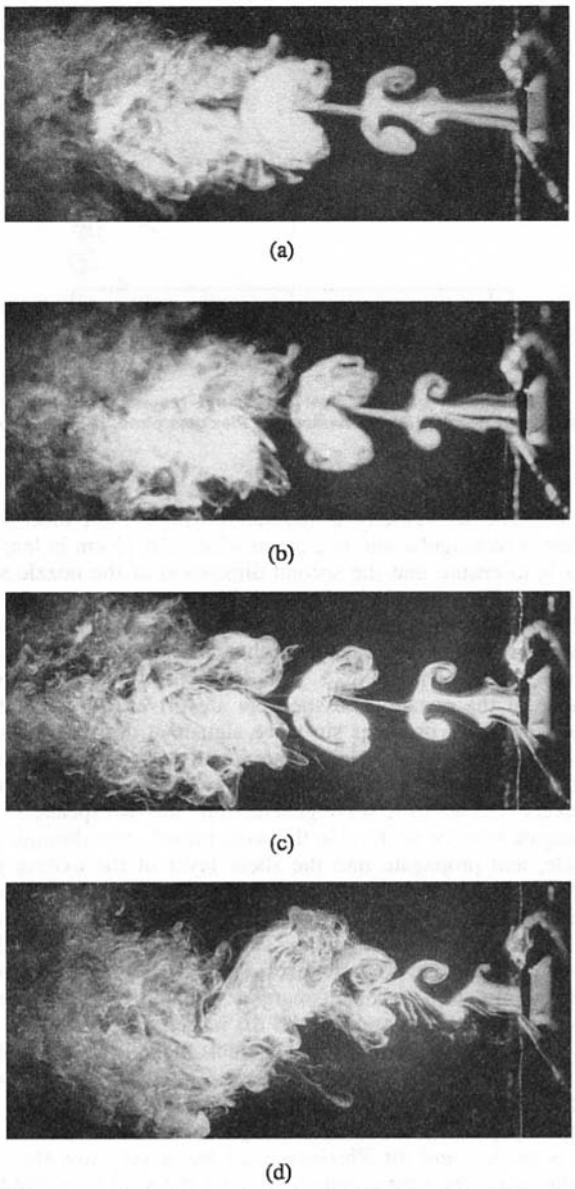

Fig. 4 Vortex flow structure of an excited jet at F_i = 0.71 and (*a*) S_{pl} = 70 dB, (*b*) S_{pl} = 80 dB, (*c*) S_{pl} = 90 dB, and (*d*) S_{pl} = 100 dB for Re = 2750

the spectral energy; however, for the noninherent frequencies the excitation can suppress the most amplified wave and decrease the spectral energy. For the inherent frequencies, the spectral energy increases with increasing excitation pressure level S_{pl}; for the noninherent frequencies, the spectral energy decreases with increasing S_{pl} when S_{pl} is small and increases when S_{pl} is large and the excitation frequency and its subharmonics become dominant in the processes of vortex formation and pairing.

In general, without acoustic excitation, the turbulence intensity in the core is constant until the formation of a vortex occurs. The formation and the pairing of vortices in the shear layer can cause a significant increase of turbulence intensity in both the shear layer and the core. Han (1991) has shown experimentally in a circular jet that the variation of turbulence intensity in the shear layer of the jet has the similar correspondence to the one in the core. Therefore, the turbulence intensity in the core along the jet flow direction can increase rapidly after the vortex formation. The turbulence intensity reaches maximum at approximately $Z/B = 8$ where transition of jet into turbulent flow occurs and decreases monotonically thereafter due to rapid mixing and diffusion of jet flow with ambient air. With acoustic excitation, the upstream shift of vortex formation and pairing process causes the upstream shift for the distribution of turbulence intensity along the jet flow direction. The effect of the upstream shift of turbulence intensity distribution increases with increasing excitation level. This can be inferred in Fig. 5 where the turbulence intensity at $Z/B = 2$ or 4 increases when the acoustic excitation is imposed or the pressure level is increased. Additional increase in the turbulence intensity is due to the amplification of the most amplified wave in the shear layer by the acoustic excitation. This can be inferred from the increase in the spectral energy as the acoustic pressure level increases (Sheu, 1993). However, the turbulence intensity near the nozzle exit before the vortex formation does not change by imposing the acoustic excitation or increasing its pressure level. At the downstream location, $Z/B = 4$, the turbulence intensity increases rapidly as the excitation pressure increases from $S_{pl} = 80$ dB to 90 dB. This is due to the occurrence of the vortex pairing process and the subsequent generation of a subharmonic wave at $F_o/8$, as shown in Figs. 3(*b*) and 3(*c*). As the acoustic level is higher than 90 dB, however, the turbulence intensity reduces significantly. This is due to the fact that large amount of excitation energy enters into the vortex and causes a partial breakdown of the vortex. At this stage, the broken vortex that is left becomes so weak that it causes a significant reduction of turbulence intensity. The reduction in the spectral energy is also noted (Sheu, 1993).

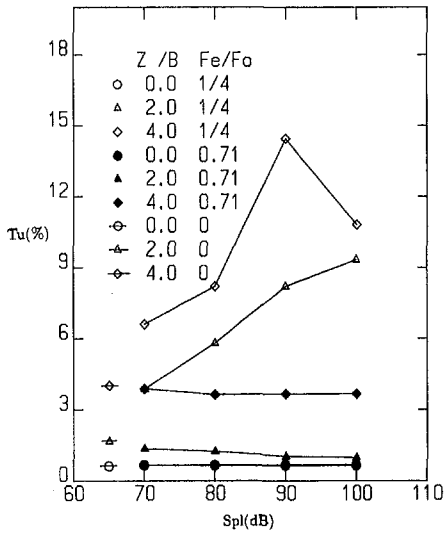

Fig. 5 Turbulence intensity along the center line of the core of an excited jet at $F_i = \frac{1}{4}$ or 0.71 and $S_{pl} = 70$ dB for Re = 11,000

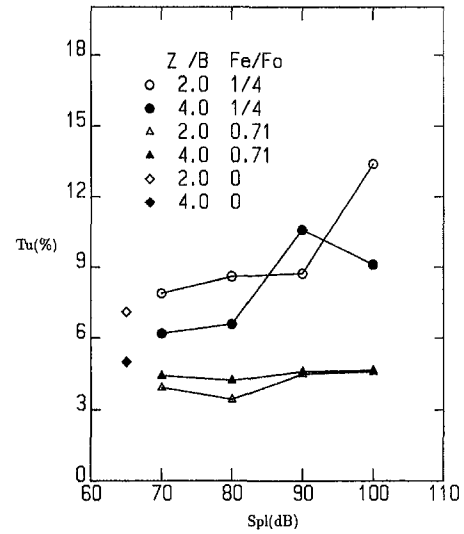

Fig. 6 Turbulence intensity at the edge of the wall jet boundary layer at $x/B = 4.0$ for an excited jet at $F_i = \frac{1}{4}$ or 0.71 and $S_{pl} = 70$ dB with Re = 11000

However, the acoustic excitation at noninherent frequency for $F_i = 0.71$ has only a slight effect on the turbulence intensity in the center line along the jet flow direction, as shown in Fig. 5, although the noninherent frequency can still cause a significant upstream shift for the vortex formation and pairing process. It appears that the upstream shift of the vortex formation and pairing process does not have a significant effect on the turbulence intensity. In fact, the turbulence intensity decreases slightly with increasing the excitation level when the level is low, and increases when the level is high. The reduction of turbulence intensity is attributed to the fact that the most amplified wave in the shear layer causing the vortex formation or pairing and resulting in generation of turbulence intensity is gradually suppressed by the excitation frequency, as the excitation level increases gradually. When the most amplified wave causing vortex formation or pairing becomes dominated by the excitation frequency and its subharmonics, the turbulence intensity in the jet increases with increasing the acoustic level. This phenomenon can be inferred from the spectral energy evolution figures (Sheu, 1993). They also occur for excitation at other noninherent frequencies. One can expect that the increase in the turbulence intensity in the jet enhances the heat transfer, or vise versa.

The heat transfer data along the wall varies significantly, especially in the transition region at approximately $x/B = 4$, as shown in the later figures with the excitation frequency and level. It is very interesting to see how the turbulence intensity at the boundary layer edge of the wall jet varies with the excitation frequency and level. Since it is difficult to define the boundary layer edge of the wall jet, we define it as being at the location having the maximum in velocity. Figure 6 indicates that the acoustic excitation at inherent frequency and the increase of its level can increase the turbulence intensity at the boundary layer edge of the wall jet, while the excitation at noninherent frequency and the increase of its level can reduce the turbulence intensity as the excitation level is low, and increase the turbulence intensity as the excitation level is high. The significant rise of turbulence intensity for S_{pl} from 80 to 90 dB at $Z/B = 4$ is due to the occurrence of vortex pairing outside the boundary layer along the wall jet. This can be inferred in the spectral energy evolution figures (Sheu, 1993) by the fact that the increase of excitation level from 80 to 90 dB causes a significant

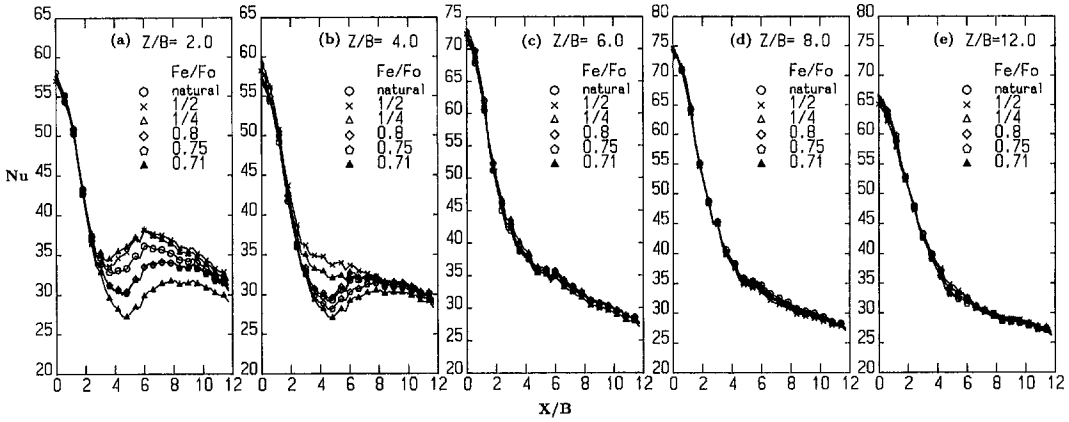

Fig. 7 The Nusselt number distribution at Re = 11,000 and (*a*) Z/B = 2.0, (*b*) Z/B = 4.0, (*c*) Z/B = 6.0, (*d*) Z/B = 8.0, and (*e*) Z/B = 12.0 for an excited jet at different frequencies and S_{pl} = 70 dB

increase of the spectral energy of the wall jet and the reduction of the most amplified frequency from F_e to $F_e/2$ at the edge of boundary layer at $x/B = 4$. The reduction of turbulence intensity for an excitation level greater than 90 dB is attributed to the partial breakdown of the vortex where the spectral energy of the vortex reduces significantly, as can be inferred in the spectral evolution figures (Sheu, 1993) and in the previous flow visualization results. Compare Fig. 5 and Fig. 6: it appears that the variation of turbulence intensity with excitation frequency and level at the boundary layer edge along the wall jet is very similar to the one at the center of the core. It has been shown in a circular jet (Han, 1992) that the variation of turbulence intensity in the shear layer of the jet has the similar correspondence to the one in the core. This is also true for a plane jet (Han, 1992). One can imagine that as the jet impinges on the wall, the shear layer of the jet will stay in the outside of the boundary layer of the wall jet and its flow structure and turbulence intensity will not be affected much by the wall jet. Therefore, one can expect that the turbulence intensity and the flow structure outside of the wall jet boundary layer is similar to the one in the shear layer of a free jet (horizontal) at the axial location where the heated plate (vertical) is to be inserted.

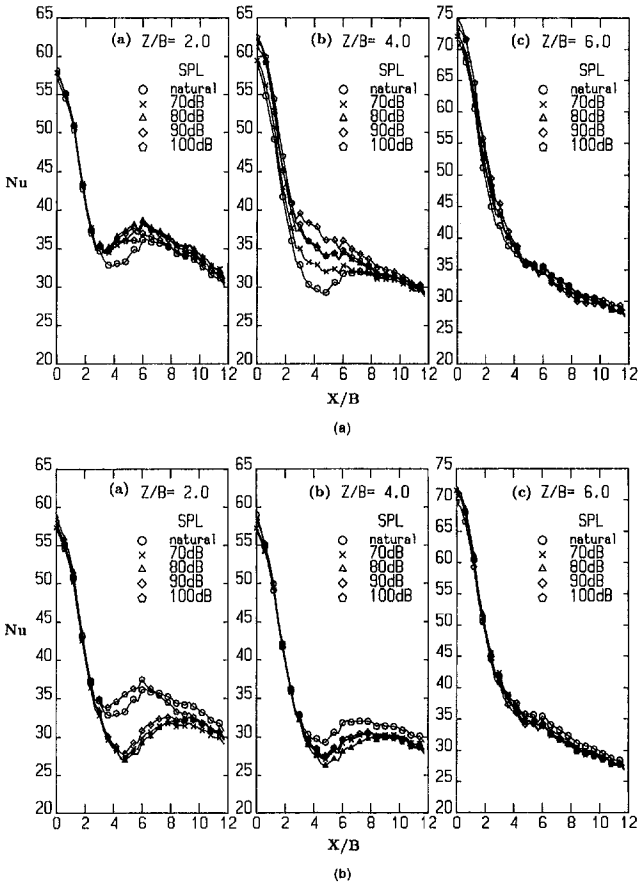

Fig. 8 The Nusselt number distribution at Re = 11,000 for an excited jet at different acoustic pressure levels and (*a*) $F_i = \frac{1}{4}$ and (*b*) F_i = 0.71

In a round jet impingement, Fox et al. (1993) made fluid visualization experiments at a very low Reynolds number (Re = 400) and found the secondary vortices induced along the wall. In a different experiment of high speed (compressible impinging jet), a significant reduction and an immediate rise in the adiabatic wall temperature was also found near the stagnation region. Therefore, Fox et al. conclude that the significant reduction and rise in the adiabatic wall temperature is due to the occurrance of the secondary vortices along the wall. However, the experimental conditions in the current experiments are different from the ones described in Fox et al. (Re = 400). One is not sure if the secondary vortices do occur as described by Fox et al. However, the variation of the turbulence intensity in the core (which is due to the occurrance of primary vortices) has a similar correspondence to the one at the region (x/B = 4) where secondary vortices are expected to occur. Even where the secondary vortices do occur, it appears that the effect of the secondary vortices on the turbulence intensity at $x/B = 4$ is similar to the effect of the primary vortices. Therefore, one can say that the enhancement or suppression of heat transfer is primarily due to the primary vortices.

3.2 Heat Transfer. From the above discussion of the flow structure it appears that the acoustic excitation affects the flow structure and the turbulence intensity only in the regions where the flow is not stable (i.e., in the shear layer of the jet where the vortex formation and pairing process occurs or in the transition region of the wall jet). However, when the turbulence intensity in the shear layer varies, this variation will propagate into the core. Therefore, one may expect that the effect of acoustic excitation on the heat transfer becomes significant only when the heated wall is placed at $Z/B < 8$ (i.e., the jet has not reached fully turbulent flow before impinging on the wall) or when the transition from laminar to turbulent flow occurs in the wall jet boundary layer. From the present experiments of jet impingement cooling with acoustic excitation, the effect of the acoustic excitation on the heat transfer becomes significant only in the region where transition from laminar to turbulent wall jet boundary layer occurs when the heated wall is at Z/B = 2 or 4. For $Z/B > 4$, the effect of acoustic excitation on the heat transfer

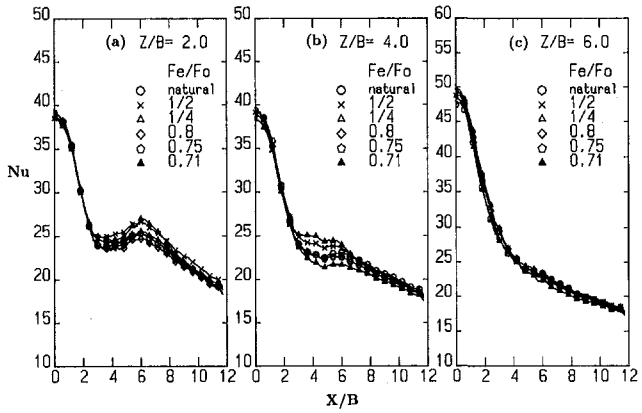

Fig. 9 The Nusselt number distribution at Re = 5500 and (*a*) Z/B = 2.0, (*b*) Z/B = 4.0, and (*c*) Z/B = 6.0 for an excited jet at different frequencies and S_{pl} = 70 dB

occurs only at the stagnation point. For $Z/B > 8$ (i.e. when the fully developed turbulent flow impinges on the wall), the acoustic excitation has no effect on the heat transfer.

The impingement cooling heat transfer data without acoustic excitation have been measured and compared with others (Gardon and Akeirat, 1966; Becko, 1976). The agreement with the data published in the literature is very good (Sheu, 1993). With excitation for Re = 11,000, the excitation of the inherent frequencies ($F_i = \frac{1}{2}, \frac{1}{4}$) can significantly enhance the heat transfer, as shown in Fig. 7, while the excitation of the noninherent frequencies (F_i = 0.71, 0.75, 0.8) can significantly reduce the heat transfer. This is due to the increase of the turbulence intensity of the wall jet by the excitation of inherent frequencies and the decrease of the turbulence intensity by the excitation of noninherent frequencies. For $Z/B > 6.0$, the acoustic excitation has only a slight effect on the stagnation point heat transfer. The effect of increasing the excitation pressure level on the heat transfer at the inherent frequency is shown in Fig. 8(a). For Z/B = 2, the wall heat transfer increases with increasing S_{pl} until S_{pl} = 80 dB, where the enhancement of the heat transfer reaches maximum. Further increase in the S_{pl} results in slightly reducing the heat transfer. However, the turbulence intensity measured at Z/B = 2 and x/B = 4 increases slightly, as shown in Fig. 6, when S_{pl} increases from 80 dB to 90 dB. The reason for this inconsistent result is not very clear at the present stage. For Z/B = 4, as shown in Fig. 8(b), higher turbulence intensity at the boundary layer edge leads to higher heat transfer. The maximum heat transfer occurs at S_{pl} = 90 dB, where the maximum turbulence intensity occurs as well. The reduction in the heat transfer for $S_{pl} > 90$ dB is attributed to the partial breakdown of the vortex that both the spectral energy of the vortex and turbulence intensity in the core or at the boundary layer edge of the wall jet reduce significantly.

For the acoustic excitation at noninherent frequency at Z/B = 2 as shown in Fig. 8(b), the decrease in the turbulence intensity at the boundary layer edge of the wall jet with increasing S_{pl} leads to the decrease in the heat transfer until S_{pl} = 80 dB, where both the turbulence intensity and the heat transfer reach minimum. The decrease in the turbulence intensity is attributed to the suppression effect of the acoustic excitation whose frequencies are completely different from the fundamental and subharmonic frequencies of the jet. When the acoustic excitation frequency becomes dominant it will cause the increase in the turbulence intensity. The heat transfer, at the present stage, increases with increasing S_{pl}. This is also true for Z/B = 4.

For Re = 5500, the effect of the acoustic excitation on the heat transfer is not so significant as those at Re = 11,000, as shown in Fig. 9; however, the enhancement of the heat transfer for acoustic excitation at inherent frequencies and the suppression and reduction of the heat transfer at noninherent frequencies can also be noted. The wall heat transfer increases with increasing the acoustic pressure level at inherent frequencies, as shown in Fig. 10(a), while it decreases with increasing S_{pl} at noninherent frequencies, as shown in Fig. 10(b). For excitation at inherent frequency, the maximum in the heat transfer occurs when S_{pl} is close to 80 dB. This suggests the occurrence of maximum turbulence intensity at the boundary layer edge of the wall jet when S_{pl} is close to 80 dB. Further increase in the excitation pressure level leads to partial breakdown of vortex and the reduction of the turbulence intensity. For excitation at noninherent frequency, the minimum in the heat transfer occurs when S_{pl} = 90 dB for Z/B = 2, or when S_{pl} = 70 dB for Z/B = 4. This suggests the occurrence of minimum turbulence intensity due to the suppression effect of the excitation. It appears that in most of the cases at low Reynolds number the excitation levels needed for the wall heat transfer or the turbulence intensity at the boundary layer edge to reach the maximum or minimum are less than the cases at high Reynolds number. The variation of the heat transfer due to the acoustic excitation at low Reynolds number is not so large as at high Reynolds number.

At high Reynolds number it appears that the acoustic excitation at both inherent or noninherent frequencies has negligible effect on the heat transfer, as shown in Fig. 11. However, as one increases the acoustic pressure level, significant enhancement in the heat transfer is found, as shown in Fig. 12(a). However, the acoustic pressure level becomes effective only when S_{pl} is greater than 80 dB. For Z/B = 2, the acoustic pressure level at 100 dB can reduce the heat transfer and make it equal to the case when the jet is not under acoustic excitation. At noninherent frequencies significant reduction in the heat transfer is also found, as shown in Fig. 12(b). The wall heat transfer reduces

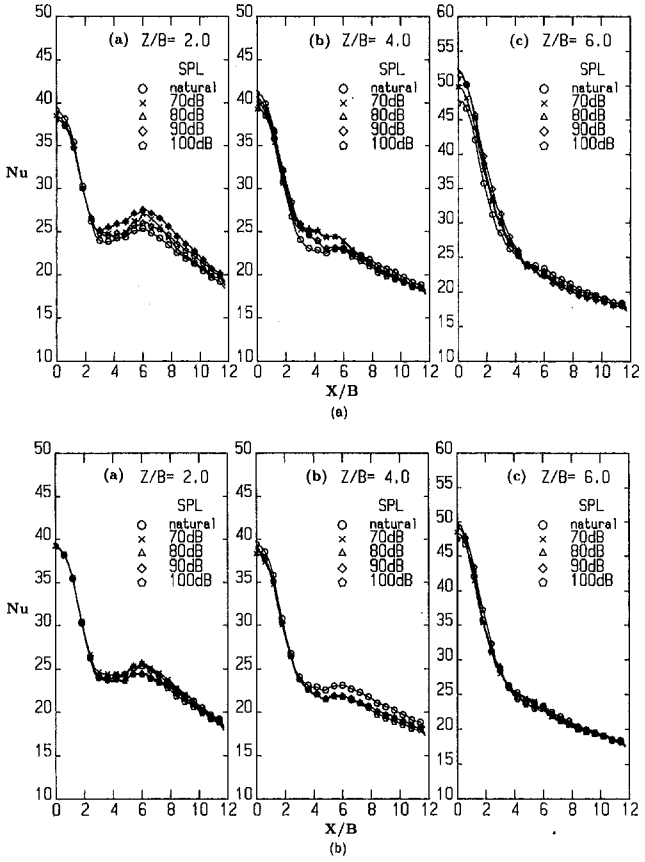

Fig. 10 The Nusselt number distribution at Re = 5500 for an excited jet at different acoustic pressure levels and (*a*) $F_i = \frac{1}{4}$ and (*b*) F_i = 0.71

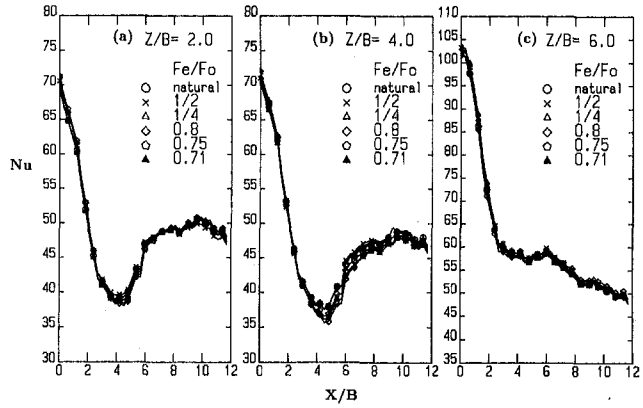

Fig. 11 The Nusselt number distribution at Re = 22,000 and (*a*) Z/B = 2.0, (*b*) Z/B = 4.0, and (c) Z/B = 6.0 for an excited jet at different frequencies and S_{pl} = 70 dB

monotonically with increasing S_{pl}. It appears that at high Reynolds number a greater excitation level is needed to reach the maximum or the minimum in the heat transfer. The variation in the heat transfer due to excitation at high Reynolds number is greater.

The acoustic excitation does have a significant effect on the heat transfer at the stagnation point, as shown in Figs. 13(a) and 13(b). However, the excitation at the inherent frequencies may reduce the heat transfer, while the one at noninherent frequencies may enhance the heat transfer. It appears that turbulence intensity measured in the core, as shown in Fig. 5, could not be used to explain the enhancement or the reduction in the heat transfer. Note that the stagnation point flow is also an

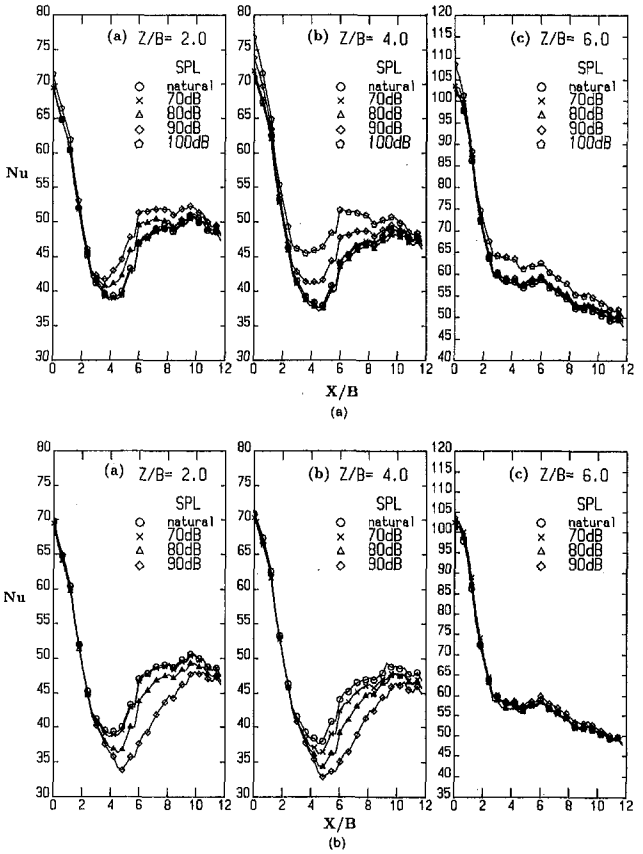

Fig. 12 The Nusselt number distribution at Re = 22,000 for an excited jet at different acoustic pressure levels and (*a*) $F_i = \frac{1}{4}$ and (*b*) F_i = 0.71

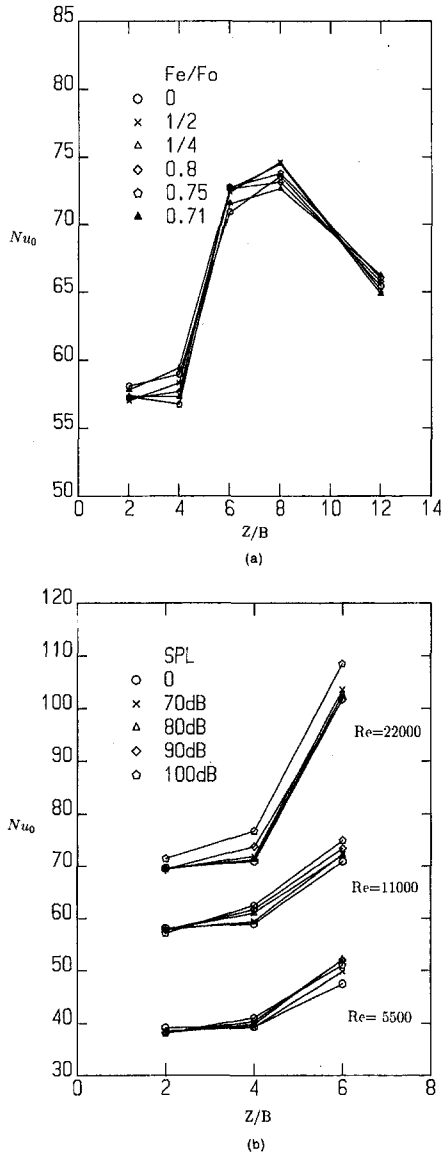

Fig. 13 The stagnation point Nusselt number at (*a*) Re = 11,000 for an excited jet at different frequencies and S_{pl} = 70 dB and (*b*) Re = 5500, 11000, 22000, and $F_i = \frac{1}{4}$ at different excitation levels

unstable flow. Although it may be significantly affected by the turbulence intensity in the core, one can expect that the acoustic excitation may have an additional effect on the flow structure at the stagnation point, as those effects in the shear layer region, and thus affect the heat transfer. From all the results of the stagnation point heat transfer, one found that the effect of acoustic excitation on the heat transfer varies significantly with the Reynolds number, the nozzle-to-plate spacing Z/B, the frequencies, and the pressure level of the excitation. However, due to the complicated flow process under the acoustic excitation it is difficult to understand physically how the stagnation point heat transfer is affected by these parameters. Further detailed measurements on the effect of the acoustic excitation on the stagnation point flow are needed.

Conclusions

The impingement cooling flow structure and wall heat transfer under the acoustic excitation at both inherent and noninherent frequencies is studied experimentally. Both the flow visualization and the spectral energy evolution measure-

ments indicate that the acoustic excitation at either inherent or noninherent frequencies can make the upsteam shift for most instability waves and the resulting vortex formation and its subsequent pairing processes. In addition, the excitation at inherent frequencies can amplify the most amplified waves in the shear layer and increase the turbulence intensity in both the shear layer and the core. This action can significantly enhance the heat transfer. Contrariwise, the excitation at noninherent frequencies can suppress the most amplified waves in the shear layer and reduce the turbulence intensity in both the shear layer and the core. This action can significantly reduce the heat transfer. At inherent frequencies the heat transfer increases with increasing S_{pl} until partial breakdown of the vortex occurs, while at the noninherent frequencies it decreases with increasing S_{pl} when S_{pl} is not small, but increases when S_{pl} is large. At high Reynolds number a greater excitation pressure level is needed to reach the maximum or the minimum in the heat transfer. In addition, the enhancement or reduction in the heat transfer becomes greater.

Since stagnation point heat transfer is significantly affected by the acoustic excitation, one expects that the stagnation point flow structure which is unstable can also be significantly affected. However, the effect of the excitation at inherent or noninherent frequencies on the stagnation point flow and heat transfer is still not understood. Detailed visualization of the flow structure and turbulence intensity measurements are needed.

Acknowledgment

This research was sponsored by the National Science Council of Taiwan under contract No. NSC 82-0401-E006-433.

References

Baughn, J. W., and Shimizu, S., 1989, "Heat Transfer Measurements from a Surface With Uniform Heat Flux and an Impinging Jet," ASME JOURNAL OF HEAT TRANSFER, Vol. 111, pp. 1097–1100.

Becko, Y., 1976, "Impingement Cooling—A Review," Lecture Series 83, Von Karman Institute for Fluid Dynamics.

Crighton, D. G., 1981, "Acoustics as Branch of Fluid Mechanics," *Journal of Fluid Mechanics,* Vol. 106, pp. 261–298.

Fox, M. D., Kurosaka, M., Hedges, L., and Hirano, K., 1993, "The Influences of Vortical Structures on the Thermal Fields of Jets," *Journal of Fluid Mechanics,* Vol. 255, pp. 447–472.

Gardon, R., and Akeirat, J. C., 1966, "Heat Transfer Characteristics of Impinging Two-Dimensional Air Jet," ASME JOURNAL OF HEAT TRANSFER, Vol. 88, pp. 101–108.

Goldstein, R. J., and Timmers, J. F., 1982, "Visualization of Heat Transfer from Arrays of Impinging Jets," *International Journal of Heat and Mass Transfer,* Vol. 25, pp. 1857–1868.

Han, J. M., 1991, "Manipulation of a Circular Jet by Acoustic Excitation," Ph.D. thesis, National Cheng Kung University, Tainan, Taiwan.

Ho, C. M., and Huerre, P., 1984, "Perturbed Free Shear Layers," *Annual Review of Fluid Mechanics,* Vol. 16, pp. 365–424.

Ho, C. M., and Huang, L. S., 1982, "Subharmonics and Vortex Merging in Mixing Layers," *Journal of Fluid Mechanics,* Vol. 119, pp. 443–473.

Hrycak, P., 1983, "Heat Transfer from Round Impinging Jets to a Flat Plate," *International Journal of Heat and Mass Transfer,* Vol. 26, pp. 1857–1865.

Kline, S. J., and McClintock, F. A., 1953, "Describing Uncertainties in Single-Sample Experiments," *Mechanical Engineering,* Vol. 73, pp. 3–8.

Mankbadi, R. R., 1985, "The Mechanism of Mixing Enhancement and Suppression in a Circular Jet under Excitation Condition," *Physics of Fluids,* Vol. 28, pp. 2062–2074.

Martin, H., 1977, "Heat and Mass Transfer Between Impinging Gas Jets and Solid Surfaces," *Advances in Heat Transfer,* J. Hartnett and T. Irvine, Jr., eds., Vol. 13, pp. 1–60.

Michalke, A., 1965, "On Spatially Growing Disturbances in an Inviscid Shear Layer," *Journal of Fluid Mechanics,* Vol. 23, Part 3, pp. 521–544.

Sheu, W. Y., 1993, "Frequency and Sound Level of Acoustic Excitation on Impingement Cooling Heat Transfer," M.S. thesis, National Cheng Kung University, Tainan, Taiwan, ROC.

Zaman, K. B. M. Q., and Hussain, A. K. M. F., 1980, "Vortex Pairing in a Circular Jet Under Controlled Excitation, Part 1: General Jet Response," *Journal of Fluid Mechanics,* Vol. 101, pp. 449–491.

M. Orme
Associate Professor.
melissao@eng.uci.edu

C. Huang
Graduate Student Researcher.

Department of Mechanical and Aerospace Engineering,
University of California, Irvine,
Irvine, CA 92717-3975

Phase Change Manipulation for Droplet-Based Solid Freeform Fabrication

Introduction

Solid Freeform Fabrication (SFF) is an emerging technology in which a useful metallic component is manufactured from the raw material without a mold in one integrated operation. A new technology under development at UCI, termed droplet-based SFF, requires less machining steps than conventional manufacturing techniques, and hence it has the potential to provide improved manufacturing quality and significant economic benefit (Orme and Muntz, 1992). In droplet-based SFF a useful structural component is fabricated by sequentially depositing molten droplets layer by layer. The usefulness of the droplet-based SFF technique is determined by the structural characteristics of the material component synthesized. Manipulation of the phase-change characteristics of the sequentially deposited droplets during the SFF process offers the potential means to control and improve the microstructure and hence the structural integrity of the part. To this purpose, conditions which cause the newly arriving droplet to locally remelt the previously deposited and solidified droplet structure are sought. Under these conditions, the solid/liquid interface changes direction after solidification and on the onset of remelting, and subsequently again on the onset of resolidification. Therefore, its motion cannot be assumed to vary with time t as t^m, as is commonly assumed (e.g., Stefan solution).

Figure 1 is a conceptual schematic of the droplet-based SFF technique under development at UCI. In operation, molten droplets on the order of 100 μm in diameter are formed from capillary stream break-up and are injected into either a vacuum or an inert environment. As the droplets are formed, they acquire a charge by passing through a charged electrode (not shown in the figure) at the time of droplet break-off from the stream. The intrinsic angular stability of the droplet stream allows the droplets to travel a vertical distance of 0.3 m prior to deposition. This is practically important since a longer flight allows for a larger lateral deposition area to be covered by electrostatic deflection. Details about the charging techniques are given elsewhere (Orme et al., 1996). Lateral motion of the x–y table from CAD information coupled with electrostatic deflection allows subsequent droplet deliveries to build the three-dimensional part microlayer by microlayer without any mold. Since the droplets rapidly solidify, complex structures can be fabricated in the absence of macroscopic fluid flow.

Droplet-based SFF bears similarities with the technology under development by Prinz et al. (1995), Amon et al. (1996), and Chin et al. (1995) termed Shape Deposition Manufacturing (SDM). In SDM a feedstock wire located directly over the substrate is melted using a plasma welding torch. A discrete droplet of typical dimensions, 1–10 mm (depending on plasma conditions), falls off the wire and onto the substrate, thereby building the material component.

Another materials synthesis technology which utilizes molten droplets as the deposition element is spray forming. There, a spray of molten metal is formed by atomizing a fluid column of molten metal. Thus, the droplet diameters and speeds vary and the precision of fabrication is limited by the angular extent of the spray cone angle. The spray is then deposited onto a substrate building a near-net shaped part. Recent developments in spray forming are described in the review article by Lavernia et al. (1992).

The droplet-based SFF technique is set apart from other methods of droplet deposition net-form, or near net-form, manufacturing in that the droplet streams can be precisely controlled and manipulated. Precise control refers to droplet streams which have an angular stability on the order of 1 micro-radian (Orme, 1994), and speed dispersions as low as 3×10^{-7} times the average stream speed (Orme, 1991). The high degree of control over the droplet dynamics allows the possibility of precise control over the droplet solidification/melting characteristics.

Although the droplet generation and deposition processes are different in the aforementioned techniques, the numerical method and results presented in this paper are applicable. The objective of this paper is to outline a computationally simple one-dimensional simulation model that can be used to study phase-change manipulation strategies for the droplet-based solid freeform fabrication of structural parts. Locally remelting the previously deposited and solidified droplet material provides a flexible approach to removing boundaries between successive splats without sacrificing the benefits of rapid solidification. The model utilizes a coordinate transformation to convert the moving boundary into a fixed one, thus simplifying immensely the numerical simulations. This model is far more computationally efficient than competing phase-change models and can be used for simulation studies of large-scale problems (requiring numerous repetitions of the same elemental event, i.e., droplet deposition and remelting) for this and other applications with moving boundaries.

Related Research

There is a vast body of literature which investigates the problem of one-dimensional phase change by heat conduction where the phase change is assumed to occur at the melting temperature and the molten phase is not in motion (e.g., Carslaw and Jaeger, 1962; Goodrich, 1978; Frederick and Greif, 1985; Amon et al., 1996). In most of the investigations only pure melting or pure solidification is possible, but not sequential remelting and solidification. In general, the sequential melting and solidification problem is difficult because of the moving boundary which is not known a priori. Many authors have assumed that the interface moves with time t as t^m (where m is usually taken to be

Contributed by the Heat Transfer Division for publication in the JOURNAL OF HEAT TRANSFER. Manuscript received by the Heat Transfer Division April 22, 1996; revision received June 13, 1997; Keywords: Conduction; Materials Processing and Manufacturing Process; Moving Boundaries. Associate Technical Editor: A. S. Lavine.

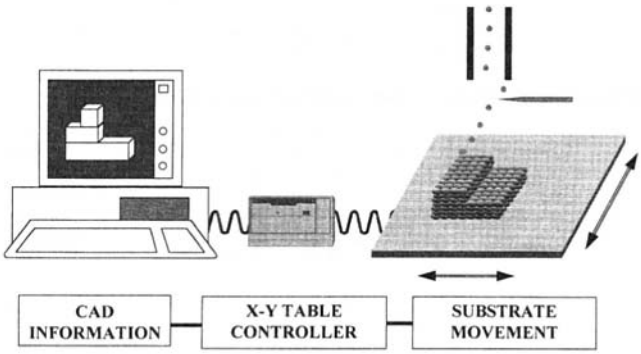

Fig. 1 Conceptual schematic of the droplet-based SFF technique

0.5). In solidification followed by remelting, the solid/liquid interface cannot be described by a simple function of time since the interface motion oscillates in a direction away from the substrate and towards the substrate. The current work is different from existing studies in that the moving boundary problem has been transformed to a fixed boundary problem where the moving interface is found as part of the solution. This eliminates the need to postulate the time-course of the moving boundary that is required by other methods in order to numerically solve the discretized governing partial differential equations. Under the proposed transformation of coordinates, the interface condition becomes a transcendental algebraic equation which provides a unique solution for the interface location as a function of time.

Other recent work has concentrated on two-dimensional equilibrium conduction in a droplet which is undergoing deformation (Madejski, 1976; Trapaga et al., 1992; Liu et al., 1993, 1995; San Marchi et al., 1993; Delplanque et al., 1996; Zhao et al., 1996; Waldvogel and Poulikakos, 1997). In several of these works (Madjeski, 1976; Liu et al., 1993, 1995; San Marchi et al., 1993; Delplanque et al., 1996), the solid/liquid interface is determined by solving the Stefan problem of solidification, and hence its location varies with the square root of time, i.e., the solid/liquid interface always moves away from the substrate for solidification or towards the substrate for melting. In the work of Trapaga et al. (1992), the enthalpy method was used to simulate the phase-change problem of the deforming splat in an effort to predict the deformation process of the impinging and solidifying splat. The model was also used to predict the temperature profile in the "heat affected zone" of the substrate, but not the time-course of the solid/liquid interface. This model can be used to estimate the remelting characteristics of the previously deposited material (substrate), though it is very computationally intensive, i.e., simulation of 5×10^{-3} seconds of real time requires more than 100 hours on a 3100 VAXSTATION due to the complexity of the model. Zhao et al. (1996) theoretically investigated presolidification splat cooling and spreading using the Lagrangian formulation and hence phase change is not considered in their work. The numerical and experimental work of Waldvogel and Poulikakos (1997) present the most complete model of droplet deformation and phase change to date, in which the heat affected zone of the substrate can be studied. They used the Lagrangian formulation to simulate the motion of the deforming free surface and focused on the determination of single solidified splat shapes as a function of impacting droplet conditions. However, this model is also computationally intensive—they report that an example simulation of one drop deformation requires 54 CPU hours on a HP 9000 Series 735 workstation.

The model proposed in this paper provides a quick estimate of the one-dimensional sequential remelting and solidification characteristics of sequentially deposited droplets by use of a transformed interface equation. Comparison of this model with a two-dimensional model such as that provided by Waldvogel and Poulikakos (1997) is inappropriate since the objectives of the two models are notably different. The model given in this work is intended to be applied to the droplet-based SFF application in which a multitude of droplets is deposited sequentially to fabricate the component. For instance, a SFF component with a height of 1 cm requires approximately 1000 droplets to be deposited on the vertical axis. The computational simplicity of this model enables simulation of remelting through 1000 sequentially deposited droplets in approximately 8 minutes on a DEC workstation. As the component grows layer by layer, the droplet temperatures can be adjusted to insure that local remelting occurs. Thus, the study of the manufacturing process of a component is distinct from the study of a single splat. Furthermore, and perhaps more importantly, the model provided in this paper can be applied to other one-dimensional moving boundary problems of finite domain with a sharp moving boundary.

Model Development

Values used in the simulations of the injecting environment, substrate, and droplet are given in the table below where the subscript ∞ refers to the ambient inert environment, m refers to the melting point of aluminum, l and s refer to the liquid and solid state of the aluminum, and *sub* refers to the lower face of the substrate. In the table, T is the temperature, L is the latent heat of fusion, C_p is the specific heat capacity, k is the thermal conductivity, and ρ is the density.

Because the rapid solidification time of the droplets is of the order of a microsecond, in most practical circumstances the molten droplets will impinge on a layer of previously delivered droplets which has solidified. Thus, we explore the possibility of remelting the solidified droplets with the thermal energy from the arriving droplets in an effort to drive the two materials to unite, thereby removing the boundaries between the different layers of droplet depositions.

Since it is the objective of this work to cause remelting, droplets will necessarily be deposited at high superheats, making the assumption that they spread to flat disks not entirely unrealistic for the conditions sought in the application of droplet-based SFF. In this case, the physical dimension of the splat in the direction normal to the substrate (height) is small compared to the lateral dimension (width) and the remelting depth is small compared to the splat height, hence the problem is approximated as a one-dimensional phase-change situation as

Nomenclature

1 = subscript used to denote conditions through the substrate
2 = subscript used to denote the droplet material in the solid state
3 = subscript used to denote the droplet material in the liquid state
a = splat thickness
C_p = specific heat capacity
k = thermal conductivity
L = latent heat of fusion
Da = substrate thickness
M = number of droplet layers
$s(t)$ = solid/liquid interface location
sub = subscript used to denote properties of substrate at lower face
T_i = initial droplet impact temperature
T_m = melting temperature of metal
T_∞ = ambient temperature
t = time
α = thermal diffusivity equal to $k/\rho C_p$
ρ = density of metal

Table 1 Material properties used in thermal analysis

T_∞	300 K	k_1	103W/mK
T_m	933 K	k_s	249 W/mK
L	402 J/kg	k_{sub}	386 W/mK
C_{p1}	1084 J/kg K	ρ_1	2380 kg/m^3
C_{ps}	895 J/g K	ρ_s	2707 kg/m^3
C_{psub}	383 J/g K	ρ_{sub}	8955 kg/m^3

sketched in Figure 2(a). While it is recognized that the heat transfer could occur two-dimensionally in many circumstances, Amon et al. (1996) showed experimentally that superheated carbon steel droplets experience predominantly unidirectional conduction heat transfer from the droplet/substrate interface. Furthermore, by comparing one-dimensional numerical simulations with multidimensional simulations, it was shown that during the time required to accomplish remelting action the one-dimensional model simulations are in excellent agreement with the multidimensional model simulations. Since the objective of this work is to investigate the conditions required for remelting, a one-dimensional model is therefore suitable. For investigations which are focused on the detailed evolution of the droplet deformation and phase change on longer time scales, a multidimensional model such as that given by Waldvogel and Poulikakos (1997) is more appropriate.

In this model, molten aluminum splats of thickness a are deposited onto a copper substrate which is D times the thickness of the splat. M subsequent layers of droplets are deposited onto the previously deposited material (refer to Fig. 2). For convenience, in the model we use the subscript "1" to represent the conditions through the copper substrate, subscript "2" to represent the aluminum in the solid state, subscript "3" to represent the aluminum in the liquid state, and subscript "sub" to represent the conditions at the lower boundary of the substrate ($x = -Da$). At time $t = 0$, a droplet makes contact with a substrate whose surface at $x = -Da$ is maintained at temperature T_{sub} at all times which is not an unreasonable assumption for the case when the dimensions of the substrate are large compared to those of the component. The molten liquid of the splat causes the previously solidified material to remelt and then begins to resolidify. The liquid/solid interface defined by $s(t)$ travels through the deposited material until it reaches the upper surface of the splat. We assume that the phase transition takes place at the unique temperature T_m and that the two phases are separated by a sharp interface.

The equations and boundary conditions governing this process can be written in dimensionless form as (Carslaw and Jaeger, 1962)

$$\frac{\partial T_1^*}{\partial t^*} = \alpha_1^* \frac{\partial^2 T_1^*}{\partial x^{*2}} \quad \text{in} \quad -D < x^* < 0 \tag{1}$$

$$\frac{\partial T_2^*}{\partial t^*} = \alpha_2^* \frac{\partial^2 T_2^*}{\partial x^{*2}} \quad \text{in} \quad 0 < x^* < s^*(t^*) \tag{2}$$

$$\frac{\partial T_3^*}{\partial t^*} = \alpha_3^* \frac{\partial^2 T_3^*}{\partial x^{*2}} \quad \text{in} \quad s^*(t^*) < x^* < M + 1 \tag{3}$$

$$k_1^* \frac{\partial T_1^*}{\partial x^*} - k_2^* \frac{\partial T_2^*}{\partial x^*} = 0 \quad \text{at} \quad x^* = 0 \tag{4}$$

$$k_2^* \frac{\partial T_2^*}{\partial x^*} - k_3^* \frac{\partial T_3^*}{\partial x^*} = L^* \frac{ds^*}{dt^*} \quad \text{at} \quad x^* = s^*(t^*) \tag{5}$$

$$T_1^* = -1 \quad \text{at} \quad x^* = -D \tag{6}$$

$$T_2^* = T_3^* = 0 \quad \text{at} \quad x^* = s^*(t^*) \tag{7}$$

$$\frac{\partial T_3^*}{\partial x^*} = 0 \quad \text{at} \quad x^* = M + 1. \tag{8}$$

Where the nondimensional quantities are defined by

$$T^* = \frac{T - T_m}{T_m - T_{sub}} \tag{9}$$

$$L^* = \frac{L}{C_{p2}(T_m - T_{sub})} \tag{10}$$

$$x^* = \frac{x}{a} \tag{11}$$

$$\alpha_1^* = \frac{\alpha_1}{\alpha_2}, \quad \alpha_2^* = 1, \quad \alpha_3^* = \frac{\alpha_3}{\alpha_2} \tag{12}$$

$$k_1^* = \frac{k_1}{k_2}, \quad k_2^* = 1, \quad k_3^* = \frac{k_3}{k_2} \tag{13}$$

$$t^* = \frac{a^2}{\alpha_2}. \tag{14}$$

The time-varying interface condition (Eq. 5) has limited the analytical solution to the specific case of a semi-infinite slab with constant boundary conditions. No analytic solutions exist for a finite slab. In this work we seek to develop an appropriate simulation methodology to investigate sequential solidification and remelting in a finite slab. Since a strategy for sequential solidification and remelting is desired for successive droplet depositions, the solid/liquid interface cannot be presumed to vary as $\propto\sqrt{t}$, but rather its motion is sought as part of the solution. The adiabatic boundary condition is an oversimplification which may be relaxed in future studies.

Solidification. The solidification portion of the problem is straightforward, and the central difference scheme is used to discretize Eqs. (1–5) (Croft and Lilley, 1977).

Remelting. When a droplet is delivered to the previously solidified material, the solid/liquid interface will regress due to the phase-change transition from solidification to remelting. The transition is defined by a turning point of the solid/liquid interface as it travels back towards the substrate during remelting. The remelted material will subsequently resolidify, as will the molten material of the droplet which caused the remelting action. This phase change transition is also marked by a turning

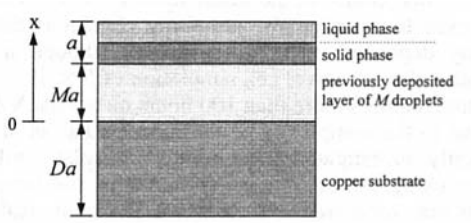

Fig. 2(a) Nomenclature for one-dimensional solidification and remelting problem

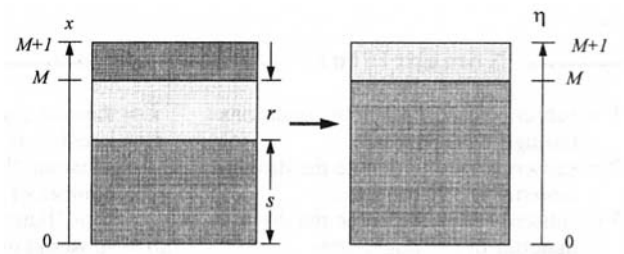

Fig. 2(b) Nomenclature for transformation from a moving boundary to a fixed boundary

point of the solid/liquid interface as it travels upward away from the substrate. The solid/liquid interface is difficult to track with the fixed grid approach since it may not necessarily fall on a grid point. To overcome this difficulty, we have transformed the moving boundary problem into a fixed boundary problem. Figure 2(*b*) illustrates the following problem transformation which is presented in this work:

$$\eta = \frac{M - s}{s[s - (M + 1)]} x^2 + \frac{s^2 - M(M + 1)}{s[s - (M + 1)]} x. \quad (15)$$

In Eq. (15) and for the remainder of this paper we have dropped the asterisk which denotes dimensionless quantities for convenience. Under this transformation, which maps the dynamically moving values in the x plane $(0, s, M + 1)$ to the fixed values in the η plane $(0, M, M + 1)$, the governing equations for the liquid and solid state become

$$\frac{\partial T_2}{\partial t} = (4A\eta + B^2)\alpha \frac{\partial^2 T_2}{\partial \eta^2} + 2A\alpha \frac{\partial T_2}{\partial \eta} \quad \text{in} \quad 0 < \eta < M \quad (16)$$

$$\frac{\partial T_3}{\partial t} = (4A\eta + B^2)\alpha \frac{\partial^2 T_3}{\partial \eta^2} + 2A\alpha \frac{\partial T_3}{\partial \eta} \quad \text{in} \quad M < \eta < M + 1 \quad (17)$$

with the following boundary conditions at $\eta = M$:

$$T_2 = T_3 = 0 \quad (18)$$

$$k_2 \frac{\partial T_2}{\partial \eta} - k_3 \frac{\partial T_3}{\partial \eta} = \frac{L}{(2As + B)} \frac{ds}{dt}. \quad (19)$$

A and B are defined in terms of the relative displacement of the interface, $r = s - M$.

$$A = \frac{-r}{(r + M)(r - 1)}, \quad B = \frac{r^2 + 2Mr - M}{(r + M)(r - 1)}. \quad (20)$$

In the transformation, r is negative during remelting and positive during solidification. The interface condition given above in Eq. (19) may be rewritten as

$$r + \frac{M - 1}{2} \ln\left[1 + \left(\frac{r}{\sqrt{M}}\right)^2\right] - 2\sqrt{M} \times \arctan\frac{r}{\sqrt{M}} + \frac{1}{L}\int_0^t \left(k_2 \frac{\partial T_2}{\partial \eta} - k_3 \frac{\partial T_3}{\partial \eta}\right) dt = 0. \quad (21)$$

Since the temperature gradients at the interface in the transformed η plane can be evaluated from the temperatures at the previous time step, Eq. (21) can be numerically integrated for each time step, leaving the solution for the solid/liquid interface to be found from the resulting transcendental algebraic equation. This equation has a zero solution for $t = 0$ (which is the initial condition) and a unique solution for $t > 0$ because of the monotonic shape of the nonlinear functions involved (logarithmic and arctangent) in the region of interest. The above equation for the moving interface of phase change provides an efficient method of tracking the solid/liquid interface through the sequential solidification and remelting process.

Cooling. Following remelting, the molten material solidifies. The splats cool prior to subsequent droplet deposition. To simulate the cooling process we use the Crank-Nicholson scheme (Croft and Lilley, 1977).

Results and Discussion

The simulations presented in this paper have been constructed using realistic values of droplet size and deposition rates. As a representative example, we choose the droplet fluid to be molten aluminum, a nozzle diameter of 100 μm, and a stream speed of 8 m/s. Using Lord Rayleigh's relation for droplet production from capillary stream break-up and assuming an inviscid fluid, the droplet production frequency is 17,857 droplets/s (Rayleigh, 1879). Droplet diameters are found from conservation of mass and are 189 μm. We have chosen a few representative scenarios which may likely be considered in future droplet-based Solid Freeform Fabrication endeavors, though other deposition scenarios may also be employed.

Figure 3 illustrates the solid/liquid interface depth versus time for the second splat after it has made contact with the first solidified splat which is 10 μm thick. Each curve represents the solid/liquid interface history for a different value of the ratio $(T_i - T_m)/(T_m - T_{sub})$ where T_i is the initial liquid droplet impact temperature. For the conditions considered in this work, it can be seen that remelting can be initiated by adjusting this ratio to values above approximately 1.6. Increasing the ratio to higher values, i.e., increasing either T_i or T_{sub}, will cause the remelt depth to increase. This result is of practical significance since it allows heating of the substrate to compensate for the otherwise high impact temperatures required.

Due to the nature of the proposed application, the remelting behavior through a series of deposited droplets is of interest. We examined the conditions required to remelt constant thicknesses of 1 μm for nine sequentially deposited splats. Figure 4 illustrates the T_i required to achieve the aforementioned remelting action as a function of droplet deposition rate and substrate temperature. In the figure, the circle, triangle, and square symbols correspond to deposition rates of 56, 112, and 560 μs, respectively (56 μs is the inverse of the frequency of most uniform droplet production from 100 μm diameter orifices) and the open and solid symbols correspond to T_{sub} equal to 20 and 220°C, respectively. From the simulations, it can be seen that high superheats required (e.g., when depositing onto a substrate whose lower face is held constant at 20°C) can be compensated for by increasing the substrate temperature T_{sub} as discussed earlier. Figure 4 also illustrates that deposition at short time intervals (e.g., 56 μs) requires a dramatic variation in temperature of the incoming droplets if a constant remelt thickness is desired. This is because at short time intervals, the deposit has insufficient time to cool to the temperature of the lower surface of the substrate, T_{sub}, and the rapid depositions cause heating of the deposited structure thereby reducing the required incoming temperature of the next droplet. If the temperature of the incoming droplets were to be held constant at this quick delivery rate, the molten region in the material structure would grow to

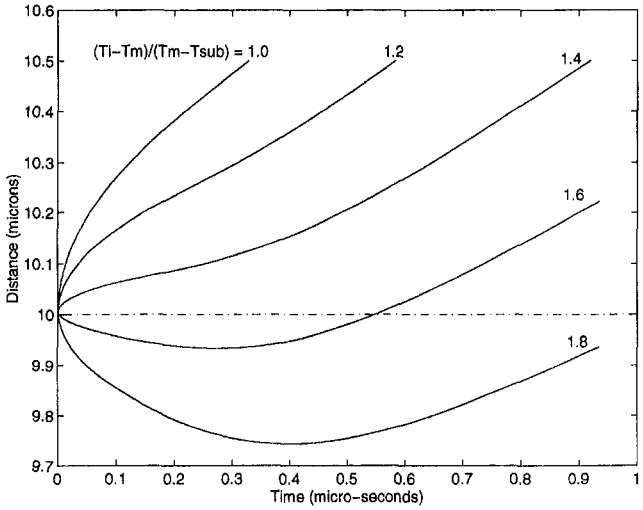

Fig. 3 Solid/liquid interface depth versus time resulting when a superheated droplet impacts on a solidified 10 μm thick aluminum droplet. Each curve represents a different value of the ratio $(T_i - T_m)/(T_m - T_{sub})$.

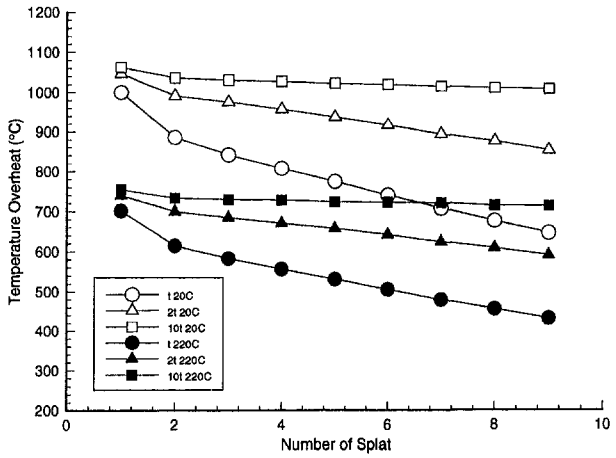

Fig. 4 Temperature superheat required to remelt 1 μm of the previously solidified substrate prior to solidification as a function of droplet deposition time interval and substrate temperature T_{sub}. Circle, triangle, and square symbols correspond to times between droplet depositions of 56 μs, 112 μs, and 560 μs, respectively. Open and closed symbols correspond to temperatures at the lower boundary of the substrate of 20°C and 220°C, respectively.

undesirable thicknesses and expanses, thereby increasing the microstructure dimensions and possibly eliminating macroscopic geometric fidelity. When the time between droplet depositions is sufficient to allow substrate cooling, the variation in incoming temperature required as a function of the number of splats delivered is reduced. It can be seen from Fig. 4 that an increase in droplet delivery rate by a factor of 10 causes nearly uniform incoming temperatures to be required to remelt 1 μm of the material structure. Increasing the time between droplet deliveries to greater values will have little considerable effect, and for the conditions chosen for this simulation, a droplet deposition time of 560 μs corresponds to the approximate minimum droplet deposition rate for which no variation of incoming temperature is required. This situation is the most flexible since it is difficult to vary the droplet temperature on a drop-to-drop basis in practice.

Figure 5 illustrates the result that the remelt depth and phase change time will increase with each droplet deposited if the incoming droplet temperature is held constant and the time between droplet depositions is short (56 μs). Shown in the figure are the solid/liquid interface histories for four sequentially deposited droplets incoming at a temperature of 980°C above the melting point and T_{sub} is held constant at 20°C. The variation in remelt depth and phase change time can be reduced drastically by increasing the time between droplet depositions to 560 μs as shown in Fig. 6 (note the difference in scales between Fig. 5 and Fig. 6). All conditions in Figs. 5 and 6 are identical except for droplet deposition time interval; hence, allowing the solidified splats to cool prior to subsequent droplet depositions reduces the variation in remelt depth and the variation in T_i required to achieve a nearly constant remelt depth.

Summary

The one-dimensional moving boundary phase change problem has been transformed into a fixed boundary problem which results in a transcendental algebraic relation for the solid/liquid interface. The model enables efficient tracking of the solid/liquid interface through the sequential solidification and remelting regimes, and more importantly, through the turning point defining the transition between solidification and remelting.

Use of the model allows efficient deposition strategies to be studied with computer simulations for desired remelt thicknesses and droplet deposition rates. The remelt depth of the previously deposited material due to the arrival of superheated droplets and the subsequent solidification time can be estimated as a function of deposit thickness, substrate temperature far away from the deposition surface, arriving droplet temperature, and deposition time interval. It has been found that droplet deposition at short time intervals requires considerable variations in incoming droplet temperature if a constant remelt depth is sought. Increasing the deposition time interval eliminates the variation in incoming droplet temperature. For constant incoming temperature, droplet depositions at short time intervals result in increasing remelt depth with increasing component thickness. Increasing the time between depositions reduces the variations in remelt depth. It was also found that moderately increasing the substrate temperature T_{sub} allows the reduction in temperature superheat for remelting.

Thus, in summary, the model provides an efficient computational method of tracking the solid/liquid interface through sequential solidification and remelting during successive droplet deliveries, and since the interface continuously changes direction, its solution is not given by the Stefan solution, i.e., it is not expressed as being proportional to the square root of time.

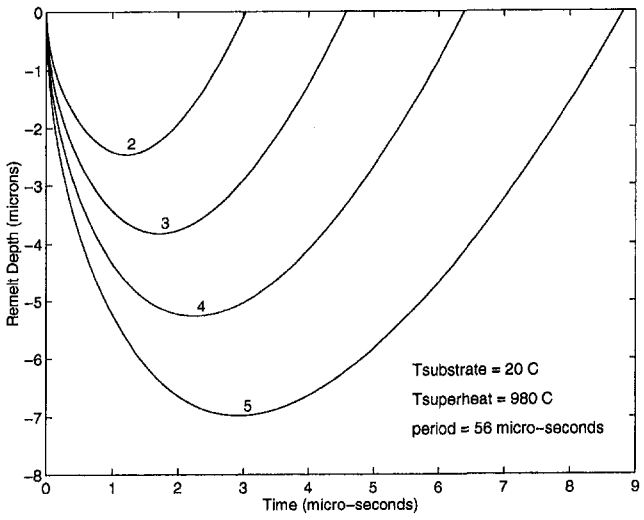

Fig. 5 Solid/liquid interface through four aluminum splats deposited sequentially every 56 μs with a constant incoming droplet temperature overheat of 980°C

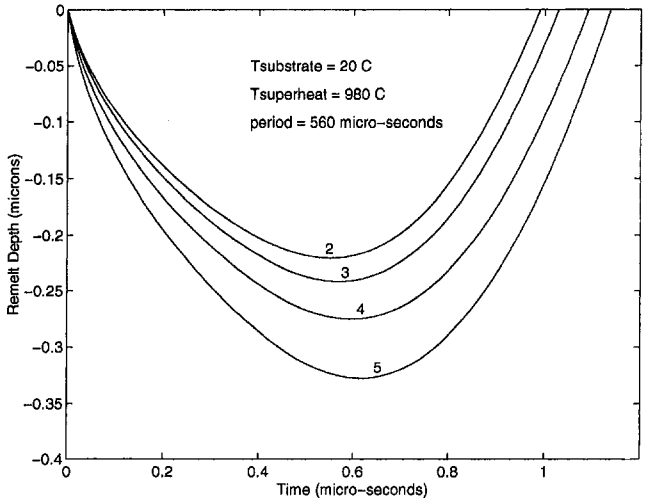

Fig. 6 Solid/liquid interface through four aluminum splats deposited sequentially every 560 μs with a constant incoming droplet temperature overheat of 980°C. Note the difference in scales between Fig. 5 and Fig. 6.

Since the model requires minimal computational time, the remelting and solidification of a multitude of droplets can be computed for use with the droplet-based SFF application. Hence, deposition strategies can be studied computationally in an effort to manipulate the phase change characteristics in order to provide the desired material characteristics of the overall SFF structure (e.g., fine microstructure and minimum porosity). Additionally, the methodology provided in this model can be applied to other one-dimensional moving boundary problems of finite domain.

Acknowledgments

The authors acknowledge the National Science Foundation, grants DMI-9396221 and DMI-9457205 for support of this research project, as well as the generous support from Delphi Interior and Lighting Division of General Motors.

References

Amon, C. H., Schmaltz, K. S., Merz, R., and Prinz, F. B., 1996, "Numerical and Experimental Investigation of Interface Bonding Via Substrate Remelting of an Impinging Molten Metal Droplet," ASME JOURNAL OF HEAT TRANSFER, Vol. 118, pp. 164–172.

Carslaw, H. S. and Jaeger, J. C., 1962, *Conduction of Heat in Solids,* 2nd ed. Clardon Press, Oxford, pp. 282–296.

Chin, R. K., Beuth, J. L., and Amon, C. H., 1995, "Control of Residual Thermal Stresses in Shape Deposition Manufacturing," *Solid Freeform Fabrication Symposium,* Austin, TX, pp. 221–228.

Croft, D. R., and Lilley, D. G., 1977, *Heat Transfer Calculations Using Finite Difference Equations,* Applied Science Publishers LTD, London, pp. 181–197.

Delplanque, J. P., Lavernia, E. J., and Rangel, R. H., 1996, "Multidirectional Solidification Model for the Description of Micropore Formation in Spray Deposition Processes," *Numerical Heat Transfer, Part A,* pp. 1–18.

Frederick, D., and Greif, R., 1985, "A Method for the Solution of Heat Transfer Problems With a Change of Phase," ASME JOURNAL OF HEAT TRANSFER, Vol. 107, pp. 520–526.

Goodrich, L. E., 1978, "Efficient Numerical Technique for One-Dimensional Thermal Problems With Phase Change," *Int. J. Heat and Mass Transfer,* Vol. 21, pp. 615–621.

Lavernia, E. J., Ayers, J. D., and Srivatsan, T. S., 1992, "Rapid Solidification Processing With Specific Application to Aluminum Alloys," *International Materials Reviews,* Vol. 37, No. 1, pp. 1–44.

Liu H., Lavernia E. J., and Rangel, R., 1993, "Numerical Simulation of Substrate Impact and Freezing of Droplets in Plasma Spray Processes," *J. Phys. D: Appl Phys.,* Vol. 26, pp. 1900–1908.

Liu, H., Lavernia, E. J., and Rangel, R. H., 1995, "Modeling of Molten Droplet Impingement on a Non-Flat Surface," *Acta Metall. Mater.,* Vol. 43, No. 5, pp. 2053–2072.

Madejski, J., 1976, "Droplets on Impact with a Solid Surface," *Int. J. Heat and Mass Transfer,* Vol. 19, pp. 1009–1013.

Orme, M. E., 1991 "On the Genesis of Droplet Stream Microspeed Dispersions," *Physics of Fluids,* Vol. 3, No. 12, pp. 2936–2947.

Orme, M. E., 1994 "Rapid Solidification Materials Synthesis with Nano-Liter Droplets," *SAE Tech Paper Series 932566,* Aerotech '93, September 27–30.

Orme, M. E., and Muntz, E. P., 1990 "The Manipulation of Capillary Stream Breakup Using Amplitude-Modulated Disturbances: A Pictorial and Quantitative Representation," *The Physics of Fluids A,* Vol. 2, No. 7, pp. 1124–1140.

Orme, M. E., and Muntz, E. P., 1992 "Method for Droplet Stream Manufacturing," U.S. Patent Number 5,171,360.

Orme, M. E., Huang, C., and Courter, C, 1996 "Precision Droplet Based Manufacturing and Material Synthesis: Fluid Dynamic and Thermal Control Issues," *J. Atomization and Sprays,* Vol. 6, pp. 305–329.

Prinz, F. B., Weiss, L. E., Amon, C. H., and Beuth, J. L., 1995 "Processing, Thermal and Mechanical Issues in Shape Deposition Manufacturing," *Solid Freeform Fabrication Symposium,* Austin, TX pp. 118–129.

Rayleigh, Lord, 1879, "On the Instability of Jets," *Proc. Lond Math. Soc.,* Vol. 10, pp. 4–13.

San Marchi, C., Liu, H., Lavernia, E. J., Rangel, R., Sickinger, A., and Muehlberger, E, 1993, "Numerical Analysis of the Deformation and Solidification of a Single Droplet Impinging Onto a Flat Substrate," *J. Mat. Sci.,* Vol. 28, pp. 3313–3321.

Trapaga, G., Matthys, E. F., Valencia, J. J., and Szekely, J., 1992, "Fluid Flow, Heat Transfer, and Solidification of Molten Metal Droplets Impinging on Substrates: Comparison of Numerical and Experimental Results," *Metallurgical Transactions B,* Vol. 23B, pp. 701–718.

Waldvogel, J. M., and Poulikakos, D., 1997, "Solidification Phenomena in Picoliter Size Solder Droplet Deposition on a Composite Substrate," *Int. J. Heat Mass Transfer,* Vol. 40, No. 2, pp. 295–309.

Zhao Z., Poulikakos, D., and Fukai, J., 1996, "Heat Transfer and Fluid Dynamics During the Collision of a Liquid Droplet on a Substrate," *Int. J. Heat Mass Transfer,* Vol. 39, No. 13, pp. 2771–2789.

Observation, Prediction, and Correlation of Geometric Shape Evolution Induced by Non-Isothermal Sintering of Polymer Powder

M. Kandis
Department of Mechanical Engineering,
The University of Texas at Austin,
Austin, TX 78712

T. L. Bergman
tberg@eng2.uconn.edu
Fellow ASME

Department of Mechanical Engineering,
University of Connecticut,
Storrs, CT 06269

Sintering of powders occurs in a wide array of manufacturing technologies and geophysical phenomena. Despite the prevalence of powder sintering, little attention has been paid to sintering of macroscopic shapes under non-isothermal conditions. In this paper (1) features of a representative, experimentally grown solid shape produced by non-isothermal sintering are discussed, (2) prediction of the solid shape evolution is achieved using a hybrid heat transfer, sintering, and consolidation model, (3) comparison of the actual and predicted solid shapes is made, (4) parametric simulation of solid part growth in conjunction with void expansion is attained, and (5) analytical predictions of the void space evolution are developed and discussed.

Introduction

Powder sintering occurs in materials processing and geophysical phenomena ranging from glass fiber manufacture (Rabinovich, 1985), to fabrication of high performance net shape structures (Kipphut et al., 1988), to glaciology (Feldt and Ballard, 1966). In addition to more traditional situations involving powder sintering, an emerging technology which relies upon non-isothermal sintering is Selective Laser Sintering (SLS); a technique to fabricate parts that may be impossible to build with conventional material-removal methods. The raw material used in SLS is micron-sized powder (plastics, waxes, or metals) which is sintered using directed laser beams to form three-dimensional parts. Applications of SLS include the following: prototyping net shape parts (Deckard and Beaman, 1989), fabricating human prostheses (Ashley, 1993), and quickly producing casting molds with tailored thermophysical properties (Bourell, 1990).

In all applications involving non-isothermal sintering, nearly solid objects or parts may evolve as local densification proceeds. In conjunction with part growth, formation of large voids is possible. In net shape manufacturing, for example, fabricated parts can be slightly larger (or smaller) than desired and, in critical applications, might need to be hand worked after processing. To develop appropriate ways to limit or control the growth of solids or voids within the powder, it is necessary to develop an understanding of the link between heat transfer processes within the powder, and microscale and macroscale sintering phenomena.

Microscale and Macroscale Sintering Phenomena. Existing studies of powder sintering have been concerned almost exclusively with microscale phenomena. Typically, particle dimensions are on the order of μm, and consideration of the thermodynamics and microscale fluid dynamics associated with particle-particle interaction allows development of constitutive relations for local densification rates. Constitutive descriptions for $d\phi/dt$ (for amorphous materials) often take the form of Frenkel's (1949) corrected expression (Scherer, 1992) which embodies the notions that sintering rates (i) increase exponentially with temperature (due to the reduction of material viscosity and, consequently, the reduction of the resistance to material flow) and (ii) decrease as ϕ becomes smaller (due to reduction in volume-averaged surface energy and, in turn, reduction in the driving force for material flow). Spatial temperature differences are negligible at the microscale, so heat transfer phenomena are not important (e.g., Jagota and Scherer, 1993; Soppe et al., 1994; Martinez-Herrera and Derby, 1994, 1995).

If a large heated volume of powder is considered, global sintering induces shrinkage of the overall volume (consolidation of the powder volume). Modeling of isothermal consolidation of macroscale volumes has proceeded at a very slow pace due to the difficulty of incorporating knowledge of microscale sintering rates into macroscopic descriptions of part shape evolution (Reid and Oakberg, 1990). Only a few modeling efforts aimed at predicting formation and evolution of large voids have been reported. In general, the modeling proceeds by treating the material to be sintered as a continuous medium with spatially varying ϕ. Local descriptions of mass conservation and force balance, coupled with microscale sintering submodels complete the mathematical description of the shape evolution for the isothermal material (Reid, 1992). Similarly, prediction of part distortion and gravitational slumping during isothermal liquid phase sintering has been achieved by developing models based upon solution of appropriate forms of the momentum equation applied to the entire compact (Raman and German, 1995).

Non-isothermal consolidation is extremely complex since $d\phi/dt$ varies from location-to-location and heat transfer is induced by the spatial temperature gradients. Internal temperatures respond to the heat transfer and subsequently modify local sintering rates. The resulting spatial variation of $d\phi/dt$ can lead to unusual consolidation phenomena. For example, when sintering a large bed of powder, macroscopic voids must develop within the bulk powder compact to compensate for the local density increase associated with sintering since initial porosities are much greater than the final (ultimate) porosities which can be achieved.

Objectives. Despite the pervasiveness of thermally induced sintering, only a few researchers have investigated non-isothermal effects and their impact on consolidation. The overall objec-

Contributed by the Heat Transfer Division for publication in the JOURNAL OF HEAT TRANSFER. Manuscript received by the Heat Transfer Division March 10, 1997; revision received June 27, 1997; Keywords: Conduction; Materials Processing and Manufacturing Process; Porous Media. Associate Technical Editor: M. Modest.

tive of this study is, therefore, to develop a better understanding of powder sintering in the presence of significant spatial temperature differences via a combined experimental, theoretical, and computational approach. To attain the objective (i) solid shapes are grown under controlled laboratory conditions, (ii) an analytical description of consolidation phenomena is proposed, (iii) predictions of solid shape evolution are achieved and, finally, (iv) development of an approximate analytical solution for macroscopic void growth during non-isothermal powder sintering is presented.

Experimental Apparatus and Procedure

Simple experiments were performed in order to grow solid shapes and observe macroscopic voids which evolve during powder sintering under highly non-isothermal conditions. The equipment consists of a test cell, a constant temperature bath, a furnace, a data acquisition system and associated hardware. The raw powder is amorphous, bisphenol-A polycarbonate with a mean particle size of 30 μm (and a particle size distribution ranging from 5 to 125 μm). The powder is used in SLS, its thermophysical properties have been measured, and a constitutive relation for $d\phi/dt$ has been reported (Nelson et al., 1993). Sintering occurs primarily above $T_g \approx 145$°C.

The test cell is composed of two concentric square tubes and two 5 mm thick balsa end-caps. The powder is placed in the annular region between the tubes which are maintained at temperatures above and below T_g during the experiment. The outer aluminum tube has inside dimensions of 25.4 mm × 25.4 mm, a wall thickness of 3.2 mm, and a length of 102 mm. The thin walled, inner square tube is made of brass with outside dimensions of 4.8 mm × 4.8 mm. In a typical experiment, the inner tube is connected to the constant temperature bath (which is set to a relatively low temperature), and the test cell is placed (horizontally or vertically) inside the furnace which is preset to a relatively high temperature.

Tube wall temperatures are monitored with K thermocouples connected to the data acquisition system (Keithley 500A). Three, 10 mil thermocouples were soldered to the outer aluminum tube at locations $\frac{1}{4}$, $\frac{1}{2}$, and $\frac{3}{4}$ along the tube axis. The lead wire was wound around the large tube several times and epoxied into place to minimize conduction error. Two thermocouples were placed inside the inner brass tube at its inlet and outlet. Measured temperatures are estimated to be accurate to within 3 degrees, and it was found that the tube temperatures are uniform to within ±0.5°C at any time.

Prior to each experiment, the test cell was filled with powder to provide $\phi_i \approx 0.5$ as reported by Nelson et al. (1993) and measured independently through a simple weighing technique. Relatively large ϕ_i are due to the non-spherical shape of the particles. After the second end-cap was secured, the test cell was placed into position. Although the oven and bath serve as constant temperature reservoirs, the outer tube required some time (≈1 hour) to reach steady-state temperature (defined as when desired boundary temperatures are reached and fluctuate by less than ±1°C). The experimental results presented here correspond to experiments lasting 6 hours (including the warming time).

After completion of each experiment, the solid shape was extracted and subsequently dusted with a room-temperature compressed air source to remove loose powder. The solid was dissected with a jeweler's saw, and distinguishing features were photographed. Local porosities were measured with a coring technique to be described later.

Mathematical Model

In the experiments just described, macroscopic voids must form because of the reduction in local ϕ with time. An initial and a hypothetical "final" condition are shown in Fig. 1 for the case when the test cell is horizontal. Local heat transfer drives the evolution of the local temperatures and, in turn, influences local values of $d\phi/dt$. Since the periphery of the powder is at a relatively high temperature, the powder will densify in these regions rapidly (relative to the powder nearer the cold inner tube). With time, single phase heat transfer (natural convection) and surface radiation may develop within the powderless regions. Natural convection may also exist within the permeable powder, and loose powder may drop from the ceiling of the void and collect at the void's base.

In lieu of treating the various heat transfer and solid mechanics phenomena in detail, a basic model is developed here which only includes description of conduction heat transfer in the powder and gas regions, along with advection of energy due to consolidation which is linked to variations in local $d\phi/dt$. As such, the bases for the macroscopic sintering model are (i) the continuity and energy equations applied to the solid and gas phases, (ii) a constitutive relation for $d\phi/dt$, and (iii) a description of instantaneous local solid and gas phase velocities associated with, and induced by, consolidation. The equations are as follows:

Conservation of mass:

$$\text{Solid:}\quad \partial/\partial t([1-\phi]\rho)_s + \partial/\partial x([1-\phi]\rho u)_s + \partial/\partial y([1-\phi]\rho v)_s = 0 \quad (1)$$

$$\text{Gas:}\quad \partial/\partial t(\phi\rho)_g + \partial/\partial x(\phi\rho u)_g + \partial/\partial y(\phi\rho v)_g = 0 \quad (2)$$

Energy equation:

$$\text{Solid:}\quad \partial/\partial t([1-\phi]\rho U)_s + \partial/\partial x([1-\phi]\rho u h)_s + \partial/\partial y([1-\phi]\rho v h)_s = \partial/\partial x(k_{\text{eff}}\partial T/\partial x)_s + \partial/\partial y(k_{\text{eff}}\partial T/\partial y)_s + S_s \quad (3)$$

$$\text{Gas:}\quad \partial/\partial t(\phi\rho U)_g + \partial/\partial x(\phi\rho u h)_g + \partial/\partial y(\phi\rho v h)_g = \partial/\partial x(k_{\text{eff}}\partial T/\partial x)_g + \partial/\partial y(k_{\text{eff}}\partial T/\partial y)_g + S_g \quad (4)$$

where S_s and S_g are source terms which, in general, would include the effects associated with the latent heat of fusion, the

Nomenclature

A = sintering rate constant, s^{-1}
Ar = ratio of initial powder volume to total volume
c_p, c_v = specific heats, J kg^{-1} K^{-1}
E_a = activation energy, kJ mol^{-1}
h = enthalpy, J kg^{-1}
H, L = enclosure dimensions, m
k = thermal conductivity, W m^{-1} K^{-1}
R = universal gas constant
S = source term, W m^{-3}
t = time, s
T = temperature, K or °C
u, v = horizontal and vertical velocities, m s^{-1}
U = internal energy, J kg^{-1}
x, y = horizontal and vertical coordinate directions

Greek symbols

λ = heat of fusion, J kg^{-1}
ρ = density, kg m^{-3}
ϕ = local porosity (gas volume fraction)
Φ = fraction of volume which is powderless
τ = dimensionless time

Subscripts and Superscripts

eff = effective
g = glass transition or gas
i = initial
pt = part
pw = powder
s = solid
∞ = ultimate (final) value

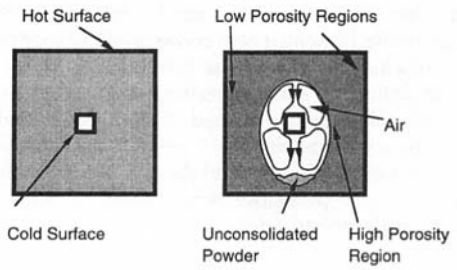

Fig. 1 Hypothetical initial (left) and ultimate (right) shapes during non-isothermal sintering in the experimental apparatus

radiative flux divergence, viscous dissipation, and interphase heat transfer (Whitaker, 1977).

To focus attention on the interplay between heat transfer, sintering, and consolidation, several assumptions are made and restrictions are applied. The gas is assumed to be incompressible, the material is amorphous ($\lambda = 0$), volumetric radiation heat transfer and viscous dissipation are neglected, and local thermal equilibrium is assumed between the gas and solid within the two phase regions. Combining Eqs. (1) and (2) yields

$$\partial/\partial t([1-\phi]\rho_s + \phi\rho_g) + \partial/\partial x([1-\phi]\rho_s u_s + \phi\rho_g u_g) + \partial/\partial y([1-\phi]\rho_s v_s + \phi\rho_g v_g) = 0. \quad (5)$$

Adding Eqs. (3) and (4), and rewriting U and h in terms of specific heats produces

$$\partial/\partial t([1-\phi]\rho_s c_{v,s}T + \phi\rho_g c_{v,g}T) + \partial/\partial x([1-\phi]\rho_s u_s c_{p,s}T + \phi\rho_g u_g c_{p,g}T) + \partial/\partial y([1-\phi]\rho_s v_s c_{p,s}T + \phi\rho_g v_g c_{p,g}T) - \partial/\partial x([k_{\text{eff},s} + k_{\text{eff},g}]\partial T/\partial x) - \partial/\partial y([k_{\text{eff},s} + k_{\text{eff},g}]\partial T/\partial y) = 0 \quad (6)$$

where, for the material used here, $k_{\text{eff},s} + k_{\text{eff},g} = k_s\,[1-\phi] + k_g\phi$ in which $k_s = 0.02504 + (5 \times 10^{-4}) \cdot T$ and k_g is that of air (Nelson et al., 1993). Note that the effective thermal conductivity of porous media is dependent upon a number of material properties including the ratio of solid to gas conductivities and the porosity (Kaviany, 1991). The simple linear expression used here provides values of k_{eff} which agree well with variational formulations (Hashin and Shtrikman, 1962) typically applied to porous media.

The constitutive relation for $d\phi/dt$ is based upon experimental measurement (Nelson et al., 1993) and is of similar form to Frenkel's equation for viscous sintering (Frenkel, 1949):

$$-d\phi/dt = A \cdot \exp(-E_a/RT)(\phi - \phi_\infty) \quad (7)$$

where the ultimate porosity is in the range $0.05 \leq \phi_\infty \leq 0.1$. (Note that $\phi_\infty \neq 0$ because interstitial voids ultimately become pendular; Nelson et al., 1993). Equation (7) takes an Arrhenius form primarily because of the dependence of the material viscosity upon temperature and the equation has been discussed extensively in the literature (Kuczynski, 1949; Cutler, 1969; Venkatu and Johnson, 1971).

Equations (5)–(7) complete the description of non-isothermal isotropic sintering except for a relation to determine the direction and magnitude of the local solid and gas phase velocities (the consolidation model). No theory exists for macroscale consolidation induced by non-isothermal sintering. In our initial approach in developing the consolidation model, it was assumed that (i) the solid phase at the most dense point within the domain is stationary, and (ii) the solid phase undergoes isotropic sintering (Beruto et al., 1988). Physically, the first assumption is based upon the expectations that low porosity regions (i) are typically of high strength, (ii) offer greater resistance to motion due to their high volume-averaged mass, and (iii) are usually physically attached to solid parts or walls (hot bounding surfaces). Without application of external forces or pressures, no reason exists to expect anisotropic sintering. The constraints which represent global consolidation and, in turn, the local solid phase velocity distribution are incorporated numerically as described in the next section.

Numerical Approach

A control volume method is used to solve the descriptive equations along with the constraints associated with the consolidation-related assumptions. Solid phase velocities are determined in a multistep scanning procedure. Specifically, Eq. (7) is first used to determine the future porosity distribution at each time step. Then, each control volume is ranked according to its predicted future ϕ (strength). The point of lowest ϕ (highest strength) accumulates solid material from its neighbors (incorporating the assumption of isotropic sintering). The process of strong (low ϕ) control volumes consuming solid material from weaker (high ϕ) neighbors is repeated until all regions within the computational domain are attended to. After the future solid phase mass fluxes are determined, solid and gas phase velocity distributions are found using Eq. (5), again incorporating the assumption of locally isotropic gas expulsion from the lowest ϕ control volume. Eventually, all of the solid phase is pulled from some control volumes resulting in the evolution of macroscopic voids.

Once solid and gas phase velocity distributions are determined at each time step, Eq. (6) is used to predict local temperatures. Iterative solution of the porosity, consolidation, and thermal equations is not necessary within each time step since the predictions are time step independent. Advection has been accounted for in Eq. (6) since these terms become more pronounced as the computational domain becomes larger (e.g., as larger parts are fabricated with SLS). The derivation of the discretized form of the energy (and continuity) equations is straightforward and is analogous to that of Patankar (1980). The discretized energy equation is solved implicitly using the ADI method, and the central-differencing scheme is used to determine advective and diffusive fluxes through the control surfaces. Interface effective thermal conductivities are estimated with harmonic-mean averaging (Patankar, 1980). Measured temperature values are specified for the thermal boundary conditions when simulation of the experiments is performed.

Since locations of the solid-gas interface of macroscopic voids are unknown a priori, control volumes are square and uniformly distributed throughout the computational domain. The predicted void-solid interfaces, therefore, are established only to the nearest control surfaces. Results presented here were obtained using a 141×141 (for simulation of the experimental results) and a 81×81 mesh (for the parametric simulations) along with a time step of 1 s. Time step and grid dependence studies are discussed in the Appendix.

Results

The Experimentally Grown Part. The experiments involved total sintering times of 6 hours. Significantly shorter experimentation resulted in small parts which were too fragile to handle. Once an appropriate total sintering time was found, the experiments were performed under the same applied thermal conditions, but with the test cell placed in either a horizontal or a vertical position. Each experiment was repeated once with no modification in the features of the resulting solid shape, except as noted.

Figure 2 shows features of a solid part which was grown in the vertical orientation. The initial powder temperature was 25°C, the steady-state warm wall temperature was 180°C, and the steady-state inner tube temperature was 50°C. The top photograph (Fig. 2(*a*)) includes the aluminum (hot) enclosure, the

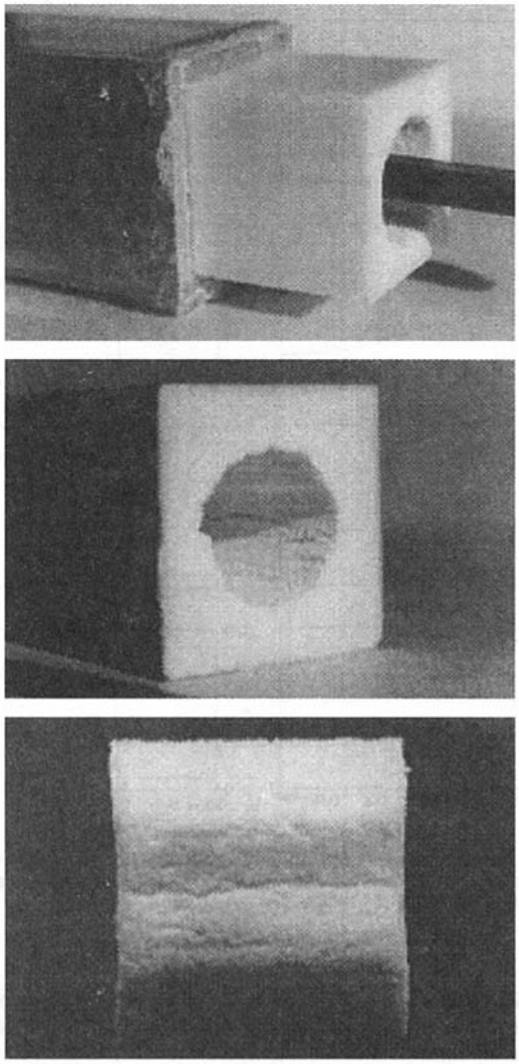

Fig. 2 Photographs of (*a*) an exploded view of the aluminum mold (left), the sintered part (middle), and the inner brass tube (right), (*b*) a cross section of the macroscopic void, and (c) the crack on the inside surface of the solid. The piece in (*c*) is 20 mm long.

sintered (white) solid piece, and the inner (cold) brass tube in an exploded view. Note that a very large macroscopic void separates the cool inner tube from the solid piece and has a nominally circular shape (Fig. 2(*b*)). The solid piece is relatively strong, and its texture varies from delicate and rough adjacent to the void to nearly that of pure acrylic next to the hot wall. For subsequent discussion it is helpful to note that, upon dismantling, loose powder (not shown) was collected within (approximately) the bottom $\frac{1}{3}$ of the macroscopic void. Slight variations (less than 5 percent) in the average void diameter were noted from top to bottom. A similar void formed when the experiment was performed in the horizontal orientation—suggesting that natural convection was of minor importance in the experiments.

Figure 2(*c*) is a photograph of the interior of the solid piece (from an observer standing on the center tube). Of particular note is the crack which runs (at mid-height) along the length of the solid. These cracks were found after every experiment involving the square enclosure and were always located midway along the vertical and horizontal walls of the test cell (the cracks can be seen upon careful inspection of Fig. 2(*b*)). Moreover, the cracks were not as evident in the lower $\frac{1}{3}$ of the vertically oriented parts and were considerably smaller in the horizontally grown piece. Several experiments were also performed with a

Table 1 Thermophysical properties of the solid phase (Nelson et al., 1993)

ρ_s	= 1278 kg/m^3
A	= 3.55 × 10^{15} s^{-1}
E_a	= 41,700 kcal/mol
c_s	= 1395.4 J/kg·K
c_g	= 1017 J/kg·K
k_s	= 0.02504 + (5 × 10^{-4})·T
k_g	= 0.004372 + (7.384 × 10^{-5})·T
λ	= 0

concentric circular tube test cell, and similar growth of an internal void adjacent to the cold inner tube was noted. Cracks were not observed in the parts grown in the circular tube test cell.

Predicted Part Features. To generate the results, the thermophysical properties listed in Table 1 were used. Note that the value of A used here is slightly different than the value reported by Nelson et al. (1993) based upon their isothermal sintering investigation. The few studies which have considered non-isothermal sintering effects (in other materials) have shown that sintering rates (and consolidation) can change dramatically in the presence of temperature gradients when compared to isothermal sintering scenarios (Beruto et al., 1989). Today, the physical mechanisms which are responsible for sintering rate sensitivity to temperature gradients are not understood, although it may be expected that non-isothermal conditions result in thermally induced stresses which simultaneously (i) change the driving forces for consolidation and (ii) modify the effective viscosity of the powder compacts and, in turn, their resistance to consolidation (Rybakov and Semenov, 1996).

Predicted ϕ distributions are shown in Fig. 3. At early times ($t = 3h$) the void (which coincides with the $\phi = 0.9$ contour) is nominally circular (the texture of the void is due to the numerical procedure), and the smallest values of ϕ are in the warmest regions (corners) of the computational domain. The isotherms bear similarity to the porosity contours, as such they are not shown.

As time proceeds ($t = 4h$), cracks are predicted to form along $x/L = 0.5$ (but are not evident along $y/H = 0.5$). The predicted crack formation is thermally driven and is due to the global migration of the powder to the low ϕ regions (corners). Because of the problem symmetry, crack formation should occur in the x and y-directions simultaneously. The preferential direction of crack formation is due to the scanning direction

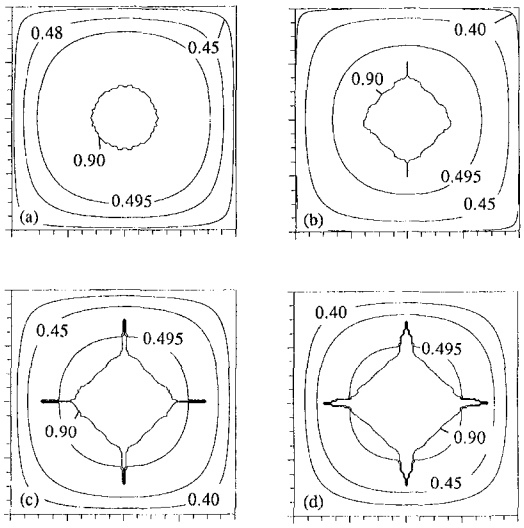

Fig. 3 Predicted porosity distributions at (*a*) t = 3 h, (*b*) t = 4 h, (*c*) t = 5 h, and (*d*) t = 6 h

associated with the numerical step used to identify control volumes of minimum porosity (scanning vertically then horizontally induces initial crack formation in the x-direction, but not in the y-direction). The extreme sensitivity of crack formation to a very minor aspect of the numerical methodology suggests that crack formation is highly sensitive to small perturbations in the system behavior. In the limit of infinite grid resolution, consideration of the descriptive equations reveals that infinitely thin cracks should form instantaneously upon heating and travel at infinite speed along $y/H = x/L = 0.5$.

At $t = 5\ h$, cracks exist in all compass directions and nearly symmetric system behavior is regained. The large void continues to grow and ultimately ($t = 6\ h$) occupies a considerable portion of the original powder volume. A casual comparison of Figs. 2(b) and 3(d) shows that the powder-air interface ($\phi = 0.9$) takes on a diamond shape numerically, while it is more circular in reality. A possible explanation for the discrepancy is outlined in the remainder of the section.

Recall that loose powder was extracted from the void and the photograph of Fig. 2(b) was taken of the part which occupied the upper region of the test cell. Since loose powder fell to the bottom of the void during the experiments, some of the solid material shown in Fig. 3(d) was not available for sintering. In fact, the amount of solid in the region $0.495 \leq \phi \leq 0.9$ over $\frac{2}{3}$ of the test cell length is the same as the amount of loose powder which was extracted after curtailment of the experiment. When viewed in this light (computationally removing the loose powder), comparison of the solid shape in Fig. 2(b) to the $\phi = 0.495$ contour of Fig. 3(d) shows remarkably good agreement. Apparently, slight densification ($\phi = 0.5$ to 0.495) is sufficient to hold the relatively loose powder in place during processing.

Porosities were measured at various locations within the part by drilling small diameter (2.4 mm) holes in the object in the axial direction. The mass of solid removed by coring was determined by weighing the part before and after the operation using a precision laboratory balance. The estimated uncertainty in the measured porosity (averaged over the core volume) is ± 0.03 and is associated with uncertainties in the solid density, the volume of the core hole, and the accuracy of the balance. Measured and predicted local porosities are in fair agreement, but conclusions regarding quantitative agreement cannot be made because of the relatively large uncertainty in the measured porosity. However, measured and predicted porosity differences from location-to-location (between locations of predicted ϕ values of 0.45, 0.40, and 0.38) are in agreement to within the uncertainty of the measurement, which is ± 0.001.

Parametric Simulations. With agreement noted between the experimental results and the model predictions, the model was subsequently used to predict part growth of an initially warm, buried object (a situation similar to SLS, except surface heating and/or cooling is not included). In the parametric simulations, a two-dimensional square (25.4 × 25.4 mm) computational domain is considered. A part (at T_i, ϕ_i) is placed in the central region ($0.3 \leq y/H \leq 0.7$, $0.3 \leq x/L \leq 0.7$) of the domain. The solid part is surrounded by loose powder ($\phi = 0.5$) at an initially uniform temperature of 150°C. Adiabatic conditions are applied to the boundaries of the computational domain.

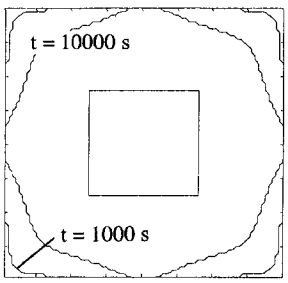

Fig. 4 Predicted time evolution of the solid and void shape. The $\phi = 0.9$ contour is shown at the times indicated. The initial solid shape is shown in the center of the domain.

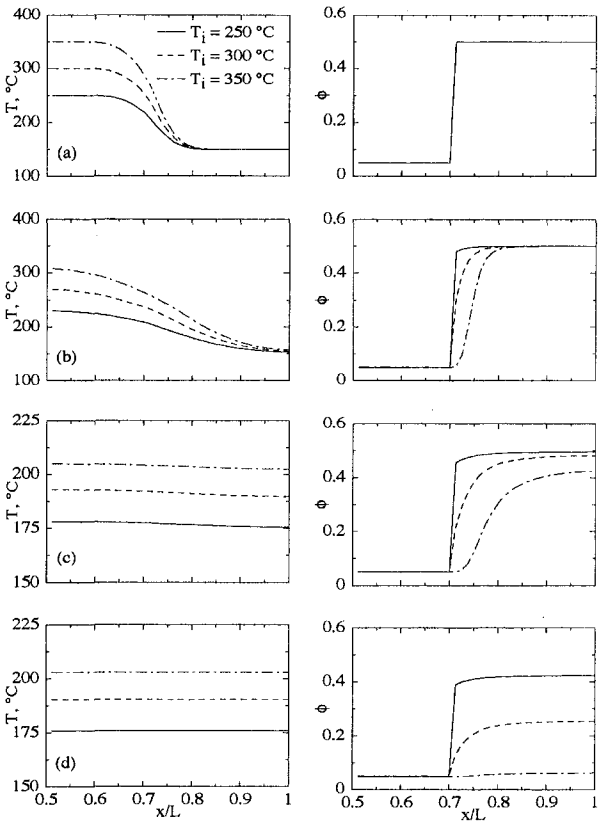

Fig. 5 Predicted centerline temperature (left) and porosity (right) distributions for $\phi_i = 0.05$ and $T_i = 250$, 300, and 350°C. Predictions are shown at (*a*) 10 s, (*b*) 100 s, (*c*) 1000 s, and (*d*) 10,000 s.

With the preceding scenario, the initially hot part will lose energy to the surrounding powder. As such, the loose powder will densify and (if $\phi_i > \phi_\infty$ within the central piece) the central piece will also contract in size. Powder will be pulled toward $x/L = y/H = 0.5$ and, at infinite time, in the absence of gravitational acceleration the solid phase will coalesce into a circular shape in the center of the computational domain (German et al., 1995). The steady-state temperature will vary as T_i and ϕ_i are modified. All told, a rather wide array of potential ultimate part shapes is expected.

The transient development of the part shape within the computational domain is shown in Fig. 4 for $T_i = 300$°C and $\phi_i = \phi_\infty$ (no sintering of the central square region). Figure 5 includes predicted temperature and porosity distributions at $y/H = 0.5$ (at $t = 10$, 100, 1000, and 10,000 s) for $\phi_i = 0.05$. Initial part temperatures of 250, 300, and 350°C are considered. As is evident, the temperature distribution evolves quite rapidly relative to the porosity distribution. Slight variations in the slope of the temperature distribution can be noted at $x/L \approx 0.7$ (due to variations in k_{eff}). Eventually ($t \approx 1000$ s), nearly uniform temperatures exist throughout the computational domain. Inspection of the porosity distributions reveals that (i) part growth (expansion of regions for which $\phi < 0.495$) is more severe at higher T_i (as expected), (ii) the surrounding powder continues to sinter after steady-state thermal conditions are reached, and (iii) for $T_i = 350$°C, the entire solid has consolidated to $\phi \approx 0.05$ and is just ready to pull away from the adiabatic wall (at $t = 10{,}000$ s).

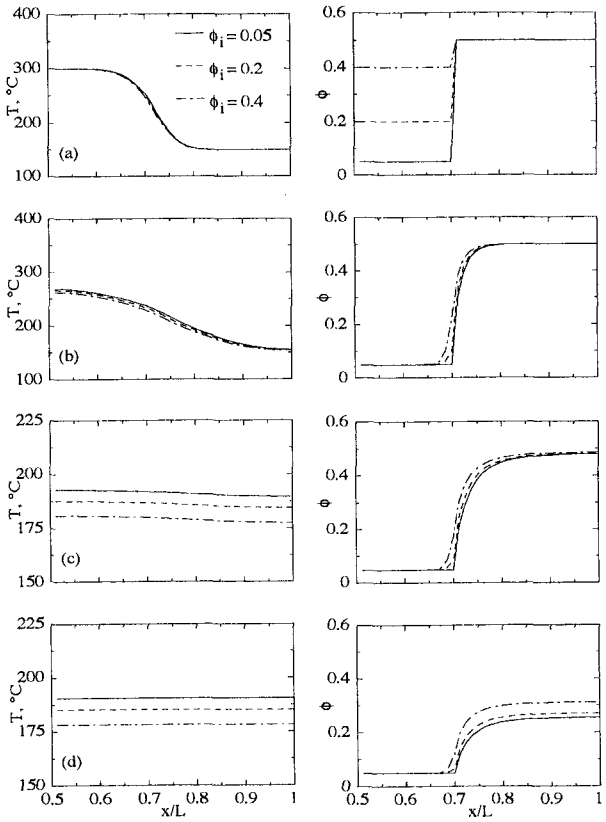

Fig. 6 Predicted centerline temperature (left) and porosity (right) distributions for ϕ_i = 0.05, 0.2, and 0.4 at T_i = 300°C. Predictions are shown at (*a*) 10 s, (*b*) 100 s, (*c*) 1000 s, and (*d*) 10,000 s.

Sensitivity to ϕ_i is reported in Fig. 6. Here, the interior part is at T_i = 300°C, with ϕ_i at its ultimate value (0.05) or at partially sintered initial values of 0.2 and 0.4. Inspection of the temperature distributions along $y/H = 0.5$ again reveals a relatively rapid response compared to the ϕ time scale. Different steady-state temperatures evolve because of the variation of the thermal mass with the initial porosity. Inspection of the porosity distributions shows that the initially hot central region sinters rapidly ($t < 100$ s) with maximum sintering occurring in regions of warmest temperature ($x/L = 0.5$). Once the temperatures approach their steady-state values ($t \approx 1000$ s) sintering is slowed considerably and the porosity distribution evolves gradually. The part boundary is not clearly defined for $t \geq 10$ s and the entire solid has agglomerated into a single piece by t = 10,000 s. Additional results for T_i = 250°C are available elsewhere (Kandis and Bergman, 1996).

Analytical Expression for Void Growth. As evident so far, the non-isothermal sintering model can be used to predict detailed features of the formation and growth of macroscopic voids and cracks which were observed repeatedly in experimentation. Parametric simulation results are as expected.

Since the time scale of temperature evolution is short relative to the time scale associated with sintering, a significant portion of the sintering time (for a buried part) proceeds under nearly isothermal conditions (as noted in Figs. 5 and 6). With adiabatic conditions applied to the computational domain, the steady-state temperature can be determined a priori with knowledge of the initial temperatures and porosities of the solid and powder, along with the specific heats and densities of the solid and gas phases. Assuming the entire domain is at T_∞, Eq. (7) may be individually applied to (i) the buried part and (ii) the powder region to predict the (spatially uniform) porosity evolution of each. Using conservation of mass, an expression may be derived

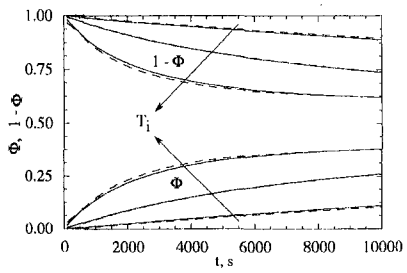

Fig. 7 Predicted variation of Φ with time for the conditions of Fig. 5. Solid lines are predictions using Eq. (9).

to describe the time variation of the dimensionless size of the single phase, powderless region Φ:

$$\Phi = 1 - (1 - \phi_i)/(1 - [\phi_\infty + (\phi_i - \phi_\infty) \times \exp(-A \cdot \exp(-E_a/RT_\infty) \cdot t)]) \quad (8)$$

where Eq. (8) is individually applied to the part and powder such that Φ for the entire domain is calculated using

$$\Phi = \Phi_{pt} \cdot (1 - Ar) + \Phi_{pw} \cdot Ar. \quad (9)$$

Comparisons of predicted Φ histories, as obtained by the detailed numerical model and Eq. (9), are shown in Figs. 7 and 8 for the conditions associated with Figs. 5 and 6. As seen in Fig. 7, when the buried part is initially at its ultimate porosity, Eq. (9) may be used to predict the Φ variation with remarkable accuracy. This encouraging result is due to the fact that the time scale of temperature evolution is short relative to that of the porosity distribution.

Figure 8(a) shows the Φ evolution for central pieces characterized by T_i = 250°C at three different ϕ_i. The predictions based upon Eq. (9) exhibit slight sensitivity to ϕ_i due to the fact that, for $\phi_i \neq \phi_\infty$, the central piece shrinks at a rate which accelerates with its initial porosity, as evident from Eq. (7). In contrast, the predictions of the detailed model show higher sensitivity to the initial central piece porosity. At very early time, Φ increases extremely rapidly as the very hot central piece shrinks before it can lose significant thermal energy to the surrounding loose powder. Figure 8(b) includes the Φ time evolution for T_i = 300°C, and similar features are noted as in Fig. 8(a). The nearly instantaneous increase in Φ at $t = 0$ is of the same magnitude as for the T_i = 250°C case, and Φ attains overall larger values than for the case illustrated in Fig. 8(a), as expected.

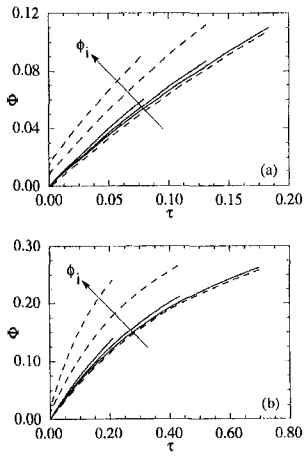

Fig. 8 Predicted variation of Φ with time for (*a*) ϕ_i = 0.05, 0.2, and 0.4 at T_i = 250°C and (*b*) ϕ_i = 0.05, 0.2, and 0.4 at T_i = 300°C. Solid lines are predictions using Eq. (9).

As is evident, the time evolution of Φ cannot be accurately estimated using Eqs. (8) and (9) when sintering is assumed to occur isothermally at T_∞ if a part with an initial porosity greater than the ultimate value is considered. In addition, the magnitude of the nearly instantaneous jump in Φ is overestimated if one assumes that initial sintering of the part and powder occurs isothermally at their initial temperatures. In general, therefore, it is necessary to use the detailed numerical model to predict the Φ evolution during sintering under highly non-isothermal conditions.

Summary and Conclusions

This study has been motivated by the desire to develop an initial understanding of the link between heat transfer, sintering, and consolidation during the thermal processing of powder compacts. The parts grown under non-isothermal conditions have revealed highly repeatable macroscopic void formation and thermally induced crack growth. Although somewhat limited in scope, the detailed model developed here can be used to predict many of the features which were observed in the experimentally grown part. Parametric simulations were performed to outline the sensitivity of part growth to different initial thermal and porosity conditions. Finally, an analytical approximate solution was developed to estimate void space evolution associated with parts which are buried in adiabatic containers. When the buried piece is initially at its ultimate porosity, predictions of Eqs. (8) and (9) are in remarkable agreement with those of the more detailed two-dimensional description of non-isothermal sintering and consolidation. The parametric simulations have revealed high sensitivity of part growth to thermal conditions within the powder bed.

As a more extreme physical response is induced (e.g., larger voids and more significant temperature differences within the domain), buoyancy-induced convection and radiative heat transfer will become more important and will need to be incorporated into the heat transfer submodel. More challenging, however, is the ultimate development of constitutive models or fundamental descriptions of the thermomechanical effects associated with breakage and settling of unsintered powder from the contracting sections of the consolidating part. Modeling two or three-dimensional consolidation in different materials, especially powdered metals, will be extremely challenging due to the complicating effects of non-zero λ, as well as the high thermal conductivity and low viscosity of molten metal relative to polymer (Mughal and Plumb, 1993). Development of a more fundamental understanding of the effects of temperature gradients upon local sintering rates is highly desirable.

Acknowledgment

This material is based upon work supported by the National Science Foundation under Grant No. CTS-9796186. The authors extend their gratitude to Jeff Norrell and Suman Das of the University of Texas at Austin.

References

Ashley, S., 1993, "Rapid Prototyping for Artificial Body Parts," *Mech. Engr.*, Vol. 115, pp. 50–53.

Beruto, D., Botter, R., and Searcy, A. W., 1988, "The Influence of Thermal Cycling on Densification: Further Tests of a Theory," in *Ceramic Transactions, Ceramic Powder Science II, B,* G. L. Messing et al., eds., American Ceramic Society, Westerville, Ohio, Vol. 1, pp. 911–918.

Beruto, D., Botter, R., and Searcy, A. W., 1989, "Influence of Temperature Gradients on Sintering: Experimental Tests of a Theory," *J. Am. Ceram. Soc.*, Vol. 72, pp. 232–235.

Bourell, D. L., 1990, "Solid Freeform Fabrication: An Advanced Manufacturing Approach," *Solid Freeform Fabrication Symposium,* University of Texas at Austin, pp. 1–7.

Carslaw, H. S., and Jaeger, J. C., 1959, *Conduction of Heat in Solids,* Oxford University Press, London.

Cutler, I. B., 1969, "Sintering of Glass Powders During Constant Rates of Heating," *J. Amer. Ceram. Soc.*, Vol. 52, pp. 14–17.

Deckard, C., and Beaman, J. J., 1989, "Recent Advances in Selective Laser Sintering," *Proceedings, 14th Conf. on Production Research and Technology,* Ann Arbor, MI, pp. 623–630.

Feldt, E. D., and Ballard, G. E. H., 1966, "A Theory of the Consolidation of Snow," *J. Glaciology,* Vol. 9, pp. 145–157.

Frenkel, J., 1949, "Viscous Flow of Crystalline Bodies under the Action of Surface Tension," *J. Phys.*, Vol. 9, pp. 385–391.

German, R. M., Iacocca, R. G., Johnson, J. L., Liu, Yixiong, and Upadhyaya, A., 1995, "Liquid-Phase Sintering under Microgravity Conditions," *J. Met.*, Vol. 47, pp. 46–48.

Hashin, Z., and Shtrikman, S., 1962, "A Variational Approach to the Theory of the Effective Magnetic Permeability of Multiphase Materials," *J. Appl. Phys.*, Vol. 10, pp. 3125–3131.

Jagota, A., and Scherer, G. W., 1993, "Viscosities and Sintering Rates of a Two-Dimensional Granular Composite," *J. Am. Ceram. Soc.*, Vol. 76, pp. 3123–3135.

Kandis, M., and Bergman, T. L., 1996, "Void Formation and Crack Propagation in Polymer Parts Grown by Non-Isothermal Sintering," in *Thermal Transport in Solidification Processing,* V. Prasad et al., eds., ASME HTD-Vol. 323, pp. 199–206.

Kaviany, M., 1991, *Principles of Heat Transfer in Porous Media,* Springer-Verlag, New York.

Kipphut, C. M., Bose, A., Farooq, S., and German, R. M., 1988, "Gravity and Configurational Energy Induced Microstructural Changes in Liquid Phase Sintering," *Metall. Trans.*, Vol. 19A, pp. 1905–1913.

Kuczynski, G. C., 1949, "Study of the Sintering of Glass," *J. Appl. Phys.*, Vol. 20, pp. 1160–1163.

Martinez-Herrera, J. I., and Derby, J. J., 1994, "Analysis of Capillary-Driven Viscous Flows During the Sintering of Ceramic Powders," *AIChE J.*, Vol. 40, pp. 1794–1803.

Martinez-Herrera, J. I., and Derby, J. J., 1995, "Viscous Sintering of Spherical Particles via Finite Element Analysis," *J. Am. Ceram. Soc.*, Vol. 78, pp. 645–649.

Mughal, M. P., and Plumb, O. A., 1993, "Thermal Densification of Metal-Ceramic Composites," *Scripta Metallurgica et Materialia,* Vol. 29, pp. 383–388.

Nelson, J. C., Xue, S., Barlow, J. W., Beaman, J. J., Marcus, H. L., and Bourell, D. L., 1993, "Model of Selective Laser Sintering of Bisphenol-A Polycarbonate," *Ind. Eng. Chem. Res.*, Vol. 32, pp. 2305–2317.

Patankar, S. V., 1980, *Numerical Heat Transfer and Fluid Flow,* Hemisphere Publishing Company, Washington.

Rabinovich, E. M., 1985, "Preparation of Glass by Sintering," *J. Mater. Sci.*, Vol. 20, pp. 4259–4297.

Raman, R., and German, R. M., 1995, "A Mathematical Model for Gravity-Induced Distortion During Liquid Phase Sintering," *Met. and Mater. Trans. A,* Vol. 26A, pp. 653–658.

Reid, C. R., and Oakburg, R. G., 1990, "A Continuum Theory for the Mechanical Response of Materials to the Thermodynamic Stress of Sintering," *Mech. Materials,* Vol. 10, pp. 201–213.

Reid, C. R., 1992, "Applications of a Continuum Theory for Sintering to Densification Rates," in *Mechanics of Granular Materials and Powder Systems,* M. M. Mehrabadi, ed., ASME MD-Vol. 37, pp. 19–27.

Rybakov, K. I., and Semenov, V. E., 1996, "Densification of Powder Materials in Non-Uniform Temperature Fields," *Philosophical Magazine A,* Vol. 73, pp. 295–307.

Scherer, G. W., 1992, "Constitutive Models for Viscous Sintering," in *Mechanics of Granular Materials and Powder Systems,* M. M. Mehrabadi, ed., ASME MD-Vol. 37, pp. 1–18.

Soppe, W. J., Janssen, B. C., Bonekamp, B. C., Correia, L. A., and Veringa, H. J., 1994, "A Computer Simulation Method for Sintering in Three-Dimensional Powder Compacts," *J. Mater. Sci.*, Vol. 29, pp. 754–761.

Venkuta, D. A., and Johnson, D. L., 1971, "Analysis of Sintering Equations Pertaining to Constant Rates of Heating," *J. Amer. Ceram. Soc.*, Vol. 54, p. 641.

Whitaker, S., 1977, "A Theory of Drying in Porous Media," in *Advances in Heat Transfer,* J. P. Hartnett and T. F. Irvine, Jr., eds., Academic Press, pp. 119–203.

APPENDIX

The main feature of the numerical procedure (incorporation of advective transfer induced by local ϕ variations) was verified by comparing predictions with one-dimensional analytical solutions for solid-liquid phase change with significant differences in the solid and liquid densities (Carslaw and Jaeger, 1959). Specifically, the algorithm discussed here was modified to include non-zero λ, using an enthalpy method approach. Inputs to the simulations include solid to liquid phase density ratios ranging from 0.6 to unity, solid to liquid thermal conductivity ratios ranging from 0.1 to unity, and solid and liquid Stefan numbers of 0.2, 0.4, and 0.6. The predicted solid-liquid interface location was within 3 percent of the analytically determined interface position for all cases when grid independent and time step independent predictions were achieved.

Time step dependence was determined by using increments ranging from 0.1 to 4 s. A comparison between predictions using time steps of 0.1 and 1 s showed that no difference in porosity contour locations could be noted visually.

A comparison of predicted ϕ distributions was made for the experiment at $t = 6$ h using 31×31, 61×61, and 141×141 uniform control volumes. Crack formation was found to be highly grid size dependent (as it should be). As the spatial resolution is increased, however, the midplane cracks propagate further toward the heated walls. The overall size of the macroscopic void is adequately resolved with the 141×141 mesh with differences in Φ estimated to be less than 1 percent between the 61×61 and 141×141 numerical predictions. In the parametric simulations, cracks do not form and so moderate grid sizes (81×81) were adequate, along with a time step of 1 s, to produce nearly time step and grid size independent predictions of the $\phi = 0.9$ contour.

Three-Dimensional Electron-Beam Deflection and Missed Joint in Welding Dissimilar Metals

P. S. Wei
Professor.

F. K. Chung
Graduate Student.

Department of Mechanical Engineering,
National Sun Yat-Sen University,
Kaohsiung, Taiwan 80424,
China

Three-dimensional deflection of the electron beam resulting in a missed joint due to thermoelectric magnetism generated while welding dissimilar metals is systematically investigated. The incident energy rate distribution is assumed to be Gaussian and the deep and narrow welding cavity induced is idealized as a paraboloid of revolution. With a three-dimensional analytical solution for the temperature and by solving Maxwell's electromagnetic equations, thermoelectric currents, magnetic flux densities, and deflections of the beam are found. The predictions agree with available experimental data. The results find that missed joints can be reduced by increasing the dimensionless accelerating voltage-to-Seebeck e.m.f. parameter, Peclet number, and effective electrical contact resistance parameter, and decreasing dimensionless beam power, magnetic permeabilities, and electrical conductivity ratio between metals 1 and 2. Tilting workpieces and shifting the electron gun from the joint line are also feasible. A three-dimensional analysis is required for a successful determination of beam deflection.

Introduction

The major advantage of welding with a high-power-density electron beam is the ability to weld dissimilar metals that cannot be accomplished by using other techniques. The joint, however, can be missed. When a small diameter (around 0.1–1.0 mm) electron beam is used to make a deep weld (Tong and Giedt, 1969), the beam must be aligned with the joint along its entire length of travel. Even when the beam from the electron gun is properly aligned with the joint, subsequent deflection of the beam can result in nonsymmetric fusion along a joint, or the fusion zone may miss the joint completely. One reason for the beam deflection is due to the presence of thermoelectric magnetic fields as proposed by Watanabe et al. (1975), reviewed by Nazarenko (1982) and Blakeley and Sanderson (1984), and analyzed theoretically by (Wei and Lee 1989; Wei and Lii, 1990) and Paulini et al. (1990).

Since temperature gradients exist between the top and bottom and in front of and behind the deep and narrow cavity near the joint plane (Schauer and Giedt, 1978; Wei et al., 1990), thermoelectric currents due to the Seebeck effect are produced in dissimilar metals (Wei and Lee 1989; Wei and Lii, 1990). Thermoelectric currents which are quite independent of the electron beam current were measured by Blakeley and Sanderson (1984) to be several hundred amperes while the measured flux density was at a constant level around 10 gauss. The induced magnetic field above and below the top surface therefore deflects the electron beam and induces a missed joint. The missed joint is attributed to vertical currents on a plane transverse to the welding line. (Wei and Lee 1989; Wei and Lii, 1990) proposed a simple two-dimensional analytical model on a transverse plane crossing the cavity and investigated which factors affect the missed joint. Apart from the thermoelectric currents that are induced, it was found that for a given incident angle of the beam, the deflection of the beam can be reduced by decreasing the difference in the Seebeck coefficients of dissimilar metals, relative magnetic permeability, thermal conductivity, welding speed and electrical conductivity, and by increasing the effective electrical contact resistance. The predictions agreed with available experimental data (Nazarenko, 1982). The incident angle is an important factor which, unfortunately, cannot be obtained from a two-dimensional model. A more realistic three-dimensional thermoelectric field model is therefore required.

Paulini et al. (1990) have calculated the approximate trajectory of the electron beam (not a laser beam). By using two-dimensional temperature distribution based on an assumed focus temperature, the effects of horizontal temperature gradient on magnetic fields, which are a function of the horizontal coordinate, and beam deflection were investigated. The beam was considered to be deflected by an unknown constant vertical temperature gradient with unrealistic high and low temperatures at the top and bottom of the cavity (Schauer and Giedt, 1978; Wei et al. 1990; Wei and Chow, 1992). Magnetic permeabilities of dissimilar metals were unity since temperatures of the heat-affected region are usually higher than the Curie temperature above which the ferromagnetic behavior is lost. It was found that horizontal currents were negligibly small compared to vertical currents. Three-dimensional magnetic fields were obtained by superposing the horizontal and vertical currents. Factors such as relative magnetic permeability, electrical conductivity, electrical contact resistance, and beam power, however, were not treated.

In this study, a three-dimensional thermoelectric and heat conduction model is proposed to predict the deflection of the electron beam from an electron gun to the top surfaces and into bulk metals. By extending the two-dimensional work of (Wei and Lee 1989; Wei and Lii, 1990), the entire trajectory of the beam can be determined. A more systematic and realistic understanding on missed joints is provided.

System Model and Analysis

As illustrated in Fig. 1, two dissimilar metals are joined by a high-power-density electron beam moving at a constant speed

Contributed by the Heat Transfer Division for publication in the JOURNAL OF HEAT TRANSFER. Manuscript received by the Heat Transfer Division January 23, 1997; revision received July 7, 1997; Keywords: Conduction; High-Temperature Phenomena; Materials Processing and Manufacturing Process. Associate Technical Editor: P. Ayyaswamy.

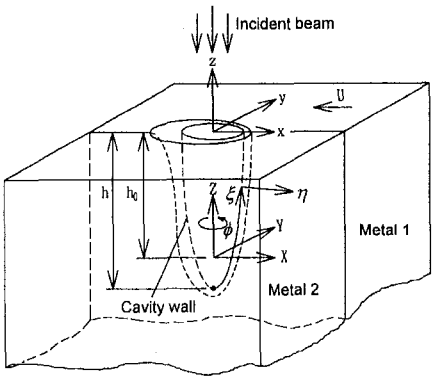

Fig. 1 Schematic sketch of the model and coordinate system

in the negative x direction. The metal having a larger Seebeck coefficient is called metal 1, which is placed on the positive y-coordinate. Thermoelectric currents occur as a result of the difference in the Seebeck coefficients of dissimilar metals and temperature gradients on the joint plane (Wei and Lee, 1989; Wei and Lii, 1990). The relative magnetic permeability of the metal reduces to unity as temperature is greater than the melting or Curie temperatures. To simplify the model without loss of generosity, the assumptions made are as follows:

1 A quasi-steady state is assumed during a sufficient welding length or time.
2 The cavity is located on the contact plane to calculate temperature fields. In reality, the missed joint represents the deep and narrow cavity deviated from the joint plane. Hence, as the deflection of the beam becomes large accuracy is reduced.
3 Electric and magnetic fields are not affected by the motion of workpieces or fluid flow in the weld pool. Magnetic diffusivity is typically around 1 m^2/s which is 10^7 times larger than kinematic viscosity. Magnetic Reynolds number is therefore between 10^{-2} and 10^{-4}, based on a length scale of 10^{-2} m from the the cavity depth and welding speed of 10^{-2} m/s and liquid velocity of 1 m/s (Wei and Chiou, 1988).
4 Thermal diffusivities are averaged within the considered temperature range and between dissimilar metals. In most metals, thermal diffusivities are within 10^{-5}–10^{-6} m^2/s. The predicted temperature field based on this assumption inevitably suffers inaccuracy. An investigation of the temperature field affected by temperature-dependent and distinct thermal diffusivities is required. Since only the temperature gradient on the contact plane is responsible for the generation of thermoelectric currents, the use of averaged thermal diffusivity to calculate the interface temperature can be considered as a first approximation. Latent heats for melting are neglected by comparison with incident flux (Wei and Ho, 1990). On the other hand, this work considers the primary electrical and thermoelectric properties such as the Seebeck coefficient, magnetic permeability, and electrical conductivity to be distinct between dissimilar metals. Hence this model still holds general features of beam deflection. Zero electrical conductivity and unity relative permeability are assumed in the cavity and surroundings.
5 An enhanced diffusivity is introduced to approximately simulate the effects of convection. Since the flow of liquid enhances energy transport, the diffusivity in the flow direction is increased by a constant multiple of around five, as chosen by Gau and Viskanta (1984), Giedt et al.

Nomenclature

$\mathbf{A}$ = vector potential
B = magnetic flux density, $B = \hat{B}/[\mu_0\sigma_2(S_1 - S_2)(T_m - T_\infty)]$
e = electron charge, coulomb
E = electric field intensity, V/m
G = dimensionless effective electrical contact resistance parameter = $\tau\sigma_2/\sigma_q$
h = dimensionless cavity depth = $\hat{h}/\sigma_q$
H = magnetic field strength = B/μ_r
h_{lg} = latent heat of evaporation, = $\hat{h}_{lg}/[R(T_m - T_\infty)]$
j = electric current density = $\hat{j}\sigma_q/[\sigma_2(S_1 - S_2)(T_m - T_\infty)]$, or Cartesian unit vector
k = liquid thermal conductivity or Cartesian unit vector
L_p^m = Laguerre function
m = electron mass
p_b = boiling pressure
$P = \hat{p}_b\sigma_q/\gamma_m$
Pe = Peclet number = $U\sigma_q/\alpha$
q, Q = incident flux and power
Q^* = dimensionless beam power = $Q/[k\sigma_q(T_m - T_\infty)]$
R = gas constant
r_0 = dimensionless cavity opening radius = $\hat{r}_0/\sigma_q$
S = Seebeck coefficient, V/K
S_α = parameter approximating convection = α/α_z
T, T_m, T_∞ = temperature, averaged melting and ambient temperature
U = welding speed
v = electron speed
V = accelerating voltage, V
x, y, z = Cartesian coordinates as shown in Fig. 1, $x = \hat{x}/\sigma_q$, $y = \hat{y}/\sigma_q$, $z = \hat{z}/\sigma_q$
X, Y, Z = Cartesian coordinates as shown in Fig. 1, $X = \hat{X}/\sigma_q$, $Y = \hat{Y}/\sigma_q$, $Z = \hat{Z}/\sigma_q$
y_e, z_e = position of electron gun

Greek Letters

α, α_z = liquid diffusivity and enhanced diffusivity
γ, γ_m = surface tension at T and T_m
Γ = gamma function or metals 1-to-2 electrical conductivity ratio = σ_1/σ_2
η, η_0 = parabolic coordinate and coordinate on cavity wall
θ = dimensionless temperature = $(T - T_\infty)/(T_m - T_\infty)$
θ_b, θ_B = boiling, base temperature
θ_c = Curie temperature
$\theta_\infty = T_\infty/(T_m - T_\infty)$
Λ = dimensionless accelerating voltage-to-Seebeck e.m.f. parameter = $(2Vm/e)^{1/2}/[\sigma_q\mu_0\sigma_2(S_1 - S_2)(T_m - T_\infty)]$
μ_r, μ_0 = relative and free space permeability, $\mu_0 = 4\pi \times 10^{-7}$ N/amp^2
ξ = parabolic coordinate
σ = electrical conductivity, ohm^{-1}m^{-1}
σ_q = energy flux distribution parameter, m
τ = effective electrical contact resistance, ohm-m^2
$Y = (T_m - T_\infty)(d\gamma/dT)/\gamma_m$ where $d\gamma/dT$ is a constant
ϕ = electric potential or parabolic coordinate
χ_e = tilt angle of workpiece
Ψ = confluent hypergeometric function of the second kind
ω, Ω = dimensional and dimensionless electrostatic potential, $\omega = \phi + ST$, $\Omega = \omega/[(S_1 - S_2)(T_m - T_\infty)]$

Superscript

$\hat{}$ = dimensional quantity

Subscript

1,2 = metal 1 and 2 having larger and smaller Seebeck coefficient and lying on $y > 0$, and $y < 0$, respectively.

(1984), and Wei et al. (1997), to achieve good agreement with experimental data.

Governing Equations for Thermoelectric Magnetism. Maxwell's electromagnetic field equations are (see, for example, Cramer and Pai, 1973; Nayfeh and Brussel, 1985)

$$\nabla \times \mathbf{E} = 0 \quad \text{or} \quad \mathbf{E} = -\nabla\phi \tag{1}$$

$$\nabla \cdot \mathbf{B} = 0 \tag{2}$$

$$\nabla \times \mathbf{H} = \mathbf{j} \tag{3}$$

where magnetic flux density is related to magnetic field intensity by the relation $\mathbf{B} = \mu_r\mathbf{H}$. Current density in Eq. (3) is determined from a generalized Ohm's law

$$\frac{\mathbf{j}}{\sigma} = \mathbf{E} - S\nabla T \tag{4}$$

where the last term on the right-hand side accounts for the thermoelectric Seebeck effect (Giedt, 1971; Shercliff, 1979). By substituting Eqs. (1) and (4) into Eq. (3), and taking the divergence lead to (Shercliff, 1979; Wei and Lii, 1990)

$$\nabla^2\Omega = 0, \tag{5}$$

Eq. (2) implies the existence of a magnetic vector potential $\mathbf{A}$ such that

$$\nabla \times \mathbf{A} = \mathbf{B}. \tag{6}$$

To assure uniqueness of the magnetic vector potential, a Coulomb's gauge is introduced. That is,

$$\nabla \cdot \mathbf{A} = 0. \tag{7}$$

Substituting Eqs. (6) and (7) into Eq. (3) gives

$$\nabla^2\mathbf{A} = -\mu_r\mathbf{j} \tag{8}$$

where electric currents are taken to vanish in the surroundings and in the cavity.

Boundary Conditions. Normal current density across an interface is conserved. This gives

$$\frac{\partial\Omega_2}{\partial y} = \Gamma\frac{\partial\Omega_1}{\partial y}. \tag{9}$$

Interfacial temperature gradients parallel to the contact surface are responsible for the occurrence of thermoelectric currents and are governed by (Shercliff, 1979; Wei and Lii, 1990)

$$\frac{\partial\Omega_1}{\partial z} - \frac{\partial\Omega_2}{\partial z} - G\frac{\partial^2\Omega_1}{\partial z\partial y} = \frac{\partial\theta_1}{\partial z} \tag{10}$$

$$\frac{\partial\Omega_1}{\partial x} - \frac{\partial\Omega_2}{\partial x} - G\frac{\partial^2\Omega_1}{\partial x\partial y} = \frac{\partial\theta_1}{\partial x}. \tag{11}$$

Other applicable boundary conditions are that the electrostatic potential gradients vanish at the top surface and far from the electron beam. Boundary conditions at the contact surface parallel to z-x plane for Eq. (8) are continuities of normal magnetic flux density and tangential magnetic field strength. They are, respectively,

$$\left(\frac{\partial A_x}{\partial z} - \frac{\partial A_z}{\partial x}\right)^- = \left(\frac{\partial A_x}{\partial z} - \frac{\partial A_z}{\partial x}\right)^+ \tag{12}$$

$$\frac{1}{\mu_r^-}\left(\frac{\partial A_y}{\partial x} - \frac{\partial A_x}{\partial y}\right)^- = \frac{1}{\mu_r^+}\left(\frac{\partial A_y}{\partial x} - \frac{\partial A_x}{\partial y}\right)^+ \tag{13}$$

$$\frac{1}{\mu_r^-}\left(\frac{\partial A_z}{\partial y} - \frac{\partial A_y}{\partial z}\right)^- = \frac{1}{\mu_r^+}\left(\frac{\partial A_z}{\partial y} - \frac{\partial A_y}{\partial z}\right)^+. \tag{14}$$

Similar equations can be obtained for contact surfaces parallel to x-y and y-z planes.

Three-Dimensional Analytical Temperature Field. Temperature gradients at the contact surface are required in Eqs. (10) and (11). The energy equation in a quasi-steady state is

$$-U\frac{\partial T}{\partial\hat{X}} = \alpha\left(\frac{\partial^2 T}{\partial\hat{X}^2} + \frac{\partial^2 T}{\partial\hat{Y}^2}\right) + \alpha_z\frac{\partial^2 T}{\partial\hat{Z}^2}. \tag{15}$$

The incident flux is given by a Gaussian distribution,

$$\hat{q} = \frac{3\hat{Q}}{\pi\sigma_q^2}\exp\left[-\frac{3(\hat{x}^2 + \hat{y}^2)}{\sigma_q^2}\right]. \tag{16}$$

An analytical solution of Eq. (15) subject to boundary condition (16) was found to be (Wei and Shian, 1993; Wei et al., 1997)

$$\theta = \frac{3Q^*\sqrt{S_\alpha}\eta_0}{\pi\mathrm{Pe}}\exp(-\sqrt{\xi\eta}\cos\phi) \times \left\{\sum_{p=1}^{\infty}\Gamma(p)\left(\frac{12\eta_0}{\mathrm{Pe}^2} + \frac{1}{2}\right)^{-p}\left(\frac{12\eta_0}{\mathrm{Pe}^2} - \frac{1}{2}\right)^{p-1} \times \left[\exp\left(-\frac{\eta+\xi}{2}\right)L_{p-1}^0(\xi)\Psi(p, 1, \eta) + \exp\left(-\frac{\eta'+\xi'}{2}\right)L_{p-1}^0(\xi')\Psi(p, 1, \eta')\right]\right\} \tag{17}$$

$$\eta \geq \eta_0$$

where the parabolic coordinates are related to Cartesian coordinates as given by

$$\xi = \frac{\mathrm{Pe}}{2}\left(Z\sqrt{S_\alpha} + \sqrt{X^2 + Y^2 + S_\alpha Z^2}\right),$$

$$\eta = \frac{\mathrm{Pe}}{2}\left(-Z\sqrt{S_\alpha} + \sqrt{X^2 + Y^2 + S_\alpha Z^2}\right),$$

$$\phi = \tan^{-1}\left(\frac{Y}{X}\right). \tag{18}$$

The relations between parabolic and its image coordinates are (a) $\xi\eta = \xi'\eta'$ and (b) $(\xi - \eta)/2 + (\xi' - \eta')/2 = 2h_0$. The coordinate of the cavity wall, η_0, can be obtained from force balance between vapor pressure and surface tension at the cavity base

$$\eta_0 = \frac{\mathrm{Pe}[1 + Y(\theta_B - 1)]}{P\sqrt{S_\alpha}}\exp\left[\frac{h_{lg}(\theta_b - \theta_B)}{(\theta_B + \theta_\infty)(\theta_b + \theta_\infty)}\right] \tag{19}$$

where the cavity depth obtained from η_0 is

$$h = r_0^2\frac{\mathrm{Pe}}{4\eta_0\sqrt{S_\alpha}}. \tag{20}$$

Deflection of the Electron Beam. The electron beam is deflected by Lorentz force

$$\Lambda\frac{d\mathbf{v}}{dt} = \mathbf{v} \times \mathbf{B} \tag{21}$$

where the accelerating voltage-to-Seebeck e.m.f. parameter Λ can be seen to be a crucial factor. Since Lorentz force acting on an electron is perpendicular to local velocity, the magnitude of $\mathbf{v}$ is constant, which can be determined from energy conservation $v = (2eV/m)^{1/2}$. Substituting velocity $\mathbf{v} = v\mathbf{e}_t$ into Eq. (21) gives

$$\Lambda \frac{d\mathbf{e}_t}{dt} = \mathbf{e}_t \times \mathbf{B}. \tag{22}$$

The displacement of the electron is

$$\Delta\mathbf{r} = v \int_t^{t+\Delta t} \mathbf{e}_t dt. \tag{23}$$

The location of the electrode is specified by $\mathbf{r} = y_e\mathbf{j} + z_e\mathbf{k}$. Titlting workpieces is available to reduce deflection. For a tilt angle χ_e, the direction of an emitted electron at the electrode yields $\mathbf{e}_t = \sin\chi_e\mathbf{j} - \cos\chi_e\mathbf{k}$.

Solution Procedure. After temperature is obtained (Wei et al. 1993, 1997), thermoelectric fields are found as follows:

1 Electrostatic potential is calculated by Eq. (5) associated with boundary conditions (9)–(11).
2 Electric currents are found from $\mathbf{j}_1 = -\Gamma\nabla\Omega_1$, $\mathbf{j}_2 = -\nabla\Omega_2$.
3 Magnetic flux densities in dissimilar metals are determined by Eq. (8) with boundary conditions (12)–(14).
4 Deflection of the electron beam is determined from Eqs. (22) and (23) until the cavity depth is reached.

Since scalar potential Ω is discontinuous at the contact surface, as can be seen from Eqs. (10) and (11), the contact surface is conveniently selected as the surface of a half control volume (Patankar, 1980). Equation (12) is automatically satisfied for the continuous vector potential $\mathbf{A}$. Equation (13) (or Eq. (14)) implies that $\partial A_x/\partial y$ (or $\partial A_z/\partial y$) have a finite jump across the interface. As a result, Eq. (13) (or equation (14)) was discretized by introducing an interface conductivity (Patankar, 1980).

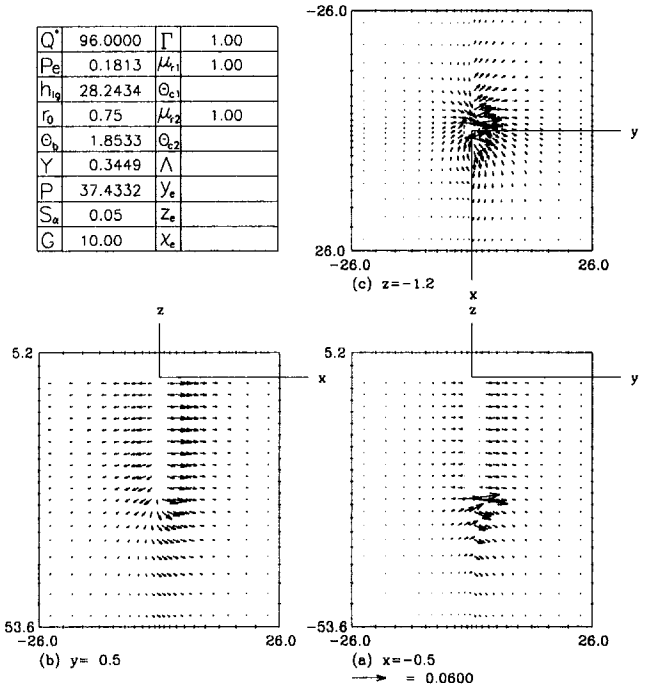

Fig. 2 Distribution of dimensionless electric current density on (a) transverse, (b) longitudinal, and (c) horizontal planes crossing the cavity in rear region of metal 1

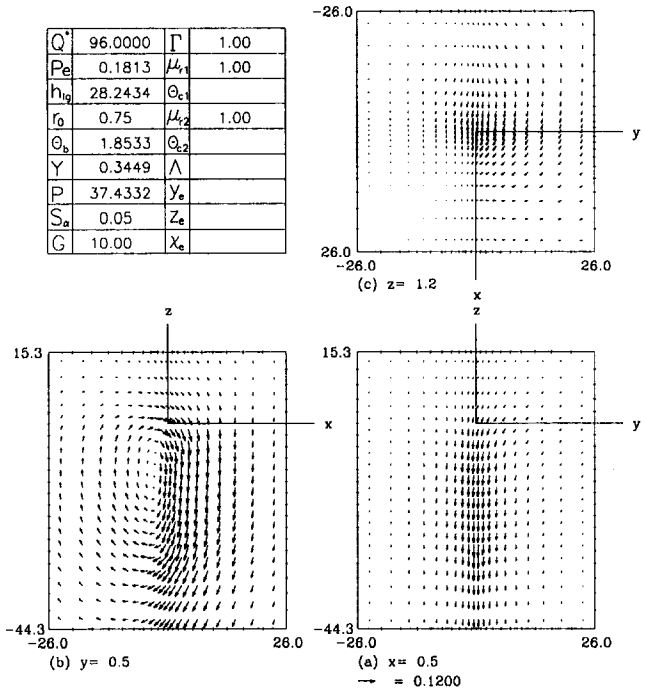

Fig. 3 Distribution of dimensionless magnetic flux density on (a) transverse, (b) longitudinal, and (c) horizontal planes crossing a point in the surroundings, front region, and on the side of metal 1

Discretized equations were solved by an SOR method (Patankar, 1980). For sufficient accuracy, a nonuniform grid of 41 × 41 × 45 nodal points were selected. The spacing ratios between adjacent grids were 1.1 for depths $z < -h$ and $z > 0$ and unity between $-h \le z \le 0$, while those in the x and y directions outwards from the cavity were 1.2. Convergence was checked by examining the iterated scalar and vector potentials with relative deviations less than 10^{-4}. Electrostatic potential and magnetic flux density in each discretized cell are also satisfied by

$$\iint \nabla\Omega \cdot \mathbf{n} dA < 10^{-6}, \quad \iint \mathbf{B} \cdot \mathbf{n} dA < 10^{-8} \tag{24}$$

where dA is the differential area on the surface of a cell.

Results and Discussion

The independent parameters controlling the process for welding dissimilar metals are those governing the thermoelectric field, μ_{r1}, μ_{r2}, Γ, G, temperature field, Q^*, Pe, and beam deflection, Λ. Values of these parameters were estimated from properties of iron, nickel, and copper, and working conditions for beam power, energy distribution parameter, and welding speed

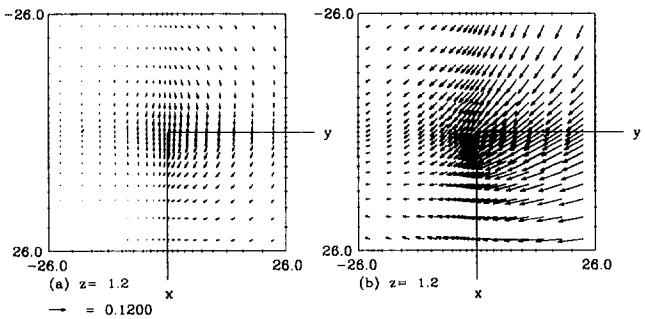

Fig. 4 Distribution of dimensionless magnetic flux density on horizontal plane in the surroundings for (a) Pe = 0.04532 and (b) Γ = 100

between 2400 and 5000 W, 1.5×10^{-4} and 10^{-3} m, and 2×10^{-4} and 2×10^{-3} m/s, respectively.

The computed dimensionless thermoelectric currents on typical transverse, longitudinal, and horizontal planes crossing the cavity in dissimilar metals are presented in Fig. 2(*a*), (*b*), and (*c*), respectively. Values of dimensionless parameters are listed in the table on the upper left. Evidently, no electric currents exist in the surroundings and cavity, as shown in Figs. 2(*a*) and (*b*). In the upper region above the cavity base, thermoelectric currents flow in a nearly horizontal direction from metal 2 to metal 1. Currents become radially divergent in metal 1. The *z*-components of currents in metal 1 are downward while those in metal 2 are upwards near the contact surface below the cavity. This can be interpreted from Eq. (10) for a positive temperature gradient. The horizontal plane result from Fig. 2(*c*) shows that thermoelectric currents in metal 2 primarily flow toward the cavity, while the currents mostly generated on the contact surface near the cavity in metal 1 flow outwards and gradually turn to the front region of the cavity. Therefore, the *x*-components of currents in the front region of metals 1 and 2 are, respectively, positive and negative. This is attributed to a negative temperature gradient in Eq. (11). Opposite results can be found in the rear region. The contact surface evidently provides both a source and sink for thermoelectric currents. In view of a larger Seebeck coefficient, current densities in metal 1 are higher than those in metal 2. High temperature gradients and surface effects induce strong currents near the bottom and around the wall of the cavity. The maximum current density is 0.059, which corresponds to 2×10^6 A/m^2 for joining dissimilar metals such as nickel and copper irradiated by an electron beam of a radius 10^{-3} m. Interestingly, this current density is higher than that of the electron beam. The circulations of thermoelectric currents on horizontal and transverse planes as sketched by Blakeley and Sanderson (1984) are similar to this work. Currents flow from metal 2 to 1 on a transverse plane also agree with the theoretical prediction made by Wei and Lee (1989) and Wei and Lii (1990).

The distributions of induced dimensionless magnetic flux density on typical transverse, longitudinal, and horizontal planes across a point in the surroundings and front region and on the side of metal 1 are shown in Figs. 3(*a*)–(*c*), respectively. Results can be interpreted by referring to the previous figure and applying the right-hand rule to find the direction of magnetic flux density near a current vector. Since thermoelectric currents direct in the positive *y*-direction the induced magnetic lines circulate in the surroundings and metals, as shown in Figs. 3(*a*) and (*b*). After emerging from the rear region of metals into the surroundings, magnetic lines turn to face the incoming solid, enter the front region, and complete circulations in the lower region. A top view from Fig. 3(*c*) shows that magnetic lines in the surroundings (and in the upper region of metals) on the sides of metals 1 and 2 are, respectively, in clockwise and counterclockwise directions. The directions of magnetic lines

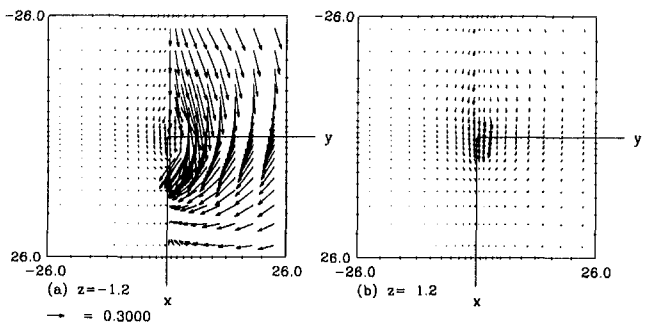

Fig. 6 Distribution of dimensionless magnetic flux density on horizontal planes at (a) $z = -1.2$ and (b) $z = 1.2$ for magnetic permeabilities $\mu_{r1} = 10$, $\mu_{r2} = 1$ ($\theta_{c1} = 0.4933$)

sketched by Blakeley and Sanderson (1984), Wei and Lii (1990), and Paulini et al. (1990) are misleading since they are towards the solidified region. In view of higher currents, magnetic field is stronger in metal 1.

The effects of the Peclet number on the magnetic field in the surroundings are presented in Fig. 4(*a*). Interestingly, a decrease in the Peclet number increases and decreases the magnitudes of the positive *x* and negative *y*-components of magnetic flux density, respectively (see Fig. 3(*c*)). This is because of a decrease in vertical temperature gradient (Wei et al., 1990) and the associated low thermoelectric currents circulating on vertical planes around the cavity. Using Eq. (3), the circulations of magnetic flux density therefore decrease. Increasing the electrical conductivity ratio between metals 1 and 2 significantly raises magnitudes of the negative-*y* component of magnetic flux density, as shown in Fig. 4(*b*).

Figure 5 shows that an increase in magnetic permeability of metal 2 enhances magnetic field, especially the positive *y*-component of magnetic flux density in metal 2 (see Fig. 3). Low magnetic flux densities in the surroundings, cavity and metal 1 are due to relative magnetic permeability of unity, which result from the existence of free space, liquid, and temperatures above the Curie point. Without accounting for the reduction of magnetic permeability magnetic field is overestimated. Magnetic field, especially the magnitudes of the negative *y*-component of magnetic flux density in metal 1, increases with magnetic permeability of metal 1, as presented in Fig. 6(*a*). From Figs. 5(*b*) and 6(*b*) it is interestingly found that the magnitudes of the negative *y*-component of magnetic flux density in the surroundings are significantly affected by magnetic permeability of metal 2 while those of the positive *x*-component are dominated by magnetic permeability of metal 1.

Deflections of the beam projected on planes parallel and perpendicular to the joint face for different values of the dimensionless accelerating voltage-to-Seebeck e.m.f. parameter are shown in Figs. 7(*a*) and (*b*), respectively. A decrease in the

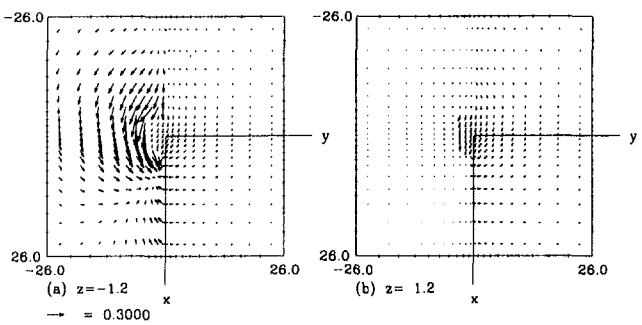

Fig. 5 Distribution of dimensionless magnetic flux density on horizontal planes at (a) $z = -1.2$ and (b) $z = 1.2$ for magnetic permeabilities $\mu_{r1} = 1$, $\mu_{r2} = 10$ ($\theta_{c2} = 0.4933$)

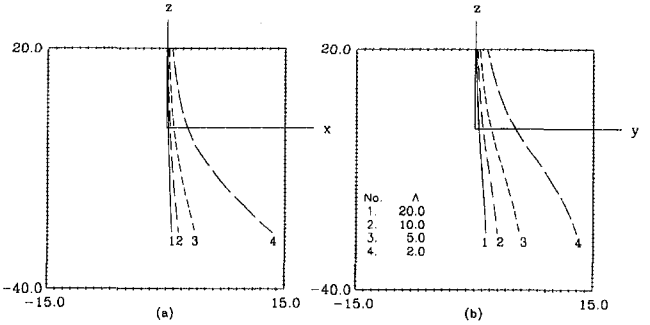

Fig. 7 Deflections of electron beam projected on (a) longitudinal and (b) transverse planes for different values of the dimensionless accelerating voltage-to-Seebeck e.m.f. parameter

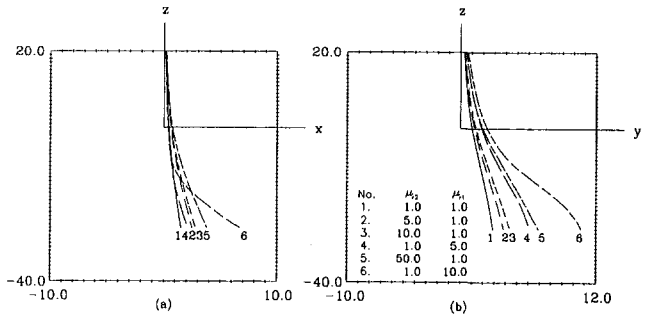

Fig. 8 Deflections of electron beam projected on (a) longitudinal and (b) transverse planes for different magnetic permeabilities

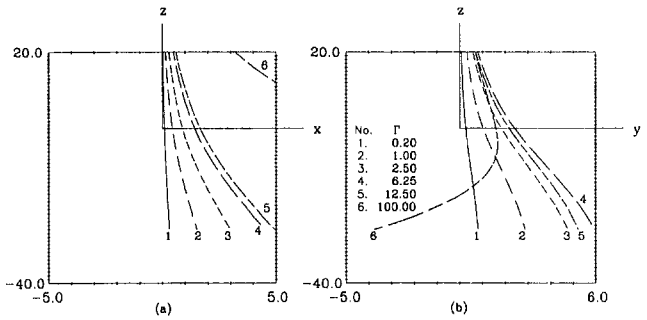

Fig. 10 Deflections of electron beam projected on (a) longitudinal and (b) transverse planes for different electrical conductivity ratios between metals 1 and 2

dimensionless accelerating voltage-to-Seebeck e.m.f. parameter or an increase in the Seebeck effect increases deflection (Wei and Lii, 1990). The maximum misalignment increases from twice to more than ten times the energy distribution parameter of the beam as the dimensionless accelerating voltage-to-Seebeck e.m.f. parameter decreases from 20 to 2. Even though the electron gun is aligned with the joint line, the deflection of the beam is toward the front region and the side of metal 1. From Lorentz force $\mathbf{j} \times \mathbf{B}$, the deflection towards positive x and y-directions is, respectively, attributed to negative y and positive x-components of the magnetic fields in front regions of the surroundings (see Fig. $3(c)$) and metal 1. The missed joint in metal 1 is in accordance with the experimental observation made by Nazarenko (1982) for welding nickel and copper and the computed results obtained from Wei and Lii (1990) by choosing a negative incident angle.

Deflections on longitudinal and transverse planes for different magnetic permeabilities of metals 1 and 2 are presented in Fig. $8(a)$ and (b), respectively. Deflections in the surroundings and bulk metals are increased with magnetic permeabilities. In contrast to the deflection in the y-direction it is interestingly found that the x-component of deflection in the surroundings are primarily affected by magnetic permeability of metal 2. This is attributed to a greater increase in the magnitude of the negative y-component of magnetic flux density (see Figs. $5(b)$ and $6(b)$). In view of a significant increase of magnetic field in metal 1 (see Figs. $5(a)$ and $6(a)$), the missed joint is dominated by magnetic permeability of metal 1.

Deflections in the x and y-directions for different values of the dimensionless parameter governing effective electric contact resistance are shown in Fig. $9(a)$ and (b), respectively. A decrease of effective electrical contact resistance implies increases in thermoelectric currents and deflection (Wei and Lii, 1990). Fig. $10(a)$ shows that deflection parallel to the joint plane increases with electrical conductivity ratio between metals 1 and 2. This is attributed to an increase in magnitudes of the negative y-component of magnetic flux density (see Fig. $4(b)$). The y-component of deflection is also enhanced by increasing the electrical conductivity ratio from 0.2 to 6.25, as can be seen from Fig. $10(b)$ (Wei and Lii, 1990). Interestingly, a further increase in the electrical conductivity ratio reduces the deflection. This is because a high electrical conductivity ratio gives rise to a large deflection in the x-direction (see Fig. $10(a)$) and the associated reduction of magnetic flux density.

Figure 11 shows that an increase of the dimensionless beam power results in an increase of deflection (Wei and Lii, 1990) due to a higher temperature gradient (Wei et al. 1990; 1997). In Fig. $12(a)$ and (b) it can be seen that increasing Peclet number enhances and reduces deflections in the x and y-directions, respectively. This is attributed to increases in the circulations of magnetic flux densities on horizontal planes around the cavity, as mentioned previously. Comparing to the opposite result obtained by Wei and Lii (1990) indicates that using the y-z two-dimensional model to investigate the effects of the Peclet number on missed joint is oversimplified. The present work also investigated the effects of the parameter approximating convection on deflection. It was found that the x and y-components of deflection are slightly increased with the parameter approximating convection.

A shift of the electron gun from the joint plane or a rotation of workpieces can reduce deflection as shown in Fig. 13. The curved weld pool encompasses almost all the joint face when the workpiece is shifted by a dimensionless distance of 3.0 towards the right side and rotated counterclockwise by 2.5 degrees relative to the electron gun at $z_e = 100$.

As shown in Fig. 14, a missed joint predicted by the present work is found to agree with available experimental data obtained from Nazarenko (1982) using a beam power of 2400 W to weld nickel and copper. Since working conditions of the experiment were insufficient, to achieve a good agreement in dimensionless parameters, Pe $= 3.162 \times 10^{-3}$, $S_\alpha = 0.14$, $G = 14.67$, $\Gamma = 10$, $\mu_{r1} = 1$, $\mu_{r2} = 600$, $\theta_{c2} = 0.292$, $\Lambda = 2000$, $x_e = 0$, $y_e =$

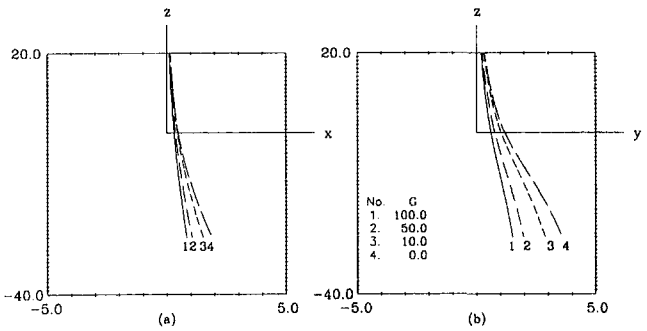

Fig. 9 Deflections of electron beam projected on (a) longitudinal and (b) transverse planes for different values of dimensionless effective electrical contact resistance parameter

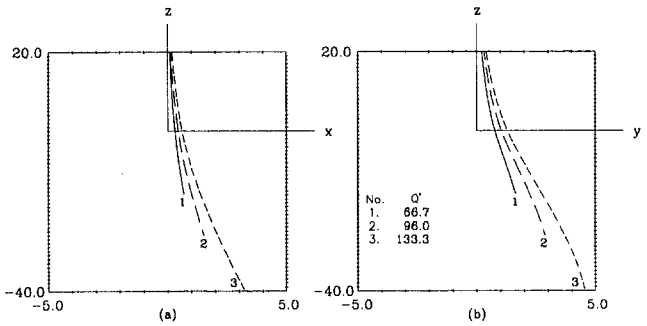

Fig. 11 Deflections of electron beam projected on (a) longitudinal and (b) transverse planes for different dimensionless beam powers

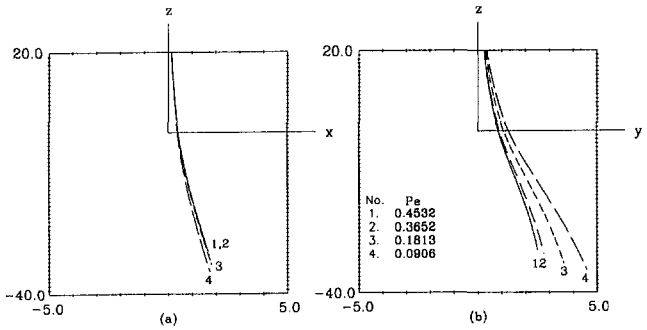

Fig. 12 Deflections of electron beam projected on (a) longitudinal and (b) transverse planes for different values of Peclet number

-6.67, $z_e = 667$ were chosen. They were evaluated from a welding speed and energy distribution parameter of 2×10^{-4} m/s and 1.5×10^{-4}m, respectively.

Conclusions

The following conclusions are drawn:

1 This study provides a general understanding of three-dimensional missed joint caused by thermoelectric phenomena in electron-beam welding dissimilar metals for the first time. Deflection of the beam from the electron gun to the top surface and into bulk metals can be predicted. A specification of the incident angle, as proposed by a two-dimensional model, is not required. The computed thermoelectric currents, magnetic and electric fields, and missed joint are found to agree with experimental observations and two-dimensional results.

2 Thermoelectric currents flow from metal 2 to metal 1 having a larger Seebeck coefficient. The contact surface provides both a source and sink for thermoelectric currents. In metal 1 thermoelectric currents are primarily generated at the contact surface near the cavity. Flows are outwards and gradually towards the front region of the cavity. On the other hand, thermoelectric currents in metal 2 mostly flow toward the cavity. The flow of currents in the upper region above the cavity base is nearly parallel to the top surface. In the lower region vertical components of currents are downwards in metal 1 near the contact surface while those in metal 2 are upwards. High currents occur at the bottom and around the cavity wall.

3 Magnetic lines emerge from the rear region of bulk metals into the surroundings, turn to face the incoming solid, enter the front region, and complete circulations in the lower region, as observed on a longitudinal plane. A top view shows that magnetic lines in the surroundings and upper region of metals on the sides of metals 1 and 2 are, respectively, in clockwise and counterclockwise directions.

4 The electron beam is deflected toward the incoming solid and metal 1. This is attributed to the negative y and positive x-components of magnetic flux density in front regions on the side of metal 1.

5 Deflection of the beam is reduced by increasing the dimensionless accelerating voltage-to-Seebeck e.m.f. parameter and effective electric contact resistance parameter, and decreasing dimensionless beam power.

6 An increase of the Peclet number enhances and reduces deflections in the x and y-directions, respectively.

7 Decreasing magnetic permeabilities of dissimilar metals reduces deflections in the surroundings and metal 1. The effect of magnetic permeability of metal 2 on the x-component of deflection in the surroundings is more pronounced than magnetic permeability of metal 1. On the other hand, the y-component of deflection in the surroundings and metal 1 is dominated by magnetic permeability of metal 1.

8 Deflection increases with the electrical conductivity ratio between metals 1 and 2 (e.g., $\Gamma < 6.25$). A further increase in the electrical conductivity ratio reduces the y-component of deflection.

9 Shifting the electron gun from the joint line and tilting workpieces are available to reduce misalignment.

10 Accounting for decreases in magnetic permeability for liquid and temperatures above the Curie point is necessary.

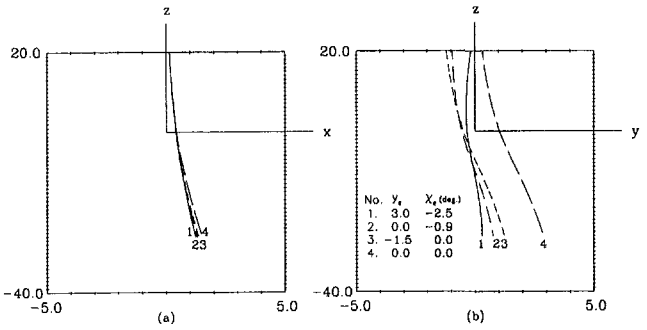

Fig. 13 Deflections of electron beam projected on (a) longitudinal and (b) transverse planes for different locations of the electron gun and tilt angles of workpieces

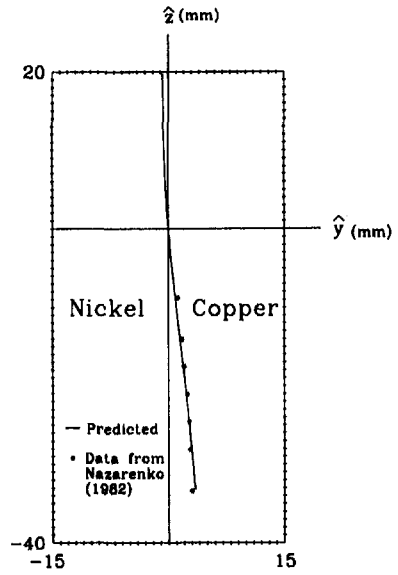

Fig. 14 Comparison of missed joint predicted by this work and experimental data from Nazarenko (1982) in welding nickel and copper

Acknowledgments

Support for this work was provided by the National Science Council, Taiwan, China, under Grant No. NSC 81-0401-E-110-03 and is gratefully acknowledged.

References

Blakeley, P. J., and Sanderson, A., 1984, "The Origin and Effects of Magnetic Fields in Electron Beam Welding," *Welding Journal,* Vol. 63, pp. 42–49.

Cramer, K. R., and Pai, S.-I., 1973, *Magnetofluid Dynamics for Engineers and Applied Physicists,* Scripta Publishing, Washington, D.C., pp. 11–46.

Gau, C., and Viskanta, R., 1984, "Melting and Solidification of a Metal System in a Rectangular Cavity," *International Journal of Heat and Mass Transfer,* Vol. 27, pp. 113–123.

Giedt, W. H., 1971, *Thermophysics,* Van Nostrand Reinhold, New York, pp. 387–388.

Giedt, W. H., Wei, X.-C., and Wei, S.-R., 1984, "Effect of Surface Convection on Stationary GTA Weld Zone Temperatures," *Welding Journal,* Vol. 63, pp. 376-s–383-s.

Nayfeh, M. H., and Brussel, M. K., 1985, *Electricity and Magnetism,* John Wiley & Sons, Inc., New York, pp. 314–316.

Nazarenko, O. K., 1982, "Deflection of the Electron Beam in Electron-Beam Welding," *Avt. Svarka,* No. 1, pp. 33–39.

Patankar, S. V., 1980, *Numerical Heat Transfer and Fluid Flow,* Hemisphere, New York, pp. 50–51, 67–68.

Paulini, J., Simon, G., and Decker, I., 1990, "Beam Deflection in Electron Beam Welding by Thermoelectric Eddy Currents," *Journal of Physics, D: Applied Physics,* Vol. 23, pp. 486–495.

Schauer, D. A., and Giedt, W. H., 1978, "Prediction of Electron Beam Welding Spiking Tendency," *Welding Journal.,* Vol. 57, pp. 189s–195s.

Shercliff, J. A., 1979, "Thermoelectric Magnetohydrodynamics," *Journal of Fluid Mechanics,* Vol. 91, pp. 231–251.

Tong, H., and Giedt, W. H., 1969, "Radiographs of the Electron Beam Welding Cavity," *The Review of Scientific Instruments,* Vol. 40, pp. 1283–1285.

Watanabe, K., Shida, T., Suzuki, M., Okamura, H., Sejima, I., Kita, H., and Yonezawa, T., 1975, "Some Problems Associated With Deep Penetration Electron Beam Welding of Heavy Section Steels," *Proceedings of Symposium of Advanced Welding Technology,* Japan Welding Society, pp. 69–74.

Wei, P. S., and Chiou, L. R., 1988, "Molten Metal Flow Around the Base of a Cavity During a High-Energy Beam Penetrating Process," ASME JOURNAL OF HEAT TRANSFER, Vol. 110, pp. 918–923.

Wei, P. S., and Chow, Y. T., 1992, "Beam Focusing Characteristics and Alloying Element Effects on High-Intensity Electron Beam Welding," *Metallurgical Transactions,* Vol. 23B, pp. 81–90.

Wei, P. S., and Ho, J. Y., 1990, "Energy Considerations in High-Energy Beam Drilling," *International Journal of Heat and Mass Transfer,* Vol. 33, pp. 2207–2217.

Wei, P. S., and Lee, T. W., 1989, "Missed Joint for Welding Dissimilar Metals with an Electron Beam," *Abstracts of Papers,* Session 27B, The 70th American Welding Society Annual Meeting, Washington, D. C., April 2–7, pp. 178–180.

Wei, P. S., and Lii, T. W., 1990, "Electron Beam Deflection When Welding Dissimilar Metals," ASME JOURNAL OF HEAT TRANSFER, Vol. 112, pp. 714–720.

Wei, P. S., and Shian, M. D., 1993, "Three-Dimensional Analytical Temperature Field Around the Welding Cavity Produced by a Moving Distributed High-Intensity Beam," ASME JOURNAL OF HEAT TRANSFER, Vol. 115, pp. 848–856.

Wei, P. S., Wu, T. H., and Chow, Y. T., 1990, "Investigation of High-Intensity Beam Characteristics on Welding Cavity Shape and Temperature Distribution," ASME JOURNAL OF HEAT TRANSFER, Vol. 112, pp. 163–169.

Wei, P. S., Ho, C. Y., Shian, M. D., and Hu, C. L., 1997, "Three-Dimensional Analytical Temperature Field and Its Application to Solidification Characteristics in High or Low-Power-Density-Beam Welding," *International Journal of Heat and Mass Transfer,* Vol. 40, pp. 2283–2292.

Journal of Heat Transfer

Technical Notes

This section contains shorter technical papers. These shorter papers will be subjected to the same review process as that for full papers.

Numerical Prediction of Heat Transfer Coefficient for a Pin-Fin Channel Flow

H.-I. You [1,3] and C.-H. Chang [2,3]

Nomenclature

A_h = wetted surface area between fluid and pin-fins structure
D = hydraulic diameter, $4V/A_h$
D^* = porosity based characteristic length, $4V_f/A_h$ (VanFossen, 1982)
k = thermal conductivity of pure substance
k^* = effective thermal conductivity
$\dot{m}$ = mass flow rate
T = temperature
u = volume averaged velocity in x-direction
V = total channel volume
V_f = volume occupied by fluid flow
x, y = coordinate axes parallel and perpendicular to the wall

Subscripts

f = fluid
i = inlet section
m = matrix
o = outlet section
w = wall

Introduction

Thermal convection in fluid saturated porous medium represents a highly efficient technique for compact heat exchangers in recent thermal applications. Porous medium is a solid body that contains pores. Pores are void spaces which are distributed randomly throughout the material. Typical compositions for porous media are packed spheres, foam metal, fibers, or screens. A bundle of series-connected capillaries, in which the flow path may branch and, later on, join together, is considered to be a theoretical model for porous structure (Scheidegger, 1974). In this regard, a large number of short pin fins embedded in a flow channel which forms a labyrinth-like flow path may also be considered a porous structure.

Staggered arrays of metallic pin fins are used to increase the heat transfer to the coolant in the internal cooling channels of gas turbine blades. Experimental structures were often utilized to investigate the effects of fin configuration, array orientation, and pin aspect ratio on the heat transfer between the endwall surfaces and flowing coolant (e.g., Lau et al., 1985; VanFossen, 1982; Metzger et al., 1984). The overall heat transfer rate, expressed as a Nusselt number, was then obtained as a function of the associated Reynolds number. The cooling effectiveness of a compact heat exchanger using pin-fins internal structure is primarily due to the significant increase in the heat transfer area. To speed the heat transfer rate and reduce the maximum temperature rise in a pin-fins matrix, high conductivity metal materials are used. For high-velocity fluid flow through a high conductivity solid matrix, local thermal nonequilibrium between the fluid and the pin-fins structure is generally encountered (Cheng, 1979; Vafai and Tien, 1981). Based on Darcian flow assumption, Koh and Colony (1974) provided a thermal analysis in a channel packed with porous materials. Using the internal heat transfer model proposed by Kar and Dybbs (1982), the forced convection heat transfer for non-Darcian fluid flow passing through sintered bronze beads was analyzed by Hwang and Chao (1994).

It was seen that to analytically obtain the thermal results for a porous channel flow, the internal heat transfer rate between the fluid and the porous medium should be known beforehand (Vafai and Sozen, 1990). In this paper, taking several temperature measurements used as the boundary conditions in the thermal analysis, the heat transfer rate of the pin-fins channel flow is predicted.

Problem Derivation

The fluid flow through a pin-fins porous structure is used to represent an efficient cooling device. The steady, two-dimensional flow is assumed. A pictorial view of the pin-fins porous channel associated with the coordinate system is shown in Fig. 1. The governing equations for flow and heat transfer are given as follows:

1 Momentum equation

$$-\frac{dp_f}{dx} = -\mu\frac{d^2u}{dy^2} + \frac{\mu}{K}u + \frac{F}{\sqrt{K}}\rho u^2 \qquad (1)$$

[1] Associate Professor; e-mail: hiyou@nchu.edu.tw
[2] Graduate Student.
[3] Department of Mechanical Engineering, National Chung-Hsing University, Taichung, Taiwan, Republic of China.

Contributed by the Heat Transfer Division of THE AMERICAN SOCIETY OF MECHANICAL ENGINEERS. Manuscript received by the Heat Transfer Division December 3, 1996; revision received June 27, 1997; Keywords: Forced Convection; Porous Media. Associate Technical Editor: K. Vafai.

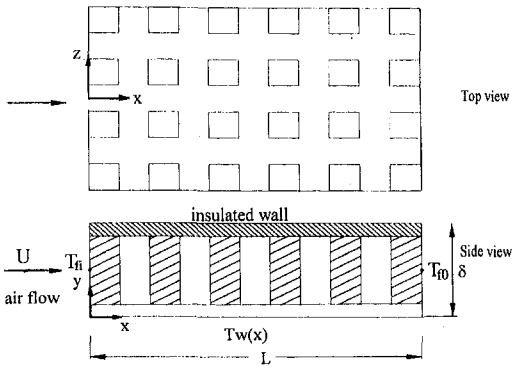

ε_f	0.462	0.599	0.679	0.782	0.943*
A_h(mm²)	51542	61042	64882	66702	
D^*(mm)	7.74	8.48	9.04	10.13	25.9
D(mm)	16.75	14.15	13.31	12.95	27.46

*Data taken and calculated from VanFossen (1982)

Fig. 1 Physical model of pin-fins channel flow

2 Continuity equation

$$\int_0^\delta u dy = U\delta \tag{2}$$

where U is the Darcian averaged velocity. The flow analysis for the determination of permeability K, inertial constant F, and the velocity solution u were described in detail by You and Chang (1997).

3 Energy equations (Cheng, 1979)

$$\text{for fluid flow} \quad (\rho c_p)_f u \frac{\partial T_f}{\partial x} = \epsilon_f k_f^* \left(\frac{\partial^2 T_f}{\partial x^2} + \frac{\partial^2 T_f}{\partial y^2} \right) - h'(T_f - T_m) \tag{3}$$

$$\text{for solid matrix} \quad \epsilon_m \left(k_{mx}^* \frac{\partial^2 T_m}{\partial x^2} + k_{my}^* \frac{\partial^2 T_m}{\partial y^2} \right) = h'(T_m - T_f) \tag{4}$$

where h' is the local convection heat transfer coefficient per unit volume between fluid and solid interfaces (Koh and Colony, 1974).

From the flow analysis it can be shown that a constant velocity flow prevails in the pin-fins channel and h' may assume a constant value. The effective thermal conductivity of the porous matrix, k_{mx}^* and k_{my}^*, is generally direction dependent and may take different values. However, an equal value, k_m^*, is assumed in the present calculation. To account for the dispersion effect in the presence of the solid matrix, an initial simulation is performed by assuming that $k_f^* = \epsilon_f k_f$ and $k_m^* = (1 - \epsilon_f) k_m$, where ϵ_f is the porosity of the pin-fins matrix. To complete the problem description, the temperature boundary conditions are described in the following sections.

Left Boundary. The incoming fluid temperature T_{fi} is assumed uniform at the inlet section. The temperature boundary conditions for the porous matrix and incoming fluid are

$$T_f = T_m = T_{fi} \quad \text{for} \quad 0 < y < \delta \quad \text{at} \quad x = 0. \tag{5}$$

Upper Boundary. The upper wall is assumed adiabatic, and the boundary conditions are mathematically defined using

$$\partial T_m / \partial y = 0 \quad \text{and} \quad T_f = T_m \quad \text{at} \quad y = \delta \quad \text{for} \quad 0 \le x \le L. \tag{6}$$

Right Boundary. A zero temperature gradient along x at the outlet section is assumed, ie.,

$$\frac{\partial T_m}{\partial x} = 0 \quad \text{for} \quad 0 < y < \delta \quad \text{at} \quad x = L. \tag{7}$$

Since internal convection heat transfer coefficient h' is not known before the computation of the temperature fields, an extra fluid temperature T_{fo} at the outlet section is measured. This exit fluid temperature is used as the matching condition for the calculation of h'.

Lower Boundary. To simulate the heat flux carried away by the pin-fins channel flow, electrical heat energy generated inside the lower wall is provided. The temperature distribution of the heated wall, $T_w(x)$, is measured, and is symbolically written as

$$T_m = T_w(x) \quad \text{and} \quad T_f = T_m \quad \text{at} \quad y = 0 \quad \text{for} \quad 0 \le x \le L. \tag{8}$$

Heat Transfer Rate

The heat energy q being dissipated from the pin-fins channel can be calculated using

$$q = \dot{m} c_p (T_{fo} - T_{fi}). \tag{9}$$

The local Nusselt number along the channel wall is determined by using

$$\mathrm{Nu}_x = \frac{h_w(x) D^*}{k_f} = D^* \left[-\epsilon_f k_f^* \left(\frac{\partial T_f}{\partial y} \right)_w - (1 - \epsilon_f) k_m^* \left(\frac{\partial T_m}{\partial y} \right)_w \right] / [k_f (T_w(x) - T_a(x))] \tag{10}$$

where T_a is the fluid average temperature defined by

$$T_a(x) = \frac{1}{\delta U} \int_0^\delta T_f(y) u dy. \tag{11}$$

The averaged Nusselt number and the Reynolds number are defined, respectively, using

$$\mathrm{Nu} = \frac{1}{L} \int_0^L \mathrm{Nu}_x dx, \quad \mathrm{Re} = \frac{\rho U D^*}{\mu}. \tag{12}$$

Note that the fluid thermal properties, ρ, c_p and μ, are evaluated at the fluid mean temperature, $(T_{fo} + T_{fi})/2$.

Numerical Method

To solve Eqs. (3) and (4) for the temperature solutions, $T_f(x, y)$ and $T_m(x, y)$, these two equations are rewritten as follows:

$$\left[\frac{\partial T_f}{\partial x} \right]_{\text{new}} = \frac{1}{(\rho c_p)_f u} \left[\epsilon_f k_f^* \left(\frac{\partial^2 T_f}{\partial x^2} + \frac{\partial^2 T_f}{\partial y^2} \right) - h'(T_f - T_m) \right]_{\text{old}} \tag{13}$$

$$\left[\left(\frac{\partial^2 T_m}{\partial x^2} + \frac{\partial^2 T_m}{\partial y^2} \right) - H' T_m \right]_{\text{new}} = -H' [T_f]_{\text{old}} \tag{14}$$

where $H' = h'/\epsilon_m k_m^*$. Equation (13) is an initial value problem of T_f which can be solved by subroutine IVPAG called from IMSL (1989). Equation (14) is a Helmholtz type boundary value problem of T_m which can be solved by the subroutine BVPFD from IMSL. Since these two temperature distributions, T_f and T_m, appear in both sides of Eqs. (13) and (14), the subscript "new" is added in the left hand side to denote the new quantities being solved, while the subscript "old" is added in the right hand side to represent the presumed trial values. Starting from an initial (old) trial solution for both temperature fields, the new temperature solutions of T_f and T_m are obtained. Iterative numerical procedures are needed in order to obtain the final convergent solutions by satisfying the following convergent criteria for T_f and T_m, i.e.:

$$\left|\frac{(T_f)_{\text{new}} - (T_f)_{\text{old}}}{(T_f)_{\text{old}}}\right| \le 10^{-3}, \quad \text{and}$$

$$\left|\frac{(T_m)_{\text{new}} - (T_m)_{\text{old}}}{(T_m)_{\text{old}}}\right| \le 10^{-3}. \tag{15}$$

Since internal convection heat transfer coefficient h' is not known during the calculation of the temperature fields, the initial estimated value of h' is given to start the computational process. The final solution of h' is obtained by matching the computed gas temperature with the measured temperature, T_{fo}, at the outlet section. The matching criterion for T_{fo} is determined by using

$$\left|\frac{(T_{fo})_{\text{mea.}} - (T_{fo})_{\text{com.}}}{(T_{fo})_{\text{mea.}}}\right| \le 10^{-3}. \tag{16}$$

To expedite the convergence, two initial trial values for h' are given, and an iterative numerical scheme similar to the shooting method is used.

Numerical Illustration

To illustrate the validity of the present numerical scheme, the heat transfer experiment for air flow through a pin-fins channel is conducted. Temperature measurements on the lower heated wall and for the incoming and outgoing air are taken. It should be noted that nonuniform wall temperatures are generally obtained because of uneven heating along the channel wall. Four pin-fin structures of different porosity ϵ_f associated with its effective heating surface area A_h are shown in Fig. 1. Since there is radiation heat loss from the insulation walls during the heat transfer test, a check is made for the dissipated heat energy calculated by Eq. (9) being less than the electrical power input

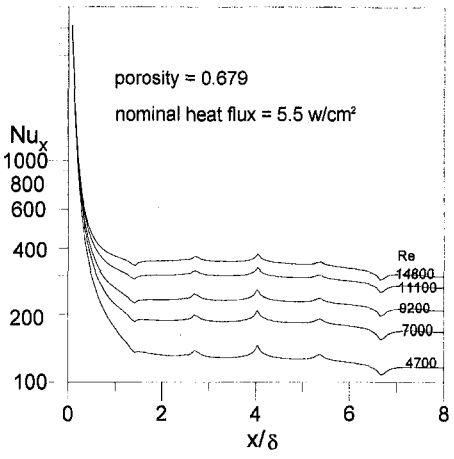

Fig. 2 Variation of the local Nusselt number along the heating wall

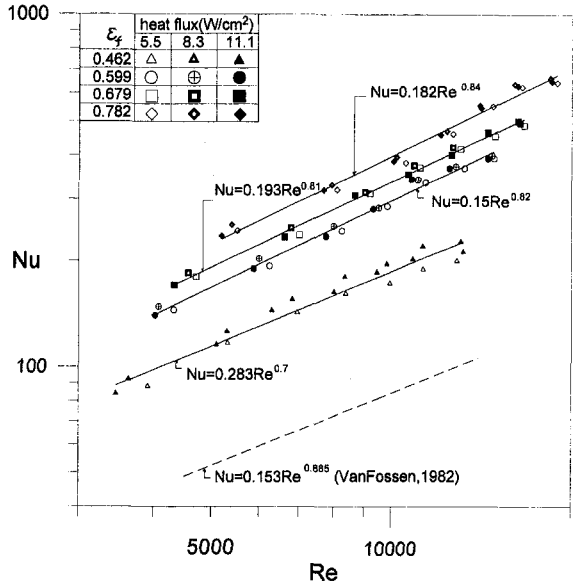

Fig. 3 Averaged Nusselt number for four units of pin-fins channel flow

denoted using the product of V (Voltage) and I (Amperes). To provide a self-check of the heat transfer result of the pin-fins channel flow, three different nominal heat flux, namely, 5.5, 8.3, and 11.1 Watts/cm^2 are imported from the heated wall to the cooling air flow.

Figure 2 shows the variations of Nu_x along the wall for several Re numbers. It was found that the value of Nu_x (and hence the convection heat transfer coefficient) is extremely large at $x = 0$ due to the zero thermal boundary thickness. However, Nu_x decays rapidly as the thermal layer developes, and a constant Nu_x value associated with the fully developed condition is reached at the downstream position. Several small wavy values for Nu_x that appeared in the line plotting were induced by the non-smooth nature of the stepwise temperature boundary conditions used in the numerical analysis. Figure 3 shows the averaged Nusselt numbers along with the best fit equations for four units of the pin-fins matrix. It should be noted that the Nusselt number is not dependent on the applied wall heat flux. The calculated Nusselt number exhibiting a random scatter within 6 percent for different dissipated heat flux is due to the experimental uncertainity during the temperature measurements. The relatively small dispersion of the thermal results can also be a self-check on the accuracy of the heat transfer rate. It is found that the heat transfer rate is higher for a high porosity matrix, which possesses a larger heating surface area. However, the heat transfer rate obtained by VanFossen (1982) was found to be much smaller than the present results as shown in Fig. 3. Since the inverse value of the hydraulic diameter D can be considered to be an indication of the effective heating surface area per unit channel volume, an increasing value of D (Fig. 1) can be used to explain the decreasing trend of the heat transfer rate (Fig. 3).

Conclusions

The forced convection heat transfer rate for a cooling fluid through a pin-fins porous channel is numerically predicted in this paper. The temperature boundary conditions were measured and a heat transfer analysis was performed. Two important results are given as follows: (1) flow experiencing a convection heat transfer process inside the pin-fins channel reaches the fully developed thermal state in the early downstream region; (2) the averaged Nusselt number for the wall shows an increasing function for Re. The heat transfer rate is higher for a porous matrix having a larger heating surface area.

Acknowledgment

This work was supported by National Science Council, Taiwan, R. O. C. under grant number NSC 83-0401-E005-068.

References

Cheng, P., 1979, "Heat Transfer in Geothermal Systems," *Advances in Heat Transfer,* Vol. 14, pp. 1–105.

Hwang, G. J., and Chao, C. H., 1994, "Heat Transfer Measurement and Analysis for Sintered Porous Channels," ASME JOURNAL OF HEAT TRANSFER, Vol. 106, pp. 456–464.

IMSL MATH/LIBRARY, 1989 Version 1.1, MALB-USM-UNBND-EN8912-1.1, IMSL Inc.

Kar, K. K., and Dybbs, A., 1982, "Internal Heat Transfer Coefficients of Porous Metals," *ASME Proceeding of the Winter Annual Meeting,* Phoenix, AZ, HTD Vol. 22, pp. 81–91.

Koh, J. C. Y., and Colony, R., 1974, "Analysis of Cooling Effectiveness for Porous Material in a Coolant Passage," ASME JOURNAL OF HEAT TRANSFER, Vol. 96, pp. 324–330.

Lau, S. C., Kim, Y. S., and Han, J. C., 1985, "Effects of Fin Configuration and Entrance Length on Local Endwall Heat/Mass Transfer in a Pin Fin Channel," ASME Paper NO. 85-WA/HT-62.

Metzger, D. E., Fan, C. S., and Haley, S. W., 1984, "Effects of Pin Shape and Array Orientation on Heat Transfer and Pressure Loss in Pin Fin Arrays," *ASME Journal of Engineering for Gas Turbines and Power,* Vol. 106, pp. 252–257.

Scheidegger, A. E., 1974, *The Physics of Flow Through Porous Media,* University of Toronto Press, Toronto, Canada.

Vafai, K., and Sozen, M., 1990, "Analysis of Energy and Momentum Transport for Fluid Flow Through a Porous Bed," ASME JOURNAL OF HEAT TRANSFER, Vol. 112, pp. 690–699.

Vafai, K., and Tien, C. L., 1981, "Boundary and Inertia Effects on Flow and Heat Transfer in Porous Media," *Int. J. of Heat Mass Transfer,* Vol. 24, pp. 195–203.

VanFossen, G. J., 1982, "Heat Transfer Coefficients for Staggered Arrays of Short Pin Fins," ASME JOURNAL OF HEAT TRANSFER, Vol. 104, pp. 268–274.

You, H. I., and Chang, C. H., 1997, "Determination of Flow Properties in Non-Darcian Flow," ASME JOURNAL OF HEAT TRANSFER, Vol. 119, pp. 190–192.

Local Heat Transfer and Velocity Measurements in a Rotating Ribbed Two-Pass Square Channel With Uneven Wall Temperatures

S.-S. Hsieh,[1,3] Y.-S. Wang,[2,3] and M.-H. Chiang[2,3]

Nomenclature

D_H = hydraulic diameter, $2WH/(W + H)$
e = rib height
Nu = Nusselt number, hD_H/k_f
p = pitch
R = mean rotation radius
Re_H = Reynolds number, UD_H/ν
Re_Ω = rotational Reynolds number, $\Omega D_H^2/\nu$
Ro = rotation number, $\mathrm{Re}_\Omega/\mathrm{Re}_H$
U = streamwise time mean velocity
U_o = entrance velocity
x = x-ordinate (streamwise) direction
y = y-ordinate (transverse) direction
y^+ = y/D_H
z = z-ordinate (spanwise) direction
z^+ = z/D_H
u' = velocity fluctuation

Greek Symbol

β = coefficient of thermal expansion and model orientation (see Fig. 1)
Ω = rotational speed
$\Delta\rho/\rho_i$ = density ratio based on the inlet bulk temperature

1 Introduction

Effective turbine blade cooling is necessary to enhance the efficiency of advanced aircraft engines. In general, convective cooling is used inside the blades by means of cooling passages. The internal cooling passages are connected at the ends, which lead to a serpentine flow path consisting of alternate channels of radially outward and inward flow. In addition, to promote turbulence and enhance heat transfer, roughened surfaces like the rib type are commonly used on the walls of these internal passages.

Rotation of turbine blade cooling passages gives rise to Coriolis and buoyancy forces that can significantly alter the local heat transfer in the inward coolant passage from the development of cross stream (Coriolis), as well as radial (buoyant) secondary flows. Consequently, the flow and hence, the heat transfer, in these rotating passages are quite different as compared to that in stationary channels. It is therefore recognized that comprehensive data as well as accurate methods for predicting flow and heat transfer are necessary. A detailed review of relevant studies was given in Hsieh and Liu (1996). For velocity measurements, it seems that there are few papers related to this topic—only one paper was found so far, Guidez (1989). For numerical study, Prakash and Zerkle (1992) reported a numerical prediction of turbulent flow and heat transfer in a radially rotating square duct, and recently, Dutta et al. (1996) conducted a numerical simulation of turbulent heat transfer in rotating smooth square ducts.

In addition, in the realistic condition the blade surface is subjected to uneven heat flux or temperature on the leading or trailing surface of the serpentine square channels. Furthermore, it is shown (Parsons et al., 1994) that the uneven wall heat flux or temperature creates local buoyancy forces that would change the effect of the rotation, resulting in different local heat transfer coefficients on the leading/trailing surface, especially for multipass flow channels. The results presented in this paper are aimed at studying the effect of uneven temperature and rotation on a two-pass square channel with two oppositely ribbed walls from both heat transfer and flow characteristics measurements.

2 Experimental Apparatus and Procedure

The present test facility initially was followed by Hsieh and Hong (1995) with a slight modification in heating element design and flow passage. It is almost the same as that of Hsieh and Liu (1996) except for different thermal boundary conditions and the extension for LDV measurements. It was comprised of a heated section, a blower, a motor, a heat source, two slip ring assemblies, a LDV, and a datalogger (shown in Fig. 1). To determine the locally averaged streamwise heat transfer coefficients in the channel along the flow direction, the two-pass test flow channel is divided into fifteen sheet copper sections followed by Zhang et al. (1995). Figure 1 illustrates the present experimental set up schematic.

The present system used for velocity measurements is a commercial two color four beam DANTEC fringe-type LDV system operated in the backward scatter mode, with the general layout

[1] Sun Yat-Sen Professor of Mechanical Engineering; Dean of Engineering; Fellow ASME; e-mail: sshsieh@mail.nsysu.edu.tw

[2] Graduate Student.

[3] Department of Mechanical Engineering, National Sun Yat-Sen University, Kaohsiung, Taiwan 80424, Republic of China.

Contributed by the Heat Transfer Division of THE AMERICAN SOCIETY OF MECHANICAL ENGINEERS. Manuscript received by the Heat Transfer Division February 6, 1996; revision received April 25, 1997; Keywords: Augmentation and Enhancement; Forced Convection; Turbines. Associate Technical Editor: R. D. Boyd.

Acknowledgment

This work was supported by National Science Council, Taiwan, R. O. C. under grant number NSC 83-0401-E005-068.

References

Cheng, P., 1979, "Heat Transfer in Geothermal Systems," *Advances in Heat Transfer,* Vol. 14, pp. 1–105.

Hwang, G. J., and Chao, C. H., 1994, "Heat Transfer Measurement and Analysis for Sintered Porous Channels," ASME JOURNAL OF HEAT TRANSFER, Vol. 106, pp. 456–464.

IMSL MATH/LIBRARY, 1989 Version 1.1, MALB-USM-UNBND-EN8912-1.1, IMSL Inc.

Kar, K. K., and Dybbs, A., 1982, "Internal Heat Transfer Coefficients of Porous Metals," *ASME Proceeding of the Winter Annual Meeting,* Phoenix, AZ, HTD Vol. 22, pp. 81–91.

Koh, J. C. Y., and Colony, R., 1974, "Analysis of Cooling Effectiveness for Porous Material in a Coolant Passage," ASME JOURNAL OF HEAT TRANSFER, Vol. 96, pp. 324–330.

Lau, S. C., Kim, Y. S., and Han, J. C., 1985, "Effects of Fin Configuration and Entrance Length on Local Endwall Heat/Mass Transfer in a Pin Fin Channel," ASME Paper NO. 85-WA/HT-62.

Metzger, D. E., Fan, C. S., and Haley, S. W., 1984, "Effects of Pin Shape and Array Orientation on Heat Transfer and Pressure Loss in Pin Fin Arrays," *ASME Journal of Engineering for Gas Turbines and Power,* Vol. 106, pp. 252–257.

Scheidegger, A. E., 1974, *The Physics of Flow Through Porous Media,* University of Toronto Press, Toronto, Canada.

Vafai, K., and Sozen, M., 1990, "Analysis of Energy and Momentum Transport for Fluid Flow Through a Porous Bed," ASME JOURNAL OF HEAT TRANSFER, Vol. 112, pp. 690–699.

Vafai, K., and Tien, C. L., 1981, "Boundary and Inertia Effects on Flow and Heat Transfer in Porous Media," *Int. J. of Heat Mass Transfer,* Vol. 24, pp. 195–203.

VanFossen, G. J., 1982, "Heat Transfer Coefficients for Staggered Arrays of Short Pin Fins," ASME JOURNAL OF HEAT TRANSFER, Vol. 104, pp. 268–274.

You, H. I., and Chang, C. H., 1997, "Determination of Flow Properties in Non-Darcian Flow," ASME JOURNAL OF HEAT TRANSFER, Vol. 119, pp. 190–192.

Local Heat Transfer and Velocity Measurements in a Rotating Ribbed Two-Pass Square Channel With Uneven Wall Temperatures

S.-S. Hsieh,[1,3] Y.-S. Wang,[2,3] and M.-H. Chiang[2,3]

Nomenclature

D_H = hydraulic diameter, $2WH/(W + H)$
e = rib height
Nu = Nusselt number, hD_H/k_f
p = pitch
R = mean rotation radius
Re_H = Reynolds number, UD_H/ν
Re_Ω = rotational Reynolds number, $\Omega D_H^2/\nu$
Ro = rotation number, $\mathrm{Re}_\Omega/\mathrm{Re}_H$
U = streamwise time mean velocity
U_o = entrance velocity
x = x-ordinate (streamwise) direction
y = y-ordinate (transverse) direction
y^+ = y/D_H
z = z-ordinate (spanwise) direction
z^+ = z/D_H
u' = velocity fluctuation

Greek Symbol

β = coefficient of thermal expansion and model orientation (see Fig. 1)
Ω = rotational speed
$\Delta\rho/\rho_i$ = density ratio based on the inlet bulk temperature

1 Introduction

Effective turbine blade cooling is necessary to enhance the efficiency of advanced aircraft engines. In general, convective cooling is used inside the blades by means of cooling passages. The internal cooling passages are connected at the ends, which lead to a serpentine flow path consisting of alternate channels of radially outward and inward flow. In addition, to promote turbulence and enhance heat transfer, roughened surfaces like the rib type are commonly used on the walls of these internal passages.

Rotation of turbine blade cooling passages gives rise to Coriolis and buoyancy forces that can significantly alter the local heat transfer in the inward coolant passage from the development of cross stream (Coriolis), as well as radial (buoyant) secondary flows. Consequently, the flow and hence, the heat transfer, in these rotating passages are quite different as compared to that in stationary channels. It is therefore recognized that comprehensive data as well as accurate methods for predicting flow and heat transfer are necessary. A detailed review of relevant studies was given in Hsieh and Liu (1996). For velocity measurements, it seems that there are few papers related to this topic—only one paper was found so far, Guidez (1989). For numerical study, Prakash and Zerkle (1992) reported a numerical prediction of turbulent flow and heat transfer in a radially rotating square duct, and recently, Dutta et al. (1996) conducted a numerical simulation of turbulent heat transfer in rotating smooth square ducts.

In addition, in the realistic condition the blade surface is subjected to uneven heat flux or temperature on the leading or trailing surface of the serpentine square channels. Furthermore, it is shown (Parsons et al., 1994) that the uneven wall heat flux or temperature creates local buoyancy forces that would change the effect of the rotation, resulting in different local heat transfer coefficients on the leading/trailing surface, especially for multipass flow channels. The results presented in this paper are aimed at studying the effect of uneven temperature and rotation on a two-pass square channel with two oppositely ribbed walls from both heat transfer and flow characteristics measurements.

2 Experimental Apparatus and Procedure

The present test facility initially was followed by Hsieh and Hong (1995) with a slight modification in heating element design and flow passage. It is almost the same as that of Hsieh and Liu (1996) except for different thermal boundary conditions and the extension for LDV measurements. It was comprised of a heated section, a blower, a motor, a heat source, two slip ring assemblies, a LDV, and a datalogger (shown in Fig. 1). To determine the locally averaged streamwise heat transfer coefficients in the channel along the flow direction, the two-pass test flow channel is divided into fifteen sheet copper sections followed by Zhang et al. (1995). Figure 1 illustrates the present experimental set up schematic.

The present system used for velocity measurements is a commercial two color four beam DANTEC fringe-type LDV system operated in the backward scatter mode, with the general layout

[1] Sun Yat-Sen Professor of Mechanical Engineering; Dean of Engineering; Fellow ASME; e-mail: sshsieh@mail.nsysu.edu.tw

[2] Graduate Student.

[3] Department of Mechanical Engineering, National Sun Yat-Sen University, Kaohsiung, Taiwan 80424, Republic of China.

Contributed by the Heat Transfer Division of THE AMERICAN SOCIETY OF MECHANICAL ENGINEERS. Manuscript received by the Heat Transfer Division February 6, 1996; revision received April 25, 1997; Keywords: Augmentation and Enhancement; Forced Convection; Turbines. Associate Technical Editor: R. D. Boyd.

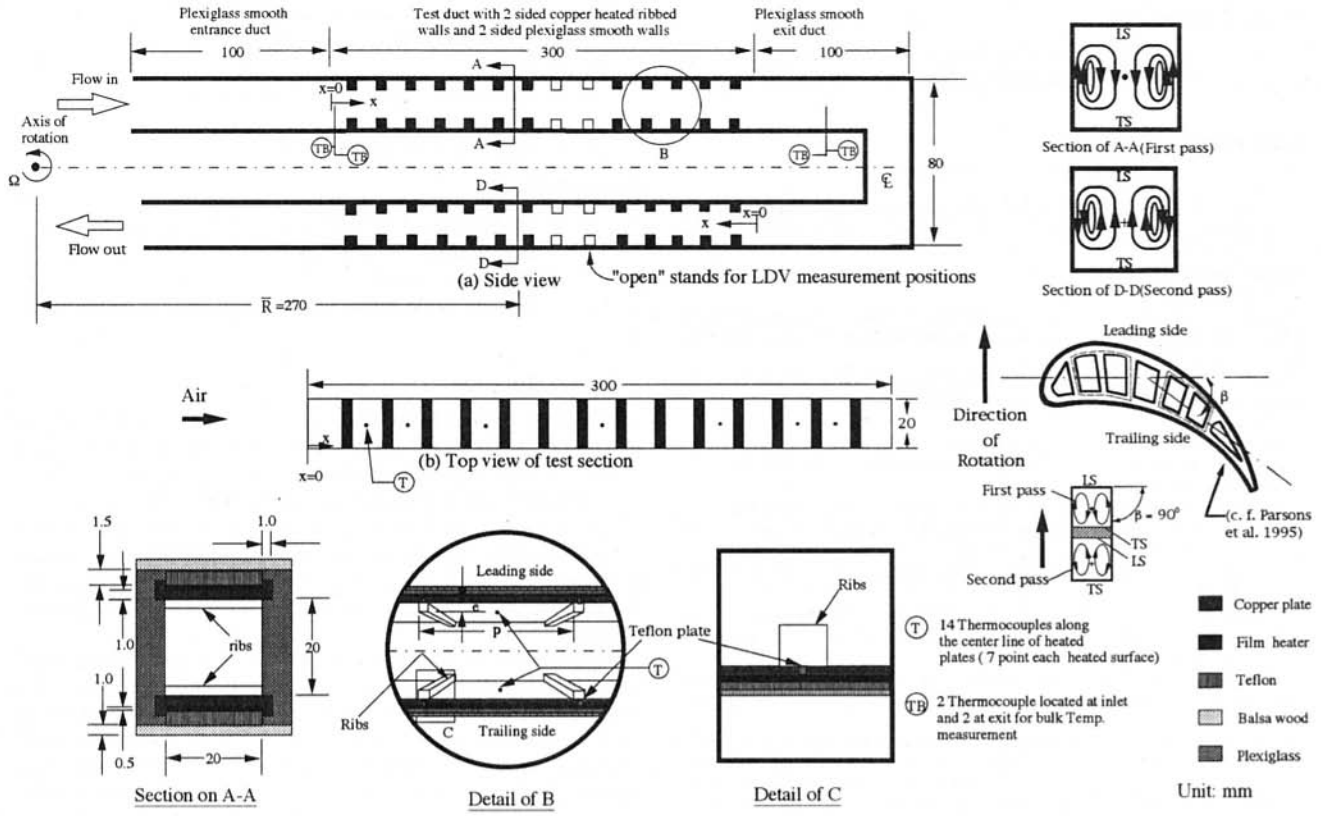

Fig. 1 Detailed thermocouple measurement position and dimensions of the test section

shown in Fig. 2. Standard DANTEC 55× modular optics and a model Stabilite 2016 4W Spectral Physics Ar^+ laser are mounted on a two-dimensional traversing system. The ellipsoidal probe volume dimensions were 640 μm × 76 μm, given, respectively, as the major and minor axes of the ellipsoid. Two separate LDV channels are formed by use of color separation; they are 514.5 nm (green light) and 488.0 nm (blue light) wavelength beams. These two beams form orthogonal fringes by means of a standard DANTEC two channels optical train. These two set of fringes allow the simultaneous measurement

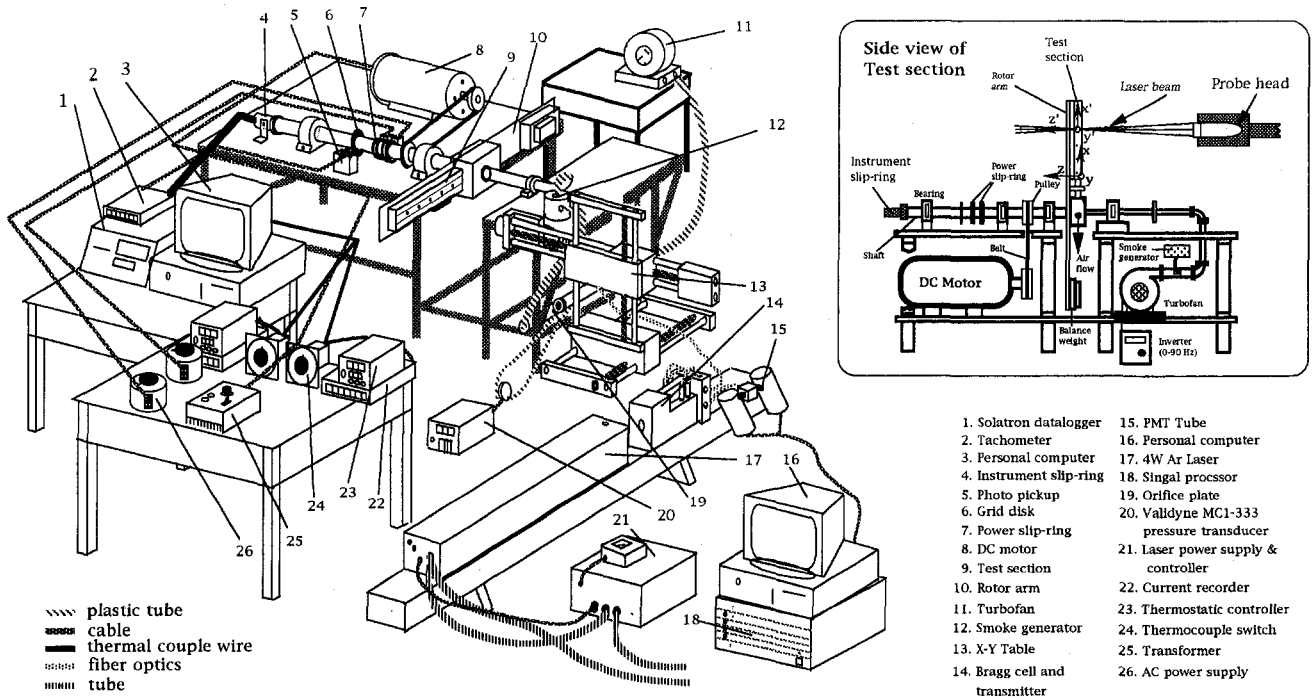

Fig. 2 Stereographic and side view of the experimental set up schematics

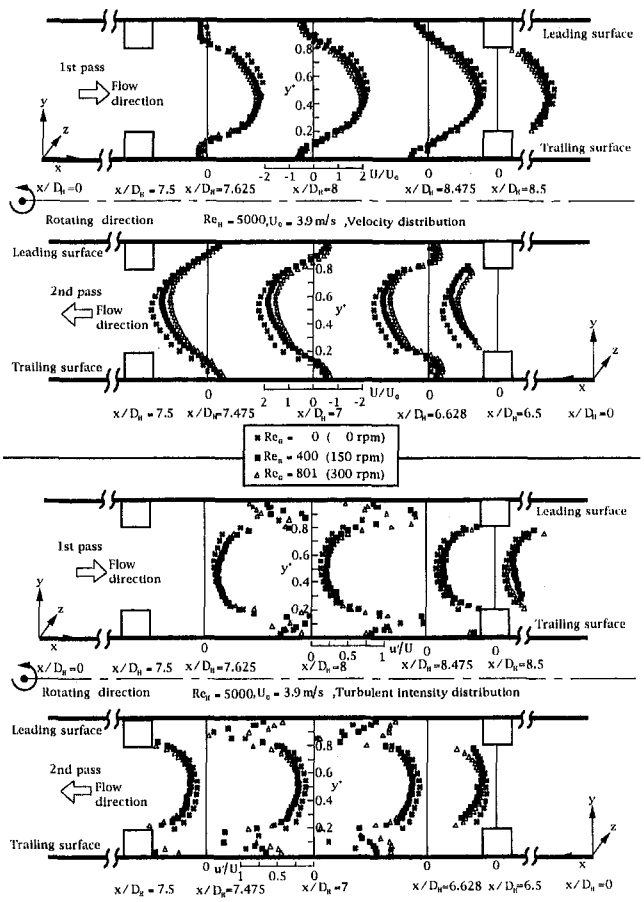

Fig. 3 LDV measurements for streamwise velocity and turbulent intensity distribution along the channels between two consecutive ribs (Re_H = 5000) at Z^+ = 0.5

of two orthogonal components. The transverse velocity component is measured (not shown here) using 488.0 nm beam, while the 514.5 nm beam measures a stremwise velocity component. A combined counter-type signal processor (Dantec model 57H00) with functions of counter, buffer interface, and coincidence filter, which is interfaced with a LEO (Intel-486) PC in the direct access mode, was employed for data processing. Statistical data were based on a sample size of 320,000 measurements, with a sampling frequency of approximately 400 samples/s, from which the time-averaged values were determined.

For the present system, the link consisted of four fiber manipulators and four single mode fibers. Each fiber manipulator was used as a launch unit to couple the beam onto the fiber. The single mode polarization preserving fiber produced a beam diameter 1.35 mm, and beam divergence angle of 0.5 ~ 0.6 mrad. It was fitted with two plugs at each end that included the microlens for focusing (at the receiving end) and/or resetting the divergence angle of the beam (at the probe end).

The selection of seed particles for laser Doppler measurements represents a compromise between large particles (diameter >10 μm), which are good light scatterers, and small particles (diameter <1 μm), which follow the air flow very accurately. A satisfactory compromise could be obtained by 4 ~ 5 μm diameter glass microbeads from a straw smoke generator. Since the flow was forced convection dominated, velocity measurements were first made without heating. Once a valid laser velocimeter signal is generated, the test section angular position is recorded with a shaft encoder. The encoder divides each revolution into 3600 parts. The two velocity signals and the shaft positions are simultaneously recorded onto floppy disks by a PC. A typical test had 40 data points in each measured downstream station. This zones two-dimensional velocity and angular position data for the measured point, which were analyzed after the test.

In order to determine the local (regionally averaged) Nusselt number, it is necessary to obtain the axial variation of heat flux from the passage wall and the difference between the wall temperature and the bulk mean temperature of the coolant. Detailed calculation procedure of heat transfer coefficients can be found from Hsieh and Liu (1996).

4 Results and Discussion

As mentioned in Wagner et al. (1991), the forced convection mechanism present in the rotating channel is influenced by the presence of Coriolis forces (rotation number) and centrifugal buoyancy (wall-to-coolant temperature difference, $\Delta\rho/\rho_i$). The tests are conducted for two channel Reynolds numbers (Re_H = 5000 and 25000) and four rotational speeds (Ω = 200, 400, 600, and 800 rpm), nine rotation numbers (Ro = 0–0.4274) are obtained. Two wall heating conditions are tested (only one case was shown). The time average, U, velocity as well as turbulent intensity (streamwise/axial direction in the test channel) was measured along a radial line at midplane and downstream distance at rotational speeds of 60, 100, 150, 200, 250, and 300 rpm.

4.1 Mean Velocity and Velocity Fluctuation. The measured mean velocity and velocity fluctuation under isothermal condition (i.e., no heating) for the specified rib configuration (see Fig. 1 for details) at Re_H = 5000, Re_Ω = 0, 160 (60 rpm), 267 (100 rpm), 400 (150 rpm), 534 (200 rpm), 667 (250 rpm), and 801 (300 rpm) are conducted. Only Re_Ω = 0, 400, and 801 are shown in Fig. 3. Generally speaking, the development of

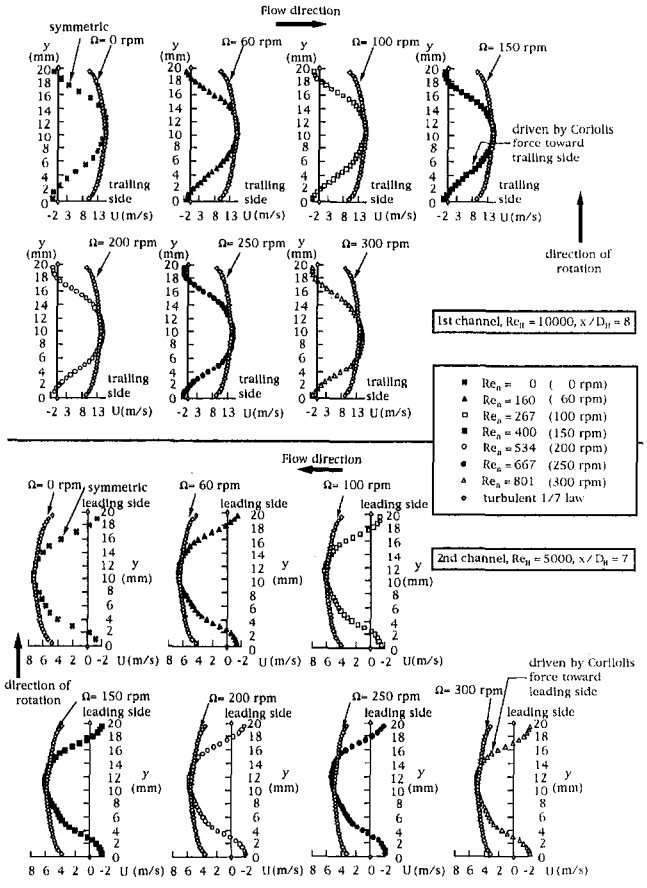

Fig. 4 Local mean velocity profile compared with one-seventh turbulent velocity profile at Z^+ = 0.5

the mean velocity between two consecutive ribs at the centerplane ($z^+ = 0.5$) is demonstrated in Fig. 3. The axial velocity profiles and velocity fluctuation obtained for eight downstream stations with and without rotation are also compared in the upper and lower part of Fig. 3. The distortion of the profiles in Fig. 3 appears clearly. Generally, the flow pattern with rotation is skewed continuously from the typical one-seventh law turbulent velocity profile. This can also be verified later in Fig. 4. The flow speeds up near the trailing (1st pass) side and leading (2nd pass) side and, consequently, the heat transfer coefficient increases. On the other hand, the flow slows down near the leading (1st pass) side and trailing (2nd pass) side and, consequently, the heat transfer coefficient decreases. The differences in axial velocity profiles with rotation seem to be not clearly noted at different rotational speeds. In spite of the present roughened surface configuration, the maximum velocity does coincide with the geometric centerline (midplane) of the duct ($y^+ = 0.5$) due to the symmetry of the duct. However, this situation becomes worse as the flow proceeds downstream (e.g, $x/D_H \geq 8$) due to rotation, especially in the second channel. Again, this behavior can also be noted in Fig. 4 as the rotational speed increases.

The continuity equation of the velocity profile in each channel at each station was assessed. It is found that the deviation is less than 8 percent (measured mass flow rate $\cong 1.56 \times 10^{-3}$kg/s and the nominal mass flow rate at $Re_H = 5000 = 1.69 \times 10^{-3}$kg/s). The measured mass flow rate was calculated based on the average of the present eight axial measurement positions (for roughened channel) plus one position ($x/D_H = 8$, 1st channel) for smooth case. The flow is significantly accelerated by the presence of the channel obstruction presented by the opposite ribs. Mean velocities at the central portion are observed somewhat higher. The increased flow velocity resulting from the channel rib has been shown to have a significant effect on the heat transfer. A large recirculation zone downstream of the upstream rib occupying the entire zone in between two consecutive ribs is evident for both channels. This reverse flow region extends from $x/D_H = 7.5$ to $x/D_H = 8.475$ (1st pass) and from $x/D_H = 6.5$ to $x/D_H = 7.475$ (2nd pass). Flow reattachment never occurs between two consecutive ribs in both channels, which indicates there is no significant change even though the flow passage has a 180 degree turn. The flow just skimmed over the two consecutive ribs. This also verifies the work in Hong and Hsieh (1993) for a stationary roughened channel, which indicates little influence from rotation on boundary layer reattachment. Although no negative velocities (flow reversal) are seen along the rib top, recirculation with reverse flow velocities as high as nearly half the channel nominal velocity U_o are seen at $x/D_H = 8.475$ (1st pass) and $x/D_H = 7$ (2nd pass). The vertical extent of this reverse flow zone is about the same for both channels at the corresponding stations. The size of this leeward recirculation zone seems not to be diminished as one proceeds downstream before touching the downstream rib. No noticeable effect was found in the present study duct at the present rotational speeds in the first channel, while the difference in axial velocity profiles with and without rotation is still noted, which can be seen in Fig. 3 at $x/D_H = 8$ (1st pass).

After leaving the upstream rib, the mean velocity profiles at $x/D_H = 7.625$ (1st pass)/ = 6.628 (2nd pass) show negative velocities adjacent to the upstream rib. Typically, between two consecutive ribs, the flow is characterized by large separation regions. Upon reaching the downstream ribs, the flow is self-adjusting to have higher streamwise mean velocity in the central portion and lower velocity near the walls. The flow near the walls is partly decelerated by the ribs with two small recirculation zones formed in the front corners of the rib and is partly accelerated due to the flow area reduction. The result is that the flow approaching the rib must accelerate over the top (as also evidenced by velocity fluctuation in the lower part of Fig. 3) and eventually merge with the mean flow. The separated flow from the upstream rib reattaches the top floor of the downstream rib, as can be inferred from the mean velocity profiles at $x/D_H = 8.475$ (1st pass)/ = 7.475 (2nd pass) in Fig. 3. After turning 180 deg from the 1st channel (i.e., flow in the 2nd pass), the mean velocity profiles at $x/D_H = 6.5$ (2nd pass) seem a little bit asymmetric and imply a noticeable transverse velocity component close to the top rib (leading side) a little bit steeper than the bottom rib (trailing side) which is perhaps due to the present rotating conditions. This situation becomes more distinct as

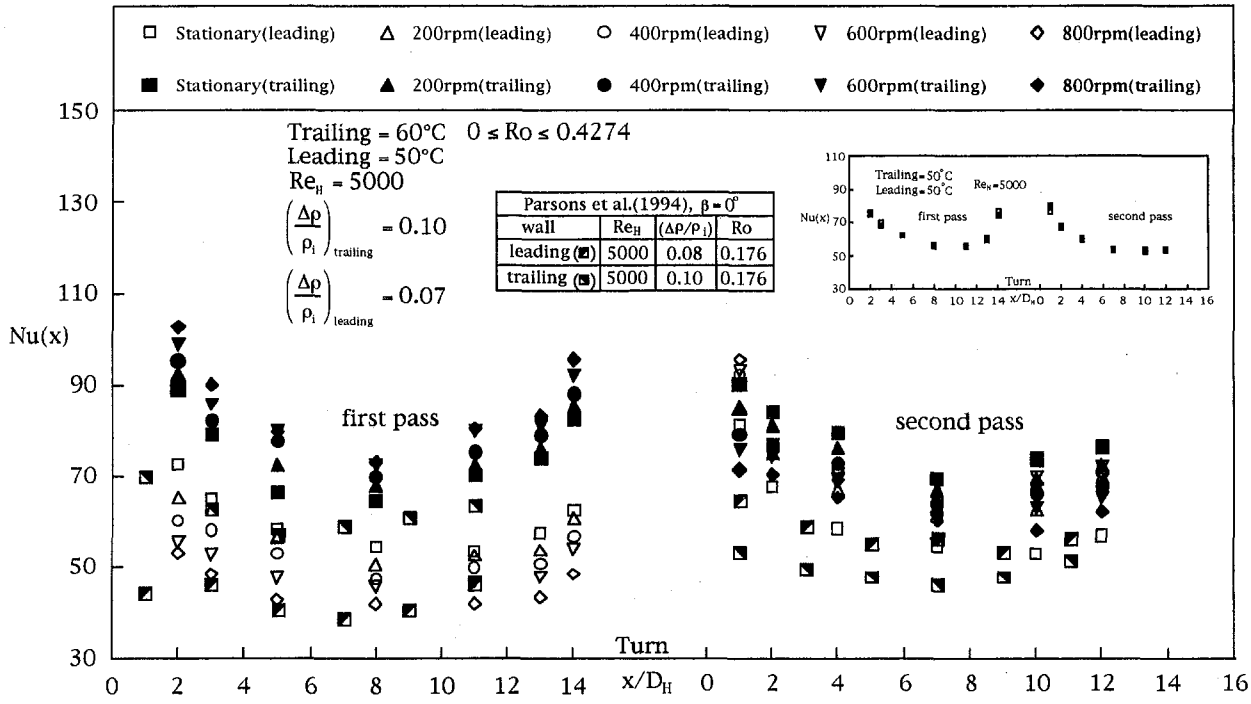

Fig. 5 Effect of uneven wall temperature on local Nusselt number at $Re_H = 5000$

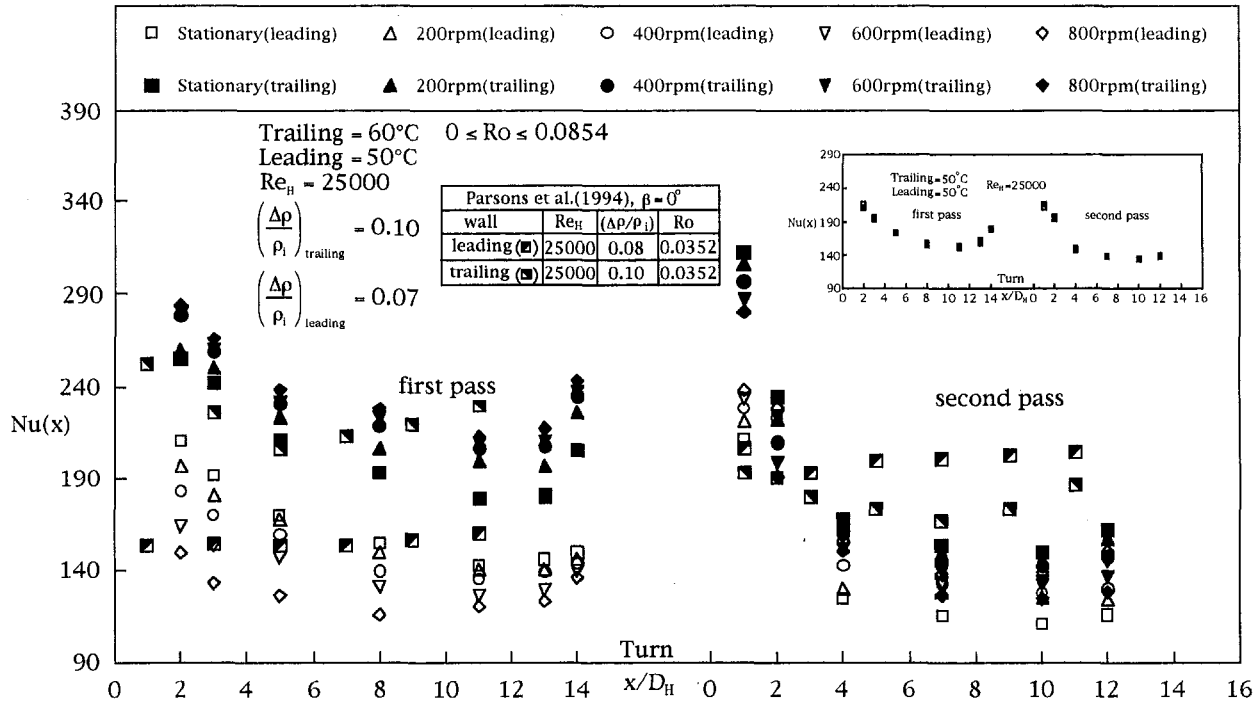

Fig. 6 Effect of uneven wall temperature on local Nusselt number at Re_H = 25000

the rotation number increases and the flow proceeds further downstream. This can be also assessed in Fig. 4. Furthermore, it should be noted in first/second channel that the axial velocity gradient on the trailing/leading wall grows steeper than that on the leading/trailing wall. This observation has two important implications. One has to do with the friction performance: higher values of the local friction factor are observed on the trailing/leading wall and lower values are observed on the leading/trailing wall in the region far from the upstream rib in first/second channel before reaching the downstream rib. The other is the physical phenomenon referred to as Ekman flow in which the main flow stream is directed toward the trailing/leading wall instead of moving parallel to the channel axis and, consequently, it enhances the convection heat transfer performance in first/second pass.

The turbulent fluctuation characteristics of the mean velocity corresponding to the data of the upper part of Fig. 3 is illustrated in the lower part of this figure. It shows that higher fluctuations near the walls are in the shear layer separating the mean flow from the recirculation zone. The higher turbulence levels in the recirculation zone promote more efficient diffusion of momentum than in the main flow. Again, as shown in the mean velocity profiles, the lower part of Fig. 3 shows that there is no influence on tubulent fluctuation at the present rotating speed. Figure 4 further assesses the previous findings for Coriolis effects under different rotational speeds at a particular downstream station x/D_H = 8 or 7 and Re_H = 10,000 or 5000 and Re_H in the first or second channel, respectively. The present results are also compared with those of the one-seventh velocity profile for smooth surfaces in Fig. 4.

4.2 Effect of Uneven Wall Temperature. The local (regionally averaged) heat transfer results are presented as the axial distributions along the channel (Nu versus x/D_H). The results shown in Fig. 5 for Re_H = 5000 and radially outward/inward flow (first/second pass) indicate that the trailing surface Nusselt number is higher than that of the corresponding value of the leading surface in the first pass. Generally speaking, the heat transfer rate increases as the rotational speed increases for trailing surface, while the reverse is true for the leading surface. The reasons can be explained as follows: for the case of trailing being hotter than leading, the uneven wall temperature superimposed on the coolant flow profile creates cooler fluid near the leading side. On the other hand, Coriolis force turns the coolant flow to the trailing surface. Furthermore, the cross stream moves this cooler fluid from the leading wall back to the trailing surface and creates more centrifugal buoyancy effects near the trailing side due to rotation. This implies that the uneven wall temperature keeps the cooler fluid close to both the trailing and leading walls and produces a greater velocity/temperature gradient near both the trailing and leading surfaces, respectively. Therefore, the hotter trailing surface and colder leading surface eventually enhances the effect of rotation on the trailing surface, but reduces the effect of rotation on the leading wall.

Figure 6 shows the flow rate effect on local heat transfer rate. The operating condition is the same as Fig. 5 with Re_H = 25,000 instead. As expected, the trailing wall Nu is higher than that of the leading wall in radially outward flow. The reverse is true in the second pass. The rotational effect still can be noted on the trailing side in the radially outward flow and also happens on the leading side in the radially inward flow. The magnitude of Fig. 6 seems much higher than the corresponding value of Fig. 5, as one would expect due to a higher Re_H = 25,000. Also shown in Figs. 5 and 6 are results from Parsons et al. (1994) for comparison. To verify the present results the results with identical wall temperatures were also shown in Figs. 5 and 6.

5 Conclusion

This paper presents an extensive study of experimental data from both heat transfer experiments and LDV measurements in a rotating two pass oppositely rib-roughened square channel with uneven wall temperatures. In general, Coriolis-induced secondary flows are shown to enhance local heat transfer over the trailing/leading surface in the first/second pass compared to a duct without rotation. Centrifugal buoyancy is shown to influence the heat transfer response with heat transfer being imposed on both leading and trailing surfaces as the wall-to-bulk fluid temperature difference is increased with other controlling parameters fixed. Moreover, LDV measurements further

verify the present and previous heat transfer measurements with and without rotation.

6 References

Dutta, S., Andrews, M. J., and Han, J. C., 1996, "Prediction of Turbulent Heat Transfer in Rotating Smooth Square Ducts," *Int. J. Heat Mass Transfer,* Vol. 39, pp. 2505–2514.

Guidez, J., 1989, "Study of the Convective Heat Transfer in Rotating Coolant Channel," *ASME Journal of Turbomachinery,* Vol. 111, pp. 43–50.

Hong, Y. J., and Hsieh, S. S., 1993, "Heat Transfer and Friction Factor Measurements in Ducts With Staggered and In-Line Ribs," ASME JOURNAL OF HEAT TRANSFER, Vol. 115, pp. 58–65.

Hsieh, S. S., and Hong, Y. J., 1995, "Heat Transfer Coefficents in an Orthogonally Rotating Duct With Turbulators," ASME JOURNAL OF HEAT TRANSFER, Vol. 117, pp. 69–78.

Hsieh, S. S., and Liu, W. J., 1996, "Uneven Wall Heat Flux Effect on Local Heat Transfer in Rotating Two-Pass Channels With Two Oppositely Ribbed Walls," ASME JOURNAL OF HEAT TRANSFER, Vol. 118, pp. 864–876.

Parsons, J. A., Han, J. C., and Zhang, Y. M., 1994, "Wall Heating Effect on Local Heat Transfer in a Rotating Two-Pass Square Channel with 90° Rib Turbulators," *Int. J. Heat Mass Transfer,* Vol. 37, pp. 1411–1420.

Parsons, J. A., Han, J. C., and Zhang, Y. M., 1995, "Effect of Model Orientation and Wall Heating Condition on Local Heat Transfer in a Rotating Two-Pass Square Channel with Rib Turbulators," *Int. J. Heat Mass Transfer,* Vol. 38, pp. 1151–1159.

Prakash, C., and Zerkle, R., 1992, "Prediction of Turbulent Flow and Heat Transfer in a Radially Rotating Square Duct," *ASME Journal of Turbomachinery,* Vol. 114, pp. 835–846.

Wagner, J. H., Johnson, B. V., and Hajek, T. J., 1991, "Heat Transfer in Rotating Passages With Smooth Walls and Radial Outward Flow," *ASME Journal of Turbomachinery,* Vol. 113, pp. 42–51.

Zhang, Y. M., Han, J. C., Parsons, J. A., and Lee, C. P., 1995, "Surface Heating Effect on Local Heat Transfer in a Rotating Two-Pass Square Channel With 60 deg Rib Turbulators," *ASME Journal of Turbomechinery,* Vol. 117, pp. 272–280.

Effect of Surface Undulations on Natural Convection in a Porous Square Cavity

B. V. Rathish Kumar[1], P. Singh[2], and P. V. S. N. Murthy[2]

1 Introduction

Natural convection in enclosures has been a subject of intense research because of its fundamental nature and interesting applications. The enclosure related studies can be organized into two classes, viz., enclosures heated from the side and enclosures heated from below. Various flow patterns are possible depending on the imposed thermal boundary conditions, aspect ratio, and the geometry of the enclosure. Nield and Bejan (1992) give a review of the natural convection in fluid saturated porous enclosures.

Natural convection in an enclosure with vertical sides at a different temperature is most representative of porous insulation layers oriented vertically as in building technology, industrial cold-storage installations, etc. Heat transfer in such systems may be affected by intentionally roughening the surfaces by the attachment of baffles, fins, or other suitable protrusions to the walls of the enclosure (Riley 1988; Lai, 1991). There has been considerable interest in the intentional roughening of surfaces to enhance heat transfer. Bhavnani and Bergles (1991) give a literature review of free convection heat transfer from vertical surfaces with surface roughness elements in continuum fluids. By approximating the small-scale roughness as periodic (sine or cosine) functions, Watson and Poots (1971), Vajravelu and Sastri (1978), Yao (1983), Moulic and Yao (1989), and Bhavnani and Bergles (1991) have studied the free convection in clear fluids, where as Riley (1988), Rees and Pop (1994a, b), and Murthy et al., (1997) studied the free convection heat transfer in porous media.

The effect of sinusoidal protrusions on laminar free convection between vertical walls has been reported by Watson and Poots (1971), where as the free convection heat transfer in a viscous incompressible fluid confined between a long vertical cosine wavy wall and a parallel flat wall has been analysed by Vajravelu and Sastri (1978). A deviation in the Nusselt number results from that of the flat wall has been observed in both the cases. Natural convection along a vertical sinusoidal wavy surface has been analyzed by Yao (1983) and Moulic and Yao (1989) for isothermal and uniform surface heat flux conditions, respectively. In both the cases, they observe a decrease in the total Nusselt number when compared with the flat wall case in spite of increase in the surface area.

Literature connected with the free convection in porous media show that a little attention has been paid to the investigations in this direction, though porous insulation has wide range of industrial applications. Riley (1988) analyzed the effect of surface undulations approximated with cosine waves in the vertical porous slot. His results are confined to the conduction zone only. Rees and Pop (1994a, b) studied the free convection along a sinusoidal vertical and horizontal (respectively) wavy walls embedded in a fluid saturated porous media. For the vertical configuration, their results show that the local Nusselt number is less than or equal to that of a plane heated surface and the total heat transfer rate is unchanged by the presence of the sinusoidal surface undulations. The study with the horizontal wavy wall revealed an increase in the global heat flux results with the increase in the amplitude of the wave. The flow separation and reattachment on the wall has also been reported.

The situation of enclosures with the bottom wall being isothermal and of sinusoidal wavy nature (analogue of Lapwood convection) as analyzed by Murthy et al. (1997) revealed sev-

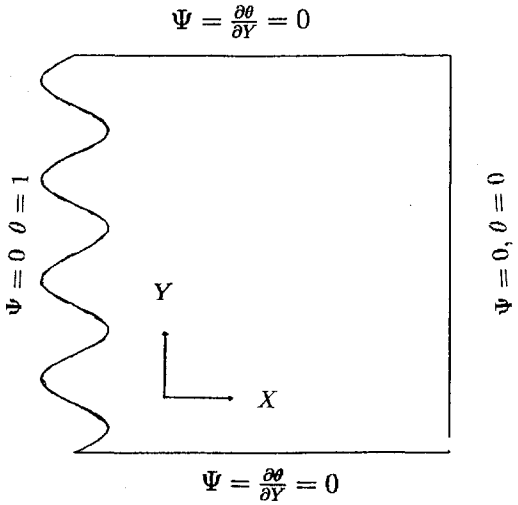

Fig. 1 Square enclosure with vertical wavy wall

[1] Department of Mathematics, Indian Institute of Technology, Kanpur 208016, V.P., India: bvrk@iitk.ernet.in

[2] Department of Mathematics, Indian Institute of Technology, Kanpur 208016, V.P., India.

Contributed by the Heat Transfer Division of THE AMERICAN SOCIETY OF MECHANICAL ENGINEERS. Manuscript received by the Heat Transfer Division June 28, 1996; revision received April 25, 1997; Keywords: Natural Convection; Numerical Methods; Porous Media. Associate Technical Editor: K. Vafai.

verify the present and previous heat transfer measurements with and without rotation.

6 References

Dutta, S., Andrews, M. J., and Han, J. C., 1996, "Prediction of Turbulent Heat Transfer in Rotating Smooth Square Ducts," *Int. J. Heat Mass Transfer,* Vol. 39, pp. 2505–2514.

Guidez, J., 1989, "Study of the Convective Heat Transfer in Rotating Coolant Channel," *ASME Journal of Turbomachinery,* Vol. 111, pp. 43–50.

Hong, Y. J., and Hsieh, S. S., 1993, "Heat Transfer and Friction Factor Measurements in Ducts With Staggered and In-Line Ribs," ASME JOURNAL OF HEAT TRANSFER, Vol. 115, pp. 58–65.

Hsieh, S. S., and Hong, Y. J., 1995, "Heat Transfer Coefficents in an Orthogonally Rotating Duct With Turbulators," ASME JOURNAL OF HEAT TRANSFER, Vol. 117, pp. 69–78.

Hsieh, S. S., and Liu, W. J., 1996, "Uneven Wall Heat Flux Effect on Local Heat Transfer in Rotating Two-Pass Channels With Two Oppositely Ribbed Walls," ASME JOURNAL OF HEAT TRANSFER, Vol. 118, pp. 864–876.

Parsons, J. A., Han, J. C., and Zhang, Y. M., 1994, "Wall Heating Effect on Local Heat Transfer in a Rotating Two-Pass Square Channel with 90° Rib Turbulators," *Int. J. Heat Mass Transfer,* Vol. 37, pp. 1411–1420.

Parsons, J. A., Han, J. C., and Zhang, Y. M., 1995, "Effect of Model Orientation and Wall Heating Condition on Local Heat Transfer in a Rotating Two-Pass Square Channel with Rib Turbulators," *Int. J. Heat Mass Transfer,* Vol. 38, pp. 1151–1159.

Prakash, C., and Zerkle, R., 1992, "Prediction of Turbulent Flow and Heat Transfer in a Radially Rotating Square Duct," *ASME Journal of Turbomachinery,* Vol. 114, pp. 835–846.

Wagner, J. H., Johnson, B. V., and Hajek, T. J., 1991, "Heat Transfer in Rotating Passages With Smooth Walls and Radial Outward Flow," *ASME Journal of Turbomachinery,* Vol. 113, pp. 42–51.

Zhang, Y. M., Han, J. C., Parsons, J. A., and Lee, C. P., 1995, "Surface Heating Effect on Local Heat Transfer in a Rotating Two-Pass Square Channel With 60 deg Rib Turbulators," *ASME Journal of Turbomechinery,* Vol. 117, pp. 272–280.

Effect of Surface Undulations on Natural Convection in a Porous Square Cavity

B. V. Rathish Kumar[1], P. Singh[2], and P. V. S. N. Murthy[2]

1 Introduction

Natural convection in enclosures has been a subject of intense research because of its fundamental nature and interesting applications. The enclosure related studies can be organized into two classes, viz., enclosures heated from the side and enclosures heated from below. Various flow patterns are possible depending on the imposed thermal boundary conditions, aspect ratio, and the geometry of the enclosure. Nield and Bejan (1992) give a review of the natural convection in fluid saturated porous enclosures.

Natural convection in an enclosure with vertical sides at a different temperature is most representative of porous insulation layers oriented vertically as in building technology, industrial cold-storage installations, etc. Heat transfer in such systems may be affected by intentionally roughening the surfaces by the attachment of baffles, fins, or other suitable protrusions to the walls of the enclosure (Riley 1988; Lai, 1991). There has been considerable interest in the intentional roughening of surfaces to enhance heat transfer. Bhavnani and Bergles (1991) give a literature review of free convection heat transfer from vertical surfaces with surface roughness elements in continuum fluids. By approximating the small-scale roughness as periodic (sine or cosine) functions, Watson and Poots (1971), Vajravelu and Sastri (1978), Yao (1983), Moulic and Yao (1989), and Bhavnani and Bergles (1991) have studied the free convection in clear fluids, where as Riley (1988), Rees and Pop (1994a, b), and Murthy et al., (1997) studied the free convection heat transfer in porous media.

The effect of sinusoidal protrusions on laminar free convection between vertical walls has been reported by Watson and Poots (1971), where as the free convection heat transfer in a viscous incompressible fluid confined between a long vertical cosine wavy wall and a parallel flat wall has been analysed by Vajravelu and Sastri (1978). A deviation in the Nusselt number results from that of the flat wall has been observed in both the cases. Natural convection along a vertical sinusoidal wavy surface has been analyzed by Yao (1983) and Moulic and Yao (1989) for isothermal and uniform surface heat flux conditions, respectively. In both the cases, they observe a decrease in the total Nusselt number when compared with the flat wall case in spite of increase in the surface area.

Literature connected with the free convection in porous media show that a little attention has been paid to the investigations in this direction, though porous insulation has wide range of industrial applications. Riley (1988) analyzed the effect of surface undulations approximated with cosine waves in the vertical porous slot. His results are confined to the conduction zone only. Rees and Pop (1994a, b) studied the free convection along a sinusoidal vertical and horizontal (respectively) wavy walls embedded in a fluid saturated porous media. For the vertical configuration, their results show that the local Nusselt number is less than or equal to that of a plane heated surface and the total heat transfer rate is unchanged by the presence of the sinusoidal surface undulations. The study with the horizontal wavy wall revealed an increase in the global heat flux results with the increase in the amplitude of the wave. The flow separation and reattachment on the wall has also been reported.

The situation of enclosures with the bottom wall being isothermal and of sinusoidal wavy nature (analogue of Lapwood convection) as analyzed by Murthy et al. (1997) revealed sev-

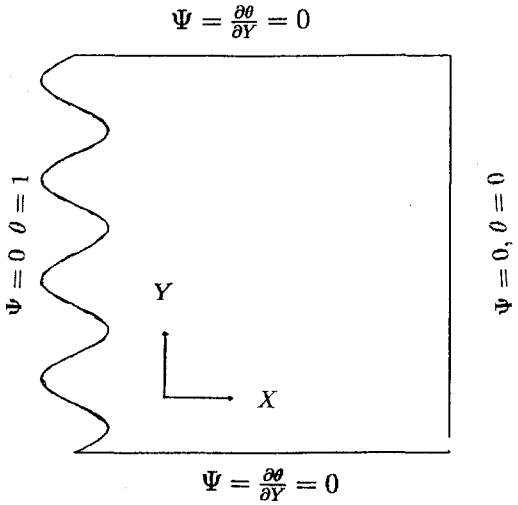

Fig. 1 Square enclosure with vertical wavy wall

[1] Department of Mathematics, Indian Institute of Technology, Kanpur 208016, V.P., India: bvrk@iitk.ernet.in

[2] Department of Mathematics, Indian Institute of Technology, Kanpur 208016, V.P., India.

Contributed by the Heat Transfer Division of THE AMERICAN SOCIETY OF MECHANICAL ENGINEERS. Manuscript received by the Heat Transfer Division June 28, 1996; revision received April 25, 1997; Keywords: Natural Convection; Numerical Methods; Porous Media. Associate Technical Editor: K. Vafai.

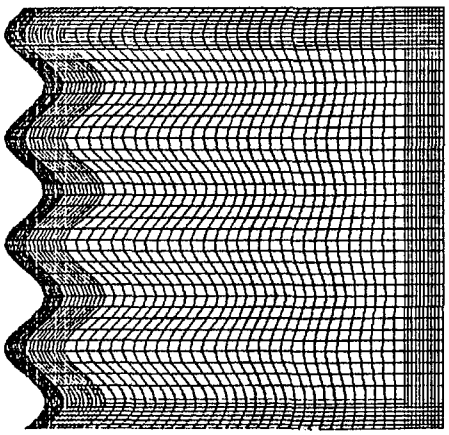

Fig. 2 Graded finite element mesh

eral interesting features like (1) flow separation and reattachment on the wavy wall of the enclosure, (2) recirculation zones which trap the heat and hinder the convective process, in the porous medium away from the walls, and (3) increase in heat transfer results with increasing Ra and the decrease of the same with increasing amplitude of waves etc. So special attention is required for studying the effect of nonlinearities in the geometries of the enclosure on the free convection heat transfer.

The present analysis is aimed at examining the effect of sinusoidal surface imperfections on the free convection in porous enclosure heated from side. The observations reveal that the heat transfer decreases as the amplitude of the wave increases. This is due to the loss in the buoyancy component. Also, the total heat transfer rate is less when compared with the heat transfer in an enclosure with plane walls.

2 Governing Equations

Consider the problem of free convection heat transfer from the isothermal sinusoidal wavy surface into the fluid saturated porous enclosure as shown in Fig. (1). The porous enclosure is assumed to be homogeneous and isotropic. The flow conditions are such that the Darcy law is valid. Following Prasad and Kulacki (1984), the governing equations in terms of nondimensional stream function and temperature distribution can be written as

$$\frac{\partial^2\Psi}{\partial X^2} + \frac{\partial^2\Psi}{\partial Y^2} = \mathrm{Ra}\,\frac{\partial\theta}{\partial X} \tag{1}$$

$$\frac{\partial\Psi}{\partial X}\frac{\partial\theta}{\partial Y} - \frac{\partial\Psi}{\partial Y}\frac{\partial\theta}{\partial X} = \frac{\partial^2\theta}{\partial X^2} + \frac{\partial^2\theta}{\partial Y^2} \tag{2}$$

with the boundary conditions being

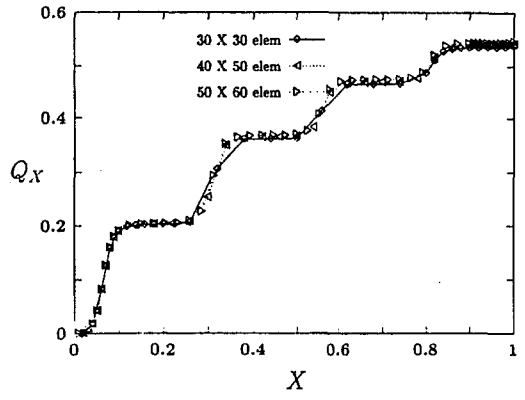

Fig. 3 Comparison of cumulative global heat flux for 30 × 30, 40 × 40 and 50 × 60 mesh systems

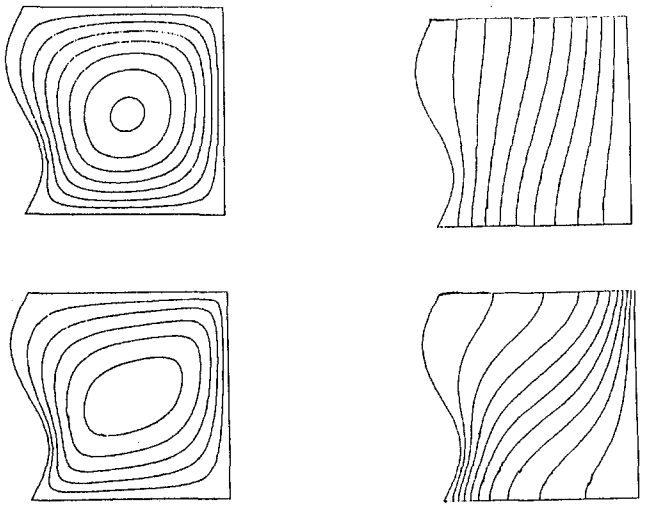

Fig. 4 Streamlines and isotherms for single wave case for (*a*) Ra = 10 and (*b*) Ra = 50 with $a = 0.1$ and $\phi = 0$ deg

$$\left.\begin{aligned} &\Psi = 0,\ \theta = 1 \quad \text{on} \quad X = a\sin(N\pi Y - \phi)\\ &\Psi = 0,\ \theta = 0 \quad \text{on} \quad X = 1\\ &\Psi = 0,\ \frac{\partial\theta}{\partial Y} = 0 \quad \text{on} \quad Y = 0 \quad \text{and} \quad Y = 1 \end{aligned}\right\}. \tag{3}$$

The nondimensional variables are

$$X = \frac{x}{L},\quad Y = \frac{y}{L},\quad \Psi = \frac{\psi}{\alpha},\quad \theta = \frac{T - T_a}{T_w - T_a}.$$

Here, X and Y are the Cartesian coordinates, Ψ is the stream function, θ is the temperature distribution, Ra is the Rayleigh number based on the vertical dimension of the enclosure defined as $K_g\beta\theta_w L/\alpha\nu$. K is the permeability of the medium, g is the gravitational constant, β is the thermal expansion coefficient, L is the height and average width of the wavy wall, α is the effective thermal diffusivity, ν is the kinematic viscosity of the fluid, $\theta_w = T_w - T_a$, T_w, T_a are the wall and reference temperatures, respectively, a is the amplitude, ϕ is the phase of the wave, and N is the number of waves considered in the vertical dimension of the enclosure.

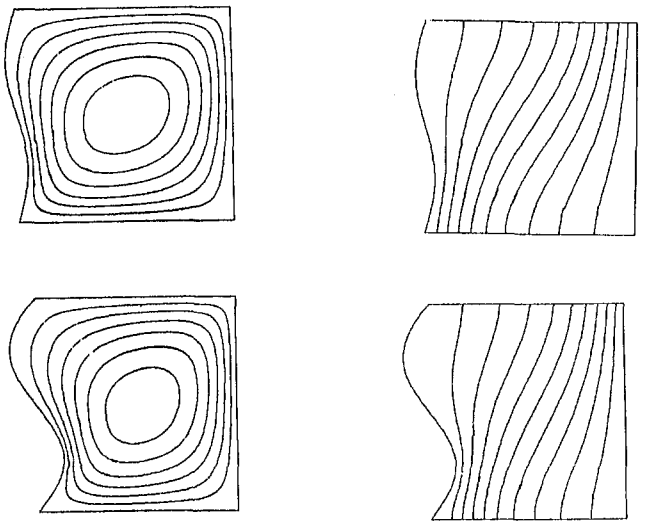

Fig. 5 Streamlines and isotherms for single wave case for (*a*) $a = 0.05$ and (*b*) $a = 0.15$ with Ra = 20 and $\phi = 0$ deg

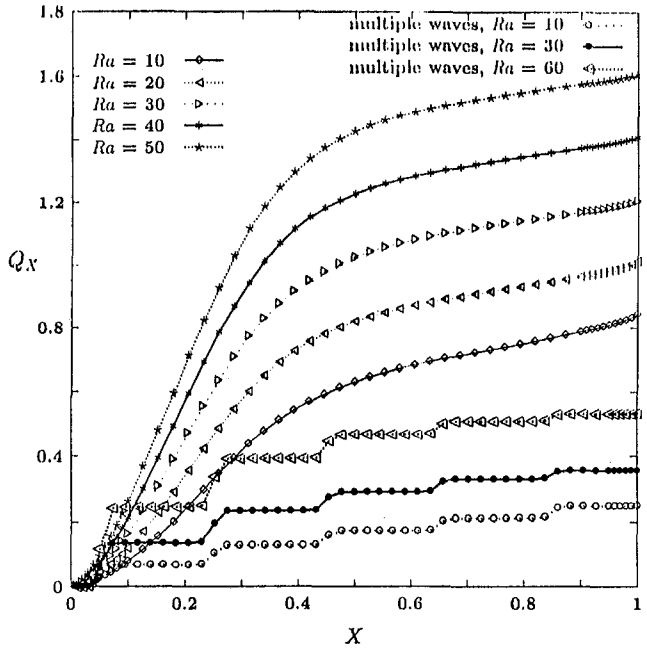

Fig. 6 Cumulative global heat flux for single wave case for varying Ra with $a = 0.1$ and $\phi = 0$ deg. The multiple wave plots correspond to $a = 0.2$, $\phi = 0$ deg and $N = 5$.

Clearly with $a = 0$ in the boundary conditions, the problem will become the free convection in a rectangular porous enclosure. This fundamental configuration has been studied thoroughly by numerous researchers. The governing partial differential Eqs. (1) and (2) along with the hydrodynamic and thermal boundary conditions (3) have been solved numerically using finite element method. The elemental equation details are available as presented in Murthy et al. (1997).

The fundamental interest of the present study is to evaluate the global heat flux into the system. The cumulative global heat flux has been computed from the formula

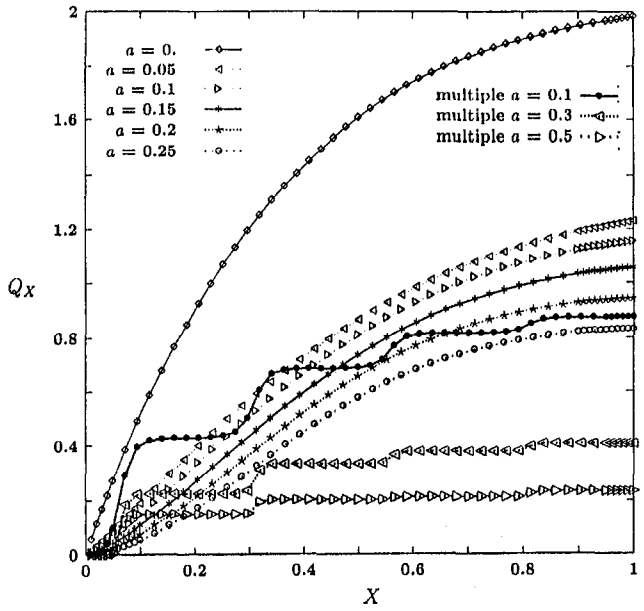

Fig. 7 Cumulative global heat flux for single wave case for varying a with Ra = 20 and $\phi = 0$ deg. The multiple wave plots correspond to Ra = 50, $\phi = 0$ deg and $N = 4$.

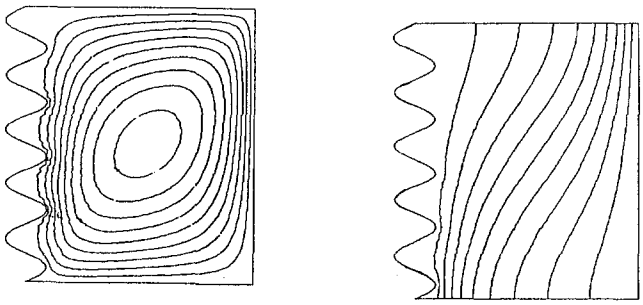

Fig. 8 Streamlines and isotherms for multiple wave case for $N = 5$ with $a = 0.1$, Ra = 30, and $\phi = 0$ deg

$$Q_X = \int_0^X -k \frac{\partial \theta}{\partial n_{|X=a\sin(N\pi Y-\phi)}} \frac{ds(\xi)}{d\xi} d\xi \qquad (4)$$

where n is the outward drawn normal to the wavy surface and $s(\xi)$ is the arc-length along the surface. $X = 1$ in the upper limit gives the global heat flux results.

Numerical simulations have been carried out over a 50×60 graded mesh as shown in Fig. 2 and the results are observed to the tolerance $\tau < 5 \times 10^{-4}$, i.e., (max $(|\Psi_i^{\text{current}} - \Psi_i^{\text{previous}}|, |\theta_i^{\text{current}} - \theta_i^{\text{previous}}|)$, for $i = 1, \ldots, n$ var) $< \tau$, where n var denotes the total number of variables. The cumulative global heat flux results obtained for fixed values of Ra, a, ϕ, and N on three different meshes are plotted in Fig. 3. It shows the improvement in the results as mesh size increases, but the difference between the results for 40×40 and 50×60 is negligibly small. This ensures the grid independency of the results.

3 Results and Discussion

The crucial parameters which influence the flow and heat transfer are the Rayleigh number Ra, the amplitude a and the phase ϕ of the wave, and the number of waves considered in the vertical dimension of the cavity. Heat transfer from a single wave for some sets of values of a, ϕ, and Ra in the ranges $0 \le a \le 0.5$, $0 \le \phi \le 315$, and $0 < \text{Ra} \le 75$, respectively, of wave amplitude, phase, and Rayleigh number are studied first. With the values considered in the present study, we can clearly study the convective transport in the enclosure. The streamlines and isotherms for Ra = 10 and Ra = 50 are presented in Fig. (4). The increase in the Ra carries the wavy nature to streamlines and isotherms in the core region too. This clearly indicates the increase in the convective transport in the medium. The isotherm pattern also supports this feature.

The stream lines and isotherms corresponding to $a = 0.05$ and $a = 0.15$ for single wave case are presented in Fig. (5).

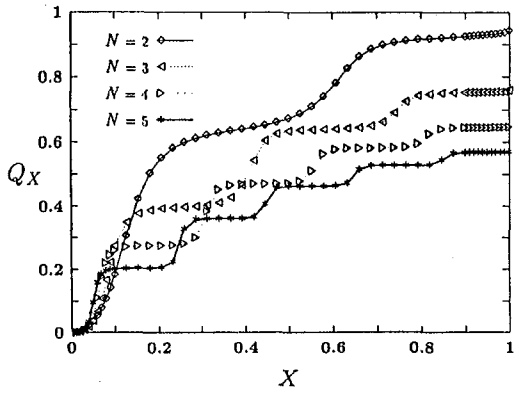

Fig. 9 Cumulative global heat flux results for varying N with $a = 0.1$, Ra = 30, and $\phi = 0$ deg

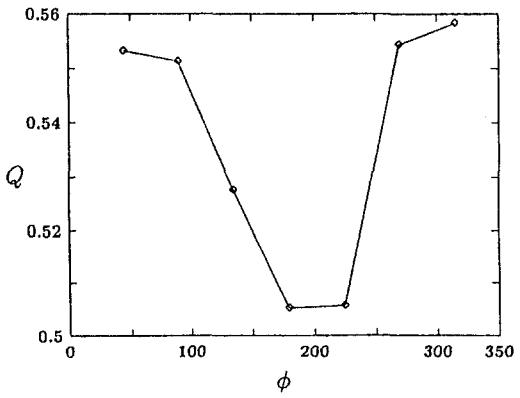

Fig. 10 Cumulative global heat flux results for varying ϕ with Ra = 20, a = 0.1, and N = 4

The increase in amplitude increases the wavy nature of the stream lines but the intensity of the flow is unaltered as clearly seen from the values of the streamlines. Also, the uniformity of the range of slopes of isotherms with an increase in amplitude reveals that it does not favor the convection process. The cumulative global heat flux for varying Ra and varying a are plotted in Figs. (6) and (7), respectively. These figures clearly indicate that the global heat flux increases with increasing Ra, whereas the same decreases with the increasing amplitude. Figure (7) also indicates that the heat transfer from wavy wall is less when compared with that of a flat surface. As pointed out by Yao (1983), the loss in the global heat flux with increasing amplitude can be attributed to the loss in the convection-favoring vertical component of the buoyancy force. The vertical component of the buoyancy force is maximum when the flat heated surface is vertical, but in the case of the wavy wall this buoyancy component is maximum only at the crest and at locations where the surface normal faces the buoyancy force. Consequently, the heat transfer from the wavy wall is less compared to that from a vertical flat plate. From Fig. (7) it is also to be noted that for any fixed a and for ϕ = 0 deg, the increase in the cumulative global heat flux, corresponding to the first half of the wavy wall leading to the crest, is larger than the subsequent increase due to the contribution from the portion of the wall leading to the trough section. This can be directly attributed to the loss in the convection-favoring bouyancy component, as one traverses from the crest to the trough section.

The study with multiple waves on the vertical dimension of the cavity also revealed the same trend, as in the one-wave case, in the global heat flux results for increasing Ra and increasing a. The wavy cumulative global heat flux curves presented for increasing Ra (Fig. 6) and for increasing a, clearly (Fig. 7) depict a continuously increasing. The wavy nature in these profiles is due to the larger contribution from the sections of wavy wall leading to crests and considerably smaller contributions from the sections leading to the troughs. This can clearly be attributed to the loss in the convection favoring bouyancy components as one moves towards the troughs. The streamlines and isotherms presented in Fig. (8) clearly indicate the wavy nature of the wall. The decrease in the global heat flux results with an increase in the number of waves, as seen in Fig. (9), can be attributed to the increase in the loss of the bouyancy force with an increase in the number of waves (i.e., number of trough sections). Finally, the varying phase between 0 deg $\leq \phi \leq$ 315 deg for fixed amplitude, Rayleigh number and Number of waves has an interesting effect on the global heat flux. With the change in the location of the each crest and trough of the wave inside the enclosure, the streamline and isotherm pattern changes accordingly, but the intensity of the flow is unchanged. Also, it can be seen from Fig. 10 that the global heat flux value decreases for increasing phase up to 180 deg, and then it increases from 180 deg onwards.

4 References

Bhavnani, S. H., and Bergles, A. E., 1991, "Natural Covection Heat Transfer From Sinusoidal Wavy Surface," *Warme-und Stoffubertrangung,* Vol. 26, pp. 341–349.

Lai, F. C., and Kulacki, F. A., 1991, "Non-Darcy Mixed Convection Along a Vertical Wall in a Saturated Porous Medium," ASME JOURNAL OF HEAT TRANSFER, Vol. 113, pp. 252–255.

Moulic, S. G., and Yao L. S., 1989, "Natural Convection Along a Vertical Wavy Surface With Uniform Heat Flux," ASME JOURNAL OF HEAT TRANSFER., Vol 111, pp. 1106–1108.

Murthy, P. V. S. N., Rathish Kumar, B. V., and Singh, P., 1997, "Natural Convection Heat Transfer From a Horizontal Wavy Surface in a Porous Enclosure," *Numerical Heat Transfer,* in press.

Nield, D. A., and Bejan, A., 1992, *Convection in Porous Media* Springer-Verlag, New York.

Prasad, V., and Kulacki, F. A., 1984, "Convective Heat Transfer in a Rectangular Porous Cavity-Effect of Aspect Ratio on Flow Structure and Heat Transfer," ASME JOURNAL OF HEAT TRANSFER, Vol. 106, pp. 158–165.

Rees, D. A. S., and Pop, I., 1994a, "A Note on Free Convection Along a Vertical Wavy Surface in a Porous Medium," ASME JOURNAL OF HEAT TRANSFER, Vol. 116, pp. 505–508.

Rees, D. A. S., and Pop, I., 1994b, "A Note on the Free Convection Along a Vertical Wavy Surface in a Porous Medium," ASME JOURNAL OF HEAT TRANSFER, Vol. 116, 505–508.

Riley, D. S., 1988, "Steady Two-Dimensional Thermal Convection in a Vertical Porous Slot With Spatially Periodic Boundary Imperfections," *Int. J. Heat Mass Transfer,* Vol. 31, pp. 2365–2380.

Vajravelu, K., and Sastri, K. S., 1978, "Free Convective Heat Transfer in a Viscous Incompressible Fluid Confined Between a Long Vertical Wall and a Parallel Flat Wall," *J. Fluid Mechanics,* Vol. 86, pp. 365–383.

Watson, A., and Poots, G., 1971, "The Effect of Sinusoidal Protrusions on Laminar Free Convection Between Vertical Walls," *J. Fluid Mechanics,* Vol. 49, pp. 33–48.

Yao, L. S., 1983, "Natural Convection Along a Vertical Wavy Surface," ASME JOURNAL OF HEAT TRANSFER Vol. 105, pp. 465–468.

An Experimental Investigation of the Capillary Performance of Triangular Versus Sinusoidal Channels

G. R. Stroes[1] and I. Catton[2]

This paper discusses an experimental investigation of the performance of capillary channels with sinusoidal versus triangular geometry. Results indicate that for equivalent cross-sectional area, angle of inclination, and heat input from below, a triangular groove geometry sustains a larger wetted area while a sinusoidal groove geometry supports a greater average heat flux.

Introduction

Much analytical and experimental work has been done regarding the local heat transfer coefficient in the evaporating region of a triple interline. For example: Das Gupta et al. (1993), Mirzamoghadam and Catton (1988), and Schonberg and Wayner (1992). But it is only in recent years that there have

[1] Graduate Student Researcher; Mem. ASME; University of California, Los Angeles, 43-132 ENGN. IV, 420 Westwood Plaza, Los Angeles, CA 90095: gustave@seas.ucla.edu

[2] Professor; Fellow ASME; University of California, Los Angeles, 48-121F ENGN. IV, 420 Westwood Plaza, Los Angeles, CA 90095.

Contributed by the Heat Transfer Division of THE AMERICAN SOCIETY OF MECHANICAL ENGINEERS. Manuscript received by the Heat Transfer Division November 11, 1995; revision received February 24, 1997; Keywords: Evaporation; Heat Pipes & Thermosyphons; Thin Film Flow. Associate Technical Editor: Y. Jaluria.

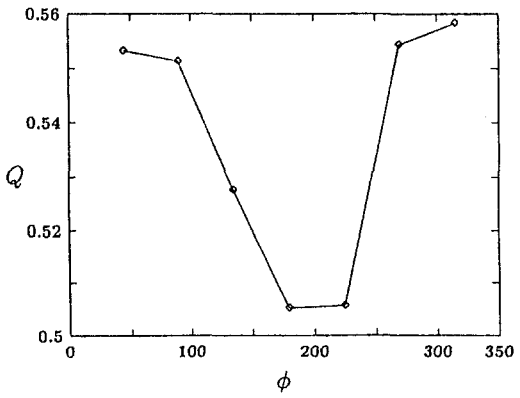

Fig. 10 Cumulative global heat flux results for varying ϕ with Ra = 20, a = 0.1, and N = 4

The increase in amplitude increases the wavy nature of the stream lines but the intensity of the flow is unaltered as clearly seen from the values of the streamlines. Also, the uniformity of the range of slopes of isotherms with an increase in amplitude reveals that it does not favor the convection process. The cumulative global heat flux for varying Ra and varying a are plotted in Figs. (6) and (7), respectively. These figures clearly indicate that the global heat flux increases with increasing Ra, whereas the same decreases with the increasing amplitude. Figure (7) also indicates that the heat transfer from wavy wall is less when compared with that of a flat surface. As pointed out by Yao (1983), the loss in the global heat flux with increasing amplitude can be attributed to the loss in the convection-favoring vertical component of the buoyancy force. The vertical component of the buoyancy force is maximum when the flat heated surface is vertical, but in the case of the wavy wall this buoyancy component is maximum only at the crest and at locations where the surface normal faces the buoyancy force. Consequently, the heat transfer from the wavy wall is less compared to that from a vertical flat plate. From Fig. (7) it is also to be noted that for any fixed a and for ϕ = 0 deg, the increase in the cumulative global heat flux, corresponding to the first half of the wavy wall leading to the crest, is larger than the subsequent increase due to the contribution from the portion of the wall leading to the trough section. This can be directly attributed to the loss in the convection-favoring bouyancy component, as one traverses from the crest to the trough section.

The study with multiple waves on the vertical dimension of the cavity also revealed the same trend, as in the one-wave case, in the global heat flux results for increasing Ra and increasing a. The wavy cumulative global heat flux curves presented for increasing Ra (Fig. 6) and for increasing a, clearly (Fig. 7) depict a continuously increasing. The wavy nature in these profiles is due to the larger contribution from the sections of wavy wall leading to crests and considerably smaller contributions from the sections leading to the troughs. This can clearly be attributed to the loss in the convection favoring bouyancy components as one moves towards the troughs. The streamlines and isotherms presented in Fig. (8) clearly indicate the wavy nature of the wall. The decrease in the global heat flux results with an increase in the number of waves, as seen in Fig. (9), can be attributed to the increase in the loss of the bouyancy force with an increase in the number of waves (i.e., number of trough sections). Finally, the varying phase between 0 deg $\leq \phi \leq$ 315 deg for fixed amplitude, Rayleigh number and Number of waves has an interesting effect on the global heat flux. With the change in the location of the each crest and trough of the wave inside the enclosure, the streamline and isotherm pattern changes accordingly, but the intensity of the flow is unchanged. Also, it can be seen from Fig. 10 that the global heat flux value decreases for increasing phase up to 180 deg, and then it increases from 180 deg onwards.

4 References

Bhavnani, S. H., and Bergles, A. E., 1991, "Natural Covection Heat Transfer From Sinusoidal Wavy Surface," *Warme-und Stoffubertrangung,* Vol. 26, pp. 341–349.

Lai, F. C., and Kulacki, F. A., 1991, "Non-Darcy Mixed Convection Along a Vertical Wall in a Saturated Porous Medium," ASME JOURNAL OF HEAT TRANSFER, Vol. 113, pp. 252–255.

Moulic, S. G., and Yao L. S., 1989, "Natural Convection Along a Vertical Wavy Surface With Uniform Heat Flux," ASME JOURNAL OF HEAT TRANSFER., Vol 111, pp. 1106–1108.

Murthy, P. V. S. N., Rathish Kumar, B. V., and Singh, P., 1997, "Natural Convection Heat Transfer From a Horizontal Wavy Surface in a Porous Enclosure," *Numerical Heat Transfer,* in press.

Nield, D. A., and Bejan, A., 1992, *Convection in Porous Media* Springer-Verlag, New York.

Prasad, V., and Kulacki, F. A., 1984, "Convective Heat Transfer in a Rectangular Porous Cavity-Effect of Aspect Ratio on Flow Structure and Heat Transfer," ASME JOURNAL OF HEAT TRANSFER, Vol. 106, pp. 158–165.

Rees, D. A. S., and Pop, I., 1994a, "A Note on Free Convection Along a Vertical Wavy Surface in a Porous Medium," ASME JOURNAL OF HEAT TRANSFER, Vol. 116, pp. 505–508.

Rees, D. A. S., and Pop, I., 1994b, "A Note on the Free Convection Along a Vertical Wavy Surface in a Porous Medium," ASME JOURNAL OF HEAT TRANSFER, Vol. 116, 505–508.

Riley, D. S., 1988, "Steady Two-Dimensional Thermal Convection in a Vertical Porous Slot With Spatially Periodic Boundary Imperfections," *Int. J. Heat Mass Transfer,* Vol. 31, pp. 2365–2380.

Vajravelu, K., and Sastri, K. S., 1978, "Free Convective Heat Transfer in a Viscous Incompressible Fluid Confined Between a Long Vertical Wall and a Parallel Flat Wall," *J. Fluid Mechanics,* Vol. 86, pp. 365–383.

Watson, A., and Poots, G., 1971, "The Effect of Sinusoidal Protrusions on Laminar Free Convection Between Vertical Walls," *J. Fluid Mechanics,* Vol. 49, pp. 33–48.

Yao, L. S., 1983, "Natural Convection Along a Vertical Wavy Surface," ASME JOURNAL OF HEAT TRANSFER Vol. 105, pp. 465–468.

An Experimental Investigation of the Capillary Performance of Triangular Versus Sinusoidal Channels

G. R. Stroes[1] and I. Catton[2]

This paper discusses an experimental investigation of the performance of capillary channels with sinusoidal versus triangular geometry. Results indicate that for equivalent cross-sectional area, angle of inclination, and heat input from below, a triangular groove geometry sustains a larger wetted area while a sinusoidal groove geometry supports a greater average heat flux.

Introduction

Much analytical and experimental work has been done regarding the local heat transfer coefficient in the evaporating region of a triple interline. For example: Das Gupta et al. (1993), Mirzamoghadam and Catton (1988), and Schonberg and Wayner (1992). But it is only in recent years that there have

[1] Graduate Student Researcher; Mem. ASME; University of California, Los Angeles, 43-132 ENGN. IV, 420 Westwood Plaza, Los Angeles, CA 90095: gustave@seas.ucla.edu

[2] Professor; Fellow ASME; University of California, Los Angeles, 48-121F ENGN. IV, 420 Westwood Plaza, Los Angeles, CA 90095.

Contributed by the Heat Transfer Division of THE AMERICAN SOCIETY OF MECHANICAL ENGINEERS. Manuscript received by the Heat Transfer Division November 11, 1995; revision received February 24, 1997; Keywords: Evaporation; Heat Pipes & Thermosyphons; Thin Film Flow. Associate Technical Editor: Y. Jaluria.

been attempts to combine the microscopic meniscus studies into a macroscopic description of the entire wetted channel. Xu and Carey (1990) as well as Swanson and Peterson (1994) are noteworthy papers in this area. It is believed that future work will increasingly bring the existing meniscus research into models of an entire groove; however, experimental data on the wetted lengths achieved in heated capillary grooves is still quite sparse. Again, Xu and Carey (1990) present some data for triangular channel geometry, and Stroes et al. (1991) give experimental results for wetted lengths in rectangular and triangular channels. The current investigation seeks to expand the experimental data base for wetted lengths in heated capillary grooves by addressing the sinusoidal channel geometry. In order to provide a standard for comparison, triangular channels are also examined.

Experimental Apparatus and Procedure

The grooves for this investigation were machined into the upper surface of two separate flat plates using wire EDM (electrical discharge machining). The plates were constructed of 304 stainless steel and measured 200 mm × 63.5 mm × 5.2 mm. The grooved section of the plates was 33.6 mm wide with the channels oriented in the axial direction. Due to the EDM process the groove surface was not perfectly smooth, and is characterized by the EDM machinists as 25 RMS (root mean square). This is a standard method of defining finish quality within the surface machining industry. The relative magnitude of the surface roughness, in contrast to the thickness of the micro-film region, undoubtedly has an effect on the experimental results. No attempt is made in this work to account for this possibility. In fact, most of the experimental micro-meniscus research in the literature completely disregards the issue of surface roughness. This is noteworthy since all existing micro-meniscus modeling has been done with the implicit assumption that the solid substrate is perfectly smooth.

The test plates were mounted in a PVC base with a 50.8 mm section separating the liquid reservoir from the heater cavity in order to reduce heat loss to the liquid. This created an adiabatic zone at the beginning of the grooved test section. Power was provided by Watlow mica strip heaters (one for each plate) capable of delivering 250 W over 48.4 cm^2.

To make a meaningful comparison between two capillary groove geometries, a standard had to be chosen which they would have in common. For this study that standard was selected to be the channel cross-sectional area A_c. The triangular groove half-angle was optimized to yield minimum friction opposing make-up flow. Ayyaswamy et al. (1974) performed a numerical study to obtain the half-angle for a triangular groove which yields the lowest coefficient of friction. Based on this

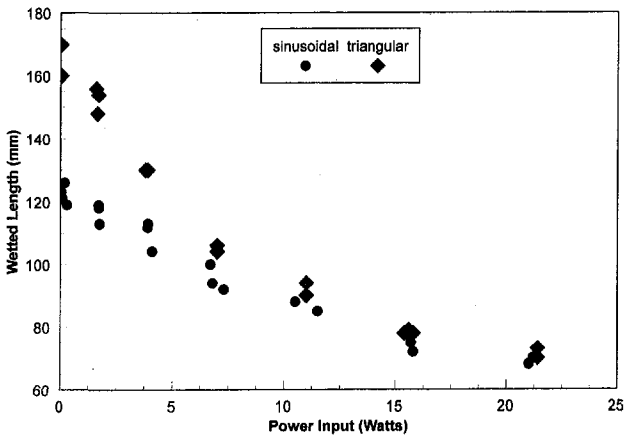

Fig. 1 Sinusoidal versus triangular groves ethanol with 4 deg inclination

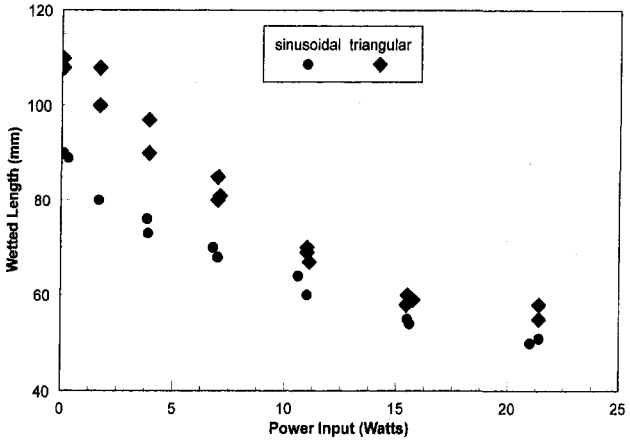

Fig. 2 Sinusoidal versus triangular groves ethanol with 6 deg inclination

work, the groove half-angle for the current triangular channels was $\beta = 40$ deg. The triangular groove width was set at $w = 3.36$ mm, which leads to a groove depth of $d = 2$ mm. Since triangular and sinusoidal channels of identical width and depth have the same cross-sectional area, the sinusoidal channels were also 3.36 mm wide by 2 mm deep.

Testing began by filling the reservoir with liquid until it just reached the top of the groove ridges at the lower end of the plate (i.e., the grooves were "full"). At this point, the liquid automatically wicked up the grooves until it reached the equilibrium distance for isothermal conditions. Then the power source was turned on and the thermal load was systematically incremented in 5 V steps until the liquid had been pushed back into the adiabatic zone of the plate. For each power setting, the wetted length (the distance to which the liquid extended up the inclined plate from the reservoir) was recorded. Because the ten separate grooves did not always support exactly the same wetted length, a visual average was taken during measurements. The maximum discrepancy between wetted lengths was rarely as much as 3 mm and usually much less. Based on this fact, an estimate of the error in the wetted length measurements is given as $x_d \pm 1.0$ mm. The angle of the grooved plates was measured using a graduated level and is estimated to have an error of $\alpha \pm 0.15$ deg.

Figures 1 and 2 show a comparison of the capillary performance of sinusoidal versus triangular channels at $\alpha = 4$ deg and $\alpha = 6$ deg, for ethanol as the working fluid. One expected result which is apparent from the graphs is that liquid is not able to wick as far up an inclined channel when a power input is imposed from below. What is more interesting is that the sinusoidal geometry displays a greater sensitivity to power input than does the triangular geometry. Before this experiment was conducted, the accepted paradigm had been that the "performance" of inclined capillary channels should be quantified by how far these channels can wick liquid up an incline while subject to an imposed heat load. By this definition, the new sinusoidal channels are no improvement over the standard triangular ones. However, there is another criteria by which the performance of grooved capillary evaporators can be quantified—namely, by how much heat a particular structure can dispel. According to this standard, the sinusoidal geometry is superior since the sinusoidal grooves were able to dissipate the same applied power as triangular grooves from a smaller wetted area. Thus, sinusoidal channels were found to support higher heat fluxes than triangular channels. This is considered to be a relevant finding.

The reason that the triangular geometry shows stronger capillary pumping than the sinusoidal geometry could be due to the rate at which the radius of curvature of the liquid-vapor interface decreases as it recedes down into the channel. This is because

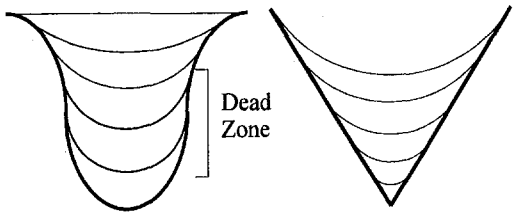

Fig. 3 Axial change in radius of curvature—"Dead Zone"

the axial pressure gradient responsible for creating capillary head is proportional to the axial rate of change of the radius of curvature of the liquid-vapor interface ($dP_l/dx \sim dr/dx$). If a zero macroscopic contact angle is assumed ($\theta = 0$ deg), then the following situation occurs: the radius of curvature initially changes faster in the axial direction for the sinusoidal geometry, but then a long section is reached where the radius of curvature in the sinusoidal groove changes very slowly (this is labeled the "dead zone"); Meanwhile, in the triangular geometry, the radius of curvature is still steadily decreasing throughout the entire wetted length—the triangular channel has no capillary "dead zone." This situation is illustrated in Fig. 3.

It is also important that for an ideally shaped triangular groove (i.e., one that comes to a sharp point at the apex) the radius of curvature of the liquid-vapor interface must eventually go to zero. As long as the macroscopic contact angle is less than 90 deg $- \beta$ (where β is the triangular groove half-angle), then this is forced to occur by geometrical constraints. However, for a sinusoidal channel the radius of curvature of the liquid-vapor interface does not go to zero at the dryout point x_d. Although the liquid height in a sinusoidal groove is equal to zero at the dryout point ($h(x) = 0$ @ $x = x_d$), the curvature of the liquid surface is a finite, nonzero value at the same location.

Thus, the last portion of the wetted length in triangular channels is an area where the radius of curvature of the liquid-vapor interface becomes very small. This factor, in combination with the lack of a capillary dead zone, could be the key to the improved wicking performance offered by the triangular groove shape. In contrast, the fact that the sinusoidal contour is more efficient at removing heat may be attributable to the increased surface area available for micro-film evaporation on the ridges between grooves.

Note that liquid creeps up onto the channel ridge much farther than would be the case if it were solely driven by capillarity since the micro-film is driven mainly by disjoining pressure. Thus, merely the fact that the film continues to thin as it climbs up the channel wall is sufficient to yield a negative liquid pressure gradient. This is not to say that the sinusoidal groove ridges are completely wetted. But, it is likely that the increase in surface area available for evaporation from a sinusoidal geometry, as opposed to a triangular geometry, is responsible for the fact that the sinusoidal grooves used in this study to supported higher heat fluxes.

Conclusion

The current paper has discussed an experimental investigation which compares the capillary performance of triangular and sinusoidal channels heated from below. For both geometries, the findings show a gradual decrease in wetting ability as the imposed heat load is increased. Furthermore, the triangular shape shows better wetting behavior than the sinusoidal shape for all heat inputs including the isothermal case. In contrast, the sinusoidal geometry is shown to remove a given power input from a smaller wetted area than the triangular geometry. Equivalently, it can be said that the sinusoidal groove shape is capable of supporting higher heat fluxes. The appropriate choice of channel geometry for a grooved capillary structure will therefore depend on the intended application.

References

Ayyaswamy, P. S., and Catton, I., "Capillary Flow in Triangular Grooves," *Journal of Applied Mechanics,* Vol. 41, No. 2, pp. 332–336.

Das Gupta, S., Schonberg, J. A., and Wayner, P. C., 1993, "Investigation of an Evaporating Extended Meniscus Based on the Augmented Young-Laplace Equation," ASME JOURNAL OF HEAT TRANSFER, Vol. 115, pp. 201–208.

Mirzamoghadam, A., and Catton, I., 1988, "Holographic Interferometry Investigation of Enhanced Tube Meniscus Behavior," ASME JOURNAL OF HEAT TRANSFER, Vol. 110, pp. 208–213.

Schonberg, J. A., and Wayner, P. C., 1992, "Analytical Solution for the Integral Contact Line Evaporative Heat Sink," *Journal of Thermophysics,* Vol. 6, No. 1, pp. 128–134.

Stroes, G. R., Rohloff, T. J., and Catton, I., 1992, "An Experimental Study of the Capillary Forces in Rectangular versus Triangular Channels," *Proceedings of the 28th National Heat Transfer Conference,* August 9–12, San Diego, HTD-Vol. 200, pp. 1–7.

Swanson, L. W., and Peterson, G. P., 1994, "Evaporating Extended Meniscus in a V-Shaped Channel," *Journal of Thermophysics and Heat Transfer,* Vol. 8, No. 1, pp. 172–180.

Xu, X., and Carey, V. P., 1990, "Film Evaporation from a Micro-Grooved Surface: An Approximate Heat Transfer Model and Its Comparison with Experimental Data," *Journal of Thermophysics and Heat Transfer,* Vol. 4, No. 4, pp. 512–520.

A Correlation for the Reordered Wave Number of the Wide-Band Absorptance of Radiating Gases

M. K. Denison[1] and W. A. Fiveland[1]

Nomenclature

A = dimensionless band absorptance
A_4 = four region expression for wide-band absorptance
a_j = blackbody weight of WSGG model
e = error function of optimized fit
$E_{b,\eta}$ = Planck's blackbody distribution function
L = path length, m
F = blackbody fraction function
n = order of correlation
n_p = number of poles
N_{wb} = number of wide bands
o_i = order of pole i
p_i = negative of pole i
s = Laplace transformed variable
t = inverse Laplace transformed variable
α = integrated band intensity, $m^2/gm\ cm^{-1}$
β = line overlap parameter ($\pi \times$ line half-width to line spacing ratio)
$\eta_{o,i}$ = spectral location of ith wide-band head, cm^{-1}
κ = absorption coefficient, m^{-1}
κ^* = dimensionless absorption coefficient ($\kappa^* = \kappa/(\rho\alpha/\omega)$)
ρ = gas density, gm/m^3
τ = dimensionless path length ($\tau = L\rho\alpha/\omega$)
ξ = reordered wave number, cm^{-1}
ξ^* = dimensionless reordered wave number ($\xi^* = \xi/\omega$)
ω = wide-band exponential decay width, cm^{-1}

[1] Research and Development Division, Babcock & Wilcox, 1562 Beeson Street, Alliance, OH 44601.

Contributed by the Heat Transfer Division of THE AMERICAN SOCIETY OF MECHANICAL ENGINEERS. Manuscript received by the Heat Transfer Division November 12, 1996; revision received June 26, 1997; Keywords: High-Temperature; Radiation; Thermophysical Properties. Associate Technical Editor: B. W. Webb.

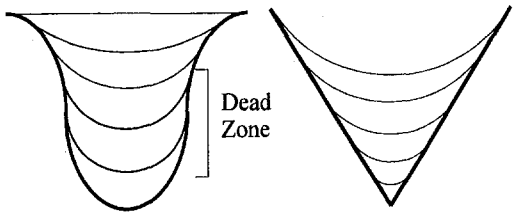

Fig. 3 Axial change in radius of curvature—"Dead Zone"

the axial pressure gradient responsible for creating capillary head is proportional to the axial rate of change of the radius of curvature of the liquid-vapor interface ($dP_l/dx \sim dr/dx$). If a zero macroscopic contact angle is assumed ($\theta = 0$ deg), then the following situation occurs: the radius of curvature initially changes faster in the axial direction for the sinusoidal geometry, but then a long section is reached where the radius of curvature in the sinusoidal groove changes very slowly (this is labeled the "dead zone"); Meanwhile, in the triangular geometry, the radius of curvature is still steadily decreasing throughout the entire wetted length—the triangular channel has no capillary "dead zone." This situation is illustrated in Fig. 3.

It is also important that for an ideally shaped triangular groove (i.e., one that comes to a sharp point at the apex) the radius of curvature of the liquid-vapor interface must eventually go to zero. As long as the macroscopic contact angle is less than 90 deg $- \beta$ (where β is the triangular groove half-angle), then this is forced to occur by geometrical constraints. However, for a sinusoidal channel the radius of curvature of the liquid-vapor interface does not go to zero at the dryout point x_d. Although the liquid height in a sinusoidal groove is equal to zero at the dryout point ($h(x) = 0$ @ $x = x_d$), the curvature of the liquid surface is a finite, nonzero value at the same location.

Thus, the last portion of the wetted length in triangular channels is an area where the radius of curvature of the liquid-vapor interface becomes very small. This factor, in combination with the lack of a capillary dead zone, could be the key to the improved wicking performance offered by the triangular groove shape. In contrast, the fact that the sinusoidal contour is more efficient at removing heat may be attributable to the increased surface area available for micro-film evaporation on the ridges between grooves.

Note that liquid creeps up onto the channel ridge much farther than would be the case if it were solely driven by capillarity since the micro-film is driven mainly by disjoining pressure. Thus, merely the fact that the film continues to thin as it climbs up the channel wall is sufficient to yield a negative liquid pressure gradient. This is not to say that the sinusoidal groove ridges are completely wetted. But, it is likely that the increase in surface area available for evaporation from a sinusoidal geometry, as opposed to a triangular geometry, is responsible for the fact that the sinusoidal grooves used in this study to supported higher heat fluxes.

Conclusion

The current paper has discussed an experimental investigation which compares the capillary performance of triangular and sinusoidal channels heated from below. For both geometries, the findings show a gradual decrease in wetting ability as the imposed heat load is increased. Furthermore, the triangular shape shows better wetting behavior than the sinusoidal shape for all heat inputs including the isothermal case. In contrast, the sinusoidal geometry is shown to remove a given power input from a smaller wetted area than the triangular geometry. Equivalently, it can be said that the sinusoidal groove shape is capable of supporting higher heat fluxes. The appropriate choice of channel geometry for a grooved capillary structure will therefore depend on the intended application.

References

Ayyaswamy, P. S., and Catton, I., "Capillary Flow in Triangular Grooves," *Journal of Applied Mechanics,* Vol. 41, No. 2, pp. 332–336.

Das Gupta, S., Schonberg, J. A., and Wayner, P. C., 1993, "Investigation of an Evaporating Extended Meniscus Based on the Augmented Young-Laplace Equation," ASME JOURNAL OF HEAT TRANSFER, Vol. 115, pp. 201–208.

Mirzamoghadam, A., and Catton, I., 1988, "Holographic Interferometry Investigation of Enhanced Tube Meniscus Behavior," ASME JOURNAL OF HEAT TRANSFER, Vol. 110, pp. 208–213.

Schonberg, J. A., and Wayner, P. C., 1992, "Analytical Solution for the Integral Contact Line Evaporative Heat Sink," *Journal of Thermophysics,* Vol. 6, No. 1, pp. 128–134.

Stroes, G. R., Rohloff, T. J., and Catton, I., 1992, "An Experimental Study of the Capillary Forces in Rectangular versus Triangular Channels," *Proceedings of the 28th National Heat Transfer Conference,* August 9–12, San Diego, HTD-Vol. 200, pp. 1–7.

Swanson, L. W., and Peterson, G. P., 1994, "Evaporating Extended Meniscus in a V-Shaped Channel," *Journal of Thermophysics and Heat Transfer,* Vol. 8, No. 1, pp. 172–180.

Xu, X., and Carey, V. P., 1990, "Film Evaporation from a Micro-Grooved Surface: An Approximate Heat Transfer Model and Its Comparison with Experimental Data," *Journal of Thermophysics and Heat Transfer,* Vol. 4, No. 4, pp. 512–520.

A Correlation for the Reordered Wave Number of the Wide-Band Absorptance of Radiating Gases

M. K. Denison[1] and W. A. Fiveland[1]

Nomenclature

A = dimensionless band absorptance
A_4 = four region expression for wide-band absorptance
a_j = blackbody weight of WSGG model
e = error function of optimized fit
$E_{b,\eta}$ = Planck's blackbody distribution function
L = path length, m
F = blackbody fraction function
n = order of correlation
n_p = number of poles
N_{wb} = number of wide bands
o_i = order of pole i
p_i = negative of pole i
s = Laplace transformed variable
t = inverse Laplace transformed variable
α = integrated band intensity, $m^2/gm\ cm^{-1}$
β = line overlap parameter ($\pi \times$ line half-width to line spacing ratio)
$\eta_{o,i}$ = spectral location of ith wide-band head, cm^{-1}
κ = absorption coefficient, m^{-1}
κ^* = dimensionless absorption coefficient ($\kappa^* = \kappa/(\rho\alpha/\omega)$)
ρ = gas density, gm/m^3
τ = dimensionless path length ($\tau = L\rho\alpha/\omega$)
ξ = reordered wave number, cm^{-1}
ξ^* = dimensionless reordered wave number ($\xi^* = \xi/\omega$)
ω = wide-band exponential decay width, cm^{-1}

[1] Research and Development Division, Babcock & Wilcox, 1562 Beeson Street, Alliance, OH 44601.

Contributed by the Heat Transfer Division of THE AMERICAN SOCIETY OF MECHANICAL ENGINEERS. Manuscript received by the Heat Transfer Division November 12, 1996; revision received June 26, 1997; Keywords: High-Temperature; Radiation; Thermophysical Properties. Associate Technical Editor: B. W. Webb.

Introduction

Recently, increased attention has been given to the development of gas spectral radiative property models which allow the use of arbitrary solution methods of the Radiative Transfer Equation (RTE) written in terms of the absorption coefficient. These models are the k-distribution method (Goody and Yung, 1989) and Weighted-Sum-of-Gray-Gases (WSGG) models (Hottel and Sarofim, 1967; Modest, 1991; Denison and Webb, 1995).

The k-distribution method using narrow-band data (Goody and Yung, 1989) has been used over the past several decades in atmospheric science. For each band, an integration over wave number is replaced by an integration over the absorption cross section of the gas.

More recently, the k-distribution method has been extended to wide bands (Lee et al., 1996; Parthasarathy et al., 1996; Marin and Buckius, 1996). These researchers have shown that the wide-band absorptance $A(\tau)$ may be represented by an integration over the absorption cross section of the gas, as follows:

$$A(\tau) = \int_0^\infty (1 - e^{-\kappa^* \tau}) \left(- \frac{d\xi^*(\kappa^*)}{d\kappa^*} \right) d\kappa^* \qquad (1)$$

where τ is a dimensionless path length ($\tau = L\rho\alpha/\omega$), κ^* is the dimensionless absorption coefficient ($\kappa^* = \kappa/(\rho\alpha/\omega)$), and $\xi^*(\kappa^*)$ is the reordered wave number of the wide band. Both A and ξ^* in Eq. (1) are normalized by the band exponential decay width, ω, and are dimensionless. $\xi^*(\kappa^*)$ is obtained from an inverse Laplace transform of $A'(\tau)$:

$$\xi^*(\kappa^*) = \int_{\kappa^*}^\infty \frac{f(t)}{t}\, dt \qquad (2a)$$

$$f(t) = \mathcal{L}^{-1}[A'(s)]. \qquad (2b)$$

The band absorptance of the popular wide-band model of Edwards (1976) is usually represented by the four-region function, herein denoted $A_4(\tau)$:

$$\begin{aligned}
\beta \le 1: \quad \tau \le \beta: &\quad A_4(\tau) = \tau \\
\beta < \tau \le 1/\beta: &\quad A_4(\tau) = 2(\beta\tau)^{1/2} - \beta \\
\tau > 1/\beta: &\quad A_4(\tau) = \ln(\beta\tau) - \beta + 2 \\
\beta > 1: \quad \tau \le 1: &\quad A_4(\tau) = \tau \\
\tau > 1: &\quad A_4(\tau) = \ln(\tau) + 1.
\end{aligned} \qquad (3)$$

Previous researchers have chosen continuous functions rather than the above four-region function. An exact inverse Laplace Transform of the four-region expression does not exist as it is not analytic or even defined in the complex plane. Lee et al. (1996) have chosen the Morizumi function and have calculated the inverse Laplace transform numerically. They present a correlated fit of $\kappa^*(\xi^*)$ which uses a spline interpolation of the fitted coefficients. Parthasarathy et al. (1996) have used the Wang function for which the inverse Laplace transform $f(t)$ is in closed form, but Eq. (2a) still requires a numerical evaluation. Although these functions are rigorous in their derivation, they under-predict the wide-band absorptance by as much as 25 to 30 percent compared with Eq. (3), and the normally recommended wide-band parameters of Edwards (Modest, 1993) were developed fitting experimental data with Eq. (3). Edwards and Balakrishnan (1973) recommend an adjusting routine to correct both the integrated band intensity, α, and the exponential decay width, ω. However, the correction is a function of path length which defeats the path length free advantage of the k-distribution method. This paper presents a correlation in closed form for the reordered wave number that closely approximates the four-region expression. The correlation allows the application of k-distribution methods using Edwards' wide-band parameters without any corrections. The form of the correlation may also be used to obtain a fit to other functions representing the band absorptance.

The Form of the Correlation

We consider the mathematical properties identified by Tien and Lowder (1966) for guidance in selecting a form for $A'(s)$. The function must satisfy the following two asymptotes:

$$\lim_{s \to 0} A'(s) = 1 \qquad (4)$$

and

$$\lim_{s \to \infty} A'(s) = \frac{1}{s}. \qquad (5)$$

The function must also be a positive, monotonically increasing function of path length, it must have the maximum slope at the optically thin limit, and it must not have inflection points. In addition to these considerations, it is desirable that the function have a closed form for both the inverse Laplace transform and the integral of Eq. (2a). If the function is analytic except at poles, all of which have a real component that is less than some finite value, then the inverse Laplace transform may be evaluated from Cauchy's residue theorem.

A form which satisfies Eqs. (4) and (5) is

$$A'(s) = \frac{s^{n-1} + \sum_{m=1}^{n-2} b_m s^m + \prod_{i=1}^{n} p_i}{\prod_{i=1}^{n} (s + p_i)}. \qquad (6)$$

The coefficients, b_m, and poles, $-p_j$, are fit to the four-region expression for each value of the mean line overlap parameter, β, which accounts for the effect of self and pressure broadening. These coefficients are therefore functions of β. Differentiation of the correlation of Tien and Lowder (1966) produces Eq. (6) for $n = 3$. Two of the poles of that correlation become complex for $\beta > 0.2$. $f(t)$ is sinusoidal for complex poles, which may result in nonphysical negative values for ξ over ranges of κ^*. Also, if the real component of any of the poles is positive (negative $\mathrm{Re}(p_j)$), the integral of Eq. (2a) diverges. Equation (6) possesses more degrees of freedom than the correlation of Tien and Lowder (1966) which enables a closer fit, especially at low values of β where the Tien and Lowder correlation is known to have serious errors.

For poles of any order, Eq. (6) can be alternatively written as the following:

$$A'(s) = \frac{s^{n-1} + \sum_{m=1}^{n-2} b_m s^m + \prod_{i=1}^{n_p} p_i^{o_i}}{\prod_{i=1}^{n_p} (s + p_i)^{o_i}}. \qquad (7)$$

where n_p is the number of poles and o_i is the order of pole i such that

$$\sum_{i=1}^{n_p} o_i = n. \qquad (8)$$

Applying partial fractions, Eq. (7) may be written in the form

$$A'(s) = \sum_{i=1}^{n_p} \sum_{j=1}^{o_i} \frac{C_{i,j}}{(s + p_i)^j}. \qquad (9)$$

Equation (9) has the following well known inverse Laplace transform:

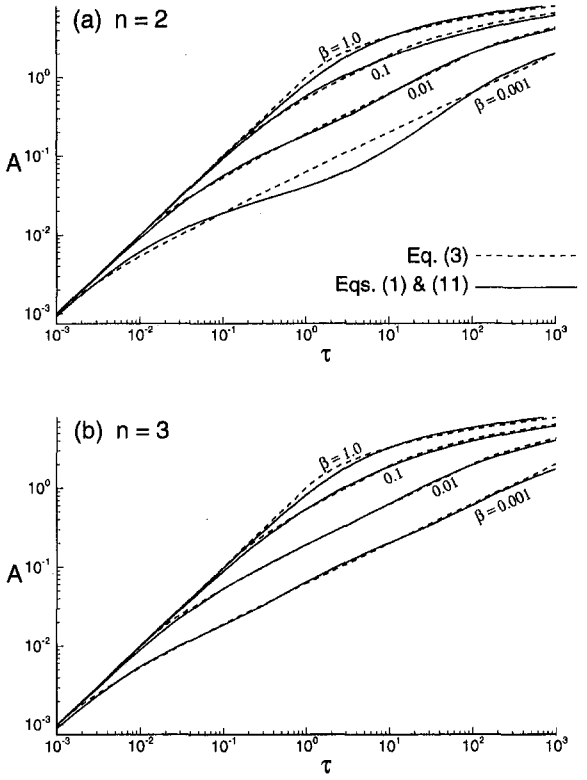

Fig. 1 Comparison of the dimensionless wide-band absorptance from the four-region function (Eq. (3)) with the absorptance calculated from Eqs. (1) and (11) for (*a*) $n = 2$ and (*b*) $n = 3$

$$f(t) = \sum_{i=1}^{n_p} \sum_{j=1}^{o_i} \frac{C_{i,j} t^{j-1}}{(j-1)!} e^{-p_i t}. \tag{10}$$

Inserting Eq. 10 into Eq. (2*a*) yields the form of the reordered wave number

$$\xi^*(\kappa^*) = \sum_{i=1}^{n_p} \sum_{j=1}^{o_i} \frac{C_{i,j}}{(j-1)!} G(j, p_i, \kappa^*) \tag{11}$$

where for $j = 1$:

$$G(1, p_i, \kappa^*) = E_1(p_i \kappa^*) \tag{12}$$

and for $j > 1$:

$$G(j, p_i, \kappa^*) = e^{-p_i \kappa^*} \sum_{k=0}^{j-2} \frac{(j-2)! \kappa^{*k}}{k! p_i^{j-k-1}}. \tag{13}$$

E_1 is the first-order exponential integral function.

Table 1 Poles, p_i, and coefficients, $C_{i,j}$, for Eq. (18)

	$0.001 < \beta \le 0.0202256$	$0.0202256 < \beta < 0.2003$	$0.2003 \le \beta \le 1$
n_p	3	2	1
p_1	$6.78622E\text{-}4 + 3.61937\beta - 30.2514\beta^2 + 2181.40\beta^3$	$7.27821E\text{-}2 - 1.39993\beta + 104.659\beta^2 - 996.743\beta^3 + 3117.65\beta^4$	$1+2.864\sqrt{1-\frac{(1-\beta)^4}{0.408986}}$
p_2	$1/p_1$	$1/p_1$	-
p_3	1	-	-
$C_{1,1}$	$p_1 C_{2,1}$	$(p_1^2 - p_1)/(p_1^2 - 1)$	1
$C_{2,1}$	$0.952246 - 12.9573\beta + 877.601\beta^2 - 14851.1\beta^3$	$(p_1 - 1)/(p_1^2 - 1)$	-
$C_{3,1}$	$1 - C_{1,1} - C_{2,1}$	-	-
$C_{1,2}$	0	0	$p_1^2 - p_1$

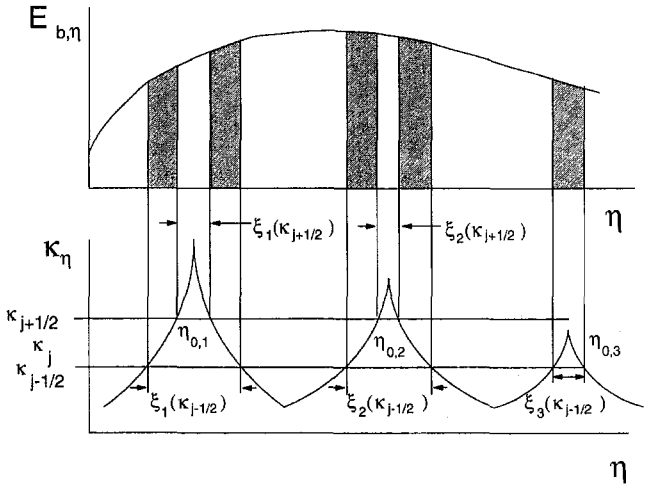

Fig. 2 Representative reordered wide bands illustrating the calculation of blackbody fractions

The Fit With the Four-Region Expression

To obtain the fit we define the following error function for optimization:

$$e = \sum_{\tau} \left(1 - \frac{A'(\tau)}{A_4'(\tau)}\right)^2. \tag{14}$$

The error was evaluated for 100 values of τ logarithmically spaced between 0.001 and 1000. The fit was obtained for β from 0.001 to 1. It was found that when fitting Eq. (6) or (7) at higher values of β, the poles become degenerate and some of the C's in Eq. (9) become negative yielding, negative-reordered wave numbers at near peak values of the absorption coefficient.

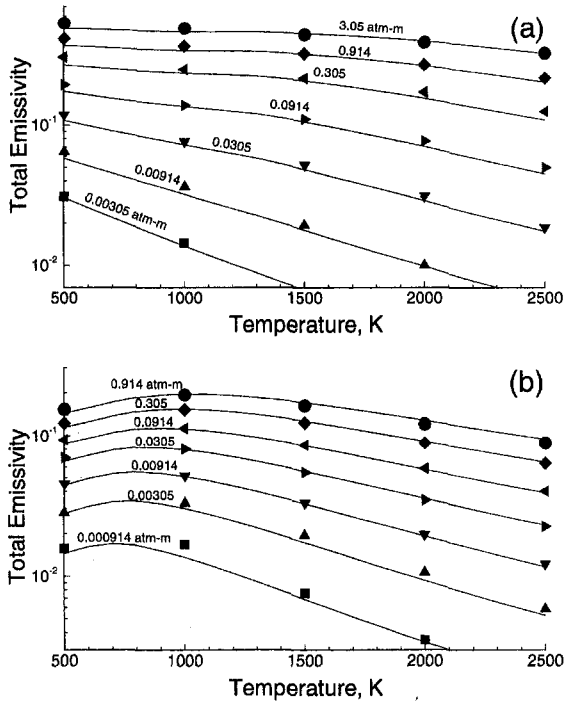

Fig. 3 Total emissivities calculated with 20 gray gases from the weighted-sum-of-gray-gas approach using Eq. (18) (lines) compared with wide-band block calculations (symbols) with the four-region function for (*a*) H_2O and (*b*) CO_2 (0.305 percent by volume at 1 atm total pressure)

Therefore, optimization of Eq. (6) was used to determine the order of the poles only and Eq. (9) was optimized with the constraint that the coefficients ($C_{i,j}$ and p_i) remain positive. The form of Eq. (9) does not guarantee that the asymptotes of Eqs. (4) and (5) will be satisfied, as does Eqs. (6) and (7). Therefore, the following additional constraints were imposed using Lagrange multipliers. Equation (4) requires that

$$\sum_{i=1}^{n_p} \sum_{j=1}^{o_i} \frac{C_{i,j}}{p_i^j} = 1 \tag{15}$$

and Eq. (5) requires that

$$\sum_{i=1}^{n_p} C_{i,1} = 1. \tag{16}$$

Figure 1 shows the optimized fit compared with the four-region function for $n = 2$ and 3, where Eqs. (1) and (11)–(13) were used to generate the curves. A finite upper limit of integration was taken assuming Elsasser lines at the band head,

$$\kappa^*_{\max} = \frac{\sinh(2\beta)}{\cosh(2\beta) - 1}. \tag{17}$$

One might expect higher n's to produce a closer fit but, by imposing positive coefficients $C_{i,j}$, the fit improves only for small β where the poles remain nondegenerate. At higher β, degeneracy occurs and the constrained optimization drives the coefficients to zero for terms of power greater than 2. The following equation was found to yield a satisfactory fit:

$$\xi^*(\kappa^*) = \sum_{i=1}^{n_p} C_{i,1} E_1(p_i \kappa^*) + C_{1,2} \frac{e^{-p_1 \kappa^*}}{p_1} \tag{18}$$

where the coefficients and poles are found in Table 1. The solid curves in Fig. 1*b* were generated with Eqs. (1) and (18).

Comparison of Total Emissivities

To demonstrate the correlation, total emissivities of H_2O and CO_2 were generated using a weighted-sum-of-gray-gas (WSGG) representation and compared with emissivities generated from the standard wide-band block calculation (Edwards and Balakrishnan, 1973). Edwards' wide-band parameters were used (Modest, 1993). The WSGG representation is expressed as

$$\epsilon = \sum_j a_j (1 - e^{-\kappa_j L}). \tag{19}$$

The emissivities were calculated using 20 gray gases with logarithmically spaced absorption coefficients, κ_j. Each discrete value, κ_j, represents the effective absorption coefficient in the portions of the high resolution spectrum where κ_η is between $\kappa_{j-1/2}$ and $\kappa_{j+1/2}$. The weights a_j were calculated as blackbody fractions illustrated in Fig. 2 showing three representative wide bands. The wave number within each wide band is reordered such that each wide band appears as a single absorption line. The weight a_j is the fraction of blackbody energy in the shaded regions under the $E_{b,\eta}$ curve in Fig. 2 where the absorption coefficient is between $\kappa_{j-1/2}$ and $\kappa_{j+1/2}$. The reordered wave number function and the band head locations, $\eta_{0,i}$, provide the wave numbers from which these blackbody fractions were calculated. The weights are then expressed mathematically in terms of the standard blackbody fraction function, $F(\eta, T)$, as

$$a_j = \sum_{i=1}^{N_{wb}} \{ F[\eta_{0,i} - \xi_i(\kappa_{j+1/2})/2, T] - F[\eta_{0,i} - \xi_i(\kappa_{j-1/2})/2, T] + F[\eta_{0,i} + \xi_i(\kappa_{j-1/2})/2, T] - F[\eta_{0,i} + \xi_i(\kappa_{j+1/2})/2, T] \} \tag{20}$$

where, in terms of dimensionless variables,

$$\xi_i(\kappa) = \omega_i \xi^*(\kappa_i^*) = \omega_i \xi^* \left(\frac{\kappa}{\rho \alpha_i / \omega_i} \right). \tag{21}$$

N_{wb} is the number of wide bands.

The emissivities are shown in Fig. 3. The agreement is very good with errors generally less than a few percent. The small differences are primarily associated with errors of the fit.

Conclusions

A function has been presented which closely approximates the four-region function for the wide-band absorptance commonly used with Edwards' wide-band parameters. The function has a reordered wave number that is in closed form. The function allows the commonly recommended wide-band parameters to be used without any corrections. The form of the function may also be used to obtain a fit to other functions representing the band absorptance.

References

Denison, M. K., and Webb, B. W., 1995, "The Spectral Line-Based Weighted-Sum-of-Gray-Gases Model in Nonisothermal Nonhomogeneous Media," ASME JOURNAL OF HEAT TRANSFER, Vol. 117, pp. 359–365.

Edwards, D. K., 1976, "Molecular Gas Band Radiation," *Advances in Heat Transfer,* Vol. 12, Academic Press, New York, pp. 115–193.

Edwards, D. K., and Balakrishnan, A., 1973, "Thermal Radiation by Combustion Gases," *International Journal of Heat and Mass Transfer,* Vol. 16, pp. 25–40.

Goody, R. M., and Yung, Y. L., 1989, *Atmospheric Radiation,* Clarendon Press, Oxford.

Hottel, H. C., and Sarofim, A. F., 1967, *Radiative Transfer,* McGraw-Hill, New York.

Lee, P. Y. C., Hollands, K. G. T., and Raithby, G. D., 1996, "Reordering the Absorption Coefficient Within the Wide Band for Predicting Gaseous Radiant Exchange," ASME JOURNAL OF HEAT TRANSFER, Vol. 118, pp. 394–400.

Marin, O., and Buckius, R. O., 1996, "Wideband Correlated-k Method Applied to Absorbing, Emitting, and Scattering Media," *Journal of Thermophysics and Heat Transfer,* Vol. 10, pp. 364–371.

Modest, M. F., 1991, "The Weighted-Sum-of-Gray-Gases Model for Arbitrary Solution Methods in Radiative Transfer," ASME JOURNAL OF HEAT TRANSFER, Vol. 113, pp. 650–656.

Modest, M. F., 1993, "Radiative Properties of Molecular Gases," chap. 9, in *Radiative Transfer,* McGraw-Hill, New York.

Parthasarathy, G., Chai, J. C., and Patankar, S. V., 1996, "A Simple Approach to Non-Gray Gas Modeling," *Numerical Heat Transfer, Part B,* Vol. 29, pp. 113–123.

Tien, C. I., and Lowder, J. E., 1966, "A Correlation for Total Band Absorptance of Radiating Gases," *International Journal of Heat and Mass Transfer,* Vol. 9, pp. 698–701.

Optimum Design of Radiating Longitudinal Fin Array Extending From a Cylindrical Surface

C. K. Krishnaprakas[1]

Nomenclature

A_p = profile area of the fin array, m^2
c = length along the cylindrical surface, m.
$dF_{d\xi-d\xi'}$ = elemental view factor from $d\xi$ to $d\xi'$
J = radiosity, W/m^2
k = thermal conductivity of fin material, W/m-K
l = fin length = $r_t - r_b$, m
n_f = total number of fins
N_c = conduction-radiation number = $kt/[2\sigma T_b^3 l^2]$
N_p = A_p/r_b^2
N_w = $2\sigma T_b^3 r_b/k$
Q = rate of total heat transfer from the fin array, W
r_b = radius of the base cylinder, m
r_t = radius of the circle through the tip of the fin, m
T = temperature of the fin, K
T_b = temperature of the base, K
x = coordinate along the length of the fin measured from tip, m

Greek Symbols

α = exponent in the equation of fin profile, $y \sim x^\alpha$
β = dimensionless radiosity = $J/\sigma T_b^4$
γ = r_t/r_b
τ = t_b/r_b
ϵ = emittance
ϕ = dimensionless rate of total heat loss from the fin array = $Q/2\pi r_b \sigma T_b^4$
σ = Stefan-Boltzmann constant = 5.67×10^{-8} W/m^2-K^4
θ = dimensionless temperature = T/T_b
ξ, ζ = dimensionless coordinates x/l and c/l

Subscripts

f = fin
b = base
max = maximum
opt = optimum

Introduction

Optimum design of radiating fins has been the subject of research by a number of investigators. However, much of the work in this area is limited to single fins freely radiating to space. Only very few investigators have considered the optimum design of a radiating fin array considering mutual interactions between the radiating elements. Sparrow et al. (1961) presented the optimum design of radiatively interacting longitudinal fins considering fin-to-fin interaction but neglecting the fin-to-base mutual irradiation. The importance of mutual radiation interaction between a fin and its base surface was later emphasized by Sparrow and Eckert (1962). The work by Karlekar and Chao (1963) also neglected fin-to-base interaction while analyzing the optimum design of trapezoidal fins. Schnurr et al. (1976) employed a nonlinear optimization technique to determine the minimum weight design for straight and circular fins of rectangular and triangular profiles protruding from a cylinder, considering fin-to-fin and fin-to-base radiation interactions. Chung and Zhang (1991a) using a variational calculus approach determined the optimum shape and minimum mass of a thin fin accounting for the fin-to-base interaction. Chung and Zhang (1991b) later extended their analysis to minimize the weight of a radiating straight fin array projecting from a cylindrical surface considering both fin-to-fin and fin-to-base interactions. The results are presented in the form of graphs and no functional form is given for the optimum profile of the fin. Krishnaprakas (1996) presented the optimum design of a rectangular plate fin array extending from a plane wall employing a nonlinear optimization method. Chung et al. (1996) developed and optimized a novel four-fin radiating array in a fuzzy environment. Here, the objective function is not precisely defined, rather the two conflicting goals of weight reduction and horizontal height minimization for space saving are fuzzily defined as fairly light and reasonably short.

Wilkins' (1960) analysis of a single fin freely radiating to space shows that the profile of the fin of least material follows a power law, i.e., $y \sim x^\alpha$, where y is the fin thickness at length x from the tip of the fin and $\alpha = 3.5$. Wilkins' profile may not be the optimum one for a fin array where the effect of mutual irradiations occurs. It is hoped that Wilkins' profile with α not a constant, but a variable depending on certain parameters governing the radiation interactions, would give a near optimum design for radiating fin array. It is the purpose of the present analysis to determine the minimum mass design of a straight thin fin array extending from a cylindrical surface considering fin-to-fin and fin-to-base radiation interactions, assuming Wilkins profile with an optimum α. Useful correlations in terms of dimensionless numbers are presented for the optimum design. The results are compared with that of Wilkins' original profile and that of Chung and Zhang (1991b).

Mathematical Model

Figure 1 shows a schematic of the configuration considered for the present analysis, i.e., a number of longitudinal fins extend from a cylindrical surface. The profile of the fin is such that

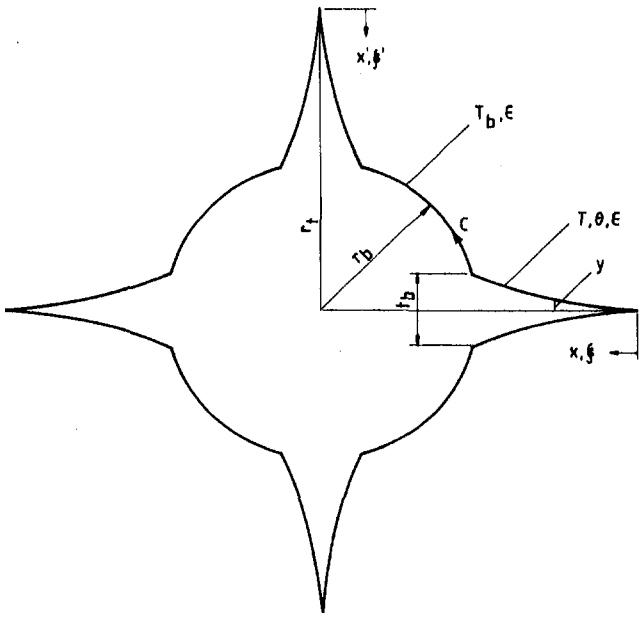

Fig. 1 Schematic of fin array

[1] Thermal Systems Group, ISRO Satellite Centre, Bangalore 560 017, India: prakas@isac.ernet.in

Contributed by the Heat Transfer Division of THE AMERICAN SOCIETY OF MECHANICAL ENGINEERS. Manuscript received by the Heat Transfer Division January 10, 1997; revision received June 5, 1997; Keywords: Finned Surfaces; Numerical Methods; Radiation Interactions. Associate Technical Editor: M. P. Menguc.

the half-thickness, y, obeys a power law along the length measured from the tip of the fin, i.e., $y = t_b x^\alpha / 2l^\alpha$. We make the following assumptions: (1) one-dimensional steady-state heat flow (thin fin assumption); (2) gray-diffuse radiating surfaces with the same emittance for both the fin and the base surfaces; (3) isothermal base surface; (4) no incident loads from any external sources; (5) surroundings at absolute zero temperature; (6) the temperature and radiosity distribution with respect to length are the same in every fin, i.e., symmetry condition; and (7) constant thermal conductivity and emittance.

Under steady-state conditions the energy conservation law requires that the net heat flux conducted across the differential element dx should be equal to the net radiative flux absorbed by dx from the adjacent fin and the base (Ozisik, 1973). The governing differential equation for the temperature distribution of the fin may be written in terms of dimensionless variables as

$$\frac{\xi^\alpha}{\sqrt{1 + \dfrac{\alpha\tau\xi^{\alpha-1}}{2(\gamma-1)}}}\left[\frac{d^2\theta(\xi)}{d\xi^2} + \frac{\alpha}{\xi}\frac{d\theta(\xi)}{d\xi}\right] = \frac{\epsilon}{N_c}\left[\theta^4(\xi) - \int_{f'}\beta_f(\xi')dF_{d\xi-d\xi'} - \int_b \beta_b(\zeta)dF_{d\xi-d\zeta}\right] \quad (1)$$

$$\frac{d\theta(\xi)}{d\xi} = 0 \quad \text{at} \quad \xi = 0 \quad (2a)$$

$$\theta = 1 \quad \text{at} \quad \xi = 1 \quad (2b)$$

$$\beta_f(\xi) = \epsilon\theta^4(\xi) + (1-\epsilon)\int_{f'}\beta_f(\xi')dF_{d\xi-d\xi'} + (1-\epsilon)\int_b \beta_b(\zeta)dF_{d\xi-d\zeta} \quad (3)$$

$$\beta_b(\zeta) = \epsilon + (1-\epsilon)\int_f \beta_f(\xi)dF_{d\zeta-d\xi} + (1-\epsilon)\int_{f'}\beta_f(\xi')dF_{d\zeta-d\xi'}. \quad (4)$$

In Eqs. (1)–(4) the subscripts f and b denote fin and base surfaces, respectively, and the primes refer to the adjacent fin.

It is to be noted that the square root term in the left-hand side of Eq. (1) appears due to the inclusion of the actual arc length of the fin profile in the analysis. We have not assumed the so-called length of arc idealization (LAI), i.e., the elemental arc length $ds \approx dx$, which is usually done by many authors. Therefore, the view factors in Eqs. (1)–(4) take into consideration the actual arc length of the fin profile.

The overall heat transfer from the fin array, Q, comprises that from the fin and base surfaces. We may define a dimensionless quantity as the ratio of the overall heat transfer from the fin array to that from a perfectly black unfinned base surface, i.e., $\phi = Q/2\pi r_b \sigma T_b^4$. ϕ may be expressed in terms of dimensionless quantities as

$$\phi = \frac{n_f(\gamma-1)}{2\pi}\left\{2\int_f\left[\beta_f(\xi) - \int_{f'}\beta_f(\xi')dF_{d\xi-d\xi'} - \int_b \beta_b(\zeta)dF_{d\xi-d\zeta}\right]d\xi + \int_b\left[\beta_b(\zeta) - \int_f \beta_f(\xi)dF_{d\zeta-d\xi} - \int_{f'}\beta_f(\xi')dF_{d\zeta-d\xi'}\right]d\zeta\right\}. \quad (5)$$

This definition of ϕ is similar but not exactly equal to the term "fin effectiveness" used in the fin heat transfer literature. Fin effectiveness is usually defined as the ratio of heat transfer with fin to that without fin. With this definition fin effectiveness becomes equal to ϕ/ϵ. We see from Eq. (5) that ϕ is a function of six variables, i.e., $\phi = \phi(\epsilon, N_c, n_f, \alpha, \gamma, \tau)$.

Numerical Scheme

The coupled nonlinear integro-differential system, Eqs. (1)–(4), was solved using the method of successive approximations to obtain the temperature and radiosity distribution in the fin (Modest, 1993). First a radiosity distribution was assumed and substituted in Eq. (1), thereby converting the integro-differential equation into a two point boundary value problem. The boundary value problem was converted to a set of nonlinear algebraic equations by replacing the derivatives with their finite difference equivalents at a number of grid points and the resulting system was solved using the Newton-Raphson method to obtain the temperatures. The Fredholm integral equation of the second kind, Eq. (3), was solved by Nystrom's method (Delves and Mohamed, 1985) employing Simpson's quadrature to obtain β_f, and then β_b was integrated out from Eq. (4). The updated radiosity profile was again used in Eq. (1) and the process was repeated till convergence, i.e., when the maximum norm of the relative difference between the successive iterates (both radiosity and temperature) was within 1.0E-5. The final radiosities were used in Eq. (5) to obtain ϕ. 40 grid points along the fin length were sufficient to give accurate results.

Optimum Design

The optimum design of a fin array accomplishes the maximum overall heat transfer from the fin and base surfaces to the surroundings for a given fin array mass or profile area A_p. We assume that all other parameters r_b, ϵ, k, and T_b are known. Therefore, a particular combination of n_f, α, r_t, and t_b out of all possible combinations gives the maximum heat transfer keeping A_p a constant. This means that in terms of dimensionless quantities, $\phi = \phi(\epsilon, N_c, n_f, \alpha, \gamma, \tau)$ should be maximum for a set of optimum values of $N_c, n_f, \alpha, \gamma, \tau$ under specified values of ϵ, dimensionless area $N_p = A_p/r_b^2$ and $N_w = 2\sigma T_b^3 r_b/k$. N_w is a dimensionless quantity defined as a Biot number for surface radiation.

The total fin array profile area is expressed as

$$A_p = \frac{n_f(\gamma-1)\tau}{(\alpha+1)}r_b^2. \quad (6)$$

N_w may be written in terms of N_c, γ, and τ using simple algebraic manipulations as

$$N_w = \frac{\tau}{N_c(\gamma-1)^2}. \quad (7)$$

The constrained optimization problem may now be stated mathematically as (for given ϵ, N_p and N_w)

$$\text{maximize} \quad \phi(\epsilon, N_c, n_f, \alpha, \gamma, \tau) \quad (8)$$

$$\text{subject to} \quad N_p = \frac{n_f\tau(\gamma-1)}{(\alpha+1)} \quad (8a)$$

$$N_w = \frac{\tau}{N_c(\gamma-1)^2}. \quad (8b)$$

The optimization problem is solved through a direct search technique employing the Nelder and Mead Simplex algorithm (Gill, et al., 1981). The motivation behind choosing this method is due to its reliability.

Results and Discussion

Analyses were carried out to find the optimum design of longitudinal fins of different profiles extending from a cylindrical surface with respect to the assumptions stated earlier. The

profiles considered were (1) rectangular, (2) triangular, (3) Wilkins profile ($y \sim x^{\alpha}$, $\alpha = 3.5$) and (4) the profile, $y \sim x^{\alpha}$, with an optimum α. Results are presented in the form of correlations to find the optimum values of n_f, r_t, t_b, and α in terms of specified values of ϵ, maximum heat flux ($\phi_{\max}$), and N_w. The range of parameters considered are ϵ between 0.5–0.9, $\phi_{\max}$ between 4–60, and N_w between 10^{-5}–10^{-3}. The correlations are applicable for only the case when the emittance of the primary surface and the extended surface is the same and the environment is at zero absolute temperature. In the correlations presented below NINT is a function which rounds the argument to the nearest integer. The correlation coefficients of the simplified curve fits are close to 0.99.

1 Rectangular profile.

$$(n_f)_{\text{opt}} = \text{NINT}(4.1392\epsilon^{-1.3813})$$

$$\left(\frac{r_t}{r_b}\right)_{\text{opt}} = 1.7718\epsilon^{-0.3028}\phi_{\max}^{1.0249}$$

$$\left(\frac{t_b}{r_b}\right)_{\text{opt}} = 2.4619\epsilon^{0.6234}\phi_{\max}^{2.1242}N_w^{1.0116}$$

2 Triangular profile.

$$(n_f)_{\text{opt}} = \text{NINT}(4.2636\epsilon^{-1.1149})$$

$$\left(\frac{r_t}{r_b}\right)_{\text{opt}} = 1.9021\epsilon^{-0.373}\phi_{\max}^{1.0298}$$

$$\left(\frac{t_b}{r_b}\right)_{\text{opt}} = 3.1221\epsilon^{0.3442}\phi_{\max}^{2.128}N_w^{1.0066}$$

3 Wilkins profile, $y \sim x^{\alpha}$, $\alpha = 3.5$.

$$(n_f)_{\text{opt}} = \text{NINT}(3.8888\epsilon^{-0.8366})$$

$$\left(\frac{r_t}{r_b}\right)_{\text{opt}} = 3.0206\epsilon^{-0.5147}\phi_{\max}^{1.0396}$$

$$\left(\frac{t_b}{r_b}\right)_{\text{opt}} = 4.3397\epsilon^{0.0892}\phi_{\max}^{2.1151}N_w^{1.0056}$$

4 The profile, $y \sim x^{\alpha}$, with the optimum α.

$$(n_f)_{\text{opt}} = \text{NINT}(3.8473\epsilon^{-1.1361})$$

$$\left(\frac{r_t}{r_b}\right)_{\text{opt}} = 2.3975\epsilon^{-0.1157}\phi_{\max}^{1.0347}$$

$$\left(\frac{t_b}{r_b}\right)_{\text{opt}} = 4.0051\epsilon^{0.4936}\phi_{\max}^{2.1284}N_w^{1.0064}$$

$$\alpha_{\text{opt}} = 2.2998\epsilon^{-0.727}$$

The above correlations indicate that for the radiating fin of optimum design the length required grows almost linearly with the heat flux, whereas the thickness varies quadratically with heat flux and linearly with N_w. This trend is similar to convecting fins. The optimum number of fins increases with decreasing emittance. This is because at lower emittances the cavity effect is more pronounced and increasing the number of fins increases the number of cavities (a cavity is formed by two adjacent fins and the base), thereby increasing the net radiative efflux. The dependence of the optimum number of fins on heat flux is very weak for large heat fluxes ($\phi_{\max} \gg \epsilon$) as understood from the correlation analysis. However, for $\phi_{\max}$ near ϵ, the dependence of $(n_f)_{\text{opt}}$ on $\phi_{\max}$ is evident as this corresponds to shorter fin lengths and hence less radiation interaction in the system, leading to a reduction in the profile area with an increase in the number of fins. Therefore, the correlations are only applicable for the case $\phi_{\max} \gg \epsilon(\phi_{\max}/\epsilon > 4.4)$. The optimum length of the fin increases with a decrease in emittance, whereas the thickness tend to decrease leading to an overall effect of increase in the least profile area. This is expected because at lower ϵ the heat transfer ability reduces calling for a large profile area. It is interesting to note that the optimum-α for Wilkins' profile is a function of only ϵ; the dependence of other parameters on α_{opt} is quite weak. As ϵ increases α_{opt} decreases. This shows that the tip of the fin of optimum profile becomes sharper at lower emittances.

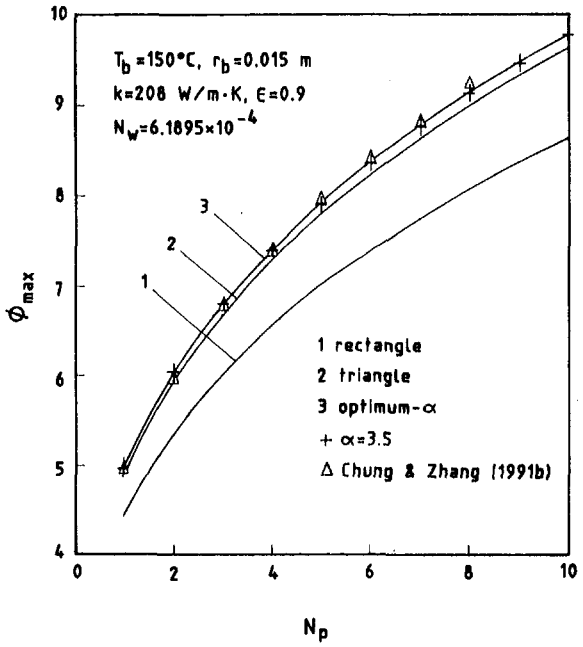

Fig. 2 Performance comparison of various profiles

Figure 2 shows a comparative performance of different fin profiles. The graph corresponding to the profile derived by Chung and Zhang (1991b) is plotted from the results of their paper. It is seen that the difference between the performances of the profile of Chung and Zhang and the optimum-α profile is very small. Also, the graphs corresponding to optimum-α and Wilkins' profile are almost the same. This shows that though the Wilkins profile is derived under the condition of no mutual irradiation, it gives a near optimum design even for the case where mutual irradiation effects are actually present. Also, in view of the difference in performances between the fin of a triangular profile and either an optimum-α profile or the profile of Chung and Zhang, being small, that a triangular profile is a good approximation to the optimum design. This study also highlights, in tune with the earlier works, the better performance of triangular fins over rectangular fins from the standpoint of more heat transfer per unit weight. The results of rectangular and triangular fin profiles were checked against that of Schnurr et al. (1976) and found to be in good agreement (the deviations in $\phi_{\max}$ are within 0.5 percent).

Acknowledgments

The author wishes to thank D. R. Bhandari, Head, Thermal Design and Analysis Division, V. K. Kaila, Group Head, H. Narayanamurthy, Group Director, Thermal Systems Group, and A. V. Patki, Deputy Director, ISRO Satellite Centre for their support and encouragement during the course of this work.

References

Chung, B. T. F., and Zhang, B. X., 1991a, "Minimum Mass Longitudinal Fins With Radiation Interaction at the Base," *Journal of the Franklin Institute,* Vol. 328, No. 1, pp. 143–161.

Chung, B. T. F., and Zhang, B. X., 1991b, "Optimization of Radiating Fin Array Including Mutual Irradiations Between Radiator Elements," ASME JOURNAL OF HEAT TRANSFER, Vol. 113, pp. 814–822.

Chung, B. T. F., Zhang, B. X., and Lee, E. T., 1996, "A Multi-Objective Optimization of Radiative Fin Array Systems in a Fuzzy Environment," ASME JOURNAL OF HEAT TRANSFER, Vol. 118, pp. 642–659.

Delves, L. M., and Mohamed, J. L., 1985, *Computational Methods for Integral Equations,* Cambridge University Press, Cambridge, UK.

Gill, P. E., Murray, W., and Wright, M. H., 1981, *Practical Optimization,* Academic Press, Inc., London.

Karlekar, B. V., and Chao, B. T., 1963, "Mass Minimization of Radiating Trapezoidal Fins With Negligible Base Cylinder Interaction," *International Journal of Heat and Mass Transfer,* Vol. 6, pp. 33–48.

Krishnaprakas, C. K., 1996, "Optimum Design of Radiating Rectangular Plate Fin Array Extending From a Plane Wall," ASME JOURNAL OF HEAT TRANSFER, Vol. 118, pp. 490–493.

Modest, M. F., 1993, *Radiative Heat Transfer,* McGraw-Hill, New York.

Ozisik, M. N., 1973, *Radiative Transfer and Interactions with Conduction and Convection,* John Wiley & Sons, Inc., New York.

Schnurr, N. M., Shapiro, A. B., and Townsend, M. A., 1976, "Optimization of Radiating Fin Arrays With Respect to Weight," ASME JOURNAL OF HEAT TRANSFER, Vol. 98, pp. 643–648.

Sparrow, E. M., Eckert, E. R. G., and Irvine, T. F., Jr., 1961, "The Effectiveness of Radiating Fins With Mutual Irradiation," *Journal of the Aerospace Sciences,* Vol. 28, pp. 763–772.

Sparrow, E. M., and Eckert, E. R. G., 1962, "Radiant Interaction Between Fin And Base Surfaces," ASME JOURNAL OF HEAT TRANSFER, Vol. 84, pp. 12–18.

Wilkins, J. E., Jr., 1960, "Minimizing the Mass of Thin Radiating Fins," *Journal of the Aerospace Sciences,* Vol. 27, No. 2, pp. 145–146.

Thermoeconomic Optimization of Constant Cross-Sectional Area Fins

S. Z. Shuja[1] and S. M. Zubair[2]

Nomenclature

C_D = drag coefficient
C_n, C_m = constants (refer to Eq. (4))
C_2, C_3 = dimensionless cost parameters
k = thermal conductivity, W/m.K
Nu = Nusselt number
q_B = base heat transfer, W
Re = Reynolds number
$\dot{S}$ = entropy generation rate, W/K
T_∞ = absolute temperature of free stream, K
U_∞ = velocity of free stream, m/s
$\dot{\Gamma}$ = total cost rate, \$/s
ρ = density of fluid, kg/m^3
ν = kinematic viscosity, m^2/s
λ_m = capital cost rate per unit volume, \$/s-m^3
λ = unit cost of lost work, \$.K/J
α = dimensionless cost ratio = λ_P/λ_H
γ = cost ratio = λ_m/λ_H, W/m^3.K

Subscripts

D = characteristic dimension (refer to Fig. 1)
f = fluid
H = heat
L = length
P = pressure
s = fin material
opt = optimum

Introduction

The optimization technique for a fin based on the second law of thermodynamics was proposed by Bejan (1979) and illustrated by Poulikakos and Bejan (1982). In this method, the total entropy generation due to heat transfer and fluid friction was formulated. Since entropy generation is proportional to the destruction of available energy (exergy), an optimum configuration generates minimum irreversible losses. This concept was applied to numerous situations in addition to heat transfer augmentation, energy storage, and insulation systems (Bejan, 1996).

The above studies do not attach monetary values to the irreversibilities generated in fin applications. Second-law-based thermoeconomic study has been carried out in a series of work by Tribus and Evans (1962), London and Shah (1983), Evans et al. (1983), and von Spakovsky and Evans (1989). Detailed sizing rules for two-phase heat exchangers with respect to thermoeconomic optimization were developed by Zubair et al. (1987). Recently Fowler and Bejan (1994) used thermoeconomic analysis to study the optimal sizes of bodies with specified external forced convection heat transfer. The objective of this paper is to present a thermoeconomic design and optimization of a constant cross-sectional area fins. In addition, a fin is designed thermoeconomically for an illustrative example and the results are compared with that obtained by Poulikakos and Bejan (1982).

Thermoeconomic Analysis and Optimization

In thermoeconomics the objective function is defined in terms of the total cost of operation and maintenance ($\dot{\Gamma}$). This includes capital costs and irreversibility penalty costs. Assuming that the capital costs are proportional to the fin volume, the objective function can be written as

$$\dot{\Gamma} = \lambda_m V + \lambda_H \dot{S}_H + \lambda_P \dot{S}_P, \qquad (1)$$

where the symbols are defined in the nomenclature section. The various methods of calculating unit cost parameters λ_H and λ_P are reviewed by Ranasinghe et al. (1987).

Referring to the analysis of Poulikakos and Bejan (1982) and introducing the circumferential area as $C = PD$, where the value of P is defined in Fig. 1 for a pin and plate fin, Shuja and Zubair (1997) have shown that

Parameter	Pin	Plate
P	π	2
A	1	2
a	1	1/2
J	2	$(2/Re_\delta)^{0.5}$
v	$\pi/4$	Re_δ

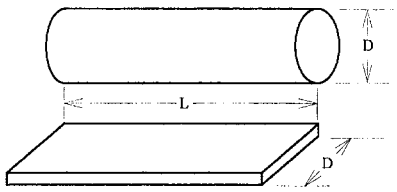

Fig. 1 Fin configuration and various geometric parameters for pin and plate fin

[1] Mechanical Engineering Department, King Fahd University of Petroleum and Minerals, Dhahran 31261, Saudi Arabia

[2] Mechanical Engineering Department, King Fahd University of Petroleum and Minerals, Dhahran 31261, Saudi Arabia. E-mail: zubair@ccse.kfupm.edu.sa

Contributed by the Heat Transfer Division of THE AMERICAN SOCIETY OF MECHANICAL ENGINEERS. Manuscript received by the Heat Transfer Division December 20, 1996; revision received August 12, 1997; Keywords: Finned Surfaces; Heat Exchanger; Thermodynamics and Second Law. Associate Technical Editor: G. M. Chrysler.

References

Chung, B. T. F., and Zhang, B. X., 1991a, "Minimum Mass Longitudinal Fins With Radiation Interaction at the Base," *Journal of the Franklin Institute,* Vol. 328, No. 1, pp. 143–161.

Chung, B. T. F., and Zhang, B. X., 1991b, "Optimization of Radiating Fin Array Including Mutual Irradiations Between Radiator Elements," ASME JOURNAL OF HEAT TRANSFER, Vol. 113, pp. 814–822.

Chung, B. T. F., Zhang, B. X., and Lee, E. T., 1996, "A Multi-Objective Optimization of Radiative Fin Array Systems in a Fuzzy Environment," ASME JOURNAL OF HEAT TRANSFER, Vol. 118, pp. 642–659.

Delves, L. M., and Mohamed, J. L., 1985, *Computational Methods for Integral Equations,* Cambridge University Press, Cambridge, UK.

Gill, P. E., Murray, W., and Wright, M. H., 1981, *Practical Optimization,* Academic Press, Inc., London.

Karlekar, B. V., and Chao, B. T., 1963, "Mass Minimization of Radiating Trapezoidal Fins With Negligible Base Cylinder Interaction," *International Journal of Heat and Mass Transfer,* Vol. 6, pp. 33–48.

Krishnaprakas, C. K., 1996, "Optimum Design of Radiating Rectangular Plate Fin Array Extending From a Plane Wall," ASME JOURNAL OF HEAT TRANSFER, Vol. 118, pp. 490–493.

Modest, M. F., 1993, *Radiative Heat Transfer,* McGraw-Hill, New York.

Ozisik, M. N., 1973, *Radiative Transfer and Interactions with Conduction and Convection,* John Wiley & Sons, Inc., New York.

Schnurr, N. M., Shapiro, A. B., and Townsend, M. A., 1976, "Optimization of Radiating Fin Arrays With Respect to Weight," ASME JOURNAL OF HEAT TRANSFER, Vol. 98, pp. 643–648.

Sparrow, E. M., Eckert, E. R. G., and Irvine, T. F., Jr., 1961, "The Effectiveness of Radiating Fins With Mutual Irradiation," *Journal of the Aerospace Sciences,* Vol. 28, pp. 763–772.

Sparrow, E. M., and Eckert, E. R. G., 1962, "Radiant Interaction Between Fin And Base Surfaces," ASME JOURNAL OF HEAT TRANSFER, Vol. 84, pp. 12–18.

Wilkins, J. E., Jr., 1960, "Minimizing the Mass of Thin Radiating Fins," *Journal of the Aerospace Sciences,* Vol. 27, No. 2, pp. 145–146.

Thermoeconomic Optimization of Constant Cross-Sectional Area Fins

S. Z. Shuja[1] and S. M. Zubair[2]

Nomenclature

C_D = drag coefficient
C_n, C_m = constants (refer to Eq. (4))
C_2, C_3 = dimensionless cost parameters
k = thermal conductivity, W/m.K
Nu = Nusselt number
q_B = base heat transfer, W
Re = Reynolds number
$\dot{S}$ = entropy generation rate, W/K
T_∞ = absolute temperature of free stream, K
U_∞ = velocity of free stream, m/s
$\dot{\Gamma}$ = total cost rate, \$/s
ρ = density of fluid, kg/m^3
ν = kinematic viscosity, m^2/s
λ_m = capital cost rate per unit volume, \$/s-m^3
λ = unit cost of lost work, \$.K/J
α = dimensionless cost ratio = λ_P/λ_H
γ = cost ratio = λ_m/λ_H, W/m^3.K

Subscripts

D = characteristic dimension (refer to Fig. 1)
f = fluid
H = heat
L = length
P = pressure
s = fin material
opt = optimum

Introduction

The optimization technique for a fin based on the second law of thermodynamics was proposed by Bejan (1979) and illustrated by Poulikakos and Bejan (1982). In this method, the total entropy generation due to heat transfer and fluid friction was formulated. Since entropy generation is proportional to the destruction of available energy (exergy), an optimum configuration generates minimum irreversible losses. This concept was applied to numerous situations in addition to heat transfer augmentation, energy storage, and insulation systems (Bejan, 1996).

The above studies do not attach monetary values to the irreversibilities generated in fin applications. Second-law-based thermoeconomic study has been carried out in a series of work by Tribus and Evans (1962), London and Shah (1983), Evans et al. (1983), and von Spakovsky and Evans (1989). Detailed sizing rules for two-phase heat exchangers with respect to thermoeconomic optimization were developed by Zubair et al. (1987). Recently Fowler and Bejan (1994) used thermoeconomic analysis to study the optimal sizes of bodies with specified external forced convection heat transfer. The objective of this paper is to present a thermoeconomic design and optimization of a constant cross-sectional area fins. In addition, a fin is designed thermoeconomically for an illustrative example and the results are compared with that obtained by Poulikakos and Bejan (1982).

Thermoeconomic Analysis and Optimization

In thermoeconomics the objective function is defined in terms of the total cost of operation and maintenance ($\dot{\Gamma}$). This includes capital costs and irreversibility penalty costs. Assuming that the capital costs are proportional to the fin volume, the objective function can be written as

$$\dot{\Gamma} = \lambda_m V + \lambda_H \dot{S}_H + \lambda_P \dot{S}_P, \qquad (1)$$

where the symbols are defined in the nomenclature section. The various methods of calculating unit cost parameters λ_H and λ_P are reviewed by Ranasinghe et al. (1987).

Referring to the analysis of Poulikakos and Bejan (1982) and introducing the circumferential area as $C = PD$, where the value of P is defined in Fig. 1 for a pin and plate fin, Shuja and Zubair (1997) have shown that

Parameter	Pin	Plate
P	π	2
A	1	2
a	1	1/2
J	2	$(2/Re_\delta)^{0.5}$
v	$\pi/4$	Re_δ

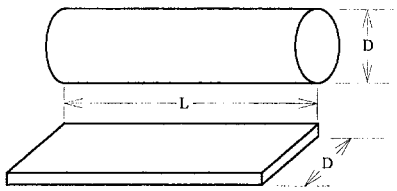

Fig. 1 Fin configuration and various geometric parameters for pin and plate fin

[1] Mechanical Engineering Department, King Fahd University of Petroleum and Minerals, Dhahran 31261, Saudi Arabia

[2] Mechanical Engineering Department, King Fahd University of Petroleum and Minerals, Dhahran 31261, Saudi Arabia. E-mail: zubair@ccse.kfupm.edu.sa

Contributed by the Heat Transfer Division of THE AMERICAN SOCIETY OF MECHANICAL ENGINEERS. Manuscript received by the Heat Transfer Division December 20, 1996; revision received August 12, 1997; Keywords: Finned Surfaces; Heat Exchanger; Thermodynamics and Second Law. Associate Technical Editor: G. M. Chrysler.

$$\dot{S}_H = F \frac{(k_s/k_f)^{1/2}}{(P/J)\sqrt{\mathrm{Nu}}\,(\mathrm{Re}_D)^a \tanh\left(J\sqrt{\frac{k_f}{k_s}}\sqrt{\mathrm{Nu}}\,\frac{\mathrm{Re}_L}{(\mathrm{Re}_D)^a}\right)}, \quad (2)$$

$$\dot{S}_P = F\frac{A}{2} B\,\mathrm{Re}_L \mathrm{Re}_D C_D, \quad (3)$$

where

$$F = \frac{q_B^2 U_\infty}{\nu k_s T_\infty^2}, \quad B = \frac{\rho \nu^3 k_s T_\infty}{q_B^2},$$

$$C_D = C_n\,\mathrm{Re}_D^n, \quad \mathrm{Nu} = C_m\,\mathrm{Re}_D^m\,\mathrm{Pr}^{1/3}, \quad (4)$$

and the parameters A, a, J, v are defined in Fig. 1. The volume "V" in Eq. (1) can also be expressed as

$$V = vFE\,\mathrm{Re}_D^{2a}\,\mathrm{Re}_L. \quad (5)$$

Note that the parameter "E" relates volume to heat transfer irreversibility. It is given by

$$E = \frac{\nu^4 k_s T_\infty^2}{q_B^2 U_\infty^4}. \quad (6)$$

On substituting Eqs. (2), (3), and (5) in Eq. (1), we get the total cost as

$$\dot{\Gamma} = \frac{F\sqrt{k_s/k_f}\,\lambda_H}{(P/J)\sqrt{\mathrm{Nu}}\,(\mathrm{Re}_D)^a \tanh\left(J\sqrt{\frac{k_f}{k_s}}\sqrt{\mathrm{Nu}}\,\frac{\mathrm{Re}_L}{(\mathrm{Re}_D)^a}\right)}$$

$$+ F\frac{A}{2} B\lambda_P\,\mathrm{Re}_L\mathrm{Re}_D C_D + \lambda_m vFE\,\mathrm{Re}_D^{2a}\,\mathrm{Re}_L. \quad (7)$$

Minimum Cost Based on Optimum Re_L. For calculating optimum $\dot{\Gamma}$, we first differentiate Eq. (7) with respect to Re_L, and then equate it to zero. This gives after some simplification (Shuja and Zubair, 1997).

$$\mathrm{Re}_{L\mathrm{opt}} = (\mathrm{Re}_D)^{a-m/2}\frac{M}{J\sqrt{C_m}}\tanh^{-1}\left(\frac{x}{\sqrt{x^2+1}}\right), \quad (8)$$

where x is given by

$$x = \frac{1}{\sqrt{C_2(\mathrm{Re}_D)^{2a+n+1} + C_3(\mathrm{Re}_D)^{4a}}}, \quad (9)$$

and the parameters are

$$M = \frac{\sqrt{k_s/k_f}}{\mathrm{Pr}^{1/6}}, \quad C_2 = \frac{\alpha PABC_n}{2J^2}, \quad C_3 = \frac{\gamma PvE}{J^2},$$

$$\alpha = \frac{\lambda_P}{\lambda_H}, \quad \gamma = \frac{\lambda_m}{\lambda_H}. \quad (10)$$

On using the definitions given by Eq. (4) and substituting the value of $\mathrm{Re}_{L\mathrm{opt}}$ from Eq. (8), we can now express Eq. (7) to give

$$\dot{\Gamma}(\mathrm{Re}_{L\mathrm{opt}}, \mathrm{Re}_D) = \frac{G}{(\mathrm{Re}_D)^{a+m/2}}\left(\frac{\sqrt{x^2+1}}{x} + \frac{\sinh^{-1}x}{x^2}\right), \quad (11)$$

where

$$G = \frac{FM\lambda_H J}{P\sqrt{C_m}}. \quad (12)$$

Equations (8) and (11) are useful when the fin dimension D is fixed due to some constraint and it is only required to find the optimum with respect to the dimension L. It should be noted that the dimension D is reflected through the variable x which is a function of Re_D, as shown in Eq. (9).

Minimum Cost Based on Optimum Re_L and Re_D. As a second step towards optimization, we now find the derivative of Eq. (11) with respect to Re_D and use Eq. (9) to get the following condition for minimum cost of operation and maintenance (Shuja and Zubair, 1997):

$$(x^2+1) + \frac{\sqrt{x^2+1}}{x}[r + 2x^2C_3\,\mathrm{Re}_D^{4a} r^*]\sinh^{-1}x = 0, \quad (13)$$

where

$$r = \frac{m - 2n - 2 - 2a}{2a+m}, \quad r^* = \frac{n+1-2a}{2a+m}. \quad (14)$$

Eliminating x using Eq. (9), the above transcedental equation remains a function of Re_D, C_2, C_3, a, m, and n. It should be noted that the solution of Eq. (13) will give optimum $\mathrm{Re}_{D\mathrm{opt}}$ which, if substituted in Eq. (8), will give optimum Re_L, and if used in Eq. (11) shall give the minimum cost ($\dot{\Gamma}_{\mathrm{opt}}$).

Simplification for a Negligible Material Cost. When λ_m is negligible compared to the two other unit cost parameters λ_H and λ_P, Eq. (9) can be simplified to give

$$x = \sqrt{\frac{1}{C_2(\mathrm{Re}_D)^{2a+n+1}}} \quad (15)$$

and Eq. (13) reduces to

$$(x^2+1) + r\frac{\sqrt{x^2+1}}{x}\sinh^{-1}x = 0. \quad (16)$$

The solution of the above equation gives the optimum value of x for any given r. It can be easily shown that the solution exists for the case when

$$r = \frac{(m-2n-2)-2a}{2a+m} < -1 \text{ or } \frac{n+2}{m} > 1. \quad (17)$$

Using this optimum value of x in Eq. (9) gives the optimum dimension D, which when used in Eq. (8) gives the optimum length for minimum operational cost. For example, it is found that for the case of pin fin, $r = -1.2336$, and for the case of plate fin, $r = -1$.

Results and Disscussion

The solution for Eq. (13) has been plotted in Fig. 2 for the case of pin fin. The Nusselt number and the drag coefficient were used from the results developed for a single cylinder in cross flow, given by (Gebhart, 1971):

$$\mathrm{Nu} = C_m\,\mathrm{Re}_D^m\,\mathrm{Pr}^{1/3}, \; C_D = C_n\,\mathrm{Re}_D^n \quad (18)$$

where the coefficients for a given Reynolds number range are given in the reference. The figure shows that for values of $C_2 < 10^{-10}$ the dependence of $\mathrm{Re}_{D\mathrm{opt}}$ remains only on the dimensionless parameter C_3. Also, it shows that for $0 < C_3 < 10^{-16}$, $\mathrm{Re}_{D\mathrm{opt}}$ is not a function of C_3.

Fig. 3 gives the solution for Eq. (13) for a plate fin. The results are given in the limit where the plate fin is slender; in this limit we rely on laminar flow ($\mathrm{Re}_D < 5\times10^5$) heat transfer, and skin friction results for a two-dimensional flat plate (Guyer and Brownell, 1989).

$$\mathrm{Nu} = 0.664\,\mathrm{Re}_D^{0.5}\,\mathrm{Pr}^{1/3}$$

$$C_D = 1.328\,\mathrm{Re}_D^{-0.5}.$$

The figure shows that for the case of a plate fin, $\mathrm{Re}_{D\mathrm{opt}}$ is independent of the dimensionless parameter C_2, however, the

$Re_{D\text{opt}}$ decreases with the dimensionless parameter C_3. For quick calculations, using the data given in Fig. 3(a), we can express

$$Re_{D\text{opt}} = 0.9484\ C_3^{-0.5}. \quad (19)$$

Illustrative example. To explain the methodology presented in the paper, we consider the case of an Aluminium pin fin (k_s = 200 W/m^{2}K) which is to be optimized for usage in an aircraft structure. The cooling fluid is air at an average temperature of 300 K (ρ = 1.1644 kg/m^3; $\nu = 1.6 \times 10^{-5}$ m^2/s; k_f = 0.0264 W/m.K; Pr = 0.712) flowing at 10 m/s and the heat transfer rate is fixed at 0.5 W per fin. The unit cost parameter associated with the heat transfer irreversibility, λ_H = 0.001 \$.K/J, and the cost ratios are as follows: $\alpha = \lambda_P/\lambda_H$ = 0.1 and $\gamma = \lambda_m/\lambda_H$ = 100 W/m^3.K.

Solution. The dimensionless parameter that accounts for the importance of fluid friction irreversibility relative to heat irreversibility (refer to Eq. (4)) is $B = 1.1447 \times 10^{-9}$, while the parameter that relates the volume to heat irreversibility (refer to Eq. (6)) is $E = 4.7186 \times 10^{-16}$ m^3/(W/K). The dimensionless parameters calculated using Eq. (10) are $C_2 = 2.47 \times 10^{-10}$ and $C_3 = 2.91 \times 10^{-14}$.

Now, using Fig. 2, $Re_{D\text{opt}}$ = 1948. Substituting these values in Eqs. (18) and (9) we find Nu = 20.806, C_D = 0.851, and x = 1.1938. When these values are used in Eq. (8) we find $Re_{L\text{opt}}$ = 18814.5.

On using Eqs. (4), (10), and (12) we find F = 0.00868 W/K, M = 92.1434, and G = 0.0006161 \$/s. Finally, using Eq. (11), the optimum operational cost shall be 2.88 \$/yr per fin. It is found for this example that the optimum operational cost is a strong function of the cost ratio α/γ. Up to $\alpha/\gamma = 1 \times 10^{-3}$, the optimum cost more or less remains constant, however, for higher values of α/γ, the optimum cost increases exponentially.

It should be noted that in the above example the unit cost parameters (λ_P, λ_m, and λ_H) are selected based on the work of Zubair et al. (1987) and Ranasinghe et al. (1987). However, these parameters are expected to change from one application to another. For example, in the cooling of electronic components

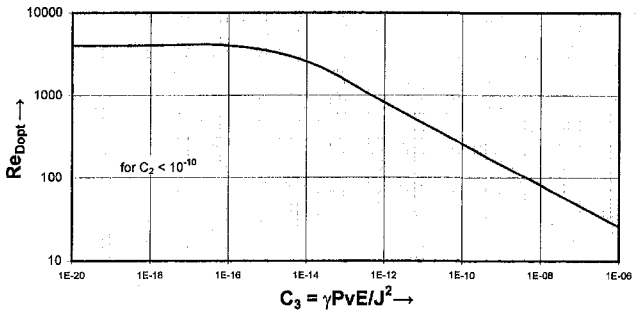

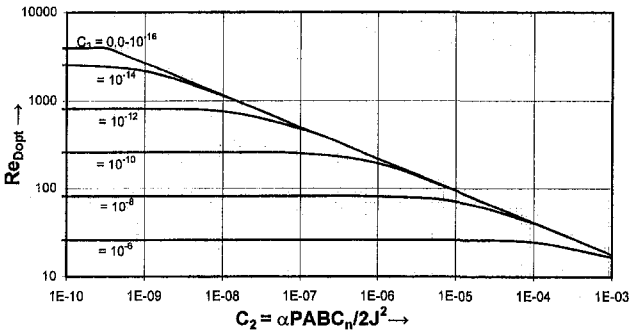

Fig. 2 Solution for Eq. (13) for optimum Re_D for the case of a pin fin

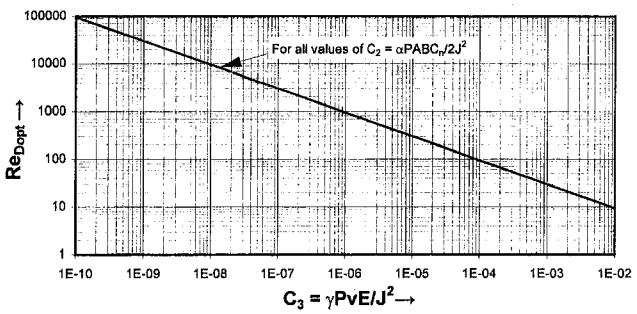

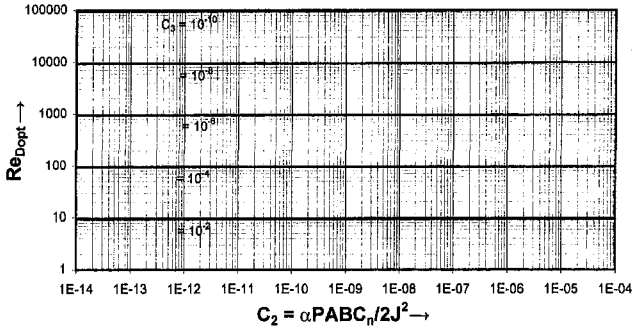

Fig. 3 Solution for Eq. (13) for optimum Re_D for the case of a plate fin

the heat transfer rate from the components is more important than the pressure drop over the surface. In this case, λ_H will be much higher than λ_P. The various methods for calculating λ_P, λ_H, and λ_m are discussed by Tribus and Evans (1962) and Ranasinghe et al. (1987).

Comparison With Previous Work. For the present study we found $r = -1.2336$ and $x = 0.6047$ for a pin fin. Now using Eq. (10) and (15), respectively, we get $C_2 = 2.15\alpha B$ and

$$Re_{D\text{opt}} = 1.09\ (\alpha B)^{-.3631}, \quad (20)$$

respectively. Note that the above equation is valid for a negligible material cost. However, when the cost ratio $\alpha = \lambda_P/\lambda_H$ = 1 we get the same result as that given by Poulikakos and Bejan (1982). It should, however, be noted that our result is an exact analytical solution and their results are numerical.

Concluding Remarks

Recognizing the need for a systematic design of thermal systems using a second, law-based procedure, this paper presents a closed form analytical solution for the thermoeconomic optimization of constant cross-sectional area fins. In order to achieve better design configurations, the present method paves the way for the more detailed thermoeconomic analysis and design of thermal systems by using the distributed unit cost data for several functional aspects of the components of a thermal system. Additional outputs of the present method are the determination of optimum diameter and length of the fin associated with specific heat transfer duty and given mass flow rate. These outputs are for any combination of thermoeconomic boundary conditions (reflected in the selection of various unit cost parameters such as λ_H, α, and γ) used in optimizing the Re_D.

Acknowledgments

The authors acknowledge the support provided by King Fahd University of Petroleum and Minerals for this research project.

References

Bejan, A., 1979, "A Study of Entropy Generation in Fundamental Convective Heat Transfer," ASME JOURNAL OF HEAT TRANSFER, Vol. 101, pp. 718–725.

Bejan, A., 1996, *Entropy Generation Minimization—The Method of Thermodynamic Optimization of Finite-Size Systems and Finite-Time Processes,* CRC Press Inc., New York.

Evans, R. B., Kadaba, P. V., and Hendrix, W. A., 1983, "Essergetic Functional Analysis for Process Design and Synthesis," *Efficiency and Costing,* ACS Symposium Series, pp. 239–261.

Fowler, A. J., and Bejan, A., 1994, "Correlation of Optimal Sizes of Bodies with External Forced Convection Heat Transfer," *Int. Comm. Heat Mass Transfer,* Vol. 21, pp. 17–27.

Guyer, E. C., and Brownell, D. L., 1989, chap. 5, *Handbook of Applied Thermal Design,* McGraw-Hill Book Company, New York.

Gebhart, B., 1971, *Heat Transfer,* McGraw-Hill Book Company, New York, pp. 212–214, 270.

London, A. L., and Shah, R. K., 1983, "Costs of Irreversibilities in Heat Exchanger Design," *Heat Transfer Engineering,* Vol. 4, No. 2, pp. 59–73.

Poulikakos, D., and Bejan, A., 1982, "Fin Geometry for Minimum Entropy Generation in Forced Convection," ASME JOURNAL OF HEAT TRANSFER, Vol. 104, pp. 616–623.

Ranasinghe, J., Aceves-Saborio, S., and Reistad, G. M., 1987, "Optimization of Heat Exchangers in Energy Conversion Systems," *Second Law Analysis of Thermal Systems,* M. J. Moran and E. Sciubba, eds., ASME, New York, pp. 29–38.

Shuja, S. Z., and Zubair, S. M., 1997, *Thermoeconomic Design and Analysis of Constant Cross-Sectional Area Fins,* KFUPM Mechanical Engineering Department Report, Saudi Arabia.

Tribus, M., and Evans, R. B., 1962, "A Contribution to the Theory of Thermoeconomics," *UCLA Engng. Dept.,* Report No. 62-36, Los Angeles, CA.

von Spakovsky, M. R., and Evans, R. B., 1989, "The Design and Performance Optimization of Thermal System Components," *ASME Journal of Energy Resources Technology,* Vol. 111, pp. 231–238.

Zubair, S. M., Kadaba, P. V., and Evans, R. B., 1987, "Second-Law-Based Thermoeconomic Optimization of Two-Phase Heat Exchangers," ASME JOURNAL OF HEAT TRANSFER, Vol. 109, pp. 287–294.

Electromagnetic Heating of Spheres

R. W. Shampine[1] and Y. Bayazitoglu[2]

Nomenclature

$\mathbf{A}_n(r, u, \phi)$ = vector potential due to the nth current source
a_0 = loop radius, m
C = capacitance, F
f = frequency of current, Hz
$H_l(q_n)$ = skin depth function for power absorbed
$I_{l+1/2}$ = modified Bessel function
$\mathbf{I}_0$ = peak coil current, A
$\mathbf{I}_{n,l,m}$ = source function for the nth current source, A
$\mathbf{J}_s$ = current density, A/m^2
$J_{l+1/2}$ = Bessel function of the first kind
L = inductance, H
N = number of loops
P_0 = characteristic power, W
P_s = power dissipated in the sphere, W
$P_l^m(\cos\phi)$ = associated Legendre polynomial of the first kind
q_n = ratio of the radius to the skin depth = $R_s\sqrt{\pi f \mu_o \sigma_s}$
R_s = sphere radius
$x_{l+1/2,k}$ = kth real root of $J_{l+1/2}(x_{l+1/2,k}) = 0$
$Y_l^m(u, \phi)$ = spherical harmonic
$\delta_{l,m}$ = kronecker delta function
σ_s = sphere electrical conductivity, $(\Omega m)^{-1}$

Introduction

A commonly encountered problem in induction heating and levitation work is the determination of the heat generated in the workpiece or, conversely, the determination of the coil and generator parameters necessary for a specified heat input. In this paper, we describe a series of experiments to verify theoretical predictions of the heating in conducting spheres.

Induction heating and electromagnetic levitation use coils of water-cooled copper tubing that carry large high frequency currents (more than 100 amps, on the order of 500 kHz) surrounding a conducting specimen. The magnetic field generated by this coil induces eddy currents in the specimen, which then dissipate energy in ohmic heating. These currents also interact with the applied field and produce Lorentz forces. However, in this paper, we are only concerned with the heat generated.

Experimental Apparatus

The experimental apparatus was designed to vary the ratio of radius-to-skin depth, q_n, over as wide a range as possible above and below 1 and to measure the heat generated in a metal sphere. The experimental set up, shown schematically in Fig. 1, consisted of a well insulated sphere with a thermocouple in it, surrounded by a water cooled coil. The coil, with a parallel resonant capacitor, was driven by a power amplifier which, in turn, was fed by a stable sine-wave oscillator. Coil current, coil frequency, change in temperature of the sphere, and time were measured during the experiment.

A coil with only a few turns, as is commonly used in induction heating, would have been impractical, as the heating rates we could achieve would have been too low to measure with the available current. More turns imply higher effective currents and thus higher heating, however, this lowers the maximum frequency of operation. A 100-turn coil was chosen with a 12.74 ± .01 cm inside diameter, a 16.00 cm outside diameter, and a height of 2.02 cm. It had a nearly square cross section and yielded an equivalent single turn radius of 7.18 cm. The coil was water cooled to eliminate an error term due to the coil heating significantly over room temperature, as seen in Shampine et. al. (1996). To increase the current in the coil, parallel resonant capacitors were used. These capacitors carry significant alternating currents and must be carefully chosen to survive this application. Ideally, this combination draws no current when driven at its resonant frequency. In reality, it draws current to make up the losses in the coil, capacitor, and sphere. The resonant frequency f_o is

$$f_0 = 1/2\pi\sqrt{LC}$$

and can be located by searching for the minimum current drawn

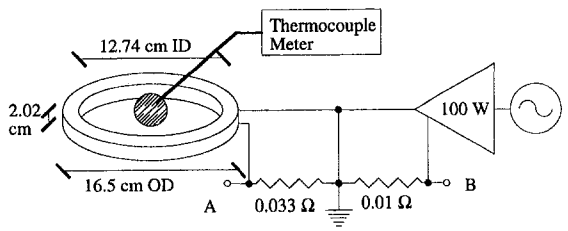

Fig. 1 Experimental apparatus for measuring electromagnetic heating

[1] Assoc. Mem. ASME, Department of Mechanical Engineering and Materials Science, Rice University, 6100 South Main Street, Houston, TX 77005.

[2] H. S. Cameron Chair Professor of Mechanical Engineering, Fellow ASME, Department of Mechanical Engineering and Materials Science, Rice University, 6100 South Main Street, Houston, TX 77005: bayaz@rice.edu

Contributed by the Heat Transfer Division of THE AMERICAN SOCIETY OF MECHANICAL ENGINEERS. Manuscript received by the Heat Transfer Division December 4, 1996; revision received May 12, 1997; Associate Technical Editor: T. L. Bergman.

References

Bejan, A., 1979, "A Study of Entropy Generation in Fundamental Convective Heat Transfer," ASME JOURNAL OF HEAT TRANSFER, Vol. 101, pp. 718–725.

Bejan, A., 1996, *Entropy Generation Minimization—The Method of Thermodynamic Optimization of Finite-Size Systems and Finite-Time Processes,* CRC Press Inc., New York.

Evans, R. B., Kadaba, P. V., and Hendrix, W. A., 1983, "Essergetic Functional Analysis for Process Design and Synthesis," *Efficiency and Costing,* ACS Symposium Series, pp. 239–261.

Fowler, A. J., and Bejan, A., 1994, "Correlation of Optimal Sizes of Bodies with External Forced Convection Heat Transfer," *Int. Comm. Heat Mass Transfer,* Vol. 21, pp. 17–27.

Guyer, E. C., and Brownell, D. L., 1989, chap. 5, *Handbook of Applied Thermal Design,* McGraw-Hill Book Company, New York.

Gebhart, B., 1971, *Heat Transfer,* McGraw-Hill Book Company, New York, pp. 212–214, 270.

London, A. L., and Shah, R. K., 1983, "Costs of Irreversibilities in Heat Exchanger Design," *Heat Transfer Engineering,* Vol. 4, No. 2, pp. 59–73.

Poulikakos, D., and Bejan, A., 1982, "Fin Geometry for Minimum Entropy Generation in Forced Convection," ASME JOURNAL OF HEAT TRANSFER, Vol. 104, pp. 616–623.

Ranasinghe, J., Aceves-Saborio, S., and Reistad, G. M., 1987, "Optimization of Heat Exchangers in Energy Conversion Systems," *Second Law Analysis of Thermal Systems,* M. J. Moran and E. Sciubba, eds., ASME, New York, pp. 29–38.

Shuja, S. Z., and Zubair, S. M., 1997, *Thermoeconomic Design and Analysis of Constant Cross-Sectional Area Fins,* KFUPM Mechanical Engineering Department Report, Saudi Arabia.

Tribus, M., and Evans, R. B., 1962, "A Contribution to the Theory of Thermoeconomics," *UCLA Engng. Dept.,* Report No. 62-36, Los Angeles, CA.

von Spakovsky, M. R., and Evans, R. B., 1989, "The Design and Performance Optimization of Thermal System Components," *ASME Journal of Energy Resources Technology,* Vol. 111, pp. 231–238.

Zubair, S. M., Kadaba, P. V., and Evans, R. B., 1987, "Second-Law-Based Thermoeconomic Optimization of Two-Phase Heat Exchangers," ASME JOURNAL OF HEAT TRANSFER, Vol. 109, pp. 287–294.

Electromagnetic Heating of Spheres

R. W. Shampine[1] and Y. Bayazitoglu[2]

Nomenclature

$\mathbf{A}_n(r, u, \phi)$ = vector potential due to the nth current source
a_0 = loop radius, m
C = capacitance, F
f = frequency of current, Hz
$H_l(q_n)$ = skin depth function for power absorbed
$I_{l+1/2}$ = modified Bessel function
$\mathbf{I}_0$ = peak coil current, A
$\mathbf{I}_{n,l,m}$ = source function for the nth current source, A
$\mathbf{J}_s$ = current density, A/m^2
$J_{l+1/2}$ = Bessel function of the first kind
L = inductance, H
N = number of loops
P_0 = characteristic power, W
P_s = power dissipated in the sphere, W
$P_l^m(\cos\phi)$ = associated Legendre polynomial of the first kind
q_n = ratio of the radius to the skin depth = $R_s\sqrt{\pi f \mu_o \sigma_s}$
R_s = sphere radius
$x_{l+1/2,k}$ = kth real root of $J_{l+1/2}(x_{l+1/2,k}) = 0$
$Y_l^m(u, \phi)$ = spherical harmonic
$\delta_{l,m}$ = kronecker delta function
σ_s = sphere electrical conductivity, $(\Omega m)^{-1}$

[1] Assoc. Mem. ASME, Department of Mechanical Engineering and Materials Science, Rice University, 6100 South Main Street, Houston, TX 77005.

[2] H. S. Cameron Chair Professor of Mechanical Engineering, Fellow ASME, Department of Mechanical Engineering and Materials Science, Rice University, 6100 South Main Street, Houston, TX 77005: bayaz@rice.edu

Contributed by the Heat Transfer Division of THE AMERICAN SOCIETY OF MECHANICAL ENGINEERS. Manuscript received by the Heat Transfer Division December 4, 1996; revision received May 12, 1997; Associate Technical Editor: T. L. Bergman.

Introduction

A commonly encountered problem in induction heating and levitation work is the determination of the heat generated in the workpiece or, conversely, the determination of the coil and generator parameters necessary for a specified heat input. In this paper, we describe a series of experiments to verify theoretical predictions of the heating in conducting spheres.

Induction heating and electromagnetic levitation use coils of water-cooled copper tubing that carry large high frequency currents (more than 100 amps, on the order of 500 kHz) surrounding a conducting specimen. The magnetic field generated by this coil induces eddy currents in the specimen, which then dissipate energy in ohmic heating. These currents also interact with the applied field and produce Lorentz forces. However, in this paper, we are only concerned with the heat generated.

Experimental Apparatus

The experimental apparatus was designed to vary the ratio of radius-to-skin depth, q_n, over as wide a range as possible above and below 1 and to measure the heat generated in a metal sphere. The experimental set up, shown schematically in Fig. 1, consisted of a well insulated sphere with a thermocouple in it, surrounded by a water cooled coil. The coil, with a parallel resonant capacitor, was driven by a power amplifier which, in turn, was fed by a stable sine-wave oscillator. Coil current, coil frequency, change in temperature of the sphere, and time were measured during the experiment.

A coil with only a few turns, as is commonly used in induction heating, would have been impractical, as the heating rates we could achieve would have been too low to measure with the available current. More turns imply higher effective currents and thus higher heating, however, this lowers the maximum frequency of operation. A 100-turn coil was chosen with a 12.74 ± .01 cm inside diameter, a 16.00 cm outside diameter, and a height of 2.02 cm. It had a nearly square cross section and yielded an equivalent single turn radius of 7.18 cm. The coil was water cooled to eliminate an error term due to the coil heating significantly over room temperature, as seen in Shampine et. al. (1996). To increase the current in the coil, parallel resonant capacitors were used. These capacitors carry significant alternating currents and must be carefully chosen to survive this application. Ideally, this combination draws no current when driven at its resonant frequency. In reality, it draws current to make up the losses in the coil, capacitor, and sphere. The resonant frequency f_o is

$$f_0 = 1/2\pi\sqrt{LC}$$

and can be located by searching for the minimum current drawn

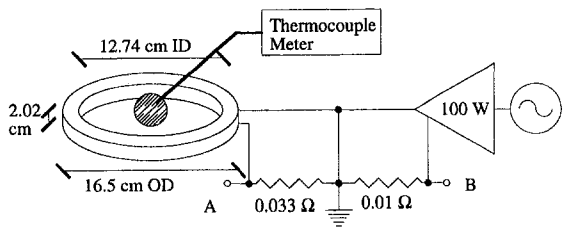

Fig. 1 Experimental apparatus for measuring electromagnetic heating

by the system. At the resonant frequency, most of the current drawn will be at twice the applied frequency (making identification easy on an oscilloscope). For very large capacitors, there will be significant losses in the capacitors and the system will still draw noticeable current at the resonant frequency. using the resonant circuit, currents in the coil were up to 15.4 times larger than the current supplied by the 100 watt amplifier used to drive the system (due to the energy storage). Coil currents between 14.4 and 22.8 Amps peak were measured using current shunt A. The very low value of this resistor minimized the unavoidable losses in the resonant system. Current shunt B was used to measure the current supplied by the amplifier to prevent overload.

A highly stable RC oscillator was used to provide sine wave drive to the power amplifier. The oscillator drifted less than 0.02 percent over 25 minutes. The period of the sine wave was measured with an eight digit counter, averaging over at least 100 cycles, yielding a frequency accurate to 1 part in 10^8.

To fully verify the heating trends, we needed to vary q_n both above and below 1. For the low range, a 2.5387 ± 0.0003 cm lead ball with a thermocouple cast into it was used. This allowed us to measure heating for q_n between 0.4 and 1.4. For the range from 1.1 to 4.4, we used machined copper and aluminum balls (2.5154 cm and 2.4928 cm, respectively) with thermocouples swaged into their centers through a drilled hole. To minimize error due to the thermocouple holes, we used 0.0251 cm wire, and oriented the thermocouple exit hole parallel to the axis of the coil. Knowing the masses of the spheres (92.40 ± 0.005 g, 75.33 g, and 23.29 g, respectively), and having measured the heating rate due to an applied magnetic field and assuming perfect insulation, the power input to the spheres is determined.

Measuring the heating rate accurately required that we minimize the heat transfer and measure the temperature. Minimizing heat transfer was done with 2.54 cm of Styrofoam insulation on all sides of the sphere. The thermal time constant of the system was measured to be 1500 s, much longer than the experimental period of 300 s (shorter if the sphere temperature change reached 19.9°C). Thus, for our experiments, the sphere can be assumed to be thermally isolated, and a transient heating analysis was valid.

To achieve reasonable accuracy with heating rates down to 32 mW, we built a thermocouple reader producing 10 millivolts per °C with an adjustable zero feeding a 3.5 digit meter. The meter was calibrated and yielded ±0.01°C measurements, an order of magnitude more accurate than conventional instruments. The device was sufficiently sensitive that it had to be shielded from air currents to prevent drift. If this was not done, it could have exhibited random drift as much as ±0.15°C in the laboratory environment. The schematic is shown in Fig. 2.

The repeatability of the apparatus was tested by taking multiple experimental runs using a variac to provide a stable 60 Hz wave. These were necessarily less repeatable than data taken with the power amplifier and function generator due to the limited accuracy of setting the variac (±0.1 amp). The tests were performed with equipment only able to measure current to ±0.1 amp (four times less accurate than the equipment used in the main experiments), yet still yielded a 95 percent confidence interval of 10.53 ± 0.09 milliwatts (or ±0.86 percent accuracy), implying that the experimental apparatus produced repeatable results.

Theoretical Predictions

The power dissipated in a sphere in a magnetic field is proportional to the square of the current induced in it and can be expressed, as in the work of Lohofer (1989), as

$$P_s = \frac{1}{2\sigma_s R_s} \sum_{n=1}^{N} \sum_{l=0}^{\infty} \sum_{m=-l}^{l} H_l(q_n) \times \left(|\mathbf{I}_{n,l,m}|^2 + 2 \sum_{n'>n} \delta_{\omega_{n'}\omega_n} \operatorname{Re}\{\mathbf{I}_{n,l,m} \cdot \mathbf{I}^*_{n,l,m}\} \right). \quad (1)$$

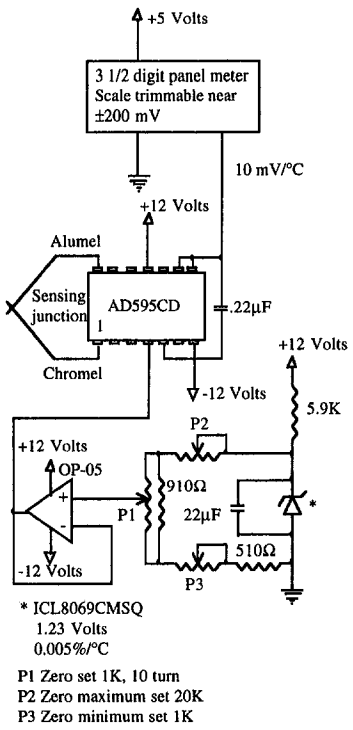

Fig. 2 High resolution thermocouple meter

The first sum, n, is over the loops. The other sums, 1 and m, are indices of spherical harmonics involved in the solution. For the case where all the loops carry currents of the same frequency (the typical implementation), this can be simplified to

$$P_s = \frac{1}{2\sigma_s R_s} \sum_{l=0}^{\infty} \sum_{m=0}^{l} H_l(q_n)(2 - \delta_{m,0}) \left| \sum_{n=1}^{N} \mathbf{I}_{n,l,m} \right|^2.$$

We are interested in the key parameter q_n and its effect on the dimensionless power P_s/N^2P_0. High frequency currents flow primarily near the surface of conductors, and the skin depth is where the current density has decayed to $1/e$ of its value at the surface. For higher frequency and higher conductivity, this depth decreases. The characteristic power P_0 is a measure of the maximum power that could be dissipated in a sphere of radius a_0.

$$P_0 = I_0^2/\sigma_s a_0$$

N is the number of turns in the coil, and I_0 is the peak coil current. The "skin depth" function $H_l(q_n)$ and the vector $\mathbf{I}_{n,l,m}$ are defined in Bayazitoglu and Sathuvalli (1994) as

$$H_l(q_n) = -4q_n^2 \operatorname{Im}\left[\frac{1}{2(1+i)q_n} \frac{I_{l+1/2}\{(1+i)q_n\}}{I_{l-1/2}\{(1+i)q_n\}} \right]$$

$$\mathbf{I}_{n,l,m} = \frac{x_{l+1/2,k}^2}{\mu_0 R_s^{5/2} J_{l+1/2}(x_{l+1/2,k})} \times \int_0^{R_s} \int_{-1}^{+1} \int_0^{2\pi} r^{3/2} J_{l+1/2}(x_{l+1/2,k} r/R_s) \times Y_l^{m^*}(u, \phi) \mathbf{A}_n(r, u, \phi) d\phi du dr$$

$$Y_l^m(u, \phi) = (-1)^m \left(\left\{ \frac{2l+1}{4\pi} \right\} \frac{(1-m)!}{(1+m)!} \right)^{1/2} P_l^m(u) e^{im\phi}$$

where $Y_l^m(u, \phi)$ are spherical harmonics, and $P_l^m(u)$ are associated Legendre polynomials of the first kind. The function $H_l(q_n)$ represents the effect of the current distribution within the sphere

on the power dissipated, and the vector $\mathbf{I}_{n,l,m}$ is known as the form function of the magnetic field.

For line currents, $\mathbf{I}_{n,l,m}$ may be expressed as in Bayazitoglu and Sathuvalli (1994):

$$\mathbf{I}_{n,l,m} = I_n R_s^l \mathbf{F}_{n,l,m}$$

where $\mathbf{F}_{n,l,m}$ is integrated over the current loop, rather than the sphere volume. It is found by integrating

$$\mathbf{F}_{n,l,m} = \oint (r_n')^{-(l+1)} Y_l^{m^*}(u_n', \phi_n') d\vec{s}_n'.$$

The primed coordinate system is centered on the sphere. If a sphere is positioned at $(x_0, 0, z_0)$ with respect to the center of a current loop of radius a_0, $\mathbf{F}_{n,l,m}$ can be evaluated using the following variables:

$$r' = \sqrt{a_0^2 + x_0^2 + z_0^2 - 2a_0 x_0 \cos\phi}$$

$$u' = \cos\left(\arctan\left(z_0/\sqrt{a_0^2 + x_0^2 - 2a_0 x_0 \cos\phi}\right)\right)$$

$$\phi' = \arctan\left(a_0 \sin\phi / a_0 \cos\phi - x_0\right)$$

$$d\vec{s}' = \hat{\phi} a_0 \cos\phi d\phi.$$

The integration is performed for ϕ from zero to two π with a ϕ directed result.

In the case of a sphere that is small relative to the coil, only the $l = 0$, $m = 0$, and $l = 1$, $m = \pm 1$ are important in the power calculations, and the following formulae from Bayazitoglu and Sathuvalli (1994) and Bayazitoglu et. al. (1996) are useful:

$$H_0(q_n) = q \frac{\sinh 2q - \sin 2q}{\cosh 2q + \cos 2q}$$

$$H_1(q_n) = q \frac{\sinh 2q + \sin 2q}{\cosh 2q - \cos 2q} - 1 \qquad (2)$$

$$\mathbf{I}_{n,0,0} = 2\sqrt{\pi}/\mu_0 \mathbf{A}_n(r_0, u_0, \phi_0)$$

$$\mathbf{I}_{n,1,1} = \sqrt{3\pi/2}(i\mathbf{u}_x + \mathbf{u}_y)(BR_s/\mu_0)$$

$$\mathbf{I}_{n,1,-1} = -\mathbf{I}_{n,1,1}^* \qquad (3)$$

where $\mathbf{A}_n(r_0, u_0, \phi_0)$ is the vector potential of the applied field at the center of the sphere, and B is the magnitude of the magnetic field at the same point. For a single loop, these can be found in Smythe (1989):

$$k^2 = 4a_0 r/[(a_0 + r)^2 + z^2]$$

$$m = [1 - (1 - k^2)^{1/2}]/[1 + (1 - k^2)^{1/2}]$$

$$\mathbf{A}_n = \frac{\mu I_0}{\pi}\left(\frac{a_0}{mr}\right)^{1/2}[K(m) - E(m)]$$

$$= \frac{\mu I_0}{4}\left(\frac{a_0}{r}\right)^{1/2} m^{3/2}\left(1 + \frac{3}{8}m^2 + \frac{15}{64}m^4 + \ldots\right)$$

$$B = [B_r^2 + B_z^2]^{1/2}$$

$$B_r = \frac{\mu I_0}{2\pi} \frac{z}{r[(a + r)^2 + z^2]^{1/2}} \times \left[-K(m) + \frac{a^2 + r^2 + z^2}{(a - r)^2 + z^2} E(m)\right]$$

$$B_z = \frac{\mu I_0}{2\pi} \frac{1}{r[(a + r)^2 + z^2]^{1/2}} \times \left[K(m) + \frac{a^2 - r^2 - z^2}{(a - r)^2 + z^2} E(m)\right].$$

K and E are complete elliptic integrals of the first and second kind, respectively. Multiple loops are treated by summing the contributions of each loop. $H_0(q_n)$ and $H_1(q_n)$ can be expressed in the following form in order to develop limiting cases for the power generation:

$$\left.\begin{aligned} \lim_{q_n \to 0} H_0(q_n) &\approx q_n^4 \\ H_1(q_n) &\approx 0.091 q_n^4 \end{aligned}\right\} q_n \leq 1$$

$$\left.\begin{aligned} H_0(q_n) &\approx q_n \\ H_1(q_n) &\approx q_n - 1 \end{aligned}\right\} q_n \geq 2.$$

These imply that the power absorbed by the sphere will vary for where q_n^4 where $q_n < 1$ and for q_n where $q_n > 1$.

Routines were developed to evaluate the small sphere approximation, a single loop exact solution, and a 100 loop exact solution. Using the model for one turn, it was verified that for this system only the $l = 0$ and $l = 1$ modes are important (the $l = 2$ mode makes a 0.3 percent contribution). Comparing the results to the highest q_n experimental value (4.4), we find that the predicted heating decreases with the accuracy of the model.

Small Sphere	$P_s/N^2P_0 = 0.785$
1 Loop	$P_s/N^2P_0 = 0.745$
100 Loops	$P_s/N^2P_0 = 0.702$
Experiment	$P_s/N^2P_0 = 2.019$

There is a 12 percent difference between the exact theoretical solution and the approximation—implying that the approximation is reasonable. However, at this extreme there is a large difference between any of the theoretical solutions and the measured value.

Experimental Results

Using Eq. (2) for $H_l(q_n)$ and Eq. (3) for $\mathbf{I}_{n,l,m}$ in solving Eq. (1), we developed a fast and simple routine for predicting the heat generation for reasonably sized spheres. Theory predicts that the function P_s/N^2P_0 will vary for q_n^4 where q_n is less than one and for q_n where q_n is greater than one. The experimental values clearly show this behavior and agree well with the predictions up to a q_n of about 2. For the low q_n regime, both the theoretical and experimental results can be fitted to the following q_n^4 curve with correlation coefficients of 0.98745 and 0.99482, respectively.

$$P_s/n^2P_0 = 0.027898 q_n^4$$

The agreement is not as good for higher q_n. While both the copper and aluminum spheres show the expected linear relationship between q_n and P_s/N^2P_0, they have different slopes and the theory shows a third slope. For q_n greater than 2, the slopes are

Copper	$0.7341\ q_n$
Aluminum	$0.9706\ q_n$
Theory	$0.2280\ q_n$

The correlation coefficients are 0.9846, 0.9755, and 0.9998, respectively.

Comparing the experimental results and theoretical predictions over two orders of magnitude of q_n and five orders of

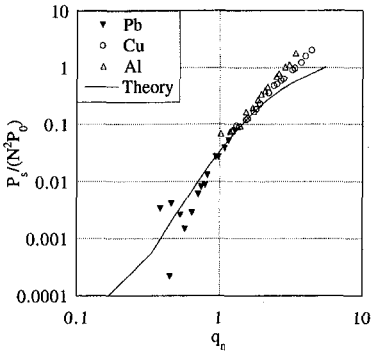

Fig. 3 Experimental and theoretical relationship between normalized power (P_s/N^2P_0) and the ratio of radius to skin depth (q_n) at x = 0.48 cm and z = 0.58 cm

magnitude of P_s/N^2P_0 (Fig. 3), the agreement is very good, except for high values of q_n. At the low end of the range, the experimental data shows increasing noise due to the very low heating values.

Uncertainty Analysis

The uncertainty analysis is based on linear regression and the method outlined by Bragg (1974). We are interested in the uncertainty in the two dimensionless groups: q_n and P_s/N^2P_0. The uncertainty in q_n can be expressed as

$$\partial q_n = (((\pi f \mu_0 \sigma_s)^{1/2} \delta R_s)^2 + (R_s(\pi \mu_0 \sigma_s / f)^{1/2} \delta f)^2 + (R_s(\pi \mu_0 \sigma_s / f)^{1/2} \delta \sigma_s)^2)^{1/2}$$

where δf is ± 0.01 ppm, δR_s is $\pm 2.54 \times 10^{-6}$, and $\delta \sigma_s$ is ± 0.39 percent; for the range of q_n considered in this work (0.4 to 4.4), this is only 0.02 percent.

For the denominator of the second dimensionless group we find

$$\delta(N^2P_0) = ((\delta I_0 2N^2 I_0/\sigma_s a_0)^2 + (-\delta a_0 N^2 I_0^2/\sigma_s a_0^2)^2 + (-\delta \sigma_s N^2 I_0^2/\sigma_s^2 a_0^2)^2)^{1/2}.$$

While there is no uncertainty in N, and a_0 is known to ± 0.001 m, I_O is only known to ± 0.03 amps, yielding a worst case N^2P_0 uncertainty of ± 1.4 percent. δP_s is found from

$$\delta P_s = ((cm\delta\beta)^2 + (\beta c \delta m)^2)^{1/2}.$$

β and $\delta\beta$ are found from the experimental data using linear regression. The 95 percent confidence limit for variance in the heating rate $\delta\beta$ is ± 2.2 percent, and δm is 5×10^{-6}. The 95 percent confidence interval for power is ± 2.2 percent. Finally, the variance in dimensionless power P_s/N^2P_O is

$$\delta(P_s/N^2P_0) = \left(\begin{array}{c} (\delta P_s/N^2P_0)^2 + \\ (-\delta(N^2P_0)P_s/(N^2P_0)^2)^2 \end{array} \right)^{1/2}.$$

The confidence interval for this is 2.6 percent.

Conclusions

The results of this work clearly indicate that a simplified theoretical model can be used to predict the heat generated in levitated or heated spheres with good accuracy. This has been verified for radius-to-skin depth ratios (q_n) between 0.4 and 4.4, covering the critical transition range where the electromagnetic field just penetrates to the center of the sphere. For q_n below 1, the experimental data agrees well with the theoretical prediction that power dissipated will be proportional to q_n^4. For q_n above 1, the experimental results provide very reliable data supporting the theoretical prediction that power absorbed is proportional to q_n. Experimental results show excellent quantitative agreement with theoretical predictions up to q_n of about 2 and some difference above this.

Acknowledgments

This work was supported in part by the Texas Advanced Technology Program under grant number 003604-041 and by the National Science Foundation under grant number CTS-9312379. The authors would also like to acknowledge the efforts of Pascal Haas.

References

Bayazitoglu, Y., and Sathuvalli, U. B., 1994, "Eddy Current Heating in an Electrically Conducting Sphere," *J. of Materials Processing and Manufacturing Science,* Vol. 3, No. 2, pp. 117–141.

Bayazitoglu, Y., Sathuvalli, U. B., Suryanarayana, P., and Mitchell, G., 1996, "Determination of Surface Tension From the Shape Oscillations of an Electromagnetically Levitated Droplet," *Physics of Fluids,* Vol. 8, No. 2, pp. 370–383.

Bragg, G. 1974. *Principles of Experimentation and Measurement,* Prentice-Hall, Inc., Englewood Cliffs, New Jersey.

Lohofer, G. 1989, "Theory of an Electromagnetically Levitated Metal Sphere I: Absorbed Power," *SIAM J. Appl. Math.,* Vol. 49, pp. 567–581.

Rony, P. B., 1969, "The Electromagnetic Levitation Melting of Metals," *Trans. Vacuum Metallurgy Conference,* American Vacuum Society, Boston, MA., pp. 55–135.

Shampine, R. W., Sathuvalli, U. B., Bayazitoglu, Y., 1996, "An Experimental Verification of Electromagnetic Heating of Spheres," presented at the ASME National Heat Transfer Conference, August 1996, HTD-Vol. 1, pp. 303–307.

Smythe, W. R., 1989, *Static and Dynamic Electricity,* Hemisphere Publishing Co., New York.